

Chromophore-specific theoretical spectroscopy: a local perspective on complex systems

a local perspective on complex systems

Habilitation Thesis

Author(s):

Neugebauer, Johannes

Publication date:

2009

Permanent link:

<https://doi.org/10.3929/ethz-a-005771925>

Rights / license:

[In Copyright - Non-Commercial Use Permitted](#)

Chromophore-Specific Theoretical Spectroscopy

A local perspective on complex systems

HABILITATIONSSCHRIFT

vorgelegt dem Departement Chemie und Angewandte Biowissenschaften

der

Eidgenössischen Technischen Hochschule Zürich

von

Dr. Johannes Neugebauer

Wenn ein Ding, das sich aus Vielem zusammensetzt, in alle seine einfachsten Teile im Denken zerlegt wird und jeder für sich [denkend] betrachtet wird, dann wird alle Verwirrung verschwinden.

Baruch de Spinoza, *Abhandlung über die Verbesserung des Verstandes*

Contents

I	Abstract	1
1	Introduction	3
1.1	The importance of subsystems in chemistry	3
1.2	Chromophore-specific theoretical spectroscopy	4
1.3	Outline of this work	6
2	Subsystem-Based Electronic-Structure Theory	7
2.1	Partitioning of quantum systems	7
2.2	Summary of Kohn–Sham density functional theory	8
2.3	Kinetic energy functionals and potentials	10
2.4	The Gordon–Kim model and the origins of subsystem DFT	12
2.4.1	The original Gordon–Kim model	13
2.4.2	The Harris functional	14
2.4.3	Approaches based on density perturbations	16
2.5	Subsystem formulation of DFT	17
2.5.1	Partitioning of the density	17
2.5.2	Effective one-particle equations	18
2.6	Frozen-density embedding	21
2.6.1	Effective embedding potential	21
2.6.2	Active part and environment	22
2.6.3	Freeze-and-thaw cycles; v_s -representability	23
2.6.4	Electron leak problem	26
2.7	Embedded cluster models	27
2.8	Energetics from frozen density embedding	29
2.9	Comparison of electron densities from Kohn–Sham and subsystem DFT	32
2.9.1	Topological analyses of electron densities	32
2.9.2	Tools for the analysis of electron densities	33
2.9.3	Criteria for the accuracy of electron densities	34
2.9.4	Factors affecting the quality of the density	37
2.9.5	Symmetric hydrogen bonds in F–H–F^-	42
2.9.6	Coordination compounds	44
2.9.7	Trends in the accuracy of electron densities from FDE	49
3	Excited States and Response Properties of Complex Systems	51
3.1	Excited-state methods suited for large systems	51
3.2	Time-dependent density functional theory	52
3.2.1	Theoretical foundations	52

3.2.2	Linear response TDDFT	54
3.2.3	Approximate solution schemes for excitation energies	59
3.3	A simple correction for the charge-transfer problem in TDDFT	61
3.3.1	Failure of TDDFT for charge-transfer excitations	61
3.3.2	Correction for the exchange–correlation kernel	62
3.3.3	Test system: He···Be	66
3.3.4	Simultaneous correction of several states	67
3.3.5	Application to solvated acetone	73
3.4	Frozen-density embedding response theory for solvatochromic effects	77
3.4.1	Models for solvent effects on excitation energies	77
3.4.2	Frozen-density embedding for excited states	78
3.4.3	Construction of the frozen environment density	79
3.4.4	Convergence with the size of the solvation shell	81
3.4.5	Simulating absorption spectra in solution	86
4	Environmental Effects on Molecular Properties and Valence Excited States	93
4.1	A review of subsystem-DFT based molecular property calculations	93
4.1.1	Structures, dynamics, and vibrational properties	93
4.1.2	Electric and magnetic properties, excited states	95
4.2	Solvation effects on ESR hyperfine coupling constants	97
4.2.1	Validation of the solvent model	98
4.2.2	Statistical analysis of snapshots	101
4.2.3	Assessment of the results	105
4.3	Solvatochromism of aminocoumarin C151	106
4.3.1	Comparison of approximate solvent models	108
4.3.2	Spectra simulations	112
4.4	Induced circular dichroism	114
4.4.1	Complexation of benzoylbenzoic acid by amphetamine	116
4.4.2	Circular dichroism induced in amino acid receptor models	122
4.4.3	Cyclodextrin inclusion compounds: Harata’s rule	125
4.4.4	Failure for coupled excitations	129
5	Time-Dependent Density-Functional Theory for Subsystems	133
5.1	A subsystem TDDFT approach for coupled excitations	133
5.1.1	The subsystem formulation of TDDFT	134
5.1.2	Effective embedding kernel	137
5.1.3	Approximate treatments	138
5.1.4	Test case: Benzaldehyde dimer	141
5.1.5	Extension to several fragments	145
5.1.6	Ground-state and excited-state interactions	146
5.1.7	Circular dichroism spectra of coupled chromophores	147
5.2	General response properties from subsystem TDDFT	148
5.2.1	Polarizabilities	149
5.2.2	Oscillator strengths	150
5.2.3	Optical rotation	151

5.2.4	Rotational strengths	152
5.2.5	Subsystem decomposition of polarizability and optical rotation	152
5.2.6	Illustrative calculations	156
5.3	Studying natural light-harvesting complexes with subsystem TDDFT	158
5.3.1	The structure of LH2	160
5.3.2	Extracting excitonic coupling constants	160
5.3.3	Chromophore–environment interactions	165
5.3.4	Chromophore–chromophore couplings	169
5.3.5	Absorption spectra of the B850 and B800 units of LH2	173
6	Chromophore-Specific Vibrational Spectroscopy	177
6.1	Selective vibrational spectroscopy	177
6.2	Resonance Raman as a chromophore-specific spectroscopy	178
6.2.1	Sum-over-states formulation	178
6.2.2	Time-dependent theory of Raman scattering	181
6.2.3	Heller’s gradient approximation	182
6.2.4	Alternative methods	183
6.3	The photochemistry of <i>o</i> -nitrobenzaldehyde	184
6.3.1	The resonance Raman spectrum of the ketene intermediate	185
6.3.2	Conclusions for photochemical intermediates	191
6.4	Photoexcitation processes in artificial photosynthesis models	192
6.4.1	Ruthenium–polypyridyl clusters as models for photosynthetic units	192
6.4.2	Analysis of resonance Raman spectra	194
7	Resonance Raman Intensity-Tracking	201
7.1	Selectivity in theoretical resonance Raman spectroscopy	201
7.2	Theory: Intensity-driven resonance Raman spectroscopy	202
7.2.1	The mode-tracking algorithm	202
7.2.2	Intensity tracking	203
7.3	Validation: Intensity-tracking for uracil	205
7.4	Resonance Raman spectra of Im7-based models	207
7.4.1	Preparatory calculations: Identification of resonating states	207
7.4.2	Root homing	212
7.4.3	Intensity tracking for Im7-based model 2	214
8	Conclusions and Outlook	217
9	Acknowledgments	221
A	List of Publications	223
B	Technical Details	227
B.1	Density-functional theory calculations	227
B.2	Spectra simulation	228
B.3	Subsystem-TDDFT calculations	231
B.4	Resonance Raman calculations	232
B.5	Visualization	233

C List of Abbreviations

235

I. Abstract

Photochemical and photophysical processes are the basis for the conversion of solar light into energy forms usable by living organisms on earth. Insight into the elementary reaction steps requires a detailed understanding of interactions between radiation and matter, which can be probed on a molecular level with spectroscopic techniques. Spectroscopy also provides the bridge to theoretical analyses, which are required to develop concepts about the underlying phenomena as well as strategies for utilizing them in other contexts. Although the fundamental physical principles needed for this purpose are known from quantum mechanics, reliable first-principles investigations are hampered by the complexity of the functional units involved in photosynthesis. Our knowledge on the basic working principles in biological photoprocesses strongly relies on the decomposition of these units into molecular or submolecular building blocks. To choose such entities as the essential ingredients in a quantum chemical framework is thus a promising route to theoretical spectroscopy of complex systems.

This work describes the development of quantum chemical methods for the purpose of chromophore-specific spectroscopy. They are designed to focus on relevant substructures without sacrificing the view on the entire system. This means that interactions of the constituent fragments must be properly described. Density functional theory provides a natural framework for such techniques, since its essential quantity, the electron density, is an observable real-space quantity, which may be decomposed into subsystem contributions.

The spectroscopic techniques that we are aiming at should be able to provide insight into photoexcitation processes. Electronic absorption and circular dichroism spectra are suited for this purpose, and resonance Raman spectroscopy can be utilized to uncover structural changes after the initial absorption events. For the underlying theoretical approaches, this necessitates the ability to describe excited electronic states for aggregates with intricate composition. This can be provided by the extension of density functional theory to time-dependent phenomena, so that the real-space separability of the electron density, now as a function of time, is retained.

In the first part of this work, a subsystem electronic-structure method within the context of density-functional theory is analyzed that employs such a real-space decomposition for the description of complex aggregates in terms of simple fragments. It is shown that this partitioning can accurately reproduce electron density distributions, even if the interactions between the constituent subsystems become rather strong.

In order to utilize density-functional theory for the excited states of extended systems composed of smaller subunits, it is necessary to understand its advantages, but also its pitfalls. It is shown that severe problems arise for the description of charge-transfer states when using conventional methods within time-dependent density-functional theory for such systems. A physically motivated correction for this problem is introduced, and

its advantages for interacting molecular subsystems are described. Subsequently, we describe an efficient partitioning scheme in the density-functional theory framework for excited states, which results in an embedding of the chromophore to be investigated in an effective environment. It is explained how this can be exploited to determine spectroscopic properties for molecules in solvents or in biological environments.

While this approach is chromophore-specific and allows efficient quantum chemical analyses of environmental effects, it fails for phenomena which can only be understood in terms of a *collective* response of an aggregate of molecules. Such phenomena occur in all photosynthetic systems, which are — as mentioned above — far too complex to be accessible to any standard quantum-chemical method. A general subsystem approach to time-dependent density functional theory is thus developed that allows one to go beyond such limitations. Furthermore, it offers the advantage to easily relate to phenomenological theories, such as excitonic coupling models. This approach actively includes the reaction of all subsystems to an electromagnetic perturbation, which is important not only under resonance conditions, but also for collective changes in the electric or magnetic properties of a functional unit. The corresponding theoretical basis and an efficient implementation for the investigation of these processes are presented in this work.

It is demonstrated that quantum chemical studies on natural light-harvesting systems are feasible with this approach without recourse to system-specific parameters or empirical corrections, which is hardly feasible with other quantum chemical approaches. The method allows to extract both site energies of pigments and excitonic splittings and thus offers a way towards a detailed understanding of photochemical reactions in complex molecular assemblies.

The more general information about the potential energy surfaces of excited states accessible from resonance Raman spectroscopy can be used to probe local excited states in larger molecules. This technique can thus serve as an intrinsically chromophore-specific method. It is shown that well-known approximations for resonance Raman calculations can efficiently be used with time-dependent density-functional theory methods to study photochemical and photophysical processes in large molecules. This is an important pre-requisite for the understanding of artificial photosynthetic systems. A great advantage of experimental resonance Raman spectroscopy for the investigation of complex biomolecules is its selectivity. In contrast to that, such systems represent true challenges to quantum chemical approaches. This problem can be circumvented by using an intensity-driven approach to resonance Raman spectroscopy that exploits the selectivity observed in experiment for an iterative determination of the high-intensity features, which is presented in this work. Its features are demonstrated for molecular biochemical building blocks.

1. Introduction

1.1 The importance of subsystems in chemistry

Quantum mechanics describes the properties of matter on the basis of fundamental interactions between elementary particles. For quantum chemistry in the non-relativistic limit, the elementary particles that have to be considered are electrons and atomic nuclei, which interact via Coulomb forces. In order to proceed from these fundamental principles to chemical concepts, many steps of abstraction have to be made. One of the most essential ones in chemistry is probably the Born–Oppenheimer approximation, which provides the basis for the concept of a molecular structure [1, p. 17].

To be more precise, the Born–Oppenheimer approximation allows us to decouple the electronic and the nuclear degrees of freedom. But even then, the underlying theoretical framework does not provide a unique criterion for identifying the border of a molecule in a larger aggregate, which we will call the supersystem or supermolecule in the following. In contrast to that, the concepts of molecules within a larger system, or even of functional groups within a molecule are essential ideas for our understanding of the structure, properties, and reactivity of chemical systems.

Although such concepts are not a *consequence* of fundamental quantum mechanics, they should be *compatible* with it, so that we can express the results of quantum chemical investigations in terms of molecules and functional groups. We can apply subsystem approaches in quantum chemistry either in an *a posteriori* or an *a priori* way. The former one serves the purpose to identify a subsystem’s contribution to a certain (super)molecular property obtained in a supermolecular calculation. By studying its transferability from one system to another, it is often possible to derive classification schemes for the properties and reactivity of molecules. Several local partitioning schemes have been defined for this purpose, which often work with a projection to atomic basis sets [2–5] or with a real-space partitioning of the electron density, either in terms of disjoint regions [6, 7], or with overlapping atomic densities [8, 9]. No attempt will be made here to review all these schemes, since detailed accounts of them have been given elsewhere (see, e.g., Refs. [6, 10–12]). However, it should be mentioned that the theory of atoms in molecules (AIM) is special among these methods because it uses a generalization of the quantum mechanical action principle to subsystems. An atom in a molecule is then identified as an open quantum system that is confined by a surface of zero flux in the gradient vectors of the electron density [7, p. 29], a definition that is compatible with fundamental quantum chemical principles.

Subsystem approaches may also be used in an *a priori* way, so that they allow the calculation of properties for (super)systems composed of subunits without recourse to a supersystem calculation. The advantages for the analysis of properties in these approaches is, of course, preserved, since the subsystem contributions are readily available

in the calculation. The subsystem approaches described in the following are of this type.

1.2 Chromophore-specific theoretical spectroscopy

Molecular spectra can be regarded as an interface between experiment and theory. Spectroscopic properties are prototypical examples for phenomena that are interpreted in terms of molecular subunits or functional groups. For example, a dye molecule in solution still shows spectroscopic features that are similar to its gas-phase properties, although the dye itself constitutes only a very small part of the new supersystem (dye plus solvent) to which it belongs to. Another example is the absorption of light with subsequent transfer of excitation energy in photosynthetic units, which is clearly related to the specific pigment molecules that are contained. Also, characteristic vibrations can be employed to target functional groups in a larger molecule. The decisive boundary condition for such a partitioning is a comparatively weak interaction of the fragments — weak compared to the intra-fragment bonds and interactions. In McWeeny’s words [13, p. 485],

The interactions that we shall consider are “weak” in the sense that the interacting subsystems retain their individuality, at least in good approximation. Thus water molecules in the liquid phase are still water molecules; naphthalene molecules in solid naphthalene are still naphthalene molecules; and so on: and even, say, different CH_3 groups in the same molecule are still recognizable as CH_3 groups.

Subsystem approaches offer two important advantages in comparison to conventional quantum chemical methods for the calculation of structural, energetic, and spectroscopic properties. The first is that a consistent and accurate description of matter in complex systems on the basis of quantum mechanics is very difficult, so that quantum chemical methods are often combined with additional approximations — especially to account for less important parts of the system. This is done because of their unfavorable scaling behavior with system size. A natural way out of this problem would be to calculate energies, properties etc. individually for a set of subsystems and to try to combine the results in a suitable way in order to obtain results for the supersystem. Increasingly complex aggregates can then be described in terms of more and more subsystems, whereas the size of each subsystem may be the same.

The other reason is that subsystem approaches are compatible with chemical intuition in the sense that all properties will be obtained in terms of subsystem properties, and effects of interactions can easily be identified. The assignment and interpretation of spectroscopic signatures to certain substructures of matter will thus be facilitated.

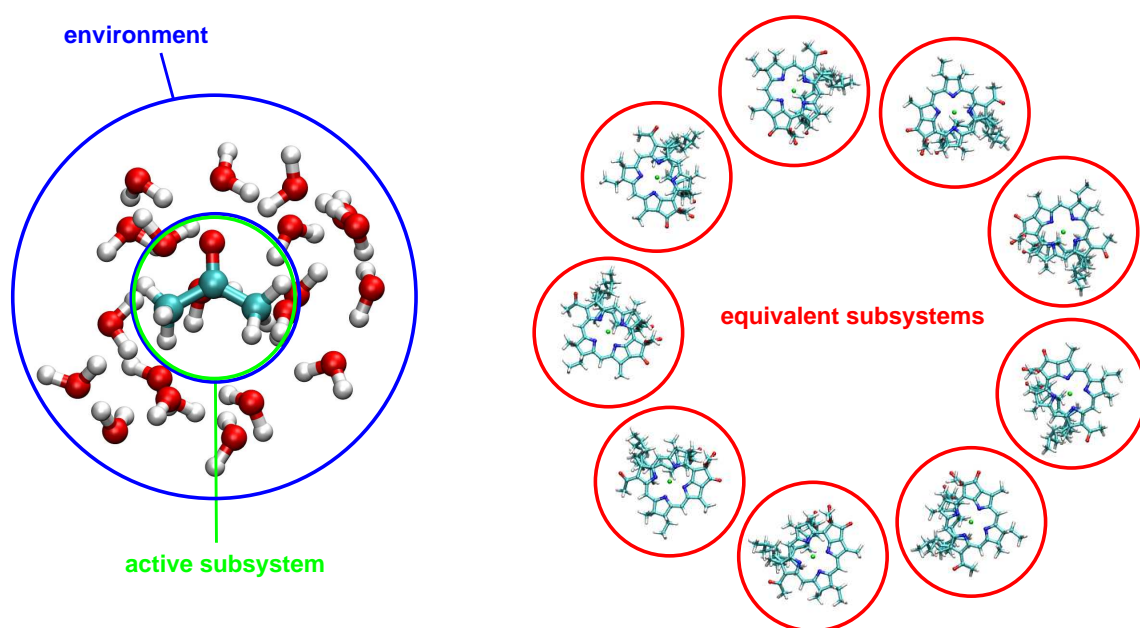
However, there is a caveat: Many such subsystem methods exist in which an active subsystem is chosen intuitively, and its environment, by construction of the method, has only indirect effects on the calculated properties. If the active subsystem is not chosen properly and the desired spectra also actively depend on parts of the environment, there is usually no way for the algorithm to correct it, since the partitioning cannot be automatically adjusted. This may concern delocalized excited electronic states that

artificially exhibit a local character due to a restricted orbital space as well as molecular vibrations that are confined by the algorithm to a particular functional group, but would couple to other parts of the system if the active fragment was chosen differently. These cases are by no means always obvious, and subsystem-based, chromophore-specific methods are desirable to offer the possibility to correct for these effects.

This work presents new developments of such schemes in the context of theoretical spectroscopic methods and response properties based on quantum chemistry. Both electronic-structure theory and the quantum mechanics of nuclear motions in molecules will be covered. Moreover, the theoretical methods developed and the practical schemes outlined here are *chromophore-specific*, since they allow one to focus on those substructures relevant for certain spectroscopic features.

We use the term “subsystem approach” in a rather general way, and we will apply these schemes in two different frameworks, which are illustrated in Figure 1.1. The first may be called “embedding approach”, since the two subsystems are not equivalent for the phenomenon investigated: There is an active subsystem (solute, adsorbate, functional group, etc.) embedded in an environment (solvent, surface, protein, etc.). In this approach, it will often be important to use a more approximate representation of the environment. The second ansatz treats all subsystems on the same footing, and only their interactions are described in a more approximate way. This will be referred to as the “general subsystem approach” and is conceptually comparable to divide-and-conquer methods.

Figure 1.1: Illustration of the two subsystem approaches. Left: In the *embedding approach*, the system (here: acetone in aqueous solution) is divided into an active subsystem (acetone as a solute) and an environment (water as a solvent); right: in the *general subsystem approach*, the system (here: B800 subunit of light-harvesting complex 2 of *Rhodospseudomonas acidophila*) can be divided into equivalent subsystems.



1.3 Outline of this work

The organization of this work is as follows: Chapter 2 introduces and analyzes subsystem and embedding approaches to ground-state electronic-structure theory with a focus on density functional theory (DFT).¹ General methods for excited states and response properties of complex systems are presented in Chapter 3, with an emphasis on time-dependent density functional theory (TDDFT) methods. This chapter also discusses a possible correction for one of the most severe problems of TDDFT when applied to extended systems, which is its failure to describe long-range charge-transfer excitations. Furthermore, an embedding version of TDDFT is presented that allows to circumvent these problems in particular for solvation phenomena. This embedding approach is then applied in Chapter 4 to investigate solvent effects on ground- and excited-state properties. Among the most interesting problems concerning absorption phenomena and excited-state properties in nature are certainly processes in photosynthetic units. Whereas the TDDFT-embedding approach fails in this context, Chapter 5 introduces a general subsystem theory that is suited for excited-state calculations of divide-and-conquer type. Subsequently, it is applied to study the photophysical properties of natural light-harvesting complexes, including the analysis of protein–pigment and pigment–pigment interactions. Chapter 6 starts with an introduction to methods that are suited for the calculation of vibrational properties of such systems and their couplings to electronic excitations. In particular, it describes the resonance Raman effect as a selective type of scattering phenomenon and demonstrates the great benefit that is provided by approximate theoretical approaches to resonance Raman spectroscopy. Chapter 7 then shows that the experimentally observed selectivity of resonance Raman spectroscopy can also be exploited in the algorithmic structure by iterative methods that directly target only intense vibrations in calculations of molecular resonance Raman spectra. A general summary and conclusion from this work is given in Chapter 8, together with an outlook to future work.

¹Note that Hartree atomic units (a.u.) are used throughout this work if not explicitly stated otherwise, i.e., the numerical values of the Planck constant \hbar , the elementary charge e , the electron mass m_e and of $1/(4\pi\epsilon_0)$ are equal to one.

2. Subsystem-Based Electronic-Structure Theory

2.1 Partitioning of quantum systems

Quantum systems are described by wave functions, which, for the fermionic systems considered here, must be antisymmetric under pairwise permutation of the particles (electrons). If a quantum system consists of several distinct subsystems, e.g., systems A and B , it should be possible to express its wave function in terms of products of wave functions for the subsystems [13, p. 485]. In the case of fermionic systems, this product wavefunction must be antisymmetrized in order to fulfill the Pauli principle,

$$\Psi(\mathbf{x}_1, \mathbf{x}_2, \dots, \mathbf{x}_{N_A+N_B}) = \tilde{N} \hat{A} [\Psi_A(\mathbf{x}_1, \dots, \mathbf{x}_{N_A}) \Psi_B(\mathbf{x}_{N_A+1}, \dots, \mathbf{x}_{N_A+N_B})], \quad (2.1)$$

where \mathbf{x}_i is a set of (spatial and spin) coordinates of particle i , N_A and N_B are the numbers of fermions (electrons) in systems A and B , Ψ_A and Ψ_B are the corresponding subsystem wavefunctions, \tilde{N} is a normalization factor, and \hat{A} is an antisymmetrizer that ensures the antisymmetry of the total wavefunction Ψ .

In principle, already the Hartree–Fock approach corresponds to such a partitioning, in which the “parts” are the one-electron functions, i.e., the orbitals. However, this does not necessarily lead to a *spatial* partitioning of the wavefunction, which is desirable for chemical concepts.

There are a number of other ways in order to partition a quantum system into subsystems, and their full discussion is far beyond the limit of this work. Therefore, only a very brief summary is given here in order to outline the relation of the methods used in the following to other approaches.

One common strategy is a Hilbert-space partitioning, in which the basis functions employed to describe the system are assigned to particular subsystems, e.g., in terms of projection operators [14–16]. The divide-and-conquer strategy by Yang [17] partitions the electron density in real space into interacting subsystem contributions, but uses a Hilbert-space partitioning of the Kohn–Sham Hamiltonian in terms of localized basis sets to calculate the subsystem densities. Recently, a more approximate scheme was proposed that only considers the electrostatic interactions based on the fragment densities in the context of density-functional theory [18]. Yang’s divide-and-conquer strategy has been transferred from the context of density-functional theory to Hartree–Fock [19], second-order Møller–Plesset (MP2) [20, 21], and coupled cluster theory [22]. A whole class of partitioning methods is provided by the fragment molecular orbital method [23], in which the entire system is partitioned into fragments that are described in terms of their localized fragment orbitals, and their energies and properties are calculated under the influence of the Coulomb field of the entire system. The total energy is calculated

in terms of an incremental scheme that can be defined for different types of quantum chemical methods. Even covalently bonded fragments are used, and the dangling bonds arising in this type of fractioning are saturated by an electrostatic capping field [24]. A Hilbert-space partitioning in terms of localized orbitals for a wavefunction-in-DFT embedding strategy has been presented in Ref. [25]. Other partitioning schemes employ the Green’s function in order to describe the effect of one subsystem on another [26], or use a partitioning of the first-order reduced density matrix [27, 28]. Also Mezey has suggested density-matrix based approaches for the quantum chemical description of complex systems, see Ref. [29, 30] and references therein. Another approach is to start from molecular fragments and incorporate their interactions in terms of an intermolecular perturbation theory, notably in the form of symmetry-adapted perturbation theory [31, 32]. In recent years, this method has successfully been combined with density-functional methods [33–39].

According to the Hohenberg–Kohn theorem [40], quantum states can equally well be described in terms of the electron density distribution $\rho(\mathbf{r})$. Since this is an observable real-space quantity which is additive for subsystems, it is, from a conceptual point of view, much better suited for a subsystem electronic-structure approach than wave functions or density matrices [41]. The general idea of subsystem-density functional theory approaches is a partitioning of the total ground-state electron density $\rho(\mathbf{r})$ into subsystem contributions according to,

$$\rho(\mathbf{r}) = \sum_I \rho_I(\mathbf{r}), \quad (2.2)$$

where the sum runs over all subsystems I . In the following, we will discuss approaches that use such a density partitioning. Before, however, a brief summary of the key equations in Kohn–Sham DFT will be presented as a basis for the subsequent sections.

2.2 Summary of Kohn–Sham density functional theory

Within the Kohn–Sham approach to density-functional theory [42], the electronic energy functional can be expressed as [43],

$$E[\rho] = T_s[\{\phi_i\}] + E_{\text{ext}}[\rho] + E_{\text{Coul}}[\rho] + E_{xc}[\rho], \quad (2.3)$$

where T_s is the kinetic energy of the non-interacting Kohn–Sham reference system with the same electron density as the interacting system of electrons under study, that depends explicitly on the Kohn–Sham orbitals ϕ_i . E_{ext} is the interaction energy of the electron density with the given local external potential $v_{\text{ext}}(\mathbf{r})$, E_{Coul} is the electron–electron Coulomb interaction energy, and E_{xc} is the exchange–correlation energy that is often divided into an exchange part E_x and an correlation part E_c . In typical quantum chemical applications, the external potential is just the Coulomb potential of the nuclei with charges Z_I at positions \mathbf{R}_I ,

$$v_{\text{ext}}(\mathbf{r}) = - \sum_I \frac{Z_I}{|\mathbf{r} - \mathbf{R}_I|}. \quad (2.4)$$

Minimization of $E[\rho]$ w.r.t. the density leads, by a comparison of the Euler–Lagrange equations of the interacting and non-interacting systems [43], to the Kohn–Sham equations,

$$\left(-\frac{\nabla^2}{2} + v_{\text{eff}}[\rho](\mathbf{r})\right) \phi_i(\mathbf{r}) = \epsilon_i \phi_i(\mathbf{r}), \quad (2.5)$$

where v_{eff} contains the functional derivatives of the energy terms E_{ext} , E_{Coul} , and E_{xc} w.r.t. the electron density $\rho(\mathbf{r})$,

$$v_{\text{eff}}[\rho](\mathbf{r}) = \frac{\delta}{\delta \rho(\mathbf{r})} (E_{\text{ext}}[\rho] + E_{\text{Coul}}[\rho] + E_{xc}[\rho]) = v_{\text{ext}}(\mathbf{r}) + v_{\text{Coul}}[\rho](\mathbf{r}) + v_{xc}[\rho](\mathbf{r}). \quad (2.6)$$

This potential depends explicitly on the electron density $\rho(\mathbf{r})$. The Coulomb (v_{Coul}) and exchange–correlation (v_{xc}) potentials are defined as the functional derivatives of the corresponding energy terms. In the Kohn–Sham formalism the density is obtained from the Kohn–Sham orbitals,

$$\rho(\mathbf{r}) = \sum_i^{\text{occ}} |\phi_i(\mathbf{r})|^2, \quad (2.7)$$

and the sum runs over all occupied orbitals $\phi_i(\mathbf{r})$. Exact analytical expressions are known for E_{ext} and E_{Coul} as explicit functionals of the electron density,

$$E_{\text{ext}}[\rho] = \int \rho(\mathbf{r}) v_{\text{ext}}(\mathbf{r}) d^3r, \quad (2.8)$$

$$E_{\text{Coul}}[\rho] = \frac{1}{2} \int \frac{\rho(\mathbf{r}) \rho(\mathbf{r}')}{|\mathbf{r} - \mathbf{r}'|} d^3r. \quad (2.9)$$

The exchange–correlation functional is, in the Kohn–Sham formalism, defined as

$$E_{xc}[\rho] := E_{ee}[\rho] - E_{\text{Coul}}[\rho] + T[\rho] - T_s[\rho], \quad (2.10)$$

where $E_{ee}[\rho]$ is the exact electron–electron interaction energy; $T[\rho]$ and $T_s[\rho]$ are the kinetic energies of the interacting and non-interacting systems, respectively. Although no exact expression for $E_{xc}[\rho]$ in terms of the electron density is known, several approximate expressions have been developed, which are reasonably accurate. The simplest approximation for the exchange part of E_{xc} is Dirac’s expression derived for a homogeneous electron gas [44] (note also the earlier work by Bloch [45]),

$$E_x^{\text{Dirac}}[\rho] = -C_x \int \rho^{4/3}(\mathbf{r}) d^3r, \quad (2.11)$$

where

$$C_x = \frac{3}{4} \left(\frac{3}{\pi}\right)^{1/3} \approx 0.7386. \quad (2.12)$$

Strategies for recent developments of exchange–correlation functionals and comparisons of their accuracies are discussed, e.g., in Refs. [46–51]. Since the terms E_{ext} , E_{Coul} , and

$E_{xc}[\rho]$ (at least for non-orbital-dependent exchange–correlation functionals) only depend on the electron density or its derivatives, they can be calculated in a straightforward way even if the electron density is provided in terms of subsystem contributions according to Eq. (2.2).

A problem for the subsystem partitioning of the energy functional arises from the kinetic energy T_s , which is only known as an implicit functional of the electron density in terms of the Kohn–Sham orbitals,

$$T_s[\{\phi_i\}] = - \sum_i^{\text{occ}} \langle \phi_i | \nabla^2 / 2 | \phi_i \rangle, \quad (2.13)$$

where the braces indicate the entire set of occupied Kohn–Sham orbitals of the full system under study and the sum runs over all occupied Kohn–Sham orbitals. What would be needed for an exact subsystem density functional theory is an expression for the kinetic energy¹ T_s that only employs the electron density (or the one-electron functions obtained for the subsystems).

2.3 Kinetic energy functionals and potentials

There have been many attempts to apply approximate, orbital-free kinetic energy functionals in DFT. A major challenge in these approaches arises from the fact that the kinetic energy is, by the virial theorem, of the same order of magnitude as the total electronic energy, whereas the exchange and correlation energy are typically one or two orders of magnitude smaller, respectively [43, 52, 53]. Therefore, the relative accuracy needed for kinetic-energy functionals must be at least one order of magnitude better than that of approximate exchange–correlation functionals if the same relative error in the total electronic energy shall be achieved.

The early DFT predecessor method by Thomas and Fermi [54, 55] employed the expression of the kinetic energy of a uniform electron gas, i.e., the local density approximation for the kinetic energy, which is

$$T_{\text{TF}}[\rho] = C_F \int \rho^{5/3}(\mathbf{r}) d^3r, \quad (2.14)$$

where

$$C_F = \frac{3}{10} (3\pi^2)^{2/3} \approx 2.8712. \quad (2.15)$$

If the Thomas–Fermi (TF) model is augmented with the exchange expression from Eq. (2.11), we arrive at the Thomas–Fermi–Dirac (TFD) model. The total electronic energy in the TFD model is calculated from the electron density according to

$$E_{\text{TFD}}[\rho] = T_{\text{TF}}[\rho] + E_{\text{ext}}[\rho] + E_{\text{Coul}}[\rho] + E_x^{\text{Dirac}}[\rho] \quad (2.16)$$

¹Note that we approximate $T_s[\rho]$ and not $T[\rho]$ because of the definition of $E_{xc}[\rho]$ in Kohn–Sham DFT; otherwise, a redefinition of the exchange–correlation functional would be required.

However, these attempts were rather unsuccessful for applications in chemistry as described for example in Ref. [43, chapter 6]. A correction term depending on the gradient of the electron density was derived by von Weizsäcker [56],

$$T_W[\rho] = \frac{1}{8} \int \frac{|\nabla \rho(\mathbf{r})|^2}{\rho(\mathbf{r})} d^3r. \quad (2.17)$$

The total kinetic energy expression used by von Weizsäcker, originally in the framework of bonding energies within atomic nuclei, is

$$T_{\text{TFW}}[\rho] = T_{\text{TF}} + \lambda T_W[\rho], \quad (2.18)$$

with $\lambda = 1$. From a systematic gradient expansion of the kinetic energy it can be shown that λ should be chosen as $1/9$, whereas empirically values close to $1/5$ seem to offer the best performance. Details on the derivation of this correction and higher-order terms in this conventional gradient expansion (CGE), which are known analytically up to sixth order, can be found in Refs. [43, p. 127 ff.] and [52]. It should also be noted that $T_W[\rho]$ represents the *exact* kinetic energy in systems that can be described by just one spatial orbital in Kohn–Sham DFT. Reliable numerical data obtained from variational TFDW calculations were recently presented in Ref. [57]. The results obtained there for diatomic molecules are only in qualitative agreement with reference data.

Because of the limited success of the CGE, work on kinetic-energy functionals within the generalized gradient approximation (GGA) was pursued, similar to the development of approximate exchange–correlation functionals [48]. In particular, Lee, Lee, and Parr [58] have outlined and rationalized a conjointness between approximate exchange- and kinetic-energy functionals, from which kinetic-energy functionals can be constructed according to

$$T_{\text{GGA}}[\rho_\alpha, \rho_\beta] = 2^{2/3} C_F \sum_\sigma \int \rho_\sigma^{5/3}(\mathbf{r}) F(s_\sigma) d^3r, \quad (2.19)$$

where ρ_σ is the spin density of spin $\sigma = \{\alpha, \beta\}$, and $s_\sigma(\mathbf{r}) = |\nabla \rho_\sigma(\mathbf{r})| / (2\rho_\sigma(\mathbf{r})k_F)$ with the Fermi vector $k_F = [6\pi\rho_\sigma(\mathbf{r})]^{1/3}$. Here, the so-called enhancement factor $F(s)$ is taken from the analogous form of the corresponding approximate exchange functional. Although quite useful in the construction of GGA-type kinetic energy functionals, it was shown later that the conjointness conjecture of Ref. [58] is not entirely correct [59]. Since the local density functionals for exchange and kinetic energy are derived for Hartree–Fock-like expressions of the first-order reduced density matrix, the conjointness conjecture may be justified for these local functionals, but not in general for gradient-corrected functionals [60]. A relationship between kinetic-energy and exchange-energy densities in terms of *non-local* generalizations obtained from the Hartree–Fock expressions for the first-order reduced density matrices was outlined by March and Santamaria [61].

While Lee, Lee, and Parr originally tested the enhancement factor from Becke’s exchange functional [62], Lembarki and Chermette [63] subsequently obtained a reparameterized kinetic-energy functional from the Perdew–Wang exchange functional [64]. Other gradient corrected kinetic-energy functionals have been proposed, e.g., by DePristo and Kress [65], Ou-Yang and Levy [66], Perdew [67], Thakkar [68], Lacks and Gordon [69],

and by Tran and Wesolowski [70]. One of the most recently developed GGA-type functionals uses a parameterization to the Kohn–Sham forces rather than energies, which is claimed to be an advantageous strategy for the further development of local kinetic-energy functionals [59]. Also for these functionals, the success in variational calculations is limited.

The data given by Wang and Carter for atoms [52] show that for fully variational calculations, the main problem of the kinetic energy functionals results from the wrong kinetic-energy potential, which enters the calculation as the functional derivative $v_{\text{kin}}(\mathbf{r}) = \delta T_s[\rho]/\delta \rho(\mathbf{r})$. (See Ref. [71] for explicit expressions of such functional derivatives for gradient-dependent kinetic-energy approximations.) None of the LDA or GGA-type functionals mentioned above is able to reproduce a shell structure in the density distribution of atoms. This failure is mainly related to the wrong linear response behavior of the kinetic-energy functionals. Another class of functionals has thus been developed that enforces the correct linear-response of the free electron gas on the basis of the so-called average-density approximation [72] and the subsequent weighted density approximation [73]. A review of this class of functionals is given in Ref. [52]. It has been demonstrated that these functionals can produce a clear shell structure of the electron densities in atoms [74]; however, the computational effort increases substantially due to the fact that these functionals are non-local.

Best results with these models are obtained for metallic systems [75–79], which come closest to the ideal of a free-electron gas, at least for valence electrons. Problems arise, however, for non-metallic systems, e.g., metal hydrides [80], although some progress has been reported recently [81]. Applications of linear-response-type functionals have largely been restricted to periodic systems because of their particular functional form, although methods for their evaluation in real space have been developed in the past years [82,83]. For a recent study on the kinetic energies of atomic systems obtained with a family of linear-response type functionals based on the von Weizsäcker functional, see Ref. [84]. It should be noted that the functional derivative

$$v_{T_s}(\mathbf{r}) = \frac{\delta T_s}{\delta \rho(\mathbf{r})}, \quad (2.20)$$

is in principle accessible from the Kohn–Sham potential, since it fulfills the Euler–Lagrange equation,

$$v_{T_s}(\mathbf{r}) + v_{\text{eff}}(\mathbf{r}) = \mu, \quad (2.21)$$

and can thus be reconstructed (up to a constant μ) from the effective Kohn–Sham potential v_{eff} . This relation was used by King and Handy [85,86] to determine kinetic potentials that are exact apart from errors introduced in the Kohn–Sham potential by the approximate exchange–correlation part.

2.4 The Gordon–Kim model and the origins of subsystem DFT

The earliest density partitioning schemes originate from the idea that the interactions between closed-shell molecules or atoms do not disturb their electron densities very

much. If we denote the electron density of the isolated subsystem (molecule) I as $\rho_I^0(\mathbf{r})$, the sum,

$$\rho^0(\mathbf{r}) = \sum_I \rho_I^0(\mathbf{r}) \quad (2.22)$$

can be regarded as a zeroth-order approximation for the density $\rho(\mathbf{r})$ of the combined system (supermolecule) [87]. More accurate schemes can be obtained by considering the change in the density upon formation of the supermolecule, i.e.,

$$\rho(\mathbf{r}) = \rho^0(\mathbf{r}) + \delta\rho(\mathbf{r}), \quad (2.23)$$

and then including the effect of the density change into the energy expression. Such methods will be discussed in the following.

2.4.1 The original Gordon–Kim model

Several methods that try to exploit the idea of a density-partitioning in real space have been proposed during the past decades. In 1970, Gaydaenko and Nikulin [88] presented calculations of interaction energies for atoms on the basis of the Thomas–Fermi and Thomas–Fermi–Dirac energy functionals applied to superpositions of unperturbed atomic electron densities from Hartree–Fock (HF) calculations. HF densities were used in order to reproduce the shell structure of atoms, which is not possible with self-consistent TF(D) densities.

A similar model was introduced in 1972 by Gordon and Kim [89], which is based on three assumptions: (i) There is no rearrangement of the electron densities when the atoms or molecules are brought together, (ii) the interaction energy can be evaluated on the basis of a free electron gas approximation for the electron density, and (iii) the electron densities of the closed-shell systems can be obtained from Hartree–Fock wavefunctions. In mathematical terms, the density of the system is partitioned into

$$\rho(\mathbf{r}) = \rho_A^{\text{HF}}(\mathbf{r}) + \rho_B^{\text{HF}}(\mathbf{r}), \quad (2.24)$$

where $\rho_A(\mathbf{r})$ and $\rho_B(\mathbf{r})$ are the HF-densities for subsystems A and B. The electronic energy of the system is then calculated as

$$E_{\text{GK}}[\rho] = T_{\text{TF}}[\rho] + E_{\text{Coul}}[\rho] + E_x^{\text{Dirac}}[\rho] + E_c^{\text{LDA}}[\rho] + \int \rho(\mathbf{r}) v_{\text{ext}}(\mathbf{r}) d^3r, \quad (2.25)$$

where the expressions for $T_{\text{TF}}[\rho]$, $E_{\text{Coul}}[\rho]$, and $E_x^{\text{Dirac}}[\rho]$ have been defined in Sections 2.1 and 2.3. In contrast to Gaydaenko and Nikulin, the Gordon–Kim model includes a local density approximation to the correlation energy of the form

$$E_c^{\text{LDA}}[\rho] = \int \rho(\mathbf{r}) \varepsilon_c[\rho] d^3r, \quad (2.26)$$

where the approximate expressions for the correlation energy density of the free electron gas, $\varepsilon_c[\rho]$, were taken from Refs. [90,91] for the limits of low and high electron densities, respectively, and an interpolation was employed for intermediate electron densities.

The main reasons for the success of this model are that the scheme is not used self-consistently, thus avoiding the failure of the kinetic-energy potentials to produce the correct shell structure in atoms, and that only *interaction* energies are calculated instead of total energies. Therefore, only differential kinetic energies need to be described by the Thomas–Fermi expression. The interaction energy in the Gordon–Kim model, including the nucleus–nucleus repulsion (V_{nn}), can be expressed as,

$$E_{\text{GK}}^{\text{int}} = V_{nn} + E_{\text{GK}}[\rho] - E_{\text{GK}}[\rho_a] + E_{\text{GK}}[\rho_b] \quad (2.27)$$

$$\begin{aligned} &= \sum_{AB} \frac{Z_A Z_B}{|\mathbf{R}_A - \mathbf{R}_B|} + \int \int \frac{\rho_a(\mathbf{r}) \rho_b(\mathbf{r}')}{|\mathbf{r} - \mathbf{r}'|} d^3r d^3r' \\ &\quad - \sum_A Z_A \int \frac{\rho_b(\mathbf{r})}{|\mathbf{r} - \mathbf{R}_A|} d^3r - \sum_B Z_B \int \frac{\rho_a(\mathbf{r})}{|\mathbf{r} - \mathbf{R}_B|} d^3r \\ &\quad + \int \{ [\rho_a(\mathbf{r}) + \rho_b(\mathbf{r})] \varepsilon_{Txc}[\rho] \\ &\quad - \rho_a(\mathbf{r}) \varepsilon_{Txc}[\rho_a] - \rho_b(\mathbf{r}) \varepsilon_{Txc}[\rho_b] \} d^3r, \end{aligned} \quad (2.28)$$

where

$$\varepsilon_{Txc}[\rho] = \varepsilon_T[\rho] + \varepsilon_x[\rho] + \varepsilon_c[\rho] \quad (2.29)$$

$$= C_F \rho^{2/3}(\mathbf{r}) - C_x \rho^{1/3}(\mathbf{r}) + \varepsilon_c[\rho]. \quad (2.30)$$

This model thus completely avoids the determination of molecular orbitals for the supersystem. It proved to be quite successful to study interaction energies between rare gas atoms [89]. Several questions concerning such a “free electron gas” model for atoms and molecules were addressed subsequently by Kim and Gordon [92], e.g., the accuracy of total energies, kinetic and exchange energy densities, one-electron energies (in comparison to HF), cases of atoms without paired electrons and open-shell atoms as well as uniform electron gas models with finite numbers of electrons and finite sizes. It was shown by DePristo [93] that the difference between the kinetic-energy, exchange, and correlation potentials for the supersystem and the noninteracting constituents (e.g., atoms) satisfies a Poisson equation in which the source is the change in the electron density upon formation of the supersystem. This equation can be solved either self-consistently in an iterative way, or by means of a perturbation expression for the change in the density (cf. also the following sections). It gives the correction terms for the neglect of density relaxation effects in the Gordon–Kim model.

2.4.2 The Harris functional

Harris introduced a method in which the change in the kinetic energies is obtained from non-self-consistent Kohn–Sham orbital energies for the supersystem [94], evaluated for a potential calculated from the density $\rho^0(\mathbf{r})$ as defined in Eq. (2.22).

We note that the exact (apart from the usual approximations in the exchange–correlation functional) electronic energy for the supersystem can be written as,

$$E[\rho] = \sum_j^{\text{occ}} \epsilon_j - \int \rho(\mathbf{r}) \left[\frac{1}{2} v_{\text{Coul}}[\rho](\mathbf{r}) + v_{xc}[\rho](\mathbf{r}) \right] d^3r + E_{xc}[\rho], \quad (2.31)$$

where the ϵ_j are the correct (self-consistent) Kohn–Sham orbital energies for the supersystem. Moreover, we define a change in the effective potential due to the density change as,

$$\Delta v_{\text{eff}}(\mathbf{r}) = v_{\text{eff}}[\rho](\mathbf{r}) - v_{\text{eff}}[\rho^0](\mathbf{r}) \quad (2.32)$$

$$= v_{\text{Coul}}[\rho](\mathbf{r}) - v_{\text{Coul}}[\rho^0](\mathbf{r}) + v_{xc}[\rho](\mathbf{r}) - v_{xc}[\rho^0](\mathbf{r}), \quad (2.33)$$

and assume that both $\Delta v_{\text{eff}}(\mathbf{r})$ and the density change upon formation of the supermolecule, $\delta\rho(\mathbf{r})$, see Eq. (2.23), are small. The (non-self-consistent) solution of the Kohn–Sham-like equations,

$$\left(-\frac{1}{2} \nabla^2 + v_{\text{eff}}[\rho^0](\mathbf{r}) \right) \tilde{\phi}_j(\mathbf{r}) = \tilde{\epsilon}_j \tilde{\phi}_j(\mathbf{r}), \quad (2.34)$$

leads to the approximate orbitals $\tilde{\phi}_j$ and orbital energies $\tilde{\epsilon}_j$ of the supersystem. The sum of the *correct* orbital energies ϵ_j of the supersystem can, within first-order perturbation theory, be written as,

$$\sum_j^{\text{occ}} \epsilon_j \approx \sum_j^{\text{occ}} \tilde{\epsilon}_j + \int \rho(\mathbf{r}) \Delta v_{\text{eff}}(\mathbf{r}) d^3r. \quad (2.35)$$

We thus get for the total energy,

$$E[\rho] \approx \sum_j^{\text{occ}} \tilde{\epsilon}_j + E_{xc}[\rho] + \int \rho(\mathbf{r}) \left[\Delta v_s(\mathbf{r}) - \frac{1}{2} v_{\text{Coul}}[\rho](\mathbf{r}) - v_{xc}[\rho](\mathbf{r}) \right] d^3r \quad (2.36)$$

$$= \sum_j^{\text{occ}} \tilde{\epsilon}_j + E_{xc}[\rho] + \int \rho(\mathbf{r}) \left[\frac{1}{2} v_{\text{Coul}}[\rho](\mathbf{r}) - v_{\text{Coul}}[\rho^0](\mathbf{r}) - v_{xc}[\rho^0](\mathbf{r}) \right] d^3r. \quad (2.37)$$

By expanding $E_{xc}[\rho]$ in powers of $\delta\rho(\mathbf{r})$ around $\rho^0(\mathbf{r})$ and neglecting all exchange–correlation and Coulomb energy terms of second order in $\delta\rho(\mathbf{r})$, Eq. (2.37) can be turned into,

$$E[\rho] \approx \sum_j^{\text{occ}} \tilde{\epsilon}_j - \int \rho^0(\mathbf{r}) \left[\frac{1}{2} v_{\text{Coul}}[\rho^0](\mathbf{r}) + v_{xc}[\rho^0](\mathbf{r}) \right] d^3r + E_{xc}[\rho^0]. \quad (2.38)$$

Eq. (2.38) just differs from the exact expression, Eq. (2.31) by the fact that the “orbital energies” are determined from the potential $v_{\text{eff}}[\rho^0](\mathbf{r})$ rather than self-consistently from $v_{\text{eff}}[\rho](\mathbf{r})$, and that the sum-of-fragment density $\rho^0(\mathbf{r})$ is plugged into the energy expression rather than the exact density ρ . The errors in total energies obtained with the Harris functional are small compared to Kohn–Sham DFT results for closed-shell dimers, and may be acceptable even for covalently bonded dimers [94]. However, this

scheme is correct only to first order in the density change. It will, thus, not be applicable if the changes in the density become larger, so that also second-order contributions need to be taken into account. For investigations of the formal properties of the Harris functional, see Refs. [95,96]. Harris has pointed out that his energy expression is equivalent to the Gordon–Kim model if the eigenvalue sum is approximated by a local density approximation for the kinetic energy change [94].

2.4.3 Approaches based on density perturbations

On the basis of density functional perturbation theory [97–100], one can derive expressions for the energy functional of a supersystem in which the interaction of the systems is treated as the perturbation (see also the analysis given in Ref. [41]). Benoit *et al.* expanded the Kohn–Sham energy functional up to second order in the Kohn–Sham orbitals [101]. The reference orbitals were chosen to be localized orbitals for each subsystem, which were orthogonalized subsequently. The first-order correction to the orbitals is accessible by the requirement that their energy functional is stationary w.r.t. the orbital corrections. Good interaction energies were obtained with this approach for hydrogen-bonded complexes, ionic systems, and silicon crystals. A very similar scheme was suggested by Zhu and Trickey [102].

A method based on the response of the subsystems’ densities ($\delta\rho_I$, where I labels the subsystems) was employed by Tabacchi *et al.* [103], following the approach used in the chemical potential equalization method by York and Yang [104]. Within this method, the energy functional is expanded in terms of a change in the external potential and in the density. For a fixed external potential, the energy expression reads,

$$E[\rho, v_{\text{ext}}] = F \left[\sum_I \rho_I^0 \right] + \int \rho(\mathbf{r}) v_{\text{ext}}(\mathbf{r}) d^3r + \sum_I \int \frac{\delta F}{\delta \rho_I(\mathbf{r})} \delta \rho_I(\mathbf{r}) d^3r + \frac{1}{2} \sum_{IJ} \int \int \delta \rho_I(\mathbf{r}) \frac{\delta^2 F}{\delta \rho_I(\mathbf{r}) \delta \rho_J(\mathbf{r}')} \delta \rho_J(\mathbf{r}') d^3r d^3r', \quad (2.39)$$

with

$$F[\rho] = T_s[\rho] + E_{\text{Coul}}[\rho] + E_{xc}[\rho]. \quad (2.40)$$

The response densities of the subsystems can be obtained by minimizing Eq. (2.39) w.r.t. the $\delta\rho_I$, e.g., after introducing a basis set expansion [103]. The first and second order response kernels derived from the density functional $F[\rho]$ contain Coulombic, exchange–correlation, and kinetic energy terms. In their original work, Tabacchi *et al.* were aiming at a quantum chemistry-based force field and replaced the exchange–correlation and kinetic-energy contributions in $F[\rho]$ by an empirical potential. The kinetic-energy component of the first-order kernel was evaluated by using the TF approximation for the kinetic-energy functional, whereas the second-order kernels for both exchange–correlation and kinetic-energy were approximated by a semi-empirical extended Hückel approach. In a subsequent study, a purely density-functional based approach was applied, where the local density approximation was used for all exchange–correlation and kinetic-energy dependent terms [105].

2.5 Subsystem formulation of DFT

2.5.1 Partitioning of the density

Whereas the preceding approaches introduce certain approximations in an *ad hoc* manner or use truncated perturbative schemes, a systematic development of a subsystem-based density functional theory will be developed in the following. The idea for this scheme was introduced by Cortona [106] for the special case of atomic subsystems in crystals, although he already mentions that the approach might be extended to molecular subunits as well. The general derivation presented here is not restricted to a particular type of subsystem; its range of applicability will be studied in Section 2.9.

The density of the total system, denoted as the supersystem in the following, is usually expressed in terms of the Kohn–Sham orbitals ϕ_i^{super} of that system, cf. Eq. (2.5),

$$\rho(\mathbf{r}) = \sum_i |\phi_i^{\text{super}}(\mathbf{r})|^2. \quad (2.41)$$

The strategy of the subsystem approach is now as follows: In order to avoid the calculation of molecular orbitals for the supersystem, we partition the density into subsystem contributions, see Eq. (2.2),

$$\rho(\mathbf{r}) = \sum_I \rho_I(\mathbf{r}), \quad (2.42)$$

where the density of each subsystem I will be expressed in terms of (yet to be determined) subsystem orbitals ϕ_{i_I} ,

$$\rho_I(\mathbf{r}) = \sum_i |\phi_{i_I}(\mathbf{r})|^2. \quad (2.43)$$

Similar to the Kohn–Sham strategy to partition the energy expression into large known (T_s , E_{ext} , E_{Coul}) and a smaller unknown part (E_{xc}), we write the kinetic energy of the supersystem formally exact as

$$T_s[\{\phi_i^{\text{super}}\}] = \underbrace{\sum_I T_s^I[\{\phi_{i_I}\}]}_{\text{subsystem kinetic energies}} + \underbrace{\left[T_s[\{\phi_i^{\text{super}}\}] - \sum_I T_s[\{\phi_{i_I}\}] \right]}_{\text{non-additive kinetic energy}}, \quad (2.44)$$

where $T_s[\{\phi_{i_I}\}]$ is the single-particle kinetic energy associated with subsystem I ,

$$T_s[\{\phi_{i_I}\}] = - \sum_i^{\text{occ}} \left\langle \phi_{i_I} \left| \frac{1}{2} \nabla^2 \right| \phi_{i_I} \right\rangle. \quad (2.45)$$

The sum runs over all occupied spin-orbitals ϕ_{i_I} in subsystem I . These spin-orbitals form an orthonormal set of orbitals for each subsystem, but spin-orbitals from different subsystems are not necessarily orthonormal. We now introduce the exact non-additive kinetic-energy functional T_s^{nadd} ,

$$T_s^{\text{nadd}}[\{\phi_i^{\text{super}}\}, \{\{\phi_{i_J}\}\}] = \left[T_s[\{\phi_i^{\text{super}}\}] - \sum_I T_s[\{\phi_{i_I}\}] \right], \quad (2.46)$$

where the double braces indicate the dependence on the sets of occupied subsystem orbitals for all subsystems J . The kinetic energy thus turns into,

$$T_s[\{\phi_i^{\text{super}}\}, \{\{\phi_{i_J}\}\}] = \sum_I T_s[\{\phi_{i_I}\}] + T_s^{\text{nadd}}[\{\phi_i^{\text{super}}\}, \{\{\phi_{i_J}\}\}]. \quad (2.47)$$

For weakly interacting subsystems, the non-additive kinetic energy T_s^{nadd} will be small compared to the sum of the subsystem kinetic energies, and indeed it will vanish in the limit of non-interacting subsystems. This justifies to introduce an orbital-free, explicitly density-dependent approximation $T_s^{\text{nadd}}[\{\rho_J\}]$,

$$T_s^{\text{nadd}}[\{\phi_i^{\text{super}}\}, \{\{\phi_{i_J}\}\}] \approx T_s^{\text{nadd}}[\{\rho_J\}] = T_s[\rho] - \sum_I T_s[\rho_I]. \quad (2.48)$$

The subsystem kinetic energies will, however, be calculated exactly on the basis of the subsystem orbitals. This results in the following expression for the total kinetic energy,

$$T_s[\{\rho_J\}, \{\{\phi_{i_J}\}\}] = \sum_I T_s[\{\phi_{i_I}\}] + T_s^{\text{nadd}}[\{\rho_J\}]. \quad (2.49)$$

Examples for $T_s^{\text{approx}}[\rho]$ are discussed in Sec. 2.3. We observe that the resulting expression does no longer depend on the supersystem orbitals explicitly, so that the bottleneck of Kohn–Sham DFT calculations for large systems can be avoided, which is the self-consistent determination of an orthonormal set of orbitals for the supersystem. Note that the derivation presented here suggests that approximations to $T_s^{\text{nadd}}[\rho]$ should necessarily be decomposable into kinetic energy contributions of the supersystem and of the subsystems. Another strategy in the development of approximations is, however, to directly approximate $T_s^{\text{nadd}}[\rho]$, leading to non-decomposable non-additive kinetic-energy functionals (see Ref. [107]).

Cortona applied this method, e.g., to study the cohesive properties of alkali halides [108], and a similar approach based on spherical atomic electron densities was employed to model interaction energies in metallic systems [109]. A study that extended Cortona’s approach to molecular subsystem densities in molecular dynamics simulations was presented in Ref. [110].

2.5.2 Effective one-particle equations

Effective one-particle equations for the determination of the subsystem orbitals can be derived from a minimization of the energy functional subject to the condition that the subsystem electron densities integrate to the correct number of electrons per subsystem. This requires that each subsystem density corresponds to an integer number of electrons N_J ,

$$\int d^3r \rho_J(\mathbf{r}) = N_J \quad \forall J. \quad (2.50)$$

In order to enforce these conditions, we construct the Lagrangian

$$L[\{\rho_J\}] = E[\{\rho_J\}] + \sum_I \mu_I \left(\int d^3r \rho_I(\mathbf{r}) - N_I \right). \quad (2.51)$$

Minimization of the Lagrangian requires that

$$\left(\frac{\delta L[\{\rho_J\}]}{\delta \rho_K} \right)_{\rho_J, J \neq K} = 0 \quad \forall K, \quad (2.52)$$

where the index on the left-hand side indicates that all other subsystem densities are kept fixed during the minimization w.r.t. ρ_I . By writing the total energy in Eq. (2.51) explicitly as

$$\begin{aligned} E[\{\rho_J\}] &= E_{\text{ext}}[\rho] + E_{\text{Coul}}[\rho] + E_{xc}[\rho] + \sum_I T_s^I[\{\phi_{i_I}\}] + T_s^{\text{nadd}}[\{\rho_J\}], \\ &= \int v_{\text{ext}}(\mathbf{r}) \left[\sum_I \rho_I(\mathbf{r}) \right] d^3r + \frac{1}{2} \int \int \frac{(\sum_I \rho_I(\mathbf{r}')) \cdot (\sum_I \rho_I(\mathbf{r}))}{|\mathbf{r} - \mathbf{r}'|} d^3r' d^3r \\ &\quad + E_{xc}[\rho] + \sum_I T_s^I[\{\phi_{i_I}\}] + T_s^{\text{nadd}}[\{\rho_J\}], \end{aligned} \quad (2.53)$$

we obtain for the conditions in Eq. (2.52),

$$\begin{aligned} 0 &= v_{\text{ext}}(\mathbf{r}) + \int \frac{(\sum_I \rho_I(\mathbf{r}'))}{|\mathbf{r} - \mathbf{r}'|} d^3r' + \frac{\delta E_{xc}[\rho]}{\delta \rho_K(\mathbf{r})} + \frac{\delta T_s[\{\phi_{i_K}\}]}{\delta \rho_K(\mathbf{r})} + \frac{\delta T_s^{\text{nadd}}[\{\rho_J\}]}{\delta \rho_K(\mathbf{r})} + \mu_K \\ &= v_{\text{ext}}(\mathbf{r}) + v_{\text{Coul}}[\rho](\mathbf{r}) + v_{xc}[\rho](\mathbf{r}) + \frac{\delta T_s[\{\phi_{i_K}\}]}{\delta \rho_K(\mathbf{r})} + \frac{\delta T_s^{\text{nadd}}[\{\rho_J\}]}{\delta \rho_K(\mathbf{r})} + \mu_K \end{aligned} \quad (2.54)$$

It should be noted that the functional derivatives of energy terms which only depend on the total density ρ can be obtained according to the chain rule for functional differentiation as

$$\frac{\delta (E_{\text{ext}}[\rho] + E_{\text{Coul}}[\rho] + E_{xc}[\rho])}{\delta \rho_K(\mathbf{r})} = \int \frac{\delta (E_{\text{ext}}[\rho] + E_{\text{Coul}}[\rho] + E_{xc}[\rho])}{\delta \rho(\mathbf{r}')} \frac{\delta \rho(\mathbf{r}')}{\delta \rho_K(\mathbf{r})} d^3r' \quad (2.56)$$

$$= \frac{\delta (E_{\text{ext}}[\rho] + E_{\text{Coul}}[\rho] + E_{xc}[\rho])}{\delta \rho(\mathbf{r})}. \quad (2.57)$$

The last line follows from the fact that

$$\frac{\delta \rho(\mathbf{r}')}{\delta \rho_K(\mathbf{r})} = \delta(\mathbf{r} - \mathbf{r}'), \quad (2.58)$$

since ρ is just the sum of the subsystem densities at each point in space. We furthermore note that the functional derivative in Eq. (2.57) is nothing but the effective Kohn–Sham potential for the supersystem, see Eq. (2.6).

The potential term arising from the non-additive kinetic energy in Eq. (2.55) can be written more explicitly as

$$\frac{\delta T_s^{\text{nadd}}[\{\rho_J\}]}{\delta \rho_K(\mathbf{r})} = \frac{\delta T_s[\rho]}{\delta \rho(\mathbf{r})} - \frac{\delta T_s[\rho_I]}{\delta \rho_K(\mathbf{r})}, \quad (2.59)$$

where we have again used the chain rule for functional differentiation for the first term on the right-hand side. If we now assume that the subsystem densities ρ_J are v_s -representable (non-interacting v -representable), which also implies that they are non-negative everywhere in space, we can express them in terms of orbitals according to Eq. (2.43). The latter point will be analyzed in Section 2.9.4. The orbitals are obtained from the one-electron equations,

$$\left(-\frac{1}{2}\nabla^2 + v_{\text{eff}}^{\text{sub}}[\rho, \rho_I](\mathbf{r}) \right) \phi_{i_I} = \epsilon_{i_I} \phi_{i_I}, \quad (2.60)$$

for all orbitals ϕ_{i_I} of all subsystems I , subject to the condition that all subsystem densities except ρ_I are fixed. In the equation above, we introduced,

$$v_{\text{eff}}^{\text{sub}}[\rho, \rho_I](\mathbf{r}) = v_{\text{eff}}[\rho](\mathbf{r}) + \frac{\delta T_s[\rho]}{\delta \rho(\mathbf{r})} - \frac{\delta T_s[\rho_I]}{\delta \rho_I(\mathbf{r})}. \quad (2.61)$$

The density of the non-interacting system described in terms of these orbitals fulfills the Euler–Lagrange equation,

$$v_{\text{eff}}^{\text{sub}}[\rho, \rho_I](\mathbf{r}) + \frac{\delta T_s[\{\phi_{i_I}\}]}{\delta \rho_I(\mathbf{r})} + \mu_I = 0, \quad (2.62)$$

and is thus the sought-after density which fulfills Eq. (2.55). The derivation of such an effective subsystem potential including the effect of the entire electron density of the system was introduced by Wesolowski and Warshel [111] in the context of a two-partitioning of the electron density (see below).

Eq. (2.60) introduces a double self-consistency problem: The orbitals ϕ_{i_I} depend on the potential $v_{\text{eff}}^{\text{sub}}$, which by itself depends on the density calculated from the orbitals. Furthermore, for the minimization of the total energy, we have to solve Eq. (2.60) for each subsystem. But in order to solve the equation for the first subsystem, a guess for all other subsystem densities is needed. When Eq. (2.60) has been solved once for each subsystem, the effective potential $v_{\text{eff}}^{\text{sub}}$ for the first subsystem will have changed due to the changes in the other subsystem densities. Therefore, the full minimization of the energy functional requires an iterative update of the other subsystem densities in $v_{\text{eff}}^{\text{sub}}$. Two different strategies are possible to solve Eq. (2.60) for all subsystems: Either, they are indeed solved self-consistently for each subsystem, and only after Eq. (2.60) has been solved for one subsystem an update of the other subsystems' potentials

is performed, based on the new subsystem densities. This corresponds to the freeze-and-thaw strategy pursued in Ref. [112], which will be explained in more detail in Section 2.6.3. The other is to perform one SCF cycle for each subsystem and then update all densities, so that all subsystem problems are converged simultaneously, which is applied in Ref. [110]. The subsystem DFT setup that was partly implemented during this work in the Amsterdam Density Functional (ADF) package allows both schemes as well as intermediate approaches, in which the SCF for each subsystem is partly converged before a density update takes place [113].

2.6 Frozen-density embedding

2.6.1 Effective embedding potential

Eq. (2.60) can be re-written in a slightly different form by separating intra-subsystem and inter-subsystem contributions to the potential. For this purpose, we explicitly assume that the external potential in the total system is given by the Coulomb potential due to the nuclei, which will also be assigned to the different subsystems. I.e., the external potential due to subsystem I will be written as

$$v_{\text{ext}}^I(\mathbf{r}) = - \sum_{A_I} \frac{Z_{A_I}}{|\mathbf{r} - \mathbf{R}_{A_I}|}. \quad (2.63)$$

A_I labels the atomic nuclei assigned to system I , with nuclear charges Z_{A_I} at positions \mathbf{R}_{A_I} . The total external potential is the sum of the external potentials from all subsystems,

$$v_{\text{ext}}(\mathbf{r}) = \sum_J v_{\text{ext}}^J(\mathbf{r}) = v_{\text{ext}}^I(\mathbf{r}) + \sum_{J, J \neq I} v_{\text{ext}}^J(\mathbf{r}). \quad (2.64)$$

Similarly, the total Coulomb potential is the sum of the Coulomb potentials due to the subsystem densities, since it is linear in the density,

$$v_{\text{Coul}}[\rho](\mathbf{r}) = \int \frac{(\sum_J \rho_J(\mathbf{r}'))}{|\mathbf{r} - \mathbf{r}'|} d^3 r' = \sum_J v_{\text{Coul}}[\rho_J](\mathbf{r}) \quad (2.65)$$

$$= v_{\text{Coul}}[\rho_I](\mathbf{r}) + \sum_{J, J \neq I} v_{\text{Coul}}[\rho_J](\mathbf{r}). \quad (2.66)$$

The exchange–correlation potential cannot be separated like this, since it is non-linear in the density. Nevertheless, we can formally write

$$v_{xc}[\rho](\mathbf{r}) = v_{xc}[\rho_I](\mathbf{r}) + \{v_{xc}[\rho](\mathbf{r}) - v_{xc}[\rho_I](\mathbf{r})\} \quad (2.67)$$

By realizing that the effective Kohn–Sham potential for subsystem I in absence of all other subsystems would be given by,

$$v_{\text{eff}}[\rho_I](\mathbf{r}) = v_{\text{ext}}^I(\mathbf{r}) + v_{\text{Coul}}[\rho_I](\mathbf{r}) + v_{xc}[\rho_I](\mathbf{r}), \quad (2.68)$$

we can write the effective subsystem potential as

$$v_{\text{eff}}^{\text{sub}}(\mathbf{r}) = v_{\text{eff}}[\rho_I](\mathbf{r}) + v_{\text{emb}}[\rho_I, \rho_I^{\text{compl.}}], \quad (2.69)$$

where we have introduced the *complementary* density to ρ_I ,

$$\rho_I^{\text{compl.}}(\mathbf{r}) = \sum_{J, J \neq I} \rho_J(\mathbf{r}) = \rho(\mathbf{r}) - \rho_I(\mathbf{r}) \quad (2.70)$$

and the effective embedding potential

$$v_{\text{emb}}[\rho_I, \rho_I^{\text{compl.}}](\mathbf{r}) = \sum_{J, J \neq I} v_{\text{ext}}(\mathbf{r}) + \sum_{J, J \neq I} v_{\text{Coul}}[\rho_J](\mathbf{r}) + \{v_{xc}[\rho](\mathbf{r}) - v_{xc}[\rho_I](\mathbf{r})\} \quad (2.71)$$

$$\begin{aligned} &= \sum_{J, J \neq I} v_{\text{ext}}(\mathbf{r}) + v_{\text{Coul}}[\rho_I^{\text{compl.}}](\mathbf{r}) + \left\{ v_{xc}[\rho_I + \rho_I^{\text{compl.}}](\mathbf{r}) - v_{xc}[\rho_I](\mathbf{r}) \right\} \\ &\quad + \frac{\delta T_s[\rho_I + \rho_I^{\text{compl.}}]}{\delta(\rho_I(\mathbf{r}) + \rho_I^{\text{compl.}}(\mathbf{r}))} - \frac{\delta T_s[\rho_I]}{\delta \rho_I(\mathbf{r})}. \end{aligned} \quad (2.72)$$

The definition of $v_{\text{eff}}^{\text{sub}}$ via Eq. (2.69) and (2.71) has the advantage that it separates the potential into a term that is also present in the isolated subsystem I and a term that introduces the effect of the surrounding subsystems in terms of an effective embedding potential. It also clearly separates $\rho_I^{\text{compl.}}$, the part of the density that is kept fixed during the solution of Eq. (2.60), from the density ρ_I that is varied. The alternative definition in Eq. (2.61) contains the total density instead, which changes whenever ρ_I is varied.

2.6.2 Active part and environment

The subsystem approach as introduced in the preceding sections treats all subsystems on the same footing, which will be the preferred starting point whenever ensembles of identical or similar molecules shall be described. In many cases, however, scientific questions are clearly focused on a certain molecule within a larger aggregate, e.g., a solute in a solvent shell. In 1993, Wesolowski and Warshel [111] introduced a subsystem DFT approach that is particularly well suited for this type of problem, in which the entire system is partitioned into two subsystems, the active subsystem with density ρ_1 and the environment with density ρ_2 . This approach can be identified as a special example of the subsystem approach outlined in the preceding sections, in which

$$\rho(\mathbf{r}) = \rho_1(\mathbf{r}) + \rho_2(\mathbf{r}), \quad \rho_1^{\text{compl.}}(\mathbf{r}) = \rho_2(\mathbf{r}). \quad (2.73)$$

The effective one-particle equations then become,

$$\left(-\frac{1}{2} \nabla^2 + v_{\text{eff}}[\rho_I](\mathbf{r}) + v_{\text{emb}}[\rho_1, \rho_2] \right) \phi_{i_1} = \epsilon_{i_1} \phi_{i_1}, \quad (2.74)$$

where the explicit form of the embedding potential is,

$$\begin{aligned}
v_{\text{emb}}[\rho_1, \rho_2](\mathbf{r}) &= \sum_{A_2} -\frac{Z_{A_2}}{|\mathbf{r} - \mathbf{R}_{A_2}|} + \int \frac{\rho_2(\mathbf{r}')}{|\mathbf{r}' - \mathbf{r}|} d^3r' \\
&+ \frac{\delta E_{xc}[\rho]}{\delta \rho(\mathbf{r})} - \frac{\delta E_{xc}[\rho_1]}{\delta \rho_1(\mathbf{r})} + \frac{\delta T_s[\rho]}{\delta \rho(\mathbf{r})} - \frac{\delta T_s[\rho_1]}{\delta \rho_1(\mathbf{r})}.
\end{aligned} \tag{2.75}$$

In the simplest and most efficient version of this approach, an approximation for the electron density of the environment is constructed at the beginning of the calculation and then kept frozen. In that way, the self-consistency problem in Eqs. (2.60), which are called Kohn–Sham equations with constrained electron densities (KSCED), is only solved once for system 1. This approach is known as frozen-density embedding (FDE) or frozen density functional theory (FDFT), although the former name is also used for more advanced variants of this embedding approach. An extension to periodic-boundary calculations within a plane-wave basis was described in Ref. [71].

The focus of the FDE scheme is clearly on the active subsystem, whereas the environment only modulates its properties. Thus, a number of approximations are possible in the description of the environment that make the calculation more efficient. One approximation that can be applied is to construct the frozen environmental density itself as a sum of fragment densities, which may be approximated by the densities of the isolated fragments, e.g., solvent molecules [114–116].

2.6.3 Freeze-and-thaw cycles; v_s -representability

Subsystem density functional theory can be regarded as exact in the limit of exact functionals for the exchange–correlation and kinetic energy contributions. In view of the present approximations that are available, in particular for the latter functional, this ideal is, however, far beyond reach. The formal exactness requires, in addition, the assumption of v_s -representability of the subsystem densities. As discussed by Wesolowski [41], one can speculate about cases in which the v_s -representability condition is not fulfilled for the supersystem (as required in the Kohn–Sham context), but is fulfilled for the subsystems, making FDE formally applicable in contrast to KS-DFT.

Also the frozen-density embedding scheme as outlined above can still be regarded as formally rigorous, as long as the density $\rho_1(\mathbf{r})$ to be optimized can indeed lead to the density complementary to the fixed $\rho_2(\mathbf{r})$. The v_s -representability condition for $\rho_1(\mathbf{r})$ is, however, more severe in this case, since many choices of $\rho_2(\mathbf{r})$ will make it impossible to express the exact $\rho_1^{\text{exact}}(\mathbf{r}) := \rho_{\text{super}}(\mathbf{r}) - \rho_2(\mathbf{r})$ in terms of the density of a non-interacting reference system (we denote the density of the supersystem explicitly as ρ_{super} here). This holds in particular if $\rho_2(\mathbf{r}) > \rho_{\text{super}}(\mathbf{r})$ for any point \mathbf{r} , since a v_s -representable density $\rho_1(\mathbf{r})$ must be non-negative everywhere in space. Especially for more strongly interacting subsystems, this condition will in general not be fulfilled.

To illustrate this point, the electron density of the $\text{H}_2\text{O} \cdots \text{F}^-$ system was studied by means of FDE calculations. Its BP86/TZP optimized structure is shown in Figure 2.1. The $\text{H} \cdots \text{F}$ distance in this planar complex is 1.32 Å, the $\text{O} - \text{H} \cdots \text{F}$ angle is 177.9 degrees and the $\text{H} - \text{O} - \text{H}$ angle is 101.1 degrees. There are two different $\text{O} - \text{H}$ bond lengths, $\text{O} - \text{H}_1 = 0.97$ Å and $\text{O} - \text{H}_2 = 1.11$ Å. The PW91k functional was employed for the

T_s^{nadd} in the FDE calculations. Figure 2.2 a) shows the difference density between the supermolecular density from a Kohn–Sham–DFT calculation on the combined system, which can be regarded as a reference for the total density ρ_{super} , and the density $\rho_{\text{frag}}(\text{F}^-)$ of the frozen fragment, which is the F^- ion in this case. As can clearly be seen, the difference $\rho_{\text{super}}(\mathbf{r}) - \rho_2(\mathbf{r})$ is *not* non-negative everywhere, and thus FDE can only give approximate results.

Figure 2.1: Optimized (BP86/TZP) structure and coordinates in the grid of the H-bonded system $\text{H}_2\text{O} \cdots \text{F}^-$.

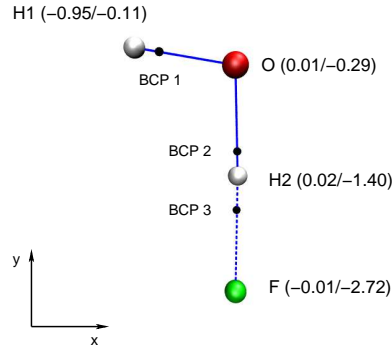
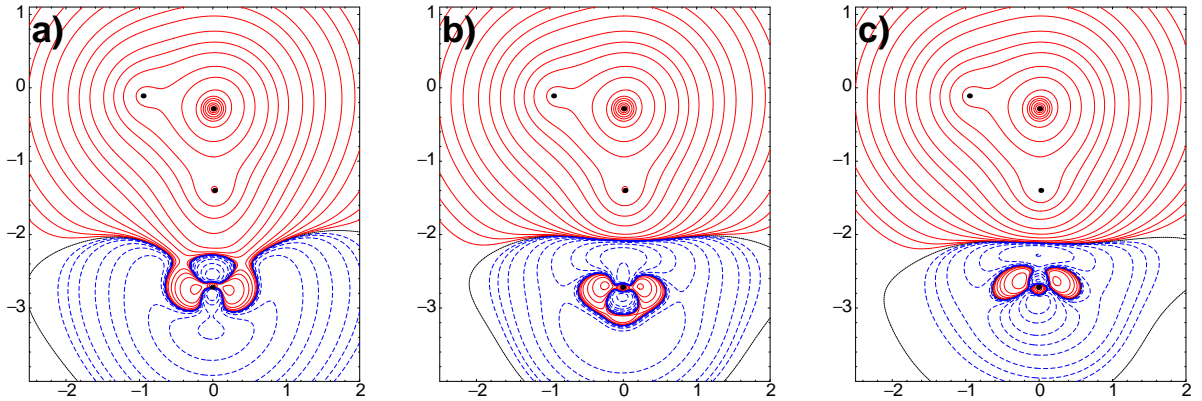


Figure 2.2: Difference densities $\rho_{\text{super}} - \rho_{\text{frag}}(\text{F}^-)$ (a), $\rho_{\text{super}} - \rho_{\text{emb}}(\text{F}^-)$ (b) and $\rho_{\text{super}} - \rho_{\text{emb,gh}}(\text{F}^-)$ (c) for $\text{H}_2\text{O} \cdots \text{F}^-$. Contour lines are drawn at $\pm 2, 4, 8 \times 10^n \text{ e}\text{\AA}^{-3}$ with $n = -4, -3, -2, -1, 0$ and for $0 \text{ e}\text{\AA}^{-3}$ for the difference densities. Positive (including zero) values and negative values are marked by solid and dashed lines, respectively. Atomic positions are indicated by dots.



In order to cure deficiencies in the initial choice of ρ_2 in FDE calculations, Wesolowski

and Weber [117] relaxed the assumption of a fixed electron density ρ_2 by introducing the freeze-and-thaw procedure, as was already mentioned for the general case of many subsystems in Section 2.6.1. Basically, the density ρ_1 resulting from an initial FDE calculation with a fixed ρ_2 is employed as the frozen environmental density in an FDE calculation, in which ρ_2 is now the active subsystem. That results in a new approximation for the environmental density that is polarized w.r.t. ρ_1 . In a subsequent FDE calculation for the optimization of ρ_1 , the v_s -representability condition might be better fulfilled. This procedure can be iteratively repeated, until no more changes occur in the resulting densities.

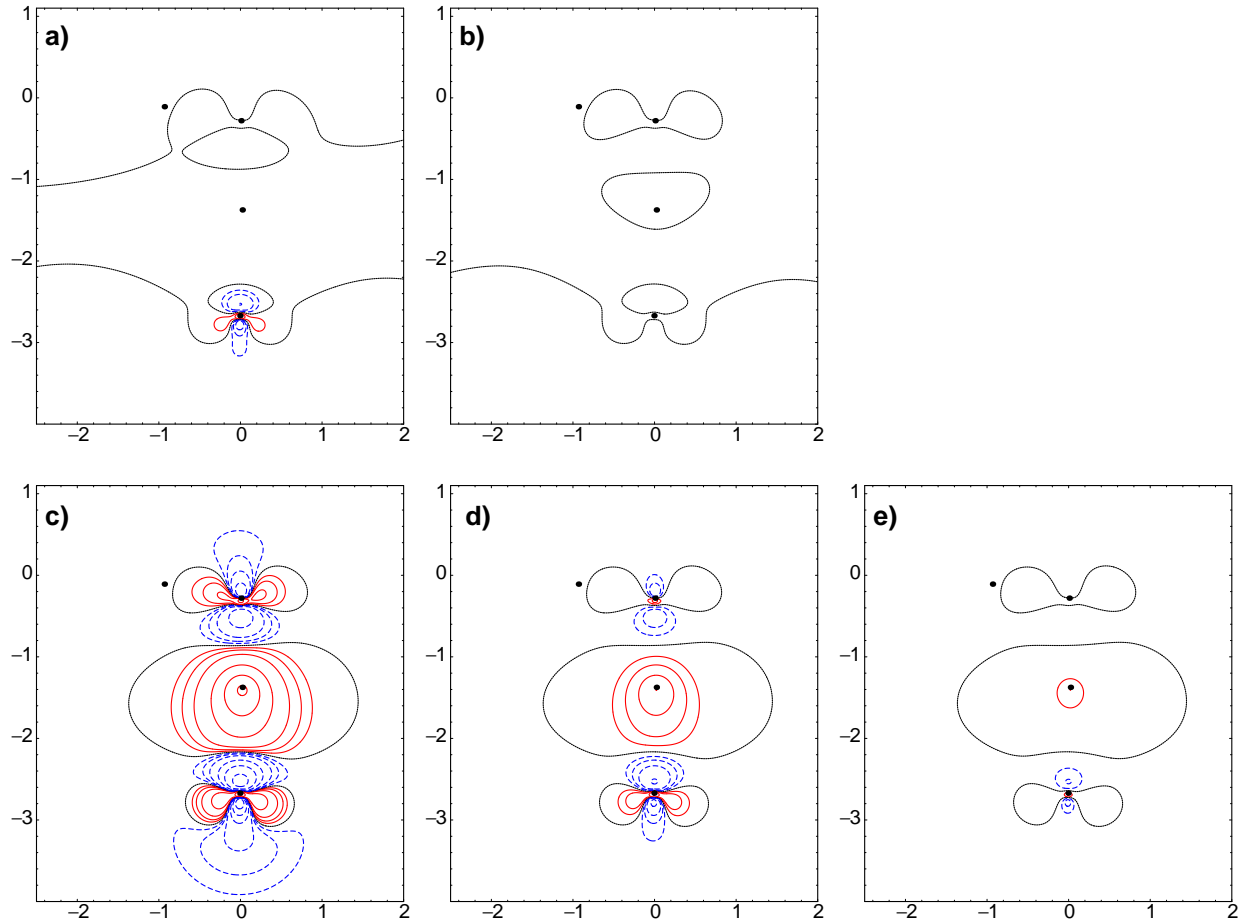
That raises questions concerning the convergence behavior of the freeze-and-thaw cycles. In principle this can be analyzed in two different ways: (i) One iterative series of calculations is performed, in which after each cycle the total density is compared to the total density of the previous cycle. A cycle consists of two calculations, in which first system 2 and then system 1 is frozen. (ii) Two series of freeze-and-thaw iterations are performed, of which the first starts with system 2 frozen, whereas the second starts with system 1 frozen. Here, the total densities of the two series are compared to each other after each iteration. This second approach has the advantage that it can also confirm whether or not both series of calculations converge to the same total density, or if the choice of the initial embedded fragment has an influence on the converged total density. Results for protocol (i) are given in the Supplementary Material to Ref. [118], so that we restrict ourselves to the second approach in the following.

In Figure 2.3 a) and b), the difference densities resulting from freeze-and-thaw cycles starting with a frozen water fragment and from those starting with a frozen fluorine fragment are shown for three and four freeze-and-thaw cycles. After three cycles, the differences are in the order of $10^{-4} \text{ e}\text{\AA}^{-3}$ and after four cycles below $10^{-4} \text{ e}\text{\AA}^{-3}$. I.e., the densities are very well converged. For calculations including ghost basis functions in the frozen region (see also Section 2.9.4) typically more cycles are needed. In Figure 2.3 c) to e), the corresponding difference density plots are shown, in which a TZP ghost basis was included. It can be seen that five cycles are needed to converge the densities to less than $10^{-4} \text{ e}\text{\AA}^{-3}$. Already after three cycles, the maximal difference is smaller than $10^{-2} \text{ e}\text{\AA}^{-3}$ and can be regarded as reasonably well converged for most purposes.

The difference density between ρ_{super} and the converged density of the F^- fragment from the freeze-and-thaw calculation without ghost basis functions in the frozen region, $\rho_{\text{emb}}(\text{F}^-)$, is shown in Figure 2.2 b). It can be seen that the areas in which ρ_1 , i.e., the density of the H_2O fragment, would have to be negative, are clearly diminished when compared to the results for $\rho_{\text{frag}}(\text{F}^-)$ in Figure 2.2 a). But even then, the condition $\rho_{\text{super}} - \rho(\text{F}^-) > 0$ is not fulfilled everywhere. The use of a TZP ghost basis leads to a further improvement in most regions, as can be seen from Figure 2.2 c), but still does not yield a v_s -representable density ρ_1 .

It should be noted that at the end of a freeze-and-thaw procedure the formal difference between the active or embedded subsystem and the environmental system vanishes, and FDE calculations which are fully converged in this respect are equivalent to a subsystem-DFT approach for the special case of two subsystems. Therefore, the acronym FDE is usually applied in a broad sense, which means that the exact conditions for the description of the environment must be provided to clearly define an FDE calculation.

Figure 2.3: Difference densities obtained from freeze-and-thaw calculations with reversed order of fragments (freeze-and-thaw cycles starting with frozen fluorine or with frozen water fragments, respectively) after 3 cycles (a) and after 4 cycles (b) for $\text{H}_2\text{O} \cdots \text{F}^-$ without ghost basis, and after 3 (c), 4 (d) and 5 cycles (e) with a TZP ghost basis. Contour lines are drawn at $\pm 2, 4, 8 \times 10^{-4} \text{ e}\text{\AA}^{-3}$. Atomic positions are indicated by dots.



2.6.4 Electron leak problem

Stefanovich and Truong mentioned the problem of electrons leaking from the embedded system to the atomic cores in the frozen system in FDE calculations [119]. This was explained in terms of an unphysical redistribution of the water electron density to the core region of the fluoride because of the strongly attractive Coulomb attraction. In supermolecular DFT calculations, this is compensated by the orthogonality requirements for the molecular orbitals, which has to be modeled in FDE calculations by the non-additive kinetic energy functional. Obviously, the repulsive effect of the potential term arising from T_s^{nadd} is not strong enough close to the nuclei. Similar observations were made in pure electrostatic embedding schemes [120], where they are typically called *electron spill-out*. The problem is most pronounced in plane-wave applications, where the electrons have the variational freedom to fully delocalize, whereas it is naturally

restricted in (small) localized basis set calculations. In Ref. [120], a pseudopotential-like approach was used to overcome these artifacts within an electrostatically coupled quantum mechanics/molecular mechanics (QM/MM) scheme.

Wesolowski *et al.*, however, reported in Ref. [121] that for the systems studied by Stefanovich and Truong no electron spill-out occurs in FDE calculations, and that flaws in the numerical implementation of the frozen-density embedding scheme in Ref. [119] are probable reasons for the observation of electron leaks. They conclude that localized unoccupied orbitals around the nuclei in the frozen region do not significantly affect the FDE calculations.

However, in a previous study on induced dipole moments in van der Waals complexes [122], similar spurious charge leaking effects were observed in cases where the environment contained atoms with larger nuclear charge numbers (heavier rare-gas atoms or mercury). Jacob *et al.* investigated the functional form of the exact embedding potential at the nuclei of the frozen system in the limit of a large distance to the embedded system, and found that approximations currently in use fail completely to describe the correct behavior [123]. They also demonstrated cases in which this can lead to non-Aufbau solutions or to spuriously low energies for virtual orbitals, which may cause problems in excitation energy calculations, and proposed a pragmatic long-distance correction to circumvent these difficulties. As will be shown in Section 2.9, the electron leak problem can lead to dramatic consequences in cases of transition metal complexes.

2.7 Embedded cluster models

One class of typical applications of embedding approaches are studies on molecules adsorbed on surfaces. A major problem in such investigations is to find an appropriate balance between the (infinite) periodic electronic structure of the solid and the local character at the bonding site of the adsorbed molecule. A possible solution to this problem is the *perturbed cluster* cluster approach. In this approach, the system under study is divided into two subsystems: the cluster, i.e., the adsorption site, and the crystalline environment, i.e., the rest of the crystal. The effect of the crystalline environment is typically introduced as an effective potential, which suggests to use approaches like the FDE scheme for such embedded cluster calculations. Several attempts to use DFT-based embedded cluster methods were made, in which the Coulomb, exchange and correlation potential of the environment was included on the basis of the environmental density. In these models, the effective Pauli repulsion was introduced *ad hoc*, either by employing small basis sets or by adding repulsive core potentials to the atoms around the embedded cluster [124,125]. A relativistic version of this approach was formulated in Ref. [126]. Embedded cluster models using a point charge array to mimic the Madelung field have proven to be helpful in connection with wavefunction methods to obtain ground- and excited-state potential-energy surfaces for small molecules on oxide surfaces (see References in Ref. [127] for cluster-in-cluster embedding methods or “dipped adcluster” embedding). However, this discrete representation of the environmental potential sometimes causes a distortion in the electron density distribution of the embedded cluster [128].

Carter and co-workers developed a wavefunction/DFT embedding scheme [129,130], in which the total electron density is calculated only once at the beginning from a periodic

DFT calculation and is kept fixed afterwards, which assumes that already the DFT calculation results in a good approximation to the correct density of the system. An effective embedding potential is then constructed for which all terms containing the total electron density ρ_{super} and also the kinetic energy contribution involving ρ_1 are kept constant during the calculation. All other terms involving ρ_1 are updated during the SCF. Pseudopotentials are applied for the ion–electron part of the interaction potential. The total energy in this scheme is thus

$$E_{\text{tot}} \approx E_{\text{tot}}^{\text{emb}} = E_I^{\text{WF}} + E_{II}^{\text{DFT}} + E_{\text{int}}^{\text{DFT}}, \quad (2.76)$$

or

$$E_{\text{tot}}^{\text{emb}} = E_{\text{tot}}^{\text{DFT}} + (E_I^{\text{WF}} - E_I^{\text{DFT}}), \quad (2.77)$$

since

$$E_{\text{tot}}^{\text{DFT}} = E_I^{\text{DFT}} + E_{II}^{\text{DFT}} + E_{\text{int}}^{\text{DFT}}. \quad (2.78)$$

The embedding can thus be understood as a local wavefunction-based correction to the total DFT energy in system I . The energy expression in Eq. (2.77) shows a structure similar to that of QM/MM [131–135], or ONIOM-type approaches [136–138].

From the interaction energy, an expression for the embedding potential is derived that is closely related to the one of the frozen-density embedding approach. It enters the wavefunction part of the calculation as an additional term in the Fock operator. For second-order Møller–Plesset perturbation theory (MP2) calculations, nothing else has to be done in addition to a normal MP2 calculation. For single-reference CI methods embedded in DFT, a single transformation step of the one-electron integrals of the embedding potential has to be carried out at the end of the Hartree–Fock calculation. For CASSCF calculations, the MO coefficients change in every CI iteration, so that a transformation of these one-electron integrals has to be performed in each step.

In their initial work [129,130], Carter and co-workers employed a frozen total electron density ρ_{super} , whereas in later work this was replaced by a frozen background (environmental) density ρ_2 [139]. The latter approach is similar to the FDE approach, where also the environmental density ρ_2 is frozen, whereas in the fully variational FDE scheme (i.e., using freeze-and-thaw cycles), both ρ_1 and ρ_2 can vary independently. Huang and Carter recently demonstrated that their embedded cluster model works very well for the description of local electronic structures at adsorption sites of adatoms on metallic surfaces [140]. A formal theoretical analysis of wavefunction-in-DFT embedding approaches is given in Ref. [141], while the importance of embedding approaches for simulations of materials and nanostructures is discussed in Refs. [142,143].

An approach for the treatment of excited states of clusters described by CI or CASSCF wavefunctions, embedded in an infinite periodic crystal described in terms of density-functional theory was proposed in Refs. [144,145] (see also Refs. [146,147]). One problem in the application of this embedding scheme for excited states is that the embedding potential should, in principle, be state-dependent. In Ref. [145], ground-state-density-based embedding operators were applied for the excited states as well, and it was proposed, though not tested, to apply a state-averaged density ρ_1 for the construction of an embedding potential in CASSCF calculations. Also in the later

work, the embedding potential determined (now self-consistently) for the *ground state* was used without further modifications for the excited-state calculations. A similar approach was used by Visscher and co-workers, though not under periodic boundary conditions, in which additional simplifications were introduced by employing a fixed embedding potential in which ρ_1 is not updated during the SCF [148].

In Chapters 3 and 5 it will be outlined how excitation energies can be obtained within the frozen-density embedding scheme or a general subsystem DFT.

2.8 Energetics from frozen density embedding

Many studies on energetics from FDE have been conducted during the past years, which addressed topics such as solvation free energies, interaction energies in hydrogen-bonded systems or van der Waals complexes, and metal–ligand interactions.

One of the first applications of FDE was to estimate the solvation free energy difference of water and methane in water [114]. In this study, the frozen electron density of the solvent water molecules was approximated by a sum of isolated water fragment densities for a number of snapshots from a molecular dynamics (MD) trajectory. The Thomas–Fermi–von Weizsäcker functional T_{TFW} from Eq. (2.18) was applied, in which the parameter λ was varied from 0 to 1. For $\lambda = 2/3$, a very good agreement of the difference in solvation free energies with experiment was obtained. In subsequent work [115], it was demonstrated that in principle also proton transfer reactions for systems of the type $\text{F}-\text{H}\cdots\text{F}^-$ can be studied in solution using FDE in combination with an empirical valence bond (EVB) reference potential. Although the absolute energy differences between FDE and KS-DFT calculations were as large as 100 kJ/mol, the shapes of the potential energy curves for proton abstraction, and thus the abstraction energies, were in much better agreement.

Free energy calculations employing frozen-density embedding techniques were also reported by Warshel and co-workers for the autodissociation of water in aqueous solution and proton transfer reactions involving methanol [149,150]. For these purposes, the FDE approach was integrated into a QM/MM framework [149], which was later also used for studies on the reduction potential of proteins [151]. For the study in Ref. [150], FDE was applied in order to describe particular valence bond structures, so that diabatic states could be defined for use in the EVB method [152]. This combined approach was also applied to study the solvent dependence of the off-diagonal elements of the EVB Hamiltonian for $\text{S}_\text{N}2$ reactions, which was found to be rather small [153]. The mechanism of the nitrate reduction by nitrate reductase models was studied in Ref. [154], where FDE was applied to model the protein environment in terms of small peptide fragments. In particular the relative energies of singlet and triplet states in the molybdenum-containing active center under influence of the protein were analyzed. FDE was compared to the ONIOM approach in that study, and only small differences could be detected. This result is probably due to the fact that FDE or ONIOM were only used to represent the environment, which was not directly involved in the reaction.

In a study on hydrogen-bonded complexes, Wesolowski found in 1997 [155] that gradient-corrected kinetic energy functionals, in particular the reparameterized PW91k functional, give good results for the interaction energies in comparison to KS-DFT reference calculations. In contrast to this, the Thomas–Fermi functional resulted in poor agreement

with KS calculations. It was concluded that the Thomas–Fermi functional does not provide a sufficiently good approximation to T_s^{nadd} . Interaction energies obtained with the PW91k functional agreed typically within less than 1.5 kJ/mol. It is interesting to note that the non-additive kinetic energy for these hydrogen-bonded dimers contributes between 20 to 40 kJ/mol around the equilibrium distance of the dimers. For distances > 4 to 5 Å, where the density overlap is typically small, KS and FDE energies agree very well for all functionals.

Stefanovich and Truong [119] compared the Thomas–Fermi kinetic energy expression with the more advanced, gradient-corrected approximation suggested by Thakkar [68]. They studied several small systems composed of two closed-shell molecules, atoms, or ions. For the He dimer, they found worse agreement than the original Gordon–Kim calculation, which underlines the role of error cancellation effects in the Gordon–Kim model. Of particular interest are the systems $X^- \cdots \text{H}_2\text{O}$ with $X = \text{F}, \text{Cl}$. For the fluoride system, a strong decrease of the total energy was observed for distances smaller than 1.5 Å. A similar observation was made for the chloride system. This could be explained in terms of an unphysical redistribution of the water electron density to the core region of the fluoride because of the strongly attractive Coulomb attraction. But as mentioned before, the FDE implementation in Ref. [119] apparently resulted in numerical instabilities, and the observed effect could not be reproduced with a different implementation of the FDE scheme [121].

The accuracy of LDA and GGA functionals for exchange–correlation and non-additive kinetic energy in FDE calculations of interaction energies in hydrogen-bonded complexes was further investigated in Ref. [60]. In this case, the results were analyzed in comparison to accurate coupled cluster or symmetry-adapted perturbation theory calculations. For a test set consisting of different stationary points on the potential energy surface of the water dimer, seven points with varying angle between the two water molecules, as well as three other hydrogen bonded complexes, average absolute errors of 3.18 and 1.05 kJ/mol were found for fully variational GGA and LDA calculations, respectively. In non-variational calculations — which are similar in spirit to the Gordon–Kim model, but start from KS rather than HF densities and may employ gradient corrected functionals — the GGA interaction energies turned out to be more accurate than the LDA energies. In a study on van der Waals complexes, the PW91 kinetic energy functional turned out to yield reliable results when compared to KS calculations [156]. Good agreement with experimental and MP2 results were reported for complexes like $\text{C}_6\text{H}_6 \cdot \text{O}_2$ or $\text{C}_6\text{H}_6 \cdot \text{N}_2$. The contribution of the non-additive kinetic energy at the equilibrium distances was found to be of the order of 10 to 20 kJ/mol. It turned out that FDE calculations are less sensitive to basis set effects than supermolecular KS calculations presented for the same systems before in Ref. [157].

Van der Waals complexes with weakly overlapping densities were studied in Ref. [158]. In that study, LDA or GGA functionals were used consistently for both the exchange–correlation and the kinetic energy contribution. The accuracy observed for GGA-FDE interaction energies was higher than that of LDA-FDE calculations when compared to *ab initio* data; the average absolute errors found for the test set studied in Ref. [158] were 1.21 kJ/mol (GGA) and 1.84 kJ/mol (LDA). For complexes with very small density overlap, however, the LDA interaction energies were superior to GGA-type functionals for E_{xc} and T_s^{nadd} . As another important result, GGA-FDE calculations agreed better

with the accurate *ab initio* data than KS-DFT. This was confirmed in an investigation of carbazole complexes [159] and in a study on the physisorption behavior of H₂ on polycyclic aromatic hydrocarbons (PAHs) [160]. Another study concerning π -stacking interactions on the basis of FDE has been presented in Ref. [161]. While it is known that Kohn–Sham DFT has problems in describing dispersion interactions unless special care is taken [50, 162–164], it could be shown that FDE provides more accurate interaction energies for the benzene dimer than MP2 calculations, when taking CCSD(T) data as a reference [165].

Some progress for the application of FDE to transition metals has been made, with the final goal of modeling metal-catalyzed reactions. In Ref. [166] it was shown that potential energy curves for proton abstraction reactions can reliably be modeled. However, the error of the FDE interaction energy in comparison to KS-DFT depends strongly on the distance of the broken bond to the border of the two subsystems. The frozen system in this case was the set of non-reactive ligands, whereas the metal center, the proton-donating water ligand, and an additional proton-accepting water molecule were chosen as the active system. For the proton transfer reaction itself, the interaction energies obtained were in very good agreement with the reference values, but in this case no bond to an atom at the border of the two subsystems was broken. The results were considerably worse if the distance between the proton-donating water ligand and the Zn²⁺ center was varied. Several different approximations for the ligands’ density $\rho_2(\mathbf{r})$ were tested in that case, e.g., a sum of (individually) prepolarized fragments. It turned out that typically this prepolarization is only necessary for one point on the potential energy curve, and the fragment densities thus obtained can be applied for all structures, at least in cases where there is no structural change involving the frozen ligands.

FDE has also been applied recently to study orbital energy splittings in lanthanide complexes [167, 168]. It was demonstrated that it can serve as a non-empirical alternative to empirical crystal-field or ligand-field splitting models. In these types of applications FDE can partly cure the problem of too large covalent contributions or too large mixing between *f* orbitals of the cation and ligand orbitals present in conventional DFT calculations. This particular point was subject of another recent study, in which the restriction to localized embedded orbitals was lifted [169].

A summary of the results obtained with FDE for interaction energies can thus be given as follows (see also the discussion in Ref. [170]): FDE employing LDA functionals for both E_{xc} and T_s^{nadd} leads to very good interaction energies for weakly overlapping densities, such as in rare gas dimers or the CH₄⋯CH₄ complex. For interactions involving hydrogen-bonded systems, GGA-type approximations result in closer agreement with KS-DFT calculations [155], while the study in Ref. [60] showed that the agreement with *ab initio* reference data for the systems studied there was better within the local density approximation. In systems where π -interactions are important, LDA does not lead to satisfactory results, and GGA-type functionals lead to significant improvements. The description of metal–ligand interactions is typically considerably more difficult.

2.9 Comparison of electron densities from Kohn–Sham and subsystem DFT

2.9.1 Topological analyses of electron densities

As mentioned before, the electron density can be regarded as a fundamental quantity for the description of matter according to the Hohenberg–Kohn theorem. In addition to quantitative calculations within density functional theory, recent work also highlights the role of the density for qualitative analyses of electronic structure and an understanding of chemical bonding in molecules, see Refs. [7,10,11]. Topological analyses of hydrogen-bonded systems have been carried out in the recent past to develop criteria for the detection of hydrogen bonds [171], to investigate the distance dependence of the electron-density topology [172], or to study the relationship between the topology and energetic properties of hydrogen bonds [173]. These theoretical approaches also gain increasing importance in transition metal chemistry; for a review see Ref. [174] as well as the recent studies in Refs. [175,176] and references therein. One interesting aspect of such analyses is the attempt to relate properties of a chemical system to those of certain constituents, e.g., molecules within a supermolecule or functional groups within molecules [177]. That such a decomposition is essential for chemical concepts is apparent in the discussion of coordination compounds in terms of an electron acceptor (e.g., a central metal ion) and electron donating ligands, which becomes manifest in crystal- or ligand-field theory. The electron density can be employed to study the effect of the ligands on the metal center, as was done in Refs. [167,169] on the basis of FDE (see also Section 2.8).

In spite of its pragmatic use as an effective environmental model, FDE should lead to the exact density of a system if the exact kinetic and exchange–correlation energy functionals were known and the density to be optimized fulfilled the v_s -representability criteria (see Section 2.5.1). The approximate functionals for the kinetic-energy component that have to be used in practice, however, limit the applicability of the FDE scheme to rather weakly interacting systems. More strongly interacting subsystems, e.g., systems connected by a covalent bond, cannot be appropriately described by the presently available approximations. However, it has not been explored in detail where the limits of these approximate functionals are. Most of the previous studies assessed the accuracy of FDE calculations in an indirect way, e.g., by analyzing their accuracy for properties, energies, or structures. Brief analyses of the electron density deformation from FDE and supermolecular calculations were presented for the $\text{FH}\cdots\text{NCH}$ complex in Ref. [117] and for the $\text{Li}^+-\text{H}_2\text{O}$ complex in Ref. [119], although the latter study apparently contained some numerical flaws [121].

In the following, an analysis of the differences in the topology of electron densities obtained from FDE calculations and from Kohn–Sham DFT calculations will be carried out. This is necessary in order to gain a more detailed understanding of factors affecting the accuracy of embedding calculations. For that purpose, we investigate a set of molecules with hydrogen-bonding interactions, i.e., the rather strongly bound systems $\text{HOH}\cdots\text{F}^-$ and $\text{F}-\text{H}-\text{F}^-$, and subsystems connected by coordination bonds. Even though there are a few applications of FDE to such systems, e.g., for MnF_6^{4-} [168], lanthanide complexes [167,169], or zinc complexes [166], subsystems connected by donor–acceptor bonds represent a big challenge and push the currently available approximations

for the non-additive kinetic energy to their limits.

After a brief outline of tools for the analysis of electron density distributions in Section 2.9.2, different criteria for the assessment of densities for the $\text{H}_2\text{O}\cdots\text{F}^-$ complex for a typical setup as employed in practical FDE calculations are compared in Section 2.9.3. Since such calculations involve both numerical approximations as well as more fundamental approximations concerning the energy functionals employed, the different factors that determine the performance of FDE separately in terms of their impact on the electron-density topology are analyzed in Section 2.9.4. The symmetric hydrogen-bonded system $\text{F}-\text{H}-\text{F}^-$ is analyzed in Section 2.9.5. As representative examples of such cases, we consider the metal complexes TiCl_4 and $\text{Cr}(\text{CO})_6$ in a subsequent section.

2.9.2 Tools for the analysis of electron densities

Since already the superposition of isolated molecular densities produces a density similar to that of the interacting complex in many cases, difference (or deformation) densities as well as the negative Laplacian of the electron density are employed as more sensitive diagnostic tools. The ability to model the binding region between the subunits in the FDE calculations is furthermore analyzed by a topological analysis of the electron density according to the theory of atoms in molecules [7]. It provides detailed insight into the electronic structure of molecules and solids that has in the past been utilized for many different purposes [178], such as analyzing the bonding scenario in transition metal ethylene and acetylene complexes [179,180] and deriving a new concept to describe agostic interactions in early transition metal complexes [174].

The topology of an electron density distribution can be summarized by a characteristic set of critical (i.e. stationary) points [7]. The so-called bond critical point (BCP) is the saddle point found between two bound atoms in a molecule, i.e., it is the minimum on a line connecting the local maxima of the electron density which correspond to the atomic positions. A second type of critical point, the ring critical point (RCP), is found when atoms form a ring structure like in benzene. The values of the electron densities at these critical points can, together with the values of the negative Laplacian, be used to characterize a chemical bond. The negative Laplacian of the electron density, $L(\mathbf{r}) = -\nabla^2\rho(\mathbf{r})$, is a measure of the curvature of the electron density at a given point. These two topological parameters, $\rho(\mathbf{r})$ and $L(\mathbf{r})$ at the critical points allow for a direct bond characterization. A positive value of $L(\mathbf{r})$, which indicates a local concentration of the electron density within the bonding region, is found for covalent bonds. Analogous to $\rho(\mathbf{r})$ stationary points can also be identified and characterized in the topology of $L(\mathbf{r})$. Of special importance are the local maxima in the positive regions of the negative Laplacian, the so-called local charge concentrations. In compounds containing only main group elements two types of local charge concentrations can be identified. The *bonding* charge concentrations are found in the valence regions of atoms connected by a covalent bond, while the *non-bonding* charge concentrations are observed at the positions where free electron pairs are located. In the following, we will refer to the latter type of maxima in short as “charge concentrations”.

The two subunits connected by hydrogen bonds were chosen as the fragments in the FDE calculations, i.e., the hydrogen bonding region forms the boundary between the subsystems. Both the density and $L(\mathbf{r})$ are linear, so that their values for a superposition

of fragment densities can be obtained by adding up the corresponding values for the subsystems. The densities of the fragments and the supermolecule were obtained on the same grid for each complex under study. The electron density and the negative Laplacian $L(\mathbf{r})$ were obtained on a grid of points (step-size 0.01 Å) from a locally modified version of the DENSF-utility program of the ADF package. The search for stationary points in the electron density was performed with the program INTEGRITY [181]. The isocontour plots of the difference densities and $L(\mathbf{r})$ were prepared using a MATHEMATICA script [182,183]. In the following figures, contour lines are drawn at $\pm 2, 4, 8 \times 10^n \text{ e}\text{\AA}^{-3}$ with $n = -2, -1, 0, 1, 2, 3$ for the densities, with $n = -4, -3, -2, -1, 0$ and for $0 \text{ e}\text{\AA}^{-3}$ for the difference densities, and at $\pm 2, 4, 8 \times 10^n \text{ e}\text{\AA}^{-5}$ with $n = -4, -3, -2, -1, 0, 1, 2$ for the negative Laplacians if not explicitly mentioned otherwise. Positive (including zero) values and negative values are marked by solid and dashed lines, respectively. Coordinates are given in units of Å. Atomic positions and bond critical points are marked by dots and open circles, respectively.

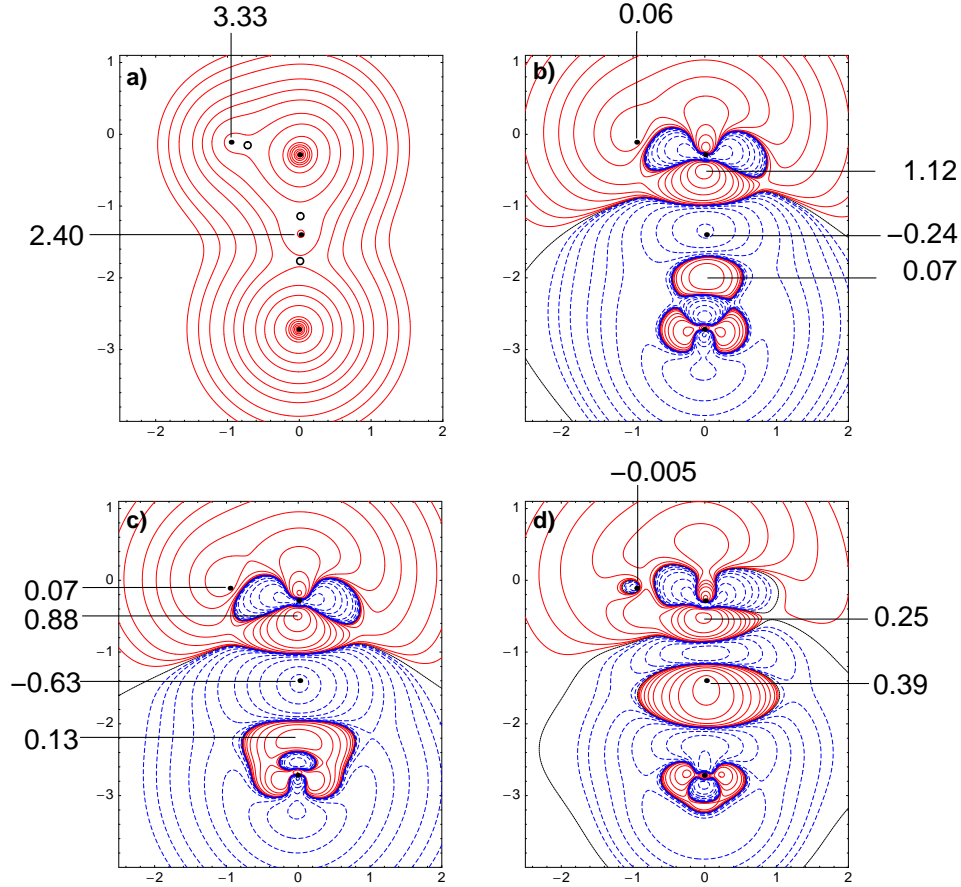
2.9.3 Criteria for the accuracy of electron densities

In this section the criteria for assessing the quality of FDE densities will be applied to the hydrogen-bonded complex of water and a fluoride ion as an example. This complex was introduced in Section 2.6.3, and its structure is shown in Figure 2.1. Subsystem densities were obtained using a TZP basis set after three freeze-and-thaw cycles. A subsystem basis set was employed in each calculation in this section; note that this is an approximation, since a supermolecular basis set is in principle needed in order to provide full flexibility for a polarization of a subsystem density by the other subsystem (see Section 2.9.4). The choice of this type of basis set was motivated by the fact that actually most practical applications of FDE as an environmental model do, similarly to QM/MM hybrid methods, not employ basis functions in the environmental region. The results in this section thus allow an assessment of the densities obtained in such calculations where FDE is applied as an approximate environmental model. But it must be kept in mind that they do not allow an assessment of the limitations of this subsystem approach to reproduce the electron densities from supermolecular KS calculations *in principle*, which requires to carefully distinguish between purely technical approximations (basis sets, convergence of freeze-and-thaw cycles) and fundamental approximations in the energy functionals applied. These effects will be analyzed in Section 2.9.4. Note that we will use the term “embedding densities” in the following for the sum of the two subsystem densities obtained from the FDE calculations. We employed the BP86 functional for the exchange–correlation part of the embedding potential, while for the non-additive kinetic energy contribution the PW91k functional was chosen as default (see Appendix B for details). These settings correspond to a standard FDE calculation that usually gives good results for molecular properties [116,184,185]. The effect of changes to these defaults will be investigated in the subsequent sections.

Probably the most obvious way to compare electron densities is to present them in a map, e.g. by plotting isodensity values in a plane. This is shown in Figure 2.4 a) for the density in the molecular plane of $\text{H}_2\text{O} \cdots \text{F}^-$, obtained in a KS-DFT calculation of the supermolecule (ρ_{super}). This map can then be compared to the densities obtained by summing up the subsystem densities from the embedding calculation, ρ_{emb} , or from

the isolated fragments' densities, ρ_{frag} . The fragments in this case are an H_2O molecule and an F^- ion. The corresponding plots for ρ_{frag} and ρ_{emb} are very similar to ρ_{super} , and no differences can be found upon visual inspection. They are therefore not presented here. Thus, this direct approach does not offer a sensitive criterion for the assessment of the differences in the density.

Figure 2.4: Density ρ_{super} (a) and deformation densities $\rho_{\text{super}} - \rho_{\text{frag}}$ (b), $\rho_{\text{emb}} - \rho_{\text{frag}}$ (c) and difference density $\rho_{\text{super}} - \rho_{\text{emb}}$ (d) for $\text{H}_2\text{O} \cdots \text{F}^-$.

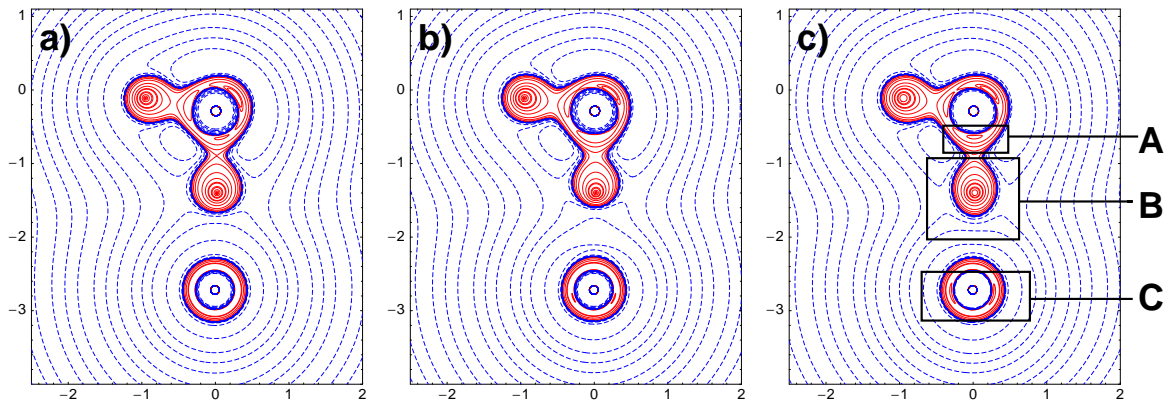


For a more detailed analysis of the FDE electron densities, we considered deformation densities, i.e. the difference between ρ_{super} and ρ_{frag} or ρ_{emb} and ρ_{frag} . These deformation densities show changes in the density upon formation of the $\text{H} \cdots \text{F}$ bond. Additionally, we also studied the difference densities $\rho_{\text{super}} - \rho_{\text{emb}}$. This offers the possibility to detect subtle deviations between the FDE and supermolecular KS electron densities in a locally resolved manner. In Figures 2.4 b) to d) deformation and difference densities are depicted for $\text{H}_2\text{O} \cdots \text{F}^-$. In part b) the deformation density upon formation of the hydrogen bond between the fluoride ion and the water molecule is presented for the supermolecular KS case. The difference density in the fluorine subsystem is positive in a ring around the fluorine ion perpendicular to the plotting plane, which originates from the electron lone pairs. It is also positive in the middle of the $\text{H} \cdots \text{F}$ connection line, while the remaining part in this subsystem is negative. In the water subsystem, the

difference density is negative around hydrogen atom H2 and in a region perpendicular to the bond axis on the oxygen, but positive elsewhere. In comparison to the two isolated subsystems, the electron density around the oxygen atom and the fluorine ion appear to be polarized towards the connecting hydrogen atom in the hydrogen-bonded complex. The corresponding difference density for the embedding calculation is shown in Figure 2.4 c). In this case, the two regions of positive difference densities around the fluorine ion are overlapping and less localized than in the supermolecular calculation. In particular, the density deformation is less directed towards the hydrogen bonding region. Nonetheless, the qualitative features of the deformation density plot agree with the supermolecular case, although it can be recognized from the data points included in Figure 2.4 that quantitative differences remain.

A direct comparison between ρ_{super} and ρ_{emb} is possible by analyzing their difference density, which is shown in Figure 2.4 d). The density ρ_{emb} in the $\text{F} \cdots \text{H2}-\text{O}$ region is too low around atom H2, but too high towards the fluorine ion and too high on the $\text{O}-\text{H2}$ bond close to H2. Regarding the changes perpendicular to the bond axis at the atoms O and F, ρ_{emb} is too high around O and too low around F. Upon formation of the bond, density appears to be shifted from this region to the hydrogen bond. Although this shift is qualitatively captured by FDE, the detailed structure of the density in the bonding region is not fully reproduced, since not enough density is transferred from the region around hydrogen atom 1 towards the hydrogen bond. The embedding calculation can thus not fully reproduce the polarization of the water molecule and the fluorine atom upon bond formation.

Figure 2.5: Negative Laplacian L_{frag} (a), L_{emb} (b) and L_{super} (c) for $\text{H}_2\text{O} \cdots \text{F}^-$. Contour lines in addition to those mentioned in Section 2.9.2 are drawn at 0, 70 and $158 \text{ e}\text{\AA}^{-5}$.



A sensitive and locally resolved probe for the differences in electron densities is the negative Laplacian. In Figure 2.5 the negative Laplacians L_{frag} , L_{emb} and L_{super} are depicted. In L_{frag} , the fluorine fragment appears spherically symmetric. Since the same geometric structure as in the hydrogen-bonded complex was used for the water molecule, the two $\text{O}-\text{H}$ bonds are not equivalent, e.g. the bonding charge concentration on the $\text{O}-\text{H2}$ bond is smaller than on the $\text{O}-\text{H1}$ bond. In L_{emb} , the Laplacian in the region of hydrogen atom H2, region B in Figure 2.5 c), looks similar to the unperturbed L_{frag} , but

the region of local charge concentration descends steeper and does not extend as far to the fluorine atom as in L_{frag} or L_{super} . In L_{super} , this local charge concentration descends more symmetrically to both sides of the $\text{F}\cdots\text{H2}-\text{O}$ connection line. Moreover, the bonding charge concentration on the oxygen atom towards H2, shown by an additional contour line at $70\text{ e}\text{\AA}^{-3}$ in Figure 2.5 c), region A, is higher than towards H1. Further maxima of the local charge concentration can be found in region C in Figure 2.5 c), shown by the contour lines at $158\text{ e}\text{\AA}^{-3}$. In L_{emb} , this ring is much less pronounced and the bonding charge concentration in region A is much smaller, but still visible. Topological parameters at the BCPs (cf. Figure 2.1) are listed in Table 2.1. The most significant differences can be seen at BCP3, which is located on the hydrogen bond where the system is divided into subsystems for FDE. The approximate ρ_{emb} obtained with the particular setup used here, i.e., without ghost basis functions in the environmental system, seems to yield worse results than ρ_{frag} for the topological parameters, as the coordinates of BCP3 are too close to the hydrogen atom and values of the density and $L(\mathbf{r})$ show larger deviations from ρ_{super} than those of ρ_{frag} .

Table 2.1: Coordinates \mathbf{r}_{BCP} (in units of \AA) of the BCPs and values of $\rho(\mathbf{r})$ in $\text{e}\text{\AA}^{-3}$ and $L(\mathbf{r})$ in $\text{e}\text{\AA}^{-5}$ at the BCPs of $\rho(\text{H}_2\text{O}\cdots\text{F}^-)$ calculated with different approximations (supermolecular density ρ_{super} , embedding density ρ_{emb} and superposition of the isolated fragment densities ρ_{frag}).

		$\mathbf{r}_{x,\text{BCP}}$	$\mathbf{r}_{y,\text{BCP}}$	$\rho(\mathbf{r}_{\text{BCP}})$	$L(\mathbf{r}_{\text{BCP}})$
BCP 1	ρ_{super}	-0.72	-0.15	2.32	10.3
	ρ_{emb}	-0.72	-0.15	2.32	10.4
	ρ_{frag}	-0.73	-0.15	2.33	11.5
BCP 2	ρ_{super}	0.02	-1.14	1.52	5.20
	ρ_{emb}	0.02	-1.17	1.52	7.96
	ρ_{frag}	0.01	-1.11	1.63	4.94
BCP 3	ρ_{super}	0.01	-1.77	0.75	-0.68
	ρ_{emb}	0.01	-1.73	0.55	-2.20
	ρ_{frag}	0.01	-1.79	0.72	-1.98

With increasing distance from the hydrogen bond, the differences in the topological parameters disappear. While at BCP2 the density is virtually the same for ρ_{super} and ρ_{emb} and only the negative Laplacians differ, at BCP1 both values are nearly identical for the two approaches. Therefore, we will in further discussions concentrate on BCP2 and BCP3 only. As will be shown in Section 2.9.4, the comparatively bad results of the FDE scheme for some of the topological parameters are partly due to the use of a monomer (i.e. subsystem) basis set in these calculations.

2.9.4 Factors affecting the quality of the density

In this section, we briefly analyze different factors which determine the overall accuracy of the electron density in frozen-density embedding calculations in comparison to supermolecular KS calculations. Among the numerical approximations made are the

number of freeze-and-thaw cycles, which were studied in Section 2.6.3 and will thus not be considered here, and the basis set. Additionally, we address questions related to the choice of the kinetic energy functional employed for the embedding potential.

Basis sets

FDE describes the polarization of densities under the influence of an environment, for which a flexible basis set is needed [186]. For the preceding results in this section, we only considered monomer (or subsystem) basis sets, in which the molecular orbitals $\phi_{i_{1/2}}$ in systems 1/2 are expanded in terms of basis functions ξ localized within the respective fragment only, i.e.,

$$\phi_{i_1} = \sum_{\nu_1} c_{i_1\nu_1} \xi_{\nu_1}, \quad (2.79)$$

$$\phi_{i_2} = \sum_{\nu_2} c_{i_2\nu_2} \xi_{\nu_2}. \quad (2.80)$$

Here, $\nu_{1/2}$ label the basis functions in systems 1/2, and $c_{i_n\nu_n}$ are the expansion coefficients. A remaining problem might therefore be that the basis is not flexible enough in the region of the frozen subsystem in order to allow for a sufficient transfer of electron density from one system to the other, so that a supermolecular basis set might be required for a quantitative modeling. In that case, the molecular orbitals would be expanded as,

$$\phi_{i_{1/2}} = \sum_{\nu_1} c_{i_{1/2}\nu_1} \xi_{\nu_1} + \sum_{\nu_2} c_{i_{1/2}\nu_2} \xi_{\nu_2}. \quad (2.81)$$

Although both sets of basis functions contribute to the total electron density in both approaches, the expressions for the density in terms of the basis functions differ. In the supermolecular expansion, Eq. (2.81), we obtain,

$$\rho = \sum_{i_1} \left| \sum_{\nu_1}^{\text{occ}_1} c_{i_1\nu_1} \xi_{\nu_1} + \sum_{\nu_2} c_{i_1\nu_2} \xi_{\nu_2} \right|^2 + \sum_{i_2} \left| \sum_{\nu_1} c_{i_2\nu_1} \xi_{\nu_1} + \sum_{\nu_2}^{\text{occ}_2} c_{i_2\nu_2} \xi_{\nu_2} \right|^2, \quad (2.82)$$

where the sums over $i_{1/2}$ run over all occupied orbitals of subsystem 1/2. Cross-terms of the form $d \cdot \xi_{\nu_1} \xi_{\nu_2}$ thus contribute to the density, where d is a product of expansion coefficients for systems 1 or 2. These terms are missing in the monomer expansion, where the density is expressed as,

$$\rho = \sum_{i_1}^{\text{occ}_1} \left| \sum_{\nu_1} c_{i_1\nu_1} \xi_{\nu_1} \right|^2 + \sum_{i_2}^{\text{occ}_2} \left| \sum_{\nu_2} c_{i_2\nu_2} \xi_{\nu_2} \right|^2. \quad (2.83)$$

It is well known that the results of FDE calculations typically depend much more strongly on the availability of ghost basis functions in the frozen region than on the particular atomic basis set [118,186]. Therefore, we will only address the second point

here. Table 2.2 lists the topological parameters at the BCPs for different ghost basis sets. The densities obtained from such calculations are denoted as $\rho_{\text{emb,gh}}$.

Table 2.2: Basis set dependence of the coordinates \mathbf{r}_{BCP} (in units of Å) of BCP2 and BCP3 in $\text{H}_2\text{O}\cdots\text{F}^-$ and of $\rho(\mathbf{r})$ in $e\text{\AA}^{-3}$ and $L(\mathbf{r})$ in $e\text{\AA}^{-5}$ at the BCPs obtained with different approximations (ρ_{super} , ρ_{emb} , $\rho_{\text{emb,gh}}$); ghost basis sets in the boundary region only are indicated by “(bd)”. Three freeze-and-thaw cycles were used for ρ_{emb} and $\rho_{\text{emb,gh}}$.

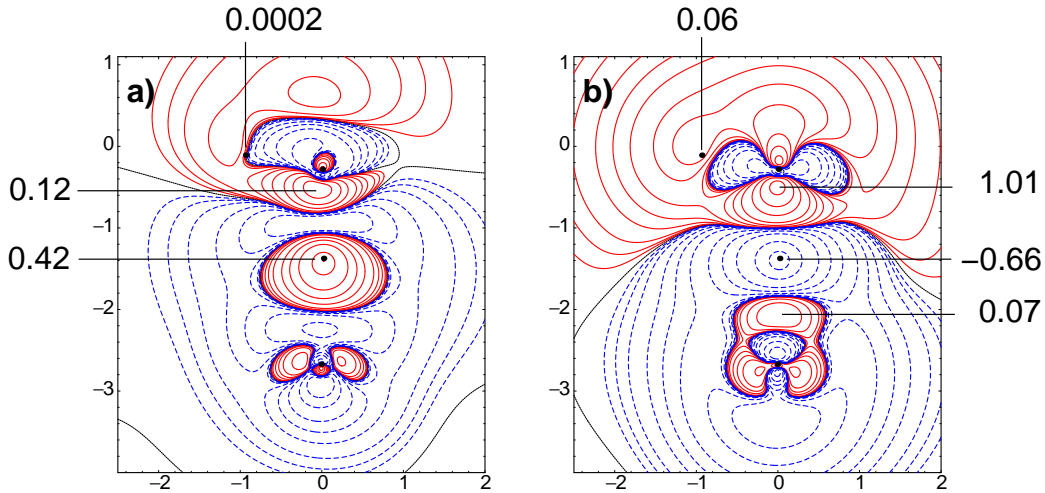
	basis	$\mathbf{r}_{x,\text{BCP}}$	$\mathbf{r}_{y,\text{BCP}}$	$\rho(\mathbf{r}_{\text{BCP}})$	$L(\mathbf{r}_{\text{BCP}})$
BCP 2	TZP	0.02	−1.14	1.52	5.20
	ρ_{emb} TZP	0.02	−1.17	1.52	7.96
	$\rho_{\text{emb,gh}}$ TZP/DZP (bd)	0.02	−1.17	1.47	7.39
	TZP/DZP	0.02	−1.17	1.47	7.33
	TZP/TZP	0.02	−1.17	1.48	7.33
BCP 3	ρ_{super} TZP	0.01	−1.77	0.75	−0.68
	ρ_{emb} TZP	0.01	−1.73	0.55	−2.20
	$\rho_{\text{emb,gh}}$ TZP/DZP (bd)	0.01	−1.73	0.66	−0.86
	TZP/DZP	0.01	−1.74	0.66	−0.85
	TZP/TZP	0.01	−1.74	0.66	−0.80

Although the precise values of the topological parameters depend on the particular combination of basis set on the embedded fragment and ghost basis on the frozen fragment, the calculations employing ghost basis sets typically lead to much better results than any of the calculations with a monomer basis set. An exception is the density at BCP2, which is slightly underestimated by the calculations with ghost basis functions, whereas the results without ghost basis functions are in good agreement with the KS reference values. The value of the Laplacian at BCP3 is an instructive example: It changes from $-2.20 e\text{\AA}^{-5}$ (TZP, monomer basis set) to $-0.80 e\text{\AA}^{-5}$ (TZP plus TZP ghost basis, in the following denoted as TZP/TZP), thus reducing the deviation from the reference from 1.52 to 0.12 $e\text{\AA}^{-5}$. The results also demonstrate that a DZP ghost basis is already sufficiently large, since the additional changes when going from a DZP to a TZP ghost basis are rather small.

To further analyze the effect of the ghost basis set we calculated the difference density between ρ_{super} (TZP) and $\rho_{\text{emb,gh}}$ (TZP/TZP), which is shown in Figure 2.6. Compared to Figure 2.4 d) it can be seen that the absolute differences in the $\text{F}\cdots\text{H}-\text{O}$ bonding region are smaller than in the calculation without the ghost basis functions, with the exception of the maximum of the difference density near H2, which is slightly higher in $\rho_{\text{super}} - \rho_{\text{emb,gh}}$ than in $\rho_{\text{super}} - \rho_{\text{emb}}$ ($0.42 e\text{\AA}^{-3}$ compared to $0.39 e\text{\AA}^{-3}$). In particular the size of the region around H2 in which the FDE electron density is too small, is decreasing, and the absolute values of the difference density are smaller in the region of negative difference density between H2 and the fluorine atom. Moreover, the density close to the fluorine ion on the side opposite to the hydrogen bond is apparently better described. The ghost basis set obviously allows for a better transfer of charge from the F^- to the H_2O fragment. Although there are still pronounced differences between

ρ_{super} and $\rho_{\text{emb,gh}}$, the ghost basis set leads to a significant improvement of the density obtained in the FDE calculation.

Figure 2.6: Difference density $\rho_{\text{super}} - \rho_{\text{emb,gh}}$ (a), and deformation density $\rho_{\text{emb,gh}} - \rho_{\text{frag}}$ (b) for $\text{H}_2\text{O} \cdots \text{F}^-$, using a TZP ghost basis and five freeze-and-thaw iterations in the FDE calculations.



Providing ghost basis functions on all atoms of the frozen fragment ρ_2 counteracts the advantages of a subsystem formalism, since it increases the basis set size for each subsystem calculation to that of the supersystem. Since our intention was to increase the flexibility of the basis to accurately describe the polarization of one subsystem by another one, it might be sufficient to provide ghost basis functions only in the boundary region between the two subsystems. We tested this by performing FDE calculations in which a minimal ghost basis was supplied, i.e., a DZP basis on the atom next to the boundary between the two subsystems only (F or H2, respectively). The results for the topological parameters are shown in Table 2.2, denoted as $\rho_{\text{emb,gh}}$ TZP/DZP (bd); they are virtually the same as in the case of the full ghost basis. It must of course be noted that even the “minimal basis” in this case already represents a large part of the full ghost basis, especially in case of F^- as the frozen system. Nevertheless, we can conclude that the basis set in the frozen region may be of lower quality than the one in the embedded region.

Choice of the kinetic-energy functional

The choice of the (non-additive) kinetic-energy functional is important for the differences between KS-DFT and FDE that have to be expected. Several approximate functionals are available, and we tested the following ones: The PW91k functional as described above, the Thomas–Fermi functional (TF) [54,55], and a purely electrostatic embedding (i.e., exchange–correlation and kinetic-energy components of the embedding potential were switched off), which is denoted as COULOMB. Additional functionals have been investigated in Ref. [118].

The results obtained for the topological parameters of $\text{H}_2\text{O}\cdots\text{F}^-$ are listed in Table 2.3. For the calculations with supermolecular basis sets we employed a TZP ghost basis and five freeze-and-thaw cycles, whereas three cycles were applied in calculations without ghost basis sets. The TF and PW91k data do not differ very much. The coordinates of the BCPs are virtually the same, the densities agree within $0.01\text{ e}\text{\AA}^{-3}$, and the Laplacian values are very similar for BCP3. Only at BCP2 the values for $L(\mathbf{r})$ from PW91k and TF without ghost basis functions differ by about $0.18\text{ e}\text{\AA}^{-5}$, but even that is small compared to the difference between KS and FDE calculations (about $2.8\text{ e}\text{\AA}^{-5}$ at BCP2 and $1.5\text{ e}\text{\AA}^{-5}$ at BCP3). As was already discussed in Section 2.9.4, the results obtained with a supermolecular basis are typically much better than those without, which holds for all kinetic-energy functionals studied here. Only the Laplacian at BCP2 is not very well reproduced even when including a ghost basis. By comparing the $\rho_{\text{emb,gh}}$ (PW91k) data to those in Table 2.2 (TZP/TZP), it can furthermore be seen that the additional two freeze-and-thaw cycles hardly change the results.

Table 2.3: Coordinates \mathbf{r}_{BCP} (in units of \AA) of the BCPs in $\text{H}_2\text{O}\cdots\text{F}^-$ and values of $\rho(\mathbf{r})$ in $\text{e}\text{\AA}^{-3}$ and $L(\mathbf{r})$ in $\text{e}\text{\AA}^{-5}$ at BCP2 and BCP3 for the supermolecular density ρ_{super} , embedding densities obtained with different kinetic energy functionals or electrostatic embedding (COULOMB) without (ρ_{emb}) and with a TZP ghost basis on the frozen subsystem ($\rho_{\text{emb,gh}}$). In calculations without ghost basis, three freeze-and-thaw cycles were used, whereas five cycles were used in calculations with ghost basis.

		$\mathbf{r}_{x,\text{BCP}}$	$\mathbf{r}_{y,\text{BCP}}$	$\rho(\mathbf{r}_{\text{BCP}})$	$L(\mathbf{r}_{\text{BCP}})$
BCP 2	ρ_{super}	0.02	−1.14	1.52	5.20
	$\rho_{\text{emb,gh}}$ PW91k	0.02	−1.17	1.47	7.35
	$\rho_{\text{emb,gh}}$ TF	0.02	−1.17	1.47	7.35
	$\rho_{\text{emb,gh}}$ COULOMB	0.06	−1.03	1.72	4.16
	ρ_{emb} PW91k	0.02	−1.17	1.52	7.96
	ρ_{emb} TF	0.02	−1.17	1.51	8.14
	ρ_{emb} COULOMB	0.02	−1.15	1.40	4.40
BCP 3	ρ_{super}	0.01	−1.77	0.75	−0.68
	$\rho_{\text{emb,gh}}$ PW91k	0.01	−1.74	0.66	−0.79
	$\rho_{\text{emb,gh}}$ TF	0.01	−1.74	0.66	−0.81
	$\rho_{\text{emb,gh}}$ COULOMB	0.02	−1.80	1.21	0.85
	ρ_{emb} PW91k	0.01	−1.73	0.55	−2.20
	ρ_{emb} TF	0.01	−1.73	0.54	−2.21
	ρ_{emb} COULOMB	0.01	−1.75	0.76	−1.06

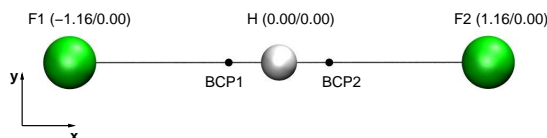
The data obtained with purely electrostatic embedding must be interpreted with care. From the data in Table 2.3 it can be seen that the results for the density and the Laplacian are rather bad if the full supermolecular basis is used. The results at BCP3 are even qualitatively wrong, as the negative Laplacian value has a wrong sign. The reason for this is that the purely electrostatic embedding is lacking the repulsive non-additive kinetic-energy contribution close to the nuclei in the frozen system, so that electron density is transferred into the frozen region (see the discussion of this electron

leak problem in Section 2.6.4). The data in Table 2.3 also show that the simple electrostatic embedding benefits from error cancellation effects if ghost basis functions in the environmental system are neglected. In that case, it leads to a better agreement with the KS reference calculations than the calculations with a kinetic-energy and exchange–correlation contribution, both for the density and the Laplacian at BCP3.

2.9.5 Symmetric hydrogen bonds in $\text{F}-\text{H}-\text{F}^-$

Because of the limitations of the available approximate functionals for the non-additive kinetic-energy component of the potential, the quality of the results from FDE calculations depends on the molecules under study, in particular the kind (and strength) of interaction between the subsystems. For this purpose, we compared FDE and supermolecular KS densities for different interaction types. In preliminary studies on systems like rare gas dimers, it turned out that almost no differences can be found, and that even the densities of the isolated fragments are almost indistinguishable from the supermolecular results. Therefore, we concentrated on cases that pose greater challenges to FDE due to stronger interactions and studied the symmetric hydrogen bond in $\text{F}-\text{H}-\text{F}^-$, starting from asymmetric fragments. Since this section mainly focuses on the practical applicability of FDE, we will work with a DZP ghost basis in case of calculations using supermolecular basis sets and employ three freeze-and-thaw iterations in all calculations. $\text{F}-\text{H}-\text{F}^-$, which contains two equivalent $\text{H}-\text{F}$ bonds, is considered to have one of the strongest hydrogen bonds. A reliable estimate for the dissociation energy D_0 into F^- and HF is 44.4 ± 1.6 kcal/mol [187,188]. The experimental estimate for the $\text{F}-\text{F}$ distance (2.278 Å) [189] is smaller than the van-der-Waals distance of two fluorine atoms (2.7 Å). This system has been subject to FDE studies in the context of proton transfer reactions before, where it was used as a test system for the evaluation of free energy calculations of chemical reactions in solution [115].

Figure 2.7: Optimized (BP86/TZP) structure and coordinates in the grid of the H-bonded system $\text{F}-\text{H}-\text{F}^-$.



The BP86/TZP optimized structure of the molecule is shown in Figure 2.7. The $\text{H}-\text{F}$ distance in this linear, symmetric molecule is 1.16 Å, so that the calculated $\text{F}-\text{F}$ distance of 2.32 Å is in fair agreement with the experimental value. The density ρ_{super} of the $\text{F}-\text{H}-\text{F}^-$ ion is symmetric [118]. The $\text{H}-\text{F}$ bond on which BCP1 is located was divided, so that a stretched HF and a fluoride ion were obtained as fragments. Consequently, the superposition of fragment densities is not symmetric, and also ρ_{emb} does not show the

required symmetry. If, however, ghost basis functions are added, the resulting $\rho_{\text{emb,gh}}$, shown in Figure 2.8 a), appears almost symmetric w.r.t. the horizontal mirror plane. Slight deviations from this symmetry can be detected in the plot of the difference density between the symmetric supermolecule density and $\rho_{\text{emb,gh}}$, Figure 2.8 b). This difference density plot also reveals that the agreement between ρ_{super} and $\rho_{\text{emb,gh}}$ is not perfect, since alternating regions of positive and negative difference density can be observed. On an absolute scale, these deviations are rather small, as can be seen from the densities at the BCPs, where $\Delta\rho = 0.12 \text{ e}\text{\AA}^{-3}$ at BCP1 and $\Delta\rho = 0.09 \text{ e}\text{\AA}^{-3}$ at BCP2.

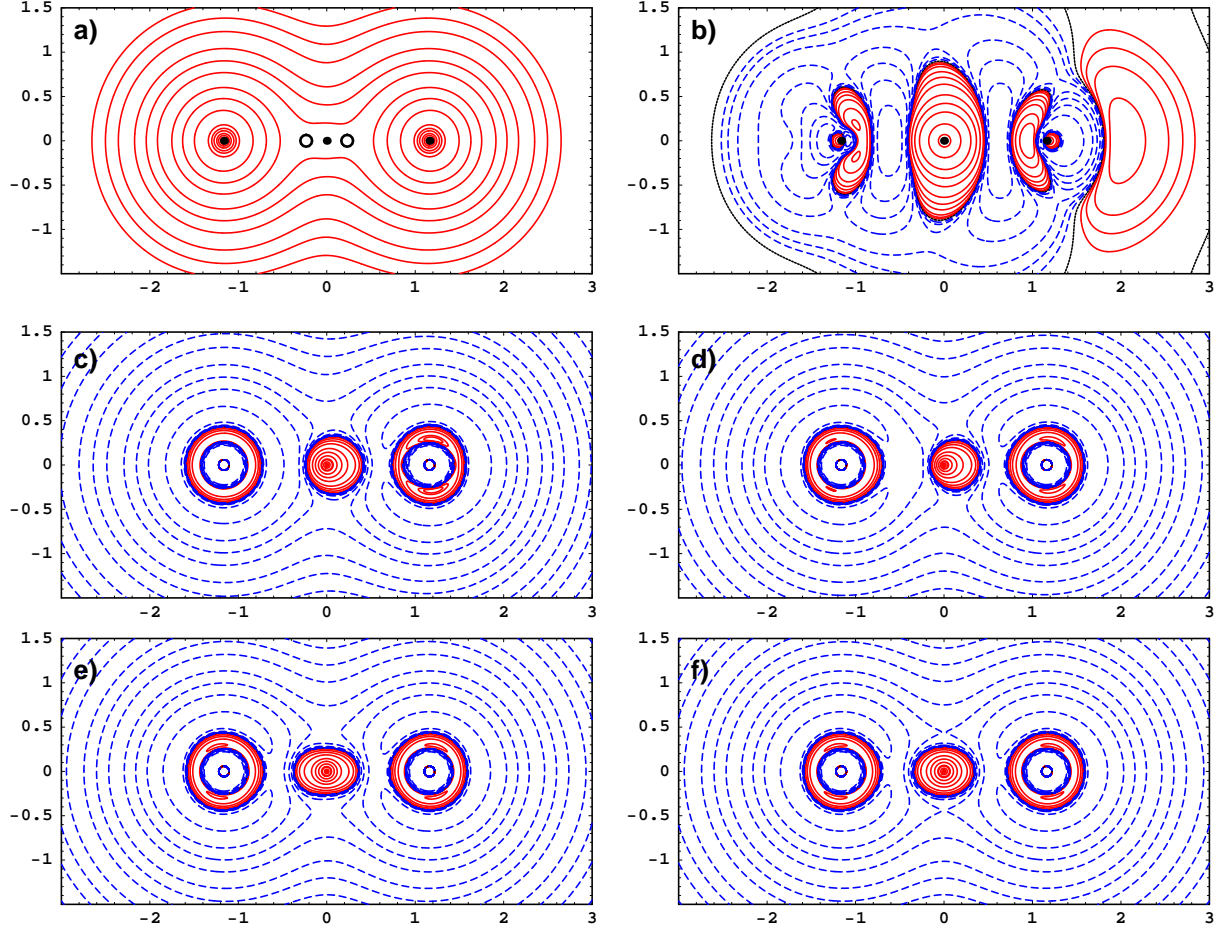
Table 2.4: Coordinates \mathbf{r}_{BCP} (in units of \AA) of the BCPs in F-H-F^- and values of $\rho(\mathbf{r})$ in $\text{e}\text{\AA}^{-3}$ and $L(\mathbf{r})$ in $\text{e}\text{\AA}^{-5}$ at the BCPs for ρ_{super} , ρ_{emb} , $\rho_{\text{emb,gh}}$ (obtained with a DZP ghost basis), and ρ_{frag} .

		$\mathbf{r}_{x,\text{BCP}}$	$\mathbf{r}_{y,\text{BCP}}$	$\rho(\mathbf{r}_{\text{BCP}})$	$L(\mathbf{r}_{\text{BCP}})$
BCP1	ρ_{super}	0.28	0.00	1.14	1.68
	ρ_{emb}	0.21	0.00	1.07	5.68
	$\rho_{\text{emb,gh}}$	0.23	0.00	1.02	2.74
	ρ_{frag}	0.30	0.00	1.30	3.08
BCP2	ρ_{super}	-0.28	0.00	1.14	1.68
	ρ_{emb}	-0.22	0.00	0.71	-1.92
	$\rho_{\text{emb,gh}}$	-0.23	0.00	1.05	2.80
	ρ_{frag}	-0.29	0.00	0.96	-1.70

The coordinates of the BCPs in ρ_{emb} are symmetrical w.r.t. the hydrogen atom, but the densities differ considerably ($|\rho(\text{BCP1}) - \rho(\text{BCP2})| = 0.37 \text{ e}\text{\AA}^{-3}$) and the sign of $L(\mathbf{r})$ at BCP1 is different from that at BCP2, see Table 2.4. FDE without ghost basis functions is thus qualitatively more similar to the isolated fragments than to the supermolecule for F-H-F^- . This is partly remedied with ghost basis functions, which do not improve the coordinates of the BCPs much, but considerably reduce the asymmetry in the density ($|\rho(\text{BCP1}) - \rho(\text{BCP2})| = 0.03 \text{ e}\text{\AA}^{-3}$). Furthermore, $L(\mathbf{r})$ has the same sign at both BCPs and also the absolute values are comparable. Hence, FDE yields a qualitatively correct description of this complex even though we started from asymmetric fragments and the interaction strength is very large.

In Figure 2.8 c) to f) also the plots of the negative Laplacian are shown. Whereas L_{frag} , part c), consists clearly of an independent, spherically symmetric fluorine fragment and an HF fragment, in L_{emb} , part d), one can already recognize local charge concentrations at atom F1 and a shift of charge concentration towards atom F1 at the hydrogen atom. $L_{\text{emb,gh}}$ in part e) is almost symmetric and already very similar to L_{super} , which is shown in part f). The negative Laplacian thus allows to quantitatively follow the improving description of the electron density from the asymmetric fragments via the fragments from the embedding approach without ghost basis to the FDE fragments including ghost basis functions, which do already capture the characteristic signatures of the supermolecule.

Figure 2.8: Density $\rho_{\text{emb,gh}}$ (a), difference density $\rho_{\text{super}} - \rho_{\text{emb,gh}}$ (b), and negative Laplacians L_{frag} (c), L_{emb} (d), $L_{\text{emb,gh}}$ (e), and L_{super} (f) for F–H–F[−]. A DZP ghost basis was employed for $\rho_{\text{emb,gh}}$ and $L_{\text{emb,gh}}$; three freeze-and-thaw cycles were carried out in all cases. An additional contour line at $165 \text{ e } \text{\AA}^{-5}$ is drawn for the negative Laplacian.



2.9.6 Coordination compounds

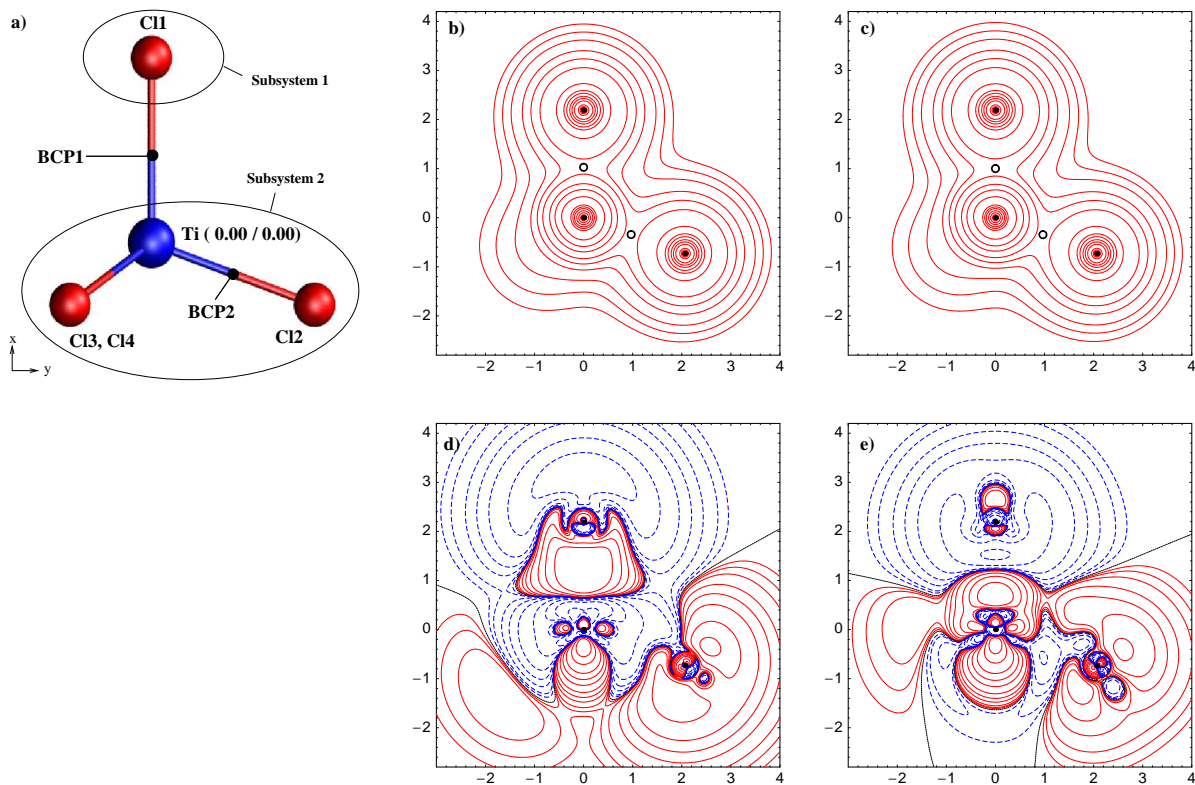
The available kinetic-energy functionals are usually assumed not to be accurate enough to be applied to covalent bonds, so that a straightforward application of the FDE scheme would not be possible in these cases. Extensions of the FDE scheme have been proposed that can handle such situations, e.g., by the introduction of capping groups, which has been successfully applied to the description of proteins [190].

In the following, the accuracy of the FDE scheme with the currently available approximate kinetic-energy functionals will be investigated for the case of subsystems connected by coordination bonds. As representative examples of such cases, we will consider the metal complexes TiCl_4 and $\text{Cr}(\text{CO})_6$. For these examples, the supermolecular basis set expansion [155] was employed in the FDE calculations, with the parameterization of the gradient-dependent enhancement factor in the PW91k kinetic-energy functional as given by Lembarki and Chermette (LC94) [63].

TiCl₄

Titaniumtetrachloride is a tetrahedral complex with T_d symmetry and strong interactions between the central metal atom and the ligands. The optimized structure is shown in Figure 2.9 a). The Ti–Cl distance is 2.19 Å (exp.: 2.18 Å) and the Cl–Ti–Cl angle is 109.47°. The reference data were taken from Ref. [191]. For the FDE calculation, the complex was divided into a negatively charged Cl[−] and a positively charged TiCl₃⁺ fragment. Initial FDE calculations converged very slowly and the electron density obtained was unreasonable. If TiCl₃⁺ was treated as the frozen fragment, a spurious charge transfer from the Cl[−] fragment to the TiCl₃⁺ fragment took place. The SCF procedure for the TiCl₃⁺ fragment only converged if one enforced a non-aufbau solution with one unoccupied orbital with a lower orbital energy than the highest occupied molecular orbital (HOMO). These difficulties are due to the well-known problem of the FDE embedding potential at the frozen system, in particular close to the nuclei (see Section 2.6.4). In earlier examples this incorrect behavior caused a wrong orbital ordering only at a very large distance between the subsystems.

Figure 2.9: a) BP86/TZP optimized structure of titaniumtetrachloride. The double labeling of some atoms means that there are two atoms, that differ only in their z -coordinate and are therefore overlaying in the picture. Note that the color change along the Ti–Cl bond is arbitrary and thus not related to the partitioning into subsystems. b) Supermolecular density, c) embedding density, d) difference density $\rho_{\text{super}} - \rho_{\text{frag}}$, e) difference density $\rho_{\text{super}} - \rho_{\text{emb}}$. The orientation of the molecule in the density plots corresponds to the one of the ball-and-stick model.



The present example demonstrates that for certain choices of subsystems the embedding potential fails to produce the correct orbital occupation even at the equilibrium distance. A practical solution to this problem was suggested in Ref. [123] by applying a position-dependent correction that enforces the right behavior of the embedding potential at the frozen subsystem. This long-distance correction resulted in an aufbau solution with the expected order of orbitals in our case, i.e., the spuriously low-lying orbital was shifted to higher energies.

Contour plots of the electron density for the supermolecular and the FDE calculation are shown in Figure 2.9 b) and c). The difference of the supermolecular density and the superposition of the densities of the isolated fragments is shown in Figure 2.9 d). Due to the complex formation, electron density is transferred from the Cl^- fragment towards the titanium atom. The most important change occurs in the center of the TiCl_3^+ fragment. The difference of the supermolecular density and the density from the FDE calculation is shown in Figure 2.9 e). Near the titanium atom the electron density from the FDE calculation is too low, whereas it is too high at Cl1 perpendicular to the Ti–Cl bond. Also in the center of the Ti–Cl2 bonding region FDE overestimates the electron density, although the differences are small.

Table 2.5: Coordinates \mathbf{r}_{BCP} (in units of Å) of the BCPs and values of $\rho(r)$ in $\text{e}\text{\AA}^{-3}$ and $L(r)$ in $\text{e}\text{\AA}^{-5}$ at the bond critical points of titaniumtetrachloride.

		$r_{x,\text{BCP}}$	$r_{y,\text{BCP}}$	$\rho(r)$	$L(r)$
BCP 1	sup	1.03	0.00	0.65	−1.73
	emb	1.00	0.00	0.59	−2.34
	diff	0.03	0.00	0.06	0.61
BCP 2	sup	−0.34	0.97	0.65	−1.73
	emb	−0.35	0.97	0.66	−1.68
	diff	0.01	0.00	−0.01	−0.05

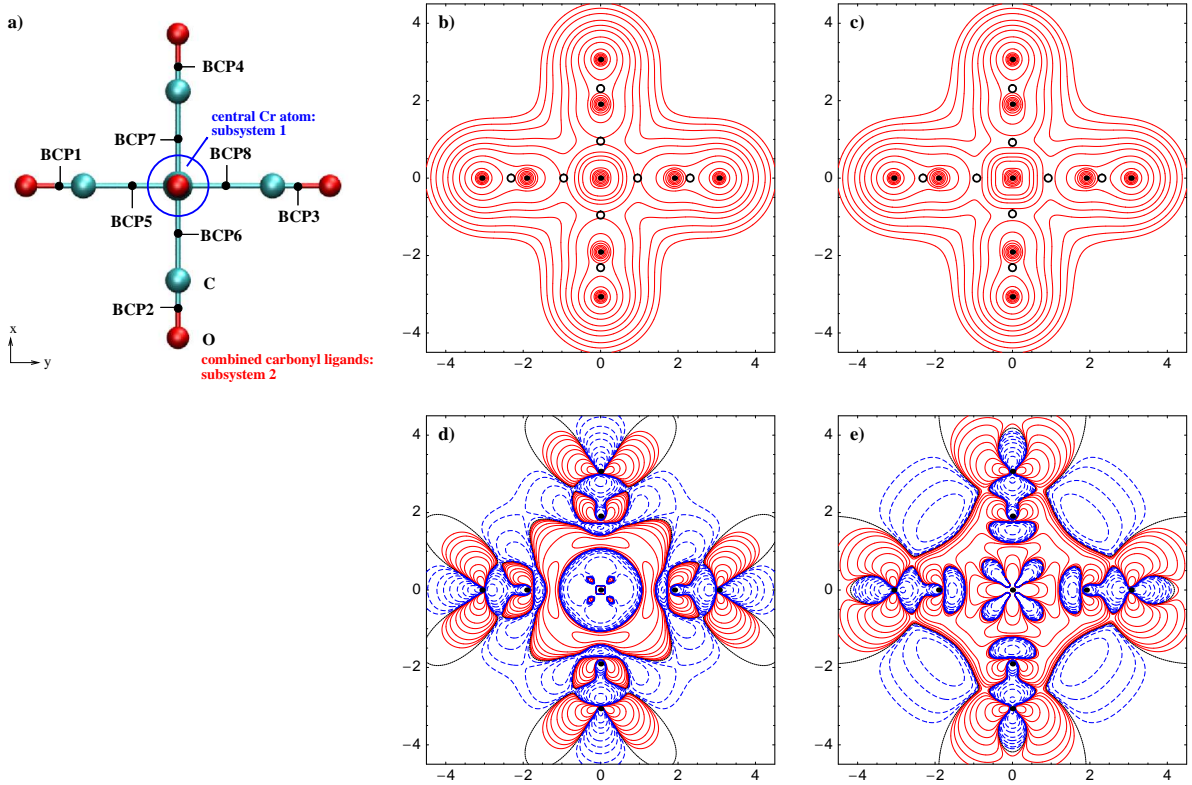
The values for the electron density and the negative Laplacian are shown in Table 2.5. At BCP1 near the border of the two subsystems the difference of the supermolecular density and the electron density from the FDE calculation and the difference of the negative Laplacians are rather small ($\sim 0.06 \text{ e}\text{\AA}^{-3}$ and $0.61 \text{ e}\text{\AA}^{-5}$, respectively); at BCP2 these deviations are even smaller. The negative Laplacian has the correct sign at both BCPs. Also the values of the difference density in titaniumtetrachloride are relatively small.

$\text{Cr}(\text{CO})_6$

The octahedral complex chromium hexacarbonyl is a prototypical example of a metal complex in which π -backdonation plays an important role, and which thus cannot be entirely understood in terms of simple ligand field theory. The optimized structure is shown in Figure 2.10 a). The Cr–C distance is 1.91 Å (exp.: 1.91 Å) and the C–O distance is 1.16 Å (exp.: 1.14 Å). The reference data were taken from Ref. [192]. The electronic structure expected for chromium in a strong octahedral ligand field would be

$[\text{Ar}](t_{2g})^6$. The FDE calculation converged to an aufbau solution with the unexpected configuration $[\text{Ar}](a_{1g})^2(e_g)^4$, caused by additional low-lying orbitals centered on the ligands. Note that the non-additive kinetic energy part of the potential should actually destabilize such ligand orbitals in the calculation of the Cr fragment in order to mimic the Pauli repulsion with the occupied orbitals in the $(\text{CO})_6$ fragment. Apparently, this destabilizing effect is too weak in the present example. This is again related to the deficiency of the available GGA kinetic-energy functionals. The electron density for this electronic structure is unreasonable, because it is very similar to the density of the superposition of the isolated fragments, except in the region around the chromium atom. The same calculation was performed enforcing the correct occupation, which resulted in a non-aufbau solution for chromium with the electronic configuration $[\text{Ar}](a_{1g})^0(t_{1u})^0(t_{2g})^6$.

Figure 2.10: a) BP86/TZP optimized structure of chromium hexacarbonyl. Note that the color change along the Cr–C bond is arbitrary and thus not related to the partitioning into subsystems. b) Supermolecular density, c) embedding density, d) difference density $\rho_{\text{super}} - \rho_{\text{frag}}$, e) difference density $\rho_{\text{super}} - \rho_{\text{emb}}$. The orientation of the molecule in the density plots corresponds to the one of the ball-and-stick model.

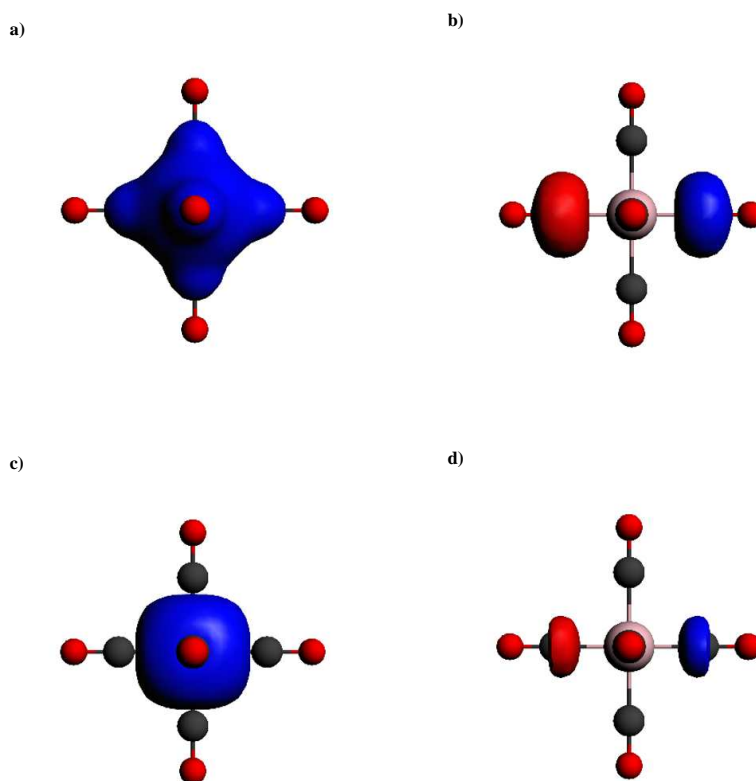


By applying the long-distance correction suggested in Ref. [123], the number of unoccupied orbitals that are lower in energy than the HOMO could be reduced. It was, however, not possible to obtain an aufbau solution with the expected occupation scheme. A set of three t_{1u} orbitals and one a_{1g} orbital were still found to be lower in energy than the metal-centered t_{2g} orbital. These orbitals are shown in Figure 2.11 a) and b) for the calculation without the long-distance correction, and in Figure 2.11 c) and d)

for the calculation with the correction. The orbitals are located on the carbon atoms of the carbonyl ligands. The long-distance correction leads to a contraction of these orbitals by raising the potential in the region of the ligand atoms. The rather sharp boundary in the isosurface plot can be explained in terms of the distance-dependence of the long-distance correction.

It should be noted that the destabilizing effect of this correction could be modified by changing the parameter α in Eq. (34) of Ref. [123], which controls the threshold to switch on the correction terms. However, it seems unreasonable to further tune this parameter since the correction enforces a limit that is only correct at large separations of the subsystems.

Figure 2.11: a) Low-lying a_{1g} orbital from the FDE calculation on $\text{Cr}(\text{CO})_6$ without long-distance correction (contour value = 0.045), b) one of the three low-lying t_{1u} orbitals from the calculation without the long-distance correction (contour value = 0.05), c) the orbital corresponding to the one shown in a) from the calculation with the long-distance correction (contour value = 0.045), d) the orbital corresponding to the one shown in b) from the calculation with the long-distance correction (contour value = 0.05).



The supermolecular and the embedding densities are shown in Figure 2.10 b) and c). The difference density is shown in Figure 2.10 d). In contrast to the other examples studied here, already the electron densities show significant differences and no sophisticated

topological analysis is needed in this case to reveal the deficiencies of the subsystem approach.

2.9.7 Trends in the accuracy of electron densities from FDE

The previous examples demonstrate that FDE is able to reproduce the qualitative changes in the electron-density topology upon hydrogen bonding of two subsystems. While the choice of the particular approximation for T_s^{nadd} had only a minor influence on the results, it turned out that monomer basis sets are often not sufficient to obtain accurate results for the densities. In case of a simple electrostatic embedding the restriction to a monomer basis set can lead to seemingly good results due to error cancellation effects. This changes drastically when a supersystem basis set is used also in the embedding calculation. In that case, an entirely electrostatic embedding leads to charge-leaking problems as discussed in Section 2.6.4.

The use of a supermolecular basis certainly limits the applicability of FDE as an effective model for large environments. However, typically only a few additional basis functions in the hydrogen-bonding region are sufficient to obtain a significant improvement of the electron-density description, which is comparable with the one obtained with a full supermolecular basis set. As will be shown in subsequent chapters, ghost basis sets in the frozen region typically have a small effect on molecular properties from FDE calculations on weakly interacting systems.

A quantitative comparison of difference densities and the Laplacian of the densities as well as the topological parameters at the bond critical points reveals that the electron densities in the hydrogen-bonding region resulting from FDE do not show the same directionality as obtained in supermolecular calculations. This could be the reason for some of the known problems related to FDE and similar approaches, e.g., in molecular dynamics simulations based on subsystem DFT [110]. A possible way to improve the FDE scheme for applications in which this directionality plays a major role may be the inclusion of terms depending on the overlap of the subsystem orbitals in the non-additive kinetic energy in some approximate manner.

We have furthermore considered cases that pose serious challenges on the embedding approach due to the fact that covalent contributions to the bonds become important. For the bonding in TiCl_4 , we experienced difficulties with the embedding approach for charged fragments when used in a naive way. We have shown that these problems, that result in an unphysical charge transfer from Cl^- to TiCl_3^+ , can be overcome in a pragmatic way by applying the long-distance correction suggested in Ref. [123].

The same approach was helpful in the attempt to employ FDE for chromium hexacarbonyl, for which orbital overlap effects play an important role. For this transition metal complex, however, the correction was only partly successful, since two sets of low-lying ligand-centered orbitals still remained. A possible explanation for this remaining deviation is the rather large covalent contribution to the $\text{Cr}-\text{C}$ bond due to the π -backdonation of the carbonyl ligands.

For the applicability of the FDE method to reproduce electron density distributions we can thus recognize a clear trend. For the densities of weak van der Waals complexes, the FDE approach is very successful [118], and it also provides accurate results for hydrogen bonds. Even for strongly hydrogen-bonded systems like $\text{F}-\text{H}-\text{F}^-$ a good

description can be achieved. Coordination bonds, however, represent borderline cases. Whereas bonds with strongly ionic character are described reasonably well, FDE fails for coordination compounds with strong covalent bonding contributions with currently available approximations for the kinetic-energy component of the embedding potential. These results indicate some important directions for the development of improved approximations to the non-additive kinetic energy functional. The examples demonstrate that the accurate description of the embedding potential at the frozen subsystem, in particular near the nuclei, is important to obtain a description that is at least qualitatively correct, i.e., that gives the correct orbital order. It was shown that the simple correction proposed in Ref. [123] works into the right direction for the systems considered here. However, it should be noted that this correction contains terms that are explicitly position-dependent, while approximations in terms of the density only would be preferable. The systems studied here will be crucial for the validation of future developments, like the most recent improved density functional approximation to the kinetic energy component of the embedding potential [107], which enforces the exact behavior near the nuclei of the frozen subsystem.

3. Excited States and Response Properties of Complex Systems

3.1 Excited-state methods suited for large systems

The methods discussed in the previous chapter allow to focus a quantum chemical description onto particular fragments within a larger system and to investigate complex aggregates by decomposing them into simpler subsystems. However, only ground-state methods have been discussed so far, whereas spectroscopic phenomena and photoexcitation processes in general also involve excited electronic states or the response of a system to an electromagnetic perturbation.

The characterization of excited electronic states is usually a much more challenging problem than the calculation of ground-state energies and properties. One difficulty is that in general no variational principle can be utilized except for special cases in which the state under consideration is the lowest of a certain irreducible representation, or if orthogonality to all lower-lying states is enforced. This holds in particular for density-functional theory, for which no ground-state wavefunction is obtained and thus no orthogonality requirements can be used directly. Furthermore, the Hohenberg–Kohn variational principle only gives access to the ground state (see, however, the work by Görling [193] or Levy and Nagy [194] as well as the discussion of variational density functional methods by Gaudoin and Burke [195]). Additional problems arise from the fact that several quantum chemical methods treat the electron correlation problem for ground and excited states in an unbalanced way, in particular those for which the computational effort is low enough to be applied to fairly complex systems. Excitation energies from configuration interaction with single substitutions (CIS) are, for example, typically much too high, since they employ Hartree–Fock molecular orbitals optimized for the ground state. Since the virtual orbitals from HF calculations effectively correspond to one-electron states of the anionic system according to Koopmans’ theorem, singly substituted HF determinants are not well suited to represent excited states. The correlation energy introduced by the CI among all singly excited states is thus too small to remedy this orbital deficiency, so that the excited states are too high in energy compared to the ground state. Also the time-dependent Hartree–Fock theory or random phase approximation (see [196–198]) typically overestimates excitation energies by 0.5 to several eV [199, 200]. If doubly substituted configurations are introduced in addition within a CISD approach, this bias is even larger, since the doubly substituted determinants are the most important ones for the correlation energy of the ground-state determinant, whereas the triply substituted determinants would be needed to include the dominant correlation contributions for singly excited states [200]. Furthermore, the CISD approach is not size-consistent.

A variety of approaches has been suggested that partly overcome these problems. Fores-

man *et al.* re-examined the CIS method and proposed an MP2-type correction to it (CIS-MP2) [201]. From an analysis and a comparison to CCSD-based excitation energies, Head-Gordon *et al.* proposed the so-called CIS(D) approach, which can be regarded as a second-order perturbation expansion of the CCSD method for excited states [202]. CIS(D) is size-consistent and shows a $O(N^5)$ scaling, and is thus a considerable improvement over the size-inconsistent CIS-MP2 method with its $O(N^6)$ scaling. Hirata presented analogous third- and fourth-order corrections, named CIS(3) and CIS(4) [203]. Several related methods have been proposed in recent years, e.g., the approximate second-order coupled cluster model CC2 [204]. Such approaches can be quite efficient in implementations that make use of the resolution-of-the-identity (RI) technique [205]. For a recent review, see Ref. [206]. Although much progress has been made with wavefunction-based excited-state methods for systems of increasing size, e.g. by introducing efficient schemes for so-called spin-component scaled and scaled opposite-spin CIS(D) variants [207], calculations for larger systems are still very costly. For a review of single-reference excited-state methods for large molecular systems, see Ref. [199].

Time-dependent density functional theory is an alternative to these wavefunction-based approaches that is often competitive in accuracy, in particular for localized valence excitations, while being applicable to molecular systems with several hundreds of atoms. However, TDDFT suffers from severe problems for certain types of excitations, e.g., Rydberg or long-range charge-transfer transitions. If one is only interested in the *absorption spectra*, this does usually not introduce major problems, since these states are typically of low oscillator strength. Nevertheless, considerable practical problems in TDDFT calculations on valence excited states may be introduced, as is described in Sections 3.3 and 3.4. In the following, an outline of the TDDFT formalism and algorithms suited for large molecular systems are presented. Furthermore, the origins of the problems in TDDFT calculations are indicated. Subsequently, we will present a simple diagnostic tool for the charge-transfer character of an excitation and a physically motivated correction for such states. Finally, an embedding version of TDDFT for use in solvation studies is described that eliminates problems due to long-range charge-transfer between different subsystems *by construction*.

3.2 Time-dependent density functional theory

3.2.1 Theoretical foundations

The theoretical basis for TDDFT is the Runge–Gross theorem [208], which is the analog of the Hohenberg–Kohn theorem for time-dependent systems. Even before the formulation of this theorem, some pioneering work on time-dependent density functional theory was conducted [209–213]. Runge and Gross presented the first general proof for a one-to-one correspondence between time-dependent external potentials $v_{\text{ext}}(\mathbf{r}, t)$ that are Taylor expandable about the initial time and the time-dependent electron density,

$$\rho(\mathbf{r}, t) = N \int d^3r_2 \dots \int d^3r_N \Psi(\mathbf{r}, \mathbf{r}_2, \dots, \mathbf{r}_N, t) \Psi^*(\mathbf{r}, \mathbf{r}_2, \dots, \mathbf{r}_N, t), \quad (3.1)$$

where N is the number of electrons and Ψ is the electronic wavefunction of the system fulfilling the time-dependent Schrödinger equation,

$$\hat{H}(t)\Psi(t) = i\frac{\partial}{\partial t}\Psi(t). \quad (3.2)$$

The proof of this one-to-one correspondence was generalized by van Leeuwen [214]. Runge and Gross furthermore established an effective one-electron scheme, i.e., a Kohn–Sham version of TDDFT. The analog of the variational principle for the ground-state energy in the time-dependent case is a stationarity condition for the action integral,

$$A[\rho] = \int_{t_0}^{t_1} dt \langle \Psi(t)[\rho] | i\partial/\partial t - \hat{H}(t) | \Psi(t)[\rho] \rangle, \quad (3.3)$$

where $\hat{H}(t)$ is the Hamiltonian of the system. This functional is stationary w.r.t. the density for densities obtained from the solutions of the time-dependent Schrödinger equation,

$$\frac{\delta A[\rho]}{\delta \rho(\mathbf{r}, t)} = 0. \quad (3.4)$$

By a comparison of the action stationarity principles for an interacting and a non-interacting system, time-dependent Kohn–Sham (TDKS) equations can be derived as,

$$\left(-\frac{1}{2}\nabla^2 + v_{\text{eff}}(\mathbf{r}, t) \right) \psi_i(\mathbf{r}, t) = i\frac{\partial}{\partial t}\psi_i(\mathbf{r}, t), \quad (3.5)$$

where

$$v_{\text{eff}}(\mathbf{r}, t) = v_{\text{ext}}(\mathbf{r}, t) + \int \frac{\rho(\mathbf{r}', t)}{|\mathbf{r} - \mathbf{r}'|} d^3r' + \frac{\delta A_{xc}[\rho]}{\delta \rho(\mathbf{r}, t)}. \quad (3.6)$$

The exchange–correlation part of the action functional is defined as

$$A_{xc}[\rho] = \int_{t_0}^{t_1} dt \left\langle \Psi(t)[\rho] \left| \frac{1}{|\mathbf{r} - \mathbf{r}'|} \right| \Psi(t)[\rho] \right\rangle - \frac{1}{2} \int_{t_0}^{t_1} dt \int d^3r \int d^3r' \frac{\rho(\mathbf{r}, t)\rho(\mathbf{r}', t)}{|\mathbf{r} - \mathbf{r}'|} + S_0[\rho] - S_1[\rho], \quad (3.7)$$

where the functional $S[\rho]$ is given by

$$S[\rho] = \int_{t_0}^{t_1} dt \langle \Psi(t)[\rho] | i\partial/\partial t - \hat{T} | \Psi(t)[\rho] \rangle, \quad (3.8)$$

and the indices 0 and 1 indicate that $S[\rho]$ should be evaluated for the wavefunction of the noninteracting and interacting system, respectively [208]. \hat{T} is the kinetic-energy operator. This action functional gives rise to causality problems when calculating response functions, which can be circumvented by modified action functionals within the so-called Keldysh formalism [215–217]. It was argued that the KS-TDDFT scheme is non-predictive due to a dependence on future densities through a second time-derivative [218], a criticism that was later disproved by Maitra, van Leeuwen, and Burke [219]. More information on the formal development and applications of TDDFT can be found in several reviews [199, 216, 220–225].

3.2.2 Linear response TDDFT

In linear response TDDFT we investigate the change in the density of the system under study due to a time-dependent perturbation $\delta v_{\text{eff}}(\mathbf{r}, t)$ in the potential.

We start from the unperturbed TDKS equations, Eq. (3.5), in the form,

$$\left(-\frac{1}{2}\nabla^2 + v_{\text{eff}}(\mathbf{r})\right) \psi_i^{(0)}(\mathbf{r}, t) = i \frac{\partial}{\partial t} \psi_i^{(0)}(\mathbf{r}, t). \quad (3.9)$$

Note that we use indices i, j, k, \dots for occupied orbitals, a, b, c, \dots for virtual orbitals, and r, s, t, \dots for general orbitals. We assume that the solutions for the unperturbed, time-independent effective KS potential $v_{\text{eff}}(\mathbf{r})$ are known as,

$$\psi_i^{(0)}(\mathbf{r}, t) = e^{-i\epsilon_i t} \phi_i(\mathbf{r}), \quad (3.10)$$

where ϵ_i is the KS orbital energy of orbital i and $\phi_i(\mathbf{r})$ is a solution of the time-independent KS equation. We now introduce a small time-dependent perturbation $\delta v_{\text{eff}}(\mathbf{r}, t)$ and write the perturbed wavefunction as

$$\psi_i(\mathbf{r}, t) = \psi_i^{(0)}(\mathbf{r}, t) + \delta\psi_i(\mathbf{r}, t), \quad (3.11)$$

so that the time-dependent Kohn–Sham equations take the form,

$$\left[-\frac{1}{2}\nabla^2 + v_{\text{eff}}(\mathbf{r}) + \delta v_{\text{eff}}(\mathbf{r}, t)\right] \left(\psi_i^{(0)}(\mathbf{r}, t) + \delta\psi_i(\mathbf{r}, t)\right) = i \frac{\partial}{\partial t} \left(\psi_i^{(0)}(\mathbf{r}, t) + \delta\psi_i(\mathbf{r}, t)\right). \quad (3.12)$$

After subtraction of the unperturbed Kohn–Sham equation, Eq. (3.9), we arrive at

$$\left[-\frac{1}{2}\nabla^2 + v_{\text{eff}}(\mathbf{r}) + \delta v_{\text{eff}}(\mathbf{r}, t)\right] \delta\psi_i(\mathbf{r}, t) + \delta v_{\text{eff}}(\mathbf{r}, t) \psi_i^{(0)}(\mathbf{r}, t) = i \frac{\partial}{\partial t} \delta\psi_i(\mathbf{r}, t). \quad (3.13)$$

These equations can formally be solved by expanding $\delta\psi(\mathbf{r}, t)$ in the set of unperturbed orbitals,

$$\delta\psi_i(\mathbf{r}, t) = \sum_r c_{ir}(t) \psi_r^{(0)}(\mathbf{r}, t), \quad (3.14)$$

and inserting this expression into Eq. (3.12). This yields a first-order differential equation in t for the expansion coefficients, which we can solve under the boundary condition that $c_{ir} = \delta_{ir}$ before switching on the perturbation. We assume that the perturbing potential has the form,¹

$$\delta v_{\text{eff}}(\mathbf{r}, t) = \delta v^{\text{pert}} \left[e^{i\omega t} + e^{-i\omega t} \right] = 2\delta v^{\text{pert}} \cos(\omega t), \quad (3.15)$$

¹Note that we actually have to introduce a damping function in order to introduce the perturbation adiabatically [220].

where δv^{pert} is hermitian and time-independent. We obtain for the expansion coefficients to first order (see, e.g., [13, 226, 227]),

$$c_{is}(t) = -\frac{1}{2} \left(\frac{e^{[i(\omega_{si}+\omega)]t}}{(\omega_{si}+\omega)} + \frac{e^{[i(\omega_{si}-\omega)]t}}{(\omega_{si}-\omega)} \right) \langle \phi_s | \delta v^{\text{pert}} | \phi_i \rangle, \quad (3.16)$$

where $\omega_{si} = \epsilon_s - \epsilon_i$.

From these coefficients, we can determine the first-order change in the density (or, alternatively, in the density matrix, see Ref. [228]),

$$\delta \rho(\mathbf{r}, t) = \rho(\mathbf{r}, t) - \rho^{(0)}(\mathbf{r}, t) \quad (3.17)$$

$$= \sum_r n_r [\psi_r^{(0)*}(\mathbf{r}, t) \delta \psi_r(\mathbf{r}, t) + \psi_r^{(0)}(\mathbf{r}, t) \delta \psi_r^*(\mathbf{r}, t)] \quad (3.18)$$

where n_r is the occupation number of orbital ψ_r . By inserting the ansatz for $\delta \psi_r(\mathbf{r}, t)$ from Eq. (3.14) and the expression from Eq. (3.16) for c_{rs} , we obtain,

$$\begin{aligned} \delta \rho(\mathbf{r}, t) = \sum_{rs} n_r & \left[\left(\frac{e^{-i\omega t}}{\omega - \omega_{sr}} - \frac{e^{i\omega t}}{\omega + \omega_{sr}} \right) \langle \phi_s | \delta v^{\text{pert}} | \phi_r \rangle \phi_r^*(\mathbf{r}) \phi_s(\mathbf{r}) \right. \\ & \left. + \left(\frac{e^{i\omega t}}{\omega - \omega_{sr}} - \frac{e^{-i\omega t}}{\omega + \omega_{sr}} \right) \langle \phi_r | \delta v^{\text{pert}} | \phi_s \rangle \phi_s^*(\mathbf{r}) \phi_r(\mathbf{r}) \right]. \end{aligned} \quad (3.19)$$

We can now identify the two Fourier components of this time-dependent density change by writing,

$$\delta \rho(\mathbf{r}, t) = \delta \rho(\mathbf{r}, \omega) e^{i\omega t} + \delta \rho(\mathbf{r}, -\omega) e^{-i\omega t}, \quad (3.20)$$

and sorting terms that oscillate with $e^{i\omega t}$ in Eq. (3.19),

$$\delta \rho(\mathbf{r}, \omega) = \sum_{rs} n_r \left[\frac{\langle \phi_r | \delta v^{\text{pert}} | \phi_s \rangle \phi_s^*(\mathbf{r}) \phi_r(\mathbf{r})}{\omega - \omega_{sr}} - \frac{\langle \phi_s | \delta v^{\text{pert}} | \phi_r \rangle \phi_r^*(\mathbf{r}) \phi_s(\mathbf{r})}{\omega + \omega_{sr}} \right], \quad (3.21)$$

as well as those that oscillate with $e^{-i\omega t}$,

$$\delta \rho(\mathbf{r}, -\omega) = \sum_{rs} n_r \left[\frac{\langle \phi_s | \delta v^{\text{pert}} | \phi_r \rangle \phi_r^*(\mathbf{r}) \phi_s(\mathbf{r})}{\omega - \omega_{sr}} - \frac{\langle \phi_r | \delta v^{\text{pert}} | \phi_s \rangle \phi_s^*(\mathbf{r}) \phi_r(\mathbf{r})}{\omega + \omega_{sr}} \right] \quad (3.22)$$

$$(3.23)$$

For pure density functionals and real (e.g., electric field-type) perturbations, we can use the fact that

$$\langle \phi_s | \delta v^{\text{pert}} | \phi_r \rangle = \delta v_{sr}^{\text{pert}} = \delta v_{rs}^{\text{pert}}. \quad (3.24)$$

We furthermore note that the unperturbed, time-independent KS orbitals $\phi_r(\mathbf{r})$ may always be chosen to be real. Since it can easily be shown from Eq. (3.19) that neither

occupied–occupied nor virtual–virtual pairs contribute to the sum, the expression for the frequency-dependent density change simplifies to,

$$\delta\rho(\mathbf{r}, \omega) = \sum_{ia} 2P_{ia}(\omega)\phi_i(\mathbf{r})\phi_a(\mathbf{r}), \quad (3.25)$$

where

$$P_{ia}(\omega) = \chi_{ia}^s(\omega)\delta v_{ia}^{\text{pert}}, \quad (3.26)$$

and²

$$\chi_{ia}^s(\omega) = \frac{\omega_{ia}}{\omega_{ia}^2 - \omega^2}. \quad (3.27)$$

The perturbation will consist of two different parts, namely (i) the external perturbation and (ii) the perturbation of the electron–electron interaction potential induced by the change in the electron density,

$$\delta v_{ia}^{\text{pert}} = \delta v_{ia}^{\text{ext}} + \delta v_{ia}^{\text{ind}}, \quad (3.28)$$

where the induced potential is approximated by the linear response of the Kohn–Sham potential, $v_{\text{eff}}(\mathbf{r})$, to a change in the density,

$$\delta v_{ia}^{\text{ind}} = \langle \phi_i | \delta v^{\text{ind}} | \phi_a \rangle \quad (3.29)$$

$$= \int d^3r_1 \left\{ \phi_i^*(\mathbf{r}_1) \left[\int d^3r_2 \frac{\delta v_{\text{eff}}(\mathbf{r}_1)}{\delta \rho(\mathbf{r}_2)} \delta \rho(\mathbf{r}_2) \right] \phi_a(\mathbf{r}_1) \right\} \quad (3.30)$$

$$= \int d^3r_1 \left\{ \phi_i^*(\mathbf{r}_1) \left[\int d^3r_2 \left(\frac{1}{|\mathbf{r}_1 - \mathbf{r}_2|} + f_{xc}(\mathbf{r}_1, \mathbf{r}_2) \right) \delta \rho(\mathbf{r}_2) \right] \phi_a(\mathbf{r}_1) \right\}. \quad (3.31)$$

The above equation already contains a simplification concerning the exchange–correlation kernel f_{xc} , since its Fourier transform is actually defined as the functional derivative of the time-dependent effective Kohn–Sham potential, which by itself is obtained as the functional derivative of the exchange–correlation part of the action functional, Eq. (3.7),

$$f_{xc}(\mathbf{r}, \mathbf{r}', t, t') = \frac{\delta v_{\text{eff}}(\mathbf{r}, t)}{\delta \rho(\mathbf{r}', t')} = \frac{\delta^2 A_{xc}}{\delta \rho(\mathbf{r}', t') \delta \rho(\mathbf{r}, t)}. \quad (3.32)$$

This definition leads to a causality problem [230], since by interchanging the order of differentiation, we would obtain $f_{xc}(\mathbf{r}, \mathbf{r}', t, t') = f_{xc}(\mathbf{r}', \mathbf{r}, t', t)$. Causality requires, however, that $f_{xc}(\mathbf{r}, \mathbf{r}', t, t') = 0$ for $t' > t$, because otherwise the potential would depend on values of the density in the future. A solution to this paradox is the Keldysh formalism introduced by van Leeuwen [215]. We will, in the following, adopt the so-called adiabatic approximation, i.e., we assume a time- or frequency-independent, respectively, exchange–correlation kernel. For brevity, we will furthermore skip the coordinate-dependence of f_{xc} . By insertion of Eq. (3.25) into Eq. (3.31) we obtain,

²Note that in comparison to the notation in Ref. [229] the sign of ω_{ia} is reversed in this work.

$$\delta v_{ia}^{\text{ind}} = \int d^3 r_1 \left\{ \phi_i^*(\mathbf{r}_1) \left[\int d^3 r_2 \left(\frac{1}{|\mathbf{r}_1 - \mathbf{r}_2|} + f_{xc} \right) \sum_{jb} 2P_{jb}(\omega) \phi_j(\mathbf{r}_2) \phi_b(\mathbf{r}_2) \right] \phi_a(\mathbf{r}_1) \right\}. \quad (3.33)$$

In terms of the coupling matrix \mathbf{K} with elements,

$$K_{ia,jb} = \int d^3 r_1 \left\{ \phi_i^*(\mathbf{r}_1) \left[\int d^3 r_2 \left(\frac{1}{|\mathbf{r}_1 - \mathbf{r}_2|} + f_{xc}(\mathbf{r}_1, \mathbf{r}_2) \right) \phi_j(\mathbf{r}_2) \phi_b^*(\mathbf{r}_2) \right] \phi_a(\mathbf{r}_1) \right\}, \quad (3.34)$$

we arrive at

$$\delta v_{ia}^{\text{ind}} = \sum_{jb} 2K_{ia,jb} P_{jb}(\omega). \quad (3.35)$$

Insertion into Eq. (3.28) leads to

$$\delta v_{ia}^{\text{pert}} = \delta v_{ia}^{\text{ext}} + \sum_{jb} 2K_{ia,jb} P_{jb}(\omega), \quad (3.36)$$

which can be put into Eq. (3.26),

$$P_{ia}(\omega) = \frac{\omega_{ia}}{\omega_{ia}^2 - \omega^2} \left[\delta v_{ia}^{\text{ext}} + \sum_{jb} 2K_{ia,jb} P_{jb}(\omega) \right]. \quad (3.37)$$

This can be re-arranged into

$$\sum_{jb} \left[\underbrace{\omega_{jb} \delta_{ij} \delta_{ab} - 2K_{ia,jb}}_{[\mathbf{A} + \mathbf{B}]_{ia,jb}} - \frac{\omega^2}{\omega_{jb}} \delta_{ij} \delta_{ab} \right] P_{jb}(\omega) = \delta v_{ia}^{\text{ext}}, \quad (3.38)$$

where we have identified elements of the sum of the matrices \mathbf{A} and \mathbf{B} , which commonly occur in other derivations of the linear response TDDFT equations [199, 220, 231, 232]. Note, however, that the definitions used for these matrices by different authors may not always be exactly the same (e.g., they may differ in sign). Furthermore, the relationship outlined above only holds for pure, i.e., non-hybrid density-functional theory. By collecting all elements P_{jb} and v_{ia}^{ext} in the vectors \mathbf{P} and \mathbf{v}^{ext} , respectively, and by introducing the diagonal matrix \mathbf{S} with elements,

$$S_{ia,jb} = \frac{1}{(\epsilon_b - \epsilon_j)} \delta_{ij} \delta_{ab}, \quad (3.39)$$

we can reformulate Eq. (3.38) in compact matrix notation as

$$[(\mathbf{A} + \mathbf{B}) + \omega^2 \mathbf{S}] \mathbf{P}(\omega) = \delta \mathbf{v}^{\text{ext}}, \quad (3.40)$$

$$\mathbf{S}^{-1/2} [(\mathbf{A} + \mathbf{B}) + \omega^2 \mathbf{S}] \underbrace{\mathbf{S}^{-1/2} \mathbf{S}^{1/2}}_{\mathbf{1}} \mathbf{P}(\omega) = \mathbf{S}^{-1/2} \delta \mathbf{v}^{\text{ext}}. \quad (3.41)$$

This equation can formally be solved for \mathbf{P} in the following way,

$$\mathbf{P}(\omega) = \mathbf{S}^{-1/2} \left[\underbrace{\mathbf{S}^{-1/2} (\mathbf{A} + \mathbf{B}) \mathbf{S}^{-1/2}}_{-\mathbf{\Omega}} + \omega^2 \mathbf{1} \right]^{-1} \mathbf{S}^{-1/2} \delta \mathbf{v}^{\text{ext}}, \quad (3.42)$$

$$\mathbf{P}(\omega) = \mathbf{S}^{-1/2} [\omega^2 \mathbf{1} - \mathbf{\Omega}]^{-1} \mathbf{S}^{-1/2} \delta \mathbf{v}^{\text{ext}}. \quad (3.43)$$

The elements of the matrix $\mathbf{\Omega}$ are given as,

$$\Omega_{ia,jb} = (\epsilon_a - \epsilon_i)^2 \delta_{ij} \delta_{ab} + 2\sqrt{(\epsilon_a - \epsilon_i)} K_{ia,jb} \sqrt{(\epsilon_b - \epsilon_j)}. \quad (3.44)$$

Eq. (3.43) has the form of a linear system of equations of the type $\mathbf{y} = \mathbf{M}^{-1} \mathbf{b}$, and the matrix \mathbf{M} in this case is of dimension $n_{\text{occ}} \times n_{\text{virt}}$, where n_{occ} and n_{virt} are the number of occupied and virtual, respectively, orbitals of the system. In typical basis set representations, a direct inversion of the matrix is thus not possible for medium-sized to large molecules, so that the equation is recast into the form,

$$[\mathbf{\Omega} - \omega^2 \mathbf{1}] \underbrace{\mathbf{S}^{1/2} \mathbf{P}(\omega)}_{\mathbf{F}} = -\mathbf{S}^{-1/2} \delta \mathbf{v}^{\text{ext}}, \quad (3.45)$$

and solved by iterative matrix-vector multiplications as outlined by Feyereisen *et al.* in the context of the related time-dependent Hartree–Fock framework [233]. This equation allows us to compute the change in the density (in terms of $\mathbf{P}(\omega)$) from the matrix elements of the external perturbation, which corresponds to the “forced oscillations” in the density in the terminology of McWeeny [13]. But we also observe that there are certain characteristic frequencies at which the inverse of $[\mathbf{\Omega} - \omega^2 \mathbf{1}]$ becomes singular, so that the density change becomes infinitely large even in the case of a vanishingly small perturbation. These are the resonance frequencies of the system, corresponding to electronic transitions or the “free oscillations” of McWeeny [13]. We can determine them by solving the eigenvalue problem that results from setting the perturbation to zero and using the above definition of the vector \mathbf{F} ,

$$[\mathbf{\Omega} - \omega_k^2 \mathbf{1}] \mathbf{F}_k = \mathbf{0}. \quad (3.46)$$

This way to calculate TDDFT excitation energies within a linear response formalism was derived by Casida [220].

3.2.3 Approximate solution schemes for excitation energies

A direct diagonalization of Eq. (3.46) would be very demanding for larger systems, although it is possible for smaller molecules. Hence, the TDDFT eigenvalue problem is usually solved by subspace iteration methods, most commonly by Davidson-type iterative solutions for the lowest eigenvalues [234,235]. In these methods, matrix–vector products of the coupling matrix \mathbf{K} with certain test vectors \mathbf{p}_{in}^k describing the excitation to be optimized are calculated [236],

$$[p_{\text{out}}^k]_{jb} = \sum_{lc} K_{jb,lc} [p_{\text{in}}^k]_{lc}. \quad (3.47)$$

The output vectors can be expressed as,

$$[p_{\text{out}}^k]_{jb} = \int \phi_j(\mathbf{r}_1) \phi_b(\mathbf{r}_1) \delta v_k^{\text{ind}}(\mathbf{r}_1) d^3 r_1, \quad (3.48)$$

where

$$\delta v_k^{\text{ind}}(\mathbf{r}_1) = \int d^3 r_2 \left\{ \left[\frac{1}{|\mathbf{r}_1 - \mathbf{r}_2|} + f_{xc} \right] \sum_{lc} [p_{\text{in}}^k]_{lc} \phi_l(\mathbf{r}_2) \phi_c(\mathbf{r}_2) \right\}, \quad (3.49)$$

is the potential induced by the density change described by the test vector \mathbf{p}_{in}^k . The test vectors actually serve as a basis in which the eigenvectors \mathbf{F}_I from Eq. (3.46) are expanded during the Davidson diagonalization. The induced potential is, for efficiency reasons, calculated in terms of the fitted density,

$$\delta \tilde{\rho}_{\text{in}}^k(\mathbf{r}_2) = \sum_i a_i f_i(\mathbf{r}_2) \approx \sum_{lc} [p_{\text{in}}^k]_{lc} \phi_l(\mathbf{r}_2) \phi_c(\mathbf{r}_2), \quad (3.50)$$

where a_i and f_i are fit coefficients and functions, respectively (for details, see Ref. [236]). Such an auxiliary-basis method is discussed already by Casida [220], and was implemented subsequently by Jamorski *et al.* [237]. Several authors have highlighted the advantages of using auxiliary-basis methods thereafter [236,238,239].

A common approximation to the TDDFT eigenvalue problem is the Tamm–Dancoff approximation (TDA), which is the TDDFT analog of CIS. A CIS-type treatment based on Kohn–Sham orbitals and orbital energies was first employed by Grimme [240]. In that work, a CIS-Hamiltonian on the basis of Kohn–Sham orbitals was diagonalized that contained additional empirical scaling factors and energy shifts to improve the resulting excitation energies. The Tamm–Dancoff approximation within a TDDFT context was introduced by Hirata and Head-Gordon in 1999 [241]. It was found that differences between TDDFT/TDA and normal TDDFT are typically small. A mean deviation of 0.04 eV for Rydberg states was reported, whereas the discrepancies can be somewhat larger for valence excited states (up to 0.3 eV). Even larger differences were found in case of hybrid functionals, where TDDFT/TDA typically yields better results since it avoids certain kinds of triplet near-instabilities. This point was emphasized in the work by Cordova *et al.* [242], where also the advantages of the TDA in photochemical applications were outlined.

Although the solution of the eigenvalue problem in Eq. (3.46) by subspace iteration methods is currently the most common approach, there are other ways and additional

technical simplifications to obtain approximate excitation energies from TDDFT. The (squares) of the orbital energy differences, which enter the diagonal elements of $\mathbf{\Omega}$, usually dominate this matrix. Furthermore, they are the exact excitation energies of the non-interacting reference system, and can thus be regarded as a zeroth-order guess for the interacting system of electrons. This is also reflected in the structure of the eigenvalue equation for excitation energies, Eq. (3.46), which we may write in the following form,

$$\mathbf{\Omega}\mathbf{F}_k = \left[\mathcal{E}^2 + 2\mathcal{E}^{1/2}\mathbf{K}\mathcal{E}^{1/2} \right] \mathbf{F}_k = \omega_k^2 \mathbf{F}_k, \quad (3.51)$$

where \mathcal{E} is the diagonal matrix of the orbital energy differences of virtual (labels a, b) and occupied (labels i, j) orbitals,

$$\mathcal{E}_{ia,jb} = (\epsilon_a - \epsilon_i)\delta_{ij}\delta_{ab}, \quad (3.52)$$

and \mathbf{K} is the coupling matrix introduced in Eq. (3.34).

One approach to improve on this zeroth-order guess for the excitation energies is to apply a Laurent expansion of the Kohn–Sham response function around the orbital energy differences [243]. In lowest order, this is now known as the single-pole approximation (SPA). However, this approach is not very accurate and may miss essential effects for certain collective excitations [244]. Later, an approximation to Casida’s matrix formulation [220] was developed that uses a continued-fraction method to obtain the excitation energies. This approach works in cases of diagonally dominant matrices and well-separated eigenvalues. The SPA is an approximation to the lowest order (called small-matrix approximation, SMA) of this method in case of small corrections to the KS excitation energies [245].

Hirao and co-workers proposed an approximate approach that uses a reduced space of occupied–virtual pairs in the calculation of excitation energies, in which first a particular row of the matrix $\mathbf{\Omega}$ is calculated, i.e., the couplings of one selected orbital transition (ia) to *all* other orbital transitions are calculated in a first step [246]. This step corresponds to one matrix–vector product in a conventional TDDFT calculation. After that, a pre-screening for the orbital transitions is performed, in which all occupied–virtual-pairs jb are neglected, for which

$$\left| \frac{\Omega_{ia,jb}}{(\epsilon_b - \epsilon_k)^2 - (\epsilon_a - \epsilon_i)^2} \right| > \theta, \quad (3.53)$$

where the threshold θ is typically of the order of 10^{-5} . The efficiency of this so-called state-specific TDDFT was later enhanced by using a combination of different basis sets and functionals during different steps of the calculation [247], at the cost of additional errors of between 0.2 to 0.3 eV compared to the reference TDDFT calculations. While this approach in principle offers a way for additional efficiency enhancement, the analysis is based on a perturbation expansion of the excitation energies similar to that in Ref. [243] and the later work by Appel *et al.* [245]. This analysis is, however, only appropriate for systems with non-degenerate excitation energies of the non-interacting system, i.e., with non-degenerate orbital-energy differences. In the state-specific TDDFT approach, problems due to degeneracy are avoided since the perturbation expression is only used to select the reduced subspace (which will always contain all excitations within a degenerate

set). Another approach that uses a reduced orbital product space in TDDFT calculations on the basis of the spatial extent of the orbitals was proposed in Ref. [248].

3.3 Assessment of a simple correction for the charge-transfer problem in time-dependent density-functional theory

3.3.1 Failure of TDDFT for charge-transfer excitations

The growing number of applications to large systems has not only shown the strengths, but also the weaknesses of TDDFT [199, 222, 249]. One of the major concerns is the complete failure of most approximate TDDFT schemes to deal with long-range charge-transfer excitations. This is caused by the approximations made for the exchange–correlation kernel f_{xc} . Since f_{xc} is usually approximated in a frequency-independent and local form from an approximate exchange–correlation potential, i.e.,

$$f_{xc}(\mathbf{r}, \mathbf{r}', \omega) \approx \frac{\delta v_{xc}^{\text{approx}}(\mathbf{r})}{\delta \rho(\mathbf{r}')} \delta(\mathbf{r} - \mathbf{r}'), \quad (3.54)$$

the coupling matrix elements $K_{ia,jb}$ vanish if the occupied and virtual orbital involved in a certain orbital transition $\phi_i \rightarrow \phi_a$ are spatially separated.

In fact, $K_{ia,jb}$ will vanish for *all* occupied–virtual pairs (j, b) if the product $\phi_i(\mathbf{r})\phi_a(\mathbf{r})$ is zero for every \mathbf{r} . This holds in particular for the adiabatic local density approximation (ALDA), but also for all kernels derived from other non-hybrid functionals. As a consequence, long-range charge transfer excitations form a subblock in the matrix Ω that is simply given by the diagonal matrix

$$\Omega_{ia,jb}^{\text{CT}} = \mathcal{E}_{ia,jb}^2 \quad (3.55)$$

and the excitation energies are obtained as the orbital energy differences. For intramolecular charge-transfer transitions, this result is independent of the separation between donor and acceptor, as long as there is no differential overlap between $\phi_i(\mathbf{r})$ and $\phi_a(\mathbf{r})$. This leads to a systematic underestimation of excitation energies ω_{CT} of long-range charge-transfer (CT) excitations, as has been discussed in detail before [250–255].

One way to correct charge-transfer excited states is to include HF exchange in the XC-kernel, i.e., by applying hybrid functionals in the TDDFT calculation [252, 256, 257]. If the fraction of HF exchange is smaller than 100 %, only a partial correction is achieved. Consequently, a hybrid approach was suggested, in which the potential energy curve for a CT excited state is calculated from a CIS calculation, and is subsequently vertically shifted to match a $\Delta\text{SCF-DFT}$ excitation energy at a large donor–acceptor distance [252]. This approach has successfully been applied to xanthophyll–chlorophyll dimers [258, 259] and complexes of zincbacteriochlorin and bacteriochlorin as well as bacteriochlorophyll and spheroidene [260]. There are, however, two drawbacks of this method: First, three different types of independent calculations are needed to get the whole set of excitation energies, namely a $\Delta\text{SCF-DFT}$ calculation for the offset, a CIS calculation for the CT states, and a TDDFT calculation for the remaining states. In particular, the user has to select which states should be taken from the CIS calculation, and which from the TDDFT calculation. Second, if applied rigorously, it would require

to do one Δ SCF-DFT calculation for each CT state that shall be corrected. This could be a problem, since the optimization of higher-energy CT states will not be a trivial task, and might be impossible in many cases. Moreover, the inclusion of exact exchange makes the calculations significantly more demanding for larger systems, as no advantage can be taken of efficient density fitting techniques for the induced potential [236]. This approach might therefore be well suited for cases where a particular charge-transfer state is of interest in the calculation. If the interest is on the contrary in a non-CT state which is hidden among a multitude of CT states, as occurs for solvated chromophores (see Section 3.4), it will not be of much use, since the main problem in those cases is to automatically detect the CT states. A promising class of charge-transfer corrections are those that use a range-separated hybrid kernel, i.e., they partition the operator $1/|\mathbf{r} - \mathbf{r}'|$ in the exact-exchange kernel into a short-range contribution, for which a local functional is used, and long-range contribution primarily based on the exact-exchange expression [253,261]. These developments are based on the corresponding functionals for ground-state calculations [262–266], and have already found considerable applications [267–273]. Although this allows for an automatic correction of CT excitations, it still has the disadvantage of requiring computationally expensive exchange integrals.

In the following, a physically motivated correction to the exchange–correlation kernel is presented, which has the property to selectively correct the CT excitation energies and which does not require the calculation of any HF exchange integrals. The corrected excitation energy depends on the quantity Δ^A (sometimes called the derivative discontinuity), which can, in principle, be calculated rigorously. Although this is certainly necessary to arrive at a high accuracy for the charge-transfer excitation energies, it is possible to find simple, transition-specific estimates for Δ^A , which can automatically be applied. The main benefit from this simple correction scheme is that low-lying valence excitations are easily isolated from artificially low CT states in one single calculation at low computational cost. The same effect can also be achieved by the TDDFT version of the frozen-density embedding scheme [116,184], as will be demonstrated in Section 3.4. However, the present exchange–correlation kernel has the advantage that couplings to orbital transitions in the embedding region are fully incorporated.

In the following, the correction to the exchange–correlation kernel and details relevant for its implementation are explained. Section 3.3.3 subsequently deals with the proper choice of the quantities needed in the correction scheme for the simple test case of two closed-shell atoms at varying distance, before we study intramolecular CT states in the benchmark system of an ethylene–tetrafluoroethylene complex, where several CT states are addressed simultaneously (Section 3.3.4). The usefulness of this simple correction scheme is then demonstrated for a solvated acetone molecule in Section 3.3.5.

3.3.2 Correction for the exchange–correlation kernel

In Ref. [254], a correction for the exchange–correlation kernel was proposed which has the correct asymptotic limit for CT excitations. An empirical switching function should guarantee that only long-range CT excitations are corrected, which are characterized by the fact that the differential overlap $\phi_i(\mathbf{r})\phi_a(\mathbf{r})$ is close to zero. Furthermore, a simpler approximation for the corrected coupling matrix elements was suggested, which

also leads to the correct asymptotic limit,

$$K_{ia,jb} = K_{ia,jb}^{\text{ALDA}} + \delta_{ij}\delta_{ab} \exp[-(O_{ia}/O_c)^2] \left[-K_{ia,ia}^{\text{ALDA}} + \Delta^A - \frac{1}{R_{ia}} + \frac{(\Delta^A - 1/R_{ia})^2}{2(\epsilon_a - \epsilon_i)} \right], \quad (3.56)$$

where $K_{ia,jb}^{\text{ALDA}}$ are the uncorrected coupling matrix elements within the adiabatic local density approximation for f_{xc} , O_{ia} is the orbital density overlap,

$$O_{ia} = \int \phi_i^2(\mathbf{r}) \phi_a^2(\mathbf{r}) d^3r, \quad (3.57)$$

which measures the magnitude of the differential overlap. Note that a few years after the first description of this approach a very similar quantity, namely,

$$\tilde{O}_{ia} = \int |\phi_i(\mathbf{r})| \cdot |\phi_a(\mathbf{r})| d^3r, \quad (3.58)$$

was introduced in Ref. [273] as a diagnostic tool for CT excitations, although no attempt was made to use it for a correction scheme. O_c in Eq. (3.57) is a small empirical parameter to ensure that the the correction term (in square brackets) is only switched on if the overlap integral O_{ia} is small, and R_{ia} is the “average distance” between the orbital densities,

$$R_{ia} = \sqrt{X_{ia}^2 + Y_{ia}^2 + Z_{ia}^2} \quad (3.59)$$

with

$$X_{ia} = \int [\phi_i^2(\mathbf{r}) - \phi_a^2(\mathbf{r})] x d^3r, \quad (3.60)$$

and the corresponding expressions for Y_{ia} and Z_{ia} . The quantity Δ^A , which is the correction applied to the excitation energies in the asymptotic limit of an infinite distance between the electron donor and acceptor in the system, is defined as the difference between the true CT excitation energy, ω_{CT} , and the TDDFT result in the asymptotic limit when employing the ALDA, $\omega_{\text{CT}}^{\text{ALDA}}$, (it also holds for GGA exchange–correlation kernels). For the lowest-energy CT transition at infinite distance, it is given by

$$\Delta^A = \omega_{\text{CT}} - \omega_{\text{CT}}^{\text{ALDA}} \approx I^D - A^A - (\epsilon_A - \epsilon_D) = -A^A - \epsilon_A \quad (3.61)$$

where ϵ_A and ϵ_D are the acceptor’s lowest unoccupied molecular orbital (LUMO) and the donor’s HOMO energies, and I^D and A^A are the ionization energy of the donor and the electron affinity of the acceptor, respectively [254]. The latter equality holds, since $I^D = -\epsilon_D$, i.e., the orbital energies of the highest occupied orbitals in Kohn–Sham theory are strictly equal to vertical ionization potentials [274,275]. For the same reason, we can write the electron affinity of the acceptor as the negative orbital energy of the HOMO of the negatively charged acceptor, ϵ_{A^-} (in case of an initially neutral acceptor), so that $\Delta^A = -A^A - \epsilon_A = \epsilon_{A^-} - \epsilon_A$.

In Ref. [254] it was proposed to use $\Delta^A \approx -\epsilon_A$ as a first approximation. Since the main goal of this study is to apply the asymptotic correction scheme to systems with many charge–transfer excitations hampering a study of intramolecular excitations, we will use

the rather simplistic guess $\Delta^A \approx \Delta_a = -\epsilon_a$ for transitions to arbitrary affinity levels ϵ_a on the acceptor fragment. It is obvious that this simple guess can introduce problems especially for higher-lying virtual orbitals, and it will be demonstrated in Section 3.3.3 that more advanced guesses can be found. In order to avoid unphysical corrections for higher-lying virtual orbitals, the asymptotic correction to a certain excitation will only be applied if $\Delta_a - 1/R_{ia}$ is a positive quantity. I.e., high-lying charge-transfer excitations, which are usually out of the energy range of interest in our examples, will not be corrected. Another consequence of this choice for Δ_a is that the corrected excitation energy in the asymptotic limit is given by

$$\omega_{\text{CT},ia}^{\text{ALDA+cor}} = \omega_{\text{CT},ia}^{\text{ALDA}} + \Delta_a = -\epsilon_i, \quad (3.62)$$

so that all CT excitations from a particular donor orbital will have the same excitation energy at long distances.

As can be seen from Eq. (3.56), our correction scheme interpolates between the ALDA version and the asymptotically correct version of the exchange–correlation kernel or, to be more precise, the corresponding coupling matrix elements. This means that we need to know the individual diagonal elements of the coupling matrix, $K_{ia,ia}^{\text{ALDA}}$, that shall be corrected. As outlined in Section 3.2.3, these coupling matrix elements are not directly calculated for efficiency reasons, and the summation in Eq. (3.47) is carried out implicitly without calculating individual matrix elements $K_{ia,jb}$. However, by combining Eqs. (3.56) and (3.47) we see that the expression for the corrected matrix–vector products still contains particular matrix elements $K_{ia,ia}^{\text{ALDA}}$,

$$\begin{aligned} [p_{\text{out}}^{k,\text{cor}}]_{ia} &= [p_{\text{out}}^{k,\text{ALDA}}]_{ia} + [p_{\text{in}}^k]_{ia} \exp[-(O_{ia}/O_c)^2] \\ &\times \left[-K_{ia,ia}^{\text{ALDA}} + \Delta^A - \frac{1}{R_{ia}} + \frac{(\Delta^A - 1/R_{ia})^2}{2(\epsilon_a - \epsilon_i)} \right], \end{aligned} \quad (3.63)$$

Our correction, thus, puts the additional problem that not only the matrix–vector products, but also the diagonal elements of the matrix \mathbf{K} need to be calculated. A number of facts can be exploited to reduce the computational effort for this task. The matrix elements are directly evaluated in molecular orbital basis. In contrast to this, the fitting of the induced density $\delta\tilde{\rho}_{\text{in}}^k$, Eq. (3.50), and the calculation of the matrix elements of Eq. (3.48) is usually carried out in atomic orbital basis to make use of linear scaling techniques [236, 276]. A second point is that we only want to correct the coupling matrix elements when $K_{ia,ia}^{\text{ALDA}}$ is small due to the vanishing differential overlap. In that case, also the orbital density overlap will be small. Therefore, we approximate $K_{ia,ia}^{\text{ALDA}} \approx 0$ if $O_{ia} < O_c/100$. Note that O_c *should* be chosen in such a way that $K_{ia,ia}^{\text{ALDA}}$ is negligible if the correction is fully switched on. This is a basic assumption in the phenomenological correction scheme applied here. Moreover, the correction will only be applied if the expression

$$T_{ia} = \exp[-(O_{ia}/O_c)^2] \left[\Delta^A - \frac{1}{R_{ia}} + \frac{(\Delta^A - 1/R_{ia})^2}{2(\epsilon_a - \epsilon_i)} \right] \quad (3.64)$$

is larger than a certain threshold (1.0E–6 a.u. per default); otherwise, the correction will not be important anyway. By testing the magnitude of O_{ia} and T_{ia} , we can therefore

reduce the number of explicitly needed diagonal \mathbf{K} -matrix elements significantly. As a further criterion, we might exploit the fact that mixings with high-energy transitions, which are not optimized in the Davidson procedure, are typically negligibly small, so that their diagonal \mathbf{K} -matrix elements need not to be corrected.

A problem can occur in calculations for very large systems: Among the n initial guess vectors for the subspace iteration, there might only be a very small number of non-CT-transitions. Subsequent iterations will in those cases almost always produce excitations which are lower in energy than the initial ones, since many of them are shifted by the kernel correction. The reason for this is that the calculation starts with a very bad guess for those excitations, since the initial vectors are good guesses for the lowest n *uncorrected* excitations. Since there might be many excitations below the corrected CT excitations which are described by the initial guess vectors, subsequently lower and lower roots of the $\mathbf{\Omega}$ matrix may be found. This will result in a rather poor convergence for the lowest excitation energies. A solution is to determine the orbital transitions for which guess vectors are created not on the basis of the orbital energy differences, but to use a corrected guess energy,

$$\Delta E_{ia}^{\text{guess}} = \sqrt{(\epsilon_a - \epsilon_i)^2 + \exp[-(O_{ia}/O_c)^2] \times \left[2(\epsilon_a - \epsilon_i) \left(\Delta^A - \frac{1}{R_{ia}} \right) + \left(\Delta^A - \frac{1}{R_{ia}} \right)^2 \right]} \quad (3.65)$$

which is the correct excitation energy under the assumptions that (i) no off-diagonal couplings exist for the orbital transition $\phi_i \rightarrow \phi_a$, and that (ii) the diagonal elements of the uncorrected coupling matrix, $K_{ia,ia}^{\text{ALDA}}$, are sufficiently small when the correction term is significant. Eq. (3.65) should provide a reasonable estimate for the excitation energies of both CT and non-CT-transitions. For the latter, Eq. (3.65) will reduce to the normal excitation energy guess, $\Delta E_{ia}^{\text{guess}} = \epsilon_a - \epsilon_i$. This guess energy should not only be used to determine which orbital transitions will be the lowest in energy, but also to set up the preconditioner in the Davidson procedure [234,235]. In the long-range limit, where $O_{ia} \approx 0$, Eq. (3.65) results in the following guess for CT excitation energies,

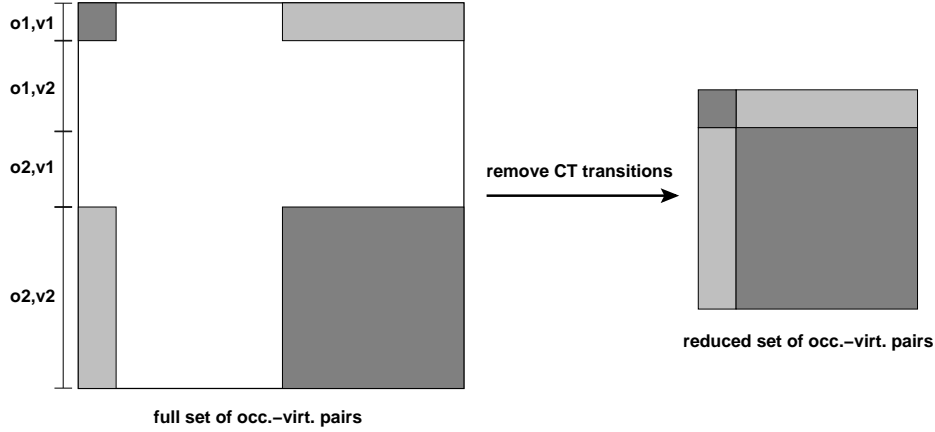
$$\Delta E_{ia}^{\text{CT}} = \sqrt{(\epsilon_a - \epsilon_i)^2 + 2(\epsilon_a - \epsilon_i) \left(\Delta^A - \frac{1}{R_{ia}} \right) + \left(\Delta^A - \frac{1}{R_{ia}} \right)^2} \quad (3.66)$$

$$= \epsilon_a - \epsilon_i + \Delta^A - \frac{1}{R_{ia}}. \quad (3.67)$$

If the differential overlap between the orbitals involved is vanishingly small, this guess energy will be identical to the optimized excitation energy, since the couplings to other orbital transitions will be small. This suggests that — based on the quantities O_{ia} — one might arrive at an even simpler scheme (not used here), in which the space of orbital transitions is restricted to those for which O_{ia} is above a certain threshold. If it is smaller, the guess energies will be sufficiently close to the optimized excitation energies, and the corresponding orbital transitions can be considered to build isolated blocks of the $\mathbf{\Omega}$ matrix.

To illustrate this further, assume that the distance between the fragments is sufficiently large. The (uncorrected) coupling matrix will then have the structure depicted in Figure 3.1. All elements for occupied–virtual orbital pairs located on different fragments

Figure 3.1: Schematic representation of the (uncorrected) coupling matrix \mathbf{K} for a system consisting of two fragments with a large separation. Left: full coupling matrix in the basis of all occupied(o1/o2)–virtual(v1/v2) orbital pairs for fragments 1 and 2. Right: coupling matrix after removal of the orbital pairs corresponding to CT excitations. The white areas correspond to matrix elements that will be (close to) zero due to a zero differential overlap.



will be zero. With that knowledge (based on O_{ia}), we might remove all orbital pairs corresponding to CT transitions to get to the reduced set of occupied–virtual orbital pairs. The correction for the CT excitations can be applied directly to the orbital energy differences. This will reduce the CPU and memory requirements for calculating the matrix–vector products in the subspace iteration procedure. For intermediate distances, some of the CT-like orbital pairs might still be included in the basis for the Davidson diagonalization.

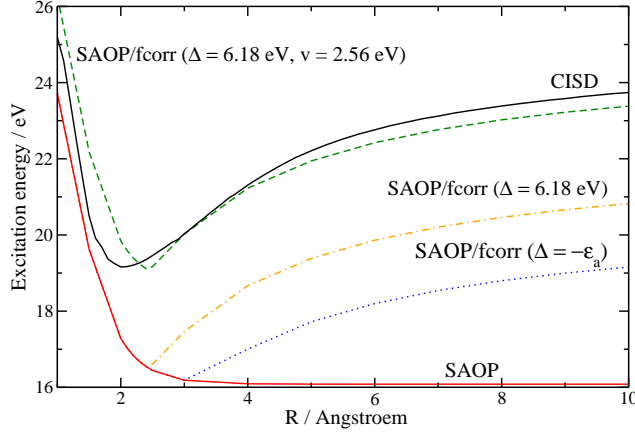
The calculations presented in the following are carried out using a modified version of the program package ADF [277,278], in which the the asymptotic correction to the coupling matrix, Eq. (3.56), was implemented.

3.3.3 Test system: $\text{He} \cdots \text{Be}$

As a simple test, we use the $\text{He} \cdots \text{Be}$ system, for which an initial study was already presented in Ref. [254].

In Figure 3.2 we show the excitation energies for the $1s(\text{He}) \rightarrow 2p_\pi(\text{Be})$ transition of the $\text{He} \cdots \text{Be}$ system as a function of the internuclear distance, obtained with SAOP/TZ2P calculations and different estimates for the quantity Δ^A . Based on some initial tests, the switching parameter O_c was set to 0.0001 a.u. in these calculations. Additionally, the CISD reference values from Ref. [254] are plotted. As mentioned before, we use $\Delta_a \approx -\epsilon_a$ as first approximation for the kernel correction Δ^A . For the excitation under study here, this means that in the asymptotic limit the excitations will be shifted by $-\epsilon_{2p_\pi(\text{Be})} = 4.52$ eV as calculated with SAOP/TZ2P.

Figure 3.2: Excitation energies for the system $\text{He} \cdots \text{Be}$ as a function of the internuclear distance R from SAOP/TZ2P calculations; fcorr: f_{xc} corrected according to Eq. (3.56). CISD data from Ref. [254] are given for comparison.



Already with this simple correction, we observe a qualitatively correct Coulombic behavior in the asymptotic limit, although the difference with respect to the CISD curve is still in the order of 4.5 eV at distances larger than 4 Å. The asymptotically corrected excitation energies presented in Ref. [254] showed a much better agreement with the CISD values, which has two reasons: First, a more sophisticated guess was used for the asymptotic shift, $\Delta_a = \Delta^{\text{Be}} \approx 0.23 \text{ eV} - \epsilon_{2p\pi(\text{Be})}^{\text{acc}} = 6.18 \text{ eV}$. Here, $\epsilon_{2p\pi(\text{Be})}^{\text{acc}} = -5.95 \text{ eV}$ is the orbital energy from an accurate KS solution for the Be atom. The electron affinity $A^{\text{Be}} = -0.23 \text{ eV}$ is taken from Ref. [279]. As can be seen from Figure 3.2, this corrects the former results towards the CISD reference, but there are still differences of $\approx 3 \text{ eV}$ for long distances. Second, the curve in Ref. [254] was corrected for the fact that — with the particular Kohn–Sham potential used — already the zero-order approximation (the orbital energy difference $\epsilon_{2p\pi(\text{Be})} - \epsilon_{1s(\text{He})}$) is too small for the system under study. Instead of the SAOP/TZ2P result for this difference in the long-range limit (16.08 eV), the “ideal” orbital energy difference was estimated from the ionization energy of He and the value of $\epsilon_{2p\pi(\text{Be})}^{\text{acc}}$, which results to 18.64 eV. The fourth curve in Fig. 3.2 was therefore obtained by applying a vertical shift of 2.56 eV (which is the difference between these zero-order guesses) to the results obtained with SAOP/TZ2P and $\Delta_a = 6.18 \text{ eV}$ in the correction to the exchange–correlation kernel. This curve closely follows the CISD data, not only in the asymptotic limit, but also close to the minimum excitation energy.

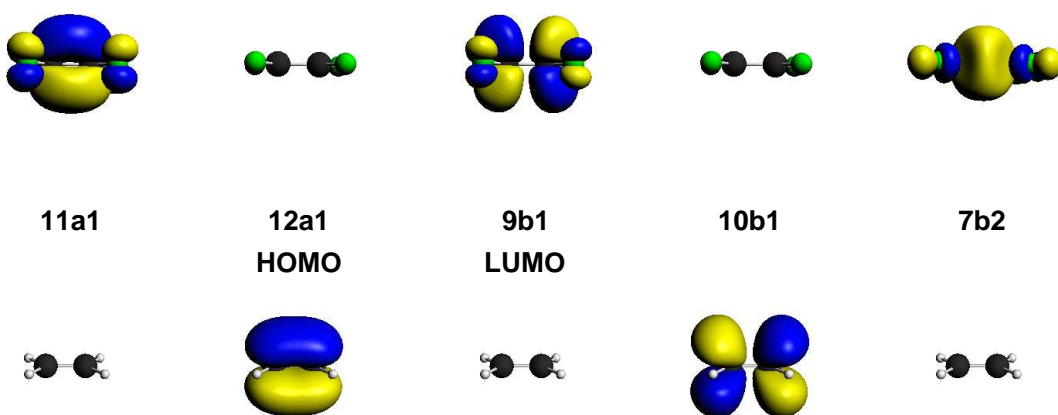
It should be emphasized that the latter correction is necessary only because of the shortcomings of the exchange–correlation *potential* for the current system, and not due to deficiencies of the correction scheme for the exchange–correlation *kernel*.

3.3.4 Simultaneous correction of several states

A second benchmark system for the problem of charge-transfer excitations in TDDFT is the complex of ethylene and tetrafluoroethylene. It was shown in Ref. [252] that typical exchange–correlation potentials, even asymptotically correct ones, show a large error

for the low-lying charge-transfer states of this system. A partial correction could be observed for hybrid functionals, but the correct asymptotic behavior was only recovered when including the full Hartree-Fock exchange in the exchange-correlation kernel, i.e., in a CIS calculation. Isosurface plots of some of the most important orbitals around the HOMO-LUMO gap are depicted in Figure 3.3.

Figure 3.3: Isosurface plots of orbitals around the HOMO-LUMO gap involved in some of the low-lying CT excitations of the ethylene-tetrafluoroethylene complex (ascending orbital energies from left to right).



In Figures 3.4 and 3.5 we show the excited-state potential energy curves for irreducible representations (irreps) A_1 and B_1 of the C_{2v} complex along the intermolecular separation coordinate calculated using SAOP/TZP with and without the kernel correction. There are no low-lying (below 8.5 eV) states in irrep A_2 , and the excitations in irrep B_2 are not given here, since no particular additional information about the performance of the correction scheme is contained in that figure. In contrast to the He-Be system, where the pure excitation energies were shown (for comparability to the CISD reference), we show here the usual energy curves by adding to the excitation energies in this case the change in ground-state energies along the distance coordinate. The ground-state energy for a separation of 10 Å was set to zero.

Figure 3.4 contains the lowest adiabatic potential energy curves for irrep A_1 and will be discussed in some more detail, since there are less states in the interesting energy region than for the other irreps. In the diagram showing the uncorrected curves, all potential energy curves are very flat and show only very small variations with increasing distance. While this is expected for the intramolecular valence transitions, $11a_1 \rightarrow 13a_1$ (tetrafluoroethylene) and $12a_1 \rightarrow 14a_1$ (ethylene), the intermolecular charge-transfer excitations, $11a_1 \rightarrow 14a_1$ (tetrafluoroethylene \rightarrow ethylene) and $12a_1 \rightarrow 13a_1$ (ethylene \rightarrow tetrafluoroethylene) are also almost independent of the distance.

Figure 3.4: Adiabatic excited-state potential energy curves (solid lines) for irrep A_1 of the ethylene-tetrafluoroethylene complex (SAOP/TZP; zero-point: ground-state energy at 10 Å). Left: no kernel correction; right: kernel correction applied. Labels correspond to the character of the excitation at a distance of 10 Å; the character of the excitations may change due to avoided crossings. In the lower diagram, also a pure $-1/R$ -like curve for the $12a_1 \rightarrow 13a_1$ state (dotted line; shifted by +0.05 eV for clarity of presentation) as well as “intuitive” diabatic states are shown, connecting data points of states with similar character (dashed lines; shifted by -0.05 eV for clarity of presentation).

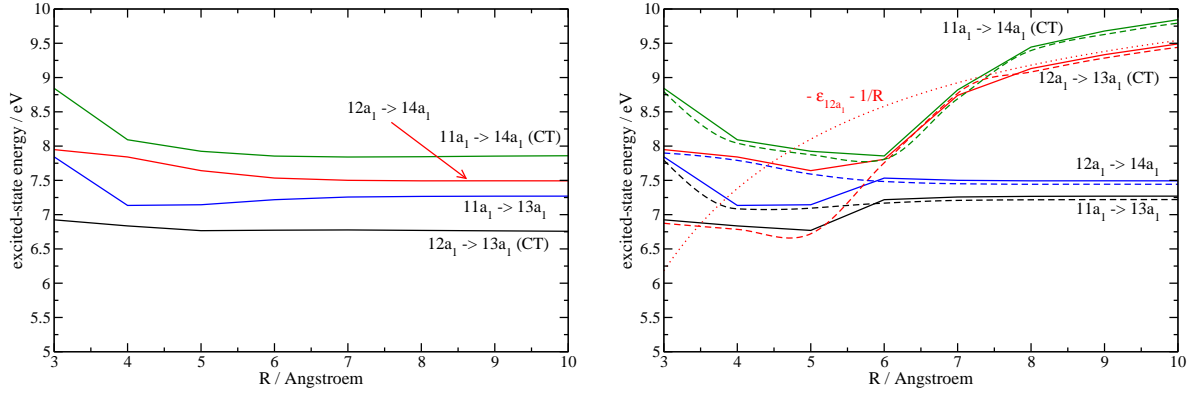
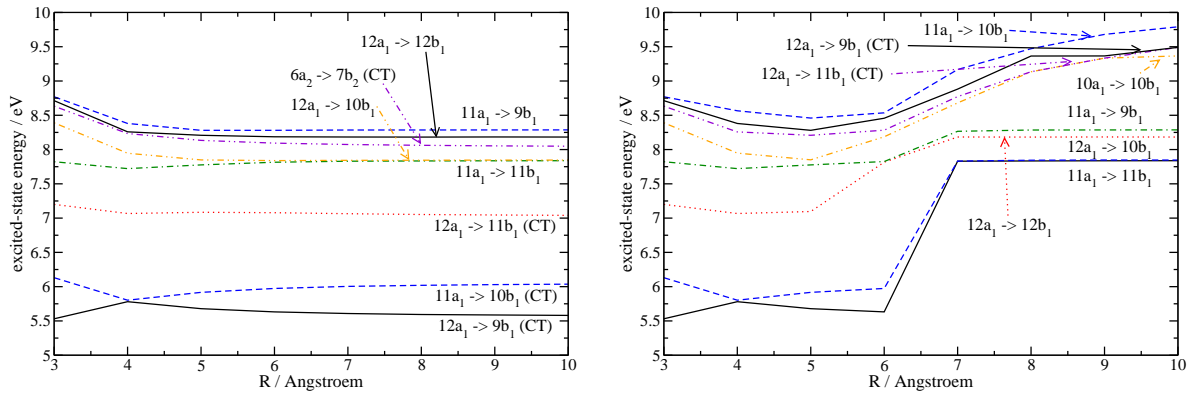


Figure 3.5: Adiabatic excited-state potential energy curves for irrep B_1 of the ethylene-tetrafluoroethylene complex (SAOP/TZP; zero-point: ground-state energy at 10 Å). Left: no kernel correction; right: kernel correction applied. Labels correspond to the character of the excitation at a distance of 10 Å; the character of the excitations may change due to avoided crossings.



In the second diagram in Figure 3.4 it can be seen that the corrected curves agree with the uncorrected results up to a distance of ≈ 5 Å. Between 5 and 6 Å, however, the correction is switched on and pushes the charge-transfer excitations to higher energies, so that avoided crossings occur. To guide the eye through these avoided crossings, we also draw “intuitive” diabatic potential energy curves, connecting data points of states with similar character (dashed lines). From these lines it becomes apparent that

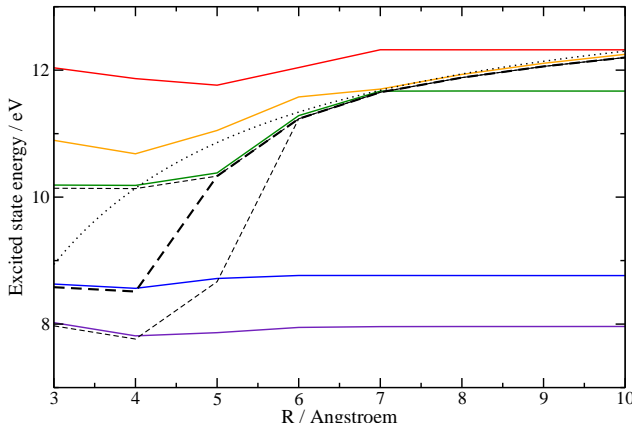
the valence transitions remain at low energies, while the charge-transfer excitations are selectively increased in energy. Although the position of the avoided crossings depends on the choice of our switching parameter O_c , it is obvious that the long-range behavior of the excited-state energies properly has Coulomb shape, as is demonstrated by the additional $-1/R$ -like curve depicted in that figure.

When comparing to the results obtained with the TDDFT-CIS hybrid approach in Ref. [252], it becomes apparent that the corrected CT state shown in that work basically has a $-1/R$ -like behavior over the full R -range between 4 and 10 Å. In our case, the CT-like states show many avoided crossings and interactions with other states, so that the Coulombic shape of the excited-state potential energy curve, even in the “intuitive” diabatic picture, gets lost at short distances. In order to assess whether our correction scheme leads to unphysical results at short distances, we carried out coupled-cluster calculations for the singlet excitations of A_1 symmetry using the CC2 model [204,280] and Ahlrichs’ basis set of valence triple- ζ quality with one set of polarization functions (TZVP) [281,282]. The (linear response) CC2 calculations for ground and excited states were carried out using the program package DALTON [283]. The 8 lowest-energy orbitals, i.e., the 1s orbitals of carbon and fluorine atoms, were kept frozen in the coupled cluster calculations.

The resulting potential energy curves are shown in Figure 3.6. It can be seen that the CC2 excitation energies are, in general, larger than the DFT excitation energies. However, it should be mentioned that initial tests with basis sets of double- ζ quality indicated that the CC2 excitation energies are rather sensitive to the quality of the basis set used, where larger basis sets lead to a decrease in excitation energies. Since the aim of this calculation is only to provide a basis for qualitative comparison, and since the memory requirements for larger calculations are quite demanding, we refrain from using even larger basis sets for these coupled-cluster calculations. Figure 3.6 also contains an “intuitive” diabatic curve, connecting data points with the same character as the lowest CT state (identified by its Coulombic shape in the long-range limit) as well as a $-1/R$ -like curve. It can be seen that also these *ab initio* calculations predict strong deviations from the Coulombic behavior at short and medium distances (up to ≈ 5 Å). At short distances, the character of the CT state spreads over the lowest three excitations, demonstrating that interactions between different excited states play a role. Similar to the results obtained with our correction scheme, the CT state is of lower energy than the $-1/R$ -like curve for intermediate distances (4 to 6 Å). The TDDFT results with the default switching function show this deviation from the Coulombic curve at somewhat larger distances (6 to 7 Å), which suggests that the correction sets in at too low orbital density overlaps. Indeed, a better switching function might be obtained by fitting to such *ab initio* reference calculations. For this work, we restrict ourselves to the default parameterization, which ensures that the asymptotic correction to the exchange–correlation kernel is applied in a “safe” manner, i.e., it is only switched on if the transition under consideration is, without any doubt, of charge-transfer type.

Similar observations as found for the A_1 states can be made for the other two irreducible representations shown: In irrep B_1 , only 3 out of the lowest 7 excitations are of intramolecular valence type for large separations ($11a_1 \rightarrow 11b_1$, $12a_1 \rightarrow 10b_1$, and $11a_1 \rightarrow 9b_1$), while all other excitations are pushed to energies > 9 eV, including the three lowest excitations in the uncorrected case (note that no “diabatic” representations

Figure 3.6: Adiabatic excited-state potential energy curves (solid lines) for irrep A_1 of the ethylene-tetrafluoroethylene complex (CC2/TZVP; zero-point: ground-state energy at 10 Å). We also show a pure $-1/R$ -like curve for the CT state (dotted line; shifted by +0.05 eV for clarity of presentation) as well as the “intuitive” diabatic potential energy curve for the lowest CT-like transition (dashed lines; shifted by -0.05 eV for clarity of presentation). For short distances, the character of this excitation spreads over the three lowest excitations in this irrep (indicated by additional dashed lines).

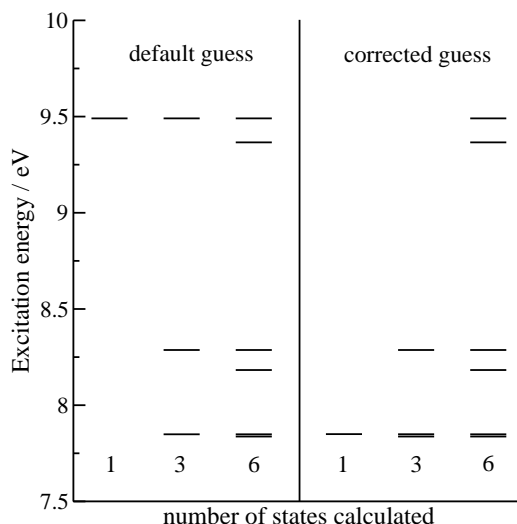


are given in this case for clarity of presentation). Note that the $10a_1 \rightarrow 10b_1$ excitation is not a CT excitation. It is only included in the diagram since it is among the lowest eight excitations at long distances (but not at short distances due to avoided crossings). The correction is typically switched on in an intermediate region of 4 to 6 Å, depending on the exact nature of the transition. For larger distances, the asymptotic correction fully replaces the ALDA kernel for long-range CT excitations, so that characteristic Coulombic potential energy curves are obtained, while the energies of the intramolecular valence excitations are not affected and are independent of the intermolecular separation. In both irreps discussed above, a multitude of avoided crossings occurs due to that fact that the CT-like excitations have low excitation energies at short distances, where the correction function is not applied due to the larger orbital density overlap. Although it is clearly necessary to find more suitable guesses for Δ_a to determine the excitation energies for the long-range CT states quantitatively, already the simple guess applied here is useful to separate the lowest valence excitations from the artificially low charge-transfer excitations. The latter are selectively and automatically shifted to higher energies, and the shapes of the potential energy curves have the correct behavior. This is an important prerequisite for a practically applicable charge-transfer correction.

A problem can be recognized in Figure 3.5: The lowest two curves in irrep B_1 correspond to the $11a_1 \rightarrow 10b_1$ and $12a_1 \rightarrow 9b_1$ transitions in the long-range limit. When the correction is applied, these transitions remain uncorrected up to a distance of 6 Å. The reason for this rather strange-looking behavior is that there is a substantial delocalization of the virtual orbitals between the different subsystems for intermediate distances. The π^* orbitals of ethylene and tetrafluoroethylene mix at intermediate distances (around 5 Å), so that the molecular orbitals extend over both fragments, and the orbital-density

overlap is not small enough to switch on the correction. It should be noted that this is not primarily a parameterization problem, since the orbital overlap is comparable to other orbital pairs localized on one of the fragments only, so that the physical conditions for fully applying the asymptotic correction are clearly not valid in this example. A possible way to correct for such problems could be an intermediate localization step, in particular in cases of purely symmetry-driven delocalization. It has recently been shown that TDDFT methods fail for these systems even if no net charge transfer occurs in the delocalized picture [284–286].

Figure 3.7: Excitation energies obtained for different numbers of optimized states in irrep B_1 of the ethylene-tetrafluoroethylene complex. Left: default guess (orbital energy differences) used to construct guesses for the lowest excitations; right: corrected guess, Eq. (3.65), applied.



If we are interested in the lowest valence transitions only, there is another point to take care of: The computational cost increases with the number of excitations to be determined, so that we usually want to keep the number of states small. On the other hand, that increases the chance of missing a low-lying state, especially if the guess for this excitation is bad. In particular in cases of symmetric molecules, there might only be a few excited states optimized per irrep, so that in each irrep there is a danger of missing important low-lying excitations. The construction of the guess vectors is usually based on the zero-order guess for the excitation energies, i.e., the orbital energy differences between occupied and unoccupied orbitals. For the excitations in irrep B_1 at an intermolecular distance of 10 Å, this is demonstrated in Figure 3.7. Shown are the excitation energies obtained when calculating 1, 3, or 6 excited states in that irrep, either with the default zero-order guess, or with the corrected guess according to Eq. (3.65). With the normal orbital energy difference guess, we get the $12a_1 \rightarrow 9b_1$ excitation if only one root is requested, since this is the excitation with the lowest orbital energy difference (5.58 eV). However, the asymptotic correction shifts this excitation to 9.49 eV due to its CT nature. With the corrected guess energy, we obtain a much lower B_1 excitation at 7.85 eV, which is the $12a_1 \rightarrow 10b_1$ transition. Also this is not the lowest

excitation, a problem that can occur in subspace iteration methods for the highest among the optimized roots. But the problem is much more severe when using the wrong guess. Only when the lowest six excitations in this irrep are calculated, we get the same excitations with both types of guesses.

3.3.5 Application to solvated acetone

The main goal of this section is to investigate the utility of the kernel correction scheme for solvated molecules. In such systems, many spuriously low charge-transfer excitations can occur, so that even a qualitative correction can be of great value if it can selectively correct CT states. As an example, we study acetone surrounded by several water molecules. The test system, which consists of one acetone and 20 water molecules, is depicted in Figure 3.8. It is a finite substructure of a snapshot from the CPMD simulation which forms the basis for the study of the frozen-density embedding TDDFT approach for solvation phenomena in Section 3.4.

19 spuriously low excitations could be found for this system below the first valence ($n \rightarrow \pi^*$) transition of acetone, many of which are transitions from the water-oxygen lone-pairs to the π^* orbital of the carbonyl group. Table 3.1 contains the excitation energies for all excitations up to the one which is identified as the $n \rightarrow \pi^*$ valence excitation of acetone according to the transition density overlap criterion defined in Ref. [116]. A characterization of the molecular orbitals involved is given in Table 3.2. In case of the conventional TDDFT calculation, there are many low-lying excitations of charge-transfer type. In particular, transitions from O_{water} lone pairs to the acetone π^* (e.g., no. 4, 5, or 10) and transitions from O_{water} lone pairs to a Rydberg-type orbital involving hydrogen atoms on a different water fragment (e.g., no. 1, 2, or 3) can be recognized. All of these transitions are shifted upwards when applying the asymptotic correction. The only exception is excitation number 16, a transition from an O_{water} lone pair to a H_{water} Rydberg-type orbital on a neighboring water molecule. Since this Rydberg-type orbital is quite diffuse, the orbital density overlap is still 5 times larger than the parameter O_c , and no significant correction is applied to this transition.

The identification of acetone valence transitions is less easy, since there is no molecular orbital of the cluster that can clearly be identified with the O_{acetone} lone pairs. Instead, these lone pairs mix with O_{water} lone pairs to form the orbitals 110a to 113a, where orbitals 111a and 113a have the largest contribution from the O_{acetone} lone pairs. One of these orbitals (111a), which are delocalized into the solvent region, is shown in Figure 3.8. Transitions from all these four orbitals with partial O_{acetone} lone pair character to the acetone π^* (118a) orbital are basically unaffected by the asymptotic correction with the default switching parameter.

Using the transition density overlap criterion defined in Ref. [116], we find that the excitation at 4.71 eV has the largest overlap with the $n \rightarrow \pi^*$ excitation of the isolated acetone molecule. This is in quite close agreement with the frozen-density embedding calculation on this cluster (see Section 3.4), which resulted in a $n \rightarrow \pi^*$ excitation energy for acetone of 4.78 eV. By construction, no long-range charge-transfer problem can occur in these frozen-density embedding calculations.

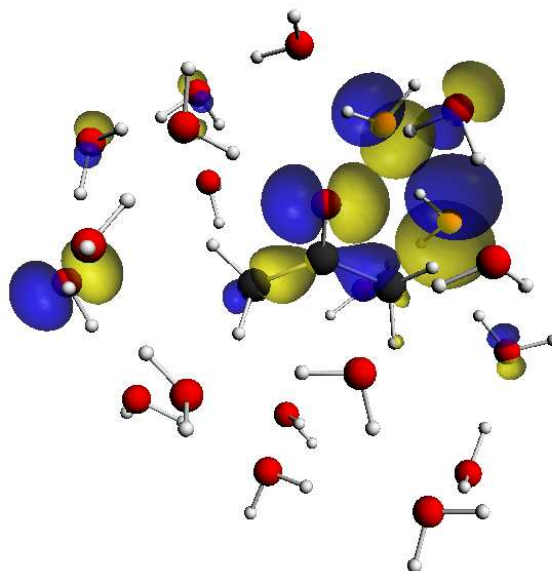
Table 3.1: Excitation energies (SAOP/TZP/DZ; in units of eV) of the lowest transitions of the acetone–water cluster shown in Figure 3.8 from a conventional TDDFT calculation (“conv.”) and calculations with the asymptotic correction. In the latter case, we either used the default switching parameter $O_c = 0.0001$, or a larger value of $O_c = 0.0005$. Also given are the oscillator strengths (in a.u.) from the conventional calculation and the dominant orbital contributions; the orbitals are characterized in Table 3.2.

n	orbitals	f	conv.	$O_c = 0.0001$	$O_c = 0.0005$
1	116a \rightarrow 117a	0.00003	3.4344		
2	115a \rightarrow 117a	0.00002	3.5271		
3	114a \rightarrow 117a	0.00012	3.8155		
4	116a \rightarrow 118a	0.00034	3.8657		
5	115a \rightarrow 118a	0.00094	3.9600		
6	113a \rightarrow 117a	0.00116	3.9747		
7	112a \rightarrow 117a	0.00025	3.9873		
8	111a \rightarrow 117a	0.00059	4.1768		
9	110a \rightarrow 117a	0.00020	4.2072		
10	114a \rightarrow 118a	0.00040	4.2471		
11	109a \rightarrow 117a	0.00011	4.3690		
12	112a \rightarrow 118a	0.00105	4.4218	4.4218	4.7863
13	116a \rightarrow 119a	0.00012	4.4366		
14	115a \rightarrow 119a	0.00125	4.5343		
15	113a \rightarrow 118a	0.01066	4.5417	4.5414	4.5167
16	108a \rightarrow 117a	0.00698	4.5980	4.5981	
17	107a \rightarrow 117a	0.00203	4.6313		
18	110a \rightarrow 118a	0.00034	4.6325	4.6329	
19	116a \rightarrow 120a	0.00016	4.6668		
20	111a \rightarrow 118a	0.00422	4.7112	4.7106	4.6875

Table 3.2: Characterization of the orbitals (SAOP/TZP/DZ) of the acetone–water cluster shown in Figure 3.8.

orbitals	description	occ./virt.
107a ... 109a	O _{water} lone pairs	occ.
110a ... 113a	O _{acetone} lone pairs + O _{water} lone pairs	occ.
114a ... 116a	O _{water} lone pairs	occ.
117a	H _{water} Rydberg	virt.
118a	acetone π^*	virt.
119a, 120a	H _{water} Rydberg	virt.

Figure 3.8: Structure of the acetone–water cluster and isosurface plot of one of the orbitals with partial O_{acetone} lone pair character (111a).

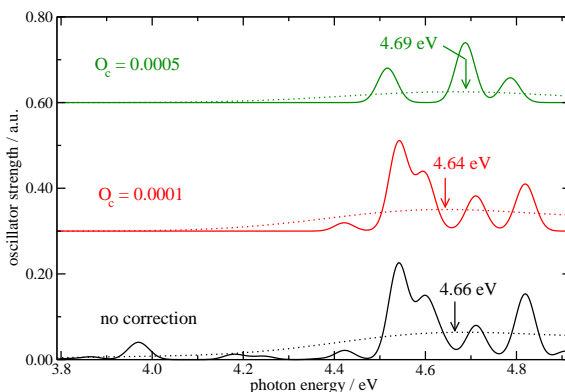


In order to study the influence of the switching parameter, which was determined for the $\text{He} \cdots \text{Be}$ system, on such excitations with mixed character, we increased O_c to 0.0005 in a second calculation. The effect is that the CT excitation to the Rydberg-type orbital is shifted out of this energy range, and also transitions no. 12 and 18 are shifted considerably, since the occupied orbitals for these transitions have only a small orbital density overlap with the acetone π^* orbital. However, the overlap is larger for orbital 112a, and the corresponding correction is smaller, so that transition 12 is still close in energy to the other two orbital transitions with partial $n \rightarrow \pi^*$ valence excitation character. No significant corrections result for the orbital transitions $113a \rightarrow 118a$ and $111a \rightarrow 118a$, but their excitation energies still change a bit because of couplings with each other and with the $112a \rightarrow 118a$ transition.

Simulated spectra resulting from the uncorrected calculation as well as from the two calculations with different switching parameters for the asymptotic correction are shown in Figure 3.9. The spectra are represented with a Gaussian broadening of half-width 0.50 eV (dotted curves) and 0.05 eV (solid curves). The former broadening is often applied to achieve a better comparability with structureless experimental spectra, especially in solution, while the latter allows to distinguish the different contributing excitations. Two important conclusions can be drawn from this picture. First, the default switching parameter does not affect the oscillator strengths of the transitions with the highest intensities in this energy range very much (all transitions have rather low oscillator strengths on an absolute scale), although most of the low-lying transitions are shifted away. If the switching parameter is increased, also excitations with relatively high intensities are shifted away, and the intensity pattern of the individual transitions changes significantly. Also the total intensity decreases. However, in all three cases the maximum of the “broad” curve, i.e., the one with a half-width of 0.50 eV applied

to each transition, is relatively stable at 4.67 ± 0.03 eV. The default parameter of $O_c = 0.0001$ a.u. is thus a safe choice which will not lead to the correction of excitations that cannot unambiguously be identified as charge-transfer transitions.

Figure 3.9: Spectra (SAOP/TZP/DZ) of the acetone-20 H₂O cluster shown in Figure 3.8 from a conventional TDDFT calculation (“no correction”) as well as from two calculations using the asymptotic correction to the coupling matrix with different values of the switching parameter O_c . The spectra are modeled by applying a Gaussian broadening of 0.50 eV (dotted lines) and 0.05 eV (solid lines). For the spectra with a halfwidth of 0.50 eV, also the positions of the maxima are indicated.



The present correction scheme is computationally simple and can be applied to rather large systems. In particular, calculations for molecules in solution will benefit from this correction, which automatically distinguishes between CT and non-CT transitions on the basis of the orbital density overlap. The example for acetone surrounded by water demonstrates that the resulting spectrum is only moderately affected by applying the asymptotic correction, while it is cleaned from many unphysically low excitations. The default choice of the parameter O_c and the switching function used in this study correspond to a “safe” type of correction, since excitations are only corrected if they are definitely of CT type. In doubtful cases, e.g., involving transitions to delocalized virtual orbitals, the conventional ALDA-TDDFT results are obtained, so that the correction scheme never makes the results accidentally worse than before.

The possibility to identify CT excitations according to the orbital density overlap of the occupied and virtual orbitals involved also opens up the way to an even simpler computational scheme, in which the corresponding orbital pairs are removed from the basis in which the matrix $\mathbf{\Omega}$ is diagonalized, as was already mentioned in Section 3.3.2. Since all couplings with other orbital transitions disappear due to the zero differential overlap, their excitation energies can be calculated directly from the orbital energy differences and the simple diagonal correction applied here.

3.4 Frozen-density embedding response theory for solvatochromic effects

3.4.1 Models for solvent effects on excitation energies

Solvatochromism denotes the shift of absorption or emission bands of solutes in solvents of different polarity [287–289]. These shifts are caused by a different stabilization of ground and excited state by the solvent within the Franck–Condon region, i.e., without a re-orientation of the solvent molecules upon absorption or emission. In recent time, several attempts have been made to model the solvatochromic shifts of simple compounds like acetone [290,291], triazines or tetrazines [292–294], solvatochromic organic dyes [295–297], or transition metal compounds [298–301] with different explicit or implicit models for the solvent.

While implicit models, i.e., continuum solvation models, are quite successful to describe non-specific effects, like dielectric medium effects [302–304], explicit models are needed for describing specific solvent effects, e.g., hydrogen bonding. An efficient example for explicit models are quantum mechanics/molecular mechanics (QM/MM) Car–Parrinello molecular dynamics (CPMD) schemes [305] in combination with TDDFT or restricted open-shell Kohn–Sham (ROKS) calculations as presented in Refs. [291,297]. A fully quantum mechanical treatment of the solvent is in principle possible using CPMD³, with a subsequent TDDFT calculation of excitation energies for snapshots of the simulation, as has been demonstrated for *s*-tetrazine [292] or acetone [256,257]. In these calculations, however, the problem of spurious or artificially too low charge-transfer excitations at low energies within TDDFT makes it cumbersome to determine the actual excitations of interest [292], although at least the problem of solute \rightarrow solvent excitations could be partially removed by including Hartree–Fock exchange in the exchange–correlation potential [257,306]. The general problem and a simple correction scheme were presented in Section 3.3. As will be explicitly demonstrated in this section, the problem becomes the more severe the more solvent molecules are involved, making supermolecular TDDFT calculations practically impossible. Even in those cases where supermolecule calculations are still feasible, it may be very difficult to extract the properties of the solvated molecule [307].

The orbital-free embedding formalism [111] outlined in Section 2.6, and its time-dependent response generalization [308] can be of great value in this context: No (or only a few) solvent molecules are explicitly considered in terms of their orbitals, so that no (or only a few) spuriously low excitations occur. Still, the full effect of the solvent molecules’ density on the potential is included. Therefore, FDE offers the possibility to describe both specific solvent effects, since the structure of the solvent is explicitly modeled, and general, non-specific solvent effects since its efficiency allows to include a large number of solvent molecules. Its ability to model hydrogen-bonding induced shifts of excitation energies has recently been demonstrated for nucleic acid base pairs [309]. An alternative method is used in Ref. [248,310], which explicitly takes the full system into account during the SCF steps, but restricts the orbital space in the TDDFT step to those orbitals important for the solute. Our method uses the frozen density embedding

³Strictly speaking, the dynamics in this scheme is still classical, although no classical force-field potentials are applied.

during the SCF procedure, enabling very large environments to be treated, see below. We would like to note that also the TDDFT extension of the fragment molecular orbital method [311,312] can be regarded as a related approach, in which, however, more pragmatic capping strategies are applied for the description of the fragment–fragment interactions than in the FDE scheme (see also Section 2.1).

The aim of this section is to elucidate the advantages and disadvantages of replacing the explicit treatment of solvent molecules in supermolecule calculations by the frozen density approach in FDE, and to develop practical schemes to efficiently model solvatochromic shifts by performing TDDFT calculations for systems with many solvent molecules for many configurations. As an example, the solvent shift of the $n \rightarrow \pi^*$ excitation of acetone in water was chosen, since it represents a benchmark for methods to model solvatochromic shifts. Many experimental [313–317] and theoretical studies [257,290,291] for this system have been carried out, so that reliable reference data are available. This solvent shift has been calculated in Ref. [290] using dielectric continuum models and explicit, polarizable molecular solvent models in a QM/MM scheme. In that work, a solvent shift of $+0.23 \pm 0.04$ eV in water was calculated using the latter, while the continuum models led to much worse results. The experimental shift is between 0.19 and 0.21 eV [313–317]. A recent QM/MM simulation [291] using the restricted open-shell Kohn–Sham approach for the QM part led to a solvent shift of +0.25 eV in water. An entirely quantum mechanical CPMD simulation [257] with a small periodic box of one acetone molecule and 14 water molecules resulted in an approximate solvent shift of 0.206 eV.

3.4.2 Frozen-density embedding for excited states

The ground-state version of the FDE method is described in detail in Section 2.6. Here, we just repeat the explicit form of the embedding potential for the particular case of a partitioning into two subsystems, i.e., $\rho(\mathbf{r}) = \rho_1(\mathbf{r}) + \rho_2(\mathbf{r})$. In Eq. (2.75) of Section 2.6.2, the expression for the embedding potential was obtained as

$$\begin{aligned} v_{\text{emb}}[\rho_1, \rho_2](\mathbf{r}) &= \sum_{A_2} -\frac{Z_{A_2}}{|\mathbf{r} - \mathbf{R}_{A_2}|} + \int \frac{\rho_2(\mathbf{r}')}{|\mathbf{r}' - \mathbf{r}|} d^3r' \\ &+ \frac{\delta E_{xc}[\rho]}{\delta \rho(\mathbf{r})} - \frac{\delta E_{xc}[\rho_1]}{\delta \rho_1(\mathbf{r})} + \frac{\delta T_s[\rho]}{\delta \rho(\mathbf{r})} - \frac{\delta T_s[\rho_1]}{\delta \rho_1(\mathbf{r})}. \end{aligned} \quad (3.68)$$

The time-dependent response formulation of the FDE scheme was given in Ref. [308] in terms of an effective environmental response function. For practical applications involving large environments, the calculation of this response function is neither feasible nor desired. Consequently, a simplification of this expression for local excited states within the active subsystem was proposed in the supplementary material to Ref. [309], which is available in ADF. Basically, the induced potential needed in the linear response TDDFT formalism, see Eq. (3.30), is now evaluated for the active subsystem, so that the change in the potential for system 1 is approximated as

$$\delta v_1^{\text{ind}}(\mathbf{r}) \approx \int d^3r' \frac{\delta v_{\text{eff}}^{\text{sub}}[\rho_1, \rho_2](\mathbf{r})}{\delta \rho_1(\mathbf{r}')} \delta \rho_1(\mathbf{r}') = \int d^3r' f_{\text{xc}}^1(\mathbf{r}, \mathbf{r}') \delta \rho_1(\mathbf{r}'). \quad (3.69)$$

This means that the FDE-TDDFT linear response calculations can just be carried out by using the orbitals and eigenvalues from the ground-state FDE calculation and replacing the exchange–correlation kernel f_{xc} for the active system 1 by an effective kernel f_{xc}^1 , which now also contains a kinetic-energy component. A test of the relative magnitude of the two effects (i.e., orbital embedding and additional kernel contribution) can be found in Ref. [185]. Also the kinetic-energy component of the kernel is, just like the exchange–correlation component, approximated on the basis of the corresponding ground-state functional,

$$f_{xc}^1(\mathbf{r}, \mathbf{r}') = \frac{\delta E_{xc}[\rho]}{\delta \rho(\mathbf{r}) \delta \rho(\mathbf{r}')} - \frac{\delta E_{xc}[\rho_1]}{\delta \rho_1(\mathbf{r}) \delta \rho_1(\mathbf{r}')} + \frac{\delta T_s[\rho]}{\delta \rho(\mathbf{r}) \delta \rho(\mathbf{r}')} - \frac{\delta T_s[\rho_1]}{\delta \rho_1(\mathbf{r}) \delta \rho_1(\mathbf{r}')}. \quad (3.70)$$

For consistency with the ALDA approach applied in ADF, the kinetic-energy component of this response kernel is calculated with the Thomas–Fermi expression for $T_s[\rho]$.

Below, we will compare the TDDFT-FDE calculations of the excitation energies of a solute molecule employing the frozen density representation of the solvent environment to supermolecule calculations.

3.4.3 Construction of the frozen environment density

Since a realistic modeling of solvent effects requires that a large number of surrounding water molecules is taken into account, we wish to perform the calculation of the frozen environment density as simply as possible. For this purpose, we tested different construction methods for the solvent density for two different systems. The first test system is an energy-minimized cluster of acetone with two water molecules, while the second is a much larger cluster of acetone with 52 water molecules, which was obtained as an arbitrary snapshot from a classical MD simulation. Note that in the following all water molecules are included in the *frozen environment* system, if not explicitly stated otherwise, in order to establish well-defined conditions for the calculation.

For both systems we employed different constructions of the solvent electron density. A fully consistent calculation would require to use the SAOP potential, which we use to calculate the vertical excitation energies of the embedded molecule, also for the construction of the solvent density. For comparison, we also tested the much simpler local density approximation in this preparation step. As a further parameter, we tested different values for the SCF convergence parameter s_{conv} in the construction of the frozen density. In our study, convergence is considered reached if the maximum element of the commutator of the Fock matrix with the density matrix used to construct this Fock matrix falls below s_{conv} and the norm of the matrix below $10 \times s$. Besides the default value of $s_{\text{conv}} = 1\text{E}-6$, we also tested larger values of up to $s_{\text{conv}} = 0.5$ for both systems. We note that an "exact" FDE calculation, including for instance basis functions in the full environment system to describe any change of ρ_2 towards ρ in this region, ought to correct automatically for differences in the frozen ρ_2 density. Since our FDE calculations are not exact, the different construction methods imply slightly different approximations, the effect of which we are testing in Table 3.3.

Excitation energies are given in Table 3.3 for two valence excitations of acetone, the experimentally known $n \rightarrow \pi^*$ excitation and a $\sigma \rightarrow \pi^*$ excitation with very low oscillator strength, which is not known from experiment. The latter is included because it shows

a large shift in the calculations, and is therefore instructive for the comparison of Kohn–Sham supermolecule and the frozen density embedding calculations in Section 3.4.4.

Table 3.3: Excitation energies (SAOP/TZP; in units of eV) of the $n \rightarrow \pi^*$ and $\sigma \rightarrow \pi^*$ valence excitations of acetone in water using the QM/QM embedding scheme for clusters with 2 water molecules (optimized structure) or 52 water molecules (structure from arbitrary snapshot of a CPMD simulation). (N.B.: Due to the different structures, the 2 H₂O and 52 H₂O results are not comparable.) For the preparation of the frozen densities, either SAOP/TZP and LDA/TZP (2 water molecules) or SAOP/DZ and LDA/DZ (52 water molecules) were applied in combination with different SCF convergence parameters s_{conv} (see text for explanation). Additionally, approximate densities from superpositions of molecular fragments (“mol. frags.”), either taking the sum of the fragment densities (“sumf.”), or the density obtained after one diagonalization of the Fock matrix based on these fragment densities (“diag.”) are employed.

		2 H ₂ O		52 H ₂ O	
	s_{conv}	SAOP	LDA	SAOP	LDA
$n \rightarrow \pi^*$	1.0E−6	4.7841	4.7873	4.8263	4.8215
	1.0E−3	4.7841	4.7873	4.8263	4.8215
	1.0E−1	4.7841	4.7870	4.8274	4.8222
	2.0E−1	4.7841	4.7878	4.8274	4.8222
	5.0E−1	4.7739	4.7705	4.8300	4.8227
	mol. frags. (sumf.)	—	4.7943	—	4.8171
	mol. frags. (diag.)	—	4.7837	—	4.8249
$\sigma \rightarrow \pi^*$	1.0E−6	7.2819	7.2906	7.2118	7.2196
	1.0E−3	7.2819	7.2907	7.2118	7.2196
	1.0E−1	7.2815	7.2909	7.2082	7.2174
	2.0E−1	7.2815	7.2904	7.2082	7.2174
	5.0E−1	7.2948	7.3157	7.2029	7.2182
	mol. frags. (sumf.)	—	7.2822	—	7.2363
	mol. frags. (diag.)	—	7.2944	—	7.2141

The results of Table 3.3 show that differences between SAOP and LDA densities for the environment are almost negligible: They are between 0.003 to 0.005 eV for a given SCF convergence parameter. Furthermore, it can be seen that even the lowest tested convergence parameter still leads to acceptable results in the FDE–TDDFT calculation. For the determination of the solvent shifts of acetone presented in Section 3.4.5, and the study of the effect of the number of water molecules on the spectrum in Section 3.4.4 we chose a parameter of $s_{\text{conv}} = 0.1$, which resulted in deviations not larger than 0.007 eV for all our tests. This is much smaller than the expected solvent shift. The calculated oscillator strengths are in similarly good agreement.

In another test (“mol. frags.” in Table 3.3) we used the density obtained from a superposition of densities of individual solvent molecules as a guess for the density of the full system of solvent molecules. First, for each solvent molecule (which all may have different O–H bond lengths and H–O–H angles) an SCF calculation is performed to obtain the density. Taking just the sum of these fragment densities as

the frozen environment density is labeled “sumf.” in Table 3.3. We also used this superposition to construct the Coulomb and exchange-correlation potentials of the KS operator, constructed a Fock matrix for the full environment system with these operators, and performed one diagonalization to obtain approximate orbitals and the density of the full frozen system (“diag.” in Table 3.3). The latter is the default for the following discussions. Note that these calculations are not carried out with the SAOP potential, since this potential always requires an intermediate step to construct the orbitals and the density of the system before setting up the potential and the Fock matrix.

The results employing molecular fragment densities are very encouraging with errors smaller than 0.006 eV for the density after one Fock matrix diagonalization, and slightly higher errors for the simple sum of fragment densities (about 0.008 eV for the $n \rightarrow \pi^*$ transition, and about twice as much for the $\sigma \rightarrow \pi^*$ transition). This is particularly important since the bottleneck in the calculation of excitation energies within the FDE approach for very large frozen systems is the SCF to prepare the frozen density. This shows the usual N^3 DFT scaling behavior with the system size N , unless the environment system becomes so large that one enters the linear scaling regime [276]. The use of molecular fragments results in a scaling behavior proportional to N with a very small prefactor in the preparation of the density, since one small SCF calculation for each solvent molecule is required (plus the superposition step). Using a “rigid molecule” approach (see Section 3.4.4), in which the density is calculated only for a limited number of different solvent molecule structures, of which copies are then used to construct the density of outer solvation shells, the preparation of the frozen density requires a constant computational effort, irrespectively of the number of solvent molecules (not considering the superposition step).

3.4.4 Convergence with the size of the solvation shell

The CPMD method will be used in Section 3.4.5 to model the solvent shift by a statistics using many solvent configurations from a CPMD run. For the TDDFT calculations using these snapshot configurations within the QM/QM embedding scheme we have to use a cluster ansatz, since our TDDFT implementation does not allow to use periodic boundary conditions.

In order to investigate the convergence of the excitation energies of acetone with respect to the size of the solvation shell, we calculated the lowest excitations for acetone and acetone embedded in clusters of water molecules of increasing size. All structures employed here are substructures of a particular snapshot from a CPMD simulation as explained in Section 3.4.5. Calculations were performed for the isolated acetone molecule in the structure from the snapshot, and for acetone in structures with 2, 5, 10, 20, 57, and 88 water molecules. For the largest system with 88 water molecules (274 atoms, including acetone; shown in Figure 3.10), we used a simplified density obtained as a superposition of molecular densities as explained in Section 3.4.3 (scheme “diag.”). In order to estimate the effect of this approximation for the current snapshot, we used this simplified method also in an additional calculation on the cluster with 57 water molecules, and similar to the observations in Section 3.4.3, this hardly affects the results. For each of these clusters, excitation energies were calculated in three different ways: (A) A TDDFT supermolecule calculation for the whole system was performed, (B) a

TDDFT calculation for the acetone molecule and the two nearest water molecules, which are bound via hydrogen bonds to the carbonyl-oxygen, is carried out, whereas the effect of the additional water molecules is included via the frozen density embedding, and (C) a TDDFT calculation for the acetone molecule only is performed in which the effect of all water molecules is included via the frozen density embedding. For the largest clusters with 57 or 88 water molecules, we only present calculations of type B and C, since supermolecule TDDFT calculations for such large systems are hardly feasible, and more important, the long-range CT problem of TDDFT would introduce an enormously large number of artificially low excitations as will be shown below. We used the local density approximation (LDA) and a DZ basis set as implemented in ADF [277] to obtain the frozen density of the solvent molecules. Results are given for the $n \rightarrow \pi^*$ and $\sigma \rightarrow \pi^*$ excitations of acetone in Table 3.4. For the smaller clusters, scheme C seems to overestimate the shift in excitation energies for the $n \rightarrow \pi^*$ transition, although the trend with increasing number of water molecules is reproduced. The agreement is usually quite good for the $\sigma \rightarrow \pi^*$ excitation. With scheme B, the results improve considerably in most cases.

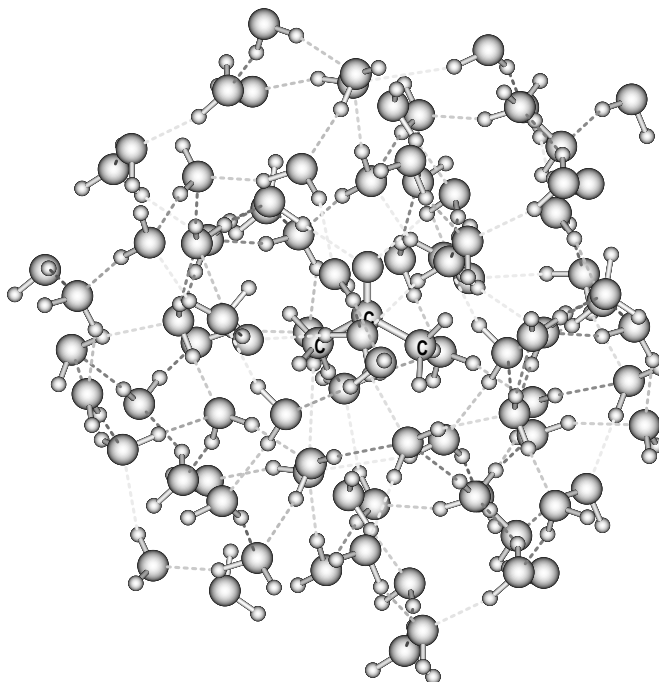
Table 3.4: Excitation energies (SAOP/TZP, LDA/DZ for the frozen part; energies in units of eV) of the $n \rightarrow \pi^*$ and $\sigma \rightarrow \pi^*$ valence excitations of acetone in water using the QM/QM embedding scheme for a snapshot from a CPMD simulation, from which subsystems with different numbers n of water molecules have been extracted. Scheme A: supermolecule calculations; scheme B: the two nearest water molecules are included in the embedded system, the other $n - 2$ water molecules are frozen; scheme C: all water molecules are frozen. For the largest cluster with $n = 88$, the frozen density was constructed as a superposition of molecular densities, see text. For the cluster with $n = 57$, both methods to construct the density are compared.

n	$n \rightarrow \pi^*$			$\sigma \rightarrow \pi^*$		
	A	B	C	A	B	C
0	4.45	—	—	7.40	—	—
2	4.57	4.57	4.69	7.09	7.09	7.15
5	4.50	4.54	4.68	7.16	7.15	7.22
10	4.60	4.66	4.74	7.20	7.13	7.22
20	4.71	4.68	4.78	7.19	7.20	7.25
57	—	4.72	4.78	—	7.14	7.24
57 (mol. frags, diag.)	—	4.72	4.79	—	7.15	7.24
88 (mol. frags, diag.)	—	4.71	4.78	—	7.26	7.28

Note that the “valence excitations” in scheme A given for comparison could only be identified on the basis of the overlap of (modified) transition densities as defined in the diabaticization scheme in Refs. [318,319] because of spurious mixings with charge-transfer-like states. This problem becomes more obvious from the graphical representation of all excitation energies for the water clusters shown in Figures 3.11 (scheme A), 3.12 (scheme B), and 3.13 (scheme C). While scheme C only produces the interesting intra-solute excitations, so that the two valence excitations under study here are always among the

lowest four excitations, scheme B already incorporates some excitations from solvent orbitals at low energies, but still the two excitations of interest ($n \rightarrow \pi^*$ and $\sigma \rightarrow \pi^*$) can always be found among the lowest ten excitations. The additional low-lying excitations found here concern mainly excitations from oxygen lone-pairs of the non-frozen water molecules to orbitals of acetone, e.g., $n(\text{OH}_2) \rightarrow \pi^*$ excitations. The two additional excitations for the isolated molecule below 7.5 eV (Figure 3.13) are of Rydberg type; they are pushed to higher energies by interaction with the solvent molecules. In scheme A, it gets more and more complicated, with increasing number of water molecules, to identify the interesting excitations: For the largest cluster considered in a supermolecule calculation (20 water molecules), the second valence transition cannot be found among the lowest 150 excitations.

Figure 3.10: Example structure of acetone and its 88 nearest water molecules as obtained from a CPMD simulation, substructures of which have been used for a comparison of (partly) frozen density embedding and supermolecule calculations.



The data in Table 3.4 also allow to draw some conclusions about the appropriate size of the solvation shell necessary to converge the shifts in the excitation energies with respect to the number of solvent molecules, and to determine the importance of different factors on these shifts. We restrict ourselves to a discussion of the calculations of scheme C here, since supermolecule calculations of excitation energies for the larger clusters could not be carried out; the calculations according to scheme B with two non-frozen water molecules show the same general trend as the calculations with full embedding, but in some cases, e.g., the $\sigma \rightarrow \pi^*$ excitation for the $n = 20$ cluster, they show strong mixings with excitations of CT type.

The first two water molecules that are considered in the calculation are bound to the

Figure 3.11: Excited states (SAOP/TZP) of acetone–water complexes with different numbers of water molecules. All water molecules have been explicitly taken into account in the TDDFT calculation (scheme A). The longer, dashed lines correspond to the $n \rightarrow \pi^*$ and $\sigma \rightarrow \pi^*$ valence transitions.

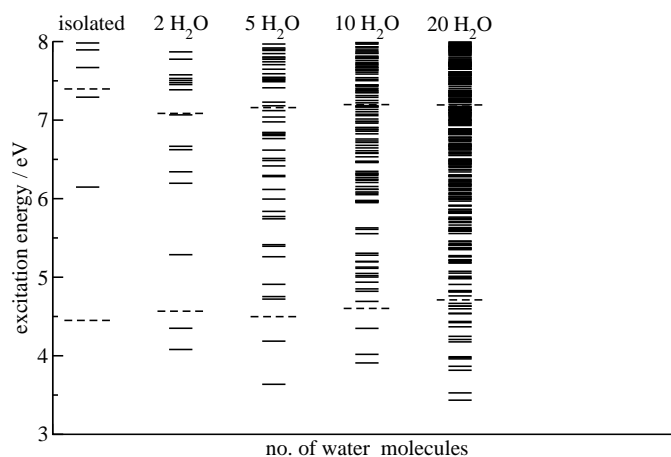


Figure 3.12: Excited states (SAOP/TZP) of acetone–water complexes with different numbers of water molecules. Two water molecules have been explicitly taken into account in the TDDFT calculation (except for the isolated molecule calculation), while all additional water molecules are included via the QM/QM embedding scheme (scheme B). The longer, dashed lines correspond to the $n \rightarrow \pi^*$ and $\sigma \rightarrow \pi^*$ valence transitions.

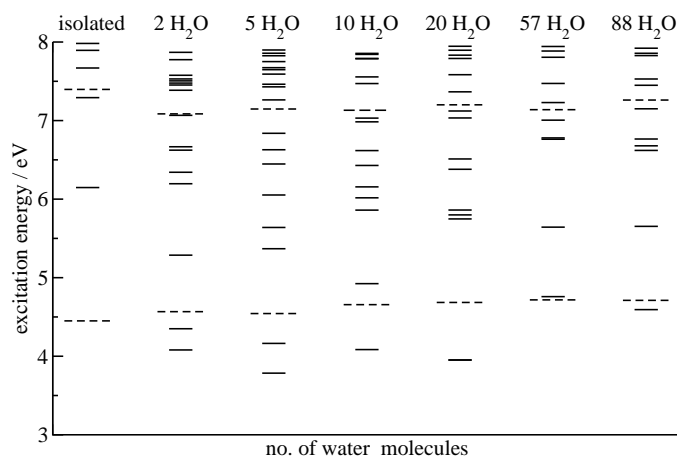
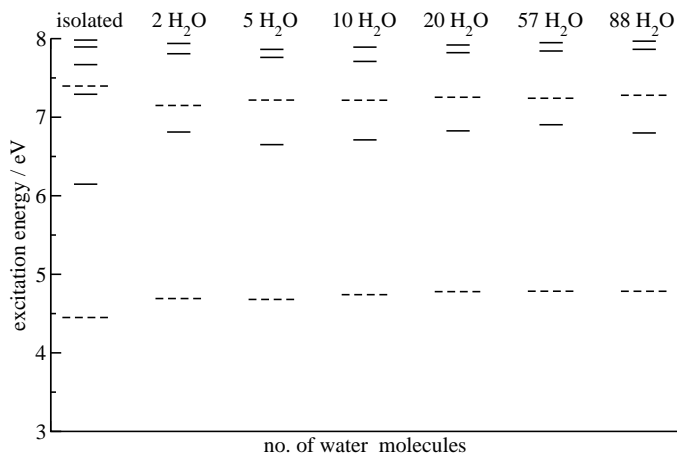


Figure 3.13: Excited states (SAOP/TZP) of acetone–water complexes with different numbers of water molecules. All water molecules are included via the QM/QM embedding scheme in the TDDFT calculation (scheme C). The longer, dashed lines correspond to the $n \rightarrow \pi^*$ and $\sigma \rightarrow \pi^*$ valence transitions.



carbonyl oxygen atom by hydrogen bonds. They have an important effect through their specific interactions: The energy for the $n \rightarrow \pi^*$ excitation increases by 0.24 eV, while for the $\sigma \rightarrow \pi^*$ transition it decreases by 0.25 eV. Further water molecules again cause a blueshift in the excitation energies for both transitions by approximately 0.1 eV. While the excitation energies vary a lot for small numbers of water molecules, the results do not show considerable deviations between the calculations with 20 or 57 water molecules. The latter structure was obtained by cutting a spherical box with a radius of 8.0 Å from the smaller but periodic box of the simulation; this approach was used for all subsequent calculations in the statistical sampling. The additional test with the more approximate density and 88 water molecules shows no change at all for the $n \rightarrow \pi^*$ excitation, while a slight increase of less than 0.04 eV can be observed for the $\sigma \rightarrow \pi^*$ excitation, which is very sensitive to solvent effects anyway.

Even larger numbers of molecules can be treated by this method if, as an additional approximation, the same frozen electron density is used for each water fragment, which appears to be reasonable in particular for those molecules which are further away from the solute. A test for the cluster with 88 water molecules described above, in which such a “rigid molecule approach” for the outer 68 water molecules was used, while the snapshot water structures were employed for the 20 nearest water molecules, resulted in changes lower than 0.003 eV for the valence transitions investigated here. With this approach, and using a simple sum-of-fragments density for the frozen part, we were able to extend the number of solvent molecules to 250. The ADF implementation of the FDE scheme developed during this work furthermore enhances the efficiency of the calculations by making use of linear scaling techniques [276, 320] and restricting the numerical grid to the embedded system only. The latter improvement can also be applied in the context of a general subsystem-TDDFT approach and will be discussed in Section 5.3.2.

The excitation energies as a function of the number of water molecules are shown in

Figure 3.14: Excitation energies (SAOP/TZP, LDA/DZ for the frozen part; energies in units of eV) of the $n \rightarrow \pi^*$ valence excitations of acetone in water using the QM/QM embedding scheme for a snapshot from a CPMD simulation, from which subsystems with different numbers n of water molecules have been extracted (for the largest clusters, also acetone molecules from neighboring cells of the CPMD simulation are included in this value). The frozen density in all cases was constructed as a sum of densities of water fragments. For clusters with more than 100 water molecules, rigid water molecules were assumed for all but the 20 water molecules nearest to the embedded acetone. For the largest clusters, the number n also includes some acetone molecules from neighboring cells of the CPMD simulation.

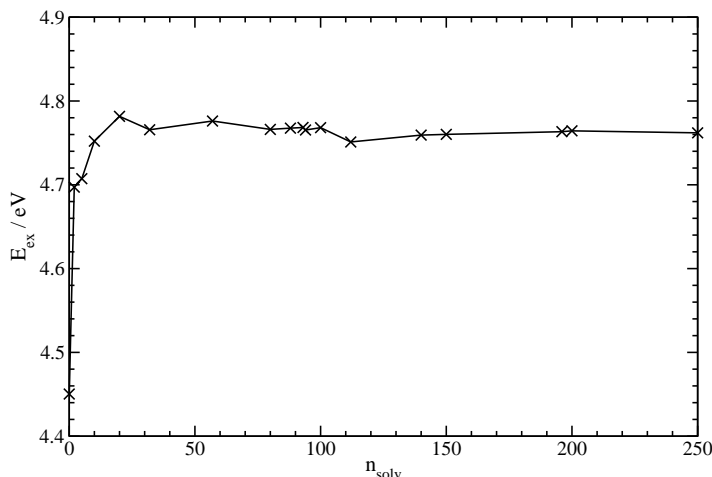


Figure 3.14; the rigid molecule approach for the outer water molecules as described above was used for all structures with more than 100 water molecules. These structures were obtained from the same CPMD snapshot, which means that for the largest clusters also acetone molecules in neighboring cells are included in the frozen density. The maximum number of atoms in this calculation is 802. Again, it can be seen that already with 20 water molecules a plateau is reached, and the changes with increasing numbers of water molecules are very modest, i.e., in the order of 0.01 to 0.02 eV.

This discussion shows that the embedding calculations have great advantages compared to normal Kohn–Sham calculations in the context of solvent effects: (i) The excitation energies are not affected by mixings with spuriously too low CT excitations from solvent to solute (or *vice versa*), (ii) the calculations are much more efficient, so that larger numbers of water molecules can be described on a quantum chemical footing, and (iii) the interpretation of the results is much easier, since only excitations within the embedded system are obtained.

3.4.5 Simulating absorption spectra in solution

The purpose of the calculations presented in Section 3.4.4 was a comparison of the frozen density approach to supersystem calculations, demonstrating the problem of the identification of certain valence transitions among spuriously too low charge transfer excitations in the latter with increasing numbers of water molecules in the calculation.

In order to describe the solvatochromic shifts, however, it is necessary to work with a larger ensemble of solvent configurations for a statistical analysis. We thus performed CPMD and classical MD simulations of acetone in water; while snapshots taken from the CPMD simulations may be more representative in terms of the structures obtained, the classical MD simulations allow to use much larger periodic box sizes to model the solvation, which is certainly necessary if this method shall be applied to larger solvated molecules. Details can be found in Appendix B.

For all following calculations, only the acetone molecule was explicitly considered, while the density of all surrounding water molecules was frozen (scheme C). Considering all water molecules within a sphere of radius $r = 8 \text{ \AA}$ as explained in Section 3.4.4, we obtained systems with between 50 and 61 water molecules from the (CP)MD snapshots, for which we calculated vertical excitation energies using the SAOP potential. A TZP basis set was used for acetone, while a DZ basis set was used for the water molecules in the calculation of the solvent density, which was obtained within the local density approximation (LDA). On average, about 175 atoms are included in the QM/QM TDDFT calculations.

The optical spectrum $f(\omega)$ of acetone was calculated through [306],

$$f(\omega) = \frac{1}{N_c} \sum_{i=1}^{n_{\max}} \sum_{j=1}^{N_c} f_i^j \delta(\omega_i^j - \omega), \quad (3.71)$$

where N_c is the number of solvent configuration snapshots taken into account, n_{\max} is the number of excitations considered for each configuration, ω_i^j is the vertical excitation frequency for a particular state and configuration, and f_i^j is the corresponding oscillator strength.

There are different ways to extract the solvent shift from the calculation, which are more or less well suited in the present case. The simplest way is just to calculate the difference between average transition energies E_{avg} for the gas phase and for the solvated molecule (so averaging over the snapshot configurations without any weighting). Another possibility is to use approximate mean transition frequencies (or the corresponding mean transition energies E_{mte}) for a particular excitation i , in which the vertical transition energies of the snapshots are weighed with the oscillator strengths (cf. Ref. [257]),

$$\langle \omega_i \rangle \approx \frac{\sum_{j=1}^{N_c} f_i^j \omega_i^j}{\sum_{j=1}^{N_c} f_i^j}. \quad (3.72)$$

These values are probably more appropriate, because they emphasize those parts of the spectrum with higher intensities. Experimentally, the solvent shifts are extracted by taking the positions of maximum intensity in the spectrum, E_{max} , which can of course also be extracted from the spectrum simulation. In contrast to E_{mte} , these values do not directly depend on the shape of an absorption band; symmetric and non-symmetric band shapes may still have the same maximum position. However, taking the position of maximum intensity in the simulated spectrum is problematic as long as the number of configurations is small, since single solvent configurations accidentally leading to high oscillator strengths can easily shift the maximum position considerably. It was recently observed [310] that several thousand configurations might be necessary to model

a complete absorption band shape correctly. Therefore, the E_{\max} values are not very reliable if it is not feasible to sample such a large number of configurations, and it seems more appropriate in such a case to extract the maximum position of a Gaussian fit to the simulated spectrum, $E_{\max,\text{fit}}$. Hence, we consider this last way the most appropriate choice in our study for a comparison of our simulated data with the results extracted from experiment.

Table 3.5: Estimations of the $n \rightarrow \pi^*$ solvent shift of acetone in water (compared to the vapor spectrum) using different ways to estimate the peak maxima. All energies given in units of eV. Also given is the number of configurations $n_{\text{conf.}}$ used to extract the values. The labels have the following meanings: mte: mean transition energy; avg: average transition energy; max: peak maximum in simulated spectrum; max, fit: peak maximum in Gaussian fit to simulated spectrum (recommended).

structure	$\rho_{\text{H}_2\text{O}}$		$n_{\text{conf.}}$	E_{mte}	E_{avg}	E_{max}	$E_{\text{max,fit}}$
vapor							
CPMD	—		300	4.4601	4.4740	4.4560	4.4746
exp. [313–315]							4.48 to 4.49
solution							
CPMD	frozen ($s_{\text{conv}} = 0.1$)		44	4.7094	4.6890	4.6940	4.7221
		shift		0.2493	0.2150	0.2380	0.2475
CPMD	frozen (mol. frags., sumf.)		44	4.6925	4.6735	4.6700	4.7131
		shift		0.2324	0.1995	0.2140	0.2385
CPMD	frozen (mol. frags., diag.)		44	4.7020	4.6818	4.6940	4.7149
		shift		0.2419	0.2078	0.2380	0.2403
CPMD	frozen ($s_{\text{conv}} = 0.1$), relaxed		44	4.7686	4.7449	4.8480	4.7832
		shift		0.3085	0.2709	0.3920	0.3086
MD	frozen ($s_{\text{conv}} = 0.1$)		25	4.6793	4.6793	4.7240	4.6963
		shift		0.2192	0.2053	0.2680	0.2217
CPMD	frozen ($s_{\text{conv}} = 0.1$)		220	4.7184	4.7000	4.6740	4.6791
		shift		0.2583	0.2260	0.2180	0.2045
CPMD	frozen ($s_{\text{conv}} = 0.1$)		219	4.6883	4.6978	4.6740	4.6791
		shift		0.2282	0.2238	0.2180	0.2045
exp. [313–317]							4.68 to 4.69
		shift					0.19 to 0.21

We carried out general analyses with a small number of snapshots for different ways to describe the solvent density. For each of these approaches, we present the calculated energies and solvent shifts extracted with all four different methods described above in Table 3.5. A gas phase CPMD simulation for isolated acetone at 300 K resulted in a value for $E_{\max,\text{fit}}$ of 4.4746 eV obtained from 300 snapshots of a 12 ps simulation time (compared to a vertical excitation energy of 4.58 eV for the optimized structure of acetone), and all other ways to estimate the band maximum agree within 0.019 eV. This is in very good agreement with the experimental value of 4.48 [313,315] to 4.49 eV [314]. Note that in the gas phase it is not possible to use a conventional thermostat, so the temperature in this CPMD simulation was kept constant by applying a very

small negative friction to the atoms.

As a starting point for the solvation models, we used 44 solvent structures from the CPMD simulation as described above. We first applied the default scheme to obtain the frozen density, i.e., all water molecules were frozen, and the density was obtained in an SCF calculation on the full set of water molecules with a convergence criterion $s_{\text{conv}} = 0.1$ (see Section 3.4.3). This results in solvent shifts between 0.2150 (based on E_{avg}) and 0.2493 eV (based on E_{mte}), so that all shifts agree within 0.034 eV. In order to show that the frozen density can also be constructed by a superposition of molecular densities as described in Section 3.4.3, we calculated the solvent shifts for the same set of structures using this approach for the density of the environment. The changes are very slight if one explicit Fock-matrix diagonalization is carried out (“diag.” in Table 3.5), with solvent shifts between 0.2078 and 0.2419 eV. The deviations are slightly larger, but still acceptably small, with solvent shifts between 0.1995 and 0.2324, if a simple superposition of water densities is performed (“sumf.” in Table 3.5). As a next test for the same set of structures, we first calculated the density of the acetone molecule for each structure, which was then frozen to calculate a relaxed density of the surrounding solvent. This relaxed solvent density was then employed in an embedding calculation for the acetone. The relaxed environment leads to solvent shifts that are a bit higher, typically in a quite systematic way by about 0.06 eV. This is a case where the maximum in the simulated spectrum is “accidentally” too high, leading to an anomalously large shift of 0.3920. The other shifts are around 0.30 eV, and agree to within 0.038 eV. These results are somewhat out of line, although we expect a significant effect (i.e., a decrease by about 0.04 eV) of using an extended set of solvent configurations (see below).

In an additional test, which is not shown in Table 3.5, we included the two nearest water molecules explicitly in the embedded system, again using the same 44 snapshots. Compared to the first simulation, this typically reduces the solvent shift by about 0.04 eV, leading to values between 0.1739 eV (based on E_{avg}) and 0.2255 eV (based on $E_{\text{max,fit}}$). The value based on E_{max} again is an exception; with 0.3240 eV it is much higher than all other shifts based on this model for the solvation. This test suffers, however, from the mixings with CT-like excitations mentioned in earlier sections of this work: For practically every snapshot, more or less strong mixings with $n(\text{OH}_2) \rightarrow \pi^*(\text{acetone})$ excitations could be observed. In many cases, the identification of the $n \rightarrow \pi^*$ excitation was only possible based on the transition density overlap criterion defined in Refs. [318,319]; some snapshots gave rise to two excitations with competing $n \rightarrow \pi^*$ contributions, which shows that the resulting statistics is not very reliable.

A last comparison was made with 25 structures obtained from a classical MD simulation. The solvent shifts are between 0.2053 (based on E_{avg}) and 0.2217 (based on $E_{\text{max,fit}}$); also here, the E_{max} value is somewhat of an outlier with 0.2680, which demonstrates again that it is a less reliable measure of the shift. No large discrepancies are observed in comparison to the CPMD simulation. However, the structures from two of the snapshots led to severe convergence problems in the SCF calculation for the solvent because of near-degenerate orbitals at the HOMO-LUMO gap, and subsequently to unreliable TDDFT results. This seems to be purely a problem of the SCF procedure, caused by an unrealistic structure of the solvent: If only the superposition of the solvent fragment densities is used (scheme “diag.”), the resulting excitation energies

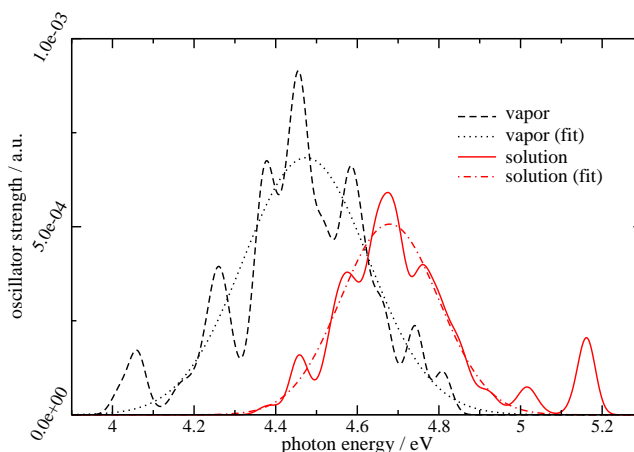
and oscillator strengths are within the normal range. Therefore, we have to conclude that the classical MD occasionally leads to structures which can induce SCF problems, so that the resulting densities are not in all cases reliable approximations. In other studies, such problems with classical MD simulations were circumvented by performing a small CPMD relaxation after a QM/MM CPMD study [291].

The final spectrum was simulated using 220 solvent configurations from the CPMD simulation, in which the total water environment density was frozen and unrelaxed; the density was obtained from an SCF calculation with a convergence threshold of $s_{\text{conv}} = 0.1$. The band of the $n \rightarrow \pi^*$ transition is shown in Figure 3.15, together with the simulation of gas-phase acetone. The solvent shift extracted from the Gaussian fit to the band is 0.2045 eV. This is 0.0430 eV lower than for the smaller set of 44 snapshots, and in excellent agreement with the experimental values of 0.19 to 0.21 eV and with former theoretical studies mentioned in the introduction. Also the maximum position of the spectrum and the average transition energies confirm this value, differing by less than 0.02 eV in the calculated shift. Only the mean transition energy results in a somewhat higher shift of 0.2583 eV, which can still be considered a good estimate for the experimental value. This somewhat too high value can exclusively be attributed to one outlier in our data set: we obtained one configuration with an excitation energy of 5.16, which has a very high oscillator strength and is therefore responsible for the peak at the high-frequency border of this band. If we neglect this one outlier, the shift computed by mean transition energies decreases to 0.2282 eV, in much better agreement with the other values. The maximum position of the spectrum does not change at all, the average transition energy changes only very little, and also the changes in the maximum of the fit are negligible. This latter point is due to the fact that we use a symmetric Gaussian function to fit our data, so that a better description of the outlier in the fit would dramatically decrease the quality of the fit in the low-frequency regime of this band. It therefore does not affect this fit very much. We would like to note that not only the solvent shift, but also the estimated band maximum of 4.6791 eV obtained in this way is in very good agreement with the experimental values of 4.68 [314] to 4.69 eV [313,315–317].

Our tests with relaxed frozen densities showed that relaxation typically leads to an increase of the excitation energies of about 0.06 eV, which was quite systematic for the structures investigated. Therefore, we expect that relaxation would also increase the solvent shift for the large set of 220 snapshots to about 0.26 eV. The solvent shifts obtained with different ways to construct the frozen density can therefore be estimated to lie in the range of 0.20 to 0.26 eV.

There is another interesting point about our simulation: In the experimental spectra in Refs. [313,314], it can be seen that the structureless vapor absorption band of the $n \rightarrow \pi^*$ transition is a bit broader than the spectrum in aqueous solution. Although it is difficult to extract exact values, the half-widths can be estimated to roughly 7000 cm^{-1} (0.87 eV, vapor) and 6000 cm^{-1} (0.74 eV, solution). The Gaussian fits to our final simulated absorption bands qualitatively agree with this observation: While the fitted gas-phase spectrum has a half-width of 0.51 eV, the solution spectrum has a reduced half-width of only 0.40 eV. But in terms of absolute values, these half-widths are still too low, and a much larger statistics might be necessary to draw definite conclusions about the full shape of the absorption band. The calculated absorption intensities are

Figure 3.15: Simulated (SAOP/TZP/DZ) absorption spectrum of acetone in water. Excitation energies have been calculated for snapshots from a CPMD simulation for acetone vapor (dashed line) or acetone in water (solid line), respectively; all water molecules within a radius of 8 Å from the acetone molecule have been considered in the latter calculations, and have been treated in a frozen density fashion. In total, 300 (vapor) or 220 (solution) configurations have been sampled. A Gaussian smearing of 0.05 eV has been applied to the peaks in the spectrum. Additionally, the curves of a Gaussian fit to the simulated absorption bands are shown for the gas-phase (dotted line) or solvated (dashed-dotted line) molecule, respectively.



less reliable; the basis set requirements for converging them are usually much larger than for the excitation energies. Moreover, the confinement of the response to the embedded system may make the electron density of the embedded system less polarizable. We therefore refrain from an interpretation of changes in the intensities in terms of physical effects in this work.

The calculations in this section clearly show the potential of the frozen density embedding in the calculation of excitation energies for solvated systems. In the first place, this embedding approach implies a restriction to the interesting intra-subsystem excitations, where the embedded system can be defined by the user. Other excitations, which might be real or spuriously shifted to the energy range investigated by failures of the (TD)DFT approach, are not obtained. This has a number of important consequences for studies on solvated systems: (i) Embedding calculations are inherently less demanding, especially for TDDFT calculations with many solvent molecules. (ii) In contrast to supermolecule calculations on systems like the one studied here, the number of low-lying excitations is constant, which makes embedding calculations even more advantageous when large solvent shells are included. (iii) The interpretation of the results is much easier, and the excitations are not affected by mixings with spuriously low CT excitations.

As demonstrated above, the excitation energies obtained from the embedding scheme are not very sensitive to approximations made in the construction of the frozen density. Of particular interest is the possibility to use superpositions of molecular densities, which replaces a calculation on a system with N molecules by N calculations on systems of

just one individual molecule; we will elaborate on this point in Section 4.3.

This gain in efficiency is decisive for the calculation of the solvatochromism for the $n \rightarrow \pi^*$ excitation of acetone in water on the basis of the CPMD trajectory. The estimated shift of 0.20 eV is in perfect agreement with the experimental shifts of 0.19 to 0.21 eV [313–317]. However, the study of density relaxation of the solvent system, which increased the calculated solvent shift by about 0.06 eV, indicates that this very good agreement is partially due to error cancellation effects. Possible error sources here could be the non-additive kinetic energy functional, the basis set limited to the embedded system, and the limited statistics of only 44 snapshots for the polarized frozen-densities. In view of the variety of factors influencing the simulation of solvatochromic shifts, these results are still very encouraging.

4. Environmental Effects on Molecular Properties and Valence Excited States

Subsystem approaches to DFT have initially been developed to enable efficient quantum chemical calculations of (interaction) energies in complex systems as outlined in Section 2.8. A variety of other schemes have been proposed and applied in the past for this purpose, and some of them were discussed already in Section 3.4.1. As particular examples, we mention continuum solvation models [302,304,321,322], effective potential methods [323,324], including the so-called *ab initio* model potentials, which are directly based on the electron densities of the environment [325,326], QM/MM schemes [131–135], or general multi-layer approaches such as the ONIOM model [136,137].

One of the advantages of subsystem DFT methods is the fact that not only a so-called “mechanical embedding” is achieved, in which the effect of the environment is only included in terms of interaction energies, but also an embedding in terms of an effective local potential as introduced by Wesolowski and Warshel [111] arises naturally. Interaction potentials with a similar aim can, of course, also be integrated into other approaches [120,327], but usually these potentials contain empirical, system-dependent terms or do not account for all types of interactions. In contrast to that, FDE incorporates both electrostatic as well as non-classical effects in a non-empirical way (apart from the usual parameterization of the density functionals employed). This allows to extract properties depending on the electron density or the orbitals of the embedded system. Furthermore, we have seen in Section 3.4.2 that the calculation of response densities and excitation energies is possible within the generalization of the FDE method for excited states [308,309].

In this chapter, we will first review previous calculations of molecular properties with FDE and related methods. Subsequently, practical schemes for the use of FDE as an explicit solvent model will be presented for calculations of electron spin resonance (ESR) hyperfine coupling constants as well as absorption spectra. In Section 4.4, it will be investigated whether induced circular dichroism phenomena, which are mediated by specific interactions between two subsystems, can be studied on the basis of FDE.

4.1 A review of subsystem-DFT based molecular property calculations

4.1.1 Structures, dynamics, and vibrational properties

The structure optimization of molecular complexes on the basis of subsystem DFT requires the availability of analytical energy gradients, except for very simple, highly symmetric molecules or partial optimizations, in which only a limited number of nuclear degrees of freedom has to be considered [165]. Such gradients also give direct access to

the forces on the nuclei as required in molecular dynamics simulations on the basis of subsystem DFT schemes. Furthermore, they allow to calculate vibrational frequencies by numerical differentiation in cases where analytical second derivatives are not available [328].

An analytical gradient implementation for the FDE scheme was described by Wesolowski *et al.* [329]. The accuracy of the structures obtained within this approach was recently investigated [170]. The largest deviations for intermolecular distances found between structures from subsystem DFT within the local density approximation and accurate wavefunction-based calculations were 0.13 Å for hydrogen-bonded complexes, 0.19 Å for dipole-bound complexes, 0.23 Å for complexes with π -interactions and 0.32 Å for rare gas dimers. GGA-type approaches resulted in worse intermolecular distances for almost all complexes studied.

Warshel and co-workers presented a QM/MM dynamics study on the autodissociation of water in aqueous solution, in which a constrained DFT treatment was tested in order to enlarge the quantum region during the calculation [149]. They constructed a frozen environment from a set of individual water molecules surrounding the active subsystem. Only the interactions between the active subsystem and each water molecule in the environment individually were treated in with the (freeze-and-thaw) frozen-density embedding approach, whereas all interactions between all frozen water molecules were evaluated classically. Barker and Sprik [330] performed a molecular dynamics study essentially based on the Gordon–Kim approach, i.e., with completely frozen electron densities. For computational simplicity, they used several pseudo-density models, in which the charge density of the valence electrons was fitted to the results of Hartree–Fock calculations. The frozen pseudo-densities were empirically modified to vary the molecular dipole moments, and the resulting potential energy curves were compared to classical force field models. Evidence for a second solvation shell, as is found in experiment, could be observed in the O–O radial distribution function only with molecular densities corresponding to a high dipole moment (2.95 D). Hutter and co-workers [110] proposed a molecular dynamics scheme based on a subsystem DFT approach as outlined in Section 2.5, in which the subsystem orbitals for all molecular fragments are optimized simultaneously, and tested it in a simulation of liquid water. It turned out that the water molecules in solution were not fully polarized. Although the first solvation shell was reasonably described, the subsystem DFT approach did not lead to the characteristics of a second solvation shell (in contrast to experiment and Kohn–Sham DFT simulations). Variation of the kinetic energy functional had a small effect on the position and peak height for the band corresponding to the first solvation shell in the O–O radial distribution function, but no functional gave rise to a second peak. This problem might be related to the lack of directionality in the deformation densities observed for the hydrogen-bonded complexes in Section 2.9.

Recently, Hodak *et al.* have presented a method very similar to the above approaches, in which an orbital-free DFT scheme was used to perform a molecular dynamics calculation of liquid water [331]. They used fixed electron densities for the water molecules described by three atom-centered Gaussian functions per water molecule, i.e., one function per atom. The parameters for the Gaussian functions were chosen in such a way that the molecular charge and dipole moment are reproduced, and the exponents were used as free parameters to fit the experimental radial distribution functions. This approach was

then combined with a Kohn–Sham treatment of an active subsystem. It can thus be regarded as a simplified version of the frozen-density embedding approach with a sum-of-fragment density for the environment (see Section 3.4.3 and Refs. [116, 184, 332]), in which the solvent molecules’ charge density is represented in a “minimal basis”, employing empirical parameters for optimizing the results.

Vibrational frequencies based on analytical gradients have been studied for complexes of the type Me^+CO ($\text{Me} = \text{K}, \text{Na}, \text{Li}$) adsorbed in zeolite ZSM5 [329]. Supermolecular KS-DFT results could be reproduced for a series of small to medium-sized model clusters for the zeolite environment, some of which were augmented by several thousand point charges to model outer coordination spheres. Also the experimental observation of a decrease in the blueshift of the CO stretching frequency upon adsorption of the Me^+CO could be observed. Another study was performed on the vibrational properties of MnF_6^{4+} [168], in which the local vibrational modes of this complex were studied in cubic fluoroperovskites.

4.1.2 Electric and magnetic properties, excited states

There are rather few studies on electric and magnetic properties from FDE, although their number is increasing in the past years. Among the first properties studied were molecular dipole moments, which are, in a certain sense, an integral measure for the accuracy of the electron density. In Ref. [114], the dipole moment of a water molecule in aqueous solution was studied and found to increase by about 0.2 D compared to the isolated molecule. This is considerably smaller than the experimental estimates or results from other quantum chemical simulations (see Refs. [327, 333, 334] and references therein). The authors argued that this small increase might be caused by the small basis set employed in their study. A later FDE calculation on water in water employing large diffuse basis sets, which did, however, not sample different snapshots from a trajectory, resulted in a change of the dipole moment from 1.80 D for the isolated molecule to 2.45 D for unpolarized surrounding electron densities, and to 2.71 D for partially relaxed environments [185]. The latter study also reported quadrupole moments calculated from FDE, which are found to be in good agreement with a discrete, polarizable classical model for the environmental effect in QM/MM-type calculations.

The dipole moments of several hydrogen-bonded dimers were studied in Ref. [155] as a function of the intermolecular distance. By comparison to supermolecular KS calculations on the dimers, it was found that changes in the dipole moments upon complex formation could be reproduced quite accurately. Even at short distances, about 70 % of the dipole moment increase could be recovered with FDE, although the results for the HCl dimer were less satisfactory. It is interesting to note that the accuracy hardly depended on the kinetic-energy functional chosen for T_s^{nadd} and its functional derivative, respectively (in contrast to the interaction energies).

Induced dipole moments in $\text{CO} \cdots \text{X}$ van der Waals complexes were analyzed in Ref. [122], where X denotes either a rare gas atom or mercury. Whereas experimental dipole moments could be reproduced within 5% for Ar, Kr, and Xe, the results for the lighter rare gas atoms were underestimated. In case of mercury, FDE leads to an overestimation of about 20%. These discrepancies were mainly attributed to the non-additive kinetic-energy functional.

A first study on polarizabilities within the FDE linear response framework outlined in Section 3.4.2 was presented in Ref. [185], which was already mentioned above in the context of dipole moment calculations. However, it turned out that the polarizability of a water molecule in a water cluster from FDE differed qualitatively from the corresponding result of the polarizable classical model. This could be traced back to the missing response of the environment by comparison with finite-field calculations. In Section 5.2 we will present cases for which FDE calculations with a response restricted to the embedded subsystem fail even more badly, and we will show how this problem can be cured.

A generalization of the FDE scheme for nuclear magnetic resonance (NMR) shieldings was recently derived by Jacob and Visscher [335] under the assumption that also the current density of the total system can be partitioned into subsystem contributions. Solvent-induced shifts on NMR shielding constants were modeled for acetonitrile in complexes with solvent molecules. The FDE results agreed with reference calculations from Kohn–Sham DFT within about 2 ppm, which is sufficiently good for solvents like water, where shifts of the order of 17 ppm were found. However, this absolute error remained the same even in solvents for which the shifts in the shielding constants were much smaller, i.e., solvent shift and FDE error are approximately of the same magnitude in those cases. The study of NMR solvent shifts on acetonitrile was later extended by Buló et al. by employing large sets of snapshots from classical force-field MD and CPMD simulations [336]. A semi-quantitative agreement with experimental data could be observed, although the results obtained with the classical force-field method and the CPMD simulation showed a significant difference.

Frozen-density embedding can easily be generalized for spin-polarized cases [337]. Under these circumstances, the embedding potential becomes spin-dependent as well. By means of freeze-and-thaw calculations, it is in principle possible to model spin-polarization effects (see also Section 4.2). This formalism was applied in Ref. [337] to study isotropic electron spin resonance (ESR) hyperfine coupling constants for Mg^+ embedded in neon and argon matrices modeled by small clusters of 8 rare gas atoms. Although the absolute values for these hyperfine coupling constants showed a strong dependence on the basis set used, the differences for the two different matrices were in very good agreement with the experimental reference. Relaxation of the frozen environmental density resulted only in very small changes in comparison with the unrelaxed FDE calculations.

Previous to the first study on solvatochromic shifts based on FDE-TDDFT, which is described in Section 3.4, Wesolowski investigated the effect of hydrogen bonding on the excited states of adenine–thymine and guanine–cytosine complexes. In these calculations, one of the nucleic acid bases was considered as the embedded system, while the other one represented the frozen environment. It was found that the hydrogen-bonding induced shifts, which varied between -0.17 and $+0.67$ eV in KS reference calculations, could be reproduced within ~ 0.05 eV by FDE. Polarization of the environmental densities resulted in only minor changes of the excitation energies for most excitations studied. An exception was the oxygen $n \rightarrow \pi^*$ transition in cytosine, for which this additional polarization changed the hydrogen-bond induced shift by 0.17 eV.

Simplified FDE studies on excited electronic states were also conducted in terms of ligand-field models by investigating the splitting in the f -orbital energies of elpasolite crystals [167, 169]. The splitting energies thus obtained showed a good agreement with

experimental data for the whole series of lanthanide ions.

The following sections describe our own investigations on environmental effects on phenomena like ESR hyperfine coupling constants, absorption spectra, and induced circular dichroism.

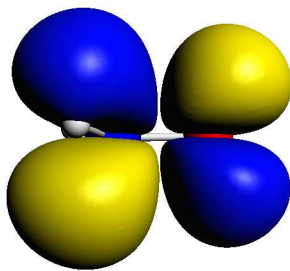
4.2 Solvation effects on ESR hyperfine coupling constants

Quantum chemical calculations of electron spin resonance (ESR) parameters have become a routinely applicable task during the past years (for an excellent overview, see the book by Kaupp, Bühl, and Malkin [338]). Particularly density functional methods are widely used to study g tensors and hyperfine splittings, and their performance was investigated in recent studies (see, e.g., Refs. [339–341]). For many systems, these parameters depend strongly on the environment.

Isotropic hyperfine coupling constants (hfcc) are very sensitive to solvent effects in two respects. First, they often show a strong dependence on the structure of the molecule, and the solvent may have a great influence on certain structural parameters. Second, also for a given distribution of structures, solvation can change the value of the hfcc significantly. Therefore, accurate calculations of these quantities must account for both structural changes between gas phase and solvent as well as for solvent effects at a given structure [342].

Among the best studied radicals are (organic) π -radicals, e.g., nitroxides, semiquinones, or phenoxy radicals. They have been subject to numerous theoretical investigations, and many aspects of solvent effects on their ESR parameters have been analyzed. [343–350]. One prototype system for the family of nitroxides is the H_2NO radical, which shows a strong dependence of the hfcc on the out-of-plane bending angle θ of the NO group from the H–N–H plane. The singly occupied molecular orbital (SOMO) in this case is a π^* -type orbital perpendicular to the molecular plane. An isosurface plot of the SOMO is shown in Figure 4.1. For $\theta = 0$, the direct contribution of the SOMO to the hyperfine coupling constants vanishes for all atoms, since there is no contribution of s -type atomic orbitals to the SOMO for symmetry reasons. It is an ideal example molecule, since many experimental studies in the gas phase [351], argon matrix [352], water [353] and methanol [354] have been carried out. Earlier theoretical studies concerning the solvent effects on this molecule employed mixed classical and quantum chemical approaches: Takase and Kikuchi used snapshots generated from classical Monte Carlo simulations, in which only the angle θ was freely varied. Hyperfine coupling constants were obtained for these structures by restricted open-shell Hartree–Fock-(ROHF-) type calculations, in which a classical point-charge model was used to include the effect of the solvent [355]. In this way, only electrostatic effects of the solvent are covered. Later, Barone *et al.* studied environmental effects by combining static hybrid density functional theory calculations of the hyperfine coupling constants with classical polarizable continuum solvent models [356]. Although the dependence of the hyperfine coupling constants on the angle θ was investigated in that study, the vibrational effect on the average ESR parameters was not explicitly given. It was, however, mentioned that in a related study on H_2NO in vacuo [356] the vibrational averaging effect for the out-of-plane vibration on this radical was small.

Studies on other nitroxide radicals showed that a more sophisticated treatment might be

Figure 4.1: Isosurface plot of the H_2NO SOMO.

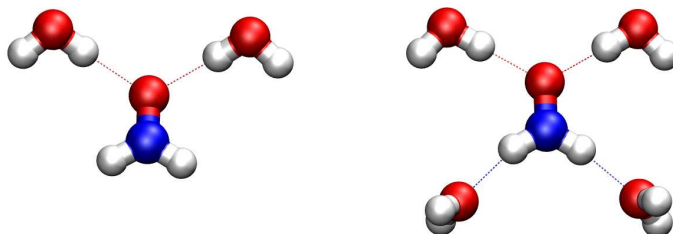
necessary in some cases, where dynamical fluctuations of hydrogen bonded systems have to be described [350]. A CPMD approach was used in Ref. [350] to sample the space of accessible configurations for the solvated system, since earlier studies [348] showed that the angular distribution around the NO group might not be reliably reproduced by studies based on classical force fields as presented in Ref. [349]. For the calculation of hyperfine coupling constants, different methods combining explicit (quantum) water molecules, classical water models, and continuum models were applied for 100 snapshots of the CPMD simulation to simulate bulk solvent effects in Ref. [350].

In this section, we are going to apply a sequential scheme of *first-principles* based CPMD or Monte Carlo simulations for the structure generation with the frozen-density embedding scheme [111] to model solvent effects on the hyperfine coupling constants. This study goes beyond earlier studies in many respects and combines the advantages of several solvent models: (i) Dynamical effects in both gas phase and solution are considered on the basis of *first-principles* electronic structure methods without restriction of the averaging process to certain degrees of freedom, (ii) problems in the gas-phase simulation due to the weak coupling between different vibrational modes are circumvented by a Monte Carlo scheme, (iii) both short-range electronic (or microsolvation) and bulk solvent effects can be studied by this efficient explicit solvent model, (vi) frozen-density embedding includes not only electrostatic effects, but also non-electrostatic effects (exchange–correlation contributions, non-additive kinetic energy effects) and (v) no empirical information enters the calculation of the hyperfine coupling constants in the presence of the solute — apart from the usual parameterization in the density functionals. A direct comparison to experimental data obtained in different media is therefore possible by this approach, which considers both the electronic and the structural changes in the solute upon solvation. We would like to note that the “gas-phase” calculations in our case have to be understood as calculations for an isolated molecule, which we assume to be a simple model for the situation in the gas phase.

4.2.1 Validation of the solvent model

The validation of the frozen-density embedding as a solvent model involves (i) an assessment of its accuracy for short-range or microsolvation effects, and (ii) a test on the convergence of the hfcc with the size of the solvent shell, to ensure a proper modeling of bulk solvent effects.

Figure 4.2: Optimized structures (BP86/ZORA-QZ4P, no symmetry constraints) of two small H_2NO –water clusters.



Short-range solvation effects on the hfcc of nitrogen and hydrogen, such as hydrogen bonding, are assessed by comparing supermolecule and frozen-density embedding calculations for small H_2NO –water clusters, which are shown in Figure 4.2. In Table 4.1 results are shown for supermolecule and frozen-density calculations on these structures. Fully converged SCF densities of the embedding $(\text{H}_2\text{O})_2$ and $(\text{H}_2\text{O})_4$ clusters are employed for the frozen-density calculations; simpler sum-of-molecular-densities superpositions are tested below. If a polarized frozen density is used, i.e., if one freeze-and-thaw cycle [357] is performed — in which the density of the water molecules is calculated in the presence of a frozen H_2NO radical density — the results for the $\text{H}_2\text{NO} \cdot 2\text{H}_2\text{O}$ cluster agree almost perfectly with the supermolecule calculations: The hfcc for hydrogen and nitrogen are -34.75 and 13.97 MHz (polarized frozen-density embedding) compared to -34.73 and 13.98 MHz (supermolecule calculation). Further freeze-and-thaw cycles change the hfcc values by less than 0.02 MHz. If the water molecules are completely omitted for this structure, we obtain values of -32.69 and 12.49 MHz for $a(^1\text{H})$ and $a(^{14}\text{N})$, respectively. As can be seen, already the non-polarized frozen-density calculation yields most of the effect of the water molecules with hyperfine splittings of -34.34 (^1H) and 13.69 MHz (^{14}N). For the cluster with 4 water molecules, there is a slightly larger deviation between supermolecule and embedding calculations, but also here the embedding captures most of the effect. This can be expected, especially for the hydrogen hfcc, since the border between the frozen and non-frozen region is much closer to the hydrogen atoms for the $\text{H}_2\text{NO} \cdot (\text{H}_2\text{O})_4$ cluster than for the $\text{H}_2\text{NO} \cdot (\text{H}_2\text{O})_2$ cluster.

We would also like to note that spin polarization of the environment can, in principle, be modeled by the frozen-density embedding. This effect can be included by using freeze-and-thaw cycles in combination with spin-unrestricted frozen-density preparation calculations. By comparing freeze-and-thaw cycles with spin-restricted frozen densities for the water molecules to those with spin-unrestricted frozen solvent densities for a small H_2NO –water cluster, we found that the spin polarization of the solvent molecules is low, leading to changes in the hyperfine coupling constants which are smaller than those of the density relaxation (ca. 0.1 to 0.3 MHz).

Table 4.1: Isotropic hfcc a (MHz) for $\text{H}_2\text{NO} \cdot 2\text{H}_2\text{O}$ and $\text{H}_2\text{NO} \cdot 4\text{H}_2\text{O}$ from unrestricted, scalar relativistic BP86/ZORA-QZ4P supermolecule and frozen-density embedding calculations. Water molecules in parenthesis denote calculations in which structures were taken from optimizations including the water molecules, while the water molecules were not considered in the ESR calculations. For all structures, we give the out-of-plane bending angle θ (degrees).

	$\text{H}_2\text{NO} \cdot 2\text{H}_2\text{O}$	$\text{H}_2\text{NO} (\cdot 2\text{H}_2\text{O})$	$\text{H}_2\text{NO} \cdot 4\text{H}_2\text{O}$	$\text{H}_2\text{NO} (\cdot 4\text{H}_2\text{O})$
	supermolecule			
θ	10.1	10.1	1.2	1.2
$a(^{14}\text{N})$	13.98	12.49	12.78	10.26
$a(^1\text{H})$	-34.73	-32.69	-38.75	-36.21
	embedding in frozen $(\text{H}_2\text{O})_n$ clusters			
$a(^{14}\text{N})$	13.69		11.85	
$a(^1\text{H})$	-34.34		-38.69	
	embedding in polarized frozen $(\text{H}_2\text{O})_n$ clusters			
$a(^{14}\text{N})$	13.97		12.32	
$a(^1\text{H})$	-34.75		-39.24	

Table 4.2: Isotropic hfcc a (MHz) for $\text{H}_2\text{NO} + 2 \text{H}_2\text{O}$ from unrestricted, scalar relativistic BP86/ZORA-QZ4P embedding calculations with different basis sets for the frozen system. Additionally, results are given for a sum-of-fragments calculation of the frozen density, in which LDA/ZORA-TZP was used to generate the water fragments.

	QZ4P	TZP	DZP	DZ	LDA/TZP, sum-of-fragments
$a(^{14}\text{N})$	13.69	13.82	13.88	13.93	13.90
$a(^1\text{H})$	-34.34	-34.53	-34.60	-34.56	-34.62

In Table 4.2, we compare the results of frozen-density calculations with different basis sets for BP86/ZORA calculations. The inclusion of scalar-relativistic effects in the frozen density does not have a significant influence on the results and is only done for internal consistency. We observe that the basis set effect for the *frozen* density is relatively small with variations of 0.13 to 0.26 MHz compared to the largest basis set.

While frozen densities from fully converged BP86 calculations were used in the above tests, such calculations are quite inefficient and can suffer from convergence problems for very large $(\text{H}_2\text{O})_n$ clusters. In Section 3.4.3, it was shown that the simpler local density approximation (LDA) may be used for the frozen part, and that it can be advantageous to calculate the frozen density from a superposition of molecular densities. We tested this method for the small $\text{H}_2\text{NO} \cdot 2\text{H}_2\text{O}$ cluster (see Table 4.2). As might be expected for these weakly interacting water molecules, the effect of the sum-of-fragment approach in combination with the simple LDA has only a minor effect on the hfcc: $a(^1\text{H})$ changes

by 0.08 MHz (from 13.82 to 13.90 MHz), and $a(^{14}\text{N})$ by 0.09 MHz (from -34.53 to -34.62 MHz) for the TZP basis set.

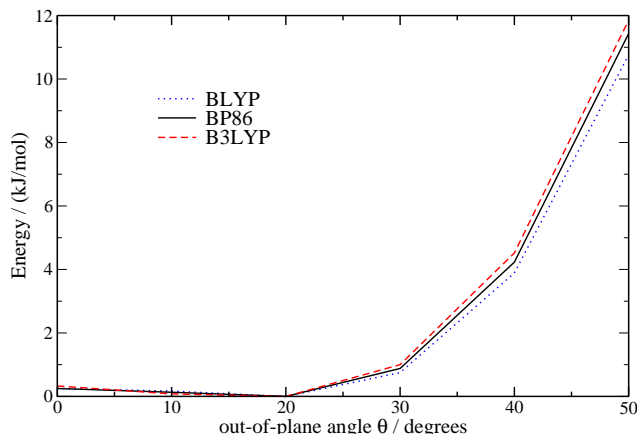
4.2.2 Statistical analysis of snapshots

A statistical analysis of the ESR parameters was performed for snapshots from a *first-principles* based MC simulation for the gas-phase and a CPMD simulation for the aqueous solution (see Appendix B for details). Two effects must be considered and accurately be described in these calculations in order to produce a reliable solvent shift for the hyperfine coupling constants. First, the electronic effect of the solvent at a given solute structure must be taken into account, and second, the effect of the solvent on the probability distribution of structural parameters. Since it is known that other radicals, like OH, can form hemibonded structures (i.e., structures with an oxygen–oxygen interaction forming a three-electron bond) in water [358], which appears to be overemphasized by the standard DFT functionals, we took a particular look at this effect for H_2NO also. However, no such hemibond is formed for this radical, since the orbital energy of the unpaired electron is too high. Otherwise, such a structure could have a significant impact on the ESR parameters.

As mentioned before, the most important structural parameter in our case is the out-of-plane bending angle θ . The probability distribution for this angle naturally depends on the potential energy curve along this internal coordinate. We calculated the potential energies along this angle using BP86/ZORA-QZ4P, where all other internal coordinates were optimized for a given out-of-plane angle. The results are shown in Figure 4.3, where we also give energies calculated (post-SCF) with the BLYP and B3LYP functionals as an internal consistency check. The lowest energy structure in this scan with steps of 10 degrees is obtained for $\theta = 20$ degrees (the angle for the fully optimized structure is 17.6 degrees). The inversion barriers are very low with 0.2 (BP86) to 0.3 (BLYP, B3LYP) kJ/mol, and they are in good agreement with the B3LYP and UQCISD[T] data from Ref. [359]. The corresponding minimum-energy out-of-plane angles found there are 16.90 (UQCISD[T]) and 16.6 degrees (B3LYP), which is — in view of the very shallow potential energy surface — in good agreement with our structure. Experimentally, there is some evidence for the planarity of the H_2NO radical, but it has been suggested that this is due to a double-minimum potential for the out-of-plane vibration with a very low barrier [351]. This is in perfect agreement with the KS-DFT and UQCISD[T] results. Also for the energies, we observe strong discrepancies between the results presented above and the ROHF results from Ref. [355]. ROHF leads to a minimum-energy structure with $\theta = 36.5$ degrees and an inversion barrier of 3.6 kJ/mol, while the energy increase for angles > 40 degrees is less steep than in our calculation. Obviously, the probability distribution resulting from the ROHF energy profile along θ cannot be considered reliable. This is important to note, since the probability distribution has a large impact on the averaged hyperfine coupling constants.

From all structures generated in the simulations, we determined the probabilities of finding particular out-of-plane bending angles θ . The results are shown in Figure 4.4. Both probability distributions are still rather noisy, but it can be recognized without doubt that the distributions in gas-phase and solution are quite similar. The maxima in the probability distributions occur at small angles (close to planarity), and the

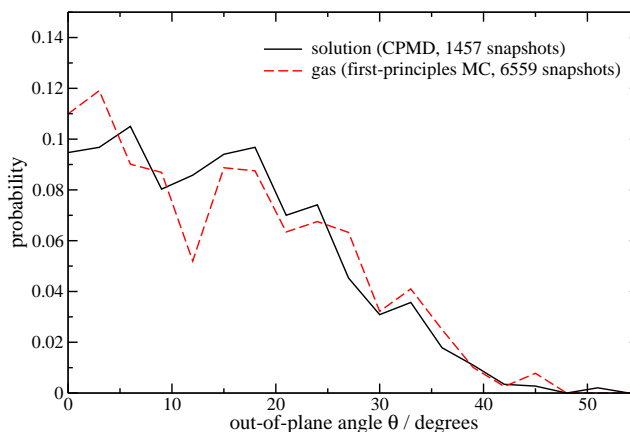
Figure 4.3: Potential energy variation along the out-of-plane bending angle θ . All other internal coordinates were optimized (BP86/ZORA-QZ4P). For comparison, results are shown for BP86, BLYP, and B3LYP (post-SCF energy calculations using a BP86/ZORA-QZ4P density). All energies are given in units of kJ/mol with respect to the structure with $\theta = 20$ degrees.



distributions are quite broad up to angles of about 25 to 30 degrees. Angles larger than 40 degrees are not very probable. This confirms the energy profile in Figure 4.3. The average out-of-plane bending angle is 16.8 degrees in the gas phase, and 16.7 degrees in solution. The difference in the average angles is thus much smaller than the standard error in the average angle (1.7 degrees for the gas phase). This is in contrast to the classical Monte Carlo study in Ref. [355] (30.7 degrees/gas phase, 19.9 degrees/solution), which used a force field fitted to ROHF energies. The potential energy minimum in that case corresponds to a much too large θ angle of 36.5 degrees. It was suggested in Ref. [355] that the inversion barrier almost completely vanishes in solution, which is in agreement with our study. But in our calculation, the barrier is also very small in the gas-phase calculation.

From the trajectories of the simulations, we calculated hyperfine coupling constants for every fifth structure of the first 1000 structures in solution and of the 6559 structures obtained from the MC simulation. Using every structure for the hfcc calculation would not add new significant information, since subsequent structures, especially in the MC simulation, often show a considerable correlation. This means that 200 snapshots were calculated in solution, while 1311 snapshots were considered for the gas-phase. We used the frozen-density embedding approach as described above to model the effect of the water molecules in these calculations. The average values and the maxima of the distributions are shown in Table 4.3. The probabilities for different values of the hfcc are shown in Figure 4.5 for the gas-phase and for aqueous solution. These plots now show the combined effect of structural and electronic changes of the hyperfine coupling constants. First, it can be seen that the maximum positions of the probabilities shift as expected from the experimental values: For $a(^{14}\text{N})$, the maximum shifts by 4.0 MHz from 10.5 (gas) to 14.5 MHz (water), and for $a(^1\text{H})$, it shifts by -2.0 MHz from -36.5 (gas) to -38.5 MHz (water). The shifts in the average values of the hyperfine coupling

Figure 4.4: Probability of finding a particular out-of-plane bending angle θ in the CPMD simulation of the H_2NO radical. The results shown are based on 1457 and 6559 snapshots for the trajectories in solution (solid line) and in the “gas phase” (isolated molecule; dashed line). The probabilities are given in intervals of 3 degrees, i.e., in units of $1/(3 \text{ degrees})$.



constants are qualitatively the same, but they differ in magnitude. The average of $a(^{14}\text{N})$ shifts by +1.8 from 19.8 MHz (gas) to 21.6 MHz (water), and the average of $a(^1\text{H})$ shifts by -5.9 from -22.6 to -28.5 . The experimental shifts are 8.8 (^{14}N) and -6.4 MHz (^1H) if the values from the microwave study in Ref. [351] are used for the gas-phase. Also the results of 30.3 MHz (^{14}N) and -33.1 MHz (^1H) from Ref. [352] are sometimes assumed as “gas-phase” values, and in combination with the results for aqueous solution from Ref. [353] they would yield solvents shift of 5.6 (^{14}N) and -2.8 MHz (^1H). These values, however, were obtained in a xenon matrix at a much lower temperature (77 K) than used in our simulation, and a rather strong temperature dependence of the hfc for H_2NO in vacuo was found in Ref. [356]. We note that the B3LYP/PCM study in Ref. [359] has even larger problems with the shift for nitrogen (0.6 MHz), and overestimates the (absolute value of the) shift for hydrogen (-10.6 MHz).

As can be seen from Figure 4.5, there is no large change in the distribution of the hyperfine coupling constants in gas phase and solution. In the gas phase, the distributions look slightly broader than in solution, but the effect is not large in view of the noise still present for this rather small number of snapshots (the classical MC simulation in Ref. [355] used two million steps for the averaging).

To investigate the electronic effect of the solvent at a given angle θ in gas phase and solution, we plot the hfc observed in our simulations as a function of θ in Figure 4.6 (only every twentieth snapshot has been used for the gas-phase simulation in that plot for clarity of presentation). Also shown are quadratic fits to these curves, the coefficients of which are collected in Table 4.4. As can be seen, the quadratic coefficients are rather similar, so that the fitted curves run almost parallel. Only for larger angles ($\theta > 20$ degrees) in case of nitrogen this is no longer well fulfilled. The offsets in the fitted curves for small angles ($\theta \approx 0$) are 4.1 MHz for ^{14}N (solution minus gas), and -3.4 MHz for ^1H , and these values can be regarded as estimates for the average electronic

Table 4.3: Isotropic hfcc a (MHz) for structures from a *first-principles* based MC (gas) or CPMD (solution) simulation, averaged over 1311 (gas) or 200 (solution) configurations. Besides the average values, we also give the maxima of the hfcc distributions as shown in Figure 4.5. The values for the optimized isolated structures of C_{2v} and C_s symmetry are included for comparison. Additionally, experimental values and results from a continuum solvation model are shown. Note that the signs of the hyperfine coupling constants are not determined in Ref. [353]. They have been inferred from the study in Ref. [351] and from our calculations.

	$a(^{14}\text{N})$	$a(\text{H})$
optimized molecule		
C_{2v}	10.0	−36.5
C_s	17.8	−25.3
gas phase simulation (1311 conf.)		
average	19.8	−22.6
max.	10.5	−36.5
exp. (Ref. [351])	27.10	−29.51
simulation aqueous solution (200 conf.)		
average	21.6	−28.5
max.	14.5	−38.5
exp. (Ref. [353])	35.9	−35.9
shift		
average	1.8	−5.9
max.	4.0	−2.0
B3LYP/PCM/EPR-3 (Ref. [359])	0.6	−10.6
exp. (Refs. [351,353])	8.8	−6.4

Figure 4.5: Distribution of the isotropic hyperfine coupling constants a from 1311 snapshots of a *first-principles* based Monte Carlo simulation of H_2NO in the gas phase (left) and in water (right). Probabilities are given for intervals of 1 MHz.

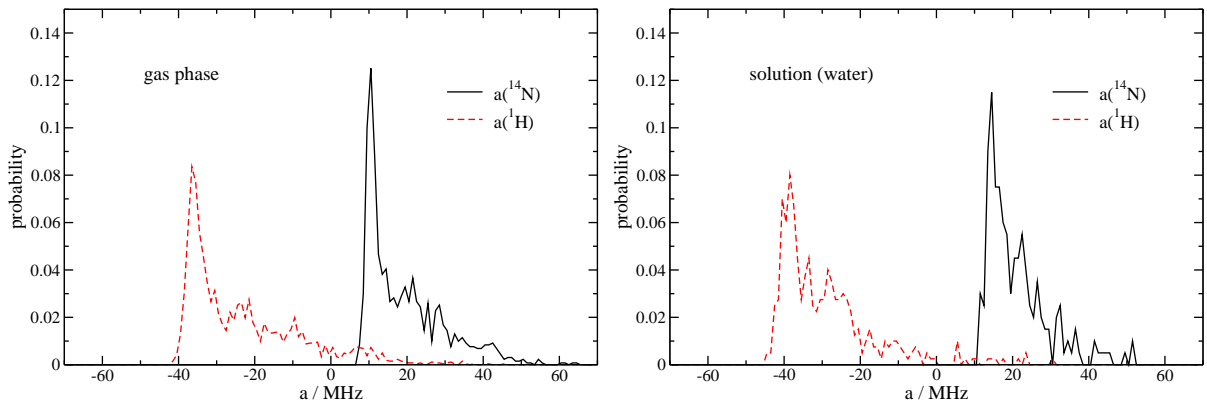


Figure 4.6: Isotropic hfcc a for ^1H and ^{14}N for H_2NO in the gas phase (left) and in aqueous solution (right) as a function of the out-of-plane bending angle θ . Shown are data points for every 20th snapshot in the gas-phase simulation (327 in total) and for every fifth of the first 1000 snapshots in solution (200 in total) for clarity of presentation (note that there are two data points for each snapshot in case of ^1H because of the two non-equivalent hydrogen atoms). Also shown are the quadratic fits to these data sets.

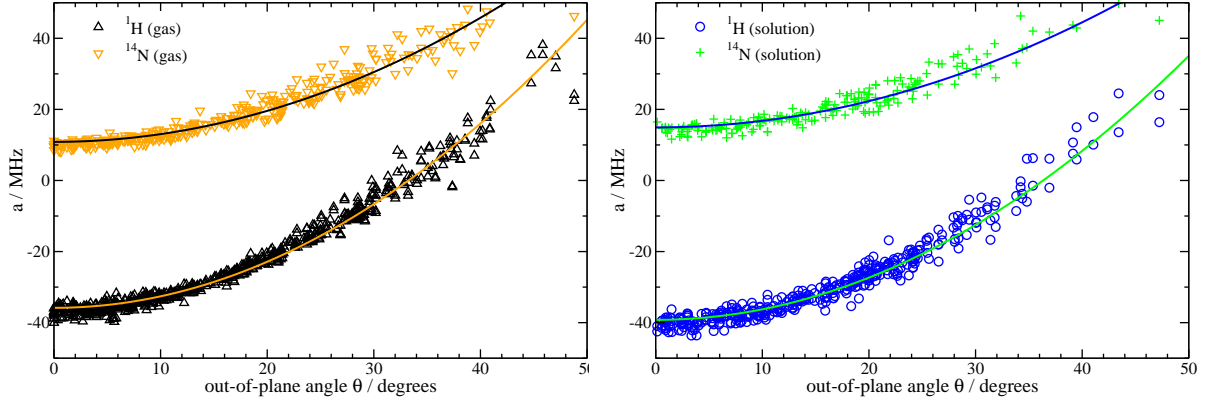


Table 4.4: Coefficients for the fits $a(\theta) = a_0 + a_1\theta^2$ of the isotropic hfcc a as a function of the out-of-plane bending angle θ . The values were obtained by fitting the data sets shown in Figure 4.6.

	a_0 / MHz	a_1 / (MHz/degree ²)
^{14}N (gas)	10.860	0.0218
^{14}N (solution)	14.935	0.0185
^1H (gas)	-39.218	0.0297
^1H (solution)	-35.831	0.0324

effect of the solvent. The results are in qualitative agreement with the experimental shifts, which again demonstrates that structural effects — although important for the average hyperfine coupling constant — are similar in gas phase and solution.

4.2.3 Assessment of the results

The example studied here demonstrates that frozen-density embedding can be used to reliably model solvent effects on ESR hyperfine coupling constants in connection with an appropriate way to sample the configurational space. A sophisticated treatment for both structural and electronic effects of macrosolvation is necessary in order to reproduce the experimental trends in particular for nitrogen, to assess which of the two effects will be stronger in solution.

In our simulations we observed that the average out-of-plane angle θ is slightly lower in solution than in the gas-phase. The strong dependence of the hfcc on θ suggests that there should be a small change towards smaller values for both $a(^1\text{H})$ and $a(^{14}\text{N})$.

The pure electronic effect can be estimated from the shift between the data sets for gas-phase and solution in Figure 4.6. In a first approximation (for small angles, which have the highest probability), the curve of $a(^1\text{H})$ is shifted by ≈ -3 MHz in solution, and the curve of $a(^{14}\text{N})$ is shifted by $\approx +4$ MHz.

To calculate the change in the average hfcc upon solvation, we also have to consider the changes in the probability for different structures, in particular for different out-of-plane angles. In contrast to the classical Monte Carlo simulation in Ref. [355], we do not find a significant difference in the probability distribution of the out-of-plane bending angle between gas-phase and solution. We attribute the differences in Ref. [355] to the ROHF-based potential energy surface with a minimum at a much too large angle θ . The total shifts in the average hfcc in our study are -5.9 MHz (^1H) and $+1.8$ MHz (^{14}N), compared to -6.4 MHz and $+8.8$ MHz, respectively, in experiment. From these calculated shifts we can — by subtracting the estimates for the electronic contribution — give rough estimates for the structural contributions of ≈ -3 MHz for hydrogen and ≈ -2 MHz for nitrogen.

Like in the microsolvation study, we see that structural and electronic effects cause shifts in opposite directions for nitrogen. But in the solution study the electronic effects dominate, so that the calculated shift for ^{14}N is too low, but it still has the same direction (plus sign) as in experiment. The quantitative modeling is complicated by the fact that already slight changes in the probability distribution have large effects on the average hyperfine coupling constants. Although the electronic effect might still be underestimated a bit by neglecting relaxation and spin-polarization effects in the frozen density, our tests showed that the (combined) errors introduced by these approximations should not be larger than ≈ 1 MHz. To arrive at full quantitative agreement with experiment, structural differences between gas-phase and solution would probably have to be modeled even more accurately (i.e., by using more sophisticated electronic structure methods in combination with large statistical test sets of snapshots). The results for hydrogen on the other hand are very encouraging and agree with the experimental shift within 0.5 MHz, although they might partially benefit from error cancellation in structural and electronic effects.

4.3 Solvatochromism of aminocoumarin C151

In this section, we extend the analysis of solvation phenomena to shifts in absorption bands of somewhat larger dye molecules, which require solvent shells of considerable size and thus pose a greater challenge to the embedding scheme. We choose a coumarin dye as a prototypical example from a class of molecules which show a strong dependence of absorption and fluorescence characteristics on the surrounding medium (see, e.g., Ref. [360]). Consequently, these molecules have been of considerable interest as laser dyes in the near-ultraviolet to green part of the spectrum [361], and as environmental or solvent probes.

The lowest singlet excitation in these aminocoumarins is a $\pi \rightarrow \pi^*$ excitation, which shows a pronounced redshift in polar solvents [362–364]. Isosurface plots of the orbitals involved in this transition in case of aminocoumarin C151 (see Figure 4.7 for the Lewis structure) are shown in Figure 4.8. Former theoretical studies on the absorption properties and excited states of these molecules in solution mainly used continuum

solvation models [365–368]. Especially in Ref. [365], the importance of specific and inhomogeneous interactions between solvent and solute, which are necessarily neglected in continuum models, was underlined. In Ref. [297], the excitation energies were calculated for C151 in water and acetonitrile. Solvent shifts were then computed with respect to the vertical excitation energy of the molecule in vacuum (as a model for a non-polar solvent), and they were found to reproduce the experimental shifts between non-polar and polar solvents quite well. A direct comparison of the simulations in acetonitrile and water, however, indicates a shift between these two solvents of 0.11 eV, compared to an experimental shift of < 0.01 eV [362]. Moreover, it is known from CPMD simulations [116] or studies of the vibrational broadening of absorption bands [319, 369, 370] that vertical excitation energies and band maxima for gas-phase molecules often differ by 0.1 to 0.2 eV, so that this aspect should be taken into account in the calculation of shifts in excitation energies. Hence, we want to assess the quality of the frozen-density embedding scheme in combination with a classical MD simulation for the calculation of solvatochromic shifts. For a direct comparison of a polar and a non-polar solvent, we conduct simulations in *n*-hexane and in water.

Figure 4.7: Structure of aminocoumarin C151.

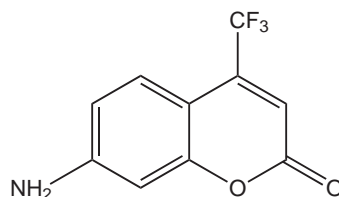
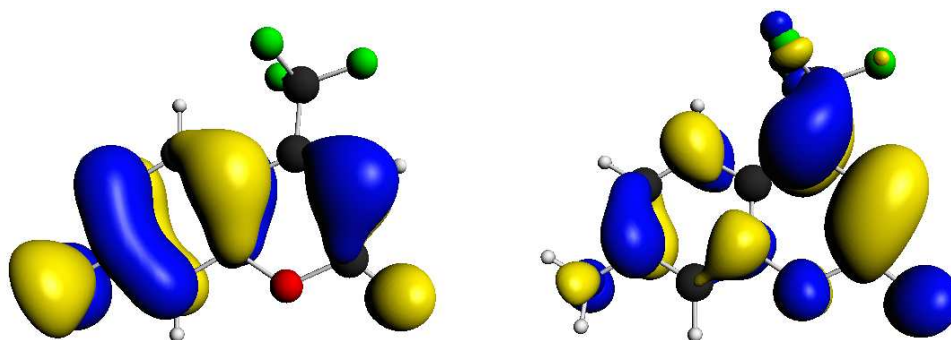


Figure 4.8: Isosurface plots of HOMO (π) and LUMO (π^*) orbitals of aminocoumarin C151.



In the following, an assessment and a validation of different types of approximations within the FDE approach as well as a closer look at the origin of the shift in our simulation are presented. We also introduce a combination of the sum-of-fragment approach for the frozen density and the freeze-and-thaw technique [357]. The results of the final spectrum simulation are shown in Section 4.3.2.

4.3.1 Comparison of approximate solvent models

The calculation of solvatochromic shifts requires to sample over the different possible structures of the solute and the surrounding solvent. In this section we want to validate our solvent model using a small set of 50 snapshots of C151 in solution for each solvent by comparing different types of embedding calculations. An extended statistical sampling with 400 snapshots from eight independent trajectories follows in the next section, which shows that the results obtained in this section are accidentally closer to experiment. Additionally, we try to separate the structural and electronic contributions to changes in the excitation energies.

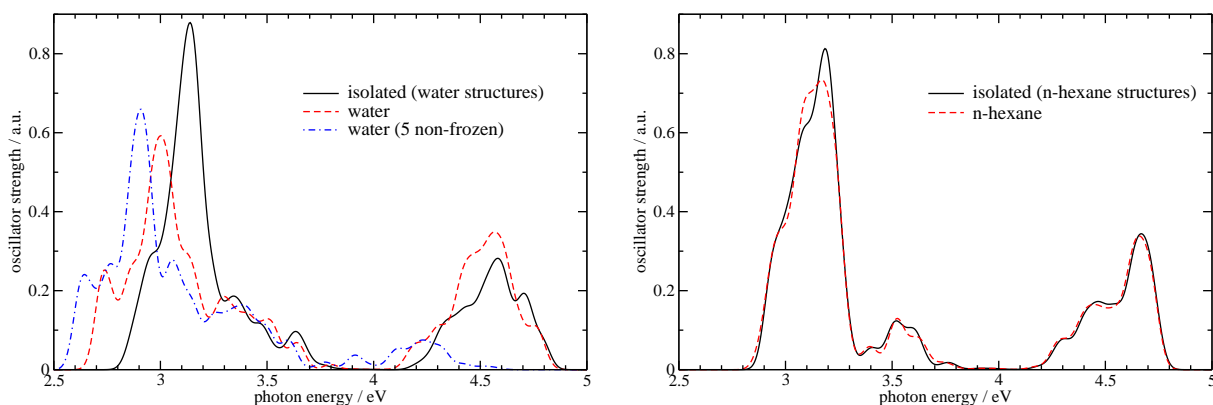
To this end, classical dynamics simulations (see Appendix B for details) were performed. For the snapshots from these simulations, a substructure was created in which the nearest 300 solvent molecules were taken into account in the case of water as a solvent, and the nearest 45 solvent molecules in case of *n*-hexane. This amounts to 900 atoms in the frozen-density system in both cases. It was tested that with this setup excitation energies are converged w.r.t. the size of the solvation shell. For the preparation of the frozen-density in the former case, the innermost 50 water molecules were treated as flexible fragments (geometries taken from the snapshots), while a uniform rigid structure (optimized in vacuo) was used for the outer water molecules. No rigid structures were assumed for the *n*-hexane molecules. The electron density of the solvent was then calculated with LDA/DZP. Tests in which a TZP basis set was used for the solvent density did not result in significant changes.

We first computed the shift in excitation energies for C151 in *n*-hexane compared to the vertical $\pi \rightarrow \pi^*$ excitation energy of the optimized, isolated molecule (3.238 eV). To separate the structural effect due to the dynamics in solution and the electronic effect due to the frozen density, we performed two series of excitation calculations: In the first, we removed all solvent molecules from the snapshots, while we kept them in the second. The first series, which includes only the structural effect, resulted in an average excitation energy of 3.096 eV, 0.142 eV lower than the vertical excitation energy for the isolated molecule. In contrast to this, the electronic effect in *n*-hexane is negligible. If the *n*-hexane molecules are included by frozen-density embedding, the average excitation energy changes by only 0.004 eV to 3.092 eV. The spectra simulated in this way are shown in Figure 4.9.

In Ref. [297] the vertical excitation energy of the isolated molecule was taken as a reference value to compute the “solvent shift” for solvation in water, which was then compared to the experimental shift between water and *n*-hexane (the latter being a solvent where both specific and non-specific solvent effects are expected to be small). In view of the difference of 0.146 eV in our calculation between the isolated molecule and the average excitation energy in *n*-hexane, we think that this is an oversimplification. This is mainly due to the fact that the (dynamic) structural effect is neglected in a (static) vertical excitation calculation. This also holds when comparing to a shift between experimental gas-phase and solution spectra, since also gas-phase dynamics may change the average excitation energy by 0.1 to 0.2 eV compared to vertical excitation energies, as is known from other CPMD [116] or vibronic coupling simulations [319].

We performed similar calculations for the snapshots obtained with water as a solvent. Considering the pure structural effect, we obtain an average excitation energy of 3.085

Figure 4.9: Simulated spectra for aminocoumarin C151 in solution based on reduced sets of 50 snapshots. Water (left) and *n*-hexane (right) have been considered as solvents. Each individual transition is represented by a Gaussian curve of half-width 0.08 eV. Shown are spectra in which the solvent is either included in a frozen-density calculation or completely omitted. In the latter case, only the structural effect of the dynamics in solution affect the spectrum. For water, we also show a simulation in which the 5 nearest water molecules are included in the embedded (non-frozen) system. In this simulation, the band at the high-frequency end of the spectrum is not obtained, since the number of excited states in the calculation was restricted to 5, and additional excitations arise due to the water molecules.



eV, which is comparable to *n*-hexane. This suggests that — within our model for the dynamics — there are no significant structural differences in the solute molecule itself for the different solvents. In contrast to *n*-hexane, however, the electronic effect is more important for the aqueous solution. Modeling this electronic effect by the frozen-density embedding including 300 frozen water molecules yields an average excitation energy of 2.955 eV, so that structural (−0.153 eV) and electronic effects (−0.130 eV) are of similar magnitude.

The solvent shift of −0.137 eV between *n*-hexane and water calculated from this limited statistics — though qualitatively correct — considerably underestimates the experimental shift of −0.22 eV. Test calculations showed that the frozen-density embedding, especially in its simplest form (i.e., without relaxation), may have some problems to accurately model the effect of hydrogen-bonded water molecules for the current system [184]. This could be improved, but in the present case not completely cured, by using at least one freeze-and-thaw cycle to polarize the frozen density. There is, however, a fundamental problem when using the sum-of-fragment approach introduced in Section 3.4.3 to generate the frozen solvent density: We can only polarize the frozen density during an SCF for the solvent system. The results in Ref. [309] suggest that polarization is most important in those cases, where direct hydrogen bonding between the frozen and the embedded system becomes important. We therefore tested the following hybrid approach: We choose a set of solvent molecules which are close to the solute, typically only five to ten molecules in the case of water, and calculate their density in an FDE calculation, in which the density of the isolated aminocoumarin C151 is kept frozen. Then, we combine the density of this polarized fragment with the density of all remaining solvent

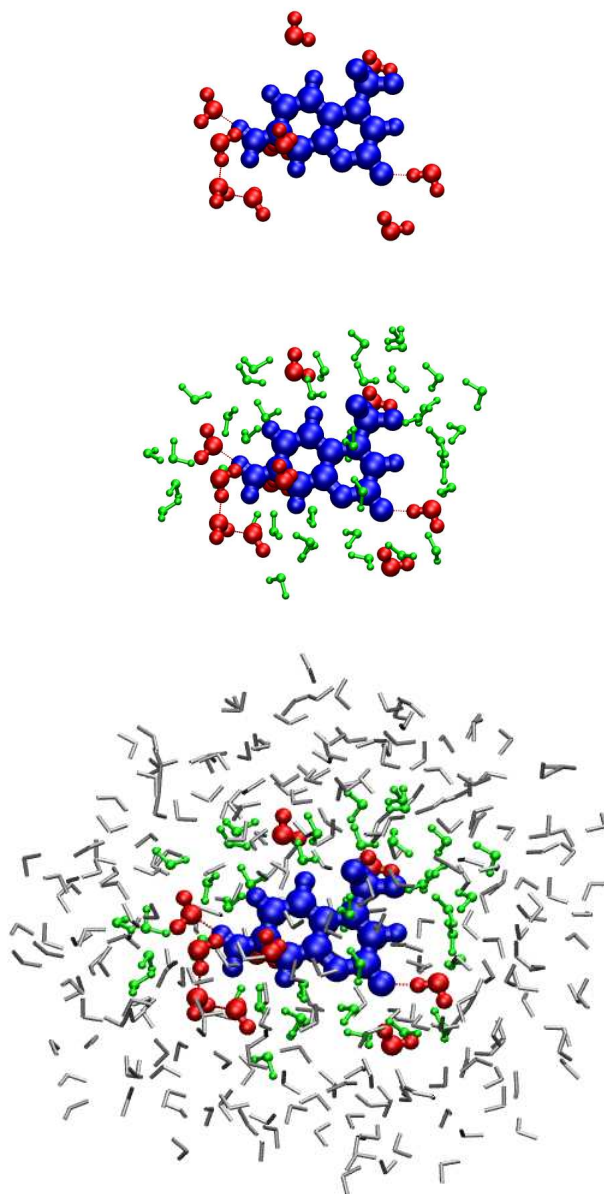
Table 4.5: Average excitation energies and solvent shifts (eV) for the $\pi \rightarrow \pi^*$ excitation of aminocoumarin C151. They are obtained from an analysis of a reduced set of 50 snapshots of MD simulations for this molecule in water and *n*-hexane, respectively. For comparison we also present calculations in which the solvent molecules have been removed in the excitation calculation, so that only the structural effect of the dynamics in solution is monitored. The acronym (fr.) stands for frozen, non-relaxed solvent molecules, (rel.) means frozen and relaxed (polarized by the C151 density) solvent molecules, (fully rel.) means frozen and fully relaxed solvent molecules (polarized by C151 and the outer water molecules), and (non-fr.) denotes non-frozen solvent molecules (included in the embedded system).

structure C151	solvent model	E_{ex} / eV
isolated, opt.	—	3.238
simulation <i>n</i> -hexane	—	3.096
simulation <i>n</i> -hexane	45 <i>n</i> -hexane (fr., non-rel.)	3.092
simulation H ₂ O	—	3.085
simulation H ₂ O	300 H ₂ O (fr., non-rel.)	2.955
simulation H ₂ O	5 H ₂ O (fr., rel.), 295 H ₂ O (fr., non-rel.)	2.930
simulation H ₂ O	10 H ₂ O (fr., rel.), 290 H ₂ O (fr., non-rel.)	2.923
simulation H ₂ O	10 H ₂ O (fr., fully rel.), 290 H ₂ O (fr., non-rel.)	2.916
simulation H ₂ O	5 H ₂ O (non-fr.), 295 H ₂ O (fr., non-rel.)	2.862

molecules using the simple sum-of-fragment approach. The resulting density is frozen and used in an FDE calculation on aminocoumarin C151. This partial relaxation leads to an average excitation energy of 2.930 eV when the nearest five water molecules are polarized, and of 2.923 eV when the nearest ten water molecules are relaxed, thus improving the shift between *n*-hexane and water solution from -0.137 eV to -0.162 or -0.169 eV, respectively. The small change from five to ten polarized water molecules confirms that polarization is only needed for the closest solvent molecules, which show the strongest interactions with the solute. We also tested the effect of relaxing the ten nearest water molecules not only with respect to the frozen C151 density, but also to the frozen density of the remaining water molecules, before this relaxed density is combined with the other water molecules and again used in an FDE calculation on aminocoumarin C151. This yields an average excitation energy of 2.916 eV, corresponding to a solvent shift of -0.176 eV.

The restriction of the response to the embedded system can be another significant source of error in the present case. Due to this restriction, changes in the solvent electron density upon excitation cannot be described. A big advantage of the embedding scheme is that the embedded system can always be extended to include also the nearest solvent molecules, if we have an indication that they might take part in the excitation process. This leads to a shell-like approach which is shown in Figure 4.10: There are three layers of water molecules in the system, of which the innermost is treated explicitly (or by relaxation, if sufficient). The next layer consists of normal frozen solvent molecules, which complete (at least) the first solvation shell. The third layer is formed by rigid water molecules modeling outer solvation shells.

Figure 4.10: Shell structure in frozen-density embedding calculations. Top: The innermost solvent molecules (red), for which hydrogen bonding to the solute (blue) is expected, can be included in the embedded system, or partial relaxation can be used for them. Middle: To complete the first solvation shell, flexible, solvent molecules (green) are added with structures according to the snapshot of the dynamics and with frozen density. Bottom: Outer solvation shells are modeled by rigid water molecules (grey).



We tested this for the simulation in water and included the five water molecules closest to the dye molecule in the non-frozen system, while the remaining 295 water molecules for each snapshot were described by the frozen-density embedding scheme. The average excitation energy for the $\pi \rightarrow \pi^*$ excitation drops to 2.862 eV, 0.093 eV lower than in the sum-of-fragment calculation. This corresponds to a solvent shift between *n*-hexane and water of 0.230 eV for this limited set of snapshots, which agrees within 0.01 eV with the experimental shift. The standard error in the average excitation energies is still larger than 0.02 eV in this case. The combination of five explicit water molecules in the embedded system with 295 frozen water molecules thus appears appropriate to be used in a more extensive statistical sampling (see below). Including further water molecules in the non-frozen region appears neither necessary nor adequate. Such water molecules, which are not hydrogen-bonded to the dye molecule, will not directly contribute to the $\pi \rightarrow \pi^*$ excitation. The calculations with partially polarized water densities already demonstrate that the influence of the nearest five water molecules on the average excitation energy is much larger than that of the following five water molecules. Additionally, the calculations with more non-frozen water molecules would suffer from two problems: First, the computer time still shows the scaling behavior of conventional DFT/TDDFT calculations with respect to the number of atoms in the non-frozen region, so that the calculations get considerably more expensive if many water molecules are included in the embedded part. Second, and even more severe, explicit water molecules increase the risk of artificially low-lying charge-transfer excitations from water-oxygen lone pairs to the π^* orbital of the aminocoumarin. Even with only five explicit water molecules, such excitations occur in rare cases. They can also affect the desired excitations by spurious mixings (see Section 3.4.4), and make the identification of these transitions cumbersome.

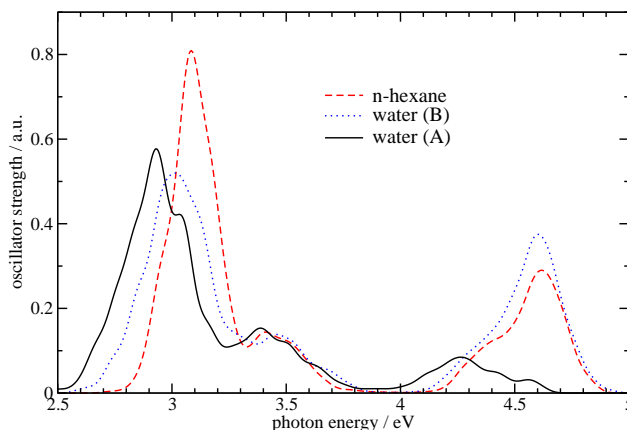
4.3.2 Spectra simulations

To improve our statistical analysis, we use 8 trajectories as explained in Section 4.3.1 for every solvent, leading to 400 snapshots in each case. In the last section it was shown that it is necessary to include those water molecules explicitly into the embedded system which interact via hydrogen bonds with the aminocoumarin. Therefore, we use five non-frozen and 295 unpolarized frozen water molecules for water as a solvent. For comparison, we also perform a calculation in which all water molecules are frozen and unpolarized. For *n*-hexane, we only use this simple scheme, since electronic effects are very small in that case anyway.

In Figure 4.11, we present the spectra resulting from 400 snapshots of the simulation in water and in *n*-hexane. Average excitation energies and solvent shifts calculated from these data are presented in Table 4.6. All solvent shifts here are extracted from average excitation energies, but using other methods to extract the mean values (cf. Section 3.4.5) changes this shift only in the order of 0.01 to 0.02 eV.

The simulation for *n*-hexane yields an average excitation energy of 3.07 eV, which is about 0.02 eV lower than for the smaller test set studied in Section 4.3.1, and 0.17 eV lower than the vertical excitation energy for the optimized, isolated structure. The average excitation energy in water is 2.90 eV for the recommended solvent model including five non-frozen water molecules, ca. 0.04 eV higher than for the limited statistics in the

Figure 4.11: Simulated spectra for aminocoumarin C151 in solution. Water and *n*-hexane have been considered as solvents. Each individual transition is represented by a Gaussian curve of half-width 0.08 eV. For water, two simulations have been carried out: (A) five non-frozen, 295 frozen water molecules; (B) all 300 water molecules frozen. In the former simulation, the band at the high-frequency end of the spectrum is not obtained, since the number of excited states in the calculation was restricted to 5, and additional excitations arise due to the water molecules.



last section. Also for the simpler model with 300 frozen water molecules, the larger statistics increases the average excitation energy by about 0.03 – 0.04 eV (compared to the single trajectory) to 2.99 eV.

The calculated solvent shift from *n*-hexane to water is -0.17 eV when including five non-frozen water molecules, which is in satisfactory agreement with the experimental shift of -0.22 eV. The simple embedding technique with all 300 water molecules frozen also shows a clear shift in negative direction, but its magnitude is somewhat underestimated with only -0.08 eV. Due to the standard errors in the average excitation energies (0.005 eV to 0.008 eV), the statistical error estimated for the solvent shifts is ca. ± 0.01 eV. In Table 4.6, we also calculate the shifts between the isolated molecule and the molecule solvated in water. Although this shift lacks a direct physical meaning, it allows a comparison to the QM/MM-CPMD study in Ref. [297]. With five non-frozen water molecules, the shift between isolated structures and aqueous solution in our calculation is identical to that in Ref. [297], where all water molecules were treated with a classical model (-0.33 eV). The simple embedding technique (300 frozen water molecules) instead yields a value of -0.25 eV for this shift. If we would use the vertical excitation energy of the optimized, isolated molecule as a first approximation to the average excitation energy in a non-polar solvent like *n*-hexane, we would have to conclude that the simpler embedding model with 300 frozen water molecules yields the better results. The direct comparison of the average excitation energies in the different solvents reveals, however, that this is not the case.

The vertical excitation energy of the isolated molecule is thus not a well-defined reference for the computation of solvatochromic shifts in a polar medium with respect to a non-polar one. For a direct comparison to experimental shifts in different media, the absorption spectra should be modeled in both solvents and then be compared.

Table 4.6: Average excitation energies and solvent shifts (eV) for the $\pi \rightarrow \pi^*$ excitation of aminocoumarin C151. They are obtained from an analysis of 400 snapshots of MD simulations for this molecule in water and *n*-hexane, respectively. Two simulations have been carried out for water: (A) five water molecules included in the embedded system, 295 frozen H₂O molecules; (B) all 300 water molecules frozen. For comparison, we give the shift w.r.t. the vertical excitation energy of the optimized isolated structure. We also include the results from a QM/MM-CPMD study (all water molecules are treated in MM fashion there) [297].

	embedding (SAOP/TZP/DZP)	QM/MM-CPMD ^a (BLYP)	exp. ^b
isolated, opt.	3.24	3.32	—
<i>n</i> -hexane	3.07	—	3.70
water (A)	2.90	2.99	3.48
water (B)	2.99		
shift <i>n</i> -hexane – water (A)	−0.17	—	−0.22
shift <i>n</i> -hexane – water (B)	−0.08		
shift isolated – water (A)	−0.33	−0.33	—
shift isolated – water (B)	−0.25		

^aRef. [297]

^bRef. [362]

In summary, almost no electronic effect on the excitation energies arises in the *n*-hexane solution for aminocoumarin C151, but such an effect is clearly visible for an aqueous solution. A considerable change in the excitation energies is induced by water molecules which are hydrogen-bonded to aminocoumarin C151. The spectra simulations show that the calculated solvent shift between the two different solvents is too small if all water molecules are kept frozen, but it is still qualitatively correct. Our tests on a limited set of 50 snapshots clearly demonstrate that the results can be improved by a relaxation of the frozen density. While this relaxation usually requires a full SCF for the frozen system, we devised a method to combine a partial relaxation of the innermost solvent shell with the sum-of-fragment approach for the construction of the frozen density.

An inclusion of a few solvent molecules in the embedded region remains important in those cases in which the first solvation shell takes part in the response of the system. In the present case, the magnitude of the experimental shift of −0.22 eV is reproduced within 0.05 eV when the closest water molecules are included in the embedded system. A quantitative prediction of solvent shifts is thus efficiently possible by this QM/QM embedding even if the response is not strictly localized on the solute molecule.

4.4 Induced circular dichroism

The environmental effects investigated in the previous sections addressed solvation phenomena on spectroscopic properties. Such phenomena can often qualitatively be described by other types of embedding schemes relying on empirical parameters for the particular solvent under study. Among the big advantages of the FDE approach are the facts that (i) specific interactions with the environment can be described since FDE is

an atomistic quantum chemical method, and (ii) it is parameter-free, so that any kind of environment can be represented if a reasonable approximation for its electron density can be obtained.

A type of spectroscopy that can act as a very sensitive probe for intermolecular interactions when chiral molecules are involved is circular dichroism (CD) spectroscopy. Of particular interest in this context is the effect of induced circular dichroism (ICD), which is the phenomenon that the CD spectrum of a mixture of two compounds differs from the sum of the spectra of the two individual compounds. Most attention has been paid to cases of ICD in which an achiral chromophore shows circular dichroism in the presence of a chiral partner, especially when the latter alone does not show CD activity in the wavelength regime investigated in a certain experiment. In those cases, a CD signal can be observed when combining the two compounds while there is no signal for either of the individual compounds.

This effect is related to interactions between the achiral chromophore and the chiral partner in its surrounding. The most important examples are symmetric compounds in optically active solvents and complexes between chiral and achiral molecules. A special case of the latter are host–guest complexes with achiral guest molecules in chiral hosts. Two basic mechanisms causing ICD can be distinguished [371], a structural perturbation of the achiral guest by the chiral partner, and an electronic perturbation of the guest due to the chiral environment. For the structural effects, a further classification can be made into (i) symmetric molecules that are inherently non-chiral, but for which a chiral, non-symmetric structure is favored in presence of the chiral environment, and (ii) molecules with inherently chiral structures, which are not optically active due to low barriers between the enantiomeric forms, but for which a chiral partner selectively stabilizes one enantiomeric form. The former molecules are non-chiral already in a static picture (e.g., benzene), whereas the latter are only non-chiral on average (or in a dynamic picture), as both enantiomeric forms will occur with equal probabilities (e.g., hydrogen peroxide).

Many systems showing ICD have been investigated experimentally. In particular the class of cyclodextrins has been studied in detail as a host system for many small, achiral molecules, e.g., benzoylbenzoic acid [372], different azi- and diazadamantanes (see Ref. [371]), 2,3-diazabicyclo[2.2.2]oct-2-ene and derivatives [373,374], substituted benzenes [375], *N*-bromophthalimide [376], maleimide [377], naphthalene [378] and its derivatives [379], as well as fluorenone and xanthone [380]. A more extensive overview over cyclodextrin inclusion compounds can be found in Refs. [381,382]. Tokura and co-workers investigated the induced circular dichroism and its solvent dependence in the 2-benzoylbenzoic acid–amphetamine system [383,384]. Another application of ICD is its use for chirality sensing, e.g., for amino acids, as demonstrated in Ref. [385].

Computational studies on induced circular dichroism are often restricted to classical molecular mechanics (MM) approaches or semiempirical approaches, especially for the relatively large systems of cyclodextrin compounds [377,380,386]. In many cases, the intensity analyses for the CD spectra are based on the Kirkwood model of coupled oscillators [387] or, to be more precise, on the modified Kirkwood expression based on bond polarizabilities developed by Tinoco [388] (see, e.g., the work in Refs. [378,380,389,390]). Such investigations resulted in Harata’s rule, which states that the ICD of a chromophore inside the cyclodextrin cavity will always be positive if its electric transition

dipole moment is parallel to the principal axis of the cyclodextrin cavity [371,378], and negative, if it is perpendicular. Additionally, Kodaka’s rule states that the situation is reversed if the chromophore is located outside the cyclodextrin cavity [391,392].

Due to the size of the host molecule, *first-principles* calculations of excitation energies and rotational strengths for these systems are rather demanding. Although TDDFT calculations may still be feasible for these systems, they suffer from spuriously low long-range inter- and intramolecular charge-transfer excitations. In particular for rather weakly bound systems, like the supramolecular complexes for which ICD is reported, many of such artificially low excitations occur, as has been demonstrated in Section 3.3. In this section, we want to study the ability of FDE to capture the effect of induced circular dichroism by more complex surroundings, consisting of chiral partners in supramolecular aggregates or symmetry-breaking host systems. Since the response of the environment (the frozen system) is explicitly assumed to be negligible in the FDE-TDDFT scheme (see Section 3.4.2) only those systems can be treated in which the circular dichroism is due to transitions within the embedded system. If transitions in both systems are important, it would still be possible to do two FDE calculations with either the one or the other system frozen, so that the contributions of the two molecules can be calculated separately. However, effects arising from a coupling of electronic transitions in the two system cannot be described correctly by this type of frozen-density embedding. But it should be a valuable tool if the ICD can be described in terms of the perturbation of the guest’s electronic structure by the host system’s charge density. Note that only electronic circular dichroism will be investigated here; for a recent study on complexation effects on vibrational circular dichroism, see Ref. [393]. We analyze the results of FDE in calculations of the CD spectra of complexes between 2-benzoylbenzoic acid and (–)-(R)-amphetamine in Section 4.4.1. A ferrocenecarboxylic acid–crown ether conjugate in a complex with protonated L-leucine serves as an example with a more complicated electronic structure in Section 4.4.2. The aim of these investigations is to analyze the advantages and shortcomings of FDE, in particular in comparison to TDDFT calculations for the full complex, while a direct comparison to experiment would require a much more extensive survey of possible low-energy structures. Section 4.4.3 deals with phenol as a guest in a cyclodextrin host molecule, a system in which the limitations of the FDE-TDDFT approach become apparent. This is due to the inability of frozen-density embedding to describe excitonic couplings to the frozen-density region, which is a consequence of its restriction to the orbital space of the embedded system. A prototypical case for this failure is the benzaldehyde dimer in Section 4.4.4.

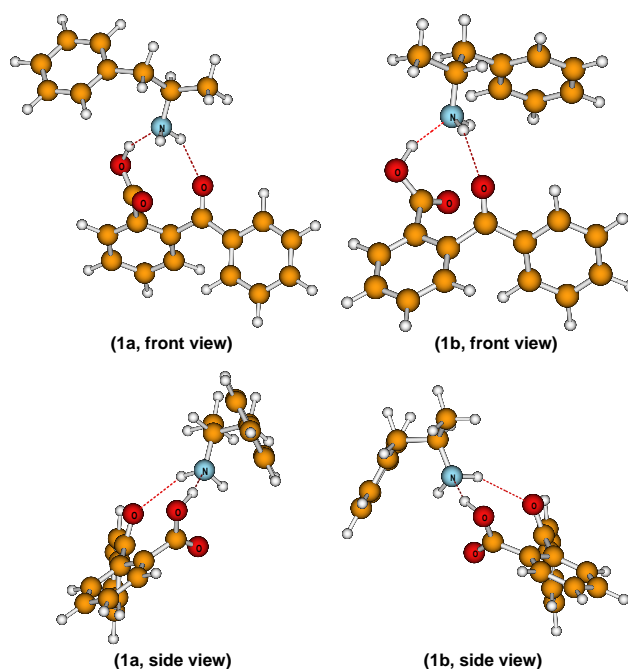
4.4.1 Complexation of benzoylbenzoic acid by amphetamine

The first compound studied here is a hydrogen-bonded complex between the non-chiral 2-benzoylbenzoic acid and (–)-(R)-amphetamine. The optimized structure of this complex is shown in Figure 4.12. This system was experimentally studied in detail by Tokura and co-workers [372,383]. They found strong evidence for the formation of a 1:1 complex between the two molecules in solution. From the vibrational frequencies and the solvent dependence of the ICD signal, they concluded that the complex was formed by the deprotonated acid and the protonated amphetamine [383]. The ICD signal was found to

be weaker in polar solvents, which favor the separation of the ion pair. Our optimization of the isolated complex did not lead to an ion-pair structure, although the hydrogen bond between the amino-N and the proton of the carboxyl-group is relatively short (1.7 Å in structure **1a**). Since the goal of this study is an assessment of frozen-density embedding for modeling the ICD effect, we refrain from a detailed discussion of this structural feature.

In this system, (–)-(R)-amphetamine acts as the chiral part that shall be described in terms of its frozen density. The isolated amphetamine in the structure of complex **1a** shows only very weak CD intensity in the wavelength range investigated here, and no transition for this molecule is observed below 4.75 eV. Furthermore, the lowest excitations of (–)-(R)-amphetamine are shifted too higher energies (> 5 eV) in complex **1a**, so that its contribution to the total CD spectrum is not relevant for our purposes and consequently will not be discussed. Benzoylbenzoic acid is the non-chiral part in this system, but it is non-chiral only in a dynamical sense. In its structure in **1a** it is chiral, and it has a non-zero CD spectrum as shown in Figure 4.13. A broad negative CD band from several overlapping transitions can be observed at 360 nm, and a weak positive band occurs at 287 nm, followed by a stronger negative band at 250 nm.

Figure 4.12: Optimized (BP86/TZP) structures of the benzoylbenzoic acid — (–)-(R)-amphetamine complex. The structure of benzoylbenzoic acid in complex **1b** is the (re-optimized) mirror image of that in complex **1a** (the mirror plane is approximately the plane of the benzoyl group; see side views on lower panel). Note that the amphetamine rotated around the C–N-bond during re-optimization. The energy difference between the two complexes is 0.6 kJ/mol.

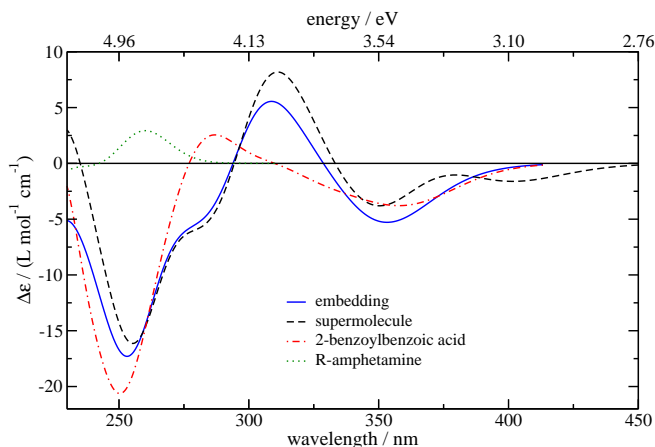


In order to see if there is an induced circular dichroism in complex **1a** we calculated the CD spectrum of this complex in a supermolecular calculation. The resulting spectrum is

included in Figure 4.13. The CD spectrum of the isolated 2-benzoylbenzoic acid in the structure of complex **1a** differs significantly from the CD spectrum of the whole complex (as obtained in the supermolecular calculation). First, we observe a weak negative band at 402 nm. However, this is a spurious transition in the supermolecular calculation, since it represents partial charge-transfer between the two molecules. ALDA-TDDFT does not describe such transitions correctly, yielding typically much too low excitation energies. Besides this feature, the most important differences are a strong positive band at 312 nm and a shoulder (at 282 nm) to the strong negative band at 256 nm, which is shifted a bit compared to the isolated 2-benzoylbenzoic acid and shows slightly lower intensity. This comparison shows that there is an important electronic contribution due to the effect arising from the amphetamine on the 2-benzoylbenzoic acid.

To answer the question whether this effect can be modeled in terms of an effective embedding potential, we carried out a calculation with a frozen-density representation of the chiral amphetamine molecule. Two freeze-and-thaw cycles were used in the embedding calculation, but the differences w.r.t. the results obtained with one freeze-and-thaw cycle are negligible. Therefore, only one freeze-and-thaw cycle is used in all the other examples studied in this section if not explicitly stated otherwise. The resulting CD spectrum is shown in Figure 4.13. In the spectra plots, all vertical excitations are represented as Gaussian curves with a half-width of 0.4 eV. The electronic contribution is very nicely reproduced by the FDE calculation, in which the amphetamine was treated as the frozen system. We observe a negative band at 353 nm, a positive band at 309 nm, and a shoulder at 281 nm to the strong negative band, which has its maximum at 254 nm. Although the rotational strengths for the bands at 353 and 309 nm differ a bit from the corresponding supermolecular values, the general agreement between the two curves is very nice. The only feature which is missing in the frozen-density calculation is the low-intensity band at 402 nm with partial intermolecular charge-transfer character, which cannot be obtained in FDE calculations.

Figure 4.13: CD spectra of the 2-benzoylbenzoic acid — (–)-(R)-amphetamine complex **1a** in Figure 4.12. Shown are spectra from an embedding calculation in which the amphetamine was represented by its frozen density (solid line), a supermolecular calculation (dashed line), as well as the spectra of isolated benzoylbenzoic acid (dashed-dotted line) and (–)-(R)-amphetamine (dotted line) in the structures they assume in complex **1a**.



While the spectra shown in Figure 4.13 are a superposition of all excitations, we report the individual excitation energies and rotational strengths in Table 4.7. That table shows data for the isolated 2-benzoylbenzoic acid, the 2-benzoylbenzoic acid with the effective embedding potential of the (–)-(R)-amphetamine, and the complex of the two molecules (“supermolecule”). Corresponding excitations were found by mapping the excitations of the supermolecule onto those excitations of the embedded or isolated molecule for which the transition densities have the largest overlap (see Ref. [116]).

Table 4.7: Excitation energies E_{ex} (SAOP/TZP; in units of eV) and rotational strengths R (in cgs units of 10^{-40} esu² cm²) for complex **1a** in Figure 4.12. For comparison, also the results for the isolated benzoylbenzoic acid in the structure of complex **1a** are given.

No.	supermolecule		embedding		isolated	
	E_{ex}	R	E_{ex}	R	E_{ex}	R
1	2.87	0.02	—	—	—	—
2	3.04	−0.48	—	—	—	—
3	3.18	−9.46	3.28	−0.84	3.66	−2.54
4	3.34	12.54	—	—	—	—
5	3.51	−16.76	3.52	−14.79	3.42	−9.36
6	3.86	6.51	3.86	8.60	4.04	4.45
7	3.92	−11.71	3.91	−13.92	3.82	−3.22
8	4.00	27.88	4.03	21.55	4.30	2.00
9	4.13	−0.15	—	—	—	—
10	4.21	−0.03	—	—	—	—
11	4.30	0.32	—	—	—	—
12	4.34	−13.49	4.33	−10.31	4.16	−5.60
13	4.37	−0.26	—	—	—	—
14	4.41	0.27	4.54	1.52	5.09	−1.45
15	4.45	0.01	—	—	—	—
16	4.49	5.37	4.56	−2.30	4.57	−2.05
17	4.51	−5.59	—	—	—	—
18	4.60	−0.14	4.52	−2.47	4.35	7.62
19	4.62	−0.05	—	—	—	—
20	4.65	0.41	—	—	—	—
21	4.72	−6.60	4.74	−3.39	4.88	−3.74
22	4.73	0.42	4.78	−3.85	4.84	−1.08
23	4.84	−20.80	4.87	−18.46	4.95	−22.98

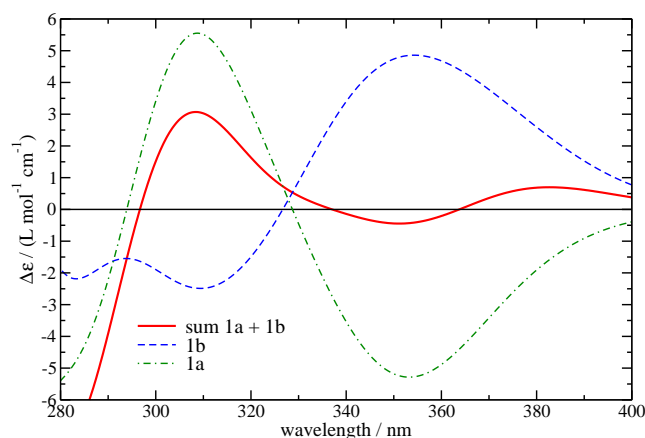
It can be observed that there are some excitations for which no corresponding transitions can be found in the embedding or isolated calculation for 2-benzoylbenzoic acid. These are charge-transfer excitations from one of the two molecules to the other. For charge-transfer excitations, the XC-kernel in ALDA-TDDFT calculations completely fails as discussed in Section 3.3: It yields a zero contribution, and the excitation energies reduce to the orbital energy differences of the orbitals involved. As can be recognized from Table 4.8, for almost all of these excitations missing in the embedded calculation, the

orbital energy difference and the excitation energy are practically identical, which is a strong hint on their CT nature. Further characteristics of CT excitations are their low transition moments and rotational strengths, which holds for all of these additional excitations except the ones at 3.34 eV and 4.51 eV. The latter also show the largest deviations from the orbital energy differences for the excitation energies. Indeed, we find a mixed character of CT and intramolecular valence transitions for these two excitations. The other supermolecular CT excitations in Table 4.7 can be regarded as artefacts of the ALDA-TDDFT method, with much too low energies.

Table 4.8: Excitation energies E_{ex} and orbital energy differences $\Delta\epsilon^{\text{orb}}$ for the most important orbital pair in those excitations in Table 4.7 for which no corresponding excitation exists in the embedding calculation (SAOP/TZP; in units of eV).

No.	E_{ex}	$\Delta\epsilon^{\text{orb}}$
1	2.87	2.87
2	3.04	3.04
4	3.34	3.30
9	4.13	4.13
10	4.21	4.21
11	4.30	4.30
13	4.37	4.37
15	4.45	4.45
17	4.51	4.41
19	4.62	4.62
20	4.65	4.63

Figure 4.14: CD spectra of the benzoylbenzoic acid — (–)-(R)-amphetamine complexes **1a** (dotted line) and **1b** (dashed line) in Figure 4.12 as well as the sum of these two spectra (solid line).



For the transitions which occur in both the supermolecular and the embedding calculation, the excitation energies typically agree very nicely within 0.03 eV, even for excitations that shift by up to 0.3 eV compared to the isolated calculation. Excitations with larger differences between embedded and supermolecular calculation typically also show larger absolute shifts with respect to the isolated 2-benzoylbenzoic acid, so that the relative deviations are still rather small. E.g., the lowest singlet excitation in the isolated molecule shifts from 3.66 eV to 3.28 eV (embedding) or 3.18 eV (supermolecule), and the excitation at 5.09 eV in the isolated molecule shifts to 4.54 eV (embedding) or 4.41 eV (supermolecule). There is no excitation for which the embedding predicts a wrong direction of the shift. Also the rotational strengths are quite similar, which leads to the very good overall agreement of the spectra. There is one exception for the rotational strengths: The excitation at 3.18 eV in the supermolecular calculation has a large negative rotational strength, while the embedding calculation predicts a transition at 3.28 eV with a small negative rotational strength. In the supermolecular calculation, there is another transition with large positive rotational strength at 3.34 eV, which also has a reasonable transition density overlap [318,319] with the excitation at 3.28 eV in the embedding calculation. This excitation at 3.34 eV is — as noted before — a spurious CT transition (cf. Table 4.8), but being accidentally close to another excitation, it distorts the rotational strengths of the two transitions, picking up much too high rotational strength itself and leaving a much too negative rotational strength for the excitation at 3.18 eV. The net effect in the spectra is quite similar: both in the supermolecular and in the embedding calculation, the total CD signal in that energy range is quite small. Also for the excitations at 4.49, 4.51, and 4.60 eV in the supermolecular calculation, we observe a rather strong mixing between different orbital transitions, one of which is of CT type, leading to a cancellation of the rotational strengths. From this example, it can be concluded that frozen-density embedding is very well suited to reproduce the change in the CD spectrum due to the interactions with the chiral, hydrogen-bonded partner molecule.

Although it is not the aim of this work to provide a detailed comparison with experiment, we would like to outline which steps would be necessary to simulate the behavior of the real system in solution. Up to now, we only looked at one particular optimized structure, although several other local minima might be energetically accessible and therefore important in solution. In particular, it could be argued that we already started from a chiral structure for the benzoylbenzoic acid, while its mirror image will occur with the same probability in solution in absence of a chiral partner. Therefore, the next step in the analysis of this system is to re-optimize the complex, but starting from the conformer of benzoylbenzoic acid that is the mirror image of the structure in **1a**. We carried out such an optimization, which resulted in structure **1b**. From the lower panel in Figure 4.12 it can be seen that indeed the benzoylbenzoic acid moiety is just mirrored w.r.t. the structure in **1a**. During re-optimization, the (–)-(R)-amphetamine rotated around the C–N-bond. The energy difference between the two conformers **1a** and **1b** is only 0.6 kJ/mol, so that both forms will exist in almost identical amounts in solution, and they would equally contribute to the total CD spectrum. Therefore, we performed another FDE calculation on structure **1b**, and the resulting CD spectrum is shown in Figure 4.14. That figure also contains the spectrum of **1a** as well as the sum of the two spectra in the wavelength range which was investigated in the experiment [383]. It can

be seen that the CD intensity for wavelengths between 340 and 400 nm more or less disappears due to different signs in the CD bands for the two conformers. Between 300 and 320 nm, however, a net positive CD signal can be observed, because the negative band of structure **1b** is much less intense than the positive band of **1a**. This positive CD band with a maximum at 309 nm arises from $\pi \rightarrow \pi^*$ transitions in **1a** and **1b**.

To really mimic the situation in solution, it would be necessary to investigate many other low-energy structures and to sample their contribution to the total CD spectrum. Nevertheless, it is gratifying to note that also in the experiment a positive CD band with a maximum at $\lambda_{\text{max}} \approx 318$ to 326 nm (depending on the solvent) is the characteristic feature in the CD spectrum of 2-benzoylbenzoic acid induced by (–)-(R)-amphetamine [383].

4.4.2 Circular dichroism induced in amino acid receptor models

Our second test system is a complex between the ferrocenecarboxylic acid–crown ether conjugate **2**, which is shown in Figure 4.15, and the protonated amino acid L-leucine. Like benzoylbenzoic acid in the first example, compound **2** is non-chiral only in a dynamical sense. I.e., stable structures of **2** are chiral, but the system is flexible enough so that the enantiomeric forms are accessible in solution. Compound **2** contains multiple binding sites for amino acids: The carboxylic acid group can form two-point hydrogen bonds to the $-\text{CO}_2\text{H}$ group of an amino acid, and the crown ether moiety can bind (protonated) amino groups. Therefore, the system can be seen as an artificial amino acid receptor, and was shown to enable efficient extraction of protonated amino acids from aqueous solution [385]. This system was employed in chirality sensing studies, since α -amino acids induce a non-zero circular dichroism in complexes with the non-chiral **2**. In this way, **2** allows to discriminate between the optical antipodes of α -amino acids, e.g., L- and D-leucine [385], which do not show own CD activity for wavelengths > 250 nm. The optimized (BP86/TZP) structure (**3a**) of this complex is shown in Figure 4.16. Again, we treat the chiral molecule, i.e., L-leucine, as the frozen part in our calculation, in order to test whether the effect of the chirality-inducing subsystem can be reproduced by frozen-density embedding. This application may seem to be somewhat unusual, since the “environmental system” in this case is smaller than the actual embedded system, and from a computational point of view also the full supermolecular calculation is feasible. But FDE not only reduces the computational cost, it also opens up the way to a simpler interpretation of the induced circular dichroism signal in terms of an effective chiral perturbation in the potential.

The lowest singlet excitation of L-leucine in a calculation on its structure in **3a** was found at 5.28 eV (235 nm). Therefore, there will be no direct contribution of this amino acid to the spectrum of the complex in the wavelength range investigated here. Since compound **2** in structure **3a** is chiral, we first calculated the CD spectrum of isolated **2**, which is shown in Figure 4.17. The lowest excitations of **2** all involve orbital transitions from Fe-*d* type orbitals to π^* type orbitals of the substituted cyclopentadienyl (Cp) ligands, which also have partly Fe-*d* contributions. At somewhat higher energies, these transitions are augmented with $\pi \rightarrow \pi^*$ excitations of the benzene moiety and $n(\text{O}) \rightarrow \pi^*(\text{Cp})$ excitations. Most of the bands observed for **2** in this structure show a rather low intensity, e.g., the negative bands with maxima at 433 nm and 528 nm.

Figure 4.15: Lewis structure of the ferrocenecarboxylic acid–crown ether conjugate **2**.

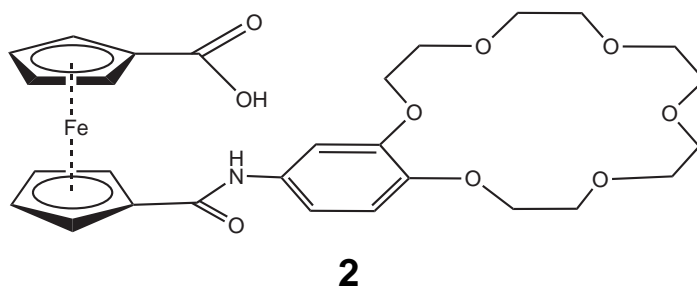
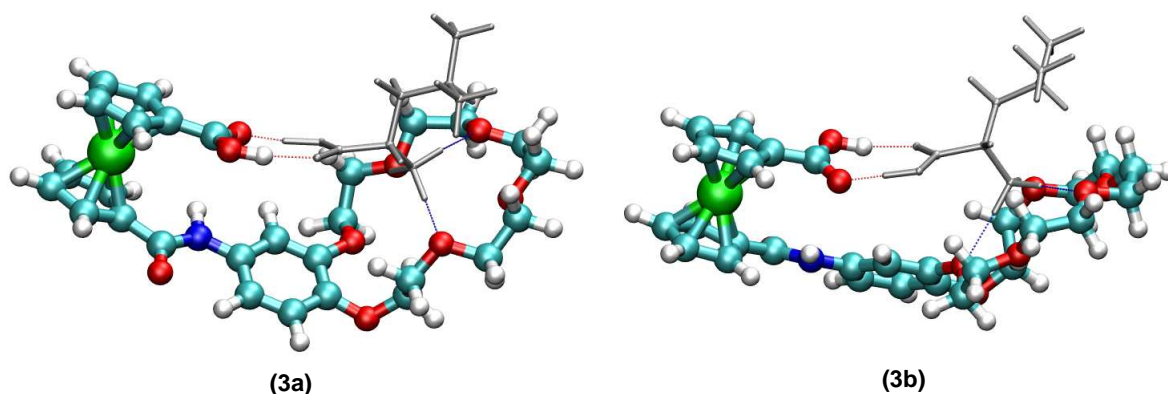


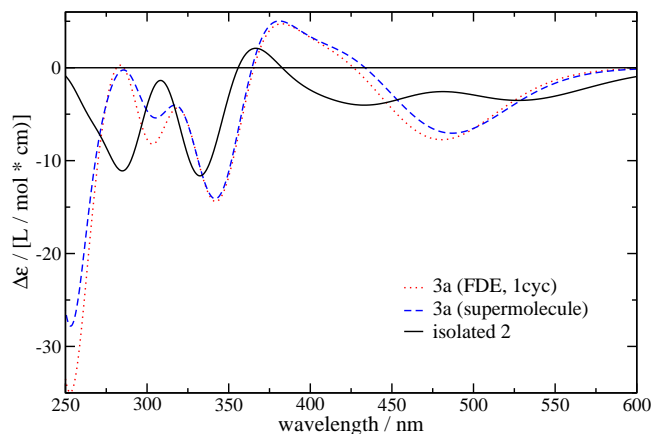
Figure 4.16: Optimized (BP86/TZP) structures of the complex between the ferrocenecarboxylic acid–crown ether conjugate (colored, ball-and-stick) and protonated L-leucine (grey, sticks only). The total charge of the complex is +1. Complex **3b** is a re-optimized complex starting from L-leucine and compound **2** in the mirror image structure of its optimum structure in complex **3a**. Structure **3a** is 1.2 kJ/mol lower in energy than structure **3b**.



However, there are also two strong negative peaks at 333 nm and 285 nm.

When we include L-leucine into the calculation by performing a supermolecular calculation on complex **3a**, we observe a strong electronic effect that completely changes the CD spectrum: A stronger negative band appears at 488 nm and a positive band at 380 nm with a shoulder at 419 nm. The strong negative peak is now shifted to 342 nm, and has even gained intensity. Another negative band can be seen at 304 nm. On the short-wavelength end of this spectrum, we see a very strong negative band centered at 253 nm. These features are very well reproduced if we use frozen-density embedding. There is only a slight disagreement in the position of the maximum of the first (negative) band (481 nm vs. 488 nm in the supermolecular calculation), and the negative bands at 304 nm and 253 nm gain some intensity in the embedding calculation. This shows that even in situations of complex interactions between a receptor-like molecule and its substrate, the effect on the circular dichroism spectrum can reliably be modeled by FDE.

Figure 4.17: CD spectra of the complex **3a** in Figure 4.16. Shown are spectra from a calculation in which L-leucine was represented by its frozen electron density (dotted line), a supermolecular calculation (dashed line), as well as the spectrum of isolated compound **2** in the structure of complex **3a** (solid line).



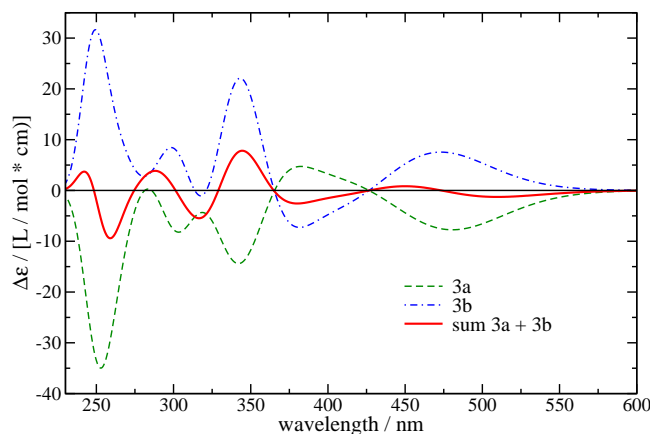
Also in this case, an extensive sampling over important conformations of this complex in solution would be necessary for a reliable comparison to experiment. Such a sampling would be even more demanding than for the system of 2-benzoylbenzoic acid and (-)-R-amphetamine. This is due to the fact that compound **2** is very flexible, and many low-energy configurations might be found. Again, a first step into this direction can be taken by optimizing the structure of the complex in which the mirror image of compound **2** in its structure in complex **3a** is employed, together with protonated L-leucine. We carried out such an optimization, which resulted in structure **3b** in Figure 4.16. The spectra of both complexes from frozen-density calculations and their sum are shown in Figure 4.18.

Unfortunately, it is very difficult to draw even qualitative conclusions from this sum spectrum in comparison to the experimental spectrum in Ref. [385]. The experimental spectrum for the complex formed with protonated L-leucine shows a weak negative CD band at 310 nm, a positive CD band at 290 nm, and a broad negative CD band at about 255 nm. This spectral feature, denoted as a W-shaped band, is followed by a more intense negative band at ca. 225 nm, i.e., at the short-wavelength end of the spectrum. Taking the sum of the spectra of complexes **3a** and **3b**, we can reproduce the cancellation of positive and negative CD signals in the wavelength regime from 365 to 600 nm. Moreover, the superimposed spectra indeed lead to a W-shaped spectral feature with a positive band at 288 nm, and two negative peaks at 317 and 259 nm. But there are also parts of the spectrum that do not match the experiment: There is a positive CD band at 344 nm, for which there is no experimental counterpart, and the strong negative band at ca. 225 nm is not observed.

We should take care not to over-interpret these results: At first glance, the spectra of **3a** and **3b** look rather symmetrical to the zero-line. The sum of the two spectra will thus depend very strongly on the exact positions and rotational strengths of the individual transitions, and the typical errors in TDDFT excitation energies might already be too large to quantitatively reproduce the experimental pattern. Second, there are several

overlapping bands, and already the type of broadening applied in the simulated spectra may change the overall shape of the spectrum considerably [394] (here, again a uniform broadening of 0.4 eV was applied to all vertical transitions). As a further complication, many more conformers of this complex may play a role in solution, as the system is highly flexible (at least in the crown-ether moiety). These structures will occur in solution with different probabilities, so that a (Boltzmann-) weighted sum of the spectra would have to be taken instead of the unweighted sum used here. We can, however, clearly conclude that our calculations strongly support the possibility of an alternating sequence of positive and negative CD signals in the wavelength regime between 250 and 350 nm by electronic transitions of the ferrocene function.

Figure 4.18: CD spectra of the complexes **3a** (dashed line) and **3b** (dashed-dotted line) in Figure 4.16 as well as the sum of these two spectra (solid line).



4.4.3 Cyclodextrin inclusion compounds: Harata's rule

As mentioned at the beginning of Section 4.4, cyclodextrin inclusion compounds are subject to extensive studies on induced circular dichroism [371]. One example of a non-chiral compound as a guest in a cyclodextrin cavity is phenol in β -cyclodextrin, which is composed of seven glucose units. It was reported that the sign of the circular dichroism depends on the orientation of the phenol molecule w.r.t. the axis of the cyclodextrin cavity [389]. From the experimental sign of a particular electronic transition, the orientation of the guest molecule in the cavity can be estimated.

Phenol as a guest molecule in its optimized conformation is non-chiral. Interactions with the chiral host may lead to a distortion of its geometry, so that a structural effect due to the host molecule induces circular dichroism. Here, we want to concentrate on possible electronic effects causing ICD and their dependence on the orientation of the phenol molecule inside the cavity. Therefore, we take an optimized (BP86/TZP) structure of an isolated phenol, which is placed inside the cavity of an optimized (BP86/TZP) conformation of β -cyclodextrin. The center-of-mass of phenol was placed in the center of the cyclodextrin cavity. The initial orientation, in which the C–O bond of phenol is in the plane of the cyclodextrin ring, is shown in Figure 4.19, as well as a 90° rotated one, where the C–O bond is perpendicular to the ring.

Figure 4.19: Structure of the host–guest complex **4** between phenol and β -cyclodextrin. Left: 0-degree orientation; right: 90-degree orientation.

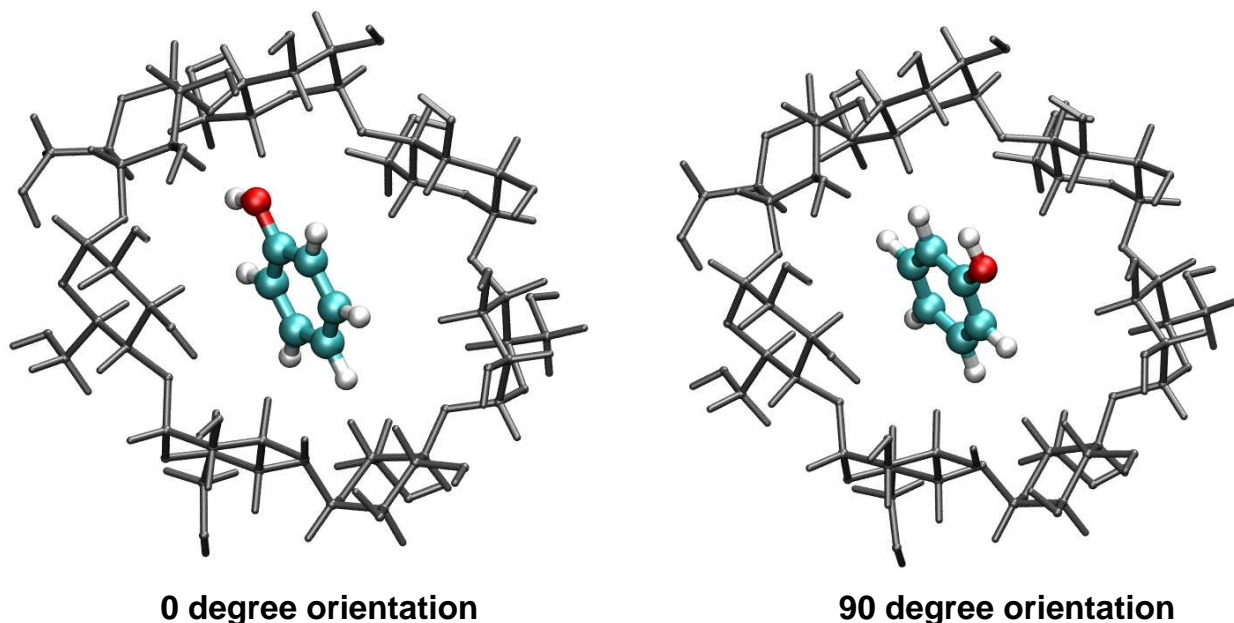
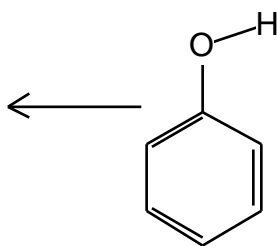


Figure 4.20: Direction of the electric transition dipole moment for the lowest singlet excitation of phenol. The transition dipole moment is located in the molecular plane.



For the isolated planar phenol molecule, the electric transition dipole moments can be either in-plane (irrep A') or perpendicular to the plane (irrep A''). According to Harata's rule, A' excitations should show a change in the sign of the CD signal when the molecule is rotated by 90° (in the way shown in Figure 4.19), as the transition moment is in the cyclodextrin plane for certain orientations, and perpendicular to it for orientations rotated by 90 degrees w.r.t. the former ones. For the transition under study here, i.e., the lowest singlet ($n \rightarrow \pi^*$) excitation of phenol, the direction of the electric transition dipole moment is in the molecular plane, approximately perpendicular to the C–O bond (see Figure 4.20).

Harata's rule was derived from the empirical Kirkwood–Tinoco model, which treats the interactions between excitations in host and guest system as a dipole–dipole coupling

between transition dipole moments. The transitions in the host system are approximated in this case as transitions of individual groups or bonds j . It was noted [391] that the most important term determining the sign of the rotational strength R_i for a given transition i in the guest molecule is the geometrical factor $(GF)_j$ in the Tinoco expression [388], which is usually defined as [378,389]

$$(GF)_j = \frac{1}{r_{ij}^3} \left[\mathbf{e}_i \cdot \mathbf{e}_j - \frac{3(\mathbf{e}_i \mathbf{r}_{ij})(\mathbf{e}_j \mathbf{r}_{ij})}{r_{ij}^2} \right] (\mathbf{e}_i \times \mathbf{e}_j) \cdot \mathbf{r}_{ij}. \quad (4.1)$$

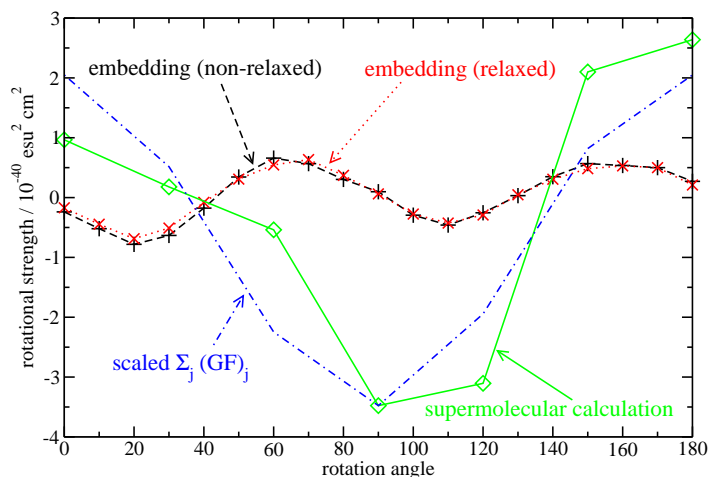
In the above equation, \mathbf{e}_i is the unit vector in the direction of the electric dipole transition moment of the guest molecule, \mathbf{e}_j is the unit vector in the direction of the bond j , and \mathbf{r}_{ij} is the vector between the two transition dipoles, which is assumed to be the vector from the center of the guest molecule to the center of bond j . Since $(GF)_j$ yields only the contribution of bond j , it is necessary to sum over all bond contributions to get the rotational strengths. The sum is a weighted sum in which bond polarizabilities parallel and perpendicular to the bond as well as an average wavenumber of the electronic transitions in that group enter as empirical parameters [378,389].

Although we do not want to perform a detailed analysis of the performance of the Kirkwood–Tinoco model for our test case, it is interesting to see if qualitatively the behavior predicted by Harata’s rule can be observed in our particular snapshot since Eq. (4.1) depends on the position and orientations of the bonds in the host system. To this end, we carried out a very simple analysis by performing an unweighted summation of the geometrical factors for all bonds. This was repeated for different orientations of the phenol molecule in the host cavity (the 0-degree and 90-degree orientations are shown in Figure 4.19). Such an approach corresponds to a very naive approximation within the Kirkwood–Tinoco model, namely, that the bond specific parameters are identical for all bonds. We only followed the common practice to neglect the effect of C–H bonds, which are usually assumed to have an isotropic bond polarizability that does not contribute to the total rotational strength. Tests indicated, however, that including the C–H bonds leads to the same qualitative behavior. For a more detailed analysis of phenol in β -cyclodextrin described by the Kirkwood–Tinoco model, we refer to Ref. [389].

The sum of the $(GF)_j$ for different angles of the C–O bond w.r.t. the plane in which the cyclodextrin molecule is located is shown in Figure 4.21. The data were obtained by using the transition dipole moment obtained for isolated phenol in each of these orientations. Since we are only interested in a qualitative behavior, the curve was scaled to match the results of a supermolecular TDDFT calculation for the axial orientation (90 degrees). Indeed, the qualitative behavior agrees with the calculations in Ref. [389], i.e., we get positive values for equatorial orientations (0 degrees and 180 degrees) while the rotational strength is negative for the axial orientation of phenol (90 degrees, corresponding to an equatorial orientation of the electric transition dipole moment). We also note that both our simple analysis and the empirical calculations in Ref. [389] lead to a behavior of the CD intensity that is symmetric w.r.t. the axial orientation (note that in Figure 11 of that reference the angle is measured for the electric transition dipole moment, not for the C–O bond).

In order to investigate whether these results are confirmed by *first principles* methods, we performed full supermolecular TDDFT calculations on this system for certain orien-

Figure 4.21: Rotational strength of the lowest singlet transition of the host–guest complex **4** between phenol and β -cyclodextrin with varying orientation of phenol inside the cavity. The 0- and 90-degree orientations are shown in Figure 4.19. Shown are results from supermolecular calculations (SAOP/TZP/DZP), employing a simple CT-correction scheme [395], and from FDE calculations, in which the cyclodextrin was treated as the frozen system (either relaxed or non-relaxed). For qualitative comparison, we also show (scaled) sums of the geometrical factors $(GF)_j$ for a given structure, which determine the rotational strength in the Kirkwood–Tinoco model.



tations. In these calculations, we used the SAOP potential in combination with a TZP basis set for phenol and a DZP basis set for β -cyclodextrin. Since the system is quite extended (160 atoms), there is a severe problem with spuriously low charge-transfer excitations. In order to remove these unphysically low excitations, we applied the simple CT correction scheme presented in Section 3.3.

The resulting rotational strengths indeed behave as expected according to Harata’s rule. Thus, they agree qualitatively with the calculations using the empirical Kirkwood–Tinoco model [389], or the simple summation of the $(GF)_j$ factors described above: For the 0-degree orientation, the electric transition dipole moment of the lowest singlet excitation is (almost) parallel to the axis of the cyclodextrin, since it is perpendicular to the C–O bond and in the molecular plane (see Figure 4.20). Indeed, this orientation results in a positive rotational strength for the lowest singlet transition. At about 45 degrees, the rotational strength becomes negative, and reaches a minimum when the C–O bond is parallel to the cyclodextrin axis (90-degree orientation; note that this corresponds to the 0-degree orientation in Ref. [389], since we measure the angle of the C–O bond w.r.t. the cyclodextrin plane, while in that work the angle of the electric transition dipole moment w.r.t. the plane is used). In the latter orientation, the transition dipole moment is perpendicular to the axis of the cyclodextrin host. However, the supermolecular calculations show that the induced rotational strength is not perfectly symmetric: The signal is, e.g., smaller at 0 degrees than at 180 degrees, but on the other hand it is larger at 60 degrees than at 120 degrees.

To test the performance of the frozen-density embedding, we calculated the rotational strengths for different orientations of the phenol molecule within the cyclodextrin cavity

representing the latter by its frozen density. We compared two calculations, in which the density of the β -cyclodextrin was either non-polarized or polarized by one freeze-and-thaw cycle. The non-polarized calculations are much more efficient¹, since the same frozen density for the host system can be used for all different orientations of the phenol molecule. The results are shown in Figure 4.21. The differences between the relaxed and non-relaxed frozen-density schemes are almost negligible, so that we will only discuss the calculations with a relaxed frozen density (and without frozen-core approximation). The rotational strength does indeed change sign for the different orientations of the phenol molecule, but it does so in an unexpected way: At 0 degrees, the rotational strength is close to zero. Then it goes down until it reaches a first minimum at 20 degrees, changes sign again at about 45 degrees, and reaches a maximum at 70 degrees, changes sign again at ca. 95 degrees and decreases until a second minimum is reached at 110 degrees. Another change in sign occurs at about 130 degrees, before the next maximum is reached at 160 degrees. This behavior is not in line with Harata’s rule, which would predict a positive rotational strength for the 0- and 180-degree orientations, and a negative one for the 90-degree orientation.

When comparing the results from the (simplified) Kirkwood–Tinoco model, the frozen-density embedding, and the supermolecular TDDFT calculation, it appears that the latter curve in Figure 4.21 is a superposition of a Kirkwood–Tinoco-model like symmetric curve and the curve resulting from FDE. Subtracting the embedding curve from the supermolecular one would lead to a more symmetric result, i.e., it would be closer to the pure Kirkwood–Tinoco model. This can be rationalized as follows: FDE is able to describe direct effects of the host system on the density and orbitals of the guest system, i.e., it shows a strong dependence on the exact position and shape of the guest molecule inside the host cavity. Due to the restricted response, however, it is not able to cover the effect of couplings with host excitations. These are, on the other hand, described by the empirical Kirkwood–Tinoco expression, whereas the only information about the guest molecule used in this empirical model is the electric transition dipole moment. Specific effects of the host on the orbitals of the embedded system are thus not included. The FDE calculations demonstrate that those are significant. The supermolecular calculation combines both effects, so that the results look like a sum of the curves obtained by FDE and the Kirkwood–Tinoco model.

4.4.4 Failure for coupled excitations

The phenomenon of coupling between host and guest molecule excitations evidently leads to discrepancy between FDE and the supermolecular benchmark calculations. To bring home this point, we briefly consider a case where the inadequacy of FDE stands out very sharply. There are some prototype systems consisting of several chromophores for which exciton coupling models predict the appearance of a so-called couplet [396]. A couplet can be understood as two interacting transitions of two similar chromophores

¹For testing, we also carried out non-polarized and polarized calculations in which a frozen-core was used for the oxygen- and carbon-1s orbitals (not shown). That further reduces the computational effort in the preparation step of the frozen density. It yields practically the same results as the calculation without frozen core, so that we can conclude that the frozen core approximation does not affect the embedding potential significantly.

that have rotational strengths of similar magnitude but opposite sign. Based on simple models employing localized wavefunctions [396] or on bond polarizabilities [388,391], it is possible to estimate the splitting between two interacting transitions and their rotational strengths. Because of the interaction of the two chromophores the positions of these transitions are not exactly the same and the CD intensities do not cancel exactly. This is demonstrated in the following for a benzaldehyde dimer as shown in Figure 4.22. The structure of the monomer was optimized using BP86/TZP. Since we only want to point out which type of interactions cannot be studied by frozen-density embedding, and not to investigate the properties of a real benzaldehyde dimer, we constructed an idealized dimer as a juxtaposition of a monomer with its mirror image. The mirror plane was chosen in the middle of the C=O bond (perpendicular to this bond), so that the positions of the carbonyl-C and O atoms are exchanged. Then, the reflected monomer was displaced along the z-axis (perpendicular to the molecular plane) by 3 Å.

Figure 4.22: Structure of the benzaldehyde dimer constructed from optimized (BP86/TZP) monomers.

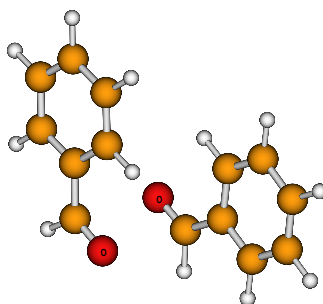


Figure 4.23: CD spectra of the benzaldehyde dimer shown in Figure 4.22 (SAOP/TZ2P). Shown are the contributions of two excitations in a supermolecular calculation as well as their sum. Additionally, the spectrum obtained in an embedding calculation is shown, which is scaled by a factor of 100.

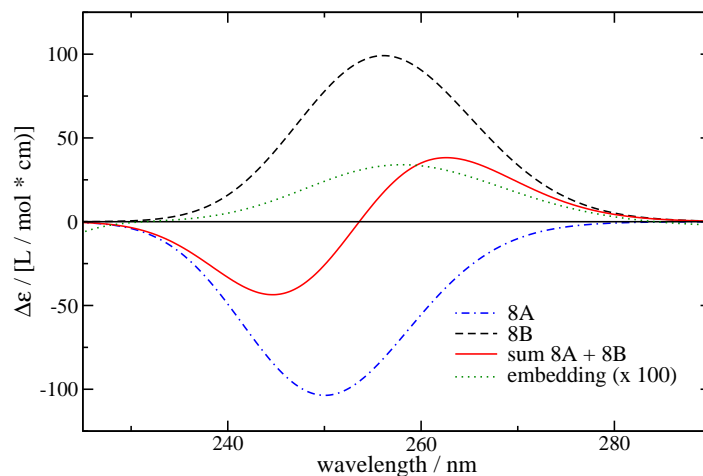


Figure 4.23 shows the results of a supermolecular calculation for a $\pi \rightarrow \pi^*$ type transition of the benzaldehyde dimer. In this particular case, we get two transitions of different symmetry for the C_2 complex: The $8B$ transition has a strong positive rotational strength, while the $8A$ transition, which is 0.12 eV higher in energy, shows a negative rotational strength of almost the same magnitude. The superposition results in a “couplet” with a positive part at the long-wavelength side and a negative part at the short-wavelength side.

As is shown in Figure 4.23, FDE is not applicable if one benzaldehyde monomer is treated as a frozen system, since the response is explicitly restricted to the embedded system. This results in a very weak, positive CD signal with a maximum at 258 nm, since there is no interaction possible with a similar excitation on the other fragment (note that the signal for the embedding calculation in Figure 4.23 is scaled by a factor of 100). Indeed, if we calculate the CD spectrum for the second monomer keeping the first one frozen, we get exactly the same result because of the imposed C_2 symmetry of the dimer.

The frozen-density embedding method is by construction not able to describe couplings to excitations that are not localized on the embedded system, which leads to a failure in cases where these effects are dominant. The reason is the same that is responsible for the advantages of the embedding method: the restriction of the orbital space to the embedded fragment. It should be kept in mind that *all* effective embedding methods, e.g., also QM/MM methods, necessarily have the same problem. However, as long as such couplings are not important, frozen-density embedding offers a way for an efficient description of interaction effects leading to induced circular dichroism, and it does not rely on any system-specific, empirical parameterization. A generalized subsystem DFT approach that can handle the coupled response of several subsystems is developed in Chapter 5.

5. Time-Dependent Density-Functional Theory for Subsystems

5.1 A subsystem TDDFT approach for coupled excitations

As was demonstrated in the previous chapters, FDE and its TDDFT generalization are very attractive approaches both from a conceptional and from a computational point of view. Excitations can still be interpreted in terms of orbital transitions, the problem of spuriously low-energetic excited states due to inter-subsystem transitions is avoided, and even very large environmental systems can be handled efficiently.

However, the study on induced circular dichroism in Section 4.4 showed that there are certain cases where FDE leads to qualitatively wrong results because couplings to the environmental response become dominant, which are neglected in the approximate FDE-TDDFT approach. As a consequence, excitation energy transfer (EET) couplings between different subsystems cannot be described in this approximate formalism.

This is a severe restriction of the FDE-TDDFT formalism, since EET couplings are essential for an understanding of many phenomena in complex aggregates containing chromophores. In particular, photoexcitation and subsequent EET processes in natural light-harvesting systems cannot be understood without such effects, as will be discussed in detail in Section 5.3.

In principle, the excitation energy splittings arising from these couplings can be extracted from quantum chemical calculations on the excited states of a supersystem composed of all chromophores under investigation. Among the first-principle methods which can be employed to describe excited states (see also Section 3.1), time-dependent density functional theory is often the method of choice for structural motifs of biological or biomimetic photosynthetic units [249, 397], and has proven to be a robust method for systems of considerable size [199, 222].

A fully quantum chemical description of a system like a natural light harvesting complex is still out of reach with conventional techniques, in particular if the surrounding medium shall also be considered. Recently, methods have been proposed to include excitation energy couplings perturbatively into TDDFT calculations starting from non-interacting fragments, in which bulk medium effects are considered in terms of continuum models [398–400]. From a chemist’s perspective, it appears that the description of aggregates of interacting chromophores and their environment should indeed be based on a subsystem-oriented approach, since the building blocks often retain their individual properties to a good approximation also in the supermolecule. This requires, however, an efficient subsystem TDDFT formalism that goes beyond the limitations of the FDE-TDDFT approach outlined in Section 3.4.2.

The original TDDFT generalization of FDE in Ref. [308] leads to an effective kernel for excitation energies of the embedded system which is still in principle exact. However, this

effective kernel would actually require to calculate the full response of the environmental system, so that no overall savings in computational effort can be expected. Furthermore, a direct implementation of the approach from Ref. [308] would suffer from numerical instabilities in the case of degenerate excitations, as will be outlined below. Here, a general subsystem TDDFT formalism for excited states will be derived. It will be shown that it is possible to find suitable approximations for the inclusion of EET couplings between the different subsystems, which can be efficiently implemented and which are thus applicable to complex systems of coupled chromophores.

Details of the formalism are presented in Section 5.1.1, followed by a discussion of possible approximations that go beyond the local response and that allow to seamlessly include excitation energy couplings in the FDE framework. A case study on a benzaldehyde dimer is carried out in Section 5.1.4. Subsequently, we demonstrate the applicability to more than two fragments and discuss cases in which both ground- and excited-state couplings are decisive to reproduce the supermolecular spectrum. In the subsequent sections of this chapter, it will be shown how general response properties can be obtained from this subsystem TDDFT approach, and that it can be applied to gain insight into the photophysical properties of natural light-harvesting complexes.

5.1.1 The subsystem formulation of TDDFT

The central assumption in the subsystem DFT approach outlined in Section 2.5 is that the total density $\rho(\mathbf{r})$ can be partitioned into subsystem densities according to Eq. (2.2), each of which is given in terms of occupied subsystem orbitals, see Eq. (2.43). The subsystem orbitals are, in turn, obtained from the Kohn–Sham-like one-electron equations given in Eq. (2.60). For brevity, we introduce the following notation for the effective potential in these equations for a subsystem J ,

$$v_J^{\text{sub}}(\mathbf{r}) = v_{\text{eff}}^{\text{sub}}[\rho, \rho_J](\mathbf{r}) = v_{\text{eff}}[\rho](\mathbf{r}) + \frac{\delta T_s[\rho]}{\delta \rho(\mathbf{r})} - \frac{\delta T_s[\rho_J]}{\delta \rho_J(\mathbf{r})}. \quad (5.1)$$

Following Ref. [308], we also partition the total density response, $\delta\rho(\mathbf{r})$, into subsystem contributions (note that we skip the frequency dependence in the following),

$$\delta\rho(\mathbf{r}) = \sum_I \delta\rho_I(\mathbf{r}). \quad (5.2)$$

In analogy to the supermolecular case, the subsystem response densities can be expanded in terms of the occupied and virtual molecular orbitals of the respective subsystems following Eq. (3.25),

$$\delta\rho_I(\mathbf{r}) = \sum_{(ia)_I} 2\delta P_{(ia)_I} \phi_{i_I}(\mathbf{r}) \phi_{a_I}(\mathbf{r}), \quad (5.3)$$

where the index I labels the subsystems. It should be noted that this is an approximation compared to the supermolecular case. It is assumed that the density response can be expanded in terms of intra-subsystem orbital transitions only, while inter-subsystem transitions do not occur. No charge-transfer excitations between the subsystems can

thus be described in the formalism. However, this approximation recovers the advantage that no artificially low long-range CT excitations between different weakly interacting fragments will be obtained, which is helpful for the analysis of the calculations. Nevertheless, this approximation clearly restricts the range of applicability of the current approach.

Also in the subsystem formulation, the expansion coefficients contain matrix elements of the perturbation, which has two parts, see Eq. (3.28),

$$\delta v_{(ia)_I} = \delta v_{(ia)_I}^{\text{ext}} + \delta v_{(ia)_I}^{\text{ind}}, \quad (5.4)$$

Assuming again a linear response of the effective one-electron potentials w.r.t. the density, we obtain for the induced effective potential in system I ,

$$\delta v_I^{\text{ind}}(\mathbf{r}_1) = \sum_J \int d^3r_2 \left(\frac{\delta v_I^{\text{sub}}(\mathbf{r}_1)}{\delta \rho_J(\mathbf{r}_2)} \right) \delta \rho_J(\mathbf{r}_2), \quad (5.5)$$

where the functional derivative has to be understood as a partial derivative in which all other subsystem densities ρ_K for $K \neq J$ are kept fixed. The effective potential for a subsystem I is given in Eq. (5.1) and consequently, its derivative w.r.t. the density ρ_J is obtained as

$$\begin{aligned} \frac{\delta v_I^{\text{sub}}(\mathbf{r}_1)}{\delta \rho_J(\mathbf{r}_2)} &= \frac{1}{|\mathbf{r}_1 - \mathbf{r}_2|} + \frac{\delta^2 E_{xc}[\rho]}{\delta \rho(\mathbf{r}_2) \delta \rho(\mathbf{r}_1)} + \frac{\delta^2 T_s[\rho]}{\delta \rho(\mathbf{r}_2) \delta \rho(\mathbf{r}_1)} - \frac{\delta^2 T_s[\rho_I]}{\delta \rho_I(\mathbf{r}_2) \delta \rho_I(\mathbf{r}_1)} \delta_{IJ}, \\ &= f_{\text{Coul}}(\mathbf{r}_1, \mathbf{r}_2) + f_{xc}^{\text{tot}}(\mathbf{r}_1, \mathbf{r}_2) - \frac{\delta^2 T_s[\rho_I]}{\delta \rho_I(\mathbf{r}_2) \delta \rho_I(\mathbf{r}_1)} \delta_{IJ}, \end{aligned} \quad (5.6)$$

$$= f_{Cxc}^{\text{tot}}(\mathbf{r}_1, \mathbf{r}_2) - \frac{\delta^2 T_s[\rho_I]}{\delta \rho_I(\mathbf{r}_2) \delta \rho_I(\mathbf{r}_1)} \delta_{IJ}, \quad (5.7)$$

where f_{Coul} is the Coulomb part of the kernel, f_{xc}^{tot} is given as,

$$f_{xc}^{\text{tot}}(\mathbf{r}_1, \mathbf{r}_2) = \frac{\delta^2 E_{xc}[\rho]}{\delta \rho(\mathbf{r}_2) \delta \rho(\mathbf{r}_1)} + \frac{\delta^2 T_s[\rho]}{\delta \rho(\mathbf{r}_2) \delta \rho(\mathbf{r}_1)} \quad (5.8)$$

and $f_{Cxc}^{\text{tot}} = f_{\text{Coul}} + f_{xc}^{\text{tot}}$. Inserting this into Eq. (5.5), we obtain

$$\delta v_I^{\text{ind}}(\mathbf{r}_1) = \int d^3r_2 \left[f_{Cxc}^{\text{tot}}(\mathbf{r}_1, \mathbf{r}_2) \delta \rho(\mathbf{r}_2) - \frac{\delta^2 T_s[\rho_I]}{\delta \rho_I(\mathbf{r}_2) \delta \rho_I(\mathbf{r}_1)} \delta \rho_I(\mathbf{r}_2) \right] \quad (5.9)$$

$$\begin{aligned} &= \int d^3r_2 \left[\left(f_{Cxc}^{\text{tot}}(\mathbf{r}_1, \mathbf{r}_2) - \frac{\delta^2 T_s[\rho_I]}{\delta \rho_I(\mathbf{r}_2) \delta \rho_I(\mathbf{r}_1)} \right) \delta \rho_I(\mathbf{r}_2) \right. \\ &\quad \left. + f_{Cxc}^{\text{tot}}(\mathbf{r}_1, \mathbf{r}_2) \sum_{J, J \neq I} \delta \rho_J(\mathbf{r}_2) \right]. \end{aligned} \quad (5.10)$$

The approximation introduced in Ref. [309] for the FDE case (see Section 3.4.2) is to assume that only the response of the embedded system itself has to be taken into account for local excitations,

$$\delta v_I^{\text{ind,approx}}(\mathbf{r}_1) = \int d^3r_2 \left[\left(f_{\text{CxcK}}^{\text{tot}}(\mathbf{r}_1, \mathbf{r}_2) - \frac{\delta^2 T_s[\rho_I]}{\delta \rho_I(\mathbf{r}_2) \delta \rho_I(\mathbf{r}_1)} \right) \delta \rho_I(\mathbf{r}_2) \right], \quad (5.11)$$

i.e., the density of the “environment” is assumed to be frozen even if an external perturbation is applied.

Going back to the full expression, Eq. (5.10), we can see that matrix elements of the induced potential are given as

$$\delta v_{(jb)_I}^{\text{ind}} = 2 \sum_{(ia)_J} K_{(jb)_I, (ia)_J}^{\text{eff}} \delta P_{(ia)_J}, \quad (5.12)$$

where the sum runs over all orbital transitions $(ia)_J$ in all subsystems J and

$$K_{(jb)_I, (ia)_J}^{\text{eff}} = \int d^3r_1 \left\{ \phi_{j_I}(\mathbf{r}_1) \phi_{b_I}(\mathbf{r}_1) \times \int d^3r_2 \left(f_{\text{CxcK}}^{\text{tot}}(\mathbf{r}_1, \mathbf{r}_2) - \frac{\delta^2 T_s[\rho_I]}{\delta \rho(\mathbf{r}_2) \delta \rho(\mathbf{r}_1)} \delta_{IJ} \right) \phi_{i_J}(\mathbf{r}_2) \phi_{a_J}(\mathbf{r}_2) \right\}. \quad (5.13)$$

Similar to the supermolecular case we arrive at

$$\delta P_{(jb)_I} = \chi_{(jb)_I}^s \left[\delta v_{(jb)_I}^{\text{ext}} + 2 \sum_{(ia)_J} K_{(jb)_I, (ia)_J}^{\text{eff}} \delta P_{(ia)_J} \right], \quad (5.14)$$

where $\chi_{(jb)_I}^s = \omega_{(jb)_I} / (\omega_{(jb)_I}^2 - \omega^2)$. In complete analogy to the supermolecular case, i.e., to conventional TDDFT, we can set up an eigenvalue equation to determine the excitation energies,

$$[\mathbf{\Omega}^s - \omega_k^2] \mathbf{F}_k^s = 0. \quad (5.15)$$

The superscript s indicates that the corresponding matrix or vector can be decomposed into subsystem blocks.¹ E.g., the matrix $\mathbf{\Omega}^s$ can be divided into intra- ($\mathbf{\Omega}_{IJ}$) and intersubsystem blocks ($\mathbf{\Omega}_{II}$; for systems $I, J = A, B, \dots, Z$), so that we obtain,

$$\left[\begin{pmatrix} \mathbf{\Omega}_{AA} & \mathbf{\Omega}_{AB} & \cdots & \mathbf{\Omega}_{AZ} \\ \mathbf{\Omega}_{BA} & \mathbf{\Omega}_{BB} & \cdots & \mathbf{\Omega}_{BZ} \\ \vdots & \vdots & \ddots & \vdots \\ \mathbf{\Omega}_{ZA} & \mathbf{\Omega}_{ZB} & \cdots & \mathbf{\Omega}_{ZZ} \end{pmatrix} - \omega_k^2 \begin{pmatrix} \mathbf{1}_{AA} & \mathbf{0}_{AB} & \cdots & \mathbf{0}_{AZ} \\ \mathbf{0}_{BA} & \mathbf{1}_{BB} & \cdots & \mathbf{0}_{BZ} \\ \vdots & \vdots & \ddots & \vdots \\ \mathbf{0}_{ZA} & \mathbf{0}_{ZB} & \cdots & \mathbf{1}_{ZZ} \end{pmatrix} \right] \begin{pmatrix} \mathbf{F}_k^A \\ \mathbf{F}_k^B \\ \vdots \\ \mathbf{F}_k^Z \end{pmatrix} = \begin{pmatrix} \mathbf{0}_A \\ \mathbf{0}_B \\ \vdots \\ \mathbf{0}_Z \end{pmatrix}. \quad (5.16)$$

Compared to the eigenvalue equations for the isolated systems I, J, \dots , this equation contains three differences: (1) The inter-system coupling blocks $\mathbf{\Omega}_{IJ}$ are absent in isolated molecule calculations, (2) the coupling matrix elements carry the effective kernel that

¹Note that this superscript will be omitted for the matrix *elements*, for which the subsystem is always indicated by an additional index

contains exchange–correlation and kinetic energy contributions from all subsystems, and (3) the orbitals and orbital energies employed in the calculation of the matrix elements are obtained from a ground-state FDE calculation. In contrast to the approaches in Refs. [399,400] the effects arising from non-orthogonal orbitals are implicitly contained in this equation by means of the non-additive kinetic energy contributions, both to the ground-state potential and to the response kernel. Nevertheless, the FDE approach may be affected if non-orthogonality effects become too strong because of the limitations of the approximate non-additive kinetic energy functionals currently in use.

While the effects (2) and (3) mentioned above are also present in the approximate form of FDE-TDDFT outlined in Section 3.4.2, the couplings to the environment are not. Assuming that we already know the eigenvectors of the subsystem matrices $\mathbf{\Omega}_{II}$ [from FDE-TDDFT calculations in the approximate form of Eq. (5.11)], we can set up a unitary transformation matrix,

$$\mathbf{U} = \begin{pmatrix} \mathbf{U}_A & \mathbf{0}_{AB} & \cdots & \mathbf{0}_{AZ} \\ \mathbf{0}_{BA} & \mathbf{U}_B & \cdots & \mathbf{0}_{BZ} \\ \vdots & \vdots & \ddots & \vdots \\ \mathbf{0}_{ZA} & \mathbf{0}_{ZB} & \cdots & \mathbf{U}_Z \end{pmatrix} \quad (5.17)$$

where \mathbf{U}_I are the square matrices containing as columns all the eigenvectors of the subsystem matrices $\mathbf{\Omega}_{II}$. Multiplying Eq. (5.15) from the left by \mathbf{U}^\dagger and inserting $\mathbf{U}\mathbf{U}^\dagger$ in front of \mathbf{F}_k yields

$$[\mathbf{U}^\dagger \mathbf{\Omega}^s \mathbf{U} - \omega_k^2] \mathbf{U}^\dagger \mathbf{F}_k^s = 0 \quad (5.18)$$

$$[\tilde{\mathbf{\Omega}}^s - \omega_k^2] \tilde{\mathbf{F}}_k^s = 0, \quad (5.19)$$

where $\tilde{\mathbf{F}}_k^s = \mathbf{U}^\dagger \mathbf{F}_k^s$ and $\tilde{\mathbf{\Omega}}^s = \mathbf{U}^\dagger \mathbf{\Omega}^s \mathbf{U}$. This transformation will bring Eq. (5.16) into the following structure,

$$\left[\begin{pmatrix} \omega_{A,0}^2 & \tilde{\mathbf{\Omega}}_{AB} & \cdots & \tilde{\mathbf{\Omega}}_{AZ} \\ \tilde{\mathbf{\Omega}}_{BA} & \omega_{B,0}^2 & \cdots & \tilde{\mathbf{\Omega}}_{BZ} \\ \vdots & \vdots & \ddots & \vdots \\ \tilde{\mathbf{\Omega}}_{ZA} & \tilde{\mathbf{\Omega}}_{ZB} & \cdots & \omega_{Z,0}^2 \end{pmatrix} - \omega_k^2 \begin{pmatrix} \mathbf{1}_{AA} & \mathbf{0}_{AB} & \cdots & \mathbf{0}_{AZ} \\ \mathbf{0}_{BA} & \mathbf{1}_{BB} & \cdots & \mathbf{0}_{BZ} \\ \vdots & \vdots & \ddots & \vdots \\ \mathbf{0}_{ZA} & \mathbf{0}_{ZB} & \cdots & \mathbf{1}_{ZZ} \end{pmatrix} \right] \begin{pmatrix} \tilde{\mathbf{F}}_k^A \\ \tilde{\mathbf{F}}_k^B \\ \vdots \\ \tilde{\mathbf{F}}_k^Z \end{pmatrix} = \begin{pmatrix} \mathbf{0}_A \\ \mathbf{0}_B \\ \vdots \\ \mathbf{0}_Z \end{pmatrix}, \quad (5.20)$$

where again a tilde denotes transformed quantities, and $\omega_{I,0}^2$ is a diagonal matrix containing the squared resonance frequencies of the subsystems in the absence of intersystem couplings. Transition dipole moments and oscillator strengths within TDDFT can be obtained from the solution vectors \mathbf{F}_k^s [237], which are obtained as

$$\mathbf{F}_k^s = \mathbf{U} \tilde{\mathbf{F}}_k^s. \quad (5.21)$$

This point will be discussed in more detail in Section 5.2.

5.1.2 Effective embedding kernel

There is a possible second approach to the solution of Eq. (5.16), which underlines the “effective embedding nature” of the approach. Assuming that we are only dealing with

a two-partitioning case (system A and environment B , which contains all subsystems other than A), we get two sets of equations from Eq. (5.16),

$$[\mathbf{\Omega}_{AA} - \omega_k^2] \mathbf{F}_k^A + \mathbf{\Omega}_{AB} \mathbf{F}_k^B = \mathbf{0} \quad (5.22)$$

$$\wedge [\mathbf{\Omega}_{BB} - \omega_k^2] \mathbf{F}_k^B + \mathbf{\Omega}_{BA} \mathbf{F}_k^A = \mathbf{0}. \quad (5.23)$$

The second equation can now be solved for \mathbf{F}_k^B ,

$$\mathbf{F}_k^B = [\omega_k^2 - \mathbf{\Omega}_{BB}]^{-1} \mathbf{\Omega}_{BA} \mathbf{F}_k^A, \quad (5.24)$$

which can be inserted into Eq. (5.22),

$$[\mathbf{\Omega}_{AA} + \mathbf{\Omega}_{AB} [\omega_k^2 - \mathbf{\Omega}_{BB}]^{-1} \mathbf{\Omega}_{BA} - \omega_k^2] \mathbf{F}_k^A = \mathbf{0}, \quad (5.25)$$

so that we can formally solve the equation,

$$[\mathbf{\Omega}_{AA}^{\text{eff}} - \omega_k^2] \mathbf{F}_k^A = \mathbf{0}, \quad (5.26)$$

where the effective matrix is

$$\mathbf{\Omega}_{AA}^{\text{eff}} = \mathbf{\Omega}_{AA} + \mathbf{\Omega}_{AB} [\omega_k^2 - \mathbf{\Omega}_{BB}]^{-1} \mathbf{\Omega}_{BA}. \quad (5.27)$$

The above equation can be used as a starting point for approximations, e.g., by treating $\mathbf{\Omega}_{AA}$ exactly and using approximations for $[\omega_k^2 - \mathbf{\Omega}_{BB}]^{-1}$ (see Ref. [13], pp. 46–48, for more details). Using Eq. (5.27) directly will, on the other hand be more problematic, since (1) the effective matrix to be diagonalized depends on the sought-for eigenvalues, so that Eq. (5.26) has to be solved iteratively. Furthermore a different matrix has to be constructed and diagonalized for each eigenvalue, and the eigenvector in question has to be identified. (2) If the diagonal elements of $\mathbf{\Omega}_{BB}$ are close to the eigenvalue ω_k^2 , the procedure will be numerically instable. Nevertheless, Eq. (5.27) can be regarded as a matrix analog to the effective kernel presented in Ref. [308].

5.1.3 Approximate treatments

A very common case will be a system composed of two parts, the embedded part A and the environment B . The environment may be further partitioned, but for clarity of presentation we restrict the discussion to two fragments. Usually, for both the environment and the embedded system only a couple of eigenvalues and eigenvectors are determined by, e.g., a Davidson-type diagonalization of the matrices $\mathbf{\Omega}_{AA}, \mathbf{\Omega}_{BB}$. In such a case, we can still set up a truncated eigenvalue problem that includes selected couplings between the previously determined subsystem excitations.

We know in those cases all the elements of subblocks of the matrices $\tilde{\mathbf{\Omega}}_{AA}, \tilde{\mathbf{\Omega}}_{BB}$, since these are diagonal matrices with squares of subsystem excitation energies on the diagonal — which were calculated with neglect of any inter-subsystem couplings, but from orbitals and orbital energies that were obtained with an effective embedding potential. Let us assume that we know a set $\{\mu_A\}$ of (uncoupled) transitions in system A and a set $\{\nu_B\}$ of transitions of subsystem B in terms of their eigenvectors stored in the columns $\nu_{A,B}$

of matrix \mathbf{U} . Then we need the following additional matrix elements in order to set up the truncated eigenvalue problem,

$$\tilde{\Omega}_{\mu_A \nu_B} = \sum_{(ia) \in A} \sum_{(jb) \in B} U_{(ia)_A \mu_A} \Omega_{(ia)_A (jb)_B} U_{(jb)_B \nu_B} \quad (5.28)$$

$$= \sum_{(ia) \in A} \sum_{(jb) \in B} 2U_{(ia)_A \mu_A} \sqrt{\omega_{(ai)_A}} K_{(ia)_A, (jb)_B}^{\text{eff}} \sqrt{\omega_{(bj)_B}} U_{(jb)_B \nu_B}. \quad (5.29)$$

Here, the sums run only over the orbital transitions within either subsystem A or B , respectively. This equation formally contains a sum over *all* inter-subsystem coupling matrix elements $K_{(ia)_A, (jb)_B}$. However, it is not necessary to calculate all these coupling elements explicitly, as will shown in the following. We write the coupling matrix elements explicitly, which results in

$$\begin{aligned} \tilde{\Omega}_{\mu_A \nu_B} &= \sum_{\substack{(ia)_A \\ (jb)_B}} 2U_{(ia)_A \mu_A} \sqrt{\omega_{(ai)_A}} \times \\ &\quad \int d^3 r_1 \int d^3 r_2 [\phi_{i_A}(\mathbf{r}_1) \phi_{a_A}(\mathbf{r}_1) f_{\text{CxcK}}^{\text{tot}} \phi_{j_B}(\mathbf{r}_2) \phi_{b_B}(\mathbf{r}_2)] \sqrt{\omega_{(bj)_B}} U_{(jb)_B \nu_B} \\ &= \int d^3 r_1 \sum_{(ia)_A} 2U_{(ia)_A \mu_A} \sqrt{\omega_{(ai)_A}} \phi_{i_A}(\mathbf{r}_1) \phi_{a_A}(\mathbf{r}_1) \int d^3 r_2 f_{\text{CxcK}}^{\text{tot}} \\ &\quad \times \left[\sum_{(jb)_B} \phi_{j_B}(\mathbf{r}_2) \phi_{b_B}(\mathbf{r}_2) \sqrt{\omega_{(bj)_B}} U_{(jb)_B \nu_B} \right]. \end{aligned} \quad (5.30)$$

Similar to conventional TDDFT calculations employing density fitting techniques, we can then express the whole term in square brackets in the last line of the above equation in terms of a fitted density [236],

$$\delta \rho_{\nu_B} = \sum_{(jb)_B} \phi_{j_B}(\mathbf{r}_2) \phi_{b_B}(\mathbf{r}_2) \sqrt{\omega_{(bj)_B}} U_{(jb)_B \nu_B} \approx \sum_{\lambda} a_{\lambda} f_{\lambda}(\mathbf{r}_2), \quad (5.31)$$

so that only matrix elements of an induced potential caused by this fitted density have to be calculated. This approach is implemented in a locally modified version of ADF [277, 278], which uses Slater-type functions (and fit functions) throughout. With this fitting procedure, the potential induced in subsystem A by transition ν_B , $\delta v_{A, \nu_B}^{\text{ind}}$, which appears in the matrix element, can be calculated analytically (compare e.g., Ref. [184]) as

$$\delta v_{A, \nu_B}^{\text{ind}}(\mathbf{r}_1) = \sum_{\lambda} a_{\lambda} \int d^3 r_2 \left(\frac{1}{|\mathbf{r}_1 - \mathbf{r}_2|} + f_{\text{xcK}}^{\text{tot}} \right) f_{\lambda}(\mathbf{r}_2), \quad (5.32)$$

where we used the superscript ν_B to indicate that the induced electronic perturbation $\delta v_{A, \nu_B}^{\text{ind}}$ has to be calculated for each electronic transition ν_B . The matrix element is then obtained by numerical integration as

$$\tilde{\Omega}_{\mu_A \nu_B} = \int d^3 r_1 \sum_{(ia)_A} 2U_{(ia)_A \mu_A} \sqrt{\omega_{(ai)_A}} \phi_{i_A}(\mathbf{r}_1) \delta v_{A, \nu_B}^{\text{ind}}(\mathbf{r}_1) \phi_{a_A}(\mathbf{r}_1). \quad (5.33)$$

This means that only the eigenvectors for the transitions $\{\mu_A, \nu_B\}$, which describe the transition densities, are needed in order to set up the truncated eigenvalue problem.

Since this procedure always involves an initial FDE-TDDFT calculation for the monomer excitations, which are subsequently coupled in the general subsystem-TDDFT formalism, we denote the monomer calculations as “uncoupled FDE” or FDEu calculations, whereas we use the term “coupled FDE” or FDEc for the coupled response calculations.

This approach is conceptually similar to the TDDFT approach for non-interacting systems used in Refs. [399,400], which can be related to Förster- and Dexter-type (or general short-range) couplings between transition densities on a donor and acceptor subsystem. These couplings occur in the present formalism as the Coulomb and exchange parts of the total matrix elements $\tilde{\Omega}_{\mu_A\nu_B}$. Excitation energy splittings for two degenerate excitations, e.g., located on two equivalent monomers, could be obtained by solving a 2×2 eigenvalue problem for the relevant excitations only (see Section 5.1.4 for an example). The general expression for these coupling constants will be discussed in the context of natural light-harvesting complexes in Section 5.3. For the special case of two equivalent monomers, the coupling constants can be directly determined from the energy splitting in the supermolecule. If we denote the excitation energy of the monomers (obtained with the uncoupled FDE approach) as ω_m , we can approximate the excitation energies ω_d in the dimer with a coupling described by a matrix element $\tilde{\Omega}_{m_1m_2}$ as

$$\omega_d = \omega_m \pm \frac{\tilde{\Omega}_{m_1m_2}}{\omega_m}, \quad (5.34)$$

provided $\omega_m^2 \gg \tilde{\Omega}_{m_1m_2}$. The matrix element $\tilde{\Omega}_{m_1m_2}$ is thus directly proportional to the coupling strength. These couplings, in turn, are important for the rate of excitation energy transfer between different chromophores [401–403]. Often, only the Coulombic (Förster) coupling is considered, which dominates at larger distances between the chromophores. It is further approximated in many cases by discrete representations of the transition densities, e.g., in terms of oscillating dipoles (for a comparison see, e.g., Ref. [404]). The approaches in Refs. [399,400] start from non-interacting subsystems, whereas a large portion of the short-range effects between subsystems in close proximity is, in the present approach, included in the effective embedding potential and the corresponding kernel contributions. It will be demonstrated in Section 5.1.6 that both ground- and excited-state interactions must be considered to accurately reproduce spectra in the general case.

Refs. [399,400] discuss the effect of condensed media on the excitation energy transfer rate, describing the medium as a dielectric continuum. Since FDE was shown to be an efficient model for solvent effects on electronic excitations when applied within the approximate expression in Eq. (5.11), it could lead to a further improvement of the description of a surrounding medium in the following way: To calculate the subsystem excitations of a given chromophore, the entire surrounding system (i.e., other chromophores and solvent) can be included according to Eq. (5.11), while couplings are afterwards only included in a selective manner between the chromophores in the system. In that way, both the effect of the solvent and the couplings between the chromophores could explicitly be included, which was not possible with the uncoupled FDE-TDDFT approach. It should be noted that such a hybrid approach between the

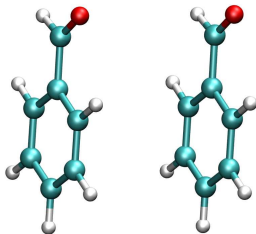
uncoupled FDE for the solvent molecules and the coupled FDE approach for solvated chromophores necessarily introduces the assumption that the entire density response can be described in terms of the changes of the chromophore densities. For a discussion of this neglect of solvent response and a comparison to a polarizable classical solvent model, see Ref. [185].

From a fundamental point of view, this approach seems very appealing to model solvent effects on coupled chromophores, since it is based entirely on density functional theory. However, such a simulation also causes some additional difficulties in comparison to continuum models: Since it is an explicit model, it requires to consider a representative set of snapshots of solvent configurations instead of just one structure [116]. Additionally, the size of the solvation shell must be sufficiently large, which can involve hundreds of solvent molecules even for medium-sized molecules [184].

5.1.4 Test case: Benzaldehyde dimer

In Section 4.4.4 it was shown that FDE-TDDFT in the previous form, i.e., with the approximation introduced in Eq. (5.11), is unable to deal with coupled identical chromophores. In order to test the approximate formalism introduced in this section, we investigated a pair of benzaldehyde molecules which are parallel displaced by varying distances (see Figure 5.1). The monomer structure was optimized with BP86/TZP. For technical details of the calculations presented here, see Appendix B.

Figure 5.1: Structure of the benzaldehyde dimer for an intermolecular distance of 5 Å.

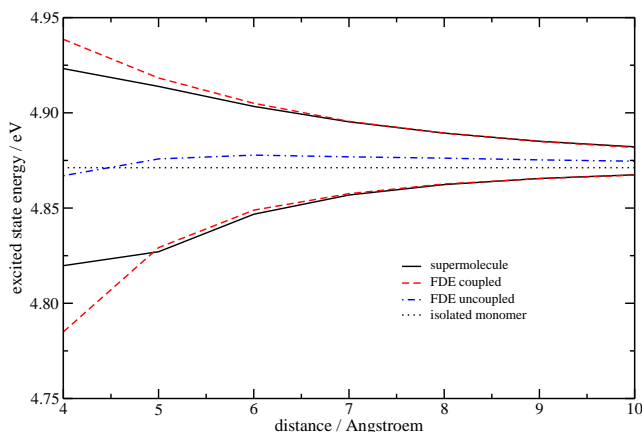


In order to test the implementation and the quality of the results obtained with the coupled FDE approach, we investigated the $3^1A'$ state, which is the lowest $\pi \rightarrow \pi^*$ singlet transition of benzaldehyde with considerable intensity (oscillator strength $f = 0.25$), and which has a dominant contribution from the (HOMO-1) \rightarrow LUMO ($4a'' \rightarrow 5a''$) orbital transition. The calculated excitation energy for this transition in the isolated monomer is 4.87 eV. Note that a lower-lying $\pi \rightarrow \pi^*$ type transition can be found at 4.24 eV, which has a dominant (HOMO-2) \rightarrow LUMO character, but a rather small oscillator strength of < 0.02 . Both orbital transitions mentioned contribute considerably to both $\pi \rightarrow \pi^*$ transitions. The transition to the $3^1A'$ state is well-suited in order to test the approach outlined above, since there is a significant coupling between excitations of this type on different monomers.

Excitation energies were calculated for distances between 4 Å, where already significant overlap of the π -systems of the monomers occurs, and 10 Å, where the couplings are already quite weak. In case of frozen-density embedding, we first calculated the lowest 20 excitation energies for both monomers employing three freeze-and-thaw cycles, so that the uncoupled FDE excitation energies were converged within < 0.0001 eV. In a second step, these excitations were coupled according to the subsystem treatment presented above.

Figure 5.2 shows the excitation energies from supermolecular and coupled FDE calculations as well as the uncoupled FDE results and the excitation energy of the isolated monomer. It can be seen that the uncoupled FDE deviates slightly from the isolated monomer due to the interaction of the two densities included in the ground-state FDE calculation, which influences the orbitals and orbital energies used in the TDDFT part. At a distance of 6 Å, this deviation is 0.007 eV and decreases to 0.003 eV at 10 Å.

Figure 5.2: Excitation energies of the benzaldehyde dimer shown in Figure 5.1 for the excited states corresponding to the $3^1A'$ state of the benzaldehyde monomer as a function of the intermolecular distance. Solid line: supermolecular TDDFT; dashed line: coupled FDE; dashed-dotted line: uncoupled FDE (no splitting); dotted line: isolated benzaldehyde monomer.

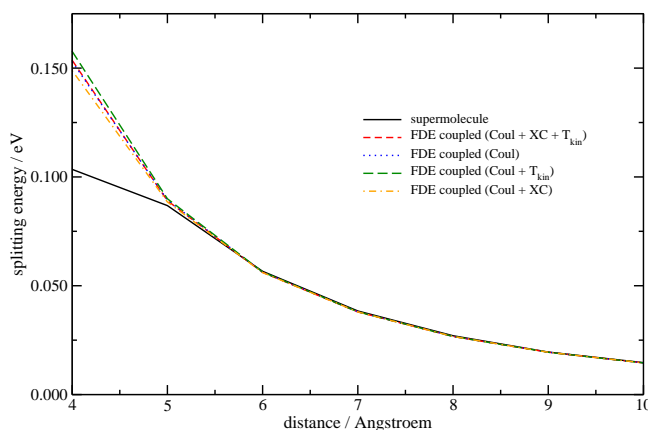


The supermolecular calculations show a significant coupling between the two monomer excitations. Even at a distance of 10 Å, there is a splitting of 15 meV, which increases to 86 meV at 5 Å distance. This behavior is very nicely reproduced by the coupled FDE calculations, especially at separations larger than 5 Å. For distances larger than 7 Å, the error in the excitation energies is smaller than 1 meV, and even at 5 Å, it is 4.4 or 2.2 meV, respectively, for the lower and the upper state. Absolute errors in the energy splitting are between 0.1 (10 Å) and 2.2 meV (5 Å), and the relative error in the splitting energy is between 0.8 (10 Å) and 2.5 % (5 Å).

At 4 Å separation, the situation changes significantly. Although there is still qualitative agreement between the coupled FDE approach and the supermolecular results, the energy gap in the FDE calculation is notably larger (0.154 eV compared to 0.103 eV in the supermolecular case). This is caused by the fact that additional excited states couple to the $\pi \rightarrow \pi^*$ excitations under study, which partly have charge-transfer character. As

explained in the Section 5.1.1, such excitations are not covered by the coupled FDE scheme. Consequently, there will be no couplings to such states in the coupled FDE formalism which could decrease the splitting between the two states under investigation. As mentioned above, interactions between such transitions are often discussed in terms of Förster- (Coulomb-) or Dexter- (exchange-) couplings. In the present formalism, we actually have to distinguish three different effects: Our effective coupling integrals contain a Coulomb- (Coul), an exchange–correlation (XC), and a kinetic-energy (T_{kin}) contribution. The latter can be associated with “Pauli-repulsion” effects, since it effectively corrects for the non-orthogonality of the subsystem orbitals. Additionally, there are interactions between the fragments taken into account in the ground-state embedding calculation, which will not be further analyzed here (see, e.g., Ref. [185] for a discussion of their influence on excitation energies). The different contributions can be analyzed by deactivating certain parts of the effective kernel for inter-subsystem coupling matrix integrals $K_{(ia)_A,(jb)_B}^{\text{eff}}$. The resulting splitting energies are shown in Figure 5.3. Obviously, the by far dominating contribution to the coupling in this case is the Coulomb coupling. Indeed, the XC and T_{kin} contributions are hardly visible for distances larger than 5 Å. Particularly interesting is that the splitting energies which only include Coulomb coupling agree almost perfectly with the fully coupled data, since the XC and T_{kin} contributions almost cancel each other even at a separation of 4 Å. However, at distances where these effects become visible, the couplings with the CT-like excitations actually have a much larger effect, which causes the deviation between the coupled FDE and the supermolecular calculations.

Figure 5.3: Splitting energies (in units of eV) of the benzaldehyde dimer shown in Figure 5.1 for the excited states corresponding to the $3^1A'$ state of the monomer, as a function of the intermolecular distance. Solid line: supermolecular TDDFT; dashed line: coupled FDE (all contributions); dashed-dotted line: coupled FDE, only Coulomb and XC contributions; long-dashed line: coupled FDE, only Coulomb and T_{kin} contributions; dotted line: coupled FDE, only Coulomb contributions.



Another question is related to the number of couplings that have to be included in order to converge the excitation energies for the coupled transitions. Simple excitonic coupling models usually assume that only pairs of identical transitions have to be coupled, so

Table 5.1: Excitation energies and splitting energies (in units of eV) for the excited states of the benzaldehyde dimer corresponding to the $3^1A'$ excitation of the monomer for different numbers of coupled states. The intermolecular distance was 5 Å.

no. of states	E_1	E_2	ΔE
1, 1	4.8311	4.9201	0.0889
10, 10	4.8310	4.9199	0.0889
15, 15	4.8293	4.9183	0.0891
20, 20	4.8292	4.9183	0.0891

that Eq. (5.19) reduces to a 2×2 matrix-eigenvalue problem. In order to investigate this point, we considered only selected states in the subsystem formalism to investigate how the number of couplings included affects the excited-state energies and the splitting between the two states. The results for an intermolecular distance of 5 Å are given in Table 5.1. It can be seen that the splitting energy is converged within 0.0002 eV even if only one excitation per monomer is taken into account. The excitation energies themselves shift slightly (by approximately -0.002 eV) if more than 15 excitations per monomer are included. Thus, the by far dominant correction to the uncoupled excitation energies originates from the coupling of the degenerate excitations, as would be expected.

The efficiency of uncoupled FDE calculations was discussed in detail in the previous chapters. The decrease in computational cost compared to supermolecular calculations can be extremely large if simple approximations for the environmental density are sufficient. In the coupled FDE approach, additional computational effort is necessary: For every subsystem for which excitations shall be coupled with the other fragments it is necessary to perform an excitation calculation in addition to the calculation of the ground-state density. Furthermore, an element of the matrix $\tilde{\Omega}^s$ has to be calculated for every pair of states that shall be coupled. The computational effort thus depends linearly on the number of couplings that are included. The effort needed to describe one of these couplings is proportional to the number of integration points N_{point} , and the number of occupied and virtual orbitals *per subsystem*, $N_{\text{occ}}^{\text{sub}}$ and $N_{\text{virt}}^{\text{sub}}$. The latter two numbers can be considered constant in systems with identical chromophores if the number of chromophores is increased. Furthermore, the matrix elements needed involve the induced potential and basis functions on one subsystem only, so that in principle also the number of grid points could be kept constant. This requires to generate one integration grid per subsystem, as will be described in Section (5.3.2). On the other hand, the CPU time needed in a supermolecular calculation is proportional to [236] $N_{\text{point}} \times N_{\text{occ}}^{\text{super}} \times N_{\text{virt}}^{\text{super}}$, where $N_{\text{occ}}^{\text{super}}$ and $N_{\text{virt}}^{\text{super}}$ are the number of occupied and unoccupied orbitals, respectively, in the supersystem. Actually, this is the scaling behavior for one matrix–vector product in the iterative solution of the eigenvalue problem. The number of matrix–vector multiplications can roughly be estimated to be proportional to the number of excited states that have to be optimized. In case of an exact diagonalization of the matrix Ω , this number would be $N_{\text{occ}}^{\text{super}} \times N_{\text{virt}}^{\text{super}}$. As was shown in Ref. [116], this number will be much larger in a supermolecular calculation than in an FDE calculation. Since

also the numbers of occupied and virtual orbitals of the supersystem scale linearly with the number of (identical) subsystems, the coupled FDE approach will be particularly valuable if couplings are only needed for a small number of excitations (as is the case here, see Table 5.1).

5.1.5 Extension to several fragments

The frozen-density approach as originally suggested by Wesolowski and Warshel divides the total system into an embedded part and an environment [111]. The initial implementations in ADF [184,309] followed this approach, so that intermediate steps were usually required in order to use sum-of-fragment approaches for the density of the environment [116,184]. This approach is preferable if FDE is used as an effective environmental model. However, the original subsystem approach by Cortona [106] was not restricted to a fixed number of fragments (see Section 2.5). The subsystem formulation for excited states given here can also be generally applied for n fragments for which excitations are calculated individually, and which are then coupled in the way described in Sections 5.1.1 and 5.1.3. This is now also possible for ground-state calculations in a new ADF implementation [190]. The matrix elements $\tilde{\Omega}_{\nu_I\mu_J}$, which are available for all pairs of fragments I and J , are then still a measure for the strength of the coupling between the excitations on the different subsystems. However, their relation to the splitting energy is of course more complicated than in the simple approximation given in Eq. (5.34) or its generalization to cases of non-equivalent subunits. Additionally, the presence of a third molecule can modify the coupling matrix elements by its influence on the molecular orbitals in the ground-state FDE calculation.

We calculated the excitation energies for a benzaldehyde trimer, which consists of three benzaldehyde molecules in a row with intermolecular distances of 5 Å. The monomer units are numbered as follows: Monomer 1 is the fragment in the middle of the trimer (molecular plane = z -plane), monomer 2 is at $z = +5$ Å, and monomer 3 is at $z = -5$ Å. Subsystems 2 and 3 are thus equivalent by symmetry.

Table 5.2: Excitation energies (in units of eV) of the coupled excitation in the benzaldehyde trimer corresponding to the $3^1A'$ excitation (at 4.871 eV) in the isolated monomer; FDEu: uncoupled FDE approach; super: supermolecular TDDFT calculation; 1- $\{2,3\}$: monomer 1 coupled to dimer $\{2,3\}$; 2- $\{1,3\}$: monomer 2 coupled to dimer $\{1,3\}$; 1-2-3: monomer 1 coupled to monomers 2 and 3. Monomer 1 is the middle fragment.

No.	iso	FDEu	super	1- $\{2,3\}$	2- $\{1,3\}$	1-2-3
1	4.871	4.880	4.812	4.819	4.814	4.816
2	4.871	4.878	4.868	4.870	4.871	4.871
3	4.871	4.878	4.932	4.942	4.937	4.941

The excitation that occurs at 4.871 eV in the isolated monomer splits into three excitations due to the couplings between the three monomers. In the case of FDE calculations, it is possible to construct the trimer either as consisting of three fragments (1,2,3) or of two fragments. In the latter case, we can either choose the monomer 1 and the dimer

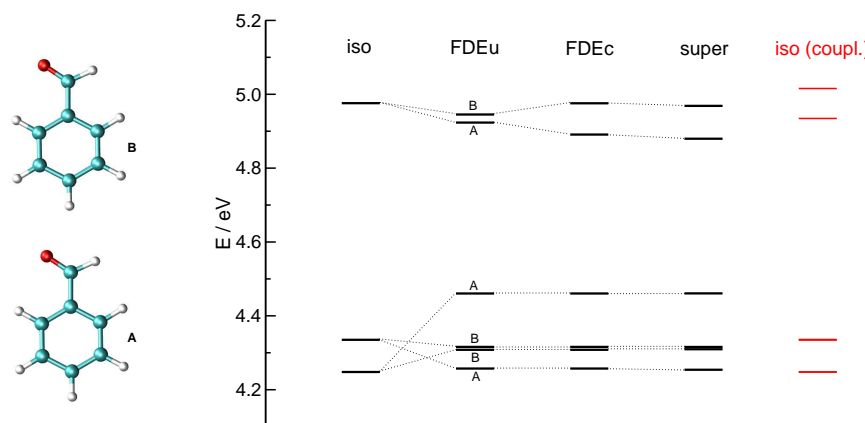
$\{2,3\}$ or the monomer 2 and the dimer $\{1,3\}$ (the third choice of monomer 3 and dimer $\{1,2\}$ is equivalent by symmetry). The results from supermolecular calculations and coupled FDE calculations with different fragments are shown in Table 5.2. The lowest 20 singlet–singlet excitations were calculated for each fragment and subsequently coupled. In the supermolecular calculation there is a splitting of 0.120 eV between the lowest and the highest of the three excitations. The coupled FDE approach starting from a monomer and a dimer yields a very similar splitting of 0.123 eV for all possible choices of monomer-dimer combinations (although the absolute positions vary slightly by 0.005 eV). The calculation based on three monomers results in a splitting that agrees well with the supermolecular approach (0.125 eV), which demonstrates the applicability of the approach to general cases with several interacting molecules.

5.1.6 Ground-state and excited-state interactions

In complex aggregates of pigment molecules, different chromophores will, in general, have non-equivalent environments. The hypothetical excitation energies of the chromophores in absence of any excited-state interaction are called site energies; the corresponding states may be regarded as quasi-adiabatic states. Their coupling by excitonic interaction then leads to the excitation energies that are observable in experiment, corresponding to adiabatic excited states.

One of the advantages of the subsystem TDDFT approach introduced here is its seamless integration into the corresponding ground-state formalism. The excitation energies from the uncoupled frozen-density embedding approach can thus be regarded as the site energies of a chromophore in an aggregate, and a subsequent coupling of the excitations as outlined above will lead to the excited states of the total system. This is demonstrated for the dimer of benzaldehyde molecules depicted in Figure 5.4. That figure also contains the excitation energies for the lowest-lying excited states of the two benzaldehyde molecules calculated in different approximations. For the isolated molecules A and B, the excitation energies are, of course, identical, as the dimer is composed of two identical benzaldehyde molecules that are lying in the same plane, but are displaced along the direction of the C–CO bond. It can be seen that already the uncoupled FDE calculation gives rise to a splitting in the excitation energies, since the two monomers are not equivalent. The differences in the excitation energies are larger for the lower-lying states, but also the upper state shows a small splitting. The excited-state couplings included in the FDEc calculation leave the energies of the lower-lying states almost unchanged, but widen the gap between the two higher-lying states. Note that the excited states in the FDEu calculation can still be assigned to either monomer A or B, whereas the excited states in the FDEc calculation are typically delocalized over both monomers. By comparison to the results of a supermolecular calculation, it can be seen that the accuracy of the FDEc calculation is very good (note that low-lying excitations of charge-transfer type in the supermolecular calculation are not shown for clarity). Figure 5.4 also contains the excitation energies obtained from a coupled calculation based on the isolated monomers instead of those from a ground-state FDE calculation (denoted as “iso”). It can be seen that the magnitude of the splitting for the higher-lying states is approximately correct, but neither the expected vertical position of these states nor the splitting in the lower-lying excitations is obtained. This clearly demonstrates that both ground-

Figure 5.4: Left: Structure of the non-symmetric dimer of two benzaldehyde molecules; right: lowest excited states for monomers A and B in isolated molecule calculations (iso), uncoupled (FDEu) and coupled FDE calculations (FDEc), a calculation on the supermolecule/dimer (super), and a coupled calculation starting from the non-interacting monomers (iso). Note that these illustrative calculations were performed with BP86/DZP.



and excited-state interactions must be properly taken into account in order to calculate excitation energies reliably within a subsystem approach.

5.1.7 Circular dichroism spectra of coupled chromophores

In Section 4.4.4 it was shown that FDE-TDDFT leads to a complete failure for the circular dichroism spectrum of a benzaldehyde dimer. Here we consider such a dimer again, which is shown in Figure 5.5. (Note that a different exchange–correlation functional was used in Section 4.4.4). The monomers are the same as employed throughout this section, and the intermolecular distance was set to 5 Å. We performed both a supermolecular calculation and a coupled FDE calculation. Rotational strengths were calculated using the dipole-velocity form for the electric transition dipole moments to obtain origin-independent results. Again, the lowest 20 excitations per monomer were included in the coupled FDE calculation. The spectra resulting from all transitions below 5 eV are shown in Figure 5.6. It can be seen that the coupled FDE approach nicely reproduces the supermolecular results. Only slight deviations can be observed in the position of the peak maxima and the intensities for the couplet dominating the spectrum. Overall, the agreement is very good.

We can thus conclude from the above examples that excitation energy couplings from supermolecular calculations can be reliably reproduced, and that the subsystem TDDFT approach is readily applicable to several subsystems. At short range, problems may arise from deficiencies in the approximate kinetic energy functionals employed here and from the fact that charge-transfer-like excitations play a role, which are excluded from the present approach. It was furthermore shown that spectral features in circular dichroism spectra arising from couplings between two chromophores are reproduced, for which the former FDE approaches failed completely (see Section 4.4.4).

Figure 5.5: Structure of the C_2 -symmetric benzaldehyde dimer for the CD calculations. The intermolecular distance is 5 Å.

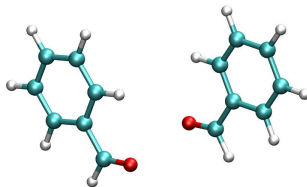
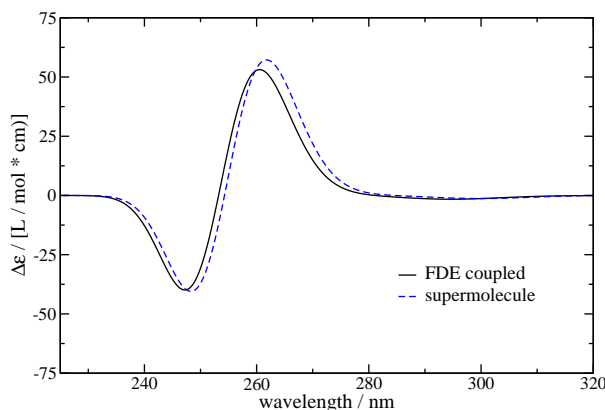


Figure 5.6: Circular dichroism spectrum (BP86/TZP) of the benzaldehyde dimer shown in Figure 5.5 (all excitations below 5 eV were taken into account).



5.2 General response properties from subsystem TDDFT

Whereas the last section concerned excitation processes exclusively, there are several other spectroscopic phenomena that are related to environmental response, and that may be of very intricate nature. To give an example, it has recently been argued that the optical rotatory dispersion of methyloxirane in benzene is caused mainly by the response of the benzene molecules due to a chiral imprinting effect [405,406]. Subsystem density functional response theory can provide an ideal means for the investigation of such phenomena, since both the entire frequency-dependent response of a system as well as the contributions of each subsystem individually can easily be assessed.

In the following, we will therefore extend the theoretical analysis given in Section 5.1 and derive explicit expressions for polarizabilities and optical rotation parameters. Additionally, we will establish the expressions for oscillator strengths and rotatory strengths in analogy to the supermolecular case. The design of efficient algorithms and an implementation of this approach will be discussed subsequently. Note that a formal derivation for polarizabilities in the two-partitioning case (embedded system and environment) was given in Ref. [308]. However, no generalization to arbitrarily many subsystems and no algorithms for practical calculations or implementations are available so far.

5.2.1 Polarizabilities

The components of the polarizability tensor are defined as the derivatives of the electric dipole moment with respect to an electric field. E.g., the xz -component of the frequency-dependent polarizability tensor is defined through the first-order perturbation in the x -component of the dipole moment, $\mu_x^{(1)}(\omega)$,

$$\mu_x^{(1)}(\omega) = \underbrace{\frac{\partial \mu_x}{\partial \mathcal{E}_z}}_{\alpha_{xz}(\omega)} \mathcal{E}_z \quad (5.35)$$

where \mathcal{E}_z is the amplitude of the frequency component with frequency ω of the external electric field. All other components can, of course, be defined analogously. The frequency-dependent electric dipole moment can be calculated as an expectation value of the electric dipole operator if the frequency-dependent density change is known. An expression for $\mu_x^{(1)}(\omega)$ can be obtained from the linear response of the density, so that the polarizability component can thus be written as

$$\alpha_{xz}(\omega) = \frac{\mu_x^{(1)}(\omega)}{\mathcal{E}_z} = \frac{1}{\mathcal{E}_z} \int d^3r \delta\rho(\omega, \mathbf{r}) \hat{\mu}_x \quad (5.36)$$

$$= \frac{2}{\mathcal{E}_z} \sum_{(ia)_I} \delta P_{(ia)_I} D_{x,(ia)_I}. \quad (5.37)$$

Again, the sum runs over all orbital transitions in all subsystems. In the last line we inserted the expression for $\delta\rho(\omega, \mathbf{r})$ according to Eqs. (5.2) and (5.3) obtained within the subsystem-TDDFT formalism and explicitly stated its frequency dependence. We have furthermore introduced the definition of the vector \mathbf{D}_x^s (the vectors \mathbf{D}_y^s and \mathbf{D}_z^s are defined correspondingly; the superscript s again indicates their subsystem block-structure), which contains matrix elements of the electric dipole operator $\hat{\boldsymbol{\mu}}$,

$$D_{x,(ia)_I} = (\mathbf{D}_x^s)_{(ia)_I} = \langle \phi_{i_I} | \hat{\mu}_x | \phi_{a_I} \rangle = -e \langle \phi_{i_I} | r_x | \phi_{a_I} \rangle. \quad (5.38)$$

In Section 3.2.2 it was shown that a formal solution for the perturbed density matrix is,

$$\delta \mathbf{P} = \mathbf{S}^{-1/2} [\omega^2 - \boldsymbol{\Omega}]^{-1} \mathbf{S}^{-1/2} \delta \mathbf{v}^{\text{ext}}, \quad (5.39)$$

and a corresponding expression can be obtained for the subsystem-TDDFT case from Eq. (5.14),

$$\delta \mathbf{P}^s = (\mathbf{S}^s)^{-1/2} [\omega^2 - \boldsymbol{\Omega}^s]^{-1} (\mathbf{S}^s)^{-1/2} \delta \mathbf{v}^{\text{ext},s}, \quad (5.40)$$

where the vector $\delta \mathbf{P}^s$ contains blocks $\delta \mathbf{P}_I$ with elements $\delta P_{(ia)_I}$ for every subsystem I , and a corresponding definition holds for the diagonal matrix \mathbf{S}^s , which contains elements,

$$S_{(ia)_I, (jb)_J} = (\mathbf{S}^s)_{(ia)_I, (jb)_J} = \frac{1}{(\epsilon_{b_J} - \epsilon_{j_J})} \delta_{(ia)_I} \delta_{(jb)_J}. \quad (5.41)$$

The differences to the conventional TDDFT response formalism are that (i) each of the matrices/vectors in this equation has a subsystem structure, thus offering new algorithmic ways and approximations for the solution (see Section 5.2.5), and that (ii) the response kernel differs as explained in Section 5.1.1.

The vector $\delta\mathbf{v}^{\text{ext},s}$ is, for an electric field in z -direction, given as

$$\delta\mathbf{v}^{\text{ext},s} = \mathcal{E}_z \mathbf{D}_z^s, \quad (5.42)$$

With Eqs. (5.42) and (5.39), we can thus rewrite Eq. (5.37) as (in analogy to the supermolecular TDDFT expression [220]),

$$\alpha_{xz}(\omega) = 2 \sum_{(ia)_I} \sum_{(jb)_J} \left\{ (\mathbf{S}^s)^{-1/2} [\mathbf{\Omega}^s - \omega^2 \mathbf{1}]^{-1} (\mathbf{S}^s)^{-1/2} \right\}_{(ia)_I, (jb)_J} D_{z, (jb)_J} D_{x, (ia)_I} \quad (5.43)$$

By using the spectral representation [220],

$$[\mathbf{\Omega}^s - \omega^2 \mathbf{1}]^{-1} = \sum_{\nu} \frac{\mathbf{F}_{\nu}^s \mathbf{F}_{\nu}^{s,\dagger}}{\omega_{\nu}^2 - \omega^2}, \quad (5.44)$$

where ω_{ν}^2 and \mathbf{F}_{ν}^s are the eigenvalues and eigenvectors of matrix $\mathbf{\Omega}^s$, see Eq. (5.15), we obtain,

$$\alpha_{xz}(\omega) = 2 \sum_{\nu} \frac{1}{\omega_{\nu}^2 - \omega^2} \mathbf{D}_x^{s,\dagger} (\mathbf{S}^s)^{-1/2} \mathbf{F}_{\nu}^s \mathbf{F}_{\nu}^{s,\dagger} (\mathbf{S}^s)^{-1/2} \mathbf{D}_z^s \quad (5.45)$$

$$= 2 \sum_{\nu} \frac{1}{\omega_{\nu}^2 - \omega^2} (\mathbf{D}_x^{s,\dagger} (\mathbf{S}^s)^{-1/2} \mathbf{F}_{\nu}^s) (\mathbf{D}_z^{s,\dagger} (\mathbf{S}^s)^{-1/2} \mathbf{F}_{\nu}^s)^{\dagger}. \quad (5.46)$$

5.2.2 Oscillator strengths

If we compare Eq. (5.46) to the sum-over-states expression of the polarizability in terms of wavefunctions and total energies (see, e.g., Refs. [220, 227]),

$$\alpha_{xz}(\omega) = 2 \sum_{\nu} \frac{\omega_{\nu}}{\omega_{\nu}^2 - \omega^2} \langle \Psi_0 | \hat{\mu}_x | \Psi_{\nu} \rangle \langle \Psi_{\nu} | \hat{\mu}_z | \Psi_0 \rangle, \quad (5.47)$$

we see that, just like in conventional TDDFT,

$$(\mathbf{D}_x^{s,\dagger} (\mathbf{S}^s)^{-1/2} \mathbf{F}_{\nu}^s) = \sqrt{\omega_{\nu}} \langle \Psi_0 | \hat{\mu}_x | \Psi_{\nu} \rangle, \quad (5.48)$$

so that the transition dipole moment is given as

$$\langle \Psi_0 | \hat{\mu}_x | \Psi_{\nu} \rangle = \frac{1}{\sqrt{\omega_{\nu}}} (\mathbf{D}_x^{s,\dagger} (\mathbf{S}^s)^{-1/2} \mathbf{F}_{\nu}^s) \quad (5.49)$$

$$= \sum_{(ia)_J} \langle \phi_{i_J} | \hat{\mu}_x | \phi_{a_J} \rangle \sqrt{\frac{(\epsilon_{a_J} - \epsilon_{i_J})}{\omega_{\nu}}} F_{\nu, (ia)_J}. \quad (5.50)$$

Oscillator strengths can be obtained as [220, 227, p. 510],

$$f_{\nu} = \frac{2}{3} \omega_{\nu} |\langle \Psi_0 | \hat{\boldsymbol{\mu}} | \Psi_{\nu} \rangle|^2 \quad (5.51)$$

$$= \frac{2}{3} (|\mathbf{D}_x^{s,\dagger} (\mathbf{S}^s)^{-1/2} \mathbf{F}_{\nu}^s|^2 + |\mathbf{D}_y^{s,\dagger} (\mathbf{S}^s)^{-1/2} \mathbf{F}_{\nu}^s|^2 + |\mathbf{D}_z^{s,\dagger} (\mathbf{S}^s)^{-1/2} \mathbf{F}_{\nu}^s|^2) \quad (5.52)$$

5.2.3 Optical rotation

The optical rotation parameter $\bar{\beta}$, which is the isotropic part (the trace divided by 3) of the corresponding optical rotation tensor β , has the form [407, 408],

$$\bar{\beta} = \frac{2}{3} \sum_{\nu} \frac{\text{Im}(\boldsymbol{\mu}_{0\nu} \cdot \mathbf{m}_{\nu 0})}{\omega_{\nu}^2 - \omega^2} = \frac{2c}{3} \sum_{\nu} \frac{R_{\nu}}{\omega_{\nu}^2 - \omega^2}, \quad (5.53)$$

where c is the speed of light, ω is the angular frequency of the external electromagnetic field, and ω_{ν} is the excitation energy from the ground state to state ν , and the rotational strengths R_{ν} are given as,

$$R_{\nu} = \text{Im}(\langle \Psi_0 | \hat{\boldsymbol{\mu}} | \Psi_{\nu} \rangle \cdot \langle \Psi_{\nu} | \hat{\mathbf{m}} | \Psi_0 \rangle) = \text{Im}(\boldsymbol{\mu}_{0\nu} \cdot \mathbf{m}_{\nu 0}), \quad (5.54)$$

where $\hat{\boldsymbol{\mu}}$ and $\hat{\mathbf{m}}$ are the electric and magnetic dipole operator, respectively. The form of the latter for a system of electrons is [409, p. 70],

$$\hat{\mathbf{m}} = - \sum_i \frac{e}{2m_i} \mathbf{r}_i \times \mathbf{p}_i = - \sum_i \frac{\mu_B}{\hbar} \mathbf{r}_i \times \mathbf{p}_i, \quad (5.55)$$

where μ_B is the Bohr magneton. In atomic units, this simplifies to,

$$\hat{\mathbf{m}} = - \sum_i \frac{1}{2} \mathbf{r}_i \times \mathbf{p}_i. \quad (5.56)$$

The tensor β can be obtained either by considering the effect of an electric perturbation on the magnetic dipole moment, or by considering the effect of a magnetic perturbation on the electric dipole moment of the molecule [407, p. 703]. Magnetic moments and perturbations cannot be represented in terms of the electron density alone. It was, however, proposed that β can be obtained from the perturbed *density matrix* of the Kohn–Sham system based on the argument that the latter not only reproduces the correct density of the interacting system, but also its current density [228]. In the case of subsystem density functional theory, this invokes the additional assumption that the total current density can be decomposed into subsystem contributions as well. This assumption was applied before in the study of nuclear magnetic resonance shieldings [335]. The xz component of the optical rotation tensor can then be obtained as [408],

$$\beta_{xz} = \frac{2}{\mathcal{E}_z} \text{Im}(\mathbf{M}_x^{s,\dagger} \mathbf{S}^s \delta \mathbf{P}^s) \quad (5.57)$$

$$= 2 \text{Im} \left(\mathbf{M}_x^{s,\dagger} \mathbf{S}^s (\mathbf{S}^s)^{-1/2} [\boldsymbol{\Omega}^s - \omega^2]^{-1} (\mathbf{S}^s)^{-1/2} \mathbf{D}_z^s \right) \quad (5.58)$$

$$= 2 \text{Im} \left(\mathbf{M}_x^{s,\dagger} (\mathbf{S}^s)^{1/2} [\boldsymbol{\Omega}^s - \omega^2]^{-1} (\mathbf{S}^s)^{-1/2} \mathbf{D}_z^s \right) \quad (5.59)$$

where the elements of the vector \mathbf{M}_x^s are defined in analogy to \mathbf{D}_x^s as matrix elements of the magnetic dipole moment operator,

$$M_{x,(ia)_I} = (\mathbf{M}_x^s)_{(ia)_I} = \langle \phi_{i_I} | \hat{\mathbf{m}}_x | \phi_{a_I} \rangle. \quad (5.60)$$

In Eq. (5.57), we have again used Eqs. (5.39) and (5.42). This shows that we can immediately calculate β once the electric-field induced perturbation of the density matrix

and the magnetic dipole integrals are available. Of course, it would also be possible to calculate β from $\delta\mathbf{P}^s$ determined for a magnetic perturbation, which in theory should lead to the same results [407, 408]. In practice, differences of the order of 1 % have been reported [410].

5.2.4 Rotational strengths

Expressions for the magnetic dipole transition moments and the rotational strengths can again be deduced by using the spectral representation of $[\mathbf{\Omega}^s - \omega^2]^{-1}$ (see also Refs. [411, 411] for the supermolecular case),

$$\beta_{xz} = 2\text{Im} \left[\sum_{\nu} \frac{1}{\omega_{\nu}^2 - \omega^2} (\mathbf{M}_x^{s,\dagger} (\mathbf{S}^s)^{+1/2} \mathbf{F}_{\nu}^s) (\mathbf{D}_z^{s,\dagger} (\mathbf{S}^s)^{-1/2} \mathbf{F}_{\nu}^s)^{\dagger} \right]. \quad (5.61)$$

From Eq. (5.61) we can identify the components of the magnetic transition dipole moment, $\mathbf{m}_{0\nu}$ by comparison with the sum-over-states expression in Eq. (5.53) and the form of the electric transition dipole moment from Eq. (5.49),

$$m_{x,0\nu} = -\omega_{\nu}^{1/2} \mathbf{M}_x^{s,\dagger} (\mathbf{S}^s)^{1/2} \mathbf{F}_{\nu}^s \quad (5.62)$$

$$= - \sum_{(ia)_J} \sqrt{\frac{\omega_{\nu}}{\epsilon_{a,J} - \epsilon_{i,J}}} M_{x,(ai)_J} F_{\nu,(ia)_J} \quad (5.63)$$

$$= \sum_{(ia)_J} \sqrt{\frac{\omega_{\nu}}{\epsilon_{a,J} - \epsilon_{i,J}}} M_{x,(ia)_J} F_{\nu,(ia)_J}. \quad (5.64)$$

In the last line we have used the fact that $M_{x,(ai)_J} = -M_{x,(ia)_J}$. Rotational strengths can then be obtained by inserting Eqs. (5.64) and (5.49) into Eq. (5.54).

5.2.5 Subsystem decomposition of polarizability and optical rotation

In order to calculate the polarizability according to Eq. (5.37), we need the occupied–virtual matrix elements of the electric dipole moment operator and the elements of the perturbed density matrix, $\delta P_{(ia)_I}$. The calculation of the former does not present a problem, whereas the latter quantities require the solution of the large linear system given in Eq. (5.39). This problem is typically tackled by iteratively solving the equation

$$\underbrace{(\mathbf{S}^s)^{1/2} [\omega^2 - \mathbf{\Omega}^s] (\mathbf{S}^s)^{1/2}}_{\mathbf{G}} \delta\mathbf{P}^s = \mathbf{G} \delta\mathbf{P}^s = \delta\mathbf{v}^{\text{ext},s}, \quad (5.65)$$

since the matrix \mathbf{G} is usually too large to be inverted directly. This corresponds to the approach used by Feyereisen *et al.* in the context of Hartree–Fock theory [233]. A similar approach starts by combining the Eqs. (5.14) for all occupied–virtual pairs $(jb)_J$ in a matrix–vector equation [412],

$$\delta\mathbf{P}^s = \chi^s [\delta\mathbf{v}^{\text{ext},s} + 2\mathbf{K}^{\text{eff}} \delta\mathbf{P}^s], \quad (5.66)$$

where χ^s is a diagonal matrix with elements,

$$\chi_{(ia)_I, (ia)_I}^s(\omega) = \frac{\omega_{(ia)_I}}{\omega_{(ia)_I}^2 - \omega^2}. \quad (5.67)$$

For the solution, a guess for $\delta\mathbf{P}^s$ is constructed by neglecting $\delta\mathbf{P}^s$ on the right-hand side of Eq. (5.66), from which the so-called uncoupled response of the density matrix is easily obtained as,

$$\delta\mathbf{P}^{s,(0)} = \chi^s \delta\mathbf{v}^{\text{ext},s}, \quad (5.68)$$

with elements,

$$\delta P_{(ia)_I}^{(0)} = \frac{\omega_{(ia)_I}}{\omega^2 - \omega_{(ia)_I}^2} \delta v_{(ia)_I}^{\text{ext}}. \quad (5.69)$$

Then, $\delta P_{(ia)_I}^{(0)}$ can be inserted into the right-hand-side of Eq. (5.66) to determine the next approximation $\delta P_{(ia)_I}^{(1)}$ and so forth until self-consistence is achieved.

At this point, we note explicitly again that all quantities in Eq. (5.66) exhibit a subsystem structure, so that we can write,

$$\begin{pmatrix} \delta\mathbf{P}_A \\ \delta\mathbf{P}_B \\ \vdots \\ \delta\mathbf{P}_Z \end{pmatrix} = \begin{pmatrix} \chi_A^s & \mathbf{0} & \cdots & \mathbf{0} \\ \mathbf{0} & \chi_B^s & \cdots & \mathbf{0} \\ \mathbf{0} & \mathbf{0} & \ddots & \vdots \\ \mathbf{0} & \mathbf{0} & \cdots & \chi_Z^s \end{pmatrix} \left[\begin{pmatrix} \delta\mathbf{v}_A^{\text{ext}} \\ \delta\mathbf{v}_B^{\text{ext}} \\ \vdots \\ \delta\mathbf{v}_Z^{\text{ext}} \end{pmatrix} + \begin{pmatrix} \mathbf{K}_{AA}^{\text{eff}} & \mathbf{K}_{AB}^{\text{eff}} & \cdots & \mathbf{K}_{AZ}^{\text{eff}} \\ \mathbf{K}_{BA}^{\text{eff}} & \mathbf{K}_{BB}^{\text{eff}} & \cdots & \mathbf{K}_{BZ}^{\text{eff}} \\ \vdots & \vdots & \ddots & \vdots \\ \mathbf{K}_{ZA}^{\text{eff}} & \mathbf{K}_{ZB}^{\text{eff}} & \cdots & \mathbf{K}_{ZZ}^{\text{eff}} \end{pmatrix} \begin{pmatrix} \delta\mathbf{P}_A \\ \delta\mathbf{P}_B \\ \vdots \\ \delta\mathbf{P}_Z \end{pmatrix} \right] \quad (5.70)$$

The solution of this system of equations for the density response seems not much simpler than in a conventional TDDFT calculation. The main simplification up to this point is that no inter-subsystem orbital transitions are included into the equation. If we assume a system composed of N identical subsystems with n_{occ} and n_{virt} occupied and virtual, respectively, orbitals per subsystem in a given one-particle basis set, then the dimension of the vector $\delta\mathbf{P}$ is $(n_{\text{occ}} \cdot N) \times (n_{\text{virt}} \cdot N)$ in the supermolecular case, whereas the dimension of $\delta\mathbf{P}^s$ is $(n_{\text{occ}} \cdot n_{\text{virt}}) \times N$ in the subsystem approach. Another big advantage of the subsystem approach is, however, that the density response of any subsystem I can be obtained as,

$$\delta\mathbf{P}_I = \chi_I^s \left[\delta\mathbf{v}_I^{\text{ext}} + 2 \sum_J \mathbf{K}_{IJ}^{\text{eff}} \delta\mathbf{P}_J \right], \quad (5.71)$$

which we can split up into,

$$\delta\mathbf{P}_I = \chi_I^s \left[\delta\mathbf{v}_I^{\text{ext}} + 2\mathbf{K}_{II}^{\text{eff}} \delta\mathbf{P}_I + 2 \sum_{J, J \neq I} \mathbf{K}_{IJ}^{\text{eff}} \delta\mathbf{P}_J \right]. \quad (5.72)$$

The coefficients of the perturbed density matrix of subsystem I can thus be partitioned into three parts: (i) a part due to the external perturbation, (ii) a part due to the change in the potential induced by the density change within the same subsystem, and (iii) a part due to the change in the potential induced by the density change in all other subsystems.

A first approximation to the perturbed density matrix for subsystem I can be obtained from a self-consistent solution of,

$$\delta\mathbf{P}_I^{(1)} = \chi_I^s \left[\delta\mathbf{v}_I^{\text{ext}} + 2\mathbf{K}_{II}^{\text{eff}}\delta\mathbf{P}_I^{(1)} \right], \quad (5.73)$$

i.e., by neglecting any inter-subsystem response couplings. Within the framework of excitation energies presented in Section 5.1, this approximation led to the “uncoupled frozen-density embedding” (FDEu) approximation. In the context of polarizabilities and response densities, the term “uncoupled” is already reserved for the (much more drastic) approximation $\delta\mathbf{P}_I^{(0)}$ in Eq. (5.69). Therefore, we will use the term “local response approximation” for Eq. (5.73). Eq. (5.73) was suggested for the calculation of polarizabilities of an embedded molecule within the FDE framework before [41]. Results calculated for water in water within the local response approximation were published in Ref. [185]. In comparison to a polarizable classical force field model for the environment, it was observed in that study that the changes in the polarizability from isolated water to the embedded water changed into the wrong direction if described by FDE. For static polarizabilities, this failure could be remedied by employing finite-field techniques [185]. A fully self-consistent solution of Eq. (5.72) can be obtained by first calculating $\delta\mathbf{P}_I^{(1)}$ for each subsystem and then iteratively solving,

$$\delta\mathbf{P}_I^{(n+1)} = \chi_I^s \left[\delta\mathbf{v}_I^{\text{ext}} + 2\mathbf{K}_{II}^{\text{eff}}\delta\mathbf{P}_I^{(n+1)} + 2 \sum_{J, J \neq I} \mathbf{K}_{IJ}^{\text{eff}}\delta\mathbf{P}_J^{(n)} \right] \quad (5.74)$$

$$= \chi_I^s \left[\delta\mathbf{v}_I^{\text{ext}} + \delta\mathbf{v}_I^{\text{inter},(n)} + 2\mathbf{K}_{II}^{\text{eff}}\delta\mathbf{P}_I^{(n+1)} \right], \quad (5.75)$$

where,

$$\delta\mathbf{v}_I^{\text{inter},(n)} = 2 \sum_{J, J \neq I} \mathbf{K}_{IJ}^{\text{eff}}\delta\mathbf{P}_J^{(n)}, \quad (5.76)$$

is the inter-subsystem contribution to the matrix elements of the potential induced by the density perturbation in iteration n . Note that in each macro-iteration, i.e., in each step from n to $n+1$ in the solution of Eq. (5.75), the perturbed density matrix for every subsystem has to be determined self-consistently according to Eq. (5.75) in a series of micro-iterations, before one can switch to the next macro-iteration.

The computational effort for one macro-iteration per subsystem is comparable to that of a conventional polarizability calculation of that subsystem. Our implementation in a development version of ADF makes use of Pulay’s direct inversion in the iterative subspace (DIIS) algorithm [413–415] in order to improve the overall convergence behavior

of each macro-iteration, i.e., in order to keep the number of micro-iterations per macro-iteration small. In addition, it turned out that oscillations in the responses of different subsystems may sometimes hamper the convergence, so that too many macroiterations would be required to converge the density response. This could be avoided by introducing a second layer of DIIS convergence acceleration for subsequent macro-iterations.

Ground-state frozen-density embedding can typically be performed in two different ways as was mentioned in the previous chapters at several points. The first is a fully self-consistent way, in which several freeze-and-thaw cycles are performed, so that the properties under study are converged. In the more approximate yet also more efficient second way, we try to find a simple approximation for the electron density of the environment and then only optimize the electron density of an active subsystem in the presence of the frozen environmental density. Both strategies can also be applied for the response. The fully self-consistent approach for the calculation of polarizabilities was already outlined above. The “pure embedding” approach would require that an approximation for the response of the other subsystems ($\delta\mathbf{P}_J$) is available, which is kept frozen during the entire calculation. Then, one can obtain an approximation for the “embedded” density response of the active system, e.g., system A , as follows,

$$\delta\mathbf{P}_A^{\text{emb}} = \chi_A^s \left[\delta\mathbf{v}_A^{\text{ext}} + 2\mathbf{K}_{AA}^{\text{eff}} \delta\mathbf{P}_A^{\text{emb}} + 2 \sum_{J, J \neq A} \mathbf{K}_{AJ}^{\text{eff}} \delta\mathbf{P}_J^{\text{approx}} \right]. \quad (5.77)$$

Although such an approximation would not be fully self-consistent, we can still expect that it allows to capture polarization effects due to the environmental response in a qualitatively correct way. The computational cost in this approximation is reduced to $N + 1$ response calculations for one of the subsystems, where N is the number of subsystems. Note that one way to perform the subsystem response formalism in embedding mode is to construct the approximate density perturbation from the local response approximation in Eq. (5.73), i.e., to stop the iterative solution of Eq. (5.75) after $\delta\mathbf{P}_A^{(2)}$ has been calculated.

In the end, one would obtain a subsystem-polarizability for each fragment according to,

$$\alpha_{xz}^I(\omega) = \frac{2}{\mathcal{E}_z} \sum_{(ia) \in I} \delta P_{(ia)_I} D_{x,(ia)_I} \quad (5.78)$$

$$= 2 \sum_{(ia) \in I} \sum_{(jb) \in J} \left\{ (\mathbf{S}^s)^{-1/2} [\boldsymbol{\Omega}^s - \omega^2 \mathbf{1}]^{-1} (\mathbf{S}^s)^{-1/2} \right\}_{(ia)_I, (jb)_J} D_{z,(jb)_J} D_{x,(ia)_I}, \quad (5.79)$$

Note that in contrast to Eq. (5.37) the first sum in both lines in the above equation is only over all occupied–virtual pairs within subsystem I , and not over all pairs and all subsystems as in the second sum, which includes the reaction of the response in system A to that of all other subsystems. The total polarizability of the system is then conveniently given as a sum of all subsystem polarizabilities,

$$\alpha_{xz}(\omega) = \sum_I \alpha_{xz}^I(\omega). \quad (5.80)$$

In a similar way, the components of the optical rotation tensor β can be decomposed into subsystem contributions, e.g.,

$$\beta_{xz}^I = \frac{2}{\mathcal{E}_z} \sum_{(ia) \in I} \text{Im} (M_{x,(ai)_I} S_{(ia)_I,(ia)_I} \delta P_{(ia)_I}) \quad (5.81)$$

$$= 2 \sum_{(ia) \in I} \sum_{(jb) \in J} \text{Im} \left(\left\{ (\mathbf{S}^s)^{1/2} [\mathbf{\Omega}^s - \omega^2]^{-1} (\mathbf{S}^s)^{-1/2} \right\}_{(ia)_I,(jb)_J} D_{z,(jb)_J} M_{x,(ai)_I} \right), \quad (5.82)$$

so that,

$$\beta_{xz}(\omega) = \sum_I \beta_{xz}^I(\omega). \quad (5.83)$$

This allows to calculate the response tensors for each subsystem individually, eventually using different types of approximations for different subsystems, so that the change in the response due to an environment can be obtained. Moreover, the overall response of the supersystem can conveniently be obtained as a sum of the subsystem contributions.

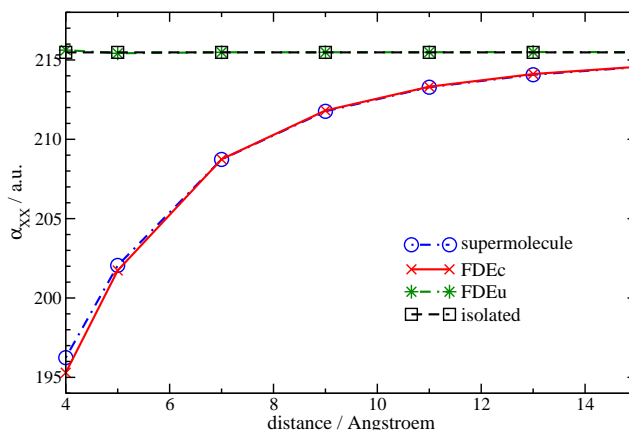
5.2.6 Illustrative calculations

As an example for the investigation of effects due to a coupled response, we study a system of two benzaldehyde molecules that are parallel displaced in z -direction by distances varying between 5 and 15 Å (see Figure 5.1). This example has already been studied in Section 5.1.4, where large excitonic couplings for the low-lying excited states were observed. It should thus serve as an ideal example of a system in which the coupled response becomes very important.

Figure 5.7 shows the distance dependence of the component α_{xx} obtained from the local response approximation (FDEu), the coupled subsystem approach (FDEc), and from a supermolecular Kohn–Sham calculation. All calculations were carried out with the BP86 functional and the large QZ4P basis set in the static limit. For the non-additive kinetic energy component of the embedding potential, the PW91k functional in the LC94 parameterization was employed. For comparison, we also give the sum of the xx -polarizability components for the two isolated monomers, which is, of course, distance-independent. The FDEu approach is clearly not suited to describe the change in the polarizability caused by a second benzaldehyde molecule. Even at rather small distances, the results hardly differ from the isolated molecule calculations, and the tiny difference that can be observed increases the total polarizability. The supermolecular approach, on the other hand, shows a significant decrease of about 15 a.u. (7 %) with respect to two isolated benzaldehyde molecules. This effect is very nicely reproduced by the coupled subsystem approach. The deviations between the FDEc and supermolecular values are 0.95 a.u. for a distance of 5 Å and decrease to 0.02 a.u. for a distance of 15 Å.

It should be noted that the agreement is slightly worse, though still qualitatively correct, if a smaller TZP basis set is employed. In that case it seems that the supermolecular

Figure 5.7: Results for the xx component of the polarizability of the benzaldehyde dimer shown in Figure 5.1 for varying distance obtained with BP86/QZ4P from local response (FDEu) and coupled subsystem approaches (FDEc) as well as from conventional supermolecular Kohn–Sham calculations (super). For comparison, also the data for two isolated benzaldehyde molecules are shown (iso).



calculation suffers from a basis set superposition-type error for the polarizability, which leads to a worse agreement at intermediate distances.

As far as optical rotation calculations are concerned, we have so far implemented only the dipole-length form of the electric transition dipole moment. The calculations are thus subject to a gauge origin dependence. It has recently been noted that the individual components of the electric dipole–magnetic dipole tensor are not gauge invariant [416–420] even in an exact theory unless contributions from the electric quadrupole tensor are taken into account. In order to minimize gauge origin effects, we again employ the very large QZ4P basis set. A benchmark calculation was carried out for the C_2 -symmetric dimer from Figure 5.5.² The optical rotation was calculated for a wavelength of 589.5932 nm, corresponding to the longer of the two wavelengths associated with the sodium D-line [421]. It should be noted that for this comparison between supermolecular and FDE results the gauge origin problem can be ignored, since it will affect both calculations in the same way. Nevertheless, the extent to which the results are affected by the gauge problem can be assessed by the calculation of the optical rotation for the isolated molecules. The isotropic optical rotation should be zero for these planar molecules. A BP86/TZP calculation resulted in an isotropic value of $\beta = 0.82$ a.u. for the sum of the two isolated molecules, which decreased to less than 0.01 with the QZ4P basis set, thus showing that gauge origin problems are not severe with the large basis.

The results for the optical rotation tensor β and its isotropic value $\bar{\beta}$ are listed in Table 5.3. It can be recognized that already the local-response version of the subsystem TDDFT approach (FDEu) leads to a change in the components of β , but this change is

²The orientation of the dimer was chosen as follows: The origin was located in the center of mass of the supermolecule. Each of the monomers was placed in plane parallel to the xy -plane, but shifted by ± 2.5 Å. The two C=O groups form a rectangle lying parallel to the xz -plane at $y = -1.707$ Å.

Table 5.3: Components of the optical rotation tensor β and its isotropic value $\bar{\beta}$ (BP86/TZP, in units of a.u.) calculated as a sum of isolated molecule contributions (iso), from FDEu, FDEc, and from a supermolecular calculation (super).

	iso	FDEu	FDEc	super
β_{xx}	76.93	77.48	80.58	80.67
β_{yy}	-76.92	-77.82	-75.17	-75.20
β_{zz}	0.00	0.53	-1.52	-1.73
β_{xy}	0.00	-0.01	-0.01	0.02
β_{xz}	37.71	37.36	37.68	37.82
β_{yz}	0.00	0.00	0.00	-0.07
β_{yx}	0.00	0.00	0.00	-0.06
β_{zx}	12.33	13.61	10.64	10.60
β_{zy}	0.00	-0.01	-0.01	-0.07
$\bar{\beta}$	0.00	0.06	1.29	1.25

not always in the direction expected from the supermolecular calculation. E.g., the zx -component increases from 12.33 to 13.61 a.u. when the ground-state interaction between the monomers is switched on. However, the supermolecular calculations yields a value of 10.60 a.u., so that there is a discrepancy of -3.01 a.u. in total. The FDEc approach corrects the FDEu value by -2.97 a.u., thus leading to a very good agreement with the supermolecular result. Also for the other components of β , the deviations between FDEc and the supermolecular results are small, with a maximum of 0.21 obtained for β_{zz} . The deviation in the isotropic value $\bar{\beta}$ is < 0.05 a.u. and thus of the order of 4 %. This underlines the reliability of the subsystem TDDFT approach for optical rotation calculations, in contrast to its FDEu approximation. The latter results in a optical rotation of 0.06 a.u. compared to 1.25 a.u. in the reference calculation, and is thus not appropriate for systems with pronounced coupled response.

5.3 Studying natural light-harvesting complexes with subsystem TDDFT

Light-harvesting complexes accomplish the first two of the essential steps in photosynthesis: They are responsible for the absorption of light and the transport of the excitation energy to the photosynthetic reaction center, where the subsequent steps, i.e., charge separation and chemical storage of the energy, take place [422–424]. A key step towards the understanding of the processes in light-harvesting complexes on a molecular level was the crystal structure determination of the integral membrane light-harvesting complexes from purple bacteria (for reviews see Ref. [425, 426]), e.g., from *Rhodospseudomonas molischanum* [427] and from *Rhodospseudomonas acidophila* [428–430].

In the present study, we will concentrate on the light-harvesting complex 2 (LH2) of the latter bacteria, for which extensive studies of pigment properties and excitation energy transfer processes have been conducted [403, 431–439]. To investigate the energy

transfer pathways in light-harvesting systems, it is necessary to calculate the excitation energy couplings between the individual chromophores [402, 440, 441]. In principle this information should be accessible from a quantum chemical calculation of the excited states of the entire light-harvesting system, but there are two basic problems. The first is the size of the antenna systems, which is — depending on the particular model chosen — in the order of several thousands to ten thousands of atoms. The second is the fact that this type of analysis necessarily requires a picture in which the excited states of the pigment complex are expressed in terms of local excited states of the individual chromophores. A quantum-chemical calculation, however, would typically result in a delocalized picture, which prohibits (or at least severely complicates) the extraction of such coupling constants.

For these two reasons, the investigation of excitonic couplings in antenna systems is usually carried out by calculating excited states of individual, isolated chromophores. Subsequently, the coupling constants are determined by calculating the interaction matrix elements between the excited states of the monomers, which effectively corresponds to an interaction of the transition densities of the isolated monomers. With these coupling matrix elements, an effective Hamiltonian matrix can be set up from which energy levels of the light-harvesting system can be extracted upon diagonalization [401].

The EET couplings relevant for these phenomena are often described in terms of Förster (Coulomb) [442] and Dexter (exchange) couplings [443] of non-interacting subunits. Several studies on these effects have been carried out during the past years, which highlight the effect of approximations introduced for the Coulomb coupling as well as short-range effects of general orbital penetration and charge-transfer type [401, 404, 436, 440, 444]. Among the methods which are most often used to approximate the Coulomb couplings are multipole expansions, e.g., the Förster-type dipole–dipole coupling [442], transition monopole interactions in terms of atomic partial transition charges [445, 446], or a real-space partitioning of the transition densities and a subsequent numerical integration of the Coulombic interactions as in the transition density cube method [435]. For a comparison of some of these approaches see Ref. [404]. More recently, density-functional and configuration-interaction type methods based on an exciton-like interaction between two local electronic transitions on isolated pigments have been suggested, which may also incorporate the effect of a dielectric medium on the coupling [398–400, 447].

In view of the structure of the light-harvesting complex, which clearly contains specific interactions between the chromophores and their environment, e.g., the apoproteins surrounding the pigments [448], it appears desirable to be able to study the electronic excitations of the antenna system including such interactions by an atomistic, quantum chemical model. The subsystem TDDFT formalism developed in Section 5.1 offers the possibility to tackle such problems.

Therefore, we are going to test the ability of this subsystem approach for the description of specific pigment–environment and excitation energy transfer interactions in the following. After a brief summary of the structural features of LH2 in Section 5.3.1, Section 5.3.2 explains how the coupling matrix elements obtained in the TDDFT treatment can be related to the phenomenological coupling constants used in model theories of EET. Subsequently, specific pigment–environment interactions on local excitations and couplings arising from interactions of excitations in different subsystems are investigated

in Section 5.3.4, before the calculated absorption spectra are presented in Section 5.3.5. Technical details of the calculations are given in Appendix B.

5.3.1 The structure of LH2

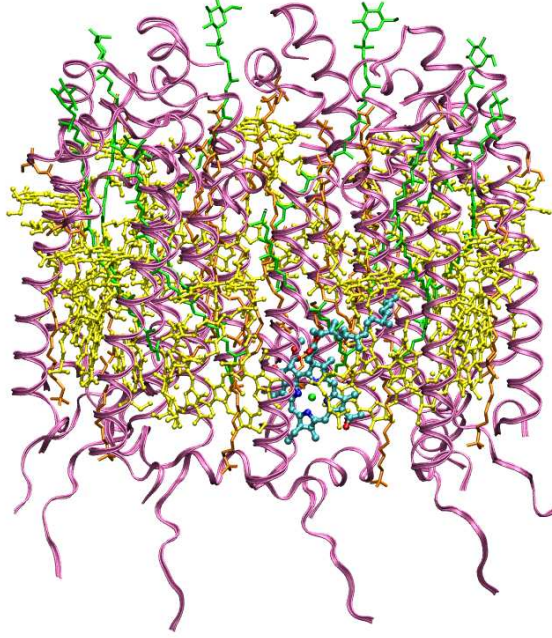
The structure of LH2 from *Rhodopseudomonas acidophila* has been described in detail before [428–430], so that only a brief summary of the most important features relevant for the present study will be given here. A crystal structure obtained at 2.0 Å resolution, which was reported in Ref. [429], showed that this antenna system has — within the experimental accuracy — C_9 symmetry. The structure is shown in Figure 5.8. It contains nine bacteriochlorophyll *a* (Bchl *a*) molecules forming a ring in such a way that the planes of the macrocycles are aligned parallel to the membrane. This set of Bchl *a* molecules is called the B800 system, since its absorption maximum is at a wavelength of 800 nm. Additionally, there is a second ring of 18 Bchl *a* molecules forming the so-called B850 system, in which the macrocycle planes are perpendicular to the membrane. These Bchl *a* molecules occur in pairs of so-called α and β B850 molecules. The Mg–Mg-distance in B800 is 21.2 Å, the distances in B850 are 9.0 Å within an (α , β)-dimer and 9.5 Å between different dimers. There is an inner ring of so-called α -apoproteins, and an outer ring of β -apoproteins. The Mg atoms in B800 interact with an oxygen atom from the COO^- -modified α -Met1 residue, while the Mg atoms in B850 ligate nitrogen atoms from α -His31 or β -His30 residues, respectively. These interactions may lead to shifts in the absorption properties of the Bchl *a* molecules, although this effect is typically small [437]. The CIS calculations in Ref. [403] showed that a red-shift of about 0.02 eV results from the His residues, although this calculation was carried out with a very small basis set (3-21G*). Additionally, the residues α -Trp45 and α -Tyr44 can form hydrogen bonds to the ring I acetyl groups of α B850 and β B850, respectively. In Ref. [437] it was reported that this causes a measurable red-shift in the absorption spectra of the light-harvesting complex. The B800 Bchl *a* molecules can form hydrogen bonds to the β -Arg20 residue, for which a significant red-shift was calculated in Ref. [433].

The asymmetric unit of the antenna system is called a protomer and consists of an α - and a β -apoprotein together with one B800 molecule and a B850 dimer as well as a carotenoid (rhodopin glucoside, RG1). In Ref. [429], part of the electron density was assigned to a second carotenoid, which was assumed to exhibit *cis*-double bonds in contrast to the all-*trans*-structure of RG1. In later work, this assignment was reversed [428].

In Sections 5.3.3 and 5.3.4, it will be demonstrated that a detailed understanding of the spectral features of the LH2 antenna system is possible on the basis of FDE calculations. We will concentrate on the interactions of the Bchl *a* pigments with their direct environment, as well as on EET coupling interactions between these chromophores, whereas the RG1 pigments are not explicitly taken into account in this study (see, e.g., Ref. [449] for an investigation on their role in excitation energy transfer processes).

5.3.2 Extracting excitonic coupling constants

The most important approximations introduced in Section 5.1 for the solution of the eigenvalue problem in Eq. (5.19) are (i) the restriction to subsets of excitations for the subsystems, which can be obtained as in conventional TDDFT calculations by means of a Davidson-type diagonalization, and additionally (ii) the use of density fitting techniques

Figure 5.8: Structure of LH2 of *Rhodopseudomonas acidophila*.

to calculate the potential induced by a transition density of a local excitation. To make the approach work for larger aggregates, some further improvements are introduced here, which make the calculation of the elements of $\tilde{\Omega}^s$ much more efficient without significant effect on the numerical accuracy.

The scheme presented in the following is implemented in a locally modified version of the ADF program package [277,278]. Most of the actual computational effort is spent on the integration of the matrix elements in Eq. (5.29), which can be written as

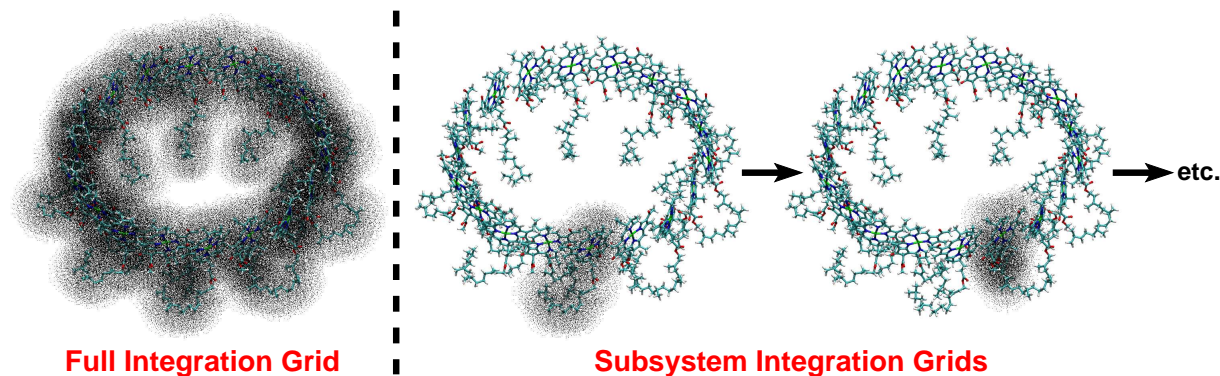
$$\tilde{\Omega}_{\mu_A \nu_B} = \int d^3 r_1 \sum_{(ia) \in A} 2U_{(ia)A\mu_A} \sqrt{\omega_{(ai)A}} \phi_{i_A}(\mathbf{r}_1) \delta v_{A,\nu_B}^{\text{ind}}(\mathbf{r}_1) \phi_{a_A}(\mathbf{r}_1), \quad (5.84)$$

where $\delta v_{A,\nu_B}^{\text{ind}}$ is the potential induced in subsystem A by transition ν located on subsystem B , which is calculated analytically from fitted transition densities. The matrix elements are determined in ADF by numerical integration, i.e.,

$$\tilde{\Omega}_{\mu_A \nu_B} \approx \sum_k w(\mathbf{r}_k) \sum_{(ia) \in A} 2U_{(ia)A\mu_A} \sqrt{\omega_{(ai)A}} \phi_{i_A}(\mathbf{r}_k) \delta v_{A,\nu_B}^{\text{ind}}(\mathbf{r}_k) \phi_{a_A}(\mathbf{r}_k), \quad (5.85)$$

where \mathbf{r}_k and $w(\mathbf{r}_k)$ are the coordinates and weights of the grid points, respectively. From this it becomes apparent that the coupling matrix elements for a certain column μ_A in the matrix $\tilde{\Omega}^s$ will only require an accurate integration grid in the region where the molecular orbitals (MOs) of system A are non-vanishing. Since the MOs are expanded in basis functions of the subsystem, the numerical grid must be accurate in regions where

Figure 5.9: Illustration of the subsystem grid technique for the calculation of coupling constants within the subsystem TDDFT approach.



the basis functions of the subsystem are non-vanishing. However, we usually have to calculate coupling matrix elements between electronic transitions of all the subsystems, and the numerical grid must be suited for all of them. This would correspond to the default grid construction used in ADF and would cover the entire supersystem for which the calculation is carried out.

For the subsystem-TDDFT approach used here we can significantly reduce the computational cost by using different subsystem grids for the coupling matrix elements involving different subsystems, so that the number of integration points per coupling matrix element is indeed small and independent of the size of the surrounding system (see Figure 5.9 for a schematic representation). Hence, the size of the integration grid can greatly be reduced without significant effect on the numerical integration accuracy. Since the computer time needed scales linearly with the number of integration points, this results in a substantial speed-up of the calculations. This was implemented in the subsystem-TDDFT module of a locally modified version of ADF. Note that also the recently presented ground-state FDE implementation in ADF, in which the densities of several subsystems can be optimized in one calculation, allows to use subsystem grids optimized for each particular subsystem [113].

It should be noted that the numerical integration is very well suited for parallelization, and full advantage of this is taken in the calculation of the coupling constants. Additionally, a pre-screening for the elements $U_{(ia)A\mu_A}$ of the subsystem-eigenvectors is carried out in order to reduce the number of occupied–virtual pairs that have to be taken into account in the summation, which also increases the speed of the calculation while allowing for full control over the numerical error introduced. In this way, an efficient calculation of the excitation energies and transition dipole moments is possible for systems that are composed of many subunits, even if the individual subunits are already comparatively large (> 100 atoms). Nevertheless, the limiting factor for the calculations is in general the size of the largest subsystem in the calculation.

Another feature that is used in ground-state FDE calculations is the superposition of subsystem densities in order to approximate the density of the full system [116]. In particular, it is possible to copy the density of a particular fragment to several positions

in space in case of identical subsystems [184]. This can also be applied for the present subsystem-TDDFT approach and has been extended so that also transition densities and (electric and magnetic) transition dipole moments can be used for multiple fragments. The cost for the preparation steps of the subsystem calculation is thus significantly reduced for systems in which several identical chromophores occur.

Coupling constants as used in phenomenological excitonic coupling schemes are usually calculated as matrix elements between local excited states. With these coupling matrix elements, a configuration-interaction-like matrix can be set up, and excited-state energies of the total system are found by diagonalization of that matrix (see, e.g., Ref. [450]). The matrix eigenvalue problem solved in the context of TDDFT in Eq. (3.51) is, however, somewhat different as it effectively involves coupling matrix elements between (energy-weighted) transition densities, and it yields squared excitation energies instead of excited-state energies. For better comparison with data from the literature, it is thus desirable to establish a relationship between the two different sets of coupling constants or to calculate CI-like coupling constants from the TDDFT data. This is possible as follows: Consider a pair of uncoupled excited states with energies $E_{a,b}$. In a CI-like case, the coupling between the two states, V_{ab} , will lead to new energy levels

$$E_{+,-} = \frac{E_a + E_b}{2} \pm \sqrt{\left(\frac{E_a - E_b}{2}\right)^2 + V_{ab}^2}. \quad (5.86)$$

The energy levels will, of course, change if couplings to other local excited states are included, although for (near-)degenerate states typically one single coupling is dominant. Nevertheless, this means that V_{ab}^2 can be obtained from the energies of the two-state problem as

$$V_{ab}^2 = \left(\frac{E_+ - E_-}{2}\right)^2 - \left(\frac{E_a - E_b}{2}\right)^2. \quad (5.87)$$

The energy differences can also be expressed in terms of excitation energy differences ω , which are the quantities occurring in the TDDFT context

$$V_{ab}^2 = \left(\frac{\omega_+ - \omega_-}{2}\right)^2 - \left(\frac{\omega_a - \omega_b}{2}\right)^2. \quad (5.88)$$

The excitation energies $\omega_{a,b}$ of the local (subsystem-) excitations are known in the calculation, and the coupled excitation energies $\omega_{+,-}$ can be obtained from the eigenvalues of the corresponding 2×2 subblock of the coupling matrix. They can also be expressed directly in terms of the coupling matrix elements $\tilde{\Omega}_{ab}$, leading to (cf. the structure of $\tilde{\Omega}^s$ in Section 5.1)

$$\omega_+ - \omega_- = \sqrt{\frac{\omega_a^2 + \omega_b^2}{2} + \sqrt{\left(\frac{\omega_a^2 - \omega_b^2}{2}\right)^2 + \tilde{\Omega}_{ab}^2}} - \sqrt{\frac{\omega_a^2 + \omega_b^2}{2} - \sqrt{\left(\frac{\omega_a^2 - \omega_b^2}{2}\right)^2 + \tilde{\Omega}_{ab}^2}}. \quad (5.89)$$

In combination with Eq. (5.88) this can be used to convert the TDDFT coupling matrix elements $\tilde{\Omega}_{ab}$ into CI-like excitonic coupling integrals V_{ab} . The information about the sign is taken from $\tilde{\Omega}_{ab}$, since only the relative signs of the matrix elements play a role,

which are the same for matrix elements between excited states or their corresponding transition densities. It should be noted that the relationship above only guarantees the same energy gaps between the two excited states, but not exactly the same excited-state energies. This is because the coupling in a CI context creates a symmetrical splitting of the energy around the mean value of the locally excited states, $(E_a + E_b)/2$, whereas the coupling in a TDDFT context induces a splitting that is symmetrical for the square of the excitation energy, ω^2 , around the mean value of the squared local excitation energies, $(\omega_a^2 + \omega_b^2)/2$. By diagonalizing the CI-like matrix constructed from such phenomenological coupling constants and the excitation energies it turns out, however, that the differences between the original TDDFT results and those from a CI-like treatment are usually very small (in the order of 0.001 eV).

It should be noted that the definition of the couplings on the basis of energy differences, i.e., following Eq. (5.86) is consistent with other DFT based approaches [399, 400], in particular for the case of identical monomer excitation energies, which is stated explicitly in Ref. [400]. Eqs. (5.88) and (5.89) implement this definition in the context of the FDEc scheme used here. A difference exists, however, in how the interactions between the monomers are taken into account (see also Section 5.1) The approaches proposed in Refs. [399, 400] evaluate the couplings starting from isolated monomers, whereas the method employed here is integrated into the FDE formalism, so that already the monomer properties and excitation energies are calculated in the presence of all other monomers included in the calculation. Thus, the starting point for the evaluation of the coupling constants are the (hypothetical) excitation energies of the monomers *in the aggregate* with excitonic coupling switched off. In a recent study based on the approaches in Refs. [399, 400], this effect was approximately taken into account by means of a set of point charges that were fitted to the other monomers' charge distributions [451] and was found to be rather small in that particular case. In contrast to such an approximate treatment, FDE can be regarded as a method that is in principle exact for the description of the ground-state interactions between different molecules (in the limit of exact functionals, see also Section 2.6.3 for the exact requirements), and its local response variant has proven to yield good results in many cases where the effect of such interactions on the absorption properties are dominant, see Chapter 4 and Refs. [116, 184, 185, 309]. Furthermore, the calculation of the interaction between the local excitations is carried out in a slightly different way compared to the other DFT-based schemes. Whereas Coulomb and exchange–correlation couplings are treated in formally the same way (although this may not hold for the approximation employed for the exchange–correlation kernel), overlap effects are treated differently. Within the FDE framework, the non-additive kinetic energy functional and its functional derivatives that enter the embedding potential and effective kernel should, in principle, take care of non-orthogonality effects, whereas an explicitly overlap-dependent term is included in the perturbative treatment of Ref. [400]. When comparing these effects it must be considered that already the subsystem orbitals and transition densities in the case of FDE are influenced by the kinetic-energy functional, and that only approximate kinetic-energy functionals can be applied. In practice, however, such effects are usually very small [229]. In Ref. [399], the overlap contribution to the coupling for the B_{1u} transition of the ethylene dimer was calculated explicitly and found to be roughly four orders of magnitude smaller than the Coulomb contribution and two orders of magnitude

smaller than the exchange–correlation contribution at the rather short intermolecular distance of 4 Å. An additional short-range effect that might be more important for the splitting energies is the interaction with charge-transfer-like configurations (see, e.g., the example in Section 5.1.4). Neither the approach originally suggested in Ref. [400] nor the coupled FDE approach used here include such effects at the present stage. Finally, it should be noted that the approaches in Refs. [399, 400] focused mainly on the inclusion of condensed-matter effects on excitation energy transfer phenomena by means of continuum models.

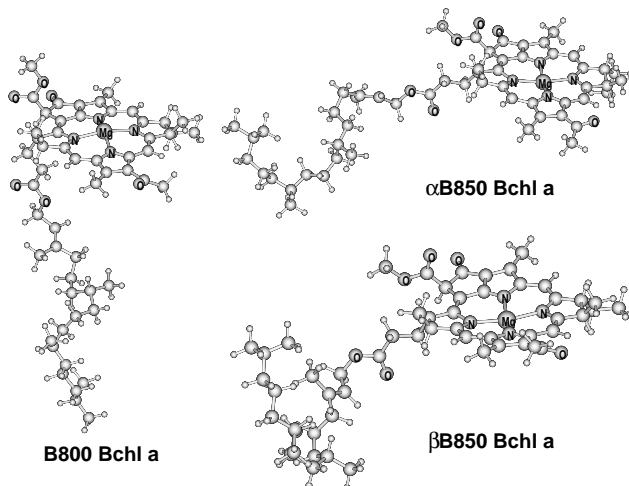
5.3.3 Chromophore–environment interactions

The absorption properties of a natural light-harvesting complex will depend on several factors, involving (i) the absorption properties of the (isolated) pigment molecules, (ii) the environmental effects on the subsystem properties (e.g., axial ligand, protein side-chains, neighboring pigments etc.), and (iii) phenomena related to the aggregation of several chromophores (i.e., excitation energy couplings). In this section, the environmental effects on local fragment properties will be studied by means of the (uncoupled) FDE approach. The following effects on the excitation energies of Bchl *a* will be analyzed: a) the structural change from an optimized structure to the crystal structure, b) the influence of neighboring Bchl *a* molecules in the aggregate, c) the effect of axial ligands and d) of hydrogen-bonding ligands. In the latter three cases, the neighboring molecule or ligand will be represented in terms of an effective embedding potential obtained from its frozen density; these densities are polarized in all cases by means of freeze-and-thaw iterations (details are described below).

The absorption spectrum of a Bchl *a* molecule consists of three prominent bands: the intense Q_y band in the region of 750 to 800 nm with a maximum at 773, the much less intense Q_x band between 550 and 600 nm (maximum at 577 nm), and the intense Soret band with a maximum at 358 nm, which extends from < 300 nm to above 400 nm (see, e.g., Ref. [423]). In Table 5.4 we compare the calculated excitation energies for the intense low-lying Q_y transition as well as the Q_x transition of bacteriochlorophyll *a* for different structural models and environments of the pigments. The general structures of the α and β B850 Bchl *a* molecules as well as that of B800 Bchl *a* are shown in Figure 5.10.

We will first concentrate on the isolated models. If these structures are fully optimized (“fully opt.” in Table 5.4), we obtain excitation energies between 1.76 and 1.79 eV for the Q_y transitions of α B850, β B850, and B800 Bchl *a*, and between 2.02 and 2.07 eV for the Q_x transitions. These excitation energies are — within the typical error bar of TDDFT results for valence excitations — in reasonable agreement with the experimental excitation energies of Bchl *a* in diethyl ether solution (taken from Ref. [423]; these values thus do not contain effects from aggregation or surrounding protein), which are 1.60 (Q_y) and 2.15 (Q_x), respectively. As a next step, we investigated the effect of constraining the positions of the non-hydrogen atoms in Bchl *a* to the positions obtained from the crystal structure for the isolated pigments, as these structures will be used in the analysis of the effect of chromophore aggregation in Section 5.3.4. Only the positions of the hydrogen atoms, which had to be added to the X-ray structure, were optimized (“H opt.” in Table 5.4; see also Appendix B). It can be seen that the excitation energies of the

Figure 5.10: Structure of the Bchl *a* monomers investigated in this study. All structures were obtained from the X-ray structure from Ref. [429], PDB code 1NKZ. Positions of added hydrogen atoms were optimized (BP86/TZP).

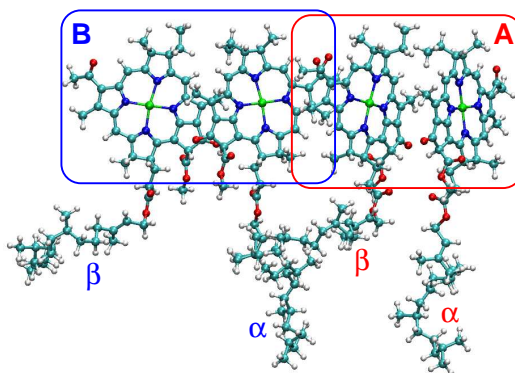


α B850 and β B850 Bchl *a* structures differ slightly by 0.02 eV for the Q_y (1.59 and 1.57 eV, respectively) and by 0.03 eV for the Q_x (1.92 and 1.95 eV, respectively) transition. The Q_y excitation energy of B800 Bchl *a* is even somewhat higher than that of α B850 Bchl *a* (1.61 eV), and its Q_x transition energy (1.94 eV) is between the corresponding values of the B850 pigments. Compared to the corresponding excitation energies of the fully optimized structure, both transitions show a pronounced blue-shift of the order of 0.1 to 0.2 eV. Apparently, the energy difference between the Q_x and the Q_y excitation energy is systematically underestimated in the SAOP/TZP calculations for all structural models tested here when compared to the experimental reference. The latter difference is 0.55 eV [423], whereas in this work energy differences of 0.25 to 0.38 eV are obtained for the isolated Bchl *a* models. This difference could be caused either by structural effects, since not all possible conformations of the Bchl *a* molecule were investigated, or by deficiencies of the SAOP potential in combination with the ALDA kernel. The energy differences obtained in Ref. [433], in which the B3LYP hybrid functional was used, are somewhat larger (> 0.4 eV), which might be a hint on the latter effect. On the other hand, only relatively small basis sets were used in that study, so that the energy differences might be subject to changes when larger basis sets are used in connection with the B3LYP functional.

In order to analyze whether the neighboring Bchl *a* molecules have an impact on the (uncoupled) excitation energies of the pigments, we investigated the B850 unit of LH2 by means of uncoupled FDE calculations as described in detail in Ref. [116]. In these calculations, the effect of the surrounding molecules is incorporated by an effective embedding potential constructed from the environmental density. This density surrounding either an α B850 or a β B850 Bchl *a* molecule was approximated in the following way: We extracted a tetrameric unit from B850, which is shown in Figure 5.11. Then, the electron densities were calculated (SAOP/TZP) for each of the monomers within the tetramer without including effects of neighboring molecules. Subsequently,

the electron densities for all four monomers were relaxed in a series of ground-state FDE calculations, in which a superposition of the densities of the other three subsystems was employed to model the environment. In each step, the latest approximation available for the density of each system in the environment was used. This cyclic optimization was carried out three times in total. Since the adjacent Bchl *a* molecules will have a much stronger impact on the electron density of a particular pigment than more distant monomers, the electron densities thus obtained for the inner two Bchl *a* molecules of the tetramer should already represent a good approximation to the monomer density in the full B850 system. In a last step, we used the densities for these inner two monomers of the tetramer to set up an approximate density of the full B850 system by superposition of these relaxed monomer densities. With this environmental density, we calculated the electron densities of one α B850 and one β B850 Bchl *a* in the full B850 complex as well as their uncoupled excitation energies in an FDE calculation. The total system in these calculations consists of 2520 atoms, of which 2380 belong to the frozen environment and 140 to the embedded system. It should be noted that this way of approximating the environmental density in an uncoupled FDE calculation is much more sophisticated than, e.g., a simple superposition of non-relaxed subsystem densities, which nevertheless often yields reasonable results (see Sections 3.4.2 and 4.3)

Figure 5.11: Structure of the tetrameric Bchl *a* substructure of the B850 unit. The labels A and B for the (α, β) dimers were introduced for comparability with the results obtained in Ref. [435], where the same notation is used.



The effect of the other Bchl *a* molecules within the B850 unit on the site energies is rather small. The excitation energies of the Q_y and Q_x transitions of both α B850 and β B850 Bchl *a* are shifted by only 0.01 eV and 0.02 eV, respectively, when this part of the environment is included (see Table 5.4).

A similar test was carried out for the B800 system, but because of the larger distance between the monomers, we only performed one relaxation step of the monomer density w.r.t. the density of all other monomers. Also here, the excitation energies for Q_y and Q_x transitions are virtually unchanged (the change in the Q_y excitation energy is in the order of 0.001 eV but leads to a roundoff effect).

Table 5.4: Calculated excitation energies (SAOP/TZP; in units of eV) of Bchl *a* for different structures and environments. The starting point for all (partial) structure optimizations carried out here was the X-ray structure with 2.0 Å resolution from Ref. [429], PDB code 1NKZ; H opt.: hydrogen atoms added and optimized (BP86/TZP); fully opt.: hydrogen atoms added, all atoms optimized (BP86/TZP). Environments: B850/B800: all other B850/B800 Bchl *a* molecules included; model compounds of different size were used for the amino acid residues α -His31, α -Trp45, β -His31, α' -Tyr44, α -Met1 and Arg20 (see text for details). Experimental values for Bchl *a* in diethyl ether were taken from Ref. [423].

structure	environment	Q_y	Q_x
α B850 Bchl <i>a</i> (fully opt.)	—	1.76	2.02
α B850 Bchl <i>a</i> (H opt.)	—	1.59	1.92
α B850 Bchl <i>a</i> (H opt.)	B850	1.60	1.94
α B850 Bchl <i>a</i> (H opt.)	α -His31	1.60	1.88
α B850 Bchl <i>a</i> (H opt.*)	α -Trp45	1.59	1.91
β B850 Bchl <i>a</i> (fully opt.)	—	1.77	2.02
β B850 Bchl <i>a</i> (H opt.)	—	1.57	1.95
β B850 Bchl <i>a</i> (H opt.)	B850	1.58	1.97
β B850 Bchl <i>a</i> (H opt.)	β -His31	1.58	1.92
β B850 Bchl <i>a</i> (H opt.*)	α' -Tyr44	1.57	1.93
B800 Bchl <i>a</i> (fully opt.)	—	1.79	2.07
B800 Bchl <i>a</i> (H opt.)	—	1.61	1.95
B800 Bchl <i>a</i> (H opt.)	B800	1.60	1.95
B800 Bchl <i>a</i> (H opt.)	α -Met1	1.61	1.90
B800 Bchl <i>a</i> (H opt.)	β -Arg20	1.55	1.85
exp. Bchl <i>a</i> [423]		1.60	2.15

In a next step, we investigated the influence of an axial ligand on the Bchl *a* pigments. For α B850 and β B850, this axial ligand is a histidine residue, which was modeled by the frozen density of an imidazole ring in a FDE calculation. Also this axial ligand results in only a small change. For α B850 Bchl *a* the Q_y excitation energy increases by 0.01 eV to 1.60 eV, and the Q_x excitation energy decreases by 0.04 eV. Similar changes are found for β B850 Bchl *a*. This is consistent with the observations made before, according to which axial ligands only lead to slight modulations of the site energies of Bchl *a* molecules [437]. In case of B800 Bchl *a*, the axial ligand reported in Refs. [428, 429], which was also used in our study, is a COO^- -modified α -Met1, i.e., the coordinating group is a carboxy group. This is in contrast to the Met ligand that was assumed in the earlier study reported in Ref. [433], where the effect of the protein environment on the excited states of Bchl *a* in B800 were investigated. In this case, we included also the following residues (Asn2–Gln3–Gly4) into the part of the protein modeled by FDE in order to test the influence of a larger protein model. But also here, the effect is rather small. The Q_y excitation energy remains unchanged at 1.61 eV, while the Q_x transition shifts by 0.05 eV to 1.90 eV.

Finally, the effects of the hydrogen-bonding residues α -Trp45 (α B850), α -Tyr44 (β B850), and β -Arg20 (B800) were investigated. These amino acids were modeled by their side-

chains only (saturated with hydrogen). Again, the positions of the hydrogen atoms were optimized in the monomers from which the hydrogen bonded complex was created. Afterwards, the positions of the atoms involved in the hydrogen bond were optimized in the hydrogen-bonded complex. For the structures obtained in this way, we performed uncoupled FDE calculations considering the amino acid side chains as the frozen part. For the B800 Bchl *a* pigment, we find rather large red-shifts of 0.06 and 0.10 eV for the Q_y and Q_x transition in comparison to the isolated molecule. This is in good agreement with the corresponding shifts of 0.05 and 0.08 eV obtained from supermolecular B3LYP/6-31G calculations in Ref. [433]. In contrast to this, rather small changes (≤ 0.02 eV) were found for α B850 and β B850 in comparison to the isolated pigment molecules.

In all the calculations reported above, the effect of either neighboring molecules, axial ligands, or hydrogen-bonding ligands was included by means of an effective embedding potential in an (uncoupled) FDE calculation. In order to assess the error introduced by the frozen-density approach, the calculation on α B850 Bchl *a* including the Trp45 ligand was repeated in a supermolecular Kohn–Sham (TD)DFT calculation. The resulting excitation energies for the Q_y and Q_x transitions agree within 0.01 eV with the FDE values, which shows that FDE does not introduce significant errors for these excitations.

5.3.4 Chromophore–chromophore couplings

The next step in the calculation of the absorption properties of LH2 is to determine the coupled excitation energies. As outlined in Section 5.3.2 this is often done by calculating CI-like matrix elements between excited monomer states, which are then used to construct an effective Hamiltonian matrix from which coupled excitations can be obtained. In order to validate the coupling constants obtained here by comparison to previous results, we will in this section concentrate on the largest coupling constants between neighboring pigments in the light-harvesting complex, whereas *all* couplings occurring between the Q_y and Q_x transitions are implicitly incorporated in the resulting spectra presented in Section 5.3.5. Couplings were calculated for the combined B850 and B800 units (3780 atoms in total) of LH2, which were separately prepared as described in the last section and then combined (i.e., no additional uncoupled FDE calculations were performed). The intra-subunit couplings obtained by considering the B850 and B800 units independently are virtually the same and are therefore not explicitly mentioned here. The pigments are labeled with a letter (A,B) indicating the protomer unit, i.e., an A–A coupling is an intrapolypeptide coupling in the nomenclature of Ref. [403], whereas an A–B coupling is an interpolypeptide coupling.

The results for the strongest couplings between pigments within the B850 subunit are compared to the (Coulomb-only) transition density cube (TDC) data based on scaled CIS transition densities from Ref. [435] as well as to the CIS results from Ref. [403] in Table 5.5. The first observation that can be made is that the coupling constants calculated here are in reasonable agreement with the ones obtained by Krueger *et al.* [435] and the scaled Coulomb results by Scholes *et al.* [403]. This is due to the fact that the couplings are dominated by the Coulomb contribution, which was scaled in Refs. [403,435] to match the experimental transition dipole moment. Scholes *et al.* assumed an experimental dipole moment of 2.51 a.u. (6.39 D), whereas their CIS/6-31G* calculation resulted in a transition moment of 4.03 and 3.98 a.u. for α B850 and β B850

Table 5.5: Calculated (SAOP/TZP; in units of cm^{-1}) coupling constants for the Q_y transition of $(\alpha, \beta)\text{B850 Bchl } a$ in a combined B850–B800 complex (FDEc: coupled FDE calculation). For comparison, also the results from Ref. [435] obtained from a Coulomb-only coupling with the transition density cube (TDC) method on the basis of scaled CIS transition densities as well as the CIS results (both original data and with scaled Coulomb contribution) from Ref. [403] are presented.

type	$\alpha_B \leftrightarrow \beta_A$	$\alpha_B \leftrightarrow \beta_B$	$\alpha_B \leftrightarrow \alpha_A$	$\beta_B \leftrightarrow \beta_A$
FDEc, B850+B800	200	232	−65	−45
TDC (scaled Coulomb only) [435]	213	238	−46	−37
CIS [403]	550	730		
CIS (scaled Coulomb) [403]	255	320		

Bchl a , respectively, so that their calculated Coulomb contribution was empirically scaled down to about 40 % of the original value. The transition dipole moment calculated in this work (SAOP/TZP) is 2.72 a.u. for αB850 and 2.71 a.u. for $\beta\text{B850 Bchl } a$ in the isolated calculation and decreases slightly to 2.67 a.u. for both αB850 and $\beta\text{B850 Bchl } a$ in the uncoupled FDE calculation on the full B850 system, thus demonstrating the reliability of transition dipole moments from TDDFT calculations.

The data from Ref. [403] suggest that short-range contributions to the total coupling are small though not negligible. The short-range contributions given there are 55 and 60 cm^{-1} , respectively, for couplings of type $\alpha_B \leftrightarrow \beta_B$ and $\alpha_B \leftrightarrow \beta_A$, respectively. However, these couplings were also found to be very sensitive to the inclusion of amino acids with hydrogen-bonding ability, which could not be explained on the basis of their calculation. Additionally, the Coulomb contributions in the results from Ref. [403] were empirically scaled down as mentioned above, whereas the short-range contribution was not modified. It is therefore not completely clear if the short-range contribution was overestimated in that work.

In the case of coupled frozen-density embedding calculations, short-range contributions are in principle included, although they cannot directly be mapped to the corresponding short-range contributions in a CIS-like treatment or in other DFT-based approaches [399,400]. The ground-state calculations in the FDE case include interactions between the monomers, so that the monomer orbitals and densities are already polarized w.r.t. the surrounding molecules in the aggregate. This can of course lead to changes in the coupling strength, e.g., in a modified Coulomb coupling due to changes in the orbitals. Furthermore, the effective kernel employed in the (uncoupled and coupled) subsystem TDDFT contains both exchange–correlation and kinetic energy contributions originating from the effective embedding potential [229], which also give rise to short-range contributions. However, the current implementation for the coupled FDE approach employs the adiabatic local density approximation (ALDA) for both XC and kinetic-energy contributions, which are usually small and of opposite sign (see Section 5.1.4). In order to analyze the role of short-range couplings in the results obtained here in more detail, we extracted an (α, β) Bchl a dimer from the B850 subunit, which shows the largest couplings in LH2. The coupling constant obtained for this dimer was 234

cm^{-1} and thus very similar to the corresponding value in the full B850+B800 system. The XC and kinetic-energy contributions in the coupled FDE calculation were analyzed by switching the corresponding terms in the kernel off in the dimer calculation. If the kinetic energy contribution is omitted, the coupling reduces from 234 to 230 cm^{-1} . If additionally the XC contribution is omitted (pure Coulomb coupling), the total coupling increases again to 233 cm^{-1} . This shows that the combined effect of kinetic energy and XC contribution is almost negligible in the present approximation for the kernel. An additional effect that may become important at small distances are charge-transfer-like excitations between the subsystems. However, the subsystem TDDFT approach introduced in Section 5.1 does by construction not account for interactions with charge-transfer excitations. Although this is — in the context of the problems for TDDFT to describe such excitations [250–255, 395] — desirable for calculations on very large systems, which would suffer substantially from the long-range charge-transfer problem [116, 395, 452] it may lead to inaccuracies in the couplings at very short range.

Because of this disagreement concerning the role of the short-range couplings, we carried out an additional test of the FDE methodology. We performed a supermolecular TDDFT calculation in comparison to a coupled FDE calculation for a model of the (α, β) B850 dimer, in which the phytol chain was omitted. The data are reported in Table 5.6. It can be seen that the splitting between the two Q_y excitations is nicely reproduced by the coupled FDE calculation. The two states resulting from the coupling appear at 1.541 and 1.606 eV (FDEc) with oscillator strengths of 0.556 and 0.036, respectively, which compares well to the supermolecular result of 1.530 and 1.596 eV (oscillator strengths: 0.574 and 0.043), respectively. The splitting energy is 518 cm^{-1} in the case of FDEc and 536 cm^{-1} in the conventional supermolecular TDDFT calculation. The coupling constants calculated according to Eq. (5.88) are 242 cm^{-1} (FDEc) and 252 cm^{-1} , respectively (in the latter case, $\omega_{+,-}$ were taken from the supermolecular calculation and $\omega_{a,b}$ were taken from the uncoupled FDE calculations), which demonstrates that the additional approximations introduced in the subsystem TDDFT approach have only a minor effect on the coupling constants.

It should be mentioned that the situation for the Q_x transitions is more complicated. While the excitation energies for the lower of the two resulting states are similar (FDEc: 1.907 eV; super: 1.910 eV), there is a larger discrepancy for the higher-energy state (FDEc: 1.943 eV; super: 1.925 eV). The splitting between the two states in the supermolecular case is even smaller than the splitting between the assumed “site energies”, which are approximated by the FDEu calculations. Therefore, this splitting cannot be analyzed in terms of Eq. (5.88), which cannot describe a decrease of the energy gap between the two excitations. Possible reasons for this problem could be (i) inaccuracies in the uncoupled excitation energies (which are not a measurable quantity anyway, since one cannot obtain uncoupled excitation energies from an interacting dimer), or (ii) an interaction with one of the many higher-lying excited states of partial charge-transfer character that can be found in the supermolecular calculation, but that are absent in the FDEc calculation. Nevertheless, both supermolecular and FDEc calculations agree on the qualitative picture that the interactions between the Q_x transitions are much smaller than for the Q_y transitions. In addition, it has been argued that it is not necessary to consider Q_x transitions as donor transitions in EET processes because of a rapid $Q_x - Q_y$ internal conversion [435].

Table 5.6: Excitation energies E (SAOP/TZP; in units of eV) and oscillator strengths f for the Q_y and Q_x transitions of a Bchl a model dimer from coupled FDE (FDEc) and supermolecular TDDFT calculations (super) (phytyl chain omitted; note that the oscillator strengths in Ref. [453] for the FDEc calculations are slightly different due to an inconsistent energy weighting of the transition moments). For comparison, also the monomer excitation energies from uncoupled FDE calculations on the dimer (FDEu) are shown.

calculation	$E(Q_y)$	$f(Q_y)$	$E(Q_y)$	$f(Q_y)$
FDEu (α)	1.585	0.298	1.911	0.071
FDEu (β)	1.563	0.293	1.940	0.074
FDEc ($\alpha + \beta$)	1.541	0.556	1.907	0.028
	1.606	0.036	1.943	0.112
super ($\alpha + \beta$)	1.530	0.574	1.910	0.037
	1.596	0.043	1.925	0.074

Table 5.7: Calculated (SAOP/TZP; in units of cm^{-1}) coupling constants for the Q_y transition of Bchl a in the combined B800 and B850 subunits (FDEc: coupled FDE calculation). For comparison, also the results from Ref. [435] obtained from a Coulomb-only coupling with the transition density cube (TDC) method on the basis of scaled CIS transition densities are shown.

type	FDEc, B800 + B850	TDC [435]
B800B \leftrightarrow B800C	-31	-27
B800A \leftrightarrow B800C	-3	-3
B800A \leftrightarrow α B850B	31	27
B800A \leftrightarrow β B850B	3	23
B800A \leftrightarrow β B850A	-3	5

After this discussion of the rather strong interactions within the B850 unit, we will now address the couplings among the B800 Bchl a molecules and between the B800 and B850 Bchl a pigments. These couplings are weaker because of the larger distances between the chromophores. Therefore, they should be almost exclusively due to Coulomb coupling. Again, we compare our results to the (Coulomb-only) transition density cube data based on the scaled CIS transition densities from Ref. [435] for the most important couplings. The data are shown in Table 5.7.

It can be seen that there is in most of the cases a reasonable agreement in the computed coupling constants with those from Ref. [435]. However, two differences can be seen: The B800A \leftrightarrow β B850B coupling is much weaker in our calculation than in the reference, and the sign differs for the coupling B800A \leftrightarrow β B850A. In order to analyze this discrepancy, we calculated the coupling constants in a dipole-dipole approximation according to [435]

$$V^{d-d} = \frac{1}{4\pi\epsilon_0} \kappa \frac{|\mu_D||\mu_A|}{R_{DA}^3}, \quad (5.90)$$

where μ_D and μ_A are the transition dipole moments of the donor and acceptor transition, respectively, κ is the so-called orientation factor

$$\kappa = \vec{r}_D \cdot \vec{r}_A - 3(\vec{r}_D \cdot \vec{R})(\vec{r}_A \cdot \vec{R}), \quad (5.91)$$

\vec{R} is a unit vector from the center of the donor to the center of the acceptor transition, R_{DA} is the distance between these two centers, and $\vec{r}_{D,A}$ are unit vectors in the direction of the transition dipole moments. In Table 5.8 we report the distances R_{DA} and orientation factors κ for the pairs of transitions from Table 5.7. For comparison, we also give the corresponding values from Ref. [435]. Differences between our data and those from that reference can be due to the different crystal structure used in that study, which leads to slightly different bond distances, and differences in the orientation and magnitude of the transition moments. However, in general there is a good agreement between the distances, orientation factors and dipole–dipole couplings obtained here and in Ref. [435], e.g., for the B800B \leftrightarrow B800C, B800A \leftrightarrow B800C, and B800A \leftrightarrow α B850B coupling. Nevertheless, the comparison suggests that the coupling constant reported for B800A \leftrightarrow β B850B may be incorrect in that reference when compared to the B800A \leftrightarrow α B850B coupling: Although the orientation factor is smaller by about a factor of five in the first case and the distance between donor and acceptor is slightly larger (both here and in Ref. [435]), the coupling constant calculated from the dipole–dipole approximation in Ref. [435] is even larger than in for B800A \leftrightarrow α B850B. Since the magnitudes of all transition dipole moments are almost identical, one would expect that the B800A \leftrightarrow β B850B coupling should be much smaller than the B800A \leftrightarrow α B850B coupling. This is confirmed by our dipole–dipole results, which yield a coupling of 33 cm^{-1} for the latter and of 5 cm^{-1} for the former pair of transitions. As far as the discrepancy for the B800A \leftrightarrow β B850A pair of transitions is concerned, we would like to note that our dipole–dipole approximation yields an orientation factor of approximately the same magnitude but opposite sign when compared to the results in Ref. [435]. The sign of a single coupling constant is actually arbitrary, since already the sign of the transition density (or the transition moment) is, in principle, arbitrary for each monomer, but of course it must be used consistently in the calculation of all coupling constants. In our case, we have chosen the same sign of the transition moment for each chromophore within the B850 ring. For this choice, the orientation factors for the B800A \leftrightarrow β B850B and B800A \leftrightarrow β B850A couplings, and consequently also the coupling constants within the dipole–dipole approximation, differ in sign.

5.3.5 Absorption spectra of the B850 and B800 units of LH2

The absorption spectra of the B850 unit have been obtained from the coupled FDE calculation described in Section 5.3.4. In Figure 5.12 we compare the monomer spectra resulting from the Q_y transitions of isolated α B850 and β B850 pigments with those obtained for the (α,β) B850 dimer, and the full B850 unit (i.e., 18 Bchl *a* molecules). The monomer peaks appear at 779 and 788 nm, respectively, for isolated α B850 and β B850. Already the coupling in the dimer leads to a considerable splitting with an intense peak at 800 nm and a less intense peak at 769 nm. In the full B850 ring of Bchl *a* monomers the intense peak (scaled with a factor of 0.1 in Figure 5.12) occurs at 812 nm, and an additional peak of low intensity can be found at 759 nm. The main

Table 5.8: Calculated (SAOP/TZP; in units of cm^{-1}) coupling constants for the Q_y transition of Bchl a in the combined B800 and B850 subunits within the dipole–dipole approximation, Eq. (5.90). Additionally given are the distances between the pigment centers (in units of Å) as well as the orientation factors κ . For comparison, also the results from Ref. [435] obtained within the dipole–dipole approximation are shown.

coupling	this work			Ref. [435]		
	R_{DA}	κ	V^{dd}	R_{DA}	κ	V^{dd}
B800B \leftrightarrow B800C	21.2	−1.20	−29	21.2	−1.33	−26
B800A \leftrightarrow B800C	39.9	−0.91	−3	39.9	−1.04	−3
B800A \leftrightarrow α B850B	17.8	0.79	33	17.6	0.79	27
B800A \leftrightarrow β B850B	21.7	0.22	5	21.8	0.17	31
B800A \leftrightarrow β B850A	18.5	−0.10	−4	18.3	0.13	4

reason for the discrepancy of the Q_y excitation energies with the absorption maxima in the natural light harvesting system (about 850 nm) are small errors in the site energies. When using the empirical site energies from Ref. [436] of 1.56 eV (α B850), 1.50 eV (β B850), which differ by only 0.04 and 0.08 eV from the energies of the monomers in the uncoupled FDE calculations (see Table 5.4), the intense peak shifts to 852 nm, while the less intense peak shifts to 785 nm. This is in nice agreement with the spectra modeled in Ref. [436], where these two peaks were found at 857 and 773 nm, respectively.

Figure 5.13 contains the spectra calculated from both the Q_y and the Q_x contributions of the B850 subunit and the combined B850 and B800 subunits of LH2. It should be noted that these spectra do not include ensemble averaging effects like static disorder or fluctuations in the environment and just serve the purpose to illustrate the results of the subsystem TDDFT calculations. The additional signals caused by the B800 ring in the lower panel of Figure 5.13 can clearly be recognized, and no significant changes occur in the bands already present in the B850 spectrum.

In summary, this application demonstrates the efficiency of the general subsystem TDDFT approach to describe both protein–pigment and pigment–pigment interactions in natural light-harvesting complexes. Site energies and excitonic coupling constants are accessible, i.e., quasi-diabatic and adiabatic pictures are provided. This is an important prerequisite for the analysis of excitation energy transfer phenomena.

As far as environmental effects are concerned, the present study investigated direct effects of neighboring molecules, but no screening effects of a surrounding medium on the coupling constants were considered. Studies concerning this point in the context of light-harvesting phenomena were recently presented by Scholes *et al.* [454] and Curutchet *et al.* [451]. On the basis of a continuum solvation model, they showed that such effects can be very important for excitation energy couplings in condensed matter. Subsystem TDDFT offers, in principle, the possibility to study also such effects in an explicit way.

Figure 5.12: Q_y contributions to the absorption spectra (SAOP/TZP) of (subunits of) the B850 ring of LH2 (*Rhodopseudomonas acidophila*). Only the Q_y transitions are considered. Note that the oscillator strengths in Ref. [453] for the FDEc calculations are slightly different due to an inconsistent energy weighting of the transition moments. The spectrum of the full B850 unit was scaled by a factor of 0.1 for better comparability. A Gaussian broadening of 0.01 eV has been applied to the peaks in the calculated absorption spectrum.

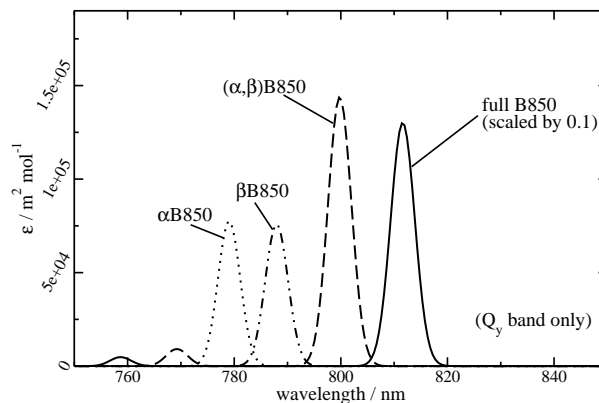
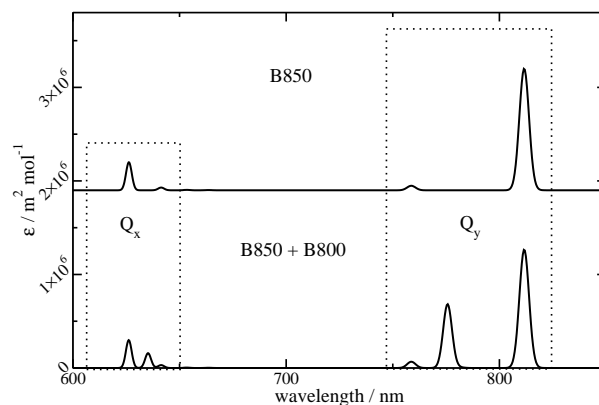


Figure 5.13: Absorption spectra (SAOP/TZP) of the B850 ring and the combined B850 and B800 rings of LH2 (*Rhodopseudomonas acidophila*). Note that the oscillator strengths in Ref. [453] for the FDEc calculations are slightly different due to an inconsistent energy weighting of the transition moments. A Gaussian broadening of 0.01 eV has been applied to the peaks in the calculated absorption spectrum.



6. Chromophore-Specific Vibrational Spectroscopy

6.1 Selective vibrational spectroscopy

As far as the investigation of molecular structure and reactivity is concerned, vibrational spectroscopy is probably an even more important tool than pure electronic spectroscopy as described in the previous chapters. The reason for this is that many more bands can be distinguished in vibrational spectra than in electronic spectra, in particular for molecules in solution or large molecules with many functional groups. These spectra thus contain much more information than electronic absorption or circular dichroism spectra, which often exhibit broad or blurred bands for such systems.

For molecules relevant in a biological context, e.g., proteins or nucleic acids, the number of peaks in a conventional vibrational spectrum, e.g., an infrared (IR) or Raman spectrum, may become prohibitively large for an assignment due to close-lying or overlapping peaks. Special experimental techniques have therefore been developed that either filter out selected parts of the total spectrum, or that spread the vibrational information over two dimensions by recording them in dependence of another parameter, e.g., the wavenumber of a previous pump pulse. Examples for the former are difference-IR [455] and -Raman techniques [456], while the latter include two-dimensional IR [457,458] or two-dimensional Raman spectroscopy (see, e.g., [459]). There are additional techniques such as vibrational circular dichroism (VCD) or vibrational Raman optical activity (VROA), which provide selective information related to chirality [460,461]. No comprehensive review of all these techniques will be given here; for details, we refer to the references given above and the general overview given in Ref. [462].

Also the theoretical description of vibrational spectroscopy has made rapid progress during the past years, so that now efficient density-functional theory implementations are available for, e.g., infrared and Raman [328,463,464], VCD [465–467], or VROA spectra [420]. A very useful method for the selective calculation of vibrational frequencies and normal modes in complex systems is the mode-tracking approach, which allows to directly target vibrations related to a specific scientific question on the basis of an intuitive guess [468]. Mode tracking has found a wide range of applications during the past years, which are reviewed in Ref. [469]. General information on the first-principles approaches to vibrational spectroscopy of biological systems is provided in Ref. [462].

Here, we will focus on chromophore-specific spectroscopic techniques which work under resonance conditions with a certain electronic transition of a chromophore. In particular, we will concentrate on theoretical resonance Raman spectroscopy, which can be regarded as a two-dimensional type of spectroscopy, in which resonance Raman intensities are not only recorded as a function of the Raman shift (i.e., the wavenumber offset from the exciting laser beam), but also in dependence of the frequency of the incident light. This requires to consider coupled electronic and vibrational degrees of freedom of the

system, and hence presents a big challenge to quantum chemistry. For this purpose, we will in the following give a brief outline of theoretical approaches for the calculation of resonance Raman spectra.¹

6.2 Resonance Raman as a chromophore-specific spectroscopy

In resonance Raman spectroscopy, the intensities of certain vibrational bands are selectively enhanced compared to normal Raman scattering, which has two important consequences for practical applications: (i) The absolute intensities are several orders of magnitude higher than in normal Raman scattering, so that the technique has a greatly enhanced sensitivity, and (ii) since only certain bands are enhanced in intensity, the resonance effect acts like a filter on the vibrational spectrum [470]. The second point is due to the fact that resonance Raman intensities can be related to structural changes in the excited state of a molecule (see below), which also means that information about excited-state processes can be deduced from resonance Raman experiments [471]. By tuning the excitation wavelength to resonances for particular chromophoric groups, it is possible to selectively enhance vibrations located on that chromophore. This makes the method well suited for applications to complex biological systems [472, 473], e.g., proteins [474–477]. Resonance Raman spectroscopy is often applied in studies on motifs in artificial or biological photosystems [478, 479], like bacteriochlorophyll *a* [480] or dendritic antenna systems [481], where electron- or excitation-energy transfer processes occur between different chromophores in a functional arrangement. It has also been used to investigate the spectroscopic properties of ruthenium–polypyridyl or related complexes [482] (see also Section 6.4).

The theory of resonance Raman scattering is, in principle, well-known, and detailed presentations are available in the literature [483–486]. The most common approaches are discussed in the following to show which approximations have to be made to arrive at schemes that are applicable to systems of considerable size.

6.2.1 Sum-over-states formulation

The starting point for the discussion of resonance Raman intensities is the Kramers–Heisenberg–Dirac expression for the scattering tensor (also sometimes called generalized or transition polarizability tensor) for a transition from an initial state $|i\rangle$ to a final state $|f\rangle$. The scattering cross section σ_{fi} for this transition is, for a randomly oriented sample, given by [485],

$$\sigma_{fi}(\omega) = \frac{8\pi\omega_s^3\omega}{9c^4} \sum_{\rho\lambda} |[\alpha_{\rho\lambda}]_{fi}|^2, \quad (6.1)$$

where c is the speed of light, ω is the angular frequency of the incident light, ω_s is the angular frequency of the scattered radiation, and $[\alpha_{\rho\lambda}]_{fi}$ is a component of the scattering tensor,

¹We will consider only *vibrational* resonance Raman spectroscopy in the absence of resolved rotational band structure.

$$[\alpha_{\rho\lambda}]_{fi} = \frac{1}{\hbar} \sum_r \left\{ \frac{\mu_{\lambda,fr} \mu_{\rho,ri}}{\omega_{rf} + \omega + i\Gamma_r} + \frac{\mu_{\rho,fr} \mu_{\lambda,ri}}{\omega_{ri} - \omega - i\Gamma_r} \right\}. \quad (6.2)$$

Here, the sum runs over all excited vibronic states $|r\rangle$, the angular frequency $\omega_{ab} = (E_a - E_b)/\hbar$ corresponds to the energy difference between vibronic states a and b , and

$$\mu_{\rho,ab} = \langle a | \hat{\mu}_\rho | b \rangle, \quad (6.3)$$

is a matrix element of a component $\rho = \{x, y, z\}$ of the electric dipole operator. The expression for α follows from standard perturbation theory. The damping constant Γ_r introduced in Eq. (6.2) accounts for the finite life time of the molecule in the excited state $|r\rangle$ due to spontaneous emission effects. While it can be rigorously derived from quantum electrodynamics [226, 487], it is often just included phenomenologically [487, p. 73]. The relative signs of the $i\Gamma_r$ terms have until recently been subject to a debate (see Ref. [483, p. 535]). In Ref. [488], which also provides a brief historical account of the discussion, it was argued on the basis of time-reversal symmetry that the damping constants should have the same sign in both terms. Subsequently, Buckingham and Fischer demonstrated that this same-sign convention (also denoted as equal-sign or constant-sign convention) leads to unphysical results [489], see also [490, 491]. Most recently, this controversy was resolved as a difference between a semiclassical linear-response and a scattering description of the process [492, 493]. In the former, a time-ordering is imposed on the process (i.e., it is assumed that first an incoming photon is absorbed, and a second photon is emitted afterwards), whereas all interactions are treated on the same footing from the scattering point of view (i.e., all time-orderings are allowed, including those in which first an emission takes place, followed by an absorption of a photon). The linear-response formalism leads to the opposite-sign prescription, whereas the scattering treatment results in equal signs for both terms. For resonance Raman calculations, this problem is usually not severe, since the term with the frequency sum in the denominator, $\omega_{fr} + \omega$, usually hardly contributes to the scattering cross section (see below). Following Ref. [483], we will adopt the opposite-sign convention in the intermediate steps, which is consistent with the derivation of $[\alpha_{\rho\lambda}]_{fi}$ as the linear response of the transition dipole moment.

Within the Born–Oppenheimer approximation, we assume that we can write the wavefunction for each vibronic state $|r\rangle$ as a product of a nuclear wavefunction χ and an electronic wavefunction Ψ . For the fundamental transitions that we will consider here, $|f\rangle$ and $|i\rangle$ are vibrational states on the ground-state electronic potential energy surface that differ by one vibrational quantum. In addition, the sum over all excited rovibronic states $|r\rangle$ in Eq. (6.2) is usually restricted to the vibrational states χ_{k_s} of the excited state Ψ_s under resonance. A slightly more general expression is obtained by assuming that there might be several excited electronic states $|\Psi_s\rangle$ that are close to resonance,

$$[\alpha_{\rho\lambda}]_{fi} = \frac{1}{\hbar} \sum_{s,k_s} \left\{ \frac{\langle \chi_{f_0} \Psi_0 | \hat{\mu}_\lambda | \chi_{k_s} \Psi_s \rangle \langle \chi_{k_s} \Psi_s | \hat{\mu}_\rho | \chi_{i_0} \Psi_0 \rangle}{\omega_{s_k,0_f} + \omega + i\Gamma_{s_k}} + \frac{\langle \chi_{f_0} \Psi_0 | \hat{\mu}_\rho | \chi_{k_s} \Psi_s \rangle \langle \chi_{k_s} \Psi_s | \hat{\mu}_\lambda | \chi_{i_0} \Psi_0 \rangle}{\omega_{s_k,0_i} - \omega - i\Gamma_{s_k}} \right\}, \quad (6.4)$$

which includes the case of a single resonating state as a special case in which the sum over the excited electronic states $|\Psi_s\rangle$ is replaced by a single excited state only. A general treatment for close-lying excited states would require to include non-adiabatic coupling effects between different electronic states [318, 319].

The terms involving the nuclear contribution to the electric dipole moment operator in Eq. (6.4) vanish due to the orthogonality of the electronic wavefunctions in the ground and excited states. The electronic contribution can be expanded in a Taylor-series in terms of normal coordinates \mathbf{Q} , e.g.,

$$\langle \chi_{k_s} \Psi_s | \hat{\mu}_\rho | \chi_{i_0} \Psi_0 \rangle = \langle \chi_{k_s} | \mu_{\rho, s0}^{\text{el}}(\mathbf{Q}) | \chi_{i_0} \rangle \quad (6.5)$$

$$= \mu_{\rho, s0}^{\text{el},(0)} \langle \chi_{k_s} | \chi_{i_0} \rangle + \sum_i \left(\frac{\partial \mu_{\rho, s0}^{\text{el},(0)}}{\partial Q_i} \right)_0 \langle \chi_{k_s} | Q_i | \chi_{i_0} \rangle + \mathcal{O}(\mathbf{Q}^2), \quad (6.6)$$

where we have introduced the notation $\mu_{\rho, s0}^{\text{el},(0)} = \mu_{\rho, s0}^{\text{el}}(\mathbf{Q}_0)$ for the electronic contribution to the electric transition dipole moment at the ground-state equilibrium position \mathbf{Q}_0 . If we invoke the Condon approximation ($\mu_{\rho, s0}^{\text{el}}(\mathbf{Q}) = \mu_{\rho, s0}^{\text{el},(0)}$), only the leading term is taken into account and we obtain,

$$[\alpha_{\rho\lambda}]_{fi} = \frac{1}{\hbar} \sum_{s, k_s} \mu_{\rho, s0}^{\text{el},(0)} \mu_{\rho, s0}^{\text{el},(0)} \left\{ \frac{\langle \chi_{f_0} | \chi_{k_s} \rangle \langle \chi_{k_s} | \chi_{i_0} \rangle}{\omega_{s_k, 0_f} + \omega + i\Gamma_{s_k}} + \frac{\langle \chi_{f_0} | \chi_{k_s} \rangle \langle \chi_{k_s} | \chi_{i_0} \rangle}{\omega_{s_k, 0_i} - \omega - i\Gamma_{s_k}} \right\}, \quad (6.7)$$

where we have used the fact that $\mu_{\rho, s0}^{\text{el},(0)} = \mu_{\rho, 0s}^{\text{el},(0)}$ etc. for real wavefunctions, which we assume here. This so-called *Franck-Condon* (FC) scattering is the dominant contribution to the resonance Raman scattering in particular for resonance with strongly allowed transitions and totally symmetric modes. The first-order correction to the electronic transition dipole moment in Eq. (6.6) gives rise to *Herzberg-Teller* scattering, which becomes important for non-totally symmetric modes [484]. These terms are in most cases much weaker than the FC-type scattering and will therefore be neglected in the studies presented here. Note that the first term on the right-hand-side of Eq. (6.7) is often neglected, because the second term contains an energy difference that approaches zero under resonance conditions. It will thus dominate the resonance Raman intensities by far.

Since the theoretical prediction of the damping constants Γ_{s_k} for state $|\chi_{k_s} \Psi_s\rangle$ is very involved (see above), they are most often introduced as phenomenological, state-independent constants, and their value is typically chosen in the range of 100 to 1600 cm^{-1} [494, 495]. Preliminary tests in this work showed that the choice of Γ within this range mainly affects the *absolute* intensities, whereas the *relative* intensities are not much changed. Since we are only interested in relative intensities, we apply a uniform damping constant of 400 cm^{-1} in all our calculations.

In order to carry out the summation in Eq. (6.7) for all but the smallest molecules, for which essentially full potential energy surfaces and the corresponding vibrational states can be determined, it is necessary to make a model assumption concerning the potential energy surfaces for ground and excited states. For larger molecules, this typically involves the harmonic approximation for both states. The reference point for the harmonic expansion in the ground state is clearly the ground-state equilibrium structure. For

the excited state, there are in principle two choices: Either, the equilibrium position of the excited-state potential energy surface is determined as well, which will be called adiabatic Franck–Condon approach, or the expansion is carried out at the ground-state equilibrium structure. The latter method, called vertical Franck–Condon approach, has two advantages. Fast processes in the excited state only probe the Franck–Condon region, so that the potential energy surface should be accurate there [485]. This point will be discussed below in the context of the time-dependent approach to resonance Raman scattering. Moreover, there is a computational advantage, since the additional effort for the excited-state structure optimization is not necessary. This gives rise to considerable savings in computer time in particular if several excited states shall be considered.

The Franck–Condon-type integrals arising from either type of approximation can be solved analytically, and efficient recursion formulae and algorithms have been designed for that purpose [369, 370, 496–504]. The simplest model for the excited-state potential energy surface, which is called the “independent mode, displace harmonic oscillator model”, corresponds to a neglect of both Duschinsky rotations, i.e., changes in the normal modes in the excited state, and frequency changes in the excited state w.r.t. the ground state [505, 506]. This is of particular interest in calculations for large molecules, e.g., transition metal complexes [507, 508], since it only requires the calculation of the excited-state gradient vector for each state under consideration within the vertical Franck–Condon approach. Therefore, this scheme is sometimes called “gradient Franck–Condon” (GFC) approach or linear electron–phonon coupling. The resulting integrals can easily be evaluated [485], and the only remaining problem is the tremendous number of integrals that is needed for large molecules.

One of the reasons why theoretical resonance Raman spectroscopy has seen such a revived interest during the past years is that robust analytical gradients for excited-state potential energy surfaces are now readily available from excited-state electronic-structure methods like CIS [201], CC2 [206, 509], CASSCF [510], and TDDFT [231, 239, 511–514]. In particular the latter are computationally cheap and usually provide reliable results for resonance Raman intensities [494, 495, 506, 508, 515–518] (see also below).

6.2.2 Time-dependent theory of Raman scattering

In the time-dependent theory of resonance Raman scattering (see, e.g., Refs. [486, 494, 519–523]), the energy denominator of the resonant term on the right-hand side of Eq. (6.7) is expressed as the half Fourier transform [520],

$$\frac{1}{\omega_{s_k,0_i} - \omega - i\Gamma} = i \int_0^\infty dt e^{[-i(\omega_{s_k,0_i} - \omega - i\Gamma)t]}, \quad (6.8)$$

where a common linewidth Γ is assumed for all vibronic transitions involved. We will, in the following, neglect the non-resonant term in Eq. (6.7), and restrict the discussion to one excited state Ψ_s .

We proceed by explicitly writing $\omega_{s_k,0_i} = \omega_{s_k} - \omega_{0_i}$ as a difference of the energy levels (in terms of angular frequencies), and by noting that $\exp[-i\omega_{s_k}t]|\chi_{k_s}\rangle = \exp[-i\hat{H}_{\text{ex}}t/\hbar]|\chi_{k_s}\rangle$, where \hat{H}_{ex} is the Hamiltonian for the nuclear motion on the excited-state potential energy

surface for electronic state $|\Psi_s\rangle$. With that, we get from Eq. (6.7),

$$\begin{aligned} [\alpha_{\rho\lambda}]_{f,i} &= \frac{i}{\hbar} \mu_{\rho,s0}^{\text{el},(0)} \mu_{\lambda,s0}^{\text{el},(0)} \int_0^\infty dt e^{[i(\omega_{0_i} + \omega)t - \Gamma t]} \langle \chi_{f0} | e^{[-i\hat{H}_{\text{ext}}t/\hbar]} \sum_{k_s} |\chi_{k_s}\rangle \langle \chi_{k_s} | \chi_{i0}\rangle \\ &= \frac{i}{\hbar} \mu_{\rho,s0}^{\text{el},(0)} \mu_{\lambda,s0}^{\text{el},(0)} \int_0^\infty dt e^{[i(\omega_{0_i} + \omega)t - \Gamma t]} \langle \chi_{f0} | e^{[-i\hat{H}_{\text{ext}}t/\hbar]} | \chi_{i0}\rangle. \end{aligned} \quad (6.9)$$

In the last transformation, we used the closure relation $\sum_{k_s} |\chi_{k_s}\rangle \langle \chi_{k_s}| = 1$. In a more compact notation, the initial vibrational wavepacket propagated by the excited-state vibrational Hamiltonian is often written as $\exp[-i\hat{H}_{\text{ext}}t/\hbar] |\chi_{i0}\rangle = |\chi_{i0}(t)\rangle$, so that

$$[\alpha_{\rho\lambda}]_{f,i} = \frac{i}{\hbar} \mu_{\rho,s0}^{\text{el},(0)} \mu_{\lambda,s0}^{\text{el},(0)} \int_0^\infty dt e^{[i(\omega_{0_i} + \omega)t - \Gamma t]} \langle \chi_{f0} | \chi_{i0}(t) \rangle. \quad (6.10)$$

The time-dependent wavepacket overlap can be evaluated analytically for the IMDHO. This requires the displacements of the excited-state equilibrium structure along the normal coordinates relative to the ground-state equilibrium structure, which are — within the IMDHO model — proportional to the excited-state gradients along the normal coordinates. The time-integral can then be evaluated numerically, where the upper limit for the integration can be chosen on the basis of the damping constant Γ . Both the time-dependent approach to resonance Raman intensities and the sum-over-states approach (within the GFC model) were implemented in the program DNR [524], which was used for the resonance Raman calculations reported in Section 6.3. Both approaches give the same results (within the specified numerical accuracy), but calculations on the basis of the time-dependent approach are typically much more efficient for molecules with many vibrational modes.

By comparison of the sum-over-states expression, Eq. (6.7), with Eq. (6.10) for the case of a single resonant state, for which we can choose the coordinate system in such a way that only one component of the transition dipole moment is non-vanishing, we see that the intensities (given in terms of the scattering cross sections) from both expressions will depend on the fourth power of the electric transition dipole moment of the state in resonance. This can be an important hint in resonance Raman calculations on the basis of approximate electronic-structure methods, since the first important task in such calculations is the identification of the electronic state in resonance. Two factors are decisive for this issue: (i) the excitation energy to the state in resonance must match the frequency of the incident light beam, and (ii) the transition must show a significant oscillator strength.

6.2.3 Heller’s gradient approximation

Under certain conditions, the time integral in Eq. (6.10) is determined by the dynamics of the system during a very short time after excitation, in which the overlap $\langle \chi_{f0} | \chi_{i0}(t) \rangle$ is large. This is in particular the case if (i) the excitation is in pre-resonance, (ii) the damping factor $\exp[-\Gamma t]$ is small enough to quench the overlap for longer times after excitation (e.g., by interactions with solvent molecules), or (iii) there are many Franck–Condon active vibrational normal modes with considerably different frequencies. As discussed in Refs. [519,521], the latter case arises from the fact that it is increasingly

difficult that all vibrational coordinates return at the same time to the Franck–Condon region, so that the overlap integral $\langle \chi_{f_0} | \chi_{i_0}(t) \rangle$ is large. I.e., it may take a rather long time before this integral becomes large again, probably so large that the quenching due to the damping factor determines the integral.

Heller *et al.* could — on the basis of an analysis of Gaussian wavepacket dynamics on classical excited-state potential energy surfaces [519] — show that in this case the polarizability tensor matrix element is determined to a good approximation only by the gradient of the excited state potential energy surface. The result for the ratio of the intensities of two modes is (see, e.g., Ref. [486]),

$$\frac{i_j}{i_k} = \left(\frac{V_j^q}{V_k^q} \right)^2 = \left(\frac{\Delta_j^q \omega_j}{\Delta_k^q \omega_k} \right)^2, \quad (6.11)$$

where V_j^q is the gradient of the excited state expressed in terms of reduced normal coordinates,

$$V_j^q = \left(\frac{\partial E^a}{\partial q_j} \right)_{q_j=0}, \quad (6.12)$$

Δ_j^q is the displacement of the excited-state equilibrium position from the ground-state equilibrium along the reduced normal mode q_j , and the definition of reduced (or dimensionless) normal coordinates q_j in terms of mass-weighted normal coordinates Q_j is,

$$q_j = Q_j \sqrt{2\pi c \tilde{\nu}_j / \hbar} = Q_j \sqrt{\omega_j / \hbar}. \quad (6.13)$$

The second equality in Eq. (6.11) only holds within the IMDHO model, because then there is a simple relationship between excited-state gradients and normal-mode displacements; in this case, the expression is known under the name of “Savin’s rule”. It should be noted that Heller’s derivation is independent from that assumption. Although only valid within clearly defined conditions, this approach has successfully been used in several studies on resonance Raman spectra (see, e.g., Refs. [506, 515, 525, 526]).

6.2.4 Alternative methods

The last section showed that it is necessary to calculate the gradients of the electronic energy in the excited state under investigation in order to use the short-time approximation for resonance Raman estimates. A quantity directly related to the excited-state gradients are the forces on the atoms on the excited-state potential energy surface. Tozzini and Giannozzi [527] used an alternative approach, in which a very short MD run on the excited-state PES was carried out in which the atoms acquired a momentum proportional to the forces without significant displacements from the equilibrium positions. Then, the system was brought back to the ground-state, and a new MD run was performed on the ground-state in which the positions and velocities were taken from

the previous excited-state run. The Fourier-transform of the mass-weighted velocity–velocity autocorrelation function then gives a spectrum with peaks corresponding to the vibrational frequencies and intensities proportional to the initial amplitude of the corresponding normal mode (in the harmonic approximation). Since this amplitude is proportional to the excited-state gradient, we are back at the short-time approximation. For systems of moderate size, this may seem like a somewhat complicated way to calculate a quantity proportional to the excited-state gradients (which actually have to be calculated intermediately to perform the MD run). The advantage of this method in the context of simulations under periodic boundary conditions is, however, that no conventional frequency analysis is needed, since the vibrational spectrum is calculated from an autocorrelation function.

Jensen *et al.* proposed a method that replaces the wavepacket propagation in the time-dependent approach to resonance Raman intensities by a classical propagator in order to arrive at an intensity expression that closely resembles the one for off-resonance Raman scattering [328,483] but contains a phenomenological damping constant as needed under resonance conditions [495]. In the case of just one excited electronic state, this method reduces to Heller’s gradient approach.

6.3 The photochemistry of *o*-nitrobenzaldehyde

Due to the enhanced intensities in resonance Raman spectroscopy when compared to off-resonance Raman, this method is well suited for the detection and investigation of transient species in low concentrations. By applying special time-resolved techniques such as femtosecond stimulated Raman spectroscopy (FSRS, see Ref. [528] for a review), it is possible to track chemical reactions following photoexcitation with high time-resolution. Basically, Raman spectra are recorded as a function of time after an initial pump laser pulse, so that intermediate products and transient species can be identified on the basis of their characteristic Raman bands.

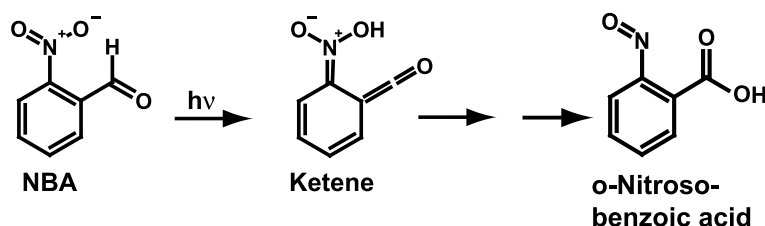
This was exploited in recent years to study the intricate photochemistry of nitroarenes, which has adverse and benevolent aspects. Nitroarenes are very common — yet toxic — industrial chemicals and thereby (potential) pollutants. In the environment nitroarenes will absorb solar UV radiation. This can degrade these components resulting in secondary pollutants. (The World Health Organization has compiled production data, environmental and health hazards of the parent compound of nitroarenes, nitrobenzene, in Ref. [529].) The benevolent aspect is that certain nitroarenes serve as photolabile protecting groups in organic synthesis [530]. These groups have been employed in numerous caged compound experiments [531] and in the automated synthesis of oligonucleotides for DNA chips [532].

The mechanisms of the primary photoprocesses of these compounds have been studied by Yip *et al.*, who performed picosecond transient absorption experiments on various nitroarenes [533–537]. Mostly, they observed the formation of the primary photoproducts within their instrumental response function of ~ 30 ps. Thus, they could only report an upper boundary for the formation time of the order of ~ 30 ps. Schwörer and Wirz [538] performed experiments with a higher time-resolution on the photo-tautomerisation of nitrotoluene. Yet, their paper does not focus on the primary processes.

An investigation on a prototypical reactive nitroarene, *ortho*-nitrobenzaldehyde (NBA),

was recently started by Laimgruber *et al.* [539]. As early as 1901 Silber and Ciamician [540] reported that when illuminated, NBA transforms into nitrosobenzoic acid. The quantum yield of the transformation is ~ 0.5 nearly irrespective of the solvent [541]. Time-resolved experiments by Yip and Sharma [535] and recent ones by Laimgruber *et al.* [539] gave evidence that this transformation involves several elementary steps. It is commonly assumed [530] that the primary step in *ortho*-substituted nitroarenes is a hydrogen transfer from the substituent to the nitro group. For NBA this transfer should result in the formation of a ketene (see Figure 6.1) [535, 539, 541, 542]. Indeed, such a ketene could be cryo-trapped in an argon matrix [542]. In a femtosecond IR experiment [539] the $\sim 2100\text{ cm}^{-1}$ resonance characteristic for a ketene [543] was seen to rise in $\sim 400\text{ fs}$. The ketene lifetime is strongly dependent on the solvent [535, 539]. In protic solvent it is $\sim 100\text{ ps}$ or below whereas it is of the order of nanoseconds in aprotic ones. In the latter solvents, e.g., in acetonitrile [518], one can therefore examine the structural details of a vibrationally relaxed ketene.

Figure 6.1: Schematic representation of the photochemistry of NBA. Photoexcitation triggers a hydrogen transfer process which results in a ketene intermediate. Subsequent reactions yield the final nitroso product.



In the following, we will present TDDFT-based Raman spectra and compare them to recent results from FSRS [518] addressing the structure of the ketene intermediate. Since the experimental spectra are subject to a resonance enhancement we expect that normal Raman calculations are not appropriate since Placzek's polarizability theory for Raman scattering [328, 483, 544] breaks down in this case. Therefore, resonance Raman calculations based on Heller's time-dependent approach (see Section 6.2.3) are carried out, for which we employ electron-phonon coupling constants from TDDFT calculations.

6.3.1 The resonance Raman spectrum of the ketene intermediate

In this section we will first validate the (TD)DFT approach by analyzing the resonance Raman spectrum of NBA, for which an experimental *steady-state* spectrum is available. Subsequently, we will use the same approach for the transient ketene intermediate and compare the theoretical findings with the FSRS spectra. Technical details of the calculations can be found in Appendix B.

Starting from the BP86/TZP optimized structure of NBA (see Figure 6.2), electronic excitations were calculated seeking states which contribute to a (pre)-resonance Raman enhancement. In the following, we will try to identify the important excited states in the experimental spectrum. Then, we will compare the calculated SAOP excitation energies and oscillator strengths to those from B3LYP calculations, so that we can finally map

the calculated states to those experimental transitions for which resonance conditions are fulfilled. Note that an assessment of the oscillator strengths obtained from different density functional schemes can be found in Ref. [545].

Figure 6.2: Optimized (BP86/TZP) structure of NBA.

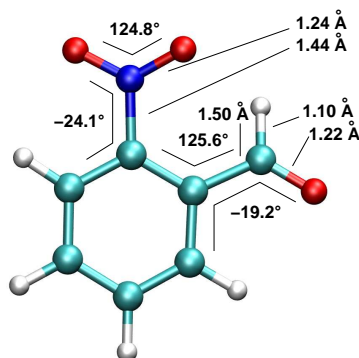
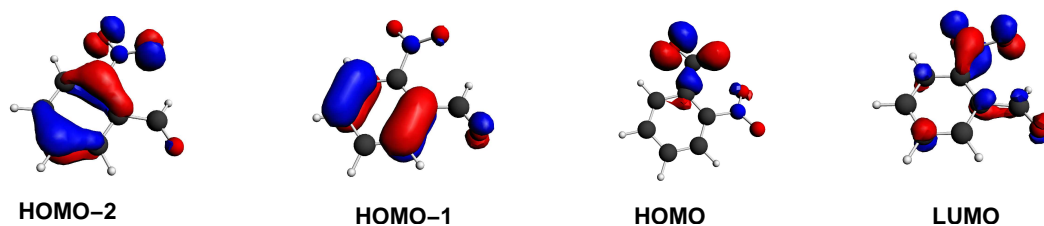


Figure 6.3: Isosurface plots of the molecular orbitals (SAOP/TZP) involved in the lowest electronic excitations of NBA.



A comparison of the laser wavelength of 388 nm with the experimental absorption spectrum of NBA shows that the incident light beam corresponds to an excitation into the long-wavelength tail of the spectrum [518]. Based on the decomposition of the experimental absorption spectrum in Ref. [518] the most probable state in resonance as deduced from experiment would be the first excited singlet state with a maximum at 343 nm in acetonitrile, which was assigned to a $n\pi^*$ transition. This state, however, has a rather low oscillator strength of $5.2 \cdot 10^{-3}$. It might thus be possible that also the second excited state plays a role for the resonance enhancement. This state is experimentally found at 297 nm in acetonitrile and was assigned to a $\pi\pi^*$ transition. Although it is much higher in energy, it could still be important since the absorption band is broad and it has a higher oscillator strength of 0.0306 (in the experiment). Table 6.1 shows the calculated excitation energies, oscillator strengths, and the dominant orbital transitions obtained from our SAOP calculation. In this calculation, the lowest unoccupied molecular orbital (LUMO) of NBA is a π^* orbital located on the nitro group (see Figure 6.3). Hence, transitions from the occupied π orbitals of the benzene ring to the LUMO are expected to suffer from the general problem of TDDFT to

Table 6.1: Calculated (SAOP/TZP and B3LYP/TZVP) excitation energies E_{ex} (in units of eV) and oscillator strengths f for NBA. Experimental values deduced from the decomposition of the absorption spectrum of for NBA [518] in acetonitrile are given for comparison.

type	dominant contr.	SAOP/TZP		B3LYP/TZVP		exp.	
		E_{ex}	f	E_{ex}	f	E_{ex}	f
$n\pi^*$	HOMO \rightarrow LUMO	2.53	0.0005	3.38	0.0006	3.61	0.0052
$\pi\pi^*(\text{CT})$	HOMO-1 \rightarrow LUMO	3.40	0.0165	4.26	0.0133	4.73	0.1012
$\pi\pi^*$	HOMO-2 \rightarrow LUMO	3.54	0.0280	3.75	0.0168	4.17	0.0306

describe charge-transfer excitations, see Section 3.3. Although this does not mean a complete failure as in the case of long-range charge-transfer excitations (see Section 3.3), it is well-known that such excitation energies in nitrobenzenes are underestimated by TDDFT [546, 547].

In order to identify problems related to the CT character of certain transitions, we also calculated excitation energies using the B3LYP hybrid functional for a structure optimized with B3LYP/TZVP. The resulting excitations were mapped to the SAOP results on the basis of the orbital transitions involved (see Table 6.1). An additional low-lying state with small oscillator strength (not shown in Table 6.1), which corresponds to a HOMO \rightarrow LUMO+1 orbital transition, was found at 3.64 eV (SAOP) and 4.12 eV (B3LYP). This state is not considered to be important for the resonance Raman scattering because of its low intensity and relatively high excitation energy. Since the B3LYP calculations partly (though not sufficiently) correct for the failure in case of CT transitions of the ALDA kernel applied in connection with SAOP TDDFT calculations, we expect significant shifts for those excitations that are of CT type. By comparing the SAOP and B3LYP data in Table 6.1 it can be seen that there are large differences for the first and second excited-state energies of the SAOP calculation in comparison to B3LYP. The reason for the deviation in case of the $\pi\pi^*(\text{CT})$ excitation is certainly its CT character, and complete active space self-consistent field calculations with second-order perturbation theory (CASPT2) on the corresponding transitions in nitrobenzene suggest typical excitation energies of 4.99 eV [548]. In contrast to this, the discrepancy for the $n\pi^*$ transition occurring within the NO₂ group is not obvious in terms of the orbital transitions. For the third excited state, which is of $\pi\pi^*$ type and also shows a partial CT contribution, SAOP and B3LYP are in much better agreement with a deviation of 0.21 eV. The calculated excitation energies from both calculations are much lower than the ones determined on the basis of a Gaussian decomposition of the experimental absorption spectrum in acetonitrile. An additional calculation using the approximate coupled cluster doubles model CC2 and Dunning’s correlation consistent valence triple- ζ basis with polarization functions (cc-pVTZ) with the RI-CC2 program of the TURBOMOLE suite [205] resulted in an excitation energy for this $\pi\pi^*(\text{CT})$ state of 4.71 eV and is thus in accordance with the experimental results. However, it turned out that this coupled-cluster approach does not provide a reliable reference wavefunction for NBA based on the so-called D1 diagnostic proposed in Ref. [549], so that also the RI-CC2 excitation energies are not fully trustworthy.

The values of the experimental excitation energies are of course also subject to uncertainties. They were obtained assuming Gaussian line shapes and a certain number of Gaussian components. Either assumption can be questioned. Nevertheless, large discrepancies between the TDDFT calculations and experiment remain. The assignment of the excited states to be considered for the resonance enhancement, i.e., the $n\pi^*$ and the $\pi\pi^*$ state identified on the basis of the experimental absorption spectrum, is less complicated. Apparently, the first transition ($n\pi^*$) from the SAOP calculation fits best to the applied laser energy of 3.20 eV (388 nm) if we take into account that the SAOP excitation energies are too small. The second excited state obtained with SAOP is severely affected by the CT problem and should appear at much higher energies, so that the third excited state ($\pi\pi^*$) in the SAOP calculation (or the second excited state in the B3LYP calculation) corresponds to the broad experimentally observed state at 4.17 eV (297 nm). These two states will thus be considered in the following. In spite of the problems of TDDFT to reproduce the correct vertical excitation energies, the derivatives of the excitation energies along the normal coordinates as needed for the calculation of resonance Raman intensities will be much less affected, since they will — to a large extent — be determined by the change in the energies of the orbitals involved in the transition. Since neither SAOP nor B3LYP are able to reproduce the *vertical* excitation energies accurately, we restrict ourselves to the discussion of the SAOP results for the resonance Raman spectra. It will be shown in Section 6.4 that non-hybrid exchange–correlation functionals yield reliable resonance Raman intensities under similar conditions.

Figure 6.4: Comparison of experimental (solid, black) and computed (SAOP/TZP) Raman spectra (dotted, colored). Lower graph NBA. Upper graph ketene. Intensities are given in arbitrary units (a.u.). To reproduce the experimental linewidth the theoretical stick spectra were convoluted with Gaussian line shape functions with a width of 25 cm^{-1} . For NBA resonance with the first excited state and for the ketene resonance with the second one was assumed.

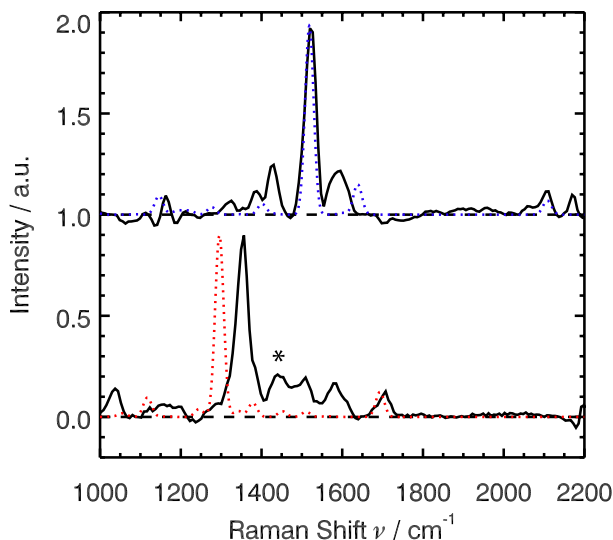
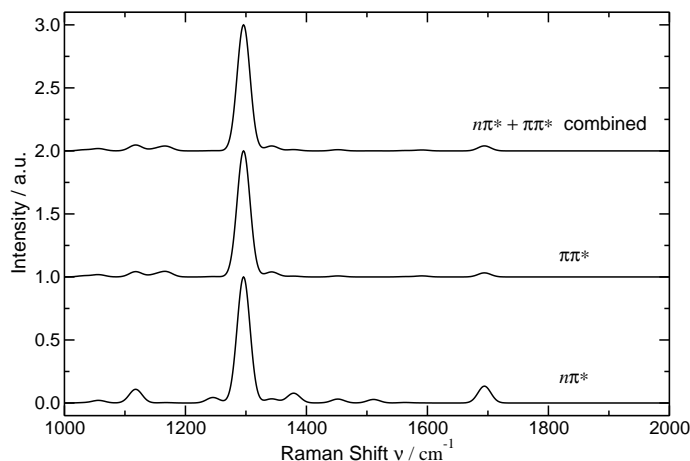


Figure 6.5: Calculated (SAOP/TZP; intensities in arbitrary units) resonance Raman spectra for NBA using Heller’s time-dependent formalism. Lower panel: resonance assumed for the first excited state ($n\pi^*$); middle panel: resonance assumed for the third excited state ($\pi\pi^*$; second excited state in experiment); upper panel: both states included in the calculation. All spectra are normalized. Stick spectra were convoluted with Gaussian line shape functions with a width of 25 cm^{-1} .



We calculated the resonance Raman intensities for the lowest excited states of NBA with SAOP/TZP based on the time-dependent formalism described in Section 6.2.2. In order to analyze the importance of the two excited states that we identified as potentially involved in the resonance Raman scattering of NBA ($n\pi^*$ and $\pi\pi^*$), we compare the spectra obtained when considering (i) only the first excited state ($n\pi^*$), (ii) only the third excited state (in the SAOP calculation; second excited state in experiment, $\pi\pi^*$), and (iii) both of these states simultaneously in Figure 6.5. Note that intensities are not in general additive in case of several excited states in resonance according to Eqs. (6.1) and (6.4), see also Refs. [550,551]. Another difficulty for several states in or close to resonance is that the energy gap between the excited states can play a crucial role for the total intensity. Since the *vertical* excitation energies from the TDDFT calculations turned out not to be fully trustworthy for NBA, we simulated the resonance Raman spectrum with the combined effect of both states assuming the *experimentally* determined excitation energies of 3.61 and 4.17 eV, and a laser wavelength of 388 nm. All spectra shown in Figure 6.5 are normalized, so that their absolute intensities are not directly comparable. The $\pi\pi^*$ transition has a larger contribution on an absolute scale than the $n\pi^*$ transition due to its much larger transition moment, so that the features of the spectrum obtained for the third excited state in resonance also dominate the spectrum in which both states were considered. In comparison to the experimental spectrum in Figure 6.4 we note that all three calculated spectra reproduce the intense feature for the NO_2 stretch vibration. The calculated wavenumber of 1296 cm^{-1} underestimates the experimental one at 1350 cm^{-1} considerably, which is rather unusual for frequency analyses based on the BP86 functional [552]. The peaks above 1350 cm^{-1} up to 1700 cm^{-1} in the experimental spectrum apparently agree best with the features in the computed spectrum where the first excited state ($n\pi^*$) is assumed to be in resonance (see Figure 6.4). This could

mean that either the ratio of the calculated transition moments for the $n\pi^*$ transition in comparison to the one obtained for the $\pi\pi^*$ transition is too small, or that inaccuracies in the experimental decomposition affect the outcome of the resonance Raman calculation. At the present stage, the best strategy to decide which state is in resonance appears to be a comparison of experimental and calculated spectra (see also Ref. [515]).

Figure 6.6: Optimized (BP86/TZP) structure of the ketene intermediate.

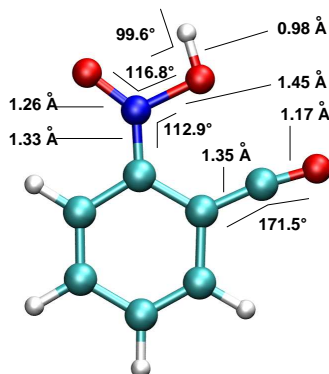
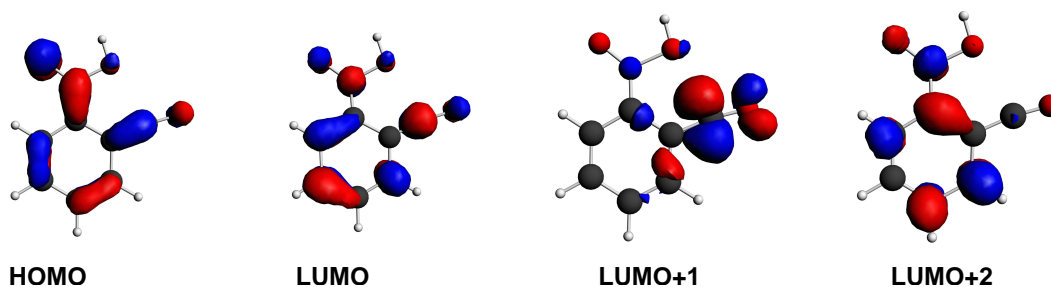


Figure 6.7: Isosurface plots of the molecular orbitals (SAOP/TZP) involved in the lowest electronic excitations of the ketene intermediate.



The ketene intermediate is formed in a hydrogen transfer process from the aldehyde substituent to the nitro group. It is most likely that after transfer the hydrogen atom is bonded to the oxygen of the nitro group next to the (former) aldehyde function (*Z*-form). The optimized structure of this *Z*-form is planar, the hydrogen atom attached to the nitro group points away from the ketene function and this function is slightly tilted (Figure 6.6). The SAOP/TZP calculation yields three transitions in the spectral range of interest which are located at 2.12 eV (oscillator strength $f = 3.5 \cdot 10^{-5}$), 2.61 eV ($f = 0.0804$), and 4.10 eV ($f = 0.0802$). The dominant orbital transitions in this case are the HOMO \rightarrow LUMO+1, HOMO \rightarrow LUMO, and HOMO \rightarrow LUMO+2, respectively (see Figure 6.7). Again, a B3LYP/TZVP calculation carried out for comparison yields larger excitation energies, but the disagreement is only about 0.2 eV for the first two

transitions (2.31 eV, $f = 3.1 \cdot 10^{-5}$ and 2.84 eV, $f = 0.1125$) and about 0.4 eV for the third one (4.51 eV, $f = 0.1180$). Hence, the deviation is much smaller than in case of NBA.

The first transition is not observed in the experimental spectrum assigned to the ketene intermediate given in Ref. [518]. This could very well be due to its low oscillator strength. The second transition, which is predicted to be more intense and to peak at 2.61 eV (480 nm, SAOP/TZP), is in line with the experimental spectrum which features a band peaking at 440 nm. The experimental spectrum hints to a further intense transition at ~ 300 nm (4.13 eV) again in accordance with the SAOP/TZP calculation. The wavelength of the Raman pump pulse is within the envelope of the 445 nm transition and so this transition will be dominantly responsible for the resonance Raman enhancement. The resonance Raman spectrum computed for this transition is in good agreement with the experimental one (Figure 6.4). In both the experimental and the theoretical spectrum a weak resonance at ~ 2100 cm^{-1} is observed. This peak is due to the stretch vibration of the central carbon atom in the ketene function. Because of the lower signal-to-noise ratio of the set-up employed in the foregoing experimental study [539] this mode was not observed by Raman spectroscopy heretofore. In that study, advantage of the large IR cross section of this mode was taken and its IR signature recorded. Improvements described in Ref. [553] subsequently enabled the detection of this resonance also by means of FSRS [518]. The next resonance in the theoretical spectrum, which is accompanied by a very weak peak at its low frequency edge, is located at 1639 cm^{-1} . These two bands might correspond to the experimental band at 1600 cm^{-1} which is broader than the other resonances pointing at overlapping bands. The 1639 cm^{-1} mode has a large N–C stretch contribution. Its high frequency points to a double bond between the nitrogen atom of the nitro group and the ring. In both the theoretical and the experimental spectrum, the most intense band is located at ~ 1520 cm^{-1} . This mode can be described as an in-phase motion of the two formal double bonds in the ring. The good agreement for these three stretch vibrations strongly support the valence bond structure of the ketene intermediate depicted in Figure 6.1. The other modes at lower frequencies have mostly hydrogen in-plane deformation character. Also for them the agreement with the experimental data is reasonable, but they are less informative in terms of structure.

6.3.2 Conclusions for photochemical intermediates

The comparison of the TDDFT calculations to the FSRS data allowed us to characterize the first ground-state intermediate in the photochemistry of NBA. This intermediate is a ketene which is formed via a hydrogen transfer from the aldehyde to the nitro-substituent. Evidence for the population of the electronic ground state of the ketene comes the fact that the experimental Raman spectrum could be well reproduced in the TDDFT-based resonance Raman calculations, which have been performed for the ground state of the ketene intermediate. The reliability of the TDDFT-based calculation of resonance Raman intensities was confirmed for the steady-state spectrum of *o*-NBA, in spite of the problems for the vertical excitation energies. The experimental and computed Raman spectra feature resonances which are very characteristic for the single-double bond pattern of the ketene intermediate, and thus underline that resonance Raman

spectroscopy can be regarded as a chromophore-specific type of spectroscopy. If the ketene were in an electronically excited state the respective bond orders should be different and thereby the Raman spectrum. Finally, we would like to note that also the transient absorption spectrum recorded in Ref. [518] supports this finding.

6.4 Photoexcitation processes in artificial photosynthesis models

6.4.1 Ruthenium–polypyridyl clusters as models for photosynthetic units

The importance of light-harvesting complexes in natural photosynthetic systems has already been discussed in Section 5.3 for the LH2 unit of purple bacteria. In general, natural antenna systems mainly consist of extended supermolecular aggregates of (bacterio)chlorophyll *a* and *b*, i.e., of substituted tetrapyrroles coordinated to a central manganese atom, and of carotenoids [554]. During the past years, more and more attempts are made to mimic these biological systems by creating artificial photosynthetic units for solar energy conversion [422]. The analogs of chlorophyll in these artificial systems are often either zinc porphyrin chromophores [555, 556], or ruthenium–polypyridyl and related complexes. The latter play a central role as photoactive components [557, 558], e.g., in dye-sensitized photovoltaic devices [559, 560], or as model compounds for energy-transfer and charge-separation processes [561]. In the context of artificial photosynthesis, ruthenium–polypyridine complexes are of particular interest in combination with an electron-donating manganese cluster as functional models for the P_{680} complex in photosystem II of green plants [562]. Related applications include the photocatalytic generation of hydrogen at room temperature and in homogeneous solution by [RuPd] complexes [563].

The initial steps involved in the photoexcitation of ruthenium–polypyridine complexes can in most cases be described as a transition from the singlet ground state to the first excited singlet state, followed by a very fast inter-system crossing to the lowest-lying triplet state [564]. Investigations using femtosecond time-resolved spectroscopy suggest that a subsequent charge transfer from Ru to Pd takes place in systems containing one or more additional Pd center(s) [564], like the tetranuclear $[Ru_2Pd_2]$ complex $\{[(tbbpy)_2Ru(tmbi)]_2[Pd(allyl)]_2\}^{2+}$ reported in Ref. [565] (*tbbpy* = 4,4'-di-*tert*-butyl-2,2'-bipyridine, *tmbi* = 5,6,5',6'-tetramethyl-2,2'-bibenzimidazolate; see the lower part of Figure 6.8 and Figure 6.9).

The tetranuclear $[Ru_2Pd_2]$ complex can therefore be regarded as a small model for an antenna system (the [Ru] subunits) linked to a possible reaction center (the [Pd] subunits) via a bibenzimidazolate bridge. Since the [Ru] subunits take part in the charge transfer, they may, in addition to their role as antennae, also be interpreted as a part of the reaction center. What makes the $[Ru_2Pd_2]$ complex special compared to, e.g., its flat $[Ru_2Cu_2]$ analogon [565], is its roof-like structure, in which the two central [Pd] fragments constitute the roof ridge and are thus easily accessible for potential reactants. Although photocatalytic activity of the $[Ru_2Pd_2]$ complex has not been shown yet, this system can serve as a prototype for photosystems with exponents reactive centers, for which our results are expected to be of significance.

The goal of this study is to investigate the very first step in the photoexcitation of

Figure 6.8: Structures of the two ruthenium–bipyridyl systems under study: $[(\text{tbbpy})_2\text{Ru}(\text{tmbiH}_2)](\text{PF}_6)_2$ (**1**; top) and $\{[(\text{tbbpy})_2\text{Ru}(\text{tmbi})]_2[\text{Pd}(\text{allyl})]_2\}(\text{PF}_6)_2$ (**2**; bottom).

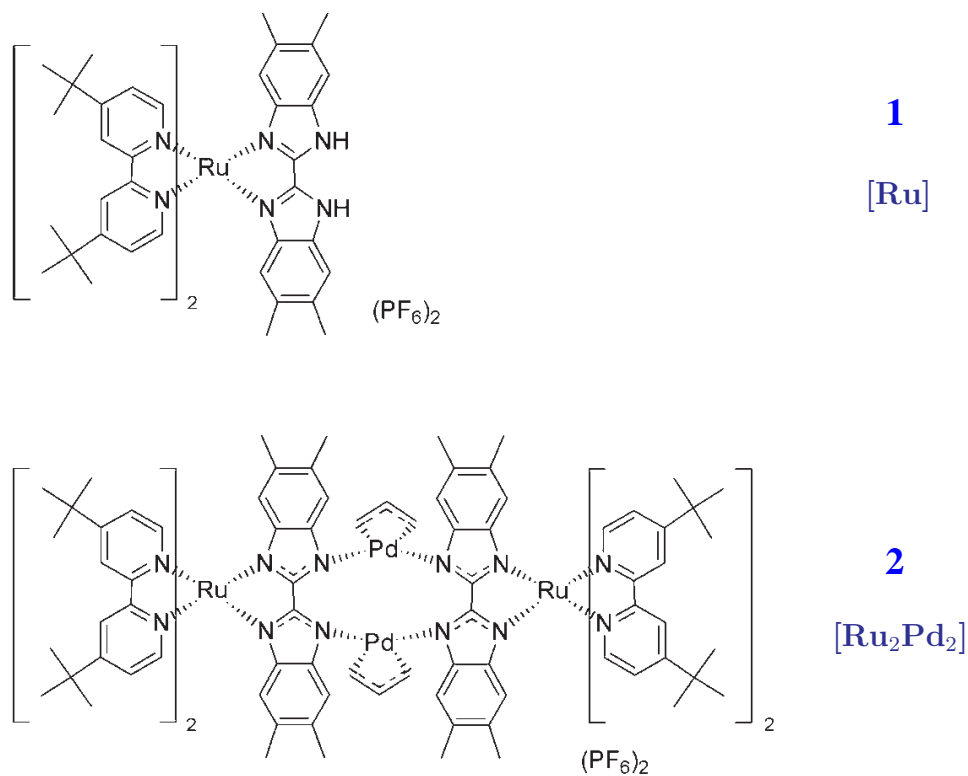
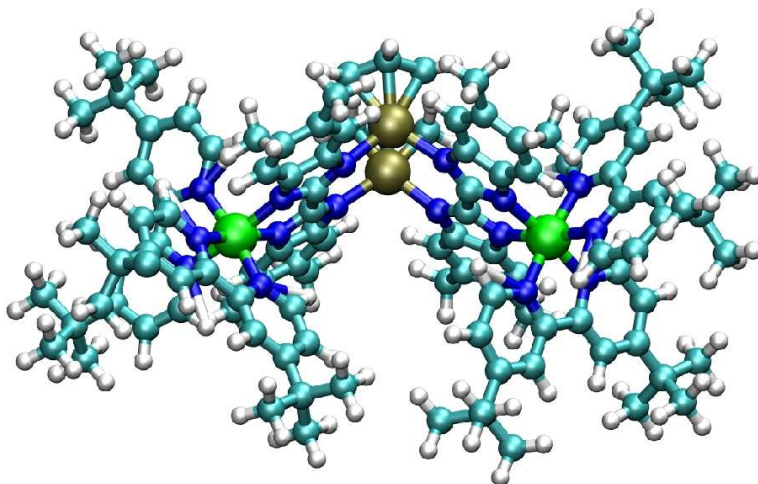


Figure 6.9: Roof-like structure of $[\text{Ru}_2\text{Pd}_2]$ (**2**). Structure optimization: BP86/TZVP.



the tetranuclear $\{[(\text{tbbpy})_2\text{Ru}(\text{tmbi})]_2[\text{Pd}(\text{allyl})]_2\}^{2+}$ complex, i.e. the transition to the excited singlet state on the basis of resonance Raman spectroscopy. We compare first-principles quantum chemical calculations relying on density functional theory to experimental resonance Raman spectra [508]. These calculations serve two purposes: First, the comparison of the calculated spectra to the measured ones provides an excellent means to assess the feasibility and reliability of currently available quantum chemical methodology. This holds in particular for the capability of the short-time approximation in connection with TDDFT to predict resonance Raman spectra of ruthenium–bipyridyl compounds. Second, and more important, the calculations provide insight into the electronic mechanisms involved in photoexcitation not available in this detailed resolution from experiment. From theory, we hence gather detailed information on the interconnection between electronic structure and vibrational modes in the photoexcitation. Local contributions to the most intense resonance Raman peaks may be identified by inspecting the associated calculated normal modes, and the nature of the transition to the excited singlet state may be characterized by analyzing the electronic structure in terms of Kohn–Sham orbitals mainly involved in the description of the excitation by TDDFT.

The photoexcitation is supposed to be located uniquely on the [Ru] fragment, the resonance Raman spectrum of the tetranuclear $[\text{Ru}_2\text{Pd}_2]$ complex is thus expected to be very similar to the one of its peripheral building block, the mononuclear complex $[(\text{tbbpy})_2\text{Ru}(\text{tmbiH}_2)]^{2+}$ (see the upper part of Figure 6.8). In order to test this assumption, resonance Raman spectra were also recorded and calculated for the smaller mononuclear [Ru] complex. Details concerning the experimental determination of the spectra are reported in Ref. [508], while technical details of the calculations presented here are given in Appendix B. The [Ru] and the $[\text{Ru}_2\text{Pd}_2]$ complexes will be denoted as **1** and **2**, respectively, in the following.

6.4.2 Analysis of resonance Raman spectra

Because of the size of the complexes under study, Heller’s gradient approximation as outlined in Section 6.2.3 in connection with TDDFT [506] is the method of choice for the calculation of the resonance Raman spectra, and was thus applied to obtain the spectra shown in the following. The comparatively small [Ru] complex **1** serves as a test case for the dependence of calculated resonance Raman spectra on the choice of the density functional. The calculation of the resonance Raman spectrum may be divided into three steps: The optimization of the geometric structure, the calculation of the vibrational normal modes and frequencies, and the subsequent calculation of the resonance Raman intensities. For the structure optimization as well as for the calculation of vibrational normal modes and frequencies, the BP86 density functional was employed. The optimized structure is in reasonable agreement with the one obtained from X-ray crystallography [565]. While bonding distances between the ruthenium centers and the ligands are reproduced very well, the bonding distances to palladium are overestimated by around 0.05 Å.

To investigate whether the BP86 functional is suited for the excited-state gradient calculations, the resonance Raman spectrum of the [Ru] complex **1** was calculated using both BP86 and B3LYP, respectively, for the excited-state gradients. For the normal

modes, BP86 was always employed. Despite the inability of BP86 to provide reasonable vertical excitation energies within a TDDFT framework (see below), the resulting spectra indeed agree very well (see Figure 6.10).

Figure 6.10: Comparison of experimental and calculated resonance Raman spectra of $[(\text{tbbpy})_2\text{Ru}(\text{tmbiH}_2)]^{2+}$ (**1**), assuming resonance with the first excited singlet state in the calculation. A Gaussian line-broadening with a half-width of 20 cm^{-1} was applied. The assignments “BP86” and “B3LYP” refer to the density functional used for the excited-state gradients needed for the intensities, while BP86/TZVP was employed for the force field in both cases. Wavenumbers in B3LYP and BP86 spectra are thus identical.

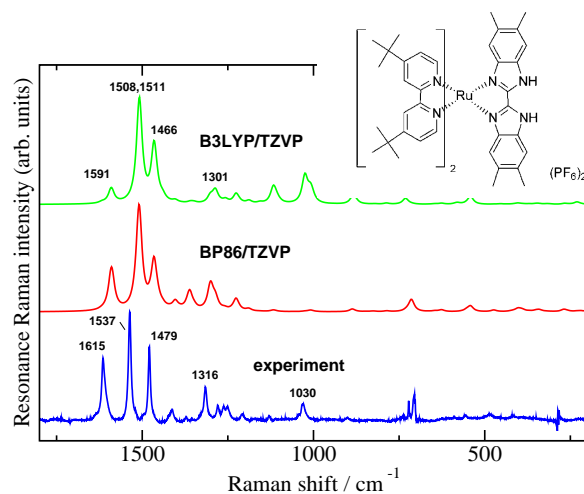
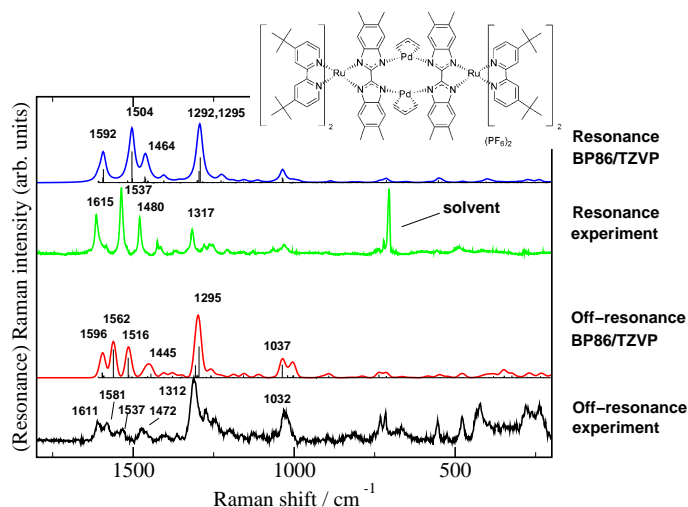


Figure 6.11: Comparison of experimental and calculated (BP86/TZVP) resonance Raman spectra of $\{[(\text{tbbpy})_2\text{Ru}(\text{tmbi})]_2[\text{Pd}(\text{allyl})_2]\}^{2+}$ (**2**). For the calculation, resonance with the second excited singlet state was assumed. Off-resonance Raman spectra are shown for comparison. A Gaussian line-broadening with a half-width of 20 cm^{-1} was applied.



This is due the fact that in the short-time approximation only the shape of the excited-state potential energy surface at the ground-state equilibrium structure is relevant, but not its vertical position. The excited-state gradient, which determines this local shape, is obviously described well with both functionals. This holds true, in particular, for the most characteristic part of the spectrum between 1200 and 1700 cm^{-1} . Small discrepancies can be observed for the spectral features between 1000 and 1200 cm^{-1} . Overall, the BP86 intensities are actually in better agreement with experiment than the B3LYP ones.

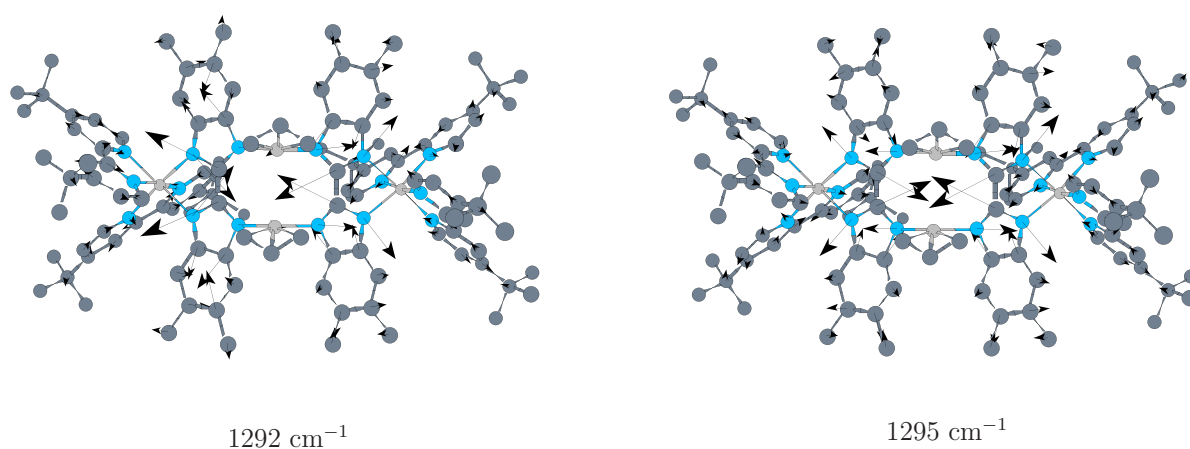
Thus, the resonance Raman spectrum of the much larger tetranuclear $[\text{Ru}_2\text{Pd}_2]$ complex **2** (containing 272 atoms) has been calculated using the BP86 density functional for both the normal modes and the resonance Raman intensities.

Figure 6.11 shows that also for the significantly larger tetranuclear complex **2**, the calculated spectrum agrees very well with the experimental one. Owing to the efficient BP86 calculations and to a combination of good parallelization and restart facilities provided by our SNF vibrational spectroscopy package [328], it is thus now possible to calculate the full spectrum of normal modes and vibrational frequencies for compounds of the size of the tetranuclear complex under study with remarkable accuracy. The calculated spectrum is indeed dominated by the $[\text{Ru}]$ fragment peaks. The most significant difference between the calculated spectra for the $[\text{Ru}]$ complex **1** and the $[\text{Ru}_2\text{Pd}_2]$ complex **2** is the peak around 1290 cm^{-1} , which is considerably more intense in the spectrum of **2**. This is mainly due to an amplification of resonance Raman scattering intensities associated with breathing-like vibrational modes of the RuN_2C_2 ring of the tmbl ligand (see Figure 6.12). In the experimental spectra, however, this amplification is much less pronounced. Furthermore, the measured spectrum shows a large signal at around 700 cm^{-1} which is not reproduced by our quantum chemical calculation. This peak is an artifact of the solvent spectrum subtraction procedure (the most intense Raman band of the CH_2Cl_2 solvent is centered around 713 cm^{-1}).

It should be noted that in the present example there is not a single excited state that is energetically clearly separated in the calculation, so that it can be unambiguously identified as the excited state in resonance with the laser beam. In experiment, an excitation into the lowest-energy absorption band of **2** is applied with a laser wavelength of 458 nm (2.71 eV). This absorption band is broad and structureless and extends from approximately 550 to 450 nm (or 2.25 to 2.75 eV) [564], so that the relative resonance Raman intensities may be expected to be rather insensitive to the exact excitation energy. As mentioned before, there are two main criteria that can be applied to identify states in the calculation that may be important for the resonance Raman spectrum: (i) the calculated energy difference for a given transition compared to the energy corresponding to the wavelength of the incident laser beam, and (ii) its oscillator strength. The comparison of transition energies is hampered by the fact that the calculated vertical TDDFT excitation energies depend strongly on the density functional. In particular, some of the low-lying excitations in the $[\text{Ru}_2\text{Pd}_2]$ complex **2** are clearly of the long-range charge-transfer type, for which generalized gradient approximation functionals such as BP86 (and the corresponding functional derivatives) are not suitable, see Section 3.3. As can be seen from Figure 6.13, there are pairs of nearly degenerate MOs located on either side of the “roof ridge”. The HOMO \rightarrow LUMO (S1 in Figure 6.13) and the HOMO-1 \rightarrow LUMO+1 (S3) transitions involve spatially separated orbitals with almost

no (differential) overlap, and the calculated excitation energies are (nearly) equal to the difference in the orbital energies. As outlined in Section 3.3, this is a characteristic feature of the long-range charge-transfer problem in TDDFT calculations. In general, the excitation energies for such transitions are dramatically underestimated, so that it is not likely that these states are in resonance under the experimental conditions employed here. In addition, pure long-range charge-transfer excitations also show a vanishing transition dipole moment, and are therefore neglected in the following.

Figure 6.12: Normal modes responsible for two of the most intense peaks in the $[\text{Ru}_2\text{Pd}_2]$ (**2**) resonance Raman spectra (BP86/TZVP). Hydrogen atoms have been left out for the sake of clarity.

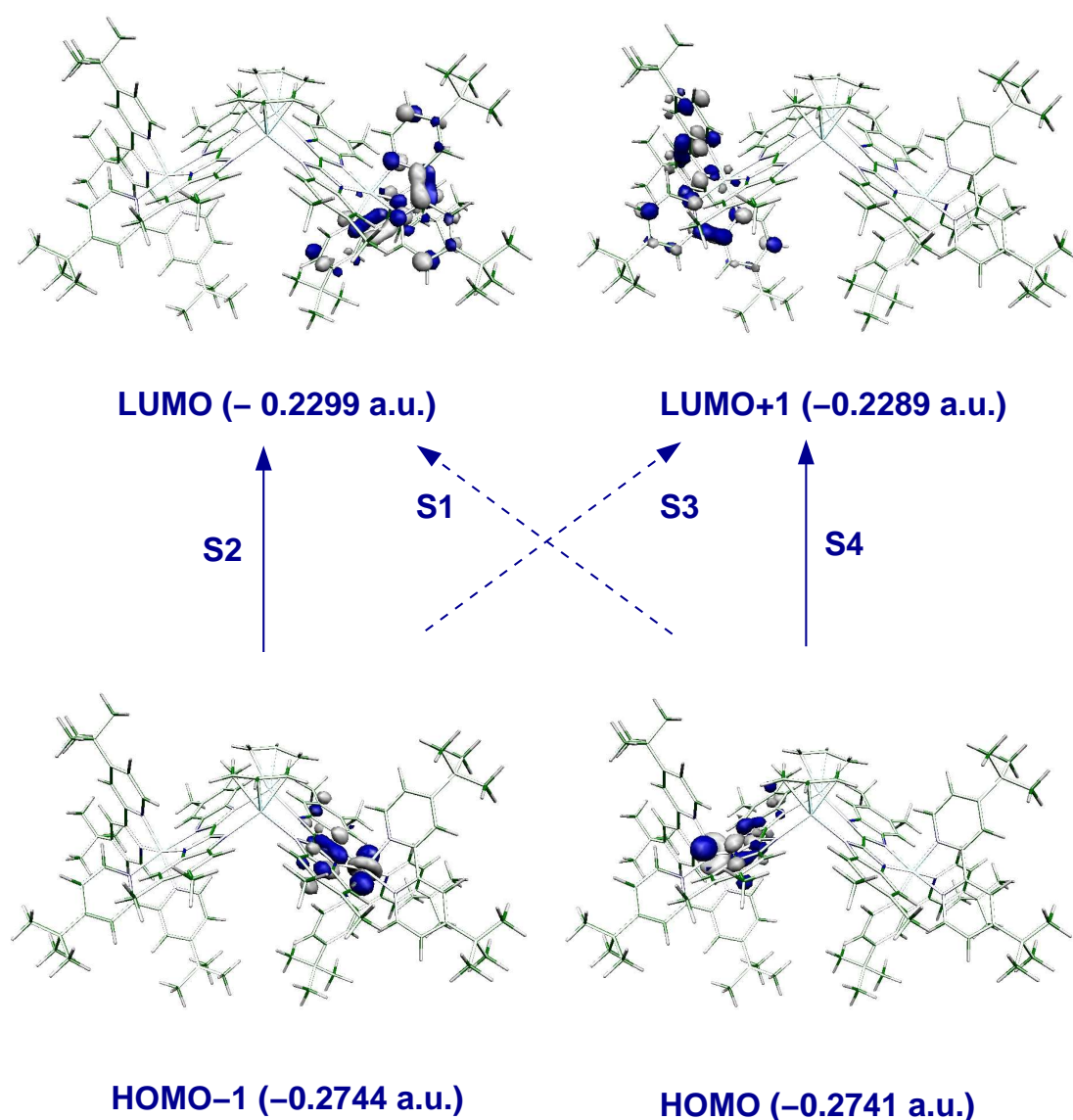


In the literature, the photoexcitation of ruthenium–bipyridyl complexes is described as initiated by an metal-to-ligand charge-transfer (MLCT) [566,567]. The four lowest-lying electronic singlet-to-singlet transitions are characterized predominantly by a transition from an occupied MO which has mainly metal d_{z^2} -character, with contributions from the π system of the bibenzimidazolate ligand, to a virtual MO with negligible metal contribution, which is delocalized over the π system of the two bipyridyl ligands. This fits very well into the picture of an initial MLCT.

We are rather interested in the MLCT excitations $\text{HOMO} \rightarrow \text{LUMO}+1$ (S4) and $\text{HOMO}-1 \rightarrow \text{LUMO}$ (S2). Transitions to both of these as well as to several other low-lying excited states have significant oscillator strengths and could therefore be important for the resonance Raman spectrum. The excitation energy again is not a very good criterion for the selection of the state in resonance: The BP86 results for the transitions denoted as S2 and S4 in Figure 6.13 are 1.23 and 1.26 eV, while the corresponding B3LYP excitation energies are 1.79 and 1.81 eV. Since these two excitations, which both have significant oscillator strengths, are spatially and energetically equivalent, we chose to concentrate on the S2 state. The choice of these two transitions is confirmed furthermore by the agreement of the qualitative picture of an MLCT transition with chemical intuition as well as by the excellent prediction of the measured spectra. It may be anticipated, however, that the measured resonance Raman spectrum contains contributions from several energetically close-lying states in resonance. To elucidate this point, we calculated spectra for six different low-lying excited states,

which all give rise to similar individual resonance Raman spectra (see the Supporting Information to Ref. [508]).

Figure 6.13: Frontier molecular orbitals dominating the excitations to the 4 lowest excited singlet states (denoted by S1 to S4) in the $[\text{Ru}_2\text{Pd}_2]$ complex **2** (BP86/TZVP). The corresponding orbital energies are given in parentheses. The orbital energies for the depicted pairs of occupied and unoccupied orbitals, respectively, indicate the somewhat imperfect C_s symmetry of the rooflike cluster, which was optimized without symmetry constraints. The small differences in these pairs of energies may be taken as an explanation for the localization of the orbitals on either half of the cluster.



We thus conclude from our results as follows: The resonance Raman spectrum of the $[\text{Ru}_2\text{Pd}_2]$ complex is dominated by vibrations located on the $[\text{Ru}]$ building blocks. This

result as well as an inspection of the Kohn–Sham molecular orbitals mainly involved in the TDDFT description of the vertical electronic excitations support the assumption that the initial photoexcitation step in the $[\text{Ru}_2\text{Pd}_2]$ system is a MLCT excitation on the $[\text{Ru}]$ fragments. The good agreement of the calculated resonance Raman spectra with the experimental ones indicates the more general ability to predict reliable resonance Raman spectra for ruthenium–polypyridyl complexes on the basis of Heller’s gradient approximation. This is of particular relevance for studies on biomimetic solar energy conversion, because ruthenium-based systems are among the most commonly employed and most intensely studied artificial light-harvesting antenna systems [557–563].

7. Resonance Raman Intensity-Tracking

7.1 Selectivity in theoretical resonance Raman spectroscopy

In Chapter 6 it was outlined that experimental resonance Raman spectroscopy is well suited to study complex molecular systems because of its selective enhancement of certain vibrations. It was also shown that the application of theoretical approaches to resonance Raman spectra has become feasible for larger molecules in recent years due to the development of reliable methods for the calculation of ground-state vibrational modes and excited electronic states [494, 495, 506, 515, 517, 523, 568, 569]. In particular the fact that frequency analyses based on density functional theory are very efficient [328] and yield harmonic frequencies that are usually in very good agreement with fundamental frequencies as obtained in experiment [552, 570] made it possible to clarify intricate features in complicated vibrational spectra [463, 571, 572]. An analysis on the basis of experimental information alone would be much more difficult in many cases, if possible at all. The development of the mode-tracking algorithm [468, 469, 573], which allows the selective calculation of a subset of pre-defined normal modes, offers the possibility to restrict the theoretical frequency analyses to subsets of the Hessian eigenvectors which are of relevance for a particular problem under study. A necessary condition for an efficient application of the mode-tracking algorithm is that at least a rough guess for the normal modes to be optimized can be provided. Various ways to obtain such a guess have been employed [397, 573–580]. For a recent review see Ref. [469].

While it is sometimes known which vibrations will get enhanced under resonance conditions, so that a guess for a mode-tracking calculation could be constructed, this may not be true in general for more complicated molecules, e.g., transition metal compounds [507]. We will therefore explore the possibility to use an algorithm based on the mode-tracking principle together with the information on the excited-state gradient in order to directly determine only the *intense* vibrations in a resonance Raman spectrum. I.e., we attempt to exploit the selectivity observed in experimental resonance Raman spectra also in the theoretical determination to enable calculations for, e.g., complex biomolecular systems. The approximate relative intensity of a vibration within Heller’s gradient approximation (see Section 6.2.3) is related to the projection of the excited-state gradient vector onto the corresponding normal mode. The method developed here uses this gradient vector as a guess vector in a mode-tracking calculation and subsequently focuses on vibrational normal modes with a large overlap with that vector. Of major importance for the efficiency of the method are the criteria according to which the intense modes are chosen and their convergence is assessed. The algorithm applied here is thus very different from, e.g., the approach presented in Ref. [463], in which the intensities were calculated in a mode-wise way *after* the vibrational frequencies and normal modes had been determined.

Although this algorithm should be of general use, we are in particular aiming at its application for resonance Raman investigations on (models for) proteins, since the structure elucidation of proteins is an important field of application for experimental resonance Raman spectroscopy. By analyzing the amide vibration wavenumbers and intensities [139,581,582], the secondary structure of proteins can be probed. If the excitation wavelength is tuned to energies at which bands of the aromatic amino acids tryptophan (Trp), tyrosine (Tyr), and phenylalanine (Phe) are selectively enhanced, information about hydrogen bonds and hydrophobicity of the environment and orientation of these chromophores can be obtained [581,583–586]. Resonance Raman spectroscopy is also a valuable method to aid the study of protein folding, as shown, e.g., in the investigation of variants of the E colicin-binding immunoprotein Im7 and their different conformational states [477].

In the following, we will first present the underlying theory and details of the algorithm and implementation (Section 7.2) before we study the approach for the calculation of resonance Raman intensities of uracil in Section 7.3. An application to models of the protein Im7 follows in Section 7.4.

7.2 Theory: Intensity-driven resonance Raman spectroscopy

In order to appreciate the algorithmic structure of the intensity-tracking approach, which focuses exclusively on the determination of high-intensity modes, we briefly review the algorithmically related, though conceptually very different mode-tracking protocol, which is solely based on the form of the collective motion provided as a guess.

7.2.1 The mode-tracking algorithm

The full details of the original mode-tracking algorithm have been presented in previous work [468,469,573]. An outline of the main steps is given in the following. In the mode-tracking algorithm the eigenvalues λ_i of the Hessian matrix are determined by employing a subspace iteration method like the Lanczos [587] or Davidson method [234]. In each iteration, approximate solutions for a subset of eigenvectors \mathbf{L}_i are obtained. This procedure can be applied to solve for a certain pre-selected mode (or, when using a block-Davidson method, several pre-selected modes), where the iterative algorithm will be carried out until the approximations of the selected eigenvectors are converged. Thus the diagonalization of the full mass-weighted Hessian \mathbf{H}^{mw} ,

$$(\mathbf{H}^{\text{mw}} - \lambda_i)\mathbf{L}_i = \mathbf{0} \quad (7.1)$$

is formally replaced by solving,

$$(\mathbf{H}^{\text{mw}} - \lambda_i^{(k)})\mathbf{L}_i^{(k)} = \mathbf{r}_i^{(k)}, \quad (7.2)$$

where $\mathbf{r}_i^{(k)}$ is the residuum vector for the approximate eigenvector $\mathbf{L}_i^{(k)}$ in iteration k . The exact eigenvectors of the Hessian provide the unitary transformation matrix from mass-weighted Cartesian (\mathbf{R}^{mw}) to mass-weighted normal coordinates (\mathbf{Q}) according to,

$$\mathbf{Q} = \mathbf{L}\mathbf{R}^{\text{mw}}, \quad \mathbf{R}^{\text{mw}} = \mathbf{L}^\dagger\mathbf{Q}. \quad (7.3)$$

In a somewhat sloppy language, the eigenvectors \mathbf{L}_i , i.e., the columns of the matrix \mathbf{L} are sometimes denoted as “normal mode vectors” or “normal modes”.

At the beginning of the mode-tracking calculation, an approximation \mathbf{b}_i for each normal mode to be optimized has to be chosen. These “guess vectors” represent the first basis vectors in which the approximate eigenvectors are expanded. In the following step, the vectors $\boldsymbol{\sigma}_i$ are determined,

$$\boldsymbol{\sigma}_i := \mathbf{H}^{\text{mw}} \mathbf{b}_i, \quad (7.4)$$

which are calculated numerically as directional derivatives of the gradient of the electronic energy with respect to the basis vectors. The vectors $\boldsymbol{\sigma}_i$ are used for the calculation of the elements of the small Davidson matrix $\tilde{\mathbf{H}}$,

$$\tilde{H}_{ji} = \mathbf{b}_j^T \mathbf{H}^{\text{mw}} \mathbf{b}_i = \mathbf{b}_j^T \boldsymbol{\sigma}_i. \quad (7.5)$$

By diagonalization of the Davidson matrix, approximate eigenvalues $\lambda_i^{(k)}$ and eigenvectors $\mathbf{L}_i^{(k)}$ of the full Hessian can be constructed. Subsequently the residuum vectors $\mathbf{r}_i^{(k)}$ are calculated for all $\mathbf{L}_i^{(k)}$ according to Eq. (7.2).

Afterwards, the root homing step is carried out, in which those approximate eigenvectors from the full set $\{\mathbf{L}_i^{(k)}\}$ are determined which correspond to the sought-for vibrations and shall thus be further optimized. This is typically done on the basis of the overlap with either the initial guess vector(s) or the approximate eigenvector(s) selected in the previous iteration.

In a subsequent convergence check it is tested whether the approximate normal modes are already sufficiently accurate. If not, new basis vectors are constructed according to

$$\mathbf{b}_{n_b+1} = \mathbf{X} \mathbf{r}_i^{(k)}, \quad (7.6)$$

where n_b is the number of basis vectors in use so far and \mathbf{X} is a preconditioner. In our previous investigations, it turned out that even without preconditioning, i.e. by formally choosing $\mathbf{X}^{(k)} = \mathbf{1}$, the algorithm can be applied very efficiently (cf. Ref. [573]).

7.2.2 Intensity tracking

Heller’s gradient approximation offers a way to estimate relative resonance Raman intensities on the basis of excited-state energy gradients (see Section 6.2.3). If this approximation is applicable, the calculation of relative intensities is even simpler than the calculation of off-resonance Raman intensities [506, 508, 515, 525, 588]. According to the criteria for the validity of the gradient approximation it can be inferred that it should work the better the more vibrational degrees of freedom there are in the molecule under study.

The mode-tracking algorithm as described above aims at finding those eigenvectors of the Hessian which resemble most closely the pre-defined collective motion. In contrast to that, intensity tracking aims at the determination of all normal modes of considerable intensity *without an intuitive guess for how these vibrations look like*. We will show in the following that Heller’s gradient approximation offers a way for such an intensity-driven approach for the case of resonance Raman spectroscopy since it can selectively provide information about the movement of the atoms in the intense vibrational modes.

The expression for the relative intensities i_j and i_k in the framework of the gradient approximation is given in Eq. (6.11), and is re-written here in terms of mass-weighted normal coordinates,

$$\frac{i_j}{i_k} = \left(\frac{V_j^Q}{V_k^Q} \right)^2 = \frac{\tilde{\nu}_k}{\tilde{\nu}_j} \left(\frac{V_j^Q}{V_k^Q} \right)^2, \quad (7.7)$$

where

$$V_j^Q = \left(\frac{\partial E_{\text{ex}}}{\partial Q_j} \right)_{\mathbf{Q}=0}. \quad (7.8)$$

The expression for relative intensities contains the wavenumbers and the gradient of the excited-state energy with respect to the mass-weighted normal coordinates. Although wavenumbers and normal modes of the spectrum are unknown before a vibrational calculation, the excited-state gradient with respect to Cartesian coordinates can be calculated analytically with a single calculation for many excited-state electronic structure methods, see Section 6.2.1.

We can write the expression for V_j^Q explicitly in terms of mass-weighted coordinates as,

$$V_j^Q = \sum_i \frac{\partial R_i^{\text{mw}}}{\partial Q_j} \left(\frac{\partial E_{\text{ex}}}{\partial R_i^{\text{mw}}} \right)_{\mathbf{R}=0} = \sum_i L_{ij} g_i^{\text{mw}} = \mathbf{L}_j \cdot \mathbf{g}^{\text{mw}}, \quad (7.9)$$

where we have introduced the mass-weighted gradient vector \mathbf{g}^{mw} ,

$$g_i^{\text{mw}} = \left(\frac{\partial E_{\text{ex}}}{\partial R_i^{\text{mw}}} \right)_{\mathbf{R}=0}, \quad (7.10)$$

and used Eq. (7.3) to determine

$$\frac{\partial R_i^{\text{mw}}}{\partial Q_j} = L_{ij}. \quad (7.11)$$

Eq. (7.9) thus shows that the excited-state derivative along a normal coordinate is equal to the corresponding expansion coefficient of the mass-weighted gradient vector in terms of normal coordinates, i.e., its projection onto the Hessian eigenvector. Since the intensity is proportional to $(V_j^Q)^2$, intense modes will have larger overlap with the excited-state gradient vector, so that the gradient resembles a particular normal coordinate the more closely the more intense it is. The excited-state gradient is thus a suitable initial vector for the mode-tracking of intense modes. Since the present approach tries to select and optimize *all* normal modes that carry a significant percentage of the total intensity, irrespective of the type of motion, the root homing procedure, i.e., the selection of eigenvector approximations for further optimization, has to be adapted, in order to choose the most intense modes.

During the intensity-tracking iterations, only approximate normal mode vectors are available at the beginning. An expression for the approximate relative intensity of mode j can be derived from Eq. (7.7),

$$i_{j,\text{rel}} = \frac{1}{\tilde{\nu}_j} \cdot (V_j^Q)^2 = \frac{1}{\tilde{\nu}_j} \cdot (\mathbf{L}_j \cdot \mathbf{g}^{\text{mw}})^2, \quad (7.12)$$

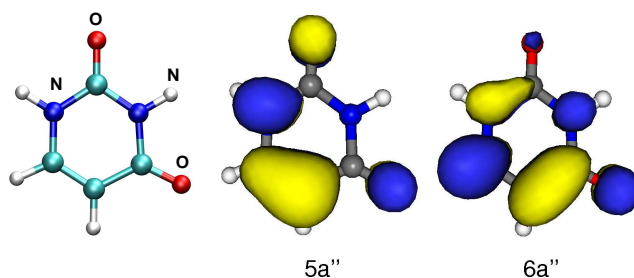
where the eigenvectors \mathbf{L}_j and wavenumbers $\tilde{\nu}_j$ have to be replaced by their current approximations.

Modes which according to Eq. (7.12) have a high approximate intensity are selected for further optimization. There are several possible schemes how to implement such a root-homing procedure, of which we have tested: (i) the selection of the N most intense modes in each iteration, (ii) the selection of all modes with a relative intensity larger than a certain threshold, or (iii) the selection of a certain number of modes in such a way that their relative intensities sum up to a certain percentage of the total intensity. The subsequent steps, i.e., convergence check and construction of new basis vectors, follow the standard mode-tracking procedure. The description of the most intense modes is iteratively improved until they are converged, so that we obtain an approximate resonance Raman spectrum which is accurate with respect to the most intense modes. The gain in efficiency compared to a conventional calculation of the resonance Raman spectrum should thus be the larger the more low-intensity modes are present in the spectrum, which will be automatically discarded in the intensity-tracking calculation.

7.3 Validation: Intensity-tracking for uracil

In order to validate the intensity-tracking algorithm, we study the resonance Raman spectrum for the second excited state of uracil, which has been well studied with various theoretical methods [495,506,589]. Uracil is a planar molecule and, within Heller's gradient approximation, resonance Raman active vibrations must be in that plane (a' symmetry). Our mode-tracking implementation does not consider the molecular symmetry for the calculations, but allows the creation of an orthogonal subspace against which new basis vectors are orthonormalized. The optimized C_s symmetric uracil structure, see Fig. 7.1, was obtained using B3LYP/TZVP and the gradient of the $2^1A'$ state at 5.25 eV was employed for the resonance Raman calculation. Since uracil is a planar molecule with $12 \times 2 = 24$ degrees of freedom in the xy -plane. Two of them represent translations and one is a rotation, so that there are 21 degrees of freedom for vibrational motion relevant for the current test.

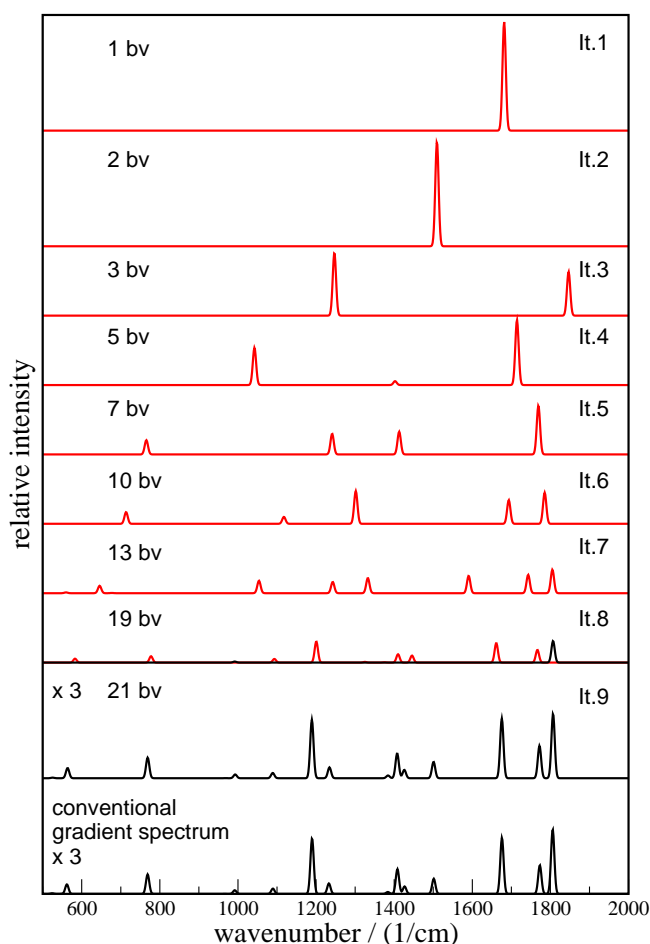
Figure 7.1: B3LYP/TZVP optimized structure of uracil (C_s symmetry) and molecular orbitals (B3LYP/TZVP) dominating the transition to the second excited state of uracil.



We expect the intensity-tracking algorithm to work best for electronic transitions localized on a small part of a larger molecule with localized vibrational modes. The uracil

molecule studied here does not at all fulfill this prerequisite, since the molecular orbitals involved in the electronic transition are basically delocalized over the entire molecule (see Fig. 7.1). Therefore, this small system represents the most critical test case for the convergence behavior of the intensity-tracking algorithm since the mode construction cannot benefit from intensity selection. This is reflected in the current example by the necessity to include all 21 basis vectors in order to converge the spectrum if rather strict convergence criteria are applied.

Figure 7.2: Intermediate results of the intensity-tracking resonance Raman calculation assuming resonance with the second excited state of uracil (B3LYP/TZVP; black: converged; red: not converged). The total number of basis vectors (bv) is given on the left. The relative intensities have a common scale, only the intensities in the lowest two panels are magnified by a factor of 3 for better comparability. The bottom panel shows a conventional gradient spectrum as a reference.



The intermediate and final spectra are depicted in Fig. 7.2 (note that all resonance Raman spectra are plotted applying a Gaussian broadening with a half-width of 10 cm^{-1}). The spectrum of the first iteration contains the intensity of all modes concentrated in one peak, which corresponds to the collective motion given by the excited-state gradient vector. Its approximate eigenvalue is already quite close to the frequency of the most

intense mode in the converged spectrum. In the following iterations, the intensity is distributed to more and better approximations of the normal modes (note that in Fig. 7.2 only vibrations between 500 and 2000 cm^{-1} are shown). Enlarging the basis leads to a shift in the wavenumbers and appearance of new modes. New approximate normal modes which carry a substantial fraction of the intensity are selected for further optimization in the root-homing step. Such modes may split up in subsequent iterations (cf. Fig. 7.2, iteration 3 to iteration 4). After a few iterations the most important features are obtained, i.e. the approximate frequencies of the intense peaks and their relative intensities do not change anymore. For example, the two most intense peaks already appear at approximately correct positions after three iterations. The spectrum of iteration 8 represents already a good approximation to the final spectrum. Several modes which are not converged according to the applied criteria hardly change compared to the next iteration. This suggests that the applied convergence criteria are too strict. Another important aspect for the convergence behavior of the spectra is the choice of the selected modes and thus the root-homing procedure, which will be analyzed in the next section. In a complete basis, the converged intensity-tracking spectrum and conventional gradient spectrum are essentially identical, see bottom of Fig. 7.2. The marginal remaining deviations are due to the fact that the numerical differentiations applied in both types of calculations make use of different basis vectors, so that they are affected by numerical noise in slightly different ways.

7.4 Resonance Raman spectra of Im7-based models

Intensity tracking is expected to be most valuable in cases of large molecules with a comparatively small number of intense vibrations. In the following, we will show how the iterative refinement of signatures in a resonance Raman spectrum can be optimized if these requirements are fulfilled. As an example, we study models derived from the Im7 protein (PDB entry: 1AYI), that all contain the skatole motif from the tryptophan residue, within Heller's gradient approximation.

This investigation requires several steps: First, the excited states of the core chromophore, i.e., the skatole moiety of the Trp residue, will be investigated in order to identify possible states in resonance, and its conventional gradient spectra are determined. Second, we will map the excited states for Im7-based models to those of skatole in order to identify the resonant states for their UV resonance Raman spectra. After these steps have been carried out, we will determine how the convergence behavior can be controlled and steered in such a way that it allows fast access to the characteristic signatures. Finally, we will apply the criteria obtained from these investigations in a model calculation of the resonance Raman spectrum for a large fragment of the Im7 protein.

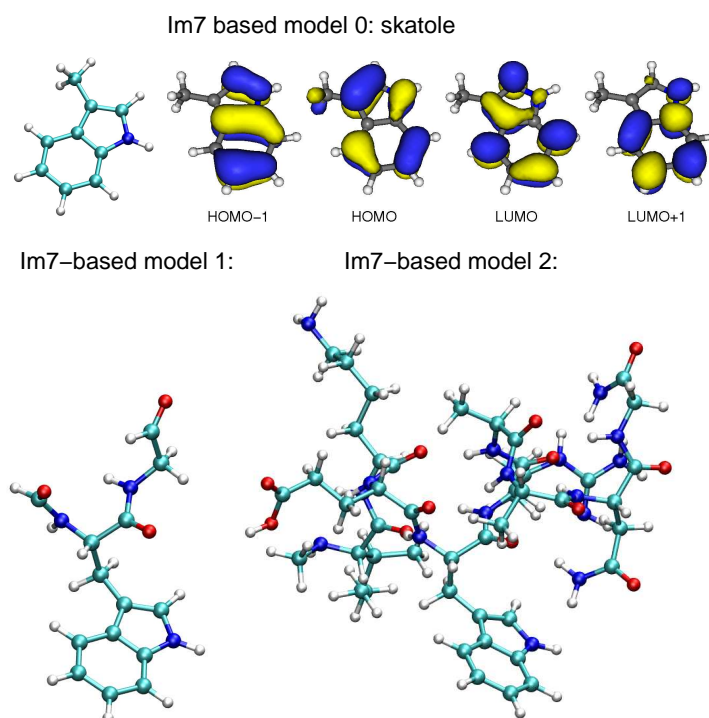
7.4.1 Preparatory calculations: Identification of resonating states

The resonance Raman spectra of Trp and its structural motif skatole show a rather strong dependence on the polarity and the hydrogen-bonding abilities of the surroundings, as was analyzed in detail before [581,584,586]. Therefore, the ultraviolet resonance Raman

spectrum of the Trp residue in Im7 was employed in order to investigate its solvent accessibility [477].

The calculation of resonance Raman spectra in Heller's gradient approximation requires as a first step the identification of the state responsible for the resonance enhancement. As mentioned in Section 6.2.3, the criteria that can be used for this purpose are the requirements that (i) the resonance condition with the incident light beam is fulfilled for the excited state and that (ii) the transition dipole moment for the corresponding transition is large. For the larger Im7-based models that we are aiming at, TDDFT is the only applicable first-principles method for excited states since it gives a good compromise between accuracy and computational cost, in particular for the valence excited states that are studied in here. However, the identification of important excited states is hampered also in the current example by the CT problem discussed in Section 3.3. The number of low-lying excited states is thus artificially increased in such calculations, and the oscillator strength of intense electronic transitions may be distributed over several close-lying excitations by spurious mixings [395].

Figure 7.3: B3LYP/TZVP optimized structures of skatole (C_s) and model **1** as well as the BP86/TZVP optimized structure of model **2**. Also shown are isosurface plots of the molecular orbitals (B3LYP/TZVP) involved in the lowest electronic excitations of skatole.



Therefore, we chose two models of different size for that part of the Im7 protein that contains the Trp fragment and mapped their excited states to those of the bare skatole chromophore. Note that the full Im7 protein also contains three tyrosine residues that are important for the total resonance Raman spectrum, which we ignored in our study in

order to set up model compounds in which one particular chromophore can be assumed to be responsible for the intensity pattern to be tracked.

In Fig. 7.3, the optimized structures of skatole as a zeroth-order model for Trp in Im7 (in a C_s symmetric minimum structure) and of the Im7-based models **1** and **2** are shown. For the optimization of the ground-state structures, frequency analyses, excitation energies and excited-state gradients of skatole and model **1**, we employed B3LYP/TZVP, whereas for the larger model **2**, BP86/TZVP was used for the ground-state structures and frequency analysis for efficiency reasons. The implications of using different functionals for ground- and excited states were discussed in Section 6.4.2, and similar observations were made for the present example.

The small Im7-based model **1** comprises 35 atoms and consists of the amino acid Trp, capped by an aldehyde at the N-terminus and a glycine fragment (instead of the arginine residue) connected to the C-terminus, see Fig. 7.3. Model **2** consists of the amino acid sequence Ile–Lys–Glu–Trp–Arg–Ala–Ala–Asn–Gly (151 atoms), in which Lys and Arg are included in their neutral form. The structures of all models were fully optimized.

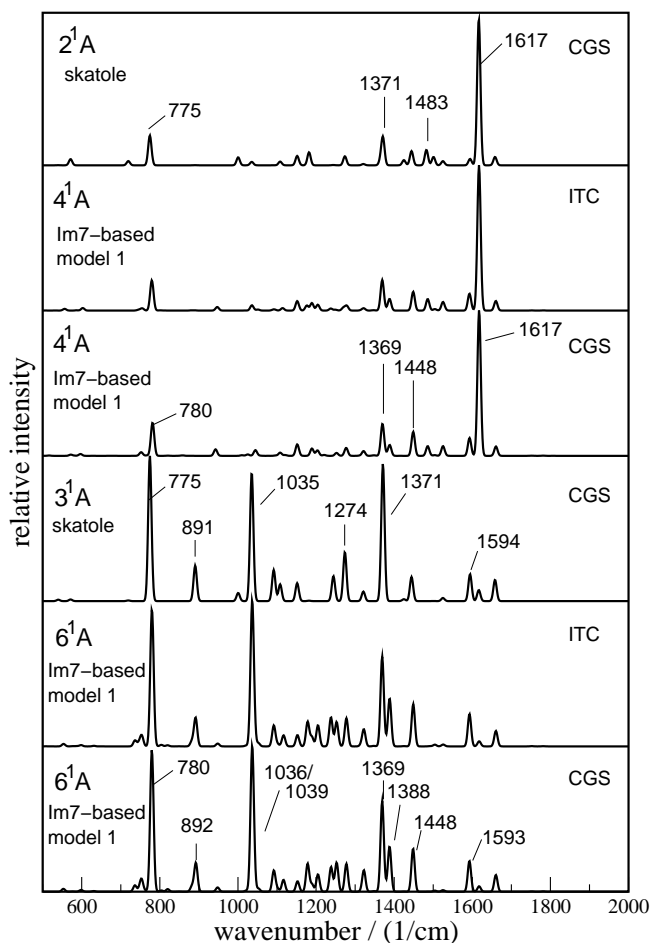
Table 7.1: Calculated excitation energies, dominant orbital transitions and corresponding transition dipole moments μ_t for skatole and model **1**. The applied functionals are given in parentheses. Where two different functionals are mentioned, the first one was used for the ground state structure and frequencies and the second one for excitation energies and the excited-state gradient. Note that the transition in the first column always refers to the corresponding transition in skatole; H: HOMO; L: LUMO.

transition	molecule	state	transition	E / eV	μ_t / a.u.
H \rightarrow L	skatole (B3LYP)	$2^1A'$	$6a'' - 7a''$ (89%)	4.62	0.78
	skatole (BP86)	$2^1A'$	$6a'' - 7a''$ (88%)	4.20	0.67
	model 1 (B3LYP)	4^1A	$72a - 74a$ (89%)	4.64	0.78
	model 1 (BP86/B3LYP)	4^1A	$72a - 74a$ (86%)	4.58	0.78
	model 1 (BP86)	8^1A	$72a - 74a$ (78%)	4.17	0.64
	model 2 (BP86/B3LYP)	15^1A	$283a - 288a$ (65%)	4.59	0.59
	model 2 (BP86)	92^1A	$279a - 288a$ (46%)	4.26	0.46
H-1 \rightarrow L + H \rightarrow L+1	skatole (B3LYP)	$3^1A'$	$5a'' - 7a''$ (60%)	4.87	0.42
			$6a'' - 8a''$ (37%)		
	skatole (BP86)	$3^1A'$	$5a'' - 7a''$ (55%)	4.57	0.25
			$6a'' - 8a''$ (44%)		
	model 1 (B3LYP)	6^1A	$71a - 74a$ (61%)	4.87	0.44
			$72a - 78a$ (25%)		
	model 1 (BP86)	12^1A	$71a - 74a$ (45%)	4.57	0.28
			$72a - 77a$ (40%)		

In Table 7.1 excitation energies, transition dipole moments and dominant orbital transitions are presented. In the wavelength regime between 250 and 280 nm (energy range from 4.4 to 5.0 eV), which we will assume for the excitation wavelength, we obtained two excited states for skatole, which are denoted as L_b (2^1A) and L_a (3^1A). The 2^1A state is dominated by the HOMO \rightarrow LUMO orbital transition while the transition to the 3^1A state can be characterized by a combination of the HOMO-1 \rightarrow LUMO and

HOMO→LUMO+1 orbital transitions. Isosurface plots of the orbitals involved are shown in Fig. 7.3. Since the 2^1A and 3^1A state are only 0.25 eV apart in energy for B3LYP and 0.37 eV for BP86, they can both be expected to contribute to a resonance Raman spectrum with an excitation energy in that range. The experimental excitation energies for both states are lower, but similarly close (4.31 eV and ~ 4.77 eV [590], respectively). A detailed theoretical study of the underlying indole motif can be found in Ref. [591].

Figure 7.4: Resonance Raman spectra for resonance with the $2^1A'$ or $3^1A'$ state of skatole obtained by a conventional gradient calculation using B3LYP/TZVP. Also shown are the spectra for the corresponding states of Im7-based model **1** obtained either in a converged intensity-tracking calculation (ITC) or as conventional gradient spectra (CGS). Wavenumbers of selected vibrations are given in units of cm^{-1} .



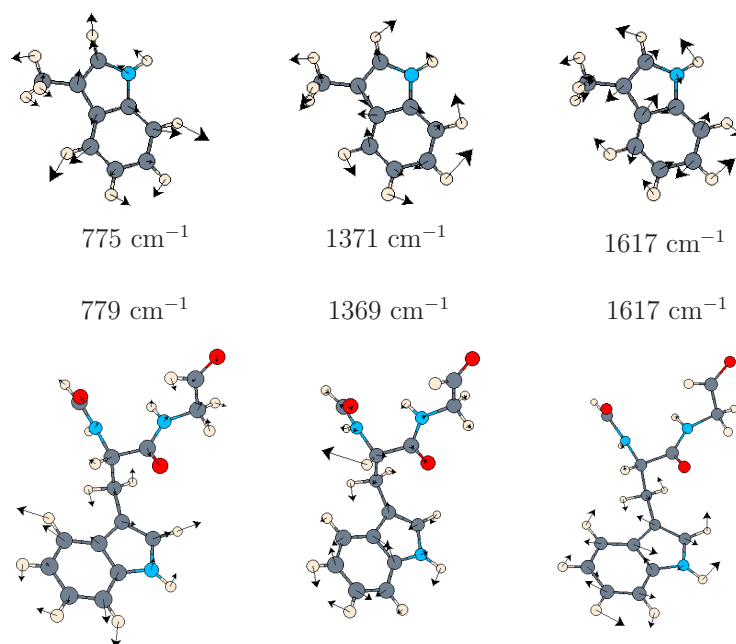
Within Heller's gradient approximation, it is always assumed that only one excited state is in resonance, which is clearly a simplification in the present case. In principle, the approach could also be applied to identify the most important modes for two or more close-lying states. Once these vibrations are identified, more sophisticated treatments taking interference effects into account could be applied subsequently in the restricted set of normal modes. For the current pilot study of the intensity tracking algorithm,

however, we will make the approximation that either the L_b or the L_a state alone determine the spectrum.

For model **1**, the identification of the L_b and L_a states is straightforward by comparing the excitation energies, transition dipole moments, and orbital transitions involved in the excitations (see Table 7.1). The situation for model **2** is more complicated and not unambiguous due to the problems outlined above for TDDFT calculations on large systems. But the choice of the resonating states made here can be assessed by comparing the final resonance Raman spectra to those of the smaller structural motifs, which will be done in Sec. 7.4.3.

While the state corresponding to the 2^1A state (L_b transition) of skatole was investigated for both models, the excited state corresponding to the 3^1A state of skatole (L_a transition) was only examined for model **1** in order to test convergence criteria and root-homing options. As will be shown below, the intensity distribution for this state is distinctly different from that of the 2^1A state, so that the requirements for the intensity-tracking algorithm to converge quickly can be tested on a broader basis.

Figure 7.5: Graphical representation of the intense vibrations (B3LYP/TZVP) in the resonance Raman spectrum of skatole (upper row) and of model **1** (lower row).



The B3LYP/TZVP resonance Raman spectrum obtained within Heller's gradient approximation by assuming resonance with the $2^1A'$ state of skatole is shown in Fig. 7.4. It is dominated by the peak at 1617 cm^{-1} , and two further intense peaks appear at 775 cm^{-1} and 1371 cm^{-1} . The corresponding normal modes are visualized in Fig. 7.5. Fig. 7.4 also shows resonance Raman spectra for model **1** of the Im7 protein, calculated for the 4^1A and 6^1A states, which correspond to the $2^1A'$ and $3^1A'$ states of skatole. Using strict convergence criteria, the intensity-tracking calculation requires almost a full

basis, and the results of the conventional gradient calculations can be reproduced apart from small numerical deviations, which again can be attributed to the different impact of numerical noise when different types of basis vectors are employed. Note that the resonance Raman spectrum of the 4^1A state is very similar to the $2^1A'$ spectrum of skatole with respect to the intensity distribution and wavenumbers of the modes. The wavenumbers of the intense modes exhibit only very small shifts, e.g. from 1371 cm^{-1} to 1369 cm^{-1} , and the vibrations are mainly localized on the skatole moiety. In Fig. 7.5, graphical representations of the normal modes are compared to the corresponding skatole modes. The spectrum of model **1** exhibits further modes in the region of 1000 to 1400 cm^{-1} carrying small percentages of the intensity, but the additional 64 vibrational degrees of freedom compared to skatole do not alter the spectrum significantly.

7.4.2 Root homing

In the preceding tests, reasonable spectra required the convergence of a rather large number of modes. This is caused by the fact that too many modes are selected with the root-homing criteria initially applied, especially when the most intense modes are already obtained. The algorithm hence tries to optimize also many lower-intensity modes that may not be relevant for the most characteristic features of a spectrum. This results in an almost simultaneous convergence of all selected modes as the basis approaches completeness. A smart root-homing should, on the contrary, lead to a directed convergence of the most intense features of the spectrum and not construct to many new basis vectors per iteration, so that a smooth development of the spectrum can be expected.

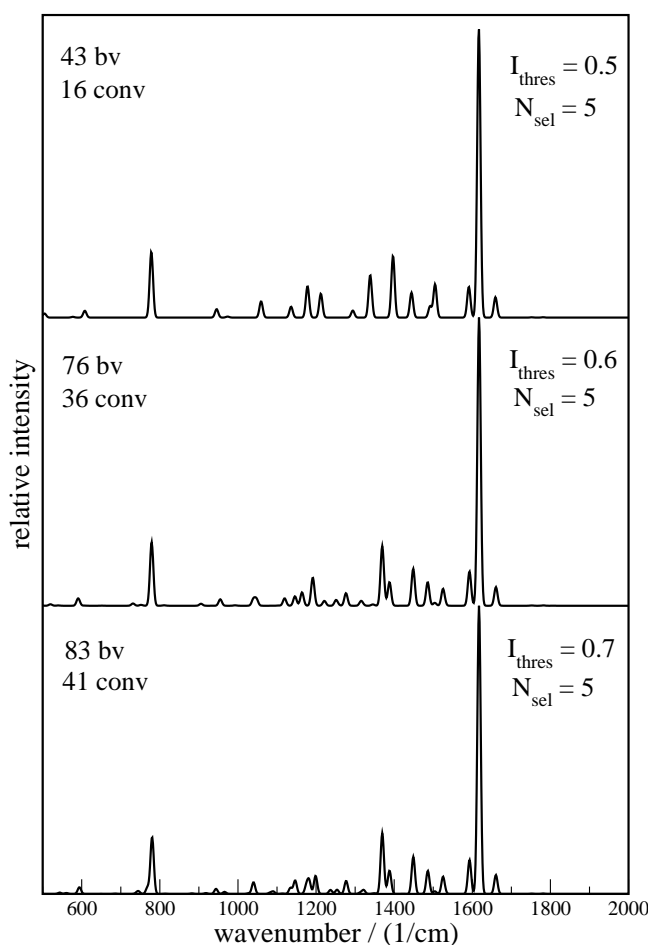
Three possible types of root homing were tested in initial calculations for Im7-based model **1**: (A) selecting the most intense modes to be optimized so that their cumulative intensity exceeds a threshold percentage of the total intensity I_{thres} , (B) choosing the integer number of N_{sel} most intense modes, or (C) optimizing those modes which carry a relative intensity exceeding the threshold value i_{thres} . It must be noted that the convergence criterion is tested for each of the modes selected for optimization. I.e., the calculation is only considered converged if all modes that are of interest (as defined by the root-homing criterion) fulfill the convergence criteria. Therefore, the root-homing somehow determines the convergence criterion for the overall spectrum, although the criterion applied to each mode may be the same for different root-homing settings.

In all three cases the number of basis vectors needed to fulfill the formal convergence criteria (maximum component of $\mathbf{r} < r_{\text{max}}^{\text{thres}} = 5 \times 10^{-4} \text{ hartree}/[\text{amu} \times \text{bohr}^2]$) were rather large. However, it turned out that option (A) is best suited for spectra with several vibrations of similar intensity, whereas option (B) is more appropriate if there is a particular interest in a small number of high-intensity modes. Root-homing option (C) is in general the least efficient one and will not be further discussed.

Neither root-homing scheme (A) nor (B) alone are completely satisfactory, and their disadvantages are complementary: With scheme (A), too many modes are chosen for optimization in each iteration, resulting in a sudden simultaneous convergence of many modes when the basis set reaches completeness. On the other hand, scheme (B) may select too few modes for optimization in spectra with several important modes and thus miss essential parts of the spectrum. To further enhance the efficiency of the algorithm,

we thus combined the two schemes in such a way that scheme (A) determines how many and which modes are checked for convergence, whereas only for a subset of them new basis vectors are constructed according to scheme (B). This leads to a much smoother convergence than scheme (A) alone and avoids unnecessary basis vectors. As an additional selection criterion, the allowed wavenumber range may be restricted for modes to be optimized.

Figure 7.6: Converged spectra for the $4^1A'$ state of model **1** for different root-homing options calculated with the convergence criterion $r_{\max}^{\text{thres}} = 5 \times 10^{-4}$. The total number of basis vectors (bv) and of converged modes (conv) is given for each spectrum.



The results for different combinations of I_{thres} and N_{sel} obtained in calculations assuming resonance with the 4^1A state of model **1** are shown in Figure 7.6. It can be seen that in particular the combination of $I_{\text{thres}} = 0.5$ and $N_{\text{sel}} = 5$ leads to convergence with a small number of only 43 basis vectors. Whereas the highest-intensity peaks at 1617 and 780 cm^{-1} are very well converged in that case, the less intense features between 1300 and 1550 cm^{-1} are only approximately reproduced. In a sense, this is exactly what one would require from an efficient intensity-tracking scheme, i.e., to accurately reproduce the most intense features with a small number of basis vectors *and* to provide a reasonable guess

for where additional peaks of lower intensity may be found. Moreover, also the less important parts of the spectrum can be systematically improved by increasing the value of I_{thres} , as is apparent in Figure 7.6.

7.4.3 Intensity tracking for Im7-based model 2

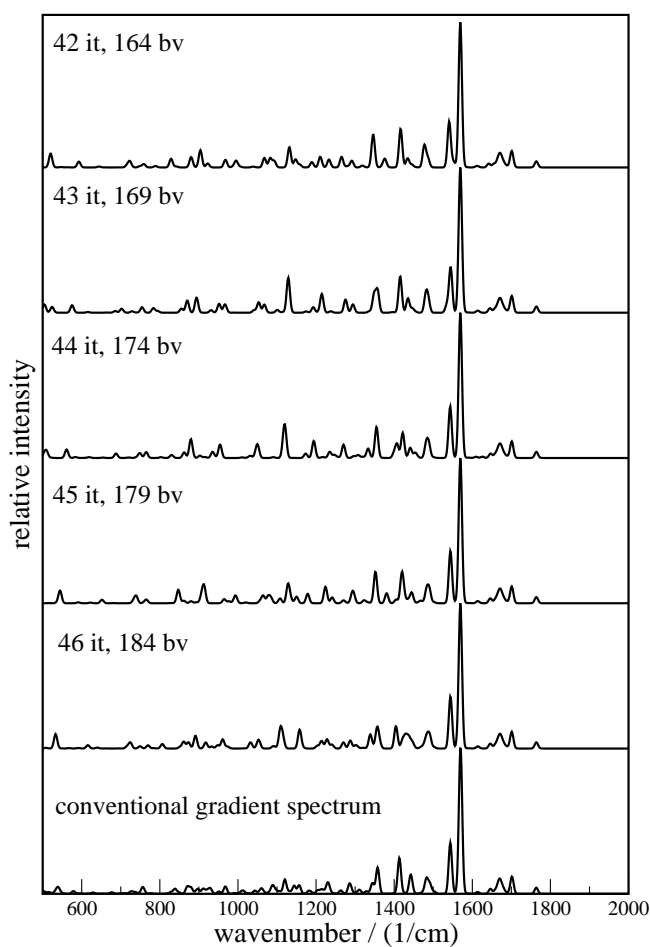
For large models of the Im7 protein, TDDFT yields a multitude of artificially low-lying excited states which mix with the excited states relevant to describe the experimentally observed spectra as can be seen from the data in Table 7.1. These data also show that B3LYP at least partly remedies this problem, since the state corresponding to the 2^1A state of skatole is the 15^1A state of model **2** with B3LYP, whereas it is the 92^1A state in case of BP86. I.e., 77 more low-lying states are found in the BP86 calculation, and it would thus be advantageous to use B3LYP for the entire calculation, as was done for the previous models. However, the pure density functional BP86 leads to an enormous increase in efficiency for large molecules, since density fitting schemes can readily be applied. We therefore again employ the hybrid approach already tested in Section 6.4.2 in which we calculated the excitation energies and excited-state gradients with B3LYP, whereas BP86 was used for the frequency analysis, which will also be applied here. Test calculations employing this hybrid approach for the smaller model **1** have shown that the main features in the spectra are the same.

In Fig. 7.7 we show approximate resonance Raman spectra obtained during an intensity-tracking calculation with this approach, i.e., using a BP86/TZVP force field in combination with a B3LYP/TZVP gradient of the $15^1A'$ state, which corresponds to the $2^1A'$ state of skatole. From the visual inspection of these spectra, it can be seen that the dominant features in this resonance Raman spectrum, which can be found in the region above 1300 cm^{-1} , appear well-converged already in iteration 42. Some smaller interferences occur for the less intense peaks in this region in intermediate steps. But in particular the two peaks at 1569 and 1544 cm^{-1} , which dominate the spectrum by far, and the neighboring peaks, are very stable. Also the intensity distribution in the whole wavenumber range plotted reproduces the intensity distribution in the reference spectrum. A remaining difficulty at the current point is the definition of convergence criteria that agree with the visual impression of a converged spectrum. To be more precise, the problem is to determine how many and which modes must be classified as converged for overall convergence. In the present example, we used the combination $I_{\text{thres}} = 0.8$ and $N_{\text{sel}} = 5$, in which apparently too many modes are checked for our purposes. However, the spectra in Figure 7.7 show that the convergence of the overall spectrum is smooth, so that it can easily be judged by inspection whether the essential parts of the spectrum are converged.

164 basis vectors are needed to obtain the approximate spectrum in iteration 42, compared to 453 that are needed in a conventional calculation. Although this gain in efficiency is not as large as in typical mode-tracking calculations for specific vibrations [318, 574, 592], it must be kept in mind that intensity-tracking calculations (i) target several vibrations, the exact number of which is unknown, (ii) start with an unspecific guess for the type of collection motion, and thus typically require more basis vectors for correction, and (iii) may partially comprise very unspecific modes that easily couple to other vibrations in the molecule, which affects the convergence behavior. In

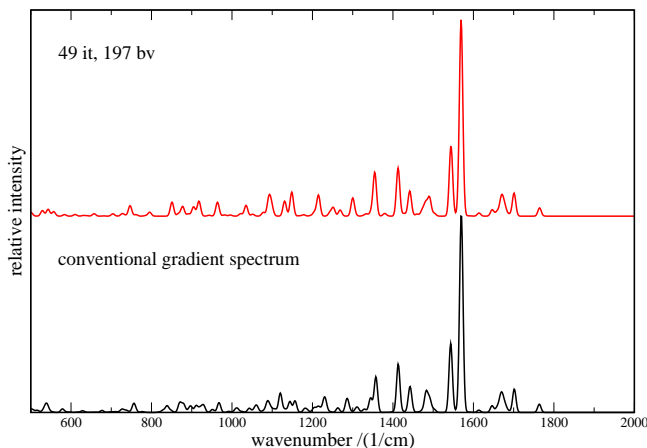
view of these points, the methodology outlined here appears quite successful in providing insight into the dominant features of the resonance Raman spectrum of large molecules at reduced cost.

Figure 7.7: Approximate resonance Raman spectra (BP86/TZVP) of model **2** for several subsequent intensity-tracking iterations. Calculations were performed using the (B3LYP/TZVP) gradient of the $15^1A'$ state, which corresponds to the $2^1A'$ state of skatole. As a reference spectrum, the conventional gradient spectrum is shown. The criteria for root-homing were $I_{\text{thres}} = 0.8$ and $N_{\text{sel}} = 5$.



In order to demonstrate that it is possible to find suitable combinations of root-homing and convergence criteria, which do not require a visual inspection as an additional convergence control, we also show the results obtained in a calculation which only employed the criterion of $N_{\text{sel}} = 5$ in Figure 7.8. In this calculation, formal convergence was reached after 49 iterations, employing a slightly higher number of 197 basis vectors. As can be seen, the resulting spectrum agrees very well with the conventional gradient spectrum and all intense features are accurately reproduced.

Figure 7.8: Approximate resonance Raman spectra (BP86/TZVP) of model **2** from an intensity-tracking calculation with root-homing criterion $N_{\text{sel}} = 5$. The calculation was performed using the (B3LYP/TZVP) gradient of the $15^1A'$ state, which corresponds to the $2^1A'$ state of skatole. As a reference spectrum, the conventional gradient spectrum is shown.



In summary, we note that conventional gradient spectra can be reproduced very well with intensity-tracking if strict convergence criteria and suitable root-homing schemes are applied, which is a necessary condition for a successful application of this algorithm. The combination of different root-homing criteria avoids the problems of either optimizing too many modes simultaneously, which typically results in bad convergence behavior, or of neglecting essential parts of the spectrum. Although the convergence in intensity-tracking calculations is intrinsically more difficult than typical examples in mode-tracking calculations, it is possible to devise root-homing schemes that lead to a smooth convergence at reduced computational cost. Further improvements in the convergence control might be possible by defining different convergence criteria for modes of different intensities, for example in such a way that tight convergence is only requested for those parts of the spectrum that stand out very sharply due to their high intensity.

8. Conclusions and Outlook

The present work focused on the development of tailor-made quantum chemical methods for targeting local properties in supermolecular assemblies. It was outlined how spectroscopic features of complex systems can be described and understood on the basis of chromophore-specific spectroscopic methods. The range of systems studied in this work covers simple hydrogen-bonded complexes, dye molecules in solution, organic inclusion compounds, artificial as well as natural light-harvesting complexes, and models for proteins. The types of spectroscopy for which subsystem-oriented methods have been devised include electronic absorption and circular dichroism, electron spin resonance, optical rotation, and resonance Raman spectroscopy.

The basis for a chromophore-specific electronic-structure theory for complex systems was developed within a subsystem DFT framework. The fundamental assumption of this approach is that the electron density of a combined system can be obtained from suitable subsystem calculations, and this assumption was tested in detail. It turned out that even in cases of strongly hydrogen-bonded systems or complexes with coordination bonds reasonably accurate electron densities can be obtained, although the limitations of this approach become apparent in cases of stronger covalent bonding. Furthermore, these applications showed that the electron leak problem in frozen-density embedding calculations is by no means irrelevant and can lead to severe problems in electronic-structure calculations for metal complexes in which the subsystem border cuts a metal–ligand bond. The range of applicability of subsystem DFT could thus be defined more clearly, which is an important prerequisite for its application to complex systems.

In order to investigate absorption and circular dichroism spectra, electronic-structure methods for excited states are needed. Although the time-dependent response approach within Kohn–Sham DFT is a rather efficient method, it becomes cumbersome to analyze the results from conventional TDDFT calculations in particular for extended systems or systems composed of many molecules. The well-known reason for this is related to the long-range charge-transfer problem of TDDFT, for which a simple, though very effective method was implemented. It could be shown that charge-transfer excitations can automatically be detected and shifted towards higher energies in a qualitatively correct way, and even quantitative corrections are possible with carefully chosen parameterizations. Such a correction is much less important within the frozen-density embedding approach to TDDFT, since it automatically restricts the active orbital space to the embedded subsystem. Hence, no inter-subsystem charge-transfer excitations are possible and an easy identification of valence excited states is facilitated.

A problem, that is deeply connected with the prediction of spectroscopic properties of complex systems with increasing number of atoms and decreasing rigidity of certain parts of the system, is the fact that it becomes more and more important to consider the explicit dynamics of the system. For small, rigid molecules, this can be done on

the basis of vibrational averaging procedures, but for, e.g., a molecule in solution, this is simply unfeasible. An alternative is to investigate a representative set of snapshots for the molecule in solution. Since the spectroscopic properties in question have to be evaluated for every structure, and several hundreds of snapshots may be needed, the electronic-structure approach applied for this purpose must be very efficient. It could be demonstrated in this work that frozen-density embedding clearly fulfills this condition. It is thus a valuable tool for explicit solvation studies. Concluding from the analyses of environmental effects on solvatochromism and induced circular dichroism we note that both specific interactions — as in the amino acid receptor model in Section 4.4.2 — and bulk environmental effects — as in the solvation study in Section 4.3 — are accurately described by frozen-density embedding. The results from Chapter 4 also highlight the ability of frozen-density embedding to account for chiral or spin-polarized environments, although the latter effect was found to be of minor importance in the examples studied. The caveat mentioned in the introduction concerning the local nature of properties in subsystem approaches became apparent in the study on induced circular dichroism. A model for environmental effects like FDE that explicitly assumes a local response of the embedded subsystem to the external perturbation cannot be expected to account for effects due to the environmental response. Consequently, the excitonic coupling effects observed in cyclodextrin inclusion compounds could not be reproduced in embedding calculations. This led to the development of a general time-dependent density-functional theory for subsystems in Chapter 5. Its relationship to FDE-TDDFT was clearly defined and it was demonstrated that approximate schemes can be implemented that make the method applicable to systems of coupled chromophores. The method was generalized for other response properties, which will be important for solvation effects that depend, e.g., on the optical rotation induced by a chiral solvation shell. In the context of polarizability and optical rotation tensors, this coupled-response description offered by the subsystem TDDFT approach is clearly needed, since the frozen-density embedding version of TDDFT yields qualitatively wrong results for such properties.

The intention to develop this subsystem approach for chromophore-specific spectroscopy was purpose-driven by the aim of enabling quantum chemical investigations for biological systems, in particular those involved in photosynthesis. The first important step into this direction was made in the investigation of pigment–protein and pigment–pigment interactions in the light-harvesting complex 2 of *Rhodospseudomonas acidophila*. Both the shifts of excitation energies due to a polarization of the electron density due to interactions with specific residues of the surrounding protein and the excitonic coupling between different pigment molecules can be described in terms of the subsystem approach developed here. Subsystem TDDFT provides both a diabatic and an adiabatic picture for the excited states of such a light-harvesting system: The excitation energies in the “local response” approach can be identified with the hypothetical site energies, whereas the subsequent coupled response formalism leads to the splitting in excitation energies due to excited-state interactions. Subsystem TDDFT thus bridges the gap between rigorous quantum chemical methods for excited states and phenomenological excitonic coupling models.

An even more informative approach to deduce properties of excited states can be provided by resonance Raman spectroscopy. Whereas accurate resonance Raman calculations are almost unfeasible already for systems of medium size, it was shown that simple ap-

proximations that are already well-known for a long-time may be successfully applied in combination with time-dependent density-functional theory calculations for the characterization of excited electronic states. A reason for this success may be the fact that these schemes, that derive from Heller’s short-time approximation [519,521], are expected to work the better the more vibrational degrees of freedom are involved, i.e., the larger the molecule is. But only with recent developments in TDDFT it has become feasible to study excited-state potential energy surfaces of molecules with hundreds of atoms. These approaches to resonance Raman spectroscopy were applied here to clarify the first intermediate in the photochemistry of *ortho*-nitrobenzaldehyde in combination with time-resolved experimental data.

The role of resonance Raman spectroscopy for the investigation of photosystems was highlighted in the study on ruthenium–polypyridyl complexes in Section 6.4, for which the calculations supported the experimental assumption of a metal-to-ligand charge-transfer as the initial photoexcitation step. In these calculations, it became apparent that the bottleneck in the determination of resonance Raman spectra with Heller’s gradient approximation is not the characterization of the excited state, but rather the calculation of the normal modes and vibrational frequencies of the system. In order to tackle this problem, an intensity-driven algorithm for the iterative determination of the high-intensity vibrations in a resonance Raman spectrum was developed and implemented in Section 7. It was shown that the algorithm converges to the exact result within the quantum chemical model chosen for the calculation of intensities and frequencies. Different options were tested to steer the convergence characteristics of this approach in an optimum way to get a balance between an accurate description of the resonance Raman spectrum and a computationally cheap method. This approach should be very well suited to study proteins, in which only a few aromatic side-chains dominate the resonance Raman spectrum at specific wavelengths. A first indication for this was provided for models of the E colicin-binding immunity protein Im7.

The developments presented in this work provide the basis for spectroscopic investigations of functional assemblies of chromophores in larger aggregates. This opens up the way to fully non-empirical studies on excitation energy-transfer pathways in photosystems, as was already indicated in the study on LH2. Many energy-transfer and energy-dissipation pathways in natural photosystems depend on a fine-tuning of energy levels in the pigment molecules involved, both by direct ground-state interactions and by excited-state interactions. In particular the role of the carotenoid pigments in these light-harvesting complexes and its role in energy transfer to bacteriochlorophyll molecules is an active field of research [593]. The subsystem TDDFT approach developed in this work can be an important tool for investigations of such systems.

Since the environmental response can explicitly be taken into account, phenomena related to solvent shielding effects on excitation energy transfer couplings can be investigated by explicit inclusion instead of by continuum models, as has been done so far in most of the studies. In particular for couplings at short range, this may provide significant new insights, since assumptions concerning the cavity in implicit solvation models can be tested. But also quite unusual phenomena may be investigated, as for example the recently reported optical rotation due to chiral imprinting and related effects [405] (see also Ref. [229]). Currently, the only way to study such phenomena is the explicit inclusion of solvent molecules into the quantum chemical description. This leads to a

dramatic increase in effort, since large solvation shells may have to be considered for many configurations in order to unambiguously prove that the results are not due to artifacts in the simulation. While this may be out of reach with standard quantum chemical methods, the subsystem response approach presented here facilitates such investigations.

The intensity-driven algorithm for resonance Raman spectroscopy provided in this work was designed for the study of components of natural photosystems, for which they can provide important insight into the initial photoexcitation steps, and for the investigation of protein structures. The latter point is related to the strong solvent-dependence of resonance Raman spectra obtained for aromatic amino acid side-chains. In order to gain a more detailed understanding into this phenomenon by means of a quantum chemical analysis, a restriction to the relevant degrees of freedom is clearly required. Since this involves both electronic and vibrational degrees of freedom, the combination of subsystem density functional theory techniques and selective approaches for vibrational spectroscopy features a unique possibility for conducting chromophore-specific studies on general spectroscopic phenomena.

9. Acknowledgments

The investigation of complex chemical systems is a complex endeavor, which requires to combine knowledge from different branches of chemistry. This can hardly be achieved by a single person, and the present work clearly benefited substantially from discussions and collaborations with other scientists, which shall be acknowledged at this point.

I am indebted to my mentor at ETH Zurich, Prof. Markus Reiher, in many respects. He granted the freedom I needed to pursue my own, independent research objectives and offered any kind of support that was necessary to achieve these goals. His continued interest in my work and our stimulating discussions were very helpful for my research activities. Additionally, the infrastructure available in his group, in particular (though not exclusively) the excellent computer facilities, provided an ideal framework for the large-scale simulations that I carried out during the past years.

I also owe a special debt of gratitude to Prof. Evert Jan Baerends, with whom I spent two and a half years as a postdoctoral research fellow at the Vrije Universiteit Amsterdam with financial support by the Deutsche Forschungsgemeinschaft (DFG). He introduced me to the field of time-dependent density-functional theory, and I learned a lot about the fundamental aspects of density-functional theory in general from him. I appreciate the independence that he gave me in all my projects very much, including the first studies on frozen-density embedding, which were conducted in Amsterdam. I would also like to thank the members of his group, in particular Dr. Oleg Gritsenko and Manuel Louwerse, who contributed to some of the projects that I carried out in the Netherlands.

For our collaborations concerning solvent effects, I would like to thank Dr. Tomasz Wesolowski from the University of Geneva, as well as for the discussions on orbital-free embedding techniques in general. Several interesting studies were (and are still) carried out in collaboration with Prof. Lucas Visscher, and I owe him my gratitude for that. The work on electron spin resonance parameters in solution was stimulated by Prof. Paola Belanzoni from Perugia during a visit in Amsterdam, which I would also like to acknowledge at this point.

For our (ongoing) collaboration on resonance Raman spectroscopy of aromatic nitro compounds, I would like to thank PD Dr. Peter Gilch from LMU München and his group. The exchange of experimental and theoretical questions we had was always very inspiring and encouraging for further research. The experimental results for the study on ruthenium–polypyridyl complexes provided by the group of Prof. Jürgen Popp (University of Jena) are also gratefully acknowledged.

Special thanks are due to Dr. Christoph Jacob, who was of great help in particular for the improved ground-state implementation of the frozen-density embedding scheme in ADF, for which he did a major part of the work. Moreover, I acknowledge the numerous contributions by my PhD student Karin Kiewisch. Many problems, in particular in the

field of resonance Raman spectroscopy, would not have been tackled in this short time without her work.

I would furthermore like to express my gratitude to all the members of the theoretical chemistry group in Zurich for the pleasant working atmosphere. In particular, I acknowledge the contributions to some of the projects presented that were made by Dr. Carmen Herrmann (now at Northwestern University, Evanston), Dr. Georg Eickerling (now at Universität Augsburg), and Samuel Fux. Carmen's work led to rapid progress in the projects on vibrational spectroscopy, and Samuel Fux carried out the FDE calculations on coordination compounds as a sequel to a former study, in which Georg shared his knowledge on topological electron density analyses. I would also like to thank Romy Isenegger for all her help in administrative questions.

For taking care of the computer infrastructure, I express my gratitude to Markus Traber, Dr. Gerrit Moritz, Dr. Stephan Schenk, and Koni Marti. I would also like to acknowledge the assistance I got for any kind of problem with the ADF package from the team of SCM (Scientific Computing & Modelling), in particular Dr. Stan van Gisbergen, Dr. Erik van Lenthe, Dr. Olivier Visser, and Dr. Alexei Yakovlev.

Financial support for my work in Zurich was granted by the Fonds der Chemischen Industrie through a Liebig-Stipendium.

A. List of Publications

This thesis is a monograph on chromophore-specific spectroscopy and its underlying quantum chemical basis. It contains parts that are based on results of previous publications, which are indicated by a star (*) in the following list. Other parts of this monograph are entirely new, and have not been published before. In particular, this includes the work on general response properties in a subsystem formulation of time-dependent density-functional theory (Section 5.2), and selective calculations of high-intensity vibrations in molecular resonance Raman spectra (Chapter 7).

- 1) **J. Neugebauer**, M. Reiher, J. Hinze, Analysis of the asymptotic and short-range behavior of quasi-local Hartree-Fock and Dirac-Fock-Coulomb electron-electron interaction potentials, *Phys. Rev. A* **65** (2002), 032518.
- 2) **J. Neugebauer**, M. Reiher, J. Hinze, Analytical local electron-electron interaction model potentials for atoms, *Phys. Rev. A* **66** (2002), 022717.
- 3) **J. Neugebauer**, M. Reiher, C. Kind, B. A. Hess, Quantum Chemical Calculation of Vibrational Spectra of Large Molecules — Raman and IR spectra for Buckminsterfullerene, *J. Comput. Chem.* **23** (2002), 895.
- 4) **J. Neugebauer**, M. Reiher, B. A. Hess, Coupled cluster Raman intensities: Assessment and comparison with multi-configuration and density functional methods, *J. Chem. Phys.* **117** (2002), 8623.
- 5) M. Reiher, **J. Neugebauer**, B. A. Hess, Quantum Chemical Calculation of Raman Intensities for Large Molecules: The Photoisomerization of $[\text{Fe}'\text{S}_4'(\text{PR}_3)_2(\text{N}_2\text{H}_2)]$ ($'\text{S}_4'^{2-} = 1,2\text{-bis}(2\text{-Mercaptophenylthio})\text{Ethane (2-)}$), *Z. Phys. Chem.* **217** (2003), 91.
- 6) **J. Neugebauer**, M. Reiher, B. A. Hess, Structure, Energetics, and Spectroscopy of Models for Enzyme Cofactors, in: S. Wagner, W. Hanke, A. Bode, F. Durst (Eds.), *High-Performance Computing in Science and Engineering 2000-2002, Transactions of the First Joint HLRB and KONWIHR Status and Result Workshop*, Springer-Verlag, Berlin 2003, pp. 157–169.
- 7) M. Reiher, **J. Neugebauer**, A mode-selective quantum chemical method for tracking molecular vibrations applied to functionalized carbon nanotubes, *J. Chem. Phys.* **118** (2003), 1634.

- 8) **J. Neugebauer**, B. A. Hess, Fundamental vibrational frequencies of small polyatomic molecules from density-functional calculations and vibrational perturbation theory, *J. Chem. Phys.* **118** (2003), 7215.
- 9) **J. Neugebauer**, B. A. Hess, Resonance Raman spectra of uracil based on Kramers–Kronig relations using time-dependent density functional calculations and multireference perturbation theory, *J. Chem. Phys.* **120** (2004), 11564.
- 10) **J. Neugebauer**, M. Reiher, Vibrational Center–Ligand Couplings in Transition Metal Complexes, *J. Comput. Chem.* **25** (2004), 587.
- 11) J. Autschbach, B. A. Hess, M. P. Johansson, **J. Neugebauer**, M. Patzschke, P. Pyykkö, M. Reiher, D. Sundholm, Properties of WAu_{12} , *Phys. Chem. Chem. Phys.* **6** (2004), 11.
- 12) **J. Neugebauer**, M. Reiher, Mode Tracking of Preselected Vibrations of One-Dimensional Molecular Wires, *J. Phys. Chem. A* **108** (2004), 2053.
- 13) M. Reiher, **J. Neugebauer**, Convergence characteristics and efficiency of mode-tracking calculations on pre-selected molecular vibrations, *Phys. Chem. Chem. Phys.* **6** (2004), 4621.
- 14) B. Le Guennic, J. Autschbach, **J. Neugebauer**, M. Reiher, The “Invisible” ^{13}C Chemical Shift of the Central Carbon Atom in $[(\text{Ph}_3\text{PAu})_6\text{C}]^{2+}$. A Theoretical Investigation, *Chem. Eur. J.* **11** (2005), 1677.
- 15) **J. Neugebauer**, E. J. Baerends, M. Nooijen, Vibronic coupling and double excitations in linear response time-dependent density functional calculations: Dipole-allowed states of N_2 , *J. Chem. Phys.* **121** (2004), 6155.
- 16) **J. Neugebauer**, E. J. Baerends, M. Nooijen, Vibronic Structure of the Permanganate Absorption Spectrum from Time-Dependent Density Functional Calculations, *J. Phys. Chem. A* **109** (2005), 1168.
- 17) **J. Neugebauer**, E. J. Baerends, E. V. Efremov, F. Ariese, C. Gooijer, Combined Theoretical and Experimental Deep-UV Resonance Raman Studies of Substituted Pyrenes, *J. Phys. Chem. A* **109** (2005), 2100.
- *18) **J. Neugebauer**, M. J. Louwerse, E. J. Baerends, T. A. Wesolowski, The merits of the frozen-density embedding scheme to model solvatochromic shifts, *J. Chem. Phys.* **122** (2005), 094115.
- 19) **J. Neugebauer**, E. J. Baerends, M. Nooijen, J. Autschbach, Importance of vibronic effects on the circular dichroism spectrum of dimethyloxirane, *J. Chem. Phys.* **122** (2005), 234305.
- 20) C. Herrmann, **J. Neugebauer**, J. Gladysz, M. Reiher, Theoretical Study on the Spin-State Energy Splittings and Local Spin in Cationic $[\text{Re}]-(\text{C})_n-[\text{Re}]$ Complexes, *Inorg. Chem.* **44** (2005), 6174.

-
- *21) **J. Neugebauer**, C. R. Jacob, T. A. Wesolowski, E. J. Baerends, An Explicit Quantum Chemical Method for Modeling Large Solvation Shells Applied to Amino-coumarin C151, *J. Phys. Chem. A* **109** (2005), 7805.
- 22) M. Reiher, **J. Neugebauer**, Comment on “Gradient-based direct normal-mode analysis” by A. L. Kaledin [*J. Chem. Phys.* **122** (2005), 184106], *J. Chem. Phys.* **123** (2005), 117101.
- *23) **J. Neugebauer**, M. J. Louwerse, P. Belanzoni, T. A. Wesolowski, E. J. Baerends, Modeling solvent effects on electron spin resonance hyperfine couplings by frozen-density embedding, *J. Chem. Phys.* **123** (2005), 114101.
- 24) C. R. Jacob, **J. Neugebauer**, L. Jensen, L. Visscher, Comparison of Frozen-Density Embedding and Discrete Reaction Field Solvent Models for Molecular Properties, *Phys. Chem. Chem. Phys.* **8** (2006), 2349.
- *25) **J. Neugebauer**, O. Gritsenko, E. J. Baerends, Assessment of a Simple Correction for the Long-Range Charge-Transfer Problem in Time-Dependent Density-Functional Theory, *J. Chem. Phys.* **124** (2006), 214102.
- *26) **J. Neugebauer**, E. J. Baerends, Exploring the Ability of Frozen-Density Embedding to Model Induced Circular Dichroism, *J. Phys. Chem. A* **110** (2006), 8786.
- 27) V.-P. Nicu, **J. Neugebauer**, S. K. Wolff, E. J. Baerends, A vibrational circular dichroism implementation within a Slater-type-orbital based density functional framework and its application to hexa- and hepta-helicenes, *Theor. Chem. Acc.* **119** (2008), 245.
- 28) C. Herrmann, **J. Neugebauer**, M. Reiher, Finding a needle in a haystack: Direct determination of vibrational signatures in complex systems, *New J. Chem.* **31** (2007), 818.
- *29) **J. Neugebauer**, Couplings between electronic transitions in a subsystem formulation of time-dependent density functional theory, *J. Chem. Phys.* **126** (2007), 134116.
- *30) C. Herrmann, **J. Neugebauer**, M. Presselt, M. Schmitt, S. Rau, J. Popp, M. Reiher, The First Photoexcitation Step of Ruthenium-Based Models for Artificial Photosynthesis Tracked by Resonance Raman Spectroscopy, *J. Phys. Chem. B* **111** (2007), 6078.
- 31) **J. Neugebauer**, Induzierte Chiralität in Achiralen Lösungsmitteln — mysteriöse Solvenseffekte, aufgeklärt mit theoretischen Methoden, *Angew. Chem.* **119** (2007), 7884; **J. Neugebauer**, Induced Chirality in Achiral Media — How Theory Unravels Mysterious Solvent Effects, *Angew. Chem. Int. Ed.* **46** (2007), 7738.
- *32) C. R. Jacob, **J. Neugebauer**, L. Visscher, A Flexible Implementation of Frozen-Density Embedding for Use in Multilevel Simulations, *J. Comput. Chem.* **29** (2008), 1011.

- 33) M. Schlangen, **J. Neugebauer**, M. Reiher, D. Schröder, J. Pitarch Lopez, M. Haryono, F. W. Heinemann, A. Grohmann, H. Schwarz, Gas-Phase C–H and N–H Bond Activation by a High Valent Nitrido–Iron Dication and $\langle\text{NH}\rangle$ -Transfer to Activated Olefins, *J. Am. Chem. Soc.* **130** (2008), 4285.
- *34) **J. Neugebauer**, Photophysical Properties of Natural Light-Harvesting Complexes Studied by Subsystem Density-Functional Theory, *J. Phys. Chem. B* **112** (2008), 2207.
- *35) K. Kiewisch, G. Eickerling, M. Reiher, **J. Neugebauer**, Topological analysis of electron densities from Kohn-Sham and subsystem density functional theory, *J. Chem. Phys.* **128** (2008), 044114.
- 36) V.-P. Nicu, **J. Neugebauer**, E. J. Baerends, Effects of Complex Formation on Vibrational Circular Dichroism Spectra, *J. Phys. Chem. A* **112** (2008), 6978.
- 37) C. Herrmann, **J. Neugebauer**, M. Reiher, QM/MM Vibrational Mode Tracking, *J. Comput. Chem.* **29** (2008), 2460.
- *38) S. Laimgruber, T. Schmierer, P. Gilch, K. Kiewisch, **J. Neugebauer**, The Ketene Intermediate in the Photochemistry of ortho-Nitrobenzaldehyde, *Phys. Chem. Chem. Phys.* **10** (2008), 3872.
- *39) S. Fux, K. Kiewisch, C. R. Jacob, **J. Neugebauer**, M. Reiher, Analysis of electron density distributions from subsystem density functional theory applied to coordination bonds, *Chem. Phys. Lett.* **461** (2008), 353.

B. Technical Details

B.1 Density-functional theory calculations

Most of the density-functional theory calculations carried out in this work were performed with the Amsterdam Density Functional (ADF) program package [277, 278], in which also all own developments within the context of subsystem DFT/TDDFT and the charge-transfer correction scheme presented in Section 3.3 were implemented. Structure optimizations were carried out with the Becke–Perdew functional denoted as BP86 [594, 595] and a triple- ζ basis set with polarization functions on all atoms (TZP) from the ADF basis set library [277] if not explicitly mentioned otherwise. This is also the default for the frozen-density embedding calculations in the topological electron density analyses presented in Section 2.9. For certain applications, larger basis sets with a second set of polarization functions on all atoms (TZ2P) or of quadruple- ζ type with four sets of polarization functions (QZ4P) from the ADF basis set library were used. These are explicitly mentioned in the main text. In DFT calculations labeled as “LDA” calculations, the exchange contribution is calculated from the Dirac exchange functional [44] and the correlation part from the Vosko–Wilk–Nusair functional (parameterization “V” in Ref. [596]).

FDE and subsystem-DFT calculations as presented in this work always employed the same exchange–correlation functional for the XC contribution of the embedding potential that is also used within the subsystems. An exception are calculations using the SAOP (“statistical averaging of molecular orbital potentials”) potential, which is orbital-dependent (see below), and can thus not be applied within the orbital-free embedding framework. In those cases, the XC part of the embedding potential is calculated with the potential derived from the BPW91c exchange–correlation functional. Although this introduces a slight inconsistency in the treatment of frozen and non-frozen subsystem, the use of different exchange–correlation potentials for different subsystems is — from a pragmatic point of view — an advantage, as a more sophisticated potential with correct asymptotic behavior can be applied for the embedded system. As a default for the non-additive kinetic energy contribution, the PW91k generalized-gradient approximation (GGA) kinetic-energy functional was employed, which has the same functional form for the enhancement factor $F(s)$ as the exchange functional of Perdew and Wang [64], and which was parameterized for the kinetic energy by Lembarki and Chermette [63]. In the course of the present work, we discovered an inconsistency in the ADF implementation of the PW91k functional for the spin-restricted case, which effectively corresponds to different parameterization of the PW91k gradient correction to the non-additive kinetic energy functional used in closed-shell calculations. We have tested the effect of this inconsistency, and found no significant discrepancies between the two different parameterizations. In particular, the differences for excitation energies and most other

properties are very small. Details can be found in Ref. [597]. In the present context, the term PW91k refers to the version originally implemented in ADF, while the calculations obtained with the Lembarki–Chermette parameterization are denoted as PW91k calculations in the LC94 parameterization.

For KS- and FDE-TDDFT calculations, we applied the ADF RESPONSE module [236]; the implementation of rotational strengths and optical rotation by Autschbach *et al.* [408,410,411] was employed for the computation of chiroptical properties in those cases. In contrast, general subsystem-TDDFT response properties and excitation energies are calculated with the new implementation described in this work. Calculations of excitation energies and excited-state gradients are in general carried out with the SAOP (“statistical averaging of molecular orbital potentials”) potential [598–600], which is a special, orbital-dependent exchange–correlation potential designed for the calculation of excitation energies. An exception are the benchmark calculations with the new subsystem TDDFT approach on small test systems presented in Sections 5.1 and 5.2, for which the BP86 functional was used. The SAOP potential is well suited for describing both valence and Rydberg excited states; this is in contrast to normal generalized gradient approximation potentials, which introduce additional problems by artificially placing Rydberg excitations at much too low energies [601]. Since no corresponding energy functional is defined for the SAOP potential, we employ the Becke–Perdew–Wang (BPW91c) exchange–correlation functional [62,64] for calculations of ground-state energies if needed in applications of the SAOP potential. All TDDFT calculations (KS, FDE, and subsystem-DFT) employ the adiabatic local density approximation (ALDA) for the exchange–correlation kernel. It should be noted that the TZP basis set is in general quite well suited for excitation energy calculations of valence excited states. Selected calculations were repeated with the much larger QZ3P–1DIFFUSE basis set from the ADF basis set library, which is of quadruple- ζ quality and contains three sets of polarization functions as well as additional diffuse functions. For the valence excited states investigated here, the excitation energies changed by about 0.05 eV compared to the TZP basis.

For the ESR calculations in Section 4.2, we employed the ZORA-QZ4P basis set from the ADF basis set. Also in this case, the BP86 functional was used, since it was shown to yield reliable results for calculations of ESR hyperfine coupling constants [340]. No frozen-core approximations were made here. Spin-unrestricted calculations were performed for the hyperfine interactions, in which we also used the zero-order regular approximation (ZORA) [602–604] for consistency with g -tensor calculations as reported in Ref. [332]. The method used here to calculate the ESR parameters is described in detail in Refs. [605] and [606].

B.2 Spectra simulation

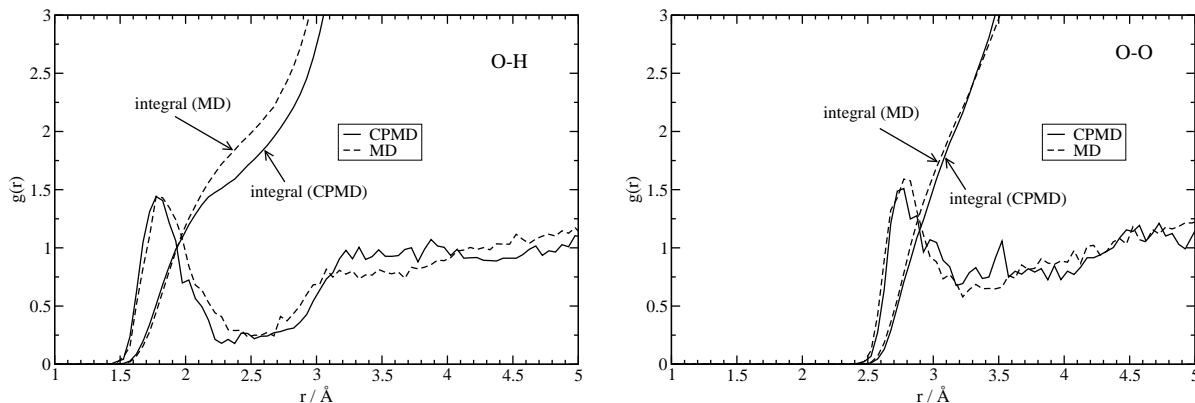
Some of the applications of the FDE approach required the simulation of spectra or spectroscopic properties in solution, or, for comparison, in the gas phase. This required the generation of snapshots, which were obtained either from molecular dynamics approaches based on classical force fields or from CPMD simulations. For classical MD simulations, we employed the General Amber Force Field (GAFF) [607] and the TIP3P water model [608] using the TINKER package [609,610] to run the calculations.

CPMD simulations were carried out with the Projector Augmented Wave (PAW) package [611] using the BLYP functional [62, 612]. For efficiency reasons, we employed deuterium isotopes for the hydrogen atoms. We used a fictitious mass for the wavefunctions of 100 a.u., a time step of 6.5 a.u. (0.157 fs) and a small friction on the wavefunctions of 0.0002 or 0.00005. The cutoff for the plane-wave basis was 30 Ry (408 eV) and 90 Ry (1225 eV) for the charge density. Using the projector augmented-wave approach rather low plane-wave cutoffs can be used, comparable to Vanderbilt’s ultrasoft pseudopotentials, and lower than those necessary with, e.g., Troullier–Martins norm-conserving pseudopotentials [611, 613]. This has been tested to give good simulations of liquid water. A Nosé thermostat with an oscillation frequency of 60000 a.u. was used to keep the temperature at 300 K. After equilibration for 11 to 15 ps with more strongly coupled thermostats, the simulations were prolonged for 8 to 12 ps.

The CPMD simulation in Section 4.2 was performed with one H_2NO molecule and 32 water molecules in a periodic cubic box of 10.05 Å. For the statistical analysis, we took the 75 water molecules closest to the radical into consideration for every snapshot in aqueous solution. In all subsequent frozen-density calculations the frozen density, ρ_2 in Eq. (2.75), was calculated from a sum of molecular densities of solvent molecules obtained within the local density approximation (LDA) and a TZP basis set. For canonical ensemble (constant temperature) gas-phase simulations of such a small molecule, (CP)MD approaches introduce the problem that it is not possible to use conventional thermostating techniques. Tests using a scheme similar to the one used in Ref. [116] for the gas-phase simulation showed that there is no exchange of energy between the different degrees of freedom in the present molecule during the simulation time, so that no proper sampling of the configurational space is achieved. We therefore used a Monte Carlo sampling in internal coordinates, in which ADF–DFT calculations were performed to determine the potential energy of the trial structures. An acceptance ratio of 0.5 was used for the Monte Carlo sampling, and the probabilities of acceptance were scaled by the factors arising from the Jacobian due to the use of non-linear coordinates (see the examples in Ref. [614, 615]).

The simulation for acetone (Section 3.4.2) was performed with one acetone molecule and 31 water molecules in a periodic cubic box of 10.168 Å. Every 36 fs, a snapshot for the final statistics was taken (220 in total), while general analyses are carried out with snapshots taken in intervals of 182 fs (44 in total). Additionally, we employed a purely classical model for acetone in water. Parameters from the GAFF [607] force field were used for acetone, combined with scaled partial charges from a Hirshfeld charge analysis for the isolated acetone molecule (SAOP/TZP). In order to verify this model, we compared the results of our MD simulations with those of the CPMD simulation with the same periodic box of 10.168 Å with one acetone molecule and 31 water molecules. The O(carbonyl)–H(water) and O(carbonyl)–O(water) radial distribution functions from both simulations are shown in Figure B.1. The partial charges for the acetone molecule were uniformly scaled in order to obtain optimum agreement of these radial distribution functions (scaling factor: 1.61). With this classical model, we performed simulations at 300 K of a periodic cubic box of 21.225 Å with 315 TIP3P water molecules and one acetone molecule. After a structure optimization and an equilibration phase of 200 ps (with 2.0 fs time steps), we carried out a simulation of 50 ps. Every 2 ps, a snapshot of the box was taken.

Figure B.1: Radial distribution function $g(r)$ and integral from a MD simulation (GAFF/TIP3P) in comparison to a CPMD simulation of the same system. Left: O(carbonyl)–H(water) distribution function; right: O(carbonyl)–O(water) distribution function.



In Figure B.1 the radial distribution functions around the carbonyl oxygen are compared. After scaling the partial charges for the acetone molecule especially the first peaks are very well reproduced by the classical MD simulations. This means that the distances and the number of hydrogen bonds to the acetone oxygen are correctly modeled. A minor difference is that the first peak in the O(carbonyl)–H(water) radial distribution function has a bit of a tail and at longer distances the peaks are slightly less pronounced. The orientation of the hydrogen bonds around the carbonyl group is much less well reproduced by the classical simulations. In the CPMD simulations the hydrogen bonds are in the plane of the acetone molecule (dihedral angles with the methyl groups: $0^\circ \pm 30^\circ$) with angles around $150^\circ (\pm 10^\circ)$ with the CO bond. In the classical simulations this chemical preference for certain angles was not present at all. Naturally, this could affect the solvent shift calculated from these structures.

The absorption spectra for the aminocoumarin C151 in Section 4.3 were simulated by calculating excitation energies for a number of solvent configurations, obtained as snapshots from a (NVT) classical MD simulation. For these MD simulations, the General Amber Force Field (GAFF) [607] and the TIP3P water model [608] were employed using the TINKER package [609,610] to run the calculations. Partial atomic charges for the aminocoumarin dye were taken from a multipole-derived charge analysis (reconstructing monopoles, dipole and quadrupole moments) [616] based on a SAOP DFT calculation. For *n*-hexane as a solvent, we used a mean value of these multipole-derived charges for an optimized structure. To improve the force-field parameters for bond stretching and valence angle bending, the equilibrium bond lengths and bond angles from an optimized structure (BP86/TZP) of C151 were used. The MD simulations for aqueous solution were carried out at a temperature of 300 K, with a cubic box of length 25 Å, containing one aminocoumarin dye molecule and 513 water molecules, leading to a density of 1.0066 kg/L. Starting from a random water structure around the aminocoumarin dye, we first optimized the structure and then equilibrated for 50 ps, heated the system to 500 K,

cooled it down to 300 K, and equilibrated again for 50 ps. After this preparation, a trajectory of 50 ps was generated with a time step of 2 fs. Every picosecond, a snapshot of the system was taken for the statistical analysis. No rigid bond constraints were used in the simulations presented here. But an additional trajectory, in which we used a Shake-like algorithm [617] to constrain bonds involving hydrogen atoms, resulted in only slight changes compared to the trajectory discussed here (the average excitation energy for a set of 50 structures changed by less than 0.03 eV). The MD simulations with *n*-hexane as a solvent were carried out in the same manner. We also used a cubic box of length 25 Å, with a density of the solution of 0.6745 kg/L (71 *n*-hexane molecules). Since this is a bit higher than the density of pure *n*-hexane at the simulation temperature, and since no accurate information about the density of the solution studied here is available, we performed an additional test with a trajectory obtained with the slightly lower density of 0.6596 kg/L (cubic box of length 25.1881 Å). No significant changes could be observed in the resulting spectra. We employed 8 trajectories for both solvents; between the individual trajectories, we heated the system to 500 K, cooled it down to 300 K and re-equilibrated for 50 ps.

B.3 Subsystem-TDDFT calculations

In the subsystem-TDDFT calculations presented in Chapter 5, fitted induced densities were employed for both the exchange–correlation and the Coulomb part (and also for the kinetic energy contribution in the case of subsystem calculations) of the induced potential for efficiency. For the benchmark tests in Section 5.1, the ground-state exchange–correlation potential was calculated from the exact densities. The ALDA-TDDFT coupling matrix is, in principle, symmetric. Due to the fitting procedure, however, there can be a slight deviation between the coupling matrix and its transpose, which is usually eliminated by taking the average of the original matrix and its transpose. In our case, however, calculating both the (A, B) - and the (B, A) -interaction blocks would double the computational cost. Hence, only the (A, B) -block is calculated explicitly, and transposed to obtain the (B, A) -block. This is done since system *A* is, by definition, the embedded system, for which we include an effective coupling to the environment. Therefore, we always employ the more approximate (fitted) representation for the environmental system. The exchange–correlation and the kinetic energy part of the kernel were obtained within the generalized ALDA, i.e., using a Thomas–Fermi-like kinetic energy contribution in addition to the conventional ALDA kernel [308].

The overall accuracy of excitation energies calculated from TDDFT depends on several parameters, like the choice of the basis set, the exchange–correlation potential used in the ground-state DFT calculation, the choice of the exchange–correlation kernel, the basis set and the fit set if density fitting techniques are used — as is the case in ADF. For a discussion of the influence of these parameters, we refer to, e.g., Ref. [222]. Details about the fitting procedure in ADF can be found in Ref. [236] and the references mentioned therein. Since ADF uses Slater-type basis functions, the calculation of the coupling matrix elements is carried out numerically, and the numerical precision of the excitation energies thus depends on the quality of the integration grid. The numerical error can be tested by increasing the number of integration points. For the examples studied in Section 5.1, we repeated a calculation of the excitation and splitting energies requesting

a numerical precision that should roughly be one order of magnitude higher than in the default calculations. The excitation energies obtained with this higher integration accuracy changed by typically 0.0001 to 0.0008 eV compared to the calculation with the smaller integration grid. It could be observed that the changes in the excitation energies are not completely random, but rather systematic, so that the precision of the splitting energies was actually better than that of the excitation energies (in the order of 0.0002 eV), and thus substantially smaller than typical splitting energies (which are in the order of 0.01 to 0.10 eV).

For the structural motives of LH2 investigated in Section 5.3, the following procedure was applied: Coordinates for non-hydrogen atoms were taken from the X-ray structure reported in Ref. [429] (PDB entry 1NKZ). Hydrogen atoms were added using default bond angles and bond lengths. Subsequently, the positions of the hydrogen atoms in the individual pigment molecules were optimized with BP86/TZP. The positions of the non-hydrogen atoms were kept fixed. For the calculation (SAOP/TZP) of excitation energies and excitation energy couplings we proceed as follows: The ground-state densities and molecular orbitals of the pigment molecules and the surrounding fragments under investigation are determined from a frozen-density embedding calculation [111] for each subsystem, including three freeze-and-thaw cycles [117]. For the pigments we calculated the local excitations within the frozen-density embedding approach as described in Section 3.4, which were subsequently coupled according to the approach presented in Section 5.1.

B.4 Resonance Raman calculations

Resonance Raman intensities within Heller’s gradient approximation were calculated either by numerical differentiation of excited-state energies along normal coordinates using ADF’s VIBRON module [318] (SAOP calculations in Section 6.3) or by a projection of analytical excited-state gradients onto the ground-state normal modes (see below). Apart from the SAOP spectra mentioned above, we employ the semi-numerical calculation of vibrational frequencies and normal modes available through the vibrational spectroscopy program package SNF [328], which allows for high-efficiency massive parallelization and excellent restart facilities necessary for systems of the size under study here. Ground- and excited-state electronic structure, gradient calculations, and geometry optimizations in Section 6.4 and Chapter 7 were performed with the quantum chemical suite of programs TURBOMOLE [618,619] using density functional theory. We employed either the BP86 functional [62,595] in combination with the resolution-of-the-identity (‘RI’) density fitting technique and auxiliary basis sets as implemented in TURBOMOLE [620–622], or the hybrid functional B3LYP [62,594,612,623]. SV(P), TZVP and TZVPP basis sets as available from the TURBOMOLE basis set library were applied [618,619,624].

Excited-state gradients were calculated analytically based on TDDFT as implemented in TURBOMOLE [231,239]. For the metal atoms in the calculations in Section 6.4, effective core potentials of the Stuttgart group were employed (which also account for scalar relativistic effects) [625]. These potentials include 28 electrons of the inner shells of both ruthenium and palladium, i.e. the 16 (Ru) or 18 (Pd) electrons belonging to the 4s, 4p, 4d and 5s shell are treated explicitly. The two PF_6^{-1} anions were not included

into the calculations, resulting in a charge of +2 for each of the two complexes under study.

No empirical scaling of the vibrational frequencies was performed. In contrast to the B3LYP functional, BP86 has proven to yield *harmonic* vibrational normal modes in close agreement with *fundamentals* from experiment [552, 570, 626] due to a fortunate error cancellation [552], which is true in particular for transition metal complexes [463, 571, 627, 628].

The intensity-tracking calculations in Chapter 7 were carried out with a modified version of the program AKIRA [468]. If not specified otherwise, standard AKIRA convergence criteria and an intensity threshold of 80 % of the total intensity for root-homing were applied. For comparison to the intensity-tracking spectra, excited-state gradients were projected onto normal modes as outlined above. These spectra are dubbed “conventional gradient spectra”.

B.5 Visualization

Graphics of the molecular structures were generated with the programs MOLDEN [629], VMD [630], and Molekel [631]. Graphical representations of normal modes, were created with the program JMOL [632].

C. List of Abbreviations

ADF	AMSTERDAM DENSITY FUNCTIONAL program
AIM	atoms in molecules
ALDA	adiabatic local density approximation
amu	atomic mass unit ($1.66056 \cdot 10^{-27}$ kg)
BCP	bond critical point
BP86	Becke's exchange functional combined with Perdew's correlation functional
BLYP	Becke's exchange functional combined with the Lee–Yang–Parr correlation functional
B3LYP	Becke's three-parameter hybrid functional
CASSCF	complete active space self-consistent field
CASPT2	CASSCF with second-order perturbation theory
cc-pVTZ	Dunning's correlation-consistent valence triple- ζ plus polarization basis
CCSD	coupled cluster with single and double excitations
CCSD(T)	CCSD with perturbative inclusion of triple excitations
CC2	approximate coupled cluster model to second order
CD	circular dichroism
CGE	conventional gradient expansion
CI	configuration interaction
CIS	configuration interaction with single excitations
CISD	configuration interaction with single and double excitations
CIS(D)	second-order perturbation expansion of CCSD
CIS(3,4)	third- and fourth-order analogs of CIS(D)
CPMD	Car–Parrinello molecular dynamics
CT	charge transfer
DFT	density-functional theory
DIIS	direct inversion in the iterative subspace
DNA	deoxyribonucleic acid
DZ	ADF's double- ζ basis set
DZP	ADF's double- ζ basis set with one set of polarization functions
EET	excitation-energy transfer
ESR	electron spin resonance
EVB	empirical valence bond
FC	Franck–Condon
FDE	frozen density embedding
FDEc	coupled FDE (i.e., including inter-subsystem response)
FDEu	uncoupled FDE (i.e., neglecting inter-subsystem response)
FDFT	frozen density functional theory
FSRS	femtosecond stimulated Raman spectroscopy
GFC	gradient Franck–Condon

GGA	generalized gradient approximation
HF	Hartree–Fock
hfcc	hyperfine coupling constant
HOMO	highest occupied molecular orbital
ICD	induced circular dichroism
IMDHO	independent mode, displaced harmonic oscillator
IR	infrared
KS	Kohn–Sham
KSCED	Kohn–Sham equations with constrained electron density
LC94	Lembarki–Chermette parameterization of the PW91k functional
LDA	local density approximation
LH2	light-harvesting complex 2 (in purple bacteria)
MC	Monte Carlo
MD	molecular dynamics
MLCT	metal-to-ligand charge transfer
MM	molecular mechanics
MO	molecular orbital
MP2	second-order Møller–Plesset perturbation theory
LUMO	lowest unoccupied molecular orbital
NBA	(<i>ortho</i> -) nitro benzaldehyde
PCM	polarizable continuum model
PES	potential-energy surface
PW91	Perdew–Wang functional
PW91c	Perdew–Wang correlation functional
PW91k	kinetic-energy functional derived from PW91x
PW91x	Perdew–Wang exchange functional
ONIOM	Morokuma’s “Our-own <i>n</i> -layered Integrated molecular Orbital + molecular mechanics Method”
QM/MM	quantum mechanics/molecular mechanics
QZ4P	ADF’s quadruple- ζ basis set with four sets of polarization functions
RCP	ring critical point
RI	resolution of the identity
ROHF	restricted open-shell Hartree–Fock
ROKS	restricted open-shell Kohn–Sham
SAOP	statistical averaging of molecular orbital potentials
SCF	self-consistent field
SMA	small matrix approximation
SOMO	singly occupied molecular orbital
SPA	single-pole approximation
SVP	Ahlrichs’ split-valence basis set with one set of polarization functions
SV(P)	like SVP, but without polarization functions on hydrogen
TDC	transition-density cube
TDDFT	time-dependent density-functional theory
TDKS	time-dependent Kohn–Sham
TF	Thomas–Fermi
TFD	Thomas–Fermi–Dirac

TFW	Thomas–Fermi–von Weizsäcker
TFWD	Thomas–Fermi–von Weizsäcker–Dirac
TZP	ADF’s triple- ζ basis set with one set of polarization functions
TZ2P	ADF’s triple- ζ basis set with two sets of polarization functions
TZVP	Ahlrichs’ triple- ζ basis set with one set of polarization functions
TZVPP	Ahlrichs’ triple- ζ basis set with two sets of polarization functions
UQCISD[T]	unrestricted quadratic CISD with approximate treatment of triple excitations
UV	ultraviolett
VCD	vibrational circular dichroism
VROA	vibrational Raman optical activity
XC	exchange–correlation
ZORA	zero-order regular approximation

Bibliography

- [1] H. Primas, U. Müller-Herold. *Elementare Quantenchemie*. Teubner, Stuttgart, 1990.
- [2] Per-Olov Löwdin. On the Non-Orthogonality Problem Connected with the Use of Atomic Wave Functions in the Theory of Molecules and Solids. *J. Chem. Phys.*, **18** (1950) 365–375.
- [3] R. S. Mulliken. Electronic Population Analysis on LCAO-MO Molecular Wave Functions. I. *J. Chem. Phys.*, **23** (1955) 1833–1840.
- [4] Alan E. Reed, Robert B. Weinstock, Frank Weinhold. Natural population analysis. *J. Chem. Phys.*, **83** (1985) 735–746.
- [5] A. E. Clark, E. R. Davidson. Population Analyses that Utilize Projection Operators. *Int. J. Quantum Chem.*, **93** (2003) 384–394.
- [6] Célia Fonseca Guerra, Jan-Willem Handgraaf, Evert Jan Baerends, F. Matthias Bickelhaupt. Voronoi deformation density (VDD) charges: Assessment of the Mulliken, Bader, Hirshfeld, Weinhold, and VDD methods for charge analysis. *J. Comput. Chem.*, **25** (2004) 189–210.
- [7] Richard Bader. *Atoms in Molecules*. Clarendon Press, Oxford, 1990.
- [8] F. L. Hirshfeld. Bonded-atom fragments for describing molecular charge densities. *Theor. Chim. Acta*, **44** (1977) 129–138.
- [9] P. Salvador, I. Mayer. Energy partitioning for “fuzzy” atoms. *J. Chem. Phys.*, **120** (2004) 5046–5052.
- [10] Roman F. Nalewaski, Paul W. Ayers, Robert G. Parr. *From Molecular Structure to Chemical Reactivity: The Density-Functional Perspective*. Oxford University Press, Oxford, 2008, to appear.
- [11] P. Geerlings, F. De Proft, W. Langenaeker. Conceptual Density Functional Theory. *Chem. Rev.*, **103** (2003) 1793–1873.
- [12] I. Mayer. Energy partitioning schemes. *Phys. Chem. Chem. Phys.*, **8** (2006) 4630–4646.
- [13] R. McWeeny. *Methods of Molecular Quantum Mechanics*. Academic Press, San Diego, 1992.

- [14] Per-Olov Löwdin. A Note on the Quantum-Mechanical Perturbation Theory. *J. Chem. Phys.*, **19** (1951) 1396–1401.
- [15] Per-Olov Löwdin. Studies in Perturbation Theory. IV. Solution of Eigenvalue Problem by Projection Operator Formalism. *J. Math. Phys.*, **3** (1962) 969–982.
- [16] A. J. Fisher. Methods for embedding for defect and surface problems. *J. Phys. C: Solid State Phys.*, **21** (1988) 3229–3249.
- [17] Weitao Yang. Direct Calculation of Electron Density in Density-Functional Theory. *Phys. Rev. Lett.*, **66** (1991) 1438–1441.
- [18] Kazuhiro Fujimoto, Weitao Yang. Density-fragment interaction approach for quantum-mechanical/molecular-mechanical calculations with application to the excited states of a Mg^{2+} -sensitive dye. *J. Chem. Phys.*, **129** (2008) 054102.
- [19] Tomoko Akama, Masato Kobayashi, Hiromi Nakai. Implementation of divide-and-conquer method including Hartree–Fock exchange interaction. *J. Comput. Chem.*, **28** (2007) 2003–2012.
- [20] Masato Kobayashi, Tomoko Akama, Hiromi Nakai. Second-order Møller–Plesset perturbation energy obtained from divide-and-conquer Hartree–Fock density matrix. *J. Chem. Phys.*, **125** (2006) 204106.
- [21] Masato Kobayashi, Yutaka Imamura, Hiromi Nakai. Alternative linear-scaling methodology for the second-order Møller–Plesset perturbation calculation based on divide-and-conquer method. *J. Chem. Phys.*, **127** (2007) 074103.
- [22] Masato Kobayashi, Hiromi Nakai. Extension of linear-scaling divide-and-conquer-based correlation method to coupled cluster theory with singles and doubles excitations. *J. Chem. Phys.*, **129** (2008) 044103.
- [23] Kazuo Kitaura, Eiji Ikeo, Toshio Asada, Tatsuya Nakano, Masami Uebayasi. Fragment molecular orbital method: an approximate computational method for large molecules. *Chem. Phys. Lett.*, **313** (1999) 701–706.
- [24] Dmitri G. Fedorov, Kazuo Kitaura. Extending the Power of Quantum Chemistry to Large Systems with the Fragment Molecular Orbital Method. *J. Phys. Chem. A*, **111** (2007) 6904–6914.
- [25] Thomas M. Henderson. Embedding wave function theory in density functional theory. *J. Chem. Phys.*, **125** (2006) 014105.
- [26] J. E. Inglesfield. A method of embedding. *J. Phys. C: Solid State Phys.*, **14** (1981) 3795–3806.
- [27] Ulrich Gutdeutsch, Uwe Birkenheuer, Sven Krüger, Notker Rösch. On cluster embedding schemes based on orbital space partitioning. *J. Chem. Phys.*, **106** (1997) 6020–6030.

-
- [28] Ulrich Gutdeutsch, Uwe Birkenheuer, Notker Rösch. A strictly variational procedure for cluster embedding based on the extended subspace approach. *J. Chem. Phys.*, **109** (1998) 2056–2064.
- [29] Paul G. Mezey. Macromolecular density matrices and electron densities with adjustable nuclear geometries. *J. Math. Chem.*, **18** (1995) 141–168.
- [30] Thomas E. Exner, Paul G. Mezey. Ab Initio-Quality Electrostatic Potentials for Proteins: An Application of the ADMA Approach. *J. Phys. Chem. A*, **106** (2002) 11791–1180.
- [31] B. Jeziorski, W. Kołos. Perturbation approach to the study of weak intermolecular interactions. In H. Ratajczak, W. J. Orville-Thomas, Eds., *Molecular Interactions, Vol. 3*, p. 1–46. Wiley, Chichester, 1982.
- [32] Bogumil Jeziorski, Robert Moszynski, Krzysztof Szalewicz. Perturbation Theory Approach to Intermolecular Potential Energy Surfaces of van der Waals Complexes. *Chem. Rev.*, **94** (1994) 1887–1930.
- [33] Hayes L. Williams, Cary F. Chabalowski. Using Kohn–Sham Orbitals in Symmetry-Adapted Perturbation Theory to Investigate Intermolecular Interactions. *J. Phys. Chem. A*, **105** (2001) 646–659.
- [34] Georg Jansen, Andreas Hesselmann. Comment on “Using Kohn–Sham Orbitals in Symmetry-Adapted Perturbation Theory to Investigate Intermolecular Interactions. *J. Phys. Chem. A*, **105** (2001) 11156–11157.
- [35] Alston J. Misquitta, Bogumil Jeziorski, Krzysztof Szalewicz. Dispersion Energy from Density-Functional Theory Description of Monomers. *Phys. Rev. Lett.*, **91** (2003) 033201.
- [36] Andreas Heßelmann, Georg Jansen. Intermolecular dispersion energies from time-dependent density functional theory. *Chem. Phys. Lett.*, **367** (2003) 778–784.
- [37] Alston J. Misquitta, Krzysztof Szalewicz. Intermolecular forces from asymptotically corrected density functional description of monomers. *Chem. Phys. Lett.*, **357** (2002) 301–306.
- [38] Andreas Heßelmann, Georg Jansen. Intermolecular induction and exchange-induction energies from coupled-perturbed Kohn–Sham density functional theory. *Chem. Phys. Lett.*, **362** (2002) 319–325.
- [39] Andreas Heßelmann, Georg Jansen. First-order intermolecular interaction energies from Kohn–Sham orbitals. *Chem. Phys. Lett.*, **357** (2002) 464–470.
- [40] Pierre Hohenberg, Walter Kohn. Inhomogeneous Electron Gas. *Phys. Rev.*, **136**(B3) (1964) 864–871.

- [41] T. A. Wesolowski. One-electron Equations for Embedded Electron Density: Challenge for Theory and Practical Payoffs in Multi-Level Modeling of Complex Polyatomic Systems. In J. Leszczynski, Ed., *Computational Chemistry: Reviews of Current Trends*, Volume 10, p. 1–82. World Scientific, Singapore, 2006.
- [42] W. Kohn, L. J. Sham. Self-Consistent Equations Including Exchange and Correlation Effects. *Phys. Rev.*, **140**(A 4) (1965) 1133–1138.
- [43] Robert G. Parr, Weitao Yang. *Density-Functional Theory of Atoms and Molecules*. Oxford University Press, Oxford, 1989.
- [44] P. A. M. Dirac. Note on exchange phenomena in the Thomas atom. *Proc. Camb. Phil. Soc.*, **26** (1930) 376–385.
- [45] F. Bloch. Bemerkung zur Elektronentheorie des Ferromagnetismus und der elektrischen Leitfähigkeit. *Z. Phys.*, **57** (1929) 545–555.
- [46] Viktor N. Staroverov, Gustavo E. Scuseria, Jianmin Tao, John P. Perdew. Comparative assessment of a new nonempirical density functional: Molecules and hydrogen-bonded complexes. *J. Chem. Phys.*, **119** (2003) 12129–12137.
- [47] J. P. Perdew, S. Kurth. Density Functionals for Non-relativistic Coulomb Systems in the New Century. In C. Fiolhais, F. Nogueira, M. Marques, Eds., *A Primer in Density Functional Theory*, p. 1–55. Springer, Berlin, 2003.
- [48] Gustavo E. Scuseria, Viktor N. Staroverov. Progress in the development of exchange–correlation functionals. In Clifford E. Dykstra, Gernot Frenking, Kwang S. Kim, Gustavo E. Scuseria, Eds., *Theory and Applications of Computational Chemistry: The First Forty Years*, p. 669–724. Elsevier, Amsterdam, 2005.
- [49] Yan Zhao, Donald G. Truhlar. A new local density functional for main-group thermochemistry, transition metal bonding, thermochemical kinetics, and noncovalent interactions. *J. Chem. Phys.*, **125** (2006) 194101.
- [50] Yan Zhao, Nathan E. Schultz, Donald G. Truhlar. Design of Density Functionals by Combining the Method of Constraint Satisfaction with Parametrization for Thermochemistry, Thermochemical Kinetics, and Noncovalent Interactions. *J. Chem. Theory Comput.*, **2** (2006) 364–382.
- [51] Yan Zhao, Donald G. Truhlar. The M06 suite of density functionals for main group thermochemistry, thermochemical kinetics, noncovalent interactions, excited states, and transition elements: two new functionals and systematic testing of four M06-class functionals and 12 other functionals. *Theor. Chem. Acc.*, **120** (2008) 215–241.
- [52] Yan Alexander Wang, Emily A. Carter. Orbital-Free Kinetic-Energy Density Functional Theory. In S. D. Schwartz, Ed., *Theoretical Methods in Condensed Phase Chemistry*, p. 117–184. Kluwer, Dordrecht, 2000.

-
- [53] Eduardo V. Ludeña, Valentin V. Karasiev, Pedro Nieto. Exact and approximate forms of the kinetic energy functional $T_s[\rho]$ for molecules obtained via local-scaling transformations. *Theor. Chem. Acc.*, **110** (2003) 395–402.
- [54] L. A. Thomas. The calculation of atomic fields. *Proc. Camb. Phil. Soc.*, **23** (1927) 542–548.
- [55] E. Fermi. Eine statistische Methode zur Bestimmung einiger Eigenschaften des Atoms und ihre Anwendung auf die Theorie des periodischen Systems der Elemente. *Z. Phys.*, **48** (1928) 73–79.
- [56] C. F. von Weizsäcker. Zur Theorie der Kernmassen. *Z. Physik*, **96** (1935) 431–458.
- [57] Garnet Kin-Lic Chan, Aron J. Cohen, Nicholas C. Handy. Thomas–Fermi–Dirac–von Weizsäcker models in finite systems. *J. Chem. Phys.*, **114** (2001) 631–638.
- [58] H. Lee, C. Lee, R. G. Parr. Conjugate gradient correction to the Hartree–Fock kinetic- and exchange-energy density functionals. *Phys. Rev. A*, **44** (1991) 768–771.
- [59] V. V. Karasiev, S. B. Trickey, Frank E. Harris. Born–Oppenheimer interatomic forces from simple, local kinetic energy density functionals. *J. Comput.-Aid. Mat. Des.*, **13** (2006) 111–129.
- [60] R. Kevorkyants, M. Dulak, T. A. Wesolowski. Interaction energies in hydrogen-bonded systems: A testing ground for subsystem formulation of density-functional theory. *J. Chem. Phys.*, **124** (2006) 024104.
- [61] N. H. March, R. Santamaria. Non-Local Relation Between Kinetic and Exchange Energy Densities in Hartree–Fock Theory. *Int. J. Quantum Chem.*, **39** (1991) 585–592.
- [62] A. D. Becke. Density-functional exchange-energy approximation with correct asymptotic behavior. *Phys. Rev. A*, **38**(6) (1988) 3098–3100.
- [63] A. Lembarki, H. Chermette. Obtaining a gradient-corrected kinetic-energy functional from the Perdew–Wang exchange functional. *Phys. Rev. A*, **50** (1994) 5328.
- [64] J. P. Perdew. In P. Ziesche, H. Eschrig, Eds., *Electronic Structure of Solids*, p. 11. Akademie Verlag, Berlin, 1991.
- [65] Andrew E. DePristo, Joel D. Kress. Kinetic-energy functionals via Padé approximations. *Phys. Rev. A*, **35** (1987) 438–441.
- [66] Hui Ou-Yang, Mel Levy. Approximate Noninteracting Kinetic Energy Functionals from a Nonuniform Scaling Requirement. *Int. J. Quantum Chem.*, **40** (1991) 379–388.
- [67] J. P. Perdew. Generalized gradient approximation for the fermion kinetic energy as a functional of the density. *Phys. Lett. A*, **165** (1992) 79–82.

-
- [68] Ajit J. Thakkar. Comparison of kinetic-energy density functionals. *Phys. Rev. A*, **46** (1992) 6920–6924.
- [69] Daniel J. Lacks, Roy G. Gordon. Tests of nonlocal kinetic energy functionals. *J. Chem. Phys.*, **100** (1994) 4446–4452.
- [70] Fabien Tran, Tomasz A. Wesolowski. Link between the Kinetic- and Exchange-Energy Functionals in the Generalized Gradient Approximation. *Int. J. Quantum Chem.*, **89** (2002) 441–446.
- [71] J. R. Trail, D. M. Bird. Density-functional embedding using a plane-wave basis. *Phys. Rev. B*, **62** (2000) 16402–16411.
- [72] O. Gunnarsson, M. Jonson, B. I. Lundqvist. Exchange and correlation in atoms, molecules and solids. *Phys. Lett.*, **59A** (1976) 177–179.
- [73] J. A. Alonso, L. A. Girifalco. Nonlocal approximation to the exchange potential and kinetic energy of an inhomogeneous electron gas. *Phys. Rev. B*, **17** (1978) 3735–3743.
- [74] P. García-González, J. E. Alvarellos, E. Chacón. Kinetic-energy density functional: Atoms and shell structure. *Phys. Rev. A*, **54** (1996) 1897–1905.
- [75] Enrico Smargiassi, Paul A. Madden. Orbital-free kinetic-energy functionals for first-principles molecular dynamics. *Phys. Rev. B*, **49** (1994) 5220–5226.
- [76] Michael Foley, Paul A. Madden. Further orbital-free kinetic-energy functionals for *ab initio* molecular dynamics. *Phys. Rev. B*, **53** (1996) 10589–10598.
- [77] Yan Alexander Wang, Niranjana Govind, Emily A. Carter. Orbital-free kinetic-energy functionals for the nearly free electron gas [Errata: *Phys. Rev. B* **60** (1998), 17162; *Phys. Rev. B* **64** (2001), 129901]. *Phys. Rev. B*, **58** (1998) 13465–13471.
- [78] Karin M. Carling, Emily A. Carter. Orbital-free density functional theory calculations of the properties of Al, Mg and Al–Mg crystalline phases. *Modelling Simul. Mater. Sci. Eng.*, **11** (2003) 339–348.
- [79] Gregory Ho, Mitchell T. Ong, Kyle J. Caspersen, Emily A. Carter. Energetics and kinetics of vacancy diffusion and aggregation in shocked aluminium *via* orbital-free density functional theory. *Phys. Chem. Chem. Phys.*, **9** (2007) 4951–5966.
- [80] Terry J. Frankcombe, Geert-Jan Kroes, Nicholas I. Choly, Efthimios Kaxiras. Orbital-Free Density Functional Theory Applied to NaAlH₄. *J. Phys. Chem. B*, **109** (2005) 16554–16562.
- [81] Baojing Zhou, Vincent L. Ligneres, Emily A. Carter. Improving the orbital-free density functional theory description of covalent materials. *J. Chem. Phys.*, **122** (2005) 044103.
- [82] Nicholas Choly, Efthimios Kaxiras. Kinetic energy density functionals for non-periodic systems. *Sol. State Commun.*, **121** (2002) 281–286.

-
- [83] Gregory S. Ho, Vincent L. Lignères, Emily A. Carter. Analytic form for a nonlocal kinetic energy functional with a density-dependent kernel for orbital-free density functional theory under periodic and Dirichlet boundary conditions. *Phys. Rev. B*, **78** (2008) 045105.
- [84] David García-Aldea, J. E. Alvarellos. Fully nonlocal kinetic energy density functionals: A proposal and a general assessment for atomic systems. *J. Chem. Phys.*, **129** (2008) 074103.
- [85] Rollin A. King, Nicholas C. Handy. Kinetic energy functionals from the Kohn–Sham potential. *Phys. Chem. Chem. Phys.*, **2** (2000) 5049–5056.
- [86] Rollin A. King, Nicholas C. Handy. Kinetic energy functionals for molecular calculations. *Mol. Phys.*, **99** (2001) 1005–1009.
- [87] P. Gombas. *Die statistische Theorie des Atoms und ihre Anwendungen*. Springer, Wien, 1949.
- [88] V. L. Gaydaenko, V. K. Nikulin. Born–Mayer Interatomic Potential for Atoms with $Z = 2$ to $Z = 36$. *Chem. Phys. Lett.*, **7** (1970) 360.
- [89] R. G. Gordon, Y. S. Kim. Theory for the Forces between Closed-Shell Atoms and Molecules. *J. Chem. Phys.*, **56** (1972) 3122.
- [90] W. J. Carr, Jr., Rosemary A. Coldwell-Horsfall, A. E. Fein. Anharmonic Contribution to the Energy of a Dilute Electron Gas — Interpolation for the Correlation Energy. *Phys. Rev.*, **124** (1961) 747–752.
- [91] W. J. Carr, Jr., A. A. Maradudin. Ground-State Energy of a High-Density Electron Gas. *Phys. Rev.*, **133** (1964) A371.
- [92] Y. S. Kim, R. G. Gordon. Study of the electron gas approximation. *J. Chem. Phys.*, **60** (1974) 1842.
- [93] Andrew E. DePristo. Hohenberg–Kohn density-functional theory as an implicit Poisson equation for density changes from summed fragment densities. *Phys. Rev. A*, **54** (1996) 3863–3869.
- [94] J. Harris. Simplified method for calculating the energy of weakly interacting fragments. *Phys. Rev. B*, **31** (1985) 1770–1779.
- [95] I. J. Robertson, Behnam Farid. Does the Harris energy functional possess a local maximum at the ground-state density? *Phys. Rev. Lett.*, **66**(25) (1991) 3265–3268.
- [96] Behnam Farid, Volker Heine, G. E. Engel, I. J. Robertson. Extremal properties of the Harris–Foulkes functional and an improved screening calculation for the electron gas. *Phys. Rev. B*, **48**(16) (1993) 11602–11621.
- [97] Stefano Baroni, Paolo Giannozzi, Andrea Testa. Green’s-Function Approach to Linear Response in Solids. *Phys. Rev. Lett.*, **58** (1987) 1861–1864.

- [98] X. Gonze, J.-P. Vigneron. Density-functional approach to nonlinear-response coefficients of solids. *Phys. Rev. B*, **39** (1989) 13120–13128.
- [99] Xavier Gonze. Adiabatic density-functional perturbation theory. *Phys. Rev. A*, **52** (1995) 1096–1114.
- [100] Anna Putrino, Daniel Sebastiani, Michele Parrinello. Generalized variational density functional perturbation theory. *J. Chem. Phys.*, **113** (2000) 7102–7109.
- [101] David M. Benoit, Daniel Sebastiani, Michele Parrinello. Accurate Total Energies without Self-Consistency. *Phys. Rev. Lett.*, **87** (2001) 226401.
- [102] Wuming Zhu, S. B. Trickey. Tests of Perturbative DFT Total Energy Estimates Implemented in a Gaussian Basis. *Int. J. Quantum Chem.*, **100** (2004) 245–253.
- [103] Gloria Tabacchi, Christopher J. Mundy, Jürg Hutter, Michele Parrinello. Classical force fields parameterized from *ab initio* calculations. *J. Chem. Phys.*, **117** (2002) 1416–1432.
- [104] Darrin M. York, Weitao Yang. A chemical potential equalization method for molecular simulations. *J. Chem. Phys.*, **104** (1996) 159–172.
- [105] Gloria Tabacchi, Jürg Hutter, Christopher J. Mundy. A density-functional approach to polarizable models: A Kim–Gordon response density interaction potential for molecular simulations. *J. Chem. Phys.*, **123** (2005) 074108.
- [106] P. Cortona. Self-consistently determined properties of solids without band-structure calculations. *Phys. Rev. B*, **44** (1991) 8454.
- [107] Juan Maria García-Lastra, Jakub W. Kaminski, Tomasz A. Wesolowski. Orbital-free effective embedding potential at nuclear cusps. *J. Chem. Phys.*, **129** (2008) 074107.
- [108] Pietro Cortona. Direct determination of self-consistent total energies and charge densities of solids: A study of the cohesive properties of the alkali halides. *Phys. Rev. B*, **46** (1992) 2008–2014.
- [109] Nicholas Choly, Gang Lu, Weinan E, Efthimios Kaxiras. Multiscale simulation in simple metals: A density-functional-based methodology. *Phys. Rev. B*, **71** (2005) 094101.
- [110] Marcella Iannuzzi, Barbara Kirchner, Jürg Hutter. Density functional embedding for molecular systems. *Chem. Phys. Lett.*, **421** (2006) 16–20.
- [111] T. A. Wesolowski, A. Warshel. Frozen Density Functional Approach for *ab Initio* Calculations of Solvated Molecules. *J. Phys. Chem.*, **97** (1993) 8050.
- [112] T. A. Wesolowski, J. Weber. Kohn-Sham equations with constrained electron density: an iterative evaluation of the ground-state electron density of interacting molecules. *Chem. Phys. Lett.*, **248** (1996) 71–76.

-
- [113] Christoph R. Jacob, Johannes Neugebauer, Lucas Visscher. A flexible implementation of frozen-density embedding for use in multilevel simulations. *J. Comput. Chem.*, **29** (2008) 1011–1018.
- [114] T. Wesolowski, A. Warshel. Ab Initio Free Energy Perturbation Calculations of Solvation Free Energy Using the Frozen Density Functional Approach. *J. Phys. Chem.*, **98** (1994) 5183 – 5187.
- [115] Tomasz Wesolowski, Richard P. Muller, Arieh Warshel. Ab Initio Frozen Density Functional Calculations of Proton Transfer Reactions in Solution. *J. Phys. Chem.*, **100** (1996) 15444–15449.
- [116] Johannes Neugebauer, Manuel J. Louwerse, Evert Jan Baerends, Tomasz A. Wesolowski. The merits of the frozen-density embedding scheme to model solvatochromic shifts. *J. Chem. Phys.*, **122** (2005) 094115.
- [117] T. A. Wesolowski, H. Chermette, J. Weber. Accuracy of approximate kinetic energy functionals in the model of Kohn–Sham equations with constrained electron density: The $\text{FH} \cdots \text{NCH}$ complex as a test case. *J. Chem. Phys.*, **105** (1996) 9182.
- [118] Karin Kiewisch, Georg Eickerling, Markus Reiher, Johannes Neugebauer. Topological analysis of electron densities from Kohn–Sham and subsystem density functional theory. *J. Chem. Phys.*, **128** (2008) 044114.
- [119] Eugene V. Stefanovich, Thanh N. Truong. Embedded density functional approach for calculations of adsorption on ionic crystals. *J. Chem. Phys.*, **104** (1996) 2946–2955.
- [120] Alessandro Laio, Joost VandeVondele, Ursula Rothlisberger. A Hamiltonian electrostatic coupling scheme for hybrid Car–Parrinello molecular dynamics simulations. *J. Chem. Phys.*, **116** (2002) 6941–6947.
- [121] Marcin Dulak, Tomasz A. Wesolowski. On the electron leak problem in orbital-free embedding calculations. *J. Chem. Phys.*, **124** (2006) 164101.
- [122] Christoph R. Jacob, Tomasz A. Wesolowski, Lucas Visscher. Orbital-free embedding applied to the calculation of induced dipole moments in $\text{CO}_2 \cdots X$ ($X=\text{He}$, Ne , Ar , Kr , Xe , Hg) van der Waals complexes. *J. Chem. Phys.*, **123** (2005) 174104.
- [123] Christoph R. Jacob, S. Maya Beyhan, Lucas Visscher. Exact functional derivative of the nonadditive kinetic-energy bifunctional in the long-distance limit. *J. Chem. Phys.*, **126** (2007) 234116.
- [124] D. E. Ellis, G. A. Benesh, E. Byrom. Molecular cluster studies of binary alloys: LiAl . *Phys. Rev. B*, **16** (1977) 3308–3313.
- [125] J. Guo, D. E. Ellis, D. J. Lam. First-principles calculations of the electronic structure of sapphire: Bulk states. *Phys. Rev. B*, **45** (1992) 3204–3214.

- [126] D. E. Ellis, G. L. Goodman. Self-Consistent Dirac-Slater Calculations for Molecules and Embedded Clusters. *Int. J. Quantum Chem.*, **25** (1984) 185–200.
- [127] T. Klüner, H.-J. Freund, V. Staemmler, R. Kosloff. Theoretical Investigation of Laser Induced Desorption of Small Molecules from Oxide Surfaces: A First Principles Study. *Phys. Rev. Lett.*, **80** (1998) 5208–5211.
- [128] T. Klüner, H.-J. Freund, J. Freitag, V. Staemmler. Laser-induced desorption of NO from NiO(100): *Ab initio* calculations of potential surfaces for intermediate excited states. *J. Chem. Phys.*, **104** (1996) 10030–10040.
- [129] N. Govind, Y. A. Wang, A. J. R. da Silva, E. A. Carter. Accurate ab initio energetics of extended systems via explicit correlation embedded in a density functional environment. *Chem. Phys. Lett.*, **295** (1998) 129–134.
- [130] N. Govind, Y. A. Wang, E. A. Carter. Electronic-structure calculations by first-principles density-based embedding of explicitly correlated systems. *J. Chem. Phys.*, **110** (1999) 7677–7688.
- [131] J. Åqvist, A. Warshel. Simulation of Enzyme Reactions Using Valence Bond Force Fields and Hybrid Quantum/Classical Approaches. *Chem. Rev.*, **93** (1993) 2523–2544.
- [132] Jiali Gao, Donald G. Truhlar. Quantum Mechanical Methods for Enzyme Kinetics. *Annu. Rev. Phys. Chem.*, **53** (2002) 467–505.
- [133] A. Shurki, A. Warshel. Structure/Function Correlations of Proteins Using MM, QM/MM, and Related Approaches: Methods, Concepts, Pitfalls, and Current Progress. *Adv. Protein Chem.*, **66** (2003) 249–313.
- [134] Richard A. Friesner, Victor Guallar. Ab Initio Quantum Chemical and Mixed Quantum Mechanics/Molecular Mechanics (QM/MM) Methods for Studying Enzymatic Catalysis. *Annu. Rev. Phys. Chem.*, **56** (2005) 389–427.
- [135] Hans-Martin Senn, Walter Thiel. QM/MM Methods for Biological Systems. *Top. Curr. Chem.*, **268** (2007) 173–290.
- [136] M. Svensson, S. Humbel, R. D. J. Froese, T. Matsubara, S. Sieber, K. Morokuma. ONIOM: A Multilayered Integrated MO + MM Method for Geometry Optimizations and Single Point Energy Predictions. A Test for Diels–Alder Reactions and Pt(P(*t*-Bu)₃)₂ + H₂ Oxidative Addition. *J. Phys. Chem.*, **100** (1996) 19357–19363.
- [137] Stéphane Humbel, Stefan Sieber, Keiji Morokuma. The IMOMO method: Integration of different levels of molecular orbital approximations for geometry optimization of large systems: Test for *n*-butane conformation and S_N2 reaction: RCl+Cl[−]. *J. Chem. Phys.*, **105** (1996) 1959–1967.
- [138] Thom Vreven, K. Suzie Byun, István Komáromi, Stefan Dapprich, John A. Montgomery, Jr., Keiji Morokuma, Michael J. Frisch. Combining Quantum Mechanics Methods with Molecular Mechanics Methods in ONIOM. *J. Chem. Theory Comput.*, **2** (2006) 815–826.

-
- [139] Patrick Huang, Emily A. Carter. Self-consistent embedding theory for locally correlated configuration interaction wave functions in condensed matter. *J. Chem. Phys.*, **125** (2006) 084102.
- [140] Patrick Huang, Emily A. Carter. Local Electronic Structure around a Single Kondo Impurity. *Nano Letters*, **6** (2006) 1146–1150.
- [141] Tomasz A. Wesolowski. Embedding a multideterminantal wave function in an orbital-free environment. *Phys. Rev. A*, **77** (2008) 012504.
- [142] Emily A. Carter. Challenges in Modeling Materials Properties Without Experimental Input. *Science*, **321** (2008) 800–803.
- [143] Patrick Huang, Emily A. Carter. Advances in Correlated Electronic Structure for Solids, Surfaces, and Nanostructures. *Annu. Rev. Phys. Chem.*, **59** (2008) 261–290.
- [144] T. Klüner, N. Govind, Y. A. Wang, E. A. Carter. Prediction of electronic excited states of adsorbates on metal surfaces from first principles. *Phys. Rev. Lett.*, **86** (2001) 5954–5957.
- [145] Thorsten Klüner, Niranjana Govind, Yan Alexander Wang, Emily A. Carter. Periodic density functional embedding theory for complete active space self-consistent field and configuration interaction calculations: Ground and excited states. *J. Chem. Phys.*, **116** (2002) 42–54.
- [146] Tomasz A. Wesolowski. Comment on “Prediction of electronic excited states of adsorbates on metal surfaces from first principles”. *Phys. Rev. Lett.*, **88** (2002) 209701.
- [147] T. Klüner, N. Govind, Y. A. Wang, E. A. Carter. Reply to Comment on “Prediction of electronic excited states of adsorbates on metal surfaces from first principles”. *Phys. Rev. Lett.*, **88** (2002) 209702.
- [148] André Severo Pereira Gomes, Christoph R. Jacob, Lucas Visscher. Calculation of local excitations in large systems by embedding wave-function theory in density-functional theory. *Phys. Chem. Chem. Phys.*, (2008) in press.
- [149] Marek Štrajbl, Gongyi Hong, Arieh Warshel. Ab Initio QM/MM Simulation with Proper Sampling: “First Principle” Calculations of the Free Energy of the Autodissociation of Water in Aqueous Solution. *J. Phys. Chem. B*, **106** (2002) 13333–13343.
- [150] Yun Xiang, Arieh Warshel. Quantifying Free Energy Profiles of Proton Transfer Reactions in Solution and Proteins by Using a Diabatic FDFT Method. *J. Phys. Chem. B*, **112** (2008) 1007–1015.
- [151] M. H. M. Olsson, G. Hong, A. Warshel. Frozen Density Functional Free Energy Simulations of Redox Proteins: Computational Studies of the Reduction Potential of Plastocyanin and Rusticyanin. *J. Am. Chem. Soc.*, **125** (2003) 5025–5039.

- [152] Arieh Warshel, Robert M. Weiss. An empirical valence bond approach for comparing reactions in solutions and in enzymes. *J. Am. Chem. Soc.*, **102** (1980) 6218–6226.
- [153] Gongyi Hong, Edina Rosta, Arieh Warshel. Using the constrained DFT Approach in Generating Diabatic Surfaces and Off Diagonal Empirical Valence Bond Terms for Modeling Reactions in Condensed Phases. *J. Phys. Chem. B*, **110** (2006) 19570–19574.
- [154] Monica Leopoldini, Nino Russo, Marirosa Toscano, Marcin Dulak, Tomasz Adam Wesolowski. Mechanism of Nitrate Reduction by *Desulfovibrio desulfuricans* Nitrate Reductase—A Theoretical Investigation. *Chem. Eur. J.*, **12** (2006) 2532–2541.
- [155] T. A. Wesolowski. Density functional theory with approximate kinetic energy functionals applied to hydrogen bonds. *J. Chem. Phys.*, **106** (1997) 8516–8526.
- [156] T. A. Wesolowski, Y. Ellinger, J. Weber. Density functional theory with an approximate kinetic energy functional applied to study structure and stability of weak van der Waals complexes. *J. Chem. Phys.*, **108** (1998) 6078.
- [157] T. A. Wesolowski, O. Parisel, Y. Ellinger, J. Weber. Comparative Study of Benzene \cdots X (X = O₂, N₂, CO) Complexes Using Density Functional Theory: The Importance of an Accurate Exchange–Correlation Energy Density at High Reduced Density Gradients. *J. Phys. Chem. A*, **101** (1997) 7818–7825.
- [158] T. A. Wesolowski, F. Tran. Gradient-free and gradient-dependent approximations in the total energy bifunctional for weakly overlapping electron densities. *J. Phys. Chem.*, **118** (2003) 2072.
- [159] T. A. Wesolowski, P.-Y. Morgantini, J. Weber. Intermolecular interaction energies from the total energy bifunctional: A case study of carbazole complexes. *J. Chem. Phys.*, **116** (2002) 6411–6421.
- [160] Fabien Tran, Jacques Weber, Tomasz A. Wesolowski. Physisorption of Molecular Hydrogen on Polycyclic Aromatic Hydrocarbons: A Theoretical Study. *J. Phys. Chem. B*, **106** (2002) 8689–8696.
- [161] Fabien Tran, Bassam Alameddine, Titus A. Jenny, Tomasz A. Wesolowski. π -Stacking Behavior of Selected Nitrogen-Containing PAHs. *J. Phys. Chem. A*, **108** (2004) 9155–9160.
- [162] S. Grimme, T. Schwabe. Towards chemical accuracy for the thermodynamics of large molecules: new hybrid density functionals including non-local correlation effects. *Phys. Chem. Chem. Phys.*, **8** (2006) 4398–4401.
- [163] S. Grimme. Semiempirical GGA-Type Density Functional Constructed with a Long-Range Dispersion Correction. *J. Comput. Chem.*, **27** (2006) 1787–1799.
- [164] S. Grimme. Seemingly simple stereoelectronic effects in alkane isomers and the implications for Kohn-Sham density functional theory. *Angew. Chem. Int. Ed.*, **45** (2006) 4460–4464.

-
- [165] Fabien Tran, Jacques Weber, Tomasz A. Wesolowski. Theoretical Study of the Benzene Dimer by the Density-Functional-Theory Formalism Based on Electron-Density Partitioning. *Helv. Chim. Acta*, **84** (2001) 1489–1503.
- [166] G. Hong, M. Strajbl, T. Wesolowski, A. Warshel. Constraining the Electron Densities in DFT Method as an Effective Way for *Ab Initio* Studies of Metal-Catalyzed Reactions. *J. Comput. Chem.*, **21** (2000) 1554–1561.
- [167] Mohamed Zbiri, Mihail Atanasov, Claude Daul, Juan Maria Garcia-Lastra, Tomasz A. Wesolowski. Application of the density functional theory derived orbital-free embedding potential to calculate the splitting energies of lanthanide cations in chloroelpasolite crystals. *Chem. Phys. Lett.*, **397** (2004) 441–446.
- [168] J. M. García-Lastra, T. A. Wesolowski, M. T. Barriuso, J. A. Aramburu, M. Moreno. Optical and vibrational properties of MnF_6^{4-} complexes in cubic fluoroperovskites: insight through embedding calculations using Kohn-Sham equations with constrained electron density. *J. Phys.: Condens. Matter*, **18** (2006) 1519–1534.
- [169] Mohamed Zbiri, Claude Daul, Tomasz A. Wesolowski. Effect of the f-Orbital Delocalization on the Ligand-Field Splitting Energies in Lanthanide-Containing Elpasolites. *J. Chem. Theory Comput.*, **2** (2006) 1106–1111.
- [170] Marcin Dułak, Jakub W. Kamiński, Tomasz A. Wesolowski. Equilibrium Geometries of Noncovalently Bound Intermolecular Complexes Derived from Subsystem Formulation of Density Functional Theory. *J. Chem. Theor. Comput.*, **3** (2007) 735–745.
- [171] U. Koch, P. L. A. Popelier. Characterization of C–H–O Hydrogen Bonds on the Basis of the Charge Density. *J. Phys. Chem.*, **99** (1995) 9747–9754.
- [172] Ignasi Mata, Ibon Alkorta, Enrique Espinosa, Elies Molins. Topological Properties of the Electron Distribution in Hydrogen-bonded Systems. In Chérif F. Matta, Russell J. Boyd, Eds., *The Quantum Theory of Atoms in Molecules*, p. 425–451. Wiley-VCH, Weinheim, 2007.
- [173] Slawomir J. Grabowski. Relationships between QTAIM and the Decomposition of the Interaction Energy — Comparison of Different Kinds of Hydrogen Bond. In Chérif F. Matta, Russell J. Boyd, Eds., *The Quantum Theory of Atoms in Molecules*, p. 453–469. Wiley-VCH, Weinheim, 2007.
- [174] W. Scherer, G. S. McGrady. Agostic interactions in d(0) metal alkyl complexes. *Angew. Chem. Int. Ed.*, **43**(14) (2004) 1782–1806.
- [175] G. Eickerling, R. Mastalerz, V. Herz, H.-J. Himmel, W. Scherer, M. Reiher. Relativistic Effects on the topology of the Electron Density. *J. Chem. Theory Comput.*, **3** (2007) 2182–2197.
- [176] G. Eickerling, M. Reiher. The shell structure of Atoms. *J. Chem. Theory Comput.*, **4** (2008) 286–296.

-
- [177] M. Reiher. A systems theory for chemistry. *Found. Chem.*, **5** (2003) 23–41.
- [178] Chérif F. Matta, Russell J. Boyd, Eds. *The Quantum Theory of Atoms in Molecules*. Wiley-VCH, Weinheim, 2007.
- [179] N. Hebben, H.-J. Himmel, G. Eickerling, C. Herrmann, M. Reiher, V. Herz, M. Presnitz, W. Scherer. The Electronic Structure of the Tris(ethylene) Complexes $[M(C_2H_4)_3]$ ($M=Ni$, Pd , and Pt): A Combined Experimental and Theoretical Study. *Chem. Eur. J.*, **13** (2007) 10078–10087.
- [180] A. Reisinger, N. Trapp, I. Krossing, S. Altmannshofer, V. Herz, M. Presnitz, W. Scherer. Homoleptische Silber(I)-Acetylen-Komplexe. *Angew. Chem.*, **119** (2007) 8445–8449.
- [181] C. Katan, P. Rabiller, C. Lecomte, M. Guezo, V. Oison, M. Souhassou. Numerical computation of critical properties and atomic basins from three-dimensional grid electron densities. *J. Appl. Cryst.*, **36** (2003) 65–73.
- [182] Mathematica Version 5.2. Wolfram Research, Inc., 2005.
- [183] M. Presnitz, F. Mayer, V. Herz, G. Eickerling, W. Scherer. calc.lap.nb: A mathematica script for the analysis of charge density distributions. Universität Augsburg (Lehrstuhl CPM), 2007.
- [184] Johannes Neugebauer, Christoph R. Jacob, Tomasz A. Wesolowski, Evert Jan Baerends. An Explicit Quantum Chemical Method for Modeling Large Solvation Shells Applied to Aminocoumarin C151. *J. Phys. Chem. A*, **109** (2005) 7805–7814.
- [185] Christoph R. Jacob, Lasse Jensen, Johannes Neugebauer, Lucas Visscher. Comparison of frozen-density embedding and discrete reaction field solvent models for molecular properties. *Phys. Chem. Chem. Phys.*, **8** (2006) 2349–2359.
- [186] Marcin Dulak, Tomasz A. Wesolowski. The Basis Set Effect on the Results of the Minimization of the Total Energy Bifunctional $E[\rho_A, \rho_B]$. *Int. J. Quantum Chem.*, **101** (2005) 543–549.
- [187] Ernest R. Davidson. Bonding in FHF^- , $(HF)_2$, and FHF . *Int. J. Quantum Chem.*, **98** (2004) 317–324.
- [188] Paul G. Wenthold, Robert R. Squires. Bond Dissociation Energies of F_2^- and HF_2 . A Gas-Phase Experimental and G2 Theoretical Study. *J. Phys. Chem.*, **99** (1995) 2002–2005.
- [189] J. E. Del Bene, M. J. Jordan. A comparative study of vibrational anharmonicity in the bihalide anions XHX^- : $X=F$, Cl , Br . *Spectrochim. Acta A*, **55** (1999) 719.
- [190] Christoph R. Jacob, Lucas Visscher. Density-functional theory approach for the quantum chemical treatment of proteins. *J. Chem. Phys.*, **128** (2008) 155102.
- [191] M. W. Lister, L. E. Sutton. The investigation by electron diffraction of the structures of some tetrahalides. *Trans. Faraday Soc.*, **37** (1941) 393–406.

-
- [192] Louis J. Farrugia, Cameron Evans. Experimental x-ray charge density studies on the binary carbonyls $\text{Cr}(\text{CO})_6$, $\text{Fe}(\text{CO})_5$ and $\text{Ni}(\text{CO})_4$. *J. Phys. Chem. A*, **109** (2005) 8834–8848.
- [193] Andreas Görling. Density-functional theory beyond the Hohenberg–Kohn theorem. *Phys. Rev. A*, **59** (1999) 3359–3374.
- [194] Mel Levy, Ágnes Nagy. Variational Density-Functional Theory for an Individual Excited State. *Phys. Rev. Lett.*, **83** (1999) 4361–4364.
- [195] R. Gaudoin, K. Burke. Lack of Hohenberg–Kohn Theorem for Excited States. *Phys. Rev. Lett.*, **93** (2004) 173001.
- [196] T. H. Dunning, V. McKoy. Nonempirical Calculations on Excited States: The Ethylene Molecule. *J. Chem. Phys.*, **47** (1967) 1735–1747.
- [197] Alexander L. Fetter, John Dirk Walecka. *Quantum Theory of Many-Particle Systems*. Dover, New York, 2003.
- [198] D. J. Thouless. *The Quantum Mechanics of Many-Body Systems*. Academic Press, New York, 1961.
- [199] Andreas Dreuw, Martin Head-Gordon. Single-Reference ab Initio Methods for the Calculation of Excited States of Large Molecules. *Chem. Rev.*, **105** (2005) 4009–4037.
- [200] Stefan Grimme, Frank Neese. Double-hybrid density functional theory for excited electronic states of molecules. *J. Chem. Phys.*, **127** (2007) 154116.
- [201] James B. Foresman, Martin Head-Gordon, John A. Pople, Michael J. Frisch. Toward a Systematic Molecular Orbital Theory for Excited States. *J. Phys. Chem.*, **96** (1992) 135–149.
- [202] Martin Head-Gordon, Rudolph J. Rico, Manabu Oumi, Timothy J. Lee. A doubles correction to electronic excited states from configuration interaction in the space of single substitutions. *Chem. Phys. Lett.*, **219** (1994) 21–29.
- [203] So Hirata. Third- and fourth-order perturbation corrections to excitation energies from configuration interaction singles. *J. Chem. Phys.*, **122** (2005) 094105.
- [204] Ove Christiansen, Henrik Koch, Poul Jørgensen. The second-order approximate coupled cluster singles and doubles model CC2. *Chem. Phys. Lett.*, **243** (1995) 409–418.
- [205] Christof Hättig, Florian Weigend. CC2 excitation energy calculations on large molecules using the resolution of the identity approximation. *J. Chem. Phys.*, **113** (2000) 5154–5161.
- [206] Christof Hättig. Structure Optimizations for Excited States with Correlated Second-Order Methods: CC2 and ADC(2). *Adv. Quantum Chem.*, **50** (2005) 37–60.

- [207] Young Min Rhee, Martin Head-Gordon. Scaled Second-Order Perturbation Corrections to Configuration Interaction Singles: Efficient and Reliable Excitation Energy Methods. *J. Phys. Chem. A*, **111** (2007) 5314–5326.
- [208] Erich Runge, E. K. U. Gross. Density-Functional Theory for Time-Dependent Systems. *Phys. Rev. Lett.*, **52** (1984) 997–1000.
- [209] Sudip Chakravarty, Martin B. Fogel, Walter Kohn. Dynamic Response of Inhomogeneous Fermi Systems. *Phys. Rev. Lett.*, **43** (1979) 775–778.
- [210] A. Zangwill, Paul Soven. Density-Functional approach to local-field effects in finite systems: Photoabsorption in the rare gases. *Phys. Rev. A*, **21** (1980) 1561–1571.
- [211] M. J. Stott, E. Zaremba. Linear-response theory within the density-functional formalism: Application to atomic polarizabilities [Erratum: *Phys. Rev. A* **22** (1980), 2293]. *Phys. Rev. A*, **21** (1980) 12–23.
- [212] S. K. Gosh, B. M. Deb. Dynamic polarizability of many-electron systems within a time-dependent density-functional theory. *Chem. Phys.*, **71** (1982) 295–306.
- [213] Libero J. Bartolotti. Variation-perturbation theory within a time-dependent Kohn–Sham formalism: An application to the determination of multipole polarizabilities, spectral sums, and dispersion coefficients. *J. Chem. Phys.*, **80** (1984) 5687–5695.
- [214] Robert van Leeuwen. Mapping from Densities to Potentials in Time-Dependent Density-Functional Theory. *Phys. Rev. Lett.*, **82** (1999) 3863–3866.
- [215] Robert van Leeuwen. Causality and Symmetry in Time-Dependent Density-Functional Theory. *Phys. Rev. Lett.*, **80** (1998) 1280–1283.
- [216] Robert van Leeuwen. Key Concepts in Time-Dependent Density-Functional Theory. *Int. J. Mod. Phys. B*, **15** (2001) 1969–2023.
- [217] R. van Leeuwen, N. E. Dahlen, G. Stefanucci, C.-O. Almbladh, U. von Barth. Introduction to the Keldysh Formalism. In M. A. L. Marques, C. A. Ullrich, F. Nogueira, A. Rubio, K. Burke, E. K. U. Gross, Eds., *Time-Dependent Density Functional Theory*, p. 33–59. Springer, Berlin, 2006.
- [218] J. Schirmer, A. Dreuw. Critique of the foundations of time-dependent density-functional theory. *Phys. Rev. A*, **75** (2007) 022513.
- [219] Neepa T. Maitra, Robert van Leeuwen, Kieron Burke. Comment on “Critique of the foundations of time-dependent density-functional theory. *arXiv:0710.0018v2*, 2008.
- [220] Mark E. Casida. Time-Dependent Density Functional Response Theory for Molecules. In Delano P. Chong, Ed., *Recent Advances in Density Functional Methods Part I*, p. 155–192. World Scientific, Singapore, 1995.

-
- [221] Miguel A. L. Marques, Eberhard K. U. Gross. Time-Dependent Density-Functional Theory. In C. Fiolhais, F. Nogueira, M. Marques, Eds., *A Primer in Density Functional Theory*, p. 144–184. Springer, Berlin, 2003.
- [222] A. Rosa, G. Ricciardi, O. V. Gritsenko, E. J. Baerends. Excitation energies of metal complexes with time-dependent density functional theory. *Struct. Bonding*, **112** (2004) 49–116.
- [223] M. A. L. Marques, E. K. U. Gross. Time-Dependent Density Functional Theory. *Annu. Rev. Phys. Chem.*, **55** (2004) 427–455.
- [224] Kieron Burke, Jan Werschnik, E. K. U. Gross. Time-dependent density functional theory: Past, present, and future. *J. Chem. Phys.*, **123** (2005) 062206.
- [225] E. K. U. Gross, K. Burke. Basics. *Lect. Notes Phys.*, **706** (2006) 1–17.
- [226] D. P. Craig, T. Thirunamachandran. *Molecular Quantum Electrodynamics*. Dover, Mineola, 1998.
- [227] P. W. Atkins, R. S. Friedman. *Molecular Quantum Mechanics*. Oxford University Press, Oxford, 3 ed., 1997.
- [228] Filipp Furche. On the density matrix based approach to time-dependent density functional response theory. *J. Chem. Phys.*, **114** (2001) 5982–5992.
- [229] Johannes Neugebauer. Couplings between electronic transitions in a subsystem formulation of time-dependent density functional theory. *J. Chem. Phys.*, **126** (2007) 134116.
- [230] E. K. U. Gross, C. A. Ullrich, U. J. Gossmann. Density Functional Theory of Time-Dependent Systems. In E. K. U. Gross, Ed., *Density Functional Theory*, p. 149–171. Plenum Press, New York, 1995.
- [231] Filipp Furche, Reinhart Ahlrichs. Adiabatic time-dependent density functional methods for excited state properties. *J. Chem. Phys.*, **117** (2002) 7433–7447.
- [232] Jochen Autschbach, Tom Ziegler. Double perturbation theory: A powerful tool in computational coordination chemistry. *Coord. Chem. Rev.*, **238/239** (2003) 83–126.
- [233] Martin Feyereisen, Jeff Nichols, Jens Oddershede, Jack Simons. Direct atomic-orbital-based time-dependent Hartree–Fock calculations of frequency-dependent polarizabilities. *J. Chem. Phys.*, **96** (1992) 2978.
- [234] Ernest R. Davidson. The Iterative Calculation of a Few of the Lowest Eigenvalues and Corresponding Eigenvectors of Large Real-Symmetric Matrices. *J. Comp. Phys.*, **17** (1975) 87–94.
- [235] Christopher W. Murray, Stephen C. Racine, Ernest R. Davidson. Improved Algorithms for the Lowest Few Eigenvalues and Associated Eigenvectors of Large Matrices. *J. Comp. Phys.*, **103** (1992) 382–389.

- [236] S. J. A. van Gisbergen, J. G. Snijders, E. J. Baerends. Implementation of time-dependent density functional response equations. *Comput. Phys. Commun.*, **118** (1999) 119–138.
- [237] Christine Jamorski, Mark E. Casida, Dennis R. Salahub. Dynamic polarizabilities and excitation spectra from a molecular implementation of time-dependent density-functional response theory: N₂ as a case study. *J. Chem. Phys.*, **104** (1996) 5134–5147.
- [238] Habbo H. Heinze, Andreas Görling, Notker Rösch. An efficient method for calculating molecular excitation energies by time-dependent density-functional theory. *J. Chem. Phys.*, **113** (2000) 2088–2099.
- [239] D. Rappoport, F. Furche. Analytical time-dependent density functional derivative methods within the RI-J approximation, an approach to excited states of large molecules. *J. Chem. Phys.*, **122** (2005) 064105.
- [240] Stefan Grimme. Density functional calculations with configuration interaction for the excited states of molecules. *Chem. Phys. Lett.*, **259** (1996) 128–137.
- [241] So Hirata, Martin Head-Gordon. Time-dependent density functional theory within the Tamm-Dancoff approximation. *Chem. Phys. Lett.*, **314** (1999) 291–299.
- [242] Felipe Cordova, L. Joubert Doriol, Andrei Ipatov, Mark E. Casida, Claudia Filippi, Alberto Vela. Troubleshooting time-dependent density-functional theory for photochemical applications: Oxirane. *J. Chem. Phys.*, **127** (2007) 164111.
- [243] M. Petersilka, U. J. Gossmann, E. K. U. Gross. Excitation Energies from Time-Dependent Density-Functional Theory. *Phys. Rev. Lett.*, **76** (1996) 1212–1215.
- [244] I. Vasiliev, Serdar Ögüt, J. R. Chelikowsky. *Ab initio* Excitation Spectra and Collective Electronic Response in Atoms and Clusters. *Phys. Rev. Lett.*, **82** (1999) 1919–1922.
- [245] H. Appel, E. K. U. Gross, K. Burke. Excitations in Time-Dependent Density-Functional Theory. *Phys. Rev. Lett.*, **90** (2003) 043005.
- [246] Mahito Chiba, Takao Tsuneda, Kimihiko Hirao. An efficient state-specific scheme of time-dependent density functional theory. *Chem. Phys. Lett.*, **420** (2006) 391–396.
- [247] Seiken Tokura, Takeshi Sato, Takao Tsuneda, Takahito Nakajima, Kimihiko Hirao. A Dual-Level State-Specific Time-Dependent Density-Functional Theory. *J. Comput. Chem.*, **29** (2007) 1187–1197.
- [248] Nicholas A. Besley. Calculation of the electronic spectra of molecules in solution and on surfaces. *Chem. Phys. Lett.*, **390** (2004) 124–129.
- [249] Andreas Dreuw. Quantum Chemical Methods for the investigation of Photoinitiated Processes in Biological Systems: Theory and Applications. *ChemPhysChem*, **7** (2006) 2259–2274.

-
- [250] Mark E. Casida, Fabien Gutierrez, Jingang Guan, Florent-Xavier Gadea, Dennis Salahub, Jean-Pierre Daudey. Charge-transfer correction for improved time-dependent local density approximation excited-state potential energy curves: Analysis within the two-level model with illustration for H₂ and LiH. *J. Chem. Phys.*, **113** (2000) 7062–7071.
- [251] David Tozer. Relationship between long-range charge-transfer excitation energy error and integer discontinuity in Kohn–Sham theory. *J. Chem. Phys.*, **119** (2003) 12697–12699.
- [252] Andreas Dreuw, Jennifer L. Weisman, Martin Head-Gordon. Long-range charge-transfer excited states in time-dependent density functional theory require non-local exchange. *J. Chem. Phys.*, **119** (2003) 2943–2946.
- [253] Yoshihiro Tawada, Takao Tsuneda, Susumu Yanagisawa, Takeshi Yanai, Kimihiko Hirao. A long-range-corrected time-dependent density functional theory. *J. Chem. Phys.*, **120** (2004) 8425–8433.
- [254] Oleg Gritsenko, Evert Jan Baerends. Asymptotic correction of the exchange correlation kernel of time-dependent density functional theory for long-range charge-transfer excitations. *J. Chem. Phys.*, **121** (2004) 655–660.
- [255] Neepa T. Maitra. Undoing static correlation: Long-range charge transfer in time-dependent density-functional theory. *J. Chem. Phys.*, **122** (2005) 234104.
- [256] Leonardo Bernasconi, Michiel Sprik, Jürg Hutter. Time dependent density functional theory study of charge-transfer and intramolecular electronic excitations in acetone–water systems. *J. Chem. Phys.*, **119** (2003) 12417–12431.
- [257] Leonardo Bernasconi, Michiel Sprik, Jürg Hutter. Hartree–Fock exchange in time dependent density functional theory: application to charge transfer excitations in solvated molecular systems. *Chem. Phys. Lett.*, **394** (2004) 141–146.
- [258] Andreas Dreuw, Graham R. Fleming, Martin Head-Gordon. Charge-Transfer State as a Possible Signature of a Zeaxanthin–Chlorophyll Dimer in the Non-photochemical Quenching Process in Green Plants. *J. Phys. Chem. B*, **107** (2003) 6500–6503.
- [259] Andreas Dreuw, Graham R. Fleming, Martin Head-Gordon. Chlorophyll fluorescence quenching by xanthophylls. *Phys. Chem. Chem. Phys.*, **5** (2003) 3247–3256.
- [260] Andreas Dreuw, Martin Head-Gordon. Failure of Time-Dependent Density Functional Theory for Long-Range Charge-Transfer Excited States: The Zincbacteriochlorin–Bacteriochlorin and Bacteriochlorophyll–Spheroidene Complexes. *J. Am. Chem. Soc.*, **126** (2004) 4007–4016.
- [261] Takeshi Yanai, David P. Tew, Nicholas C. Handy. A new hybrid exchange–correlation functional using the Coulomb-attenuating method (CAM-B3LYP). *Chem. Phys. Lett.*, **393** (2004) 51–57.

- [262] Peter M. W. Gill, Ross D. A. Adamson, John A. Pople. Coulomb-attenuated exchange energy density functionals. *Mol. Phys.*, **88** (1996) 1005–1009.
- [263] Thierry Leininger, Hermann Stoll, Hans-Joachim Werner, Andreas Savin. Combining long-range configuration interaction with short-range density functionals. *Chem. Phys. Lett.*, **275** (1997) 151–160.
- [264] Hisayoshi Iikura, Takao Tsuneda, Takeshi Yanai, Kimihiko Hirao. A long-range correction scheme for generalized-gradient-approximation exchange functionals. *J. Chem. Phys.*, **115** (2001) 3540–3544.
- [265] Iann C. Gerber, János G. Ángyán. Hybrid functional with separated range. *Chem. Phys. Lett.*, **415** (2005) 100–105.
- [266] Oleg A. Vydrov, Jochen Heyd, Aliaksandr V. Krukau, Gustavo E. Scuseria. Importance of short-range versus long-range Hartree-Fock exchange for the performance of hybrid density functionals. *J. Chem. Phys.*, **125** (2006) 074106.
- [267] Mahito Chiba, Takao Tsuneda, Kimihiko Hirao. Excited state geometry optimizations by analytical energy gradient of long-range corrected time-dependent density functional theory. *J. Chem. Phys.*, **124** (2006) 144106.
- [268] Paul N. Day, Kiet A. Nguyen, Ruth Pachter. Calculation of two-photon absorption spectra of donor– π -acceptor compounds in solution using quadratic response time-dependent density functional theory. *J. Chem. Phys.*, **125** (2006) 094103.
- [269] Michael J. G. Peach, Trygve Helgaker, Paweł Sałek, Thomas W. Keal, Ola B. Lutnæs, David J. Tozer, Nicholas C. Handy. Assessment of a Coulomb-attenuated exchange–correlation energy functional. *Phys. Chem. Chem. Phys.*, **8** (2006) 558–562.
- [270] Michael J. G. Peach, Aron J. Cohen, David J. Tozer. Influence of Coulomb-attenuation on exchange–correlation functional quality. *Phys. Chem. Chem. Phys.*, **8** (2006) 4543–4549.
- [271] Denis Jacquemin, Eric A. Perpète, Oleg A. Vydrov, Gustavo E. Scuseria, Carlo Adamo. Assessment of long-range corrected functionals performance for $n \rightarrow \pi^*$ transitions in organic dyes. *J. Chem. Phys.*, **127** (2007) 094102.
- [272] Kiet A. Nguyen, Paul N. Day, Ruth Pachter. Effects of solvation on one- and two-photon spectra of coumarin derivatives: A time-dependent density functional theory study. *J. Chem. Phys.*, **126** (2007) 094303.
- [273] Michael J. G. Peach, Peter Benfield, Trygve Helgaker, David J. Tozer. Excitation energies in density functional theory: An evaluation and a diagnostic test. *J. Chem. Phys.*, **128** (2008) 044118.
- [274] C.-O. Almbladh, U. von Barth. Exact results for the charge and spin densities, exchange–correlation potentials, and density-functional eigenvalues. *Phys. Rev. B*, **31** (1985) 3231–3244.

-
- [275] D. P. Chong, O. V. Gritsenko, E. J. Baerends. Interpretation of the Kohn–Sham orbital energies as approximate vertical ionization potentials. *J. Chem. Phys.*, **116** (2002) 1760–1772.
- [276] C. Fonseca Guerra, J. G. Snijders, G. te Velde, E. J. Baerends. Towards an order- N DFT method. *Theoret. Chem. Acc.*, **99** (1998) 391–403.
- [277] Amsterdam density functional program. Theoretical Chemistry, Vrije Universiteit, Amsterdam. URL: <http://www.scm.com>.
- [278] G. te Velde, F. M. Bickelhaupt, E. J. Baerends, S. J. A. van Gisbergen, C. Fonseca Guerra, J. G. Snijders, T. Ziegler. Chemistry with ADF. *J. Comput. Chem.*, **22** (2001) 931–967.
- [279] Chang-Guo Zhan, Jeffrey A. Nichols, David A. Dixon. Ionization Potential, Electron Affinity, Electronegativity, Hardness, and Electron Excitation Energy: Molecular Properties from Density Functional Theory Orbital Energies. *J. Phys. Chem. A*, **107** (2003) 4184–4195.
- [280] Ove Christiansen, Henrik Koch, Asger Halkier, Poul Jørgensen, Trygve Helgaker, Alfredo Sanchez de Meras. Large-scale calculations of excitation energies in coupled cluster theory: The singlet excited states of benzene. *J. Chem. Phys.*, **105** (1996) 6921–6939.
- [281] A. Schäfer, H. Horn, R. Ahlrichs. Fully Optimized Contracted Gaussian Basis Sets for Atoms Li to Kr. *J. Chem. Phys.*, **97** (1992) 2571–2577.
- [282] Ansgar Schäfer, Christian Huber, Reinhart Ahlrichs. Fully optimized contracted Gaussian basis sets of triple zeta valence quality for atoms Li to Kr. *J. Chem. Phys.*, **100**(8) (1994) 5829–5835.
- [283] C. Angeli, K. L. Bak, V. Bakken, O. Christiansen, R. Cimiraglia, S. Coriani, P. Dahle, E. K. Dalskov, T. Enevoldsen, B. Fernandez, C. Hättig, K. Hald, A. Halkier, H. Heiberg, T. Helgaker, H. Hettema, H. J. Aa. Jensen, D. Jonsson, P. Jørgensen, S. Kirpekar, W. Klopper, R. Kobayashi, H. Koch, A. Ligabue, O. B. Lutnæs, K. V. Mikkelsen, P. Norman, J. Olsen, M. J. Packer, T. B. Pedersen, Z. Rinkevicius, E. Rudberg, T. A. Ruden, K. Ruud, P. Salek, A. Sanchez de Meras, T. Saue, S. P. A. Sauer, B. Schimmelpfennig, K. O. Sylvester-Hvid, P. R. Taylor, O. Vahtras, D. J. Wilson, H. Ågren. DALTON, a molecular electronic structure program, Release 2.0 (2005), see <http://www.kjemi.uio.no/software/dalton/dalton.html>, 2005.
- [284] Wolfgang Hieringer, Andreas Görling. Failure of time-dependent density functional methods for excitations in spatially separated systems. *Chem. Phys. Lett.*, **419** (2006) 557–562.
- [285] Andreas Dreuw, Martin Head-Gordon. Comment on ‘Failure of time-dependent density functional methods for excitations in spatially separated systems’ by Wolfgang Hieringer and Andreas Görling. *Chem. Phys. Lett.*, **426** (2006) 231–233.

- [286] Wolfgang Hieringer, Andreas Görling. Reply to Comment on ‘Failure of time-dependent density functional methods for excitations in spatially separated systems’ by Andreas Dreuw and Martin Head-Gordon. *Chem. Phys. Lett.*, **426** (2006) 234–236.
- [287] Christian Reichardt. *Solvents and Solvent Effects in Organic Chemistry*. Verlag Chemie, Weinheim, 1988.
- [288] Christian Reichardt. Solvatochromic Dyes as Solvent Polarity Indicators. *Chem. Rev.*, **94** (1994) 2319–2358.
- [289] E. S. Dodsworth, M. Hasegawa, M. Brigde, W. Linert. Solvatochromism. In A. B. P. Lever, Ed., *Comprehensive Coordination Chemistry*, Volume 2, p. 351–365. Elsevier, Amsterdam, 2004.
- [290] Alex H. de Vries, Piet Th. van Duijnen. Solvatochromism of the $\pi^* \leftarrow n$ Transition of Acetone by Combined Quantum Mechanical–Classical Mechanical Calculations. *Int. J. Quant. Chem.*, **57** (1996) 1067–1076.
- [291] Ute F. Röhrig, Irmgard Frank, Jürg Hutter, Alessandro Laio, Joost VandeVondele, Ursula Rothlisberger. QM/MM Car–Parrinello Molecular Dynamics Study of the Solvent Effects on the Ground State and on the First Excited Singlet State of Acetone in Water. *ChemPhysChem*, **4** (2003) 1177–1182.
- [292] Michael Odellius, Barbara Kirchner, Jürg Hutter. *s*-Tetrazine in Aqueous Solution: A Density Functional Study of Hydrogen Bonding and Electronic Excitations. *J. Phys. Chem. A*, **108** (2004) 2044–2052.
- [293] Jun Zeng, Daiqian Xie. Hydrogen Bonding and Solvent Effects on the Lowest $^1(n, \pi^*)$ Excitations of Triazines in Water. *J. Comput. Chem.*, **25** (2004) 813–822.
- [294] Daiqian Xie, Jun Zeng. Hydrogen Bonding and Solvatochromatic Shift of the Lowest $^1(n, \pi^*)$ excitation of *s*-Tetrazine in Its Hydrated Clusters and Dilute Solutions. *J. Comput. Chem.*, **25** (2004) 1487–1494.
- [295] Wen-Ge Han, Tiqing Liu, Fahmi Himo, Alexei Touthkine, Donald Bashford, Klaus M. Hahn, Louis Noodleman. A Theoretical Study of the UV/Visible Absorption and Emission Solvatochromic Properties of Solvent-Sensitive Dyes. *ChemPhysChem*, **4** (2003) 1084–1094.
- [296] Tiqing Liu, Wen-Ge Han, Fahmi Himo, G. Matthias Ullmann, Donald Bashford, Alexei Touthkine, Klaus M. Hahn, Louis Noodleman. Density Functional Vertical Self-Consistent Reaction Field Theory for Solvatochromism Studies of Solvent-Sensitive Dyes. *J. Phys. Chem. A*, **108** (2004) 3545–3555.
- [297] M. Sulpizi, P. Carloni, J. Hutter, U. Rothlisberger. A hybrid TDDFT/MM investigation of the optical properties of aminocumarins in water and acetonitrile solution. *Phys. Chem. Chem. Phys.*, **5** (2003) 4798–4805.

-
- [298] J. Zeng, J. S. Craw, N. S. Hush, J. R. Reimers. Solvent Effects on Molecular and Ionic Spectra. 4. Photochemistry of $\text{Fe}^{2+}(\text{H}_2\text{O})_6$ in Water Revisited: Possible Mechanisms for the Primary Absorption Process Leading to Electron Ejection. *J. Phys. Chem.*, **98** (1994) 11075–11088.
- [299] S. Hush, Jeffrey R. Reimers. Solvent Effects on metal to ligand charge transfer excitations. *Coord. Chem. Rev.*, **177** (1998) 37–60.
- [300] Noel S. Hush, Jeffrey R. Reimers. Solvent Effects on the Electronic Spectra of Transition Metal Complexes. *Chem. Rev.*, **100** (2000) 775–786.
- [301] Simona Fantacci, Filippo De Angelis, Annabella Selloni. Absorption Spectrum and Solvatochromism of the $[\text{Ru}(4,4'\text{-COOH-2,2'}\text{-bpy})_2(\text{NCS})_2]$ Molecular Dye by Time Dependent Density Functional Theory. *J. Am. Chem. Soc.*, **125** (2003) 4381–4387.
- [302] Jacopo Tomasi, Maurizio Persico. Molecular Interactions in Solution: An Overview of Methods Based on Continuous Distributions of the Solvent. *Chem. Rev.*, **94** (1994) 2027–2094.
- [303] Christopher J. Cramer. *Essentials of Computational Chemistry*. Wiley, New York, 2002.
- [304] Andreas Klamt, Volker Jonas, Thorsten Bürger, John C. W. Lohrenz. Refinement and Parametrization of COSMO-RS. *J. Phys. Chem. A*, **102** (1998) 5074–5085.
- [305] R. Car, M. Parrinello. Unified Approach for Molecular Dynamics and Density-Functional Theory. *Phys. Rev. Lett.*, **55** (1985) 2471–2474.
- [306] Leonardo Bernasconi, Jochen Blumberger, Michiel Sprik, Rodolphe Vuilleumier. Optical response of Cu^+ and Ag^+ aqua ions: A DFT/TDDFT study. *J. Chem. Phys.*, **121** (2004) 11885–11899.
- [307] Anders Osted, Jacob Kongsted, Kurt V. Mikkelsen, Ove Christiansen. Linear Response Properties of Liquid Water Calculated Using CC2 and CCSD within Different Molecular Mechanics Methods. *J. Phys. Chem. A*, **108** (2004) 8646–8658.
- [308] Mark E. Casida, Tomasz A. Wesolowski. Generalization of the Kohn–Sham Equations with Constrained Electron Density Formalism and Its Time-Dependent Response Theory Formulation. *Int. J. Quantum Chem.*, **96** (2004) 577–588.
- [309] Tomasz A. Wesolowski. Hydrogen-bonding induced shifts of the excitation energies in nucleic acid bases: an interplay between electrostatic and electron density overlap effects. *J. Am. Chem. Soc.*, **126** (2004) 11444–11445.
- [310] Nicholas A. Besley, Mark T. Oakley, Alexander J. Cowan, Jonathan D. Hirst. A Sequential Molecular Mechanics/Quantum Mechanics Study of the Electronic Spectra of Amides. *J. Am. Chem. Soc.*, **126** (2004) 13502–13511.

-
- [311] Mahito Chiba, Dmitri G. Fedorov, Kazuo Kitaura. Time-dependent density functional theory with the multilayer fragment molecular orbital method. *Chem. Phys. Lett.*, **444** (2007) 346–350.
- [312] Mahito Chiba, Dmitri G. Fedorov, Kazuo Kitaura. Time-dependent density functional theory based upon the fragment molecular orbital method. *J. Chem. Phys.*, **127** (2007) 104108.
- [313] C. W. Porter, C. Iddings. The absorption spectrum and the photochemical decomposition of acetone. *J. Am. Chem. Soc.*, **48**(1) (1926) 40–44.
- [314] Noel S. Bayliss, Eion G. McRae. Solvent Effects in the Spectra of Acetone, Crotonaldehyde, Nitromethane and Nitrobenzene. *J. Phys. Chem.*, **58** (1954) 1006–1011.
- [315] N. S. Bayliss, G. Wills-Johnson. Solvent effects on the intensities of the weak ultraviolet spectra of ketones and nitroparaffins—I. *Spectrochimica Acta*, **24A** (1968) 551–561.
- [316] W. P. Hayes, C. J. Timmons. Solvent and substituent effects on the $n \rightarrow \pi^*$ absorption bands of some ketones. *Spectrochimica Acta*, **21** (1965) 529–541.
- [317] A. Balasubramanian, C. N. R. Rao. Evaluation of solute-solvent interactions from solvent blue-shifts of $n \rightarrow \pi^*$ transitions of C=O, C=S, NO₂ and N=N groups: hydrogen bond energies of various donor-acceptor systems. *Spectrochimica Acta*, **18** (1962) 1337–1352.
- [318] Johannes Neugebauer, Evert Jan Baerends, Marcel Nooijen. Vibronic coupling and double excitations in linear response time-dependent density functional calculations: Dipole-allowed states of N₂. *J. Chem. Phys.*, **121** (2004) 6155–6166.
- [319] Johannes Neugebauer, Evert Jan Baerends, Marcel Nooijen. Vibronic structure of the permanganate absorption spectrum from time-dependent density functional calculations. *J. Phys. Chem. A*, **109** (2005) 1168–1179.
- [320] S. J. A. van Gisbergen, C. Fonseca Guerra, E. J. Baerends. Towards Excitation Energies and (Hyper)polarizability Calculations of Large Molecules. Application of Parallelization and Linear Scaling Techniques to Time-Dependent Density Functional Response Theory. *J. Comput. Chem.*, **21** (2000) 1511–1523.
- [321] C. J. Cramer, D. G. Truhlar. Implicit Solvation Models: Equilibria, Structure, Spectra, and Dynamics. *Chem. Rev.*, **99** (1999) 2160–2200.
- [322] J. Tomasi, B. Mennucci, R. Cammi. Quantum Mechanical Continuum Solvation Models. *Chem. Rev.*, **105** (2005) 2999–3094.
- [323] Joachim Sauer, Marek Sierka. Combining Quantum Mechanics and Interatomic Potential Functions in *Ab Initio* Studies of Extended Systems. *J. Comput. Chem.*, **21** (2000) 1470–1493.

-
- [324] Mark S. Gordon, Mark A. Freitag, Prapdipta Bandyopadhyay, Jan H. Jensen, Visvaldas Kairys, Walter J. Stevens. The Effective Fragment Potential Method: A QM-Based MM Approach to Modeling Environmental Effects in Chemistry. *J. Phys. Chem. A*, **105** (2001) 293–307.
- [325] Zoila Barandiarán, Luis Seijo. The *ab initio* model potential representation of the crystalline environment. Theoretical study of the local distortion on NaCl:Cu⁺. *J. Chem. Phys.*, **89** (1988) 5739–5746.
- [326] Ben Swerts, Liviu F. Chibotaru, Roland Lindh, Luis Seijo, Zoila Barandiaran, Sergiu Clima, Kristin Pierloot, Marc F. A. Hendrickx. Embedding Fragment *ab Initio* Model Potentials in CASSCF/CASPT2 Calculations of Doped Solids: Implementation and Applications. *J. Chem. Theor. Comput.*, **4** (2008) 586–594.
- [327] Lasse Jensen, Piet Th. van Duijnen, Jaap G. Snijders. A discrete solvent reaction field model within density functional theory. *J. Chem. Phys.*, **118**(2) (2003) 514–521.
- [328] J. Neugebauer, M. Reiher, C. Kind, B. A. Hess. Quantum Chemical Calculation of Vibrational Spectra of Large Molecules — Raman and IR Spectra for Buckminsterfullerene. *J. Comp. Chem.*, **23** (2002) 895–910.
- [329] T. A. Wesolowski, A. Goursot, J. Weber. Properties of CO adsorbed in ZSM5 zeolite: Density functional theory study using the embedding scheme based on electron density partitioning. *J. Chem. Phys.*, **115** (2001) 4791–4797.
- [330] D. Barker, M. Sprik. Molecular dynamics study of electron gas models for liquid water. *Mol. Phys.*, **101** (2003) 1183.
- [331] Miroslav Hodak, Wenchang Lu, J. Bernholc. Hybrid *ab initio* Kohn–Sham density functional theory/frozen-density orbital-free density functional theory simulation method suitable for biological systems. *J. Chem. Phys.*, **128** (2008) 014101.
- [332] Johannes Neugebauer, Manuel J. Louwerse, Paola Belanzoni, Thomasz A. Wesolowski, Evert Jan Baerends. Modeling solvent effects on electron spin resonance hyperfine couplings by frozen-density embedding. *J. Chem. Phys.*, **123** (2005) 114101.
- [333] J. K. Gregory, D. C. Clary, K. Liu, M. G. Brown, R. J. Saykally. The Water Dipole Moment in Water Clusters. *Science*, **275** (1997) 814–817.
- [334] Pier Luigi Silvestrelli, Michele Parrinello. Water Molecule Dipole in the Gas and in the Liquid Phase. *Phys. Rev. Lett.*, **82** (1999) 3308–3311.
- [335] Christoph R. Jacob, Lucas Visscher. Calculation of nuclear magnetic resonance shieldings using frozen-density embedding. *J. Chem. Phys.*, **125** (2006) 194104.
- [336] R. E. Buló, C. R. Jacob, L. Visscher. NMR Solvent Shifts of Acetonitrile from Frozen Density Embedding Calculations. *J. Phys. Chem. A*, **112** (2008) 2640–2647.

- [337] Tomasz A. Wesolowski. Application of the DFT-based embedding scheme using an explicit functional of the kinetic energy to determine the spin density of Mg^+ embedded in Ne and Ar matrices. *Chem. Phys. Lett.*, **311** (1999) 87–92.
- [338] Martin Kaupp, Michael Bühl, Vladimir G. Malkin. *Calculation of NMR and EPR Parameters*. Wiley-VCH, Weinheim, 2004.
- [339] M. Munzarová, M. Kaupp. A Critical Validation of Density Functional and Coupled-Cluster Approaches for the Calculation of EPR Hyperfine Coupling Constants in Transition Metal Complexes. *J. Phys. Chem. A*, **103** (1999) 9966.
- [340] Paola Belanzoni, Erik van Lenthe, Evert Jan Baerends. An evaluation of the density functional approach in the zero order regular approximation for relativistic effects: Magnetic interactions in small metal compounds. *J. Chem. Phys.*, **114** (2001) 4421–4433.
- [341] L. Hermosilla, P. Calle, J. M. García de la Vega, C. Sieiro. Density Functional Theory Predictions of Isotropic Hyperfine Coupling Constants. *J. Phys. Chem. A*, **109** (2005) 1114–1124.
- [342] Roberto Improta, Vincenzo Barone. Interplay of Electronic, Environmental, and Vibrational Effects in Determining the Hyperfine Coupling Constants of Organic Free Radicals. *Chem. Rev.*, **104** (2004) 1231–1253.
- [343] Daniel M. Chipman. Hydrogen-Bonding Effects on Free-Radical Properties. *J. Phys. Chem. A*, **104** (2000) 11816–11821.
- [344] Emma Langella, Roberto Improta, Vincenzo Barone. Conformational and Spectroscopic Analysis of the Tyrosyl Radical Dipeptide Analogue in the Gas Phase and in Aqueous Solution by a Density Functional/Continuum Solvent Model. *J. Am. Chem. Soc.*, **124** (2002) 11531–11540.
- [345] Martin Kaupp, Christian Remeyi, Juha Vaara, Olga L. Malkina, Vladimir G. Malkin. Density Functional Calculations of Electronic g -Tensors for Semiquinone Radical Anions. The Role of Hydrogen Bonding and Substituent Effects. *J. Am. Chem. Soc.*, **124** (2002) 2709–2722.
- [346] Nadia Rega, Maurizio Cossi, Vincenzo Barone. Development and validation of reliable quantum mechanical approaches for the study of free radicals in solution. *J. Chem. Phys.*, **105** (1996) 11060–11067.
- [347] I. Ciofini, R. Reviakine, A. Arbuznikov, M. Kaupp. Solvent effects on g -tensors of semiquinone radical anions: polarizable continuum versus cluster models. *Theor. Chem. Acc.*, **111** (2004) 132–140.
- [348] Vincenzo Barone, Alessandro Bencini, Maurizio Cossi, Andrea Di Matteo, Maurizio Mattesini, Federico Totti. Assessment of a Combined QM/MM Approach for the Study of Large Nitroxide Systems in Vacuo and in Condensed Phases. *J. Am. Chem. Soc.*, **120** (1998) 7069–7078.

-
- [349] Toru Yagi, Osamu Kikuchi. MC/MO Study of the Electronic Structure and Hyperfine Coupling Constant of the Nitrogen of the $(\text{CH}_3)_2\text{NO}$ Radical in Hydrogen-Bonding and Non-Hydrogen-Bonding Solvents. *J. Phys. Chem. A*, **103** (1999) 9132–9137.
- [350] Michele Pavone, Caterina Benzi, Filippo De Angelis, Vincenzo Barone. Hyperfine coupling constants of dimethyl nitroxide in aqueous solution: Car–Parrinello molecular dynamics and discrete-continuum approaches. *Chem. Phys. Lett.*, **395** (2004) 120–126.
- [351] Hitomi Mikami, Shuji Saito, Satoshi Yamamoto. The microwave spectrum of the dihydronitrosyl radical, H_2NO (2B_1). *J. Chem. Phys.*, **94** (1991) 3415–3422.
- [352] M. Jinguji, T. Imamura, H. Murai, K. Obi. ESR Study of the Dihydronitroxide (H_2NO) Radical in a Xenon Matrix at Low Temperature. *Chem. Phys. Lett.*, **84** (1981) 335–338.
- [353] Om P. Chawla, Richard W. Fessenden. Electron Spin Resonance and Pulse Radiolysis Studies of Some Reactions of $\text{SO}_4^{\cdot-}$. *J. Phys. Chem.*, **79** (1975) 2693–2700.
- [354] J. Q. Adams, S. W. Nicksic, J. R. Thomas. Paramagnetic Resonance of Alkyl Nitroxides. *J. Chem. Phys.*, **45** (1966) 654–661.
- [355] Hideto Takase, Osamu Kikuchi. Monte Carlo and Molecular Orbital Study of H_2NO in Solution. Solvent Effects on the Molecular and Electronic Structures of H_2NO . *J. Phys. Chem.*, **98** (1994) 5160–5163.
- [356] Vincenzo Barone, André Grand, Camilla Minichino, Robert Subra. Theoretical Approach to the Structure and Hyperfine Coupling Constants of Nonrigid Radicals. The Case of H_2NO . *J. Phys. Chem.*, **97** (1993) 6355–6361.
- [357] T. A. Wesolowski, J. Weber. Kohn–Sham Equations with Constrained Electron Density: The Effect of Various Kinetic Energy Functional Parametrizations on the Ground-State Molecular Properties. *Int. J. Quantum Chem.*, **61** (1997) 303.
- [358] P. Vassilev, M. J. Louwerse, E. J. Baerends. Ab initio molecular dynamics simulation of the $\text{OH}\cdot$ radical in liquid water. *Chem. Phys. Lett.*, **398** (2004) 212–216.
- [359] Vincenzo Barone. Electronic, vibrational and environmental effects on the hyperfine coupling constants of nitroside radicals. H_2NO as a case study. *Chem. Phys. Lett.*, **262** (1996) 201–206.
- [360] Bernard Valeur, Jean-Claude Brochon, Eds. *New Trends in Fluorescence Spectroscopy — Applications to Chemical and Life Sciences*. Springer, Berlin, 2001.
- [361] F. P. Schäfer, Ed. *Dye Lasers*. Springer, Berlin, 3 ed., 1990.
- [362] T. Gustavsson, L. Cassara, V. Gulbinas, G. Gurzadyan, J.-C. Mialocq, S. Pommeret, M. Sorgius, P. van der Meulen. Femtosecond Spectroscopic Study of Relaxation Processes of Three Amino-Substituted Coumarin Dyes in Methanol and Dimethyl Sulfoxide. *J. Phys. Chem. A*, **102** (1998) 4229–4245.

- [363] Guilford Jones II, William R. Jackson, Chol-yoo Choi, William R. Bergmark. Solvent Effects on Emission Yield and Lifetime for Coumarin Laser Dyes. Requirements for a Rotatory Decay Mechanism. *J. Phys. Chem.*, **89** (1985) 294–300.
- [364] Christopher R. Moylan. Molecular Hyperpolarizabilities of Coumarin Dyes. *J. Phys. Chem.*, **98** (1994) 13513–13516.
- [365] Robert J. Cave, Kieron Burke, Edward W. Castner, Jr. Theoretical Investigation of the Ground and Excited States of Coumarin 151 and Coumarin 120. *J. Phys. Chem. A*, **106** (2002) 9294–9305.
- [366] Robert J. Cave, Edward W. Castner, Jr. Time-Dependent Density Functional Theory Investigation of the Ground and Excited States of Coumarins 102, 152, 153, and 343. *J. Phys. Chem. A*, **106** (2002) 12117–12123.
- [367] Koji Ando. Solvation dynamics and electronic structure development of coumarin 120 in methanol: A theoretical modeling study. *J. Chem. Phys.*, **107** (1997) 4585–4596.
- [368] M. L. Horn, J. A. Gardecki, A. Papazyan, M. Maroncelli. Subpicosecond Measurements of Polar Solvation Dynamics: Coumarin 153 Revisited. *J. Phys. Chem.*, **99** (1995) 17311–17337.
- [369] Marc Dierksen, Stefan Grimme. Density functional calculations of the vibronic structure of electronic absorption spectra. *J. Chem. Phys.*, **120** (2004) 3544–3554.
- [370] Marc Dierksen, Stefan Grimme. The Vibronic Structure of Electronic Absorption Spectra of Large Molecules: A Time-Dependent Density Functional Study on the Influence of “Exact” Hartree–Fock Exchange. *J. Phys. Chem. A*, **108** (2004) 10225–10237.
- [371] Stig Allenmark. Induced Circular Dichroism by Chiral Molecular Interaction. *Chirality*, **15** (2003) 409–422.
- [372] Shunsuke Takenaka, Norio Matsuura, Niichiro Tokura. Induced Circular Dichroism of Benzoylbenzoic Acids in β -Cyclodextrin. *Tetrahedron Lett.*, **26** (1974) 2325–2328.
- [373] Bernd Mayer, Xiangyang Zhang, Werner M. Nau, Giancarlo Marconi. Co-conformational Variability of Cyclodextrin Complexes Studied by Induced Circular Dichroism of Azoalkanes. *J. Am. Chem. Soc.*, **123** (2001) 5240–5248.
- [374] Xiangyang Zhang, Werner M. Nau. Chromophore Alignment in a Chiral Host Provides a Sensitive Test for the Orientation–Intensity Rule of Induced Circular Dichroism. *Angew. Chem. Int. Ed.*, **39** (2000) 544–547.
- [375] Mamoru Kamiya, Setsuko Mitsuhashi, Masakazu Makino, Hisashi Yoshioka. Analysis of the Induced Rotational Strength of Mono- and Disubstituted Benzenes Included in β -Cyclodextrin. *J. Phys. Chem.*, **96** (1992) 95–99.

-
- [376] Syuuta Najiwara, Masahiro Kawamura, Hiroyuki Yamaguchi. Magnetic Circular Dichroism and Induced Circular Dichroism Spectra of *N*-Bromophthalimide. *Helv. Chim. Acta*, **83** (2000) 2783–2786.
- [377] Masahiro Kawamura, Miwako Higashi. Induced Circular Dichroism and Magnetic Circular Dichroism Spectra of Maleimide and Related Molecules. *Helv. Chim. Acta*, **86** (2003) 2342–2348.
- [378] Kazuaki Harata, Hisashi Uedaira. The Circular Dichroism Spectra of the β -Cyclodextrin Complex with Naphthalene Derivatives. *Bull. Chem. Soc. Jpn*, **48** (1975) 375–378.
- [379] Masato Kodaka. Application of a General Rule to Induced Circular Dichroism of Naphthalene Derivatives Complexed with Cyclodextrins. *J. Phys. Chem. A*, **102** (1998) 8101–8103.
- [380] R. S. Murphy, T. C. Barros, J. Barnes, B. Mayer, G. Marconi, C. Bohne. Complexation of Fluorenone and Xanthone to Cyclodextrins: Comparison of Theoretical and Experimental Studies. *J. Phys. Chem. A*, **103** (1999) 137–146.
- [381] K. A. Connors. The Stability of Cyclodextrin Complexes in Solution. *Chem. Rev.*, **97** (1997) 1325–1357.
- [382] M. V. Rekharsky, Y. Inoue. Complexation Thermodynamics of Cyclodextrins. *Chem. Rev.*, **98** (1998) 1875–1917.
- [383] Niichiro Tokura, Toshikazu Nagai, Shunsuke Takenaka, Takumi Oshima. Solvent Effects on Circular Dichroism induced in Aroylarenecarboxylic Acids by Optically Active Amines. *J. Chem. Soc. Perkin II*, (1974) 337–342.
- [384] Shunsuke Takenaka, Keizo Kondo, Niichiro Tokura. Induced Circular Dichroism. Part III. Chiroptical Properties and Ionpair Equilibria in 2-Benzoylbenzoic Acid–Amphetamine. *J. Chem. Soc. Perkin II*, (1975) 1520–1524.
- [385] Hiroshi Tsukube, Hiroshi Fukui, Satoshi Shinoda. Synergistic binding and chirality sensing of unprotected amino acids with ferrocenecarboxylic acid–crown ether conjugate. *Tetrahedron Lett.*, **42** (2001) 7583–7585.
- [386] Kenny B. Lipkowitz. Applications of Computational Chemistry to the Study of Cyclodextrins. *Chem. Rev.*, **98** (1998) 1829–1873.
- [387] J. P. Kirkwood. On the Theory of Optical Rotatory Power. *J. Chem. Phys.*, **5** (1937) 479–491.
- [388] Ignacio Tinoco. Theoretical Aspects of Optical Activity. *Adv. Chem. Phys.*, **4** (1962) 113–160.
- [389] Hiroshi Shimizu, Akira Kaito, Masahiro Hatano. Induced Circular Dichroism of β -Cyclodextrin Complexes with Substituted Benzenes. *Bull. Chem. Soc. Jpn.*, **52** (1979) 2678–2684.

- [390] Hiroshi Shimizu, Akira Kaito, Masahiro Hatano. Induced Circular Dichroism of β -Cyclodextrin Complexes with *o*-, *m*-, and *p*-Disubstituted Benzenes. *Bull. Chem. Soc. Jpn.*, **54** (1981) 513–519.
- [391] M. Kodaka. Sign of Circular Dichroism Induced by β -Cyclodextrin. *J. Phys. Chem.*, **95** (1991) 2110–2112.
- [392] Masato Kodaka. A General Rule for Circular Dichroism Induced by a Chiral Macrocycle. *J. Am. Chem. Soc.*, **115** (1993) 3702–3705.
- [393] Valentin Paul Nicu, Johannes Neugebauer, Evert Jan Baerends. Effects of Complex Formation on Vibrational Circular Dichroism. *J. Phys. Chem.*, **112** (2008) 6978–6991.
- [394] Johannes Neugebauer, Evert Jan Baerends, Marcel Nooijen, Jochen Autschbach. Importance of vibronic effects on the circular dichroism spectrum of dimethyloxirane. *J. Chem. Phys.*, **122** (2005) 234305.
- [395] Johannes Neugebauer, Oleg Gritsenko, Evert Jan Baerends. Assessment of a Simple Correction for the Long-Range Charge-Transfer Problem in Time-Dependent Density-Functional Theory. *J. Chem. Phys.*, **124** (2006) 214102.
- [396] Martin Klessinger, Josef Michl. *Lichtabsorption und Photochemie organischer Moleküle*. Verlag Chemie, Weinheim, 1989.
- [397] Carmen Herrmann, Markus Reiher. Direct targeting of adsorbate vibrations with mode-tracking. *Surf. Sci.*, **9** (2006) 1891–1900.
- [398] Carles Curutchet, Benedetta Mennucci. Toward a Molecular Scale Interpretation of Excitation Energy Transfer in Solvated Bichromophoric Systems. *J. Am. Chem. Soc.*, **127** (2005) 16733–16744.
- [399] Maria Francesca Iozzi, Benedetta Mennucci, Jacopo Tomasi, Roberto Cammi. Excitation energy transfer (EET) between molecules in condensed matter: A novel application of the polarizable continuum model (PCM). *J. Chem. Phys.*, **120** (2004) 7029–7040.
- [400] Chao-Ping Hsu, Graham R. Fleming, Martin Head-Gordon, Teresa Head-Gordon. Excitation energy transfer in condensed media. *J. Chem. Phys.*, **114** (2001) 3065–3072.
- [401] Gregory D. Scholes, Kenneth P. Ghiggino. Electronic Interactions and Interchromophore Excitation Transfer. *J. Phys. Chem.*, **98** (1994) 4580–4590.
- [402] Gregory D. Scholes, Kenneth P. Ghiggino. Rate expressions for excitation transfer I. Radiationless transition theory perspective. *J. Chem. Phys.*, **101** (1994) 1251–1261.

-
- [403] Gregory D. Scholes, Ian R. Gould, Richard J. Cogdell, Graham R. Fleming. *Ab Initio* Molecular Orbital Calculations of Electronic Couplings in the LH2 Bacterial Light-Harvesting Complex of *Rps. Acidophila*. *J. Phys. Chem. B*, **103** (1999) 2543–2553.
- [404] I.A. Howard, F. Zutterman, G. Deroover, D. Lamoen, C. Van Alsenoy. Approaches to Calculations of Exciton Interaction Energies for a Molecular Dimer. *J. Phys. Chem. B*, **108** (2004) 19155–19162.
- [405] Parag Mukhopadhyay, Gérard Zuber, Peter Wipf, David N. Beratan. Contribution of a solute’s chiral solvent imprint to optical rotation. *Angew. Chem. Int. Ed.*, **46** (2007) 6450–6452.
- [406] Johannes Neugebauer. Induced Chirality in Achiral Media — How Theory Unravels Mysterious Solvent Effects. *Angew. Chem. Int. Ed.*, **46** (2007) 7738–7740.
- [407] Walter Kauzmann. *Quantum Chemistry*. Academic Press, New York, 1957.
- [408] J. Autschbach, T. Ziegler. Calculating molecular electric and magnetic properties from time-dependent density functional response theory. *J. Chem. Phys.*, **116** (2002) 891–896.
- [409] Laurence Barron. *Molecular Light Scattering and Optical Activity*. Cambridge University Press, Cambridge, 2nd ed., 2004.
- [410] Jochen Autschbach, Serguei Patchkovskii, Tom Ziegler, Stan J. A. van Gisbergen, Evert Jan Baerends. Chiroptical properties from time-dependent density functional theory. II. Optical rotations of small to medium sized organic molecules. *J. Chem. Phys.*, **117** (2002) 581–592.
- [411] J. Autschbach, T. Ziegler, S. J. A. van Gisbergen, E. J. Baerends. Chiroptical properties from time-dependent density functional theory. I. Circular dichroism spectra of organic molecules. *J. Chem. Phys.*, **116** (2002) 6930–6940.
- [412] S. J. A. van Gisbergen, J. G. Snijders, E. J. Baerends. A density functional theory study of frequency-dependent polarizabilities and Van der Waals dispersion coefficients for polyatomic molecules. *J. Phys. Chem.*, **103** (1995) 9347–9354.
- [413] Peter Pulay. Convergence Acceleration of Iterative Sequences. The Case of SCF Iteration. *Chem. Phys. Lett.*, **73** (1980) 393–398.
- [414] P. Pulay. Improved SCF Convergence Acceleration. *J. Comput. Chem.*, **3** (1982) 556–560.
- [415] Tracy P. Hamilton, Peter Pulay. Direct inversion in the iterative subspace (DIIS) optimization of open-shell, excited-state, and small multiconfiguration SCF wave functions. *J. Chem. Phys.*, **84** (1986) 5728–5734.
- [416] J. R. Cheeseman, M. J. Frisch, F. J. Devlin, P. J. Stephens. Hartree-Fock and Density Functional Theory *ab Initio* Calculation of Optical Rotation Using GIAOs: Basis Set Dependence. *J. Phys. Chem. A*, **104** (2000) 1039–1046.

- [417] K. Ruud, T. Helgaker. Optical rotation studied by density-functional and coupled-cluster methods. *Chem. Phys. Lett.*, **352** (2002) 533–539.
- [418] Mykhaylo Krykunov, Jochen Autschbach. Calculation of optical rotation with time-periodic magnetic-field-dependent basis functions in approximate time-dependent density-functional theory. *J. Chem. Phys.*, **123** (2005) 114103.
- [419] Mykhaylo Krykunov, Jochen Autschbach. Calculation of origin-independent optical rotation tensor components in approximate time-dependent density functional theory. *J. Chem. Phys.*, **125** (2006) 034102.
- [420] Sandra Luber, Markus Reiher. Raman optical activity spectra of chiral transition metal complexes. *Chem. Phys.*, **346** (2008) 212–223.
- [421] A. F. Holleman, E. Wiberg, N. Wiberg. *Lehrbuch der Anorganischen Chemie*. de Gruyter, Berlin, 102nd ed., 2007.
- [422] Anthony F. Collings, Christa Critchley, Eds. *Artificial Photosynthesis*. Wiley-VCH, Weinheim, 1st ed., 2005.
- [423] Robert E. Blankenship. *Molecular Mechanisms of Photosynthesis*. Blackwell Science, Oxford, 2002.
- [424] Rienk van Grondelle, Jan P. Dekker, Tomas Gillbro, Villy Sundstrom. Energy transfer and trapping in photosynthesis. *Biochimica et Biophysica Acta*, **1187** (1994) 1–65.
- [425] Richard J. Cogdell, Andrew Gall, Jürgen Köhler. The architecture and function of the light-harvesting apparatus of purple bacteria: from single molecules to *in vivo* membranes. *Quarterly Reviews of Biophysics*, **39** (2006) 227–324.
- [426] Xiche Hu, Thorsten Ritz, Ana Damjanović, Felix Autenrieth. Photosynthetic apparatus of purple bacteria. *Quarterly Reviews of Biophysics*, **35** (2002) 1–62.
- [427] Juergen Koepke, Xiche Hu, Cornelia Muenke, Klaus Schulten, Hartmut Michel. The crystal structure of the light-harvesting complex II (B800–850) from *Rhodospirillum rubrum*. *Structure*, **4** (1996) 581–597.
- [428] Vadim Cherezov, Jeffrey Clogston, Miroslav Z. Papiz, Martin Caffrey. Room to Move: Crystallizing Membrane Proteins in Swollen Lipidic Mesophases. *J. Mol. Biol.*, **357** (2006) 1605–1618.
- [429] Miroslav Z. Papiz, Steve M. Prince, Tina Howard, Richard J. Cogdell, Neil W. Isaacs. The Structure and Thermal Motion of the B800–850 LH2 Complex from *Rps. acidophila* at 2.0 Å Resolution and 100 K: New Structural Features and Functionally Relevant Motions. *J. Mol. Biol.*, **326** (2003) 1523–1538.
- [430] G. McDermott, S. M. Prince, A. A. Freer, A. M. Hawthornthwaite-Lawless, M. Z. Papiz, R. J. Cogdell, N. W. Isaacs. Crystal structure of an integral membrane light-harvesting complex from photosynthetic bacteria. *Nature*, **374** (1995) 517–521.

-
- [431] Rienk van Grondelle, Vladimir I. Novoderezhkin. Energy transfer in photosynthesis: experimental insights and quantitative models. *Phys. Chem. Chem. Phys.*, **8** (2006) 793–807.
- [432] Graham R. Fleming, Gregory D. Scholes. Physical chemistry: Quantum mechanics for plants. *Nature*, **431** (2004) 256–257.
- [433] Zhi He, Villy Sundström, Tõnu Pullerits. Influence of the Protein Binding Site on the Excited States of Bacteriochlorophyll: DFT Calculations of B800 in LH2. *J. Phys. Chem. B*, **106** (2002) 11606–11612.
- [434] Vijaya Subramanian, Deborah G. Evans. Excitation Energy Transfer in Model Light-Harvesting Antennae. *J. Phys. Chem. B*, **108** (2004) 1085–1095.
- [435] Brent P. Krueger, Gregory D. Scholes, Graham R. Fleming. Calculation of Couplings and Energy-Transfer Pathways between the Pigments of LH2 by the ab Initio Transition Density Cube Method. *J. Phys. Chem. B*, **102** (1998) 5378–5386.
- [436] Gregory D. Scholes, Graham R. Fleming. On the Mechanism of Light Harvesting in Photosynthetic Purple Bacteria: B800 to B850 Energy Transfer. *J. Phys. Chem. B*, **104** (2000) 1854–1868.
- [437] R. J. Cogdell, T. D. Howard, N. W. Isaacs, K. McLuskey, A. T. Gardiner. Structural factors which control the position of the Q_y absorption band of bacteriochlorophyll *a* in purple bacterial antenna complexes. *Photosynthesis Research*, **74** (2002) 135–141.
- [438] A. M. van Oijen, M. Ketelaars, J. Köhler, T. J. Aartsma, J. Schmidt. Spectroscopy of Single Light-Harvesting Complexes from Purple Photosynthetic Bacteria at 1.2 K. *J. Phys. Chem. B*, **102** (1998) 9363–9366.
- [439] Andy Freer, Steve Prince, Ken Sauer, Miroslav Papiz, Anna Hawthornthwaite-Lawless, Gerry McDermott, Richard Cogdell, Neil W. Isaacs. Pigment–pigment interactions and energy transfer in the antenna complex of the photosynthetic bacterium *Rhodospseudomonas acidophila*. *Structure*, **15** (1996) 449–462.
- [440] Richard D. Harcourt, Gregory D. Scholes, Kenneth P. Ghiggino. Rate expressions for excitation transfer. II. Electronic considerations of direct and through-configuration exciton resonance interactions. *J. Chem. Phys.*, **101** (1994) 10521–10525.
- [441] Gregory D. Scholes, Richard D. Harcourt, Kenneth P. Ghiggino. Rate expressions for excitation transfer. III. Radiationless transition theory perspective. *J. Chem. Phys.*, **102** (1995) 9574–9581.
- [442] Th. Förster. Zwischenmolekulare Energiewanderung und Fluoreszenz. *Ann. Phys.*, **2** (1948) 55.
- [443] D. L. Dexter. A Theory of Sensitized Luminescence in Solids. *J. Chem. Phys.*, **21** (1953) 836–850.

- [444] A. J. Stone. *The Theory of Intermolecular Forces*. Oxford University Press, Oxford, 1st ed., 2002.
- [445] Jane C. Chang. Monopole effects on electronic excitation interactions between large molecules. I. Application to energy transfer in chlorophylls. *J. Chem. Phys.*, **67** (1977) 3901.
- [446] M. E. Madjet, A. Abdurahman, T. Renger. Intermolecular Coulomb Couplings from Ab Initio Electrostatic Potentials: Application to Optical Transitions of Strongly Coupled Pigments in Photosynthetic Antennae and Reaction Centers. *J. Phys. Chem. B*, **110** (2006) 17268–17281.
- [447] Vincenzo Russo, Carles Curutchet, Benedetta Mennucci. Towards a Molecular Scale Interpretation of Excitation Energy Transfer in Solvated Bichromophoric Systems. II. The Trough-Bond Contribution. *J. Phys. Chem. B*, **111** (2007) 853–863.
- [448] S. M. Prince, M. Z. Papiz, A. A. Freer, G. McDermott, A. M. Hawthornthwaite-Lawless, R. J. Cogdell, N. W. Isaacs. Apoprotein Structure in the LH2 Complex from *Rhodopseudomonas acidophila* Strain 10050: Modular Assembly and Protein Pigment Interactions. *J. Mol. Biol.*, **268** (1997) 268.
- [449] Jennifer L. Herek, Wendel Wohlleben, Richard J. Cogdell, Dirk Zeidler, Marcus Motzkus. Quantum control of energy flow in light harvesting. *Nature*, **417** (2002) 533–535.
- [450] R. G. Alden, E. Johnson, V. Nagarajan, W. W. Parson, C. J. Law, R. G. Cogdell. Calculations of Spectroscopic Properties of the LH2 Bacteriochlorophyll–Protein Antenna Complex from *Rhodopseudomonas acidophila*. *J. Phys. Chem. B*, **101** (1997) 4667–4680.
- [451] C. Curutchet, G. D. Scholes, B. Mennucci, R. Cammi. How Solvent Controls Electronic Energy Transfer and Light Harvesting: Toward a Quantum-Mechanical Description of Reaction Field and Screening Effects. *J. Phys. Chem. B*, **111** (2007) 13253–13265.
- [452] Adrian Lange, John M. Herbert. Simple Methods to Reduce Charge-Transfer Contamination in Time-Dependent Density-Functional Calculations of Clusters and Liquids. *J. Chem. Theory Comput.*, **3** (2007) 1680–1690.
- [453] J. Neugebauer. Photophysical Properties of Natural Light-Harvesting Complexes Studied by Subsystem Density Functional Theory. *J. Phys. Chem. B*, **112** (2008) 2207–2217.
- [454] Gregory D. Scholes, Carles Curutchet, Benedetta Mennucci, Roberto Cammi, Jacopo Tomasi. How Solvent Controls Electronic Energy Transfer and Light Harvesting. *J. Phys. Chem. B*, **111** (2007) 6978–6982.
- [455] Carsten Kötting, Klaus Gerwert. Proteins in Action Monitored by Time-Resolved FTIR Spectroscopy. *ChemPhysChem*, **6** (2005) 881–888.

-
- [456] James M. Benevides, Stacy A. Overman, George J. Thomas, Jr. Raman, polarized Raman and ultraviolet resonance Raman spectroscopy of nucleic acids and their complexes. *J. Raman Spectrosc.*, **36** (2005) 279–299.
- [457] Valentina Cervetto, Jan Helbing, Jens Bredenbeck, Peter Hamm. Double-resonance versus pulsed Fourier transform two-dimensional infrared spectroscopy: An experimental and theoretical comparison. *J. Chem. Phys.*, **121** (2004) 5935–5942.
- [458] Jens Bredenbeck, Jan Helbing, Christoph Kolano, Peter Hamm. Ultrafast 2D-IR Spectroscopy of Transient Species. *ChemPhysChem*, **8** (2007) 1747–1756.
- [459] Peter C. Chen, Candace C. Joyner. Vibrational and Vibronic Processes in Coherent 2D Resonance Raman Spectroscopy. *J. Phys. Chem. A*, **110** (2006) 7989–7993.
- [460] Timothy A. Keiderling. Protein and peptide secondary structure determination with vibrational circular dichroism. *Curr. Opin. Chem. Biol.*, **6** (2002) 862–688.
- [461] Laurence A. Nafie. Infrared and Raman Vibrational Optical Activity: Theoretical and Experimental Aspects. *Annu. Rev. Phys. Chem.*, **48** (1997) 357–386.
- [462] Carmen Herrmann, Markus Reiher. First-Principles Approach to Vibrational Spectroscopy of Biomolecules. *Top. Curr. Chem.*, **268** (2007) 85–132.
- [463] M. Reiher, J. Neugebauer, B. A. Hess. Quantum chemical calculation of Raman intensities for large molecules: The photoisomerization of $[\{\text{Fe}'\text{S}_4'(\text{PR}_3)\}_2(\text{N}_2\text{H}_2)]$ ($\text{'S}_4'^{2-} = 1,2\text{-bis}(2\text{-mercaptophenylthio})\text{ethane}(2-)$). *Z. Physik. Chem.*, **217** (2003) 91–103.
- [464] Dmitrij Rappoport, Filipp Furche. Lagrangian approach to molecular vibrational Raman intensities using time-dependent hybrid density functional theory. *J. Chem. Phys.*, **126** (2007) 201104.
- [465] P. J. Stephens, C. S. Ashvar, F. J. Devlin, J. R. Cheeseman, M. J. Frisch. Ab initio calculation of atomic axial tensors and vibrational rotational strengths using density functional theory. *Mol. Phys.*, **89** (1996) 579–594.
- [466] J. R. Cheeseman, M. J. Frisch, F. J. Devlin, P. J. Stephens. Ab initio calculation of atomic axial tensors and vibrational rotational strengths using density functional theory. *Chem. Phys. Lett.*, **252** (1996) 211.
- [467] Valentin Paul Nicu, Johannes Neugebauer, Stephen K. Wolff, Evert Jan Baerends. A vibrational circular dichroism implementation within a Slater-type-orbital based density functional framework and its application to hexa- and hepta-helicenes. *Theor. Chem. Acc.*, **119** (2008) 245–263.
- [468] Markus Reiher, Johannes Neugebauer. A mode-selective quantum chemical method for tracking molecular vibrations applied to functionalized carbon nanotubes. *J. Chem. Phys.*, **118** (2003) 1634–1641.

- [469] Carmen Herrmann, Johannes Neugebauer, Markus Reiher. Finding a needle in a haystack: direct determination of vibrational signatures in complex systems. *New J. Chem.*, **31** (2007) 818–831.
- [470] Roman S. Czernuszewicz, Thomas G. Spiro. IR, Raman, and Resonance Raman Spectroscopy. In E.I. Solomon, A.B.P. Lever, Eds., *Inorganic Electronic Structure and Spectroscopy, Vol. 1: Methodology*, p. 353–441. Wiley, New Jersey, 1999.
- [471] Anne B. Myers. Resonance Raman Intensity Analysis of Excited-State Dynamics. *Acc. Chem. Res.*, **30** (1997) 519–527.
- [472] Reinhard Schweitzer-Stenner. Structure and dynamics of biomolecules probed by Raman spectroscopy. *J. Raman Spectrosc.*, **36** (2005) 276–278.
- [473] Renate Petry, Michael Schmitt, Jürgen Popp. Raman Spectroscopy — A Prospective Tool in the Life Sciences. *ChemPhysChem*, **4** (2003) 14–30.
- [474] Alexander V. Ruban, Peter Horton, Bruno Robert. Resonance Raman Spectroscopy of the Photosystem II Light-Harvesting Complex of Green Plants: A Comparison of Trimeric and Aggregated States. *Biochemistry*, **34** (1995) 2333–2337.
- [475] Zhenhuan Chi, Sanford A. Asher. UV Raman Determination of the Environment and Solvent Exposure of Tyr and Trp Residues. *J. Phys. Chem. B*, **102** (1998) 9595–9602.
- [476] Samir F. El-Mashtoly, Seigo Yamauchi, Masato Kumauchi, Norio Hamada, Fumio Tokunaga, Masashi Unno. Structural Changes during the Photocycle of the Photoactive Yellow Protein Monitored by Ultraviolet Resonance Raman Spectra of Tyrosine and Tryptophan. *J. Phys. Chem. B*, **109** (2005) 23666–23673.
- [477] Iñigo R. Rodriguez-Mendieta, Graham R. Spence, Christopher Gell, Sheena E. Radford, D. Alastair Smith. Ultraviolet Resonance Raman Studies Reveal the Environment of Tryptophan and Tyrosine Residues in the Native and Partially Folded States of the E Colicin-Binding Immunity Protein Im7. *Biochemistry*, **44** (2005) 3306–3315.
- [478] Agnes Cua, David H. Stewart, Michael J. Reifler, Gary W. Brudvig, David F. Bocian. Low-Frequency Resonance Raman Characterization of the Oxygen-Evolving Complex of Photosystem II. *J. Am. Chem. Soc.*, **122** (2000) 2069–2077.
- [479] Tsuyoshi Egawa, Syun-Ru Yeh. Structural and functional properties of hemoglobins from unicellular organisms as revealed by resonance Raman spectroscopy. *J. Inorg. Biochem.*, **99** (2005) 72–96.
- [480] Arne Nägele, Karine Lapouge, James N. Sturgis, Gerhard Hartwich, Ingrid Simonin, Hugo Scheer, Bruno Robert. Resonance Raman Spectroscopy of Metal-Substituted Bacteriochlorophylls: Characterization of Raman Bands Sensitive to Bacteriochlorin Conformation. *J. Raman Spectrosc.*, **28** (1997) 599–604.

-
- [481] Yu-Jun Mo, Dong-Lin Jiang, Makoto Uyemura, Takuzo Aida, Teizo Kitagawa. Energy Funneling of IR Photons Captured by Dendritic Antennae and Acceptor Mode Specificity: Anti-Stokes Resonance Raman Studies on Iron(III) Porphyrin Complexes with a Poly(aryl ether) Dendrimer Framework. *J. Am. Chem. Soc.*, **127** (2005) 10020–10027.
- [482] David J. Ma'nuel, Dennis P. Strommen, Anwar Bhuiyan, Milan Sykora, James R. Kincaid. Resonance Raman and Time-Resolved Resonance Raman Studies of Complexes of Divalent Ruthenium with Bipyridine and 4,4'-Bipyrimidine Ligands. *J. Raman Spectrosc.*, **28** (1997) 933–938.
- [483] Derek Albert Long. *The Raman Effect: A Unified Treatment of the Theory of Raman Scattering by Molecules*. John Wiley & Sons, New York, 2002.
- [484] Jeanne L. McHale. *Molecular Spectroscopy*. Prentice-Hall, Upper Saddle River, 1999.
- [485] Anne B. Myers, Richard A. Mathies. Resonance Raman Intensities: A Probe of Excited-State Structure and Dynamics. In Thomas G. Spiro, Ed., *Biological Applications of Raman Spectroscopy, Vol. 2: Resonance Raman Spectra of Polyenes and Aromatics*, p. 123–166. Wiley, New York, 1979.
- [486] Anne B. Myers. Resonance Raman Intensities and Charge-Transfer Reorganization Energies. *Chem. Rev.*, **96**(3) (1996) 911–926.
- [487] Rodney Loudon. *The quantum theory of light*. Oxford University Press, Oxford, 1973.
- [488] D. L. Andrews, S. Naguleswaran, G. E. Stedman. Phenomenological damping of nonlinear-optical response tensors. *Phys. Rev. A*, **57** (1998) 4925–4929.
- [489] A. D. Buckingham, P. Fischer. Phenomenological damping in optical response tensors. *Phys. Rev. A*, **61** (2000) 035801.
- [490] G. E. Stedman, S. Naguleswaran. Comment on “Phenomenological damping in optical response tensors”. *Phys. Rev. A*, **63** (2001) 047801.
- [491] A. D. Buckingham, P. Fischer. Reply to “Comment on ‘Phenomenological damping in optical response tensors’ ”. *Phys. Rev. A*, **63** (2001) 047802.
- [492] Iwo Bialynicki-Birula, Tomasz Sowiński. Quantum electrodynamics of qubits. *Phys. Rev. A*, **76** (2007) 062106.
- [493] Shaul Mukamel. Causal versus noncausal description of nonlinear wave mixing: Resolving the damping-sign controversy. *Phys. Rev. A*, **76** (2007) 021803.
- [494] Taras Petrenko, Frank Neese. Analysis and prediction of absorption band shapes, fluorescence band shapes, resonance Raman intensities, and excitation profiles using the time-dependent theory of electronic spectroscopy. *J. Chem. Phys.*, **127** (2007) 164319.

- [495] L. Jensen, L. L. Zhao, J. Autschbach, G. C. Schatz. Theory and method for calculating resonance Raman scattering from resonance polarizability derivatives. *J. Chem. Phys.*, **123** (2005) 174110.
- [496] C. Manneback. Computation of the intensities of vibrational spectra of electronic bands in diatomic molecules. *Physica*, **17** (1951) 1001.
- [497] T. E. Sharp, H. M. Rosenstock. Franck–Condon Factors for Polyatomic Molecules. *J. Chem. Phys.*, **41**(11) (1964) 3453–3463.
- [498] E. V. Doktorov, I. A. Malkin, V. I. Malkin. Dynamical Symmetry of Vibronic Transitions in Polyatomic Molecules and the Franck–Condon Principle. *J. Mol. Spec.*, **64** (1977) 302–326.
- [499] Per-Åke Malmqvist, Niclas Forsberg. Franck–Condon factors for multidimensional harmonic oscillators. *Chem. Phys.*, **228** (1998) 227–240.
- [500] Peder Thusgaard Ruhoff, Mark A. Ratner. Algorithms for Computing Franck–Condon Overlap Integrals. *Int. J. Quantum Chem.*, **77** (2000) 383–392.
- [501] Anirban Hazra, Marcel Nooijen. Derivation and Efficient Implementation of a Recursion Formula to Calculate Harmonic Franck–Condon Factors for Polyatomic Molecules. *Int. J. Quant. Chem.*, **95** (2003) 643–657.
- [502] Fabrizio Santoro, Alessandro Lami, Roberto Improta, Vincenzo Barone. Effective method to compute vibrationally resolved optical spectra of large molecules at finite temperature in the gas phase and in solution. *J. Chem. Phys.*, **126** (2007) 184102.
- [503] H.-C. Jankowiak, J. L. Stuber, R. Berger. Vibronic transitions in large molecular systems: Rigorous prescreening conditions for Franck–Condon factors. *J. Chem. Phys.*, **127** (2007) 234101.
- [504] Jia-Lin Chang. A new method to calculate Franck–Condon factors of multidimensional harmonic oscillators including the Duschinsky effect. *J. Chem. Phys.*, **128** (2008) 174111.
- [505] Daniel C. Blazej, Warner L. Peticolas. Ultraviolet resonance Raman excitation profiles of pyrimidine nucleotides. *J. Chem. Phys.*, **72**(5) (1980) 3134–3142.
- [506] Johannes Neugebauer, Bernd A. Hess. Resonance Raman Spectra and Excited-State Structures of Uracil from Time-Dependent Density Functional Calculations and Multi-Reference Perturbation Theory. *J. Chem. Phys.*, **120** (2004) 11564–11577.
- [507] Taras Petrenko, Kallol Ray, Karl E. Wieghardt, Frank Neese. Vibrational Markers for the Open-Shell Character of Transition Metal Bis-dithiolenes: An Infrared, Resonance Raman, and Quantum Chemical Study. *J. Am. Chem. Soc.*, **128** (2006) 4422–4436.

-
- [508] Carmen Herrmann, Johannes Neugebauer, Martin Presselt, Ute Uhlemann, Michael Schmitt, Sven Rau, Jürgen Popp, Markus Reiher. The First Photoexcitation Step of Ruthenium-Based Models for Artificial Photosynthesis Tracked by Resonance Raman Spectroscopy. *J. Phys. Chem. B*, **111** (2007) 6078–6087.
- [509] Andreas Köhn, Christof Hättig. Analytic gradients for excited-states in the coupled-cluster model CC2 employing the resolution-of-the-identity approximation. *J. Chem. Phys.*, **119** (2003) 5021–5036.
- [510] Thilo Busch, Alessandra Degli Esposti, Hans-Joachim Werner. Analytical energy gradients for multiconfiguration self-consistent field wave functions with frozen core orbitals. *J. Chem. Phys.*, **94** (1991) 6708–6715.
- [511] Carole Van Caillie, Roger D. Amos. Geometric derivatives of excitation energies using SCF and DFT. *Chem. Phys. Lett.*, **308** (1999) 249–255.
- [512] Carole Van Caille, Roger D. Amos. Raman intensities using time dependent density functional theory. *PCCP*, **2** (2000) 2123–2129.
- [513] Carole Van Caillie, Roger D. Amos. Geometric derivatives of density functional theory excitation energies using gradient-corrected functionals. *Chem. Phys. Lett.*, **317** (2000) 159–164.
- [514] J. Hutter. Excited-state nuclear forces from the Tamm–Dancoff approximation to time-dependent density functional theory within the plane wave basis set framework. *J. Chem. Phys.*, **118** (2003) 3928–3934.
- [515] Johannes Neugebauer, Evert Jan Baerends, Evtim V. Efremov, Freek Ariese, Cees Gooijer. Combined Theoretical and Experimental Deep-UV Resonance Raman Studies of Substituted Pyrenes. *J. Phys. Chem. A*, **109** (2005) 2100–2106.
- [516] Lasse Jensen, George C. Schatz. Resonance Raman Scattering of Rhodamine 6G as Calculated Using Time-Dependent Density Functional Theory. *J. Phys. Chem. A*, **110** (2006) 5973–5977.
- [517] Julien Guthmuller, Benoît Champagne. Time dependent density functional theory investigation of the resonance Raman properties of the julolidinemalononitrile push–pull chromophore in various solvents. *J. Chem. Phys.*, **127** (2007) 164507.
- [518] S. Laimgruber, T. Schmierer, P. Gilch, K. Kiewisch, J. Neugebauer. The Ketene Intermediate in the Photochemistry of *ortho*-Nitrobenzaldehyde. *Phys. Chem. Chem. Phys.*, **10** (2008) 3872–3882.
- [519] Eric J. Heller, Robert L. Sundberg, David Tannor. Simple Aspects of Raman Scattering. *J. Phys. Chem.*, **86** (1982) 1822–1833.
- [520] Anne B. Myers. ‘Time-Dependent’ Resonance Raman Theory. *J. Raman Spectr.*, **28** (1997) 389–401.
- [521] E. J. Heller. The Semiclassical Way to Molecular Spectroscopy. *Acc. Chem. Res.*, **14** (1981) 368–375.

- [522] H. Köppel, W. Domcke, L. S. Cederbaum. Multimode Molecular Dynamics Beyond the Born–Oppenheimer Approximation. *Adv. Chem. Phys.*, **57** (1984) 59.
- [523] Frank Neese, Taras Petrenko, Dmitry Ganyuschin, Gottfried Olbrich. Advanced aspects of ab initio theoretical optical spectroscopy of transition metal complexes: Multiplets, spin-orbit coupling, and resonance Raman intensities. *Coord. Chem. Rev.*, **251** (2007) 288–327.
- [524] J. Neugebauer. DNR V1.0 — A program for resonance Raman and vibronic structure calculations. ETH Zürich, 2007.
- [525] Andrzej A. Jarzęcki, Thomas G. Spiro. *Ab initio* computation of the UV resonance Raman intensity pattern of aqueous imidazole. *J. Raman Spectrosc.*, **32** (2001) 599–605.
- [526] Andrzej A. Jarzęcki, Thomas G. Spiro. *Ab initio* computation of the UV resonance Raman intensity pattern of aqueous imidazole. *J. Phys. Chem. A*, **109** (2005) 421–430.
- [527] Valentina Tozzini, Paolo Giannozzi. Vibrational Properties of DsRed Model Chromophores. *ChemPhysChem*, **6** (2005) 1786–1788.
- [528] P. Kukura, D. W. McCamant, R. A. Mathies. Femtosecond stimulated Raman spectroscopy. *Annu. Rev. Phys. Chem.*, **58** (2007) 461–488.
- [529] L. Davies. Environmental health criteria 230, nitrobenzene. WHO, Geneva 2003. URL: <http://whqlibdoc.who.int/ehc/WHO-EHC-230.pdf>.
- [530] A. P. Pelliccioli, J. Wirz. Photoremovable protecting groups: reaction mechanisms and applications. *Photochem. Photobiol. Sci.*, **1**(7) (2002) 441–458.
- [531] J. A. McCray, D. R. Trentham. Properties and uses of photoreactive caged compounds. *Annu. Rev. Biophys. Biophys. Chem.*, **18** (1989) 239–270.
- [532] X. L. Gao, E. Gulari, X. C. Zhou. In situ synthesis of oligonucleotide microarrays. *Biopolymers*, **73** (2004) 579–596.
- [533] R. W. Yip, D. K. Sharma, R. Giasson, D. Gravel. Picosecond excited-state absorption of alkyl nitrobenzenes in solution. *J. Phys. Chem.*, **88**(24) (1984) 5770–5772.
- [534] R. W. Yip, D. K. Sharma, R. Giasson, D. Gravel. Photochemistry of the ortho-nitrobenzyl system in solution — evidence for singlet-state intramolecular hydrogen abstraction. *J. Phys. Chem.*, **89** (1985) 5328–5330.
- [535] R. W. Yip, D. K. Sharma. The reactive state in the photo-rearrangement of ortho-nitrobenzaldehyde. *Research On Chem. Intermediates*, **11** (1989) 109–116.
- [536] R. W. Yip, Y. X. Wen, D. Gravel, R. Giasson, D. K. Sharma. Photochemistry of the ortho-nitrobenzyl system in solution — identification of the biradical intermediate in the intramolecular rearrangement. *J. Phys. Chem.*, **95** (1991) 6078–6081.

-
- [537] D. Gravel, R. Giasson, D. Blanchet, R. W. Yip, D. K. Sharma. Photochemistry of the ortho-nitrobenzyl system in solution — effects of O-H distance and geometrical constraint on the hydrogen transfer mechanism in the excited-state. *Can. J. Chem.-Rev. Can. Chim.*, **69** (1991) 1193–1200.
- [538] M. Schwörer, J. Wirz. Photochemical reaction mechanisms of 2-nitrobenzyl compounds in solution I. 2-nitrotoluene: Thermodynamic and kinetic parameters of the aci-nitro tautomer. *Helv. Chim. Acta*, **84** (2001) 1441–1458.
- [539] S. Laimgruber, W. J. Schreier, T. Schrader, F. Koller, W. Zinth, P. Gilch. The photochemistry of o-nitrobenzaldehyde as seen by femtosecond vibrational spectroscopy. *Angew. Chem.-Int. Edit.*, **44** (2005) 7901–7904.
- [540] G. Ciamician, P. Silber. Chemische Lichtwirkungen. *Chem. Ber.*, **35** (1901) 2040–2046.
- [541] M.V. George, J.C. Scaiano. Photochemistry of o-nitrobenzaldehyde and related studies. *J. Phys. Chem.*, **84** (1980) 492–496.
- [542] S. Kuberski, J. Gebicki. Evidence for a ketene intermediate in the photochemical transformation of matrix-isolated o-nitrobenzaldehyde. *J. Mol. Struct.*, **275** (1992) 105–110.
- [543] M. A. Mcallister, T. T. Tidwell. Structural and substituent effects on the ketene infrared stretching frequency. *Can. J. Chem.-Rev. Can. Chim.*, **72** (1994) 882–887.
- [544] G. Placzek. In E. Marx, Ed., *Handbuch der Radiologie*, Volume 6, p. 205. Akademische Verlagsgesellschaft, Leipzig, 1934.
- [545] Masanori Miura, Yuriko Aoki, Benoît Champagne. Assessment of time-dependent density functional schemes for computing the oscillator strengths of benzene, phenol, aniline, and fluorobenzene. *J. Chem. Phys.*, **127** (2007) 084103.
- [546] J. Guthmuller, D. Simon. Water solvent effect on the first hyperpolarizability of p-nitrophenol and p-nitrophenylphosphate: A time-dependent density functional study. *J. Chem. Phys.*, **124** (2006) 174502.
- [547] Habbo Hait Heinze, Fabio Della Sala, Andreas Görling. Efficient methods to calculate dynamic hyperpolarizability tensors by time-dependent density-functional theory. *J. Chem. Phys.*, **116** (2002) 9624–9640.
- [548] O. Kröhl, K. Malsch, P. Swiderek. The electronic states of nitrobenzene: electron-energy-loss spectroscopy and CASPT2 calculations. *Phys. Chem. Chem. Phys.*, **2**(5) (2000) 947–953.
- [549] Curtis L. Jansen, Ida M. B. Nielsen. New diagnostics for coupled-cluster and Møller–Plesset perturbation theory. *Chem. Phys. Lett.*, **290** (1998) 423–430.

- [550] Mark Lilichenko, Dietrich Tittelbach-Helmrich, Jan W. Verhoeven, Ian R. Gould, Anne B. Myers. Resonance Raman intensity analysis of a dicyanovinyl-azaadamantane: Mode-specific reorganization energies for charge-transfer and locally excited states. *J. Chem. Phys.*, **109** (1998) 10958.
- [551] Anne Myers Kelley. Resonance Raman and Hyper-Raman Spectroscopy of Organic Chromophores for Second-Order Nonlinear Optics. *Int. J. Quantum Chem.*, **104** (2005) 602–615.
- [552] Johannes Neugebauer, Bernd A. Hess. Fundamental Vibrational Frequencies of Small Polyatomic Molecules from Density Functional Calculations and Vibrational Perturbation Theory. *J. Chem. Phys.*, **118** (2003) 7215–7225.
- [553] S. Laimgruber, H. Schachenmayr, B. Schmidt, W. Zinth, P. Gilch. A femtosecond stimulated raman spectrograph for the near ultraviolet. *Appl. Phys. B-Lasers Opt.*, **85** (2006) 557–564.
- [554] Jeremy M. Berg, John L. Tymoczko, Lubert Stryer. *Biochemistry*. Freeman, New York, 6th ed., 2006.
- [555] G. Kodis, P. A. Liddell, L. de la Garza, P. C. Clausen, J. S. Lindsey, A. L. Moore, T. A. Moore, D. Gust. Efficient Energy Transfer and Electron Transfer in an Artificial Photosynthetic Antenna-Reaction Center Complex. *J. Phys. Chem. A*, **106** (2002) 2036–2048.
- [556] Yoshiaki Kobuke. Artificial Light-Harvesting Systems by Use of Metal Coordination. *Eur. J. Inorg. Chem.*, **12** (2006) 2333–2351.
- [557] Maria Abrahamsson, Henriette Wolpher, Olof Johansson, Jan Larsson, Mikael Kritikos, Lars Eriksson, Per-Ola Norrby, Jonas Bergquist, Licheng Sun, Björn Åkermarck, Leif Hammarström. A New Strategy for the Improvement of Photo-physical Properties in Ruthenium(II) Polypyridyl Complexes. Synthesis and Photo-physical and Electrochemical Characterization of Six Mononuclear Ruthenium(II) Bisterpyridine-Type Complexes. *Inorg. Chem.*, **44** (2005) 3215–3225.
- [558] Ming Chen, Kenneth P. Ghiggino, San H. Thang, Gerard J. Wilson. Star-Shaped Light-Harvesting Polymers Incorporating an Energy Cascade. *Angew. Chem. Int. Ed.*, **44** (2005) 4368–4372.
- [559] MD. K. Nazeeruddin, M. Grätzel. Conversion and Storage of Solar Energy using Dye-sensitized Nanocrystalline TiO₂ Cells. In Jon A. McCleverty, Thomas J. Meyer, Eds., *Comprehensive Coordination Chemistry II*, Volume 9, p. 719–758. Elsevier, Amsterdam, 2003.
- [560] Anders Hagfeldt, Michael Grätzel. Molecular Photovoltaics. *Acc. Chem. Res.*, **33** (2000) 269–277.
- [561] C. A. Bignozzi, J. R. Schoonover, F. Scandola. A Supramolecular Approach to Light Harvesting and Sensitization of Wide-Bandgap Semiconductors: Antenna

- Effects and Charge Separation. In Gerald J. Meyer, Ed., *Molecular Level Artificial Photosynthetic Materials*, p. 1–96. Wiley, New York, 1999.
- [562] Leif Hammarström. Towards artificial photosynthesis: ruthenium @ Smanganese chemistry mimicking photosystem II reactions. *Curr. Opin. Chem. Biol.*, **7** (2003) 666–673.
- [563] Sven Rau, Bernhard Schäfer, Dieter Gleich, Ernst Anders, Manfred Rudolph, Manfred Friedrich, Helmar Görls, William Henry, Johannes G. Vos. A Supramolecular Photocatalyst for the Production of Hydrogen and the Selective Hydrogenation of Tolane. *Angew. Chem. Int. Ed.*, **45** (2006) 6215–6218.
- [564] B. Dietzek, W. Kiefer, J. Blumhoff, L. Böttcher, S. Rau, D. Walther, U. Uhlemann, M. Schmitt, J. Popp. Ultrafast Excited-State Excitation Dynamics in a Quasi-Two-Dimensional Light-Harvesting Antenna Based on Ruthenium(II) and Palladium(II) Chromophores. *Chem. Eur. J.*, **12** (2006) 5105–5115.
- [565] Dirk Walther, Lars Böttcher, Jörg Blumhoff, Sebastian Schebesta, Helmar Görls, Katrin Schmuck, Sven Rau, Manfred Rudolph. Tetranuclear Complexes Containing a Luminescent Ru_2M_2 Core [$\text{M} = \text{CuI}, (\text{allyl})\text{PdII}$]: Synthesis, Structures and Electrochemical Properties. *Eur. J. Inorg. Chem.*, **2006** (2006) 2385–2392.
- [566] Niels H. Damrauer, Giulio Cerullo, Alvin Yeh, Thomas R. Boussie, Charles V. Shank, James K. McCusker. Femtosecond Dynamics of Excited-State Evolution in $[\text{Ru}(\text{bpy})_3]^{2+}$. *Science*, **275** (1997) 54–57.
- [567] Claude Daul, Evert J. Baerends, Pieter Vernooijs. A Density Functional Study of the MLCT States of $[\text{Ru}(\text{bpy})_3]^{2+}$ in D_3 Symmetry. *Inorg. Chem.*, **33** (1994) 3538–3543.
- [568] L. L. Zhao, L. Jensen, G. C. Schatz. Pyridine- Ag_{20} Cluster: A Model System for Studying Surface-Enhanced Raman Scattering. *J. Am. Chem. Soc.*, **128**(9) (2006) 2911–2919.
- [569] Maria-Andrea Mroginski, Károly Németh, Ildikó Magdó, Martin Müller, Uwe Robben, Carlos Della Védova, Peter Hildebrandt, Franz Mark. Calculation of the Vibrational Spectra of Linear Tetrapyrroles. 2. Resonance Raman Spectra of Hexamethylpyrrolmethene Monomers. *J. Phys. Chem. B*, **104** (2000) 10885–10899.
- [570] Wolfram Koch, Max C. Holthausen. *A Chemist's Guide to Density Functional Theory*. Wiley VCH, Weinheim, 2nd ed., 2001.
- [571] M. Reiher, G. Brehm, S. Schneider. Assignment of vibrational spectra of 1,10-phenanthroline by comparison with frequencies and Raman intensities from density functional calculations. *J. Phys. Chem. A*, **108** (2004) 734–742.
- [572] C. F. Leybold, M. Reiher, G. Brehm, M. O. Schmitt, S. Schneider, P. Matousek, M. Towrie. Tetracycline and derivatives-assignment of IR and Raman spectra via DFT calculations. *Phys. Chem. Chem. Phys.*, **5**(6) (2003) 1149–1157.

- [573] Markus Reiher, Johannes Neugebauer. Convergence Characteristics and Efficiency of Mode-Tracking Calculations on Pre-Selected Molecular Vibrations. *Phys. Chem. Chem. Phys.*, **6** (2004) 4621–4629.
- [574] Johannes Neugebauer, Markus Reiher. Vibrational Center–Ligand Couplings in Transition Metal Complexes. *J. Comput. Chem.*, **25** (2004) 587–597.
- [575] Johannes Neugebauer, Markus Reiher. Mode-tracking of Pre-selected Vibrations of One-Dimensional Molecular Wires. *J. Phys. Chem. A*, **108** (2004) 2053–2061.
- [576] Alexey L. Kaledin. Gradient-based direct normal-mode analysis. *J. Chem. Phys.*, **122** (2005) 184106.
- [577] Alexey L. Kaledin, Martina Kaledin, Joel M. Bowman. All-atom calculation of the normal modes of bacteriorhodopsin using a sliding block iterative diagonalization method. *J. Chem. Theory Comput.*, **2** (2006) 166–174.
- [578] Markus Reiher, Johannes Neugebauer. Comment on "Gradient-based direct normal-mode analysis" [J. Chem. Phys. 122, 184106 (2005)]. *J. Chem. Phys.*, **123** (2005) 117101.
- [579] Thomas B. Adler, Nicole Borho, Markus Reiher, Martin A. Suhm. Chirality-Induced Switch in Hydrogen-Bond Topology: Tetrameric Methyl Lactate Clusters in the Gas Phase. *Angew. Chem. Int. Ed.*, **45** (2006) 3440–3445. *Angew. Chem.* **2006**, *118*, 3518–3523.
- [580] Carmen Herrmann, Kenneth Ruud, Markus Reiher. Can Raman optical activity separate axial from local chirality? A theoretical study of helical deca-alanine. *ChemPhysChem*, **7** (2006) 2189–2196.
- [581] Janina C. Austin, Trace Jordan, Thomas G. Spiro. Ultraviolet resonance Raman studies of proteins and related compounds. *Adv. Spectrosc.*, **20** (1993) 55–127.
- [582] Robert A. Copeland, Thomas G. Spiro. Ultraviolet Raman Hypochromism of the Tropomyosin Amide Modes: A New Method for Estimating α -Helical Content in Proteins. *J. Am. Chem. Soc.*, **108** (1986) 1281–1285.
- [583] Kazuhiro Asakawa, Satoshi Masuda, Hideo Takeuchi. Indole ring orientations of Trp189 in the ground and M intermediate states of bacteriorhodopsin as studied by polarized UV resonance Raman spectroscopy. *J. Raman Spectrosc.*, **37** (2006) 255–262.
- [584] R. G. Efremov, A. V. Feofanov, I. R. Nabiev. Effect of Hydrophobic Environment on the Resonance Raman Spectra of Tryptophan Residues in Proteins. *J. Raman Spectrosc.*, **23** (1992) 69–73.
- [585] Peter G. Hildebrandt, Robert A. Copeland, Thomas G. Spiro. Tyrosine Hydrogen-Bonding and Environmental Effects in Proteins Probed by Ultraviolet Resonance Raman Spectroscopy. *Biochemistry* *1988*, **27** (1988) 5426–5433.

-
- [586] Zhenhuan Chi, Sanford A. Asher. UV Raman Determination of the Environment and Solvent Exposure of Tyr and Trp Residues. *J. Phys. Chem. B*, **102** (1998) 9595–9602.
- [587] Cornelius Lanczos. An Iteration Method for the Solution of the Eigenvalue Problem of Linear Differential and Integral Operators. *J. Res. Natl. Bur. Stand.*, **45** (1950) 255–282.
- [588] Julien Guthmuller, Benoît Champagne. Resonance Raman Scattering of Rhodamine 6G as Calculated by Time-Dependent Density Functional Theory: Vibronic and Solvent Effects. *J. Phys. Chem. A.*, **112** (2008) 3215–3223.
- [589] Warner L. Peticolas, Thomas Rush III. *Ab Initio* Calculations of the Ultraviolet Resonance Raman Spectra of Uracil. *J. Comp. Chemistry*, **16**(10) (1995) 1261–1270.
- [590] Predrag Ilich. Lowest Singlet States in Isolated Indoles. *Can. J. Spectr.*, **32** (1986) 19–27.
- [591] Luis Serrano-Andrés, Björn Roos. Theoretical Study of the Absorption and Emission Spectra of Indole in the Gas Phase and in a Solvent. *J. Am. Chem. Soc.*, **118** (1996) 185–195.
- [592] Carmen Herrmann, Johannes Neugebauer, Markus Reiher. QM/MM Vibrational Mode Tracking. *J. Comput. Chem.*, **29** (2008) 2460–2470.
- [593] Tomaáš Polívka, Dariusz Niedzwiedzki, Marcel Fuciman, Villy Sundström, Harry A. Frank. Role of B800 in Carotenoid–Bacteriochlorophyll Energy and Electron Transfer in LH2 Complexes from the Purple Bacterium *Rhodobacter sphaeroides*. *J. Phys. Chem. B*, **111** (2007) 7422–7431.
- [594] Axel D. Becke. Density-functional thermochemistry. III. The role of exact exchange. *J. Chem. Phys.*, **98**(7) (1993) 5648–5652.
- [595] John P. Perdew. Density-functional approximation for the correlation energy of the inhomogeneous electron gas. *Phys. Rev. B*, **33** (1986) 8822–8824.
- [596] S. H. Vosko, L. Wilk, M. Nusair. Accurate spin-dependent electron liquid correlation energies for local spin density calculations: a critical analysis. *Can. J. Phys.*, **58** (1980) 1200–1211.
- [597] Samuel Fux, Karin Kiewisch, Christoph R. Jacob, Johannes Neugebauer, Markus Reiher. Analysis of electron density distributions from subsystem density functional theory applied to coordination bonds. *Chem. Phys. Lett.*, **461** (2008) 353–359.
- [598] P. R. T. Schipper, O. V. Gritsenko, S. J. A. van Gisbergen, E. J. Baerends. Molecular calculations of excitation energies and (hyper)polarizabilities with a statistical average of orbital model exchange–correlation potentials. *J. Chem. Phys.*, **112** (2000) 1344–1352.

- [599] O. V. Gritsenko, P. R. T. Schipper, E. J. Baerends. Approximation of the exchange–correlation Kohn–Sham potential with a statistical average of different orbital model potentials. *Chem. Phys. Let.*, **302** (1999) 199–207.
- [600] O. V. Gritsenko, P. R. T. Schipper, E. J. Baerends. Ensuring Proper Short-Range and Asymptotic Behavior of the Exchange–Correlation Kohn–Sham potential by Modeling with a Statistical Average of Different Orbital Model Potentials. *Int. J. Quantum Chem.*, **76** (2000) 407–419.
- [601] M. Grüning, O. V. Gritsenko, S. J. A. van Gisbergen, E. J. Baerends. On the required shape corrections to the local density and generalized gradient approximations to the Kohn–Sham potentials for molecular response calculations of (hyper-) polarizabilities and excitation energies. *J. Chem. Phys.*, **116** (2002) 9591.
- [602] E. van Lenthe, E. J. Baerends, J. G. Snijders. Relativistic regular two-component Hamiltonians. *J. Chem. Phys.*, **99** (1993) 4597.
- [603] E. van Lenthe, E. J. Baerends, J. G. Snijders. Relativistic total energy using regular approximations. *J. Chem. Phys.*, **101** (1994) 9783.
- [604] E. van Lenthe, J. G. Snijders, E. J. Baerends. The zero-order regular approximation for relativistic effects: The effect of spin-orbit coupling in closed-shell molecules. *J. Chem. Phys.*, **105** (1996) 6505–6516.
- [605] E. van Lenthe, P.E.S. Wormer, A. van der Avoird. Density functional calculations of molecular *g*-tensors in the zero order regular approximation for relativistic effects. *J. Chem. Phys.*, **107** (1997) 2488–2498.
- [606] E. van Lenthe, A. van der Avoird, P.E.S. Wormer. Density functional calculations of molecular hyperfine interactions in the zero order regular approximation for relativistic effects. *J. Chem. Phys.*, **108** (1998) 4783–4796.
- [607] J. Wang, R. M. Wolf, J. W. Caldwell, P. A. Kollman, D. A. Case. Development and Testing of a General Amber Force Field [Erratum: *J. Comp. Chem.* **26** (2004), 114]. *J. Comp. Chem.*, **25** (2004) 1157–1174.
- [608] William L. Jorgensen, Jayaraman Chandrasekhar, Jeffry D. Madura. Comparison of simple potential functions for simulating liquid water. *J. Chem. Phys.*, **79** (1983) 926–935.
- [609] Jay William Ponder. TINKER — Software Tools for Molecular Design, Version 4.2. <http://dasher.wustl.edu/tinker>, 2004.
- [610] J. W. Ponder, F. M. Richards. An efficient Newton-like method for molecular mechanics energy minimization of large molecules. *J. Comput. Chem.*, **8** (1987) 1016–1024.
- [611] P. E. Blöchl. Projector augmented-wave method. *Phys. Rev. B*, **50** (1994) 17953–17979.

-
- [612] Chengteh Lee, Weitao Yang, Robert G. Parr. Development of the Colle-Salvetti correlation-energy formula into a functional of the electron density. *Phys. Rev. B*, **37** (1988) 785–789.
- [613] G. Kresse, D. Joubert. From ultrasoft pseudopotentials to the projector augmented-wave method. *Phys. Rev. B*, **59** (1999) 1758–1775.
- [614] D. Frenkel, B. Smit. *Understanding Molecular Simulation*. Academic Press, New York, 2002.
- [615] M. P. Allen, D. J. Tildesley. *Computer Simulation of Liquids*. Oxford University Press, Oxford, 1989.
- [616] M. Swart, P.Th. van Duijnen, J.G. Snijders. A charge analysis derived from an atomic multipole expansion. *J. Comput. Chem.*, **22** (2001) 79–88.
- [617] W. van Gunsteren, H. Berendsen. *Mol. Phys.*, **34** (1977) 1311–1327.
- [618] Reinhart Ahlrichs, Michael Bär, Marco Häser, Hans Horn, Christoph Kölmel. Electronic Structure Calculations on Workstation Computers: The Program System Turbomole. *Chem. Phys. Lett.*, **162** (1989) 165–169.
- [619] R. Ahlrichs et al. <http://www.cosmologic.de/turbomole.html>.
- [620] Karin Eichkorn, Oliver Treutler, Holger Öhm, Marco Häser, Reinhart Ahlrichs. Auxiliary basis sets to approximate Coulomb potentials. *Chem. Phys. Lett.*, **240** (1995) 283–290.
- [621] Karin Eichkorn, Florian Weigend, Oliver Treutler, Reinhart Ahlrichs. Auxiliary basis sets for main row atoms and transition metals and their use to approximate Coulomb potentials. *Theor. Chem. Acc.*, **97** (1997) 119–124.
- [622] <ftp://ftp.chemie.uni-karlsruhe.de/pub/jbasen>.
- [623] P. J. Stephens, F. J. Devlin, C. F. Chabalowski, M. J. Frisch. *Ab initio* Calculation of Vibrational Adsorption and Circular Dichroism Spectra Using Density Functional Force Fields. *J. Phys. Chem.*, **98**(45) (1994) 11623–11627.
- [624] <ftp://ftp.chemie.uni-karlsruhe.de/pub/basen>.
- [625] D. Andrae, U. Häussermann, M. Dolg, H. Stoll, H. Preuss. *Theor. Chim. Acta*, **77** (1990) 123.
- [626] A. P. Scott, L. Radom. Harmonic Vibrational Frequencies: An Evaluation of Hartree–Fock, Møller–Plesset, Quadratic Configuration Interaction, Density Functional Theory, and Semiempirical Scale Factors. *J. Phys. Chem.*, **100** (1996) 16502–16513.
- [627] M. Schatz, V. Raab, S. P. Foxon, G. Brehm, S. Schneider, M. Reiher, M. Holthausen, J. Sundermeyer, S. Schindler. Combined Spectroscopic and Theoretical Evidence for a Persistent End-On Copper Superoxo Complex. *Angew. Chem. Int. Ed.*, **43** (2004) 4360–4363.

- [628] Georg Brehm, Markus Reiher, Siegfried Schneider. Calculation of the vibrational contribution to the entropy change associated with the low- to high-spin transition in $\text{Fe}(\text{phen})_2(\text{NCS})_2$ complexes. *J. Phys. Chem. A*, **106** (2002) 12024–12034.
- [629] Gijs Schaftenaar. Molden3.7 — a pre- and post processing program of molecular and electronic structure. CMBI, the Netherlands, 2001.
- [630] W. Humphrey, A. Dalke, K. Schulten. VMD — Visual Molecular Dynamics. *J. Molec. Graphics*, **14.1** (1996) 33–38.
- [631] <http://www.cscs.ch/molekel/>.
- [632] <http://jmol.sourceforge.net>.